The Hadron-Parton Bridge
From the QCD Vacuum to Partons

Edward Shuryak and Ismail Zahed

Center for Nuclear Theory, Department of Physics and Astronomy,
Stony Brook University, Stony Brook NY 11794-3800, USA

arXiv:2601.15085v1 [hep-ph] 21 Jan 2026

Abstract

Quantum Chromodynamics (QCD) exhibits complementary descriptions of hadrons: a rest-frame picture based on confinement, chiral symmetry breaking and interquark forces, and a high-energy light-front picture expressed through parton distributions (PDFs,TMDs,GPDs) and form factors. This review develops a unified framework that connects these two domains. It is based mostly on multiple studies by the authors in the past few years. Using the Instanton Liquid Model (ILM) to capture essential nonperturbative features of the QCD vacuum, we derive effective interactions for mesons, baryons, and multiquark states, construct their wave functions in hyperspherical coordinates, and boost them to the light front. The resulting light-front Hamiltonians, incorporating both perturbative and instanton-induced dynamics in the Wilsonian spirit, provide realistic nonperturbative inputs for computing PDFs, DAs, GPDs, quasi-distributions, and gravitational form factors at a well-defined low scale. The connection to perturbative QCD is then established by matching gradient-flow-renormalized operators and LF wave functions to the standard $\overline{\text{MS}}$ scheme. Perturbative DGLAP and ERBL evolution then connects these predictions to experimentally accessible regimes. This approach is applied to quarkonia, glueballs, light mesons, baryons, tetraquarks, pentaquarks, and higher multiquark hadrons, yielding consistent descriptions of both their spectra and partonic structure. Special emphasis is placed on the energy-momentum tensor and the mechanical properties of hadrons, which emerge naturally from the same dynamical ingredients. Overall, the framework demonstrates a clear continuity between hadronic spectroscopy and partonic observables, offering a coherent multiscale picture of hadron structure rooted in the underlying dynamics of QCD.

Contents

Chapter 1
Preamble

The dynamics of strongly interacting matter, as encoded in Quantum Chromodynamics (QCD), remains one of the most intricate problems in theoretical physics. Although the QCD Lagrangian is deceptively simple, the richness of its nonperturbative phenomena continues to challenge our understanding, and is primary reason for the development of new analytic and numerical tools. Confinement, spontaneous chiral symmetry breaking, the proliferation of hadronic excitations, and the emergence of constituent degrees of freedom all defy simple perturbative descriptions. At the same time, high-energy scattering experiments reveal a complementary picture of hadrons in which quarks and gluons behave as nearly free, pointlike constituents carrying longitudinal momentum fractions. Reconciling these two disparate faces of QCD - the bound-state, rest-frame description and the parton-based, infinite momentum frame formulation - remains a central pursuit in contemporary hadron physics.

The purpose of this review is to assemble and expand upon a body of multiple works done in the last few years. Their unifying objective is to build a consistent theoretical bridge between traditional hadronic spectroscopy and the modern description of hadrons in terms of parton distribution functions (PDFs), distribution amplitudes (DAs), generalized parton distributions (GPDs), and gravitational form factors. A natural language for this connection is provided by light-front quantization, which renders many aspects of partonic observables transparent but is notoriously subtle when incorporating confinement and chiral symmetry breaking. The central thrust of the approach developed here is that these two essential nonperturbative features of QCD can be imported into the light-front formalism through explicit dynamical mechanisms rooted in the topological structure of the QCD vacuum.

Key among these mechanisms is the Instanton Liquid Model (ILM), which captures crucial aspects of the QCD vacuum through a semi-classical ensemble of instantons and anti-instantons. The ILM successfully accounts for the spontaneous breaking of chiral symmetry and provides nonlocal, chirally nontrivial interactions that leave observable signatures in hadron structure. Instanton-induced interactions give rise to effective constituent quark masses, characteristic spin-dependent potentials, and highly specific Dirac structures in the effective light-front Hamiltonians for both mesons and baryons. They also yield concrete predictions for higher-twist matrix elements, quasi-parton distributions, and the spin-orbit forces necessary to understand excited baryons and multiquark configurations. One central motivation of the present work is to trace these instanton effects continuously from the rest-frame description of hadrons to the light-front representation used to define partonic observables.

The first part of the review focuses on the QCD vacuum, topological fluctuations, and their impact on confinement and chiral symmetry breaking. These developments set the stage for the second major part: recent progress in spectroscopy of mesons, baryons, and (most important) the multiquark states. The hyperspherical approximation, combined with symmetry principles from the permutation group and color-spin-flavor algebra, provides a highly efficient representation of hadronic wave functions across sectors with increasing quark number. These wave functions encode the spatial correlations, spin couplings, and kinetic

structures that underlie the observed spectra. They will later serve as the initial conditions for constructing light-front wave functions through controlled boosts and matching procedures.

The transition from hadronic spectroscopy to partonic observables proceeds through the construction of effective observables (DAs,PDFs,GPDs,TMDs etc) and light-front Hamiltonians. These Hamiltonians incorporate both perturbative one-gluon exchange and instanton-induced nonperturbative interactions. They allow one to describe mesons, baryons, and even pentaquarks on the light front in a manner directly comparable to the parton model. Once the light-front wave functions are obtained, the calculation of DAs, PDFs, TMDs, GPDs, and form factors becomes a straightforward exercise in applying their standard operator definitions. The resulting observables provide a direct link between nonperturbative hadronic inputs and experimentally measurable quantities.

A critical element of this program is the evolution of observables from low to high resolution. Starting from the nonperturbative input scale determined by instanton physics, the DGLAP and ERBL equations govern the scale dependence of PDFs and DAs. The review emphasizes that this matching between low-scale models and high-scale observables is not merely a computational necessity but a conceptual synthesis: it explicitly connects the long-distance physics of the ILM with the short-distance partonic structure probed in deep inelastic scattering and hard exclusive reactions.

Beyond the traditional partonic observables, this work also incorporates gravitational form factors and the energy-momentum tensor (EMT), which encode information about the mechanical structure of hadrons, including pressure distributions, shear forces, and contributions to the mass and spin. The light-front representation of EMT matrix elements emerges naturally from the wave functions developed here and connects the mechanical interpretation of hadron structure with the same dynamical ingredients that control spectroscopy and PDFs.

Taken together, the developments presented in this review demonstrate that the hadronic and partonic pictures are not isolated but rather deeply interwoven. By constructing explicit maps between the confining, chiral-symmetry-breaking dynamics in the rest frame and the universal operator structures of the light front, we arrive at a unified, scale-resolving portrait of QCD bound states. The goal is not only to summarize a series of earlier works but to present them as a logically coherent program, highlighting the deep conceptual continuity that runs from the QCD vacuum to the partonic structure of hadrons.

Chapter 2
Introduction

This first chapter offers a broad and non-technical overview of the themes addressed in this book. The substantive material appears in the subsequent chapters, where we describe in more detail the current state of the phenomenology and theory pertinent to our subject. More technical discussions are deferred to Appendices placed at the end of individual chapters.

2.1 The QCD vacuum, correlation functions and hadrons

The QCD vacuum is the ground state of the theory, and hadrons constitute its lowest excitations. By examining how the masses and other properties of hadrons depend on their quantum numbers, we gain insight into the types of gauge and quark fields permeating the vacuum. The gauge fields composing the QCD vacuum, fall into two broad classes: the perturbative waves, or gluons, and the nonperturbative fields with amplitudes $A_\mu \sim O(1/g)$. The former resemble photons and arise from quantizing fluctuations around the (empty) perturbative vacuum defined by the quadratic part of the action, whereas the latter encompass the various topological solitons composed of glue. There is a distinction between gluons (small amplitude waves) and *glue* in general, including topological objects. The way to separate those is e.g. *gradient flow* form of renormalization group.

Since the 1980s the primary tool for exploring the QCD vacuum has been large-scale numerical simulations on supercomputers. Wilson's lattice formulation of non-Abelian gauge fields, which preserves gauge symmetry at arbitrary lattice spacing, provides the foundation for these studies. Other symmetries, however, do not fare as well: in particular, most lattice formulations of quarks recover exact chiral symmetry only in the $m_q \to 0$ limit, which in practice requires challenging extrapolations.

In parallel with this numerical, first-principles lattice approach, a number of semiclassical models have been developed that describe the vacuum as an ensemble of solitonic configurations[1]. The earliest such objects discovered in non-Abelian gauge theories were magnetic monopoles ['t Hooft, 1974, Polyakov, 1974], followed soon after by instantons [Belavin et al., 1975]. A more recent unifying picture, particularly relevant near QCD phase transitions, involves the so-called instanton-dyons (or instanton-monopoles) [Kraan and van Baal, 1998a]. While the technical details of these configurations are best sought in specialized references[2], the next chapter provides an introductory discussion of the relevant phenomena.

A central tool uniting lattice practitioners, topologists, and researchers concerned with hadronic structure is the study of vacuum correlation functions. The simplest examples are of the form $\langle O_A(x)O_A(y)\rangle$, where O_A is an operator built from fundamental fields with definite quantum numbers A. Inserting a complete

---

[1] Similarly, people who study weather and atmospheric dynamics use both numerical hydrodynamics and qualitative language such as "hurricane A moves from X to Y, while the anticyclone remains over the midwestern states."

[2] E.g. *Nonperturbative topological phenomena in QCD and related theories*, E. Shuryak, Springer 2021.

set of intermediate states between the two operators yields the so-called QCD sum rules, which connect empirical hadronic information to vacuum correlators. For operators with a current structure, $O_A = \bar{q}\Gamma_A q$, the intermediate states include mesons carrying the corresponding quantum numbers.

The theory and phenomenology of correlation functions were reviewed in [Shuryak, 1993], which emphasized that hadronic channels naturally fall into two groups with markedly different behaviors. Vector, axial, and many other mesonic channels exhibit a smooth transition from perturbative behavior at short distances to nonperturbative dynamics at longer distances. Spin zero channels (scalar and pseudoscalar) show earlier departure from perturbative correlators. This difference can be traced to single instanton contributions that strongly affect spin-zero correlators but are absent in the other channels. Figure 2.1, displaying lattice results from the MIT group [Chu et al., 1993], illustrates this contrast and compares the findings to the instanton contribution.
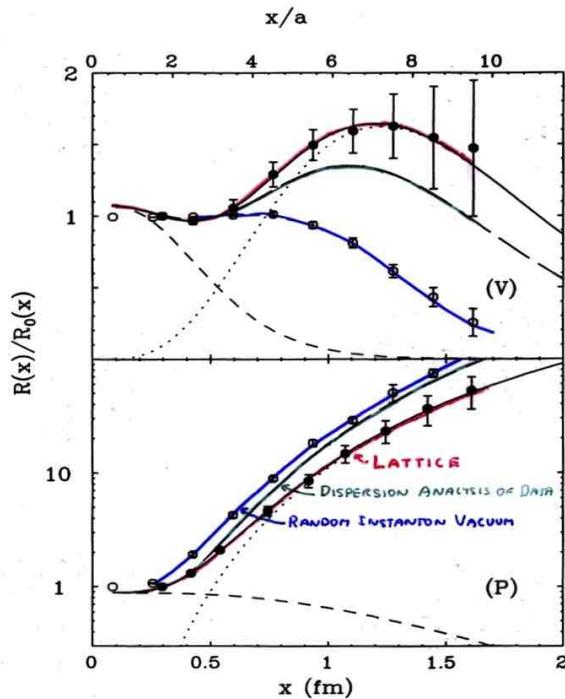
Fig. 2.1 The correlator of two local operators with the quantum numbers of the rho-meson (upper, V) and the pion (lower, P), normalized to propagation of free massless quarks. Note that the upper plot is linear and the lower logarithmic, as nonperturbative corrections in the pion channel are much larger. The dotted lines are contributions of the lowest state, the dashed ones those of non-resonance continuum.

A broader discussion of the instanton liquid and correlators within it can be found in [Schäfer and Shuryak, 1998]. Without delving into that extensive subject, Fig. 2.2 provides a qualitative picture (adapted from a talk by Negele) of how the pion and the nucleon propagate in the instanton ensemble.

Instantons (or, more precisely, the associated 't Hooft vertices) are depicted as small hills with tunnels through which quark pairs must travel.

Correlation functions reveal not merely two but three distinct types of instanton-induced effects: attraction, repulsion, and neutrality (to first order in the instanton density). For quark-based correlators, channels such as $\sigma\pi$ are attractive, while δ and η' are repulsive; many others, including vector channels such as those shown above, receive no leading-order correction. An analogous trichotomy appears even more strongly in gluonic correlators: scalar $J^P = 0^+$ channels are attractive, pseudoscalar 0^- channels are repulsive, and ten-
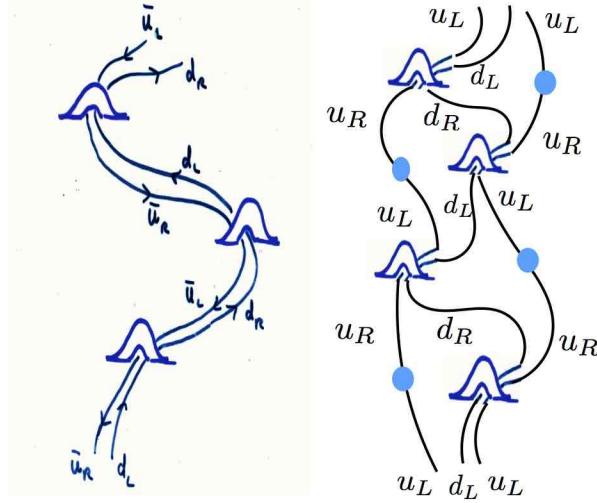
Fig. 2.2 The left sketch shows a pion propagating through the instanton vacuum; the right shows a nucleon. In the latter, the ud pair forms "good diquarks". Blue dots mark quark mass insertions where chirality flips occur.

sor 2^+ channels exhibit no first-order effect[3]. One notable prediction made in [Schäfer and Shuryak, 1995] was that the scalar glueball

has much smaller size, with the radius near

$r_{mass} \approx 0.2$ fm. After decades of hints, recent lattice works (e.g. [Abbott et al., 2025]) strongly support this prediction.

2.2 Bridging hadronic spectroscopy to partonic observables

Hadronic spectroscopy emerged in the 1950s with the discovery of numerous hadronic resonances, the excited states of mesons and baryons. The classification of these states was placed on firm footing in the 1960s through the flavor $SU(3)$ symmetry introduced by Gell-Mann and Zweig. The 1970s brought dramatic progress: asymptotic freedom and QCD was discovered [Gross and Wilczek, 1973] and [Politzer, 1973]. Then heavy-quark bound states (quarkonia) were observed experimentally. Starting around 1980s, numerical simulation on 4d lattice has evolved into a highly successful tool, with simulations now reproducing hadronic spectra and properties with impressive accuracy. One might therefore think that most conceptual developments were concluded in the late twentieth century.

Yet the field has undergone a pronounced revival, as many new hadrons have been discovered. In particularly tetraquarks and pentaquarks are in Particle Data.

Increasing attention is once again turning to six-quark (hexaquark) and twelve-quark configurations, which may play a role in the structure of the deuteron and ^{4}He.

The renewed theoretical efforts have reignited questions concerning the origin of the forces among quarks, both heavy and light, and have motivated deeper exploration of connections between these forces and the structure of the QCD vacuum. Relations between baryonic and mesonic forces have been generalized to multiquark systems, and puzzles associated with spin-dependent interactions, particularly spin-orbit couplings, have inspired new analyses. Later chapters will introduce the relevant quark symmetry group representations, methods for constructing spectra and wave functions using recent features of Mathematica, and

---

[3] This occurs because a strong instanton field nevertheless has zero stress tensor.

approaches employing multi-component wave functions. Another powerful technique borrowed from nuclear physics involves the use of hyperdistance and spherical symmetry for three-, four-, and five-body systems.

Contemporary hadron spectroscopy relies heavily on two complementary fields. The first is lattice gauge theory, which has recently reached the point where sufficiently large volumes and small quark masses allow reliable chiral and infinite-volume extrapolations. The second consists of efforts to relate spectroscopy to partonic observables, chiefly through light-front (LF) quantization.

$$Q^2 \sim \rho^{-2} \sim 0.4\,GeV^2 \qquad Q^2 \sim 1\,GeV^2 \qquad Q^2 \sim 4\,GeV^2$$
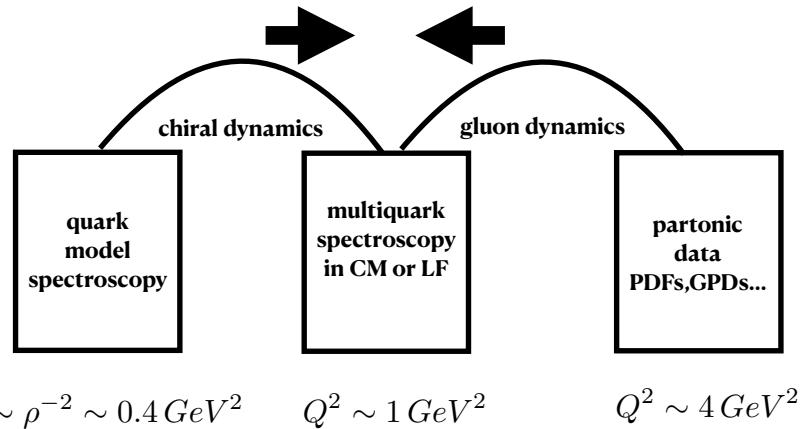
Fig. 2.3 A sketch illustrating the "bridge" to be discussed.

The project described in this review was motivated by the substantial conceptual gaps that still separate two major subfields. On one side lie models of mesons, baryons, tetraquarks, and pentaquarks formulated in terms of a fixed number of quarks. Their wave functions are eigenstates of appropriate Hamiltonians, mutually orthogonal, and built from color, flavor, and spin degrees of freedom, subject to Fermi statistics. On the other side lie partonic descriptions in which hadrons are composed of an indeterminate number of quarks, antiquarks, and gluons. These models, developed since the 1970s, rely on empirical parton distribution functions (PDFs) extracted from fits to hard-scattering data. Because PDFs include only partial information, as they are summed over all variables but one parton momentum.

Indeed, PDFs are density matrices, as as such they naturally possess nonzero entropy [Kharzeev and Levin, 2017].

Our attempt to bridge these two worlds required learning from both literatures and developing new elements as needed. These ideas are scattered through multiple papers, and the present review aims to assemble them in a coherent and pedagogical manner. We are aware that this approach is necessarily incomplete and may have omitted relevant contributions; we apologize to their authors for any such oversights. The review remains subjective and limited in scope, with the additional constraint that we deliberately chose not to involve students or postdocs except when absolutely necessary, in order to proceed quickly.

A crucial step in the program is the boosting of hadronic spectroscopy from the center-of-mass frame to the light front. This effort was pioneered by J. Vary and collaborators under what is now known as the BLFQ approach. To clarify the distinction between their program and ours, recall that solving a quantum-mechanical problem generally proceeds through three main steps: selecting the variables, choosing the Hamiltonian, and choosing the solution method. Our approach and BLFQ differ at each stage. We employ Jacobi coordinates to cleanly separate the center-of-mass motion; we adopt simple kinetic-plus-confinement Hamiltonians rather than those tailored to Brodsky's specific variable combinations such as $p_\perp^2/x$; and we emphasize that physical results must ultimately be independent of the solution method. The BLFQ basis is a technical tool that brings issues of truncation and convergence, and thus requires comparison to alternative methods. Such alternatives exist: for mesons and baryons one may directly solve the corresponding light-front Schrodinger

equations numerically or adopt various variational methods, for instance parametrized basis functions or linear combinations of Gaussians.

2.3 The multiquark hadrons and their admixtures

Even in the simplest meson systems, such as charmonia $\bar{c}c$, are not so simple. In fact we learned recently that tetraquarks $\bar{c}c\bar{q}q$ are among those and can influence the spectrum through mixing, as those may share the same quantum numbers. Over the past decade it has become increasingly clear that similar effects are ubiquitous. Baryons of the form qqq may contain admixtures of pentaquark configurations $qqqq\bar{q}$, and such components may help clarify longstanding puzzles concerning the antiquark sea.

Systems containing even larger numbers of quarks are of considerable interest as well. On the theoretical side they pose obvious challenges, and on the phenomenological side they may appear in di-nucleon reactions, which seem to hint at hexaquark (q^6) states; even four-nucleon systems may contain significant twelve quarks q^{12} admixtures.

Our discussion of multiquark hadrons rests on three broad ideas. First, we fix the center-of-mass by working in Jacobi coordinates. Second, when the relevant quarks are of equal mass, we invoke spherical symmetry, or the hyperdistance approximation. Third, we enforce Fermi statistics on the orbital, color, spin, and flavor degrees of freedom through the appropriate permutation-group representations of S_n. Although these concepts will be introduced pedagogically later, it is useful to recall their origins here. Jacobi introduced his coordinates in the mid-1800s for classical few-body problems. The hyperdistance approximation was developed in nuclear physics in the 1960s, originally applied to light nuclei such as tritium and ^{4}He. The permutation-group methods we use are of more recent vintage, developed in [Miesch and Shuryak, 2024].

2.4 The parton model

The formulation and experimental observation of Bjorken scaling in deep-inelastic electron-nucleon scattering (DIS) led Feynman to propose the parton model [Feynman, 1969]. Its conceptual basis rests on three ideas: hadrons at high energies consist of many partons; in the infinite-momentum frame these partons are effectively frozen by time dilation and behave as if free from interactions; and photon-hadron inelastic scattering is predominantly incoherent. The first concrete application of this perspective to inelastic electron-proton scattering at high energies was made by Bjorken and Paschos [Bjorken and Paschos, 1969]. Denoting by q^μ the space-like electron momentum transfer and by ν the virtual-photon energy in the nucleon rest frame, they found that inclusive electron-hadron cross sections depend only on the Bjorken variable $x_B = Q^2/(2m_N\nu)$ in the limit of large $Q^2 = -q^2$.

This naive picture of hadrons at high energies predates QCD, whose formulation by [Fritzsch et al., 1973] provided the underlying quantum field theory. Remarkably, asymptotic freedom of QCD [Gross and Wilczek, 1973, Politzer, 1973] soon gave theoretical support to the parton model. The perturbative description of scaling violation, based on anomalous dimensions and the perturbative evolution of parton distribution functions, emerges from logarithmically enhanced collinear gluon emissions and leads to the DGLAP evolution equations in the resolution scale Q^2. A related but distinct evolution in x is described by the BFKL equation.

Feynman's parton model is rooted in the infinite-momentum frame, where a hadron with large P^z is viewed as a collection of N partons (quarks and gluons) with momenta

$$p_i = x_i P^z + k_{\perp i} \qquad \sum_{i=1}^{N} x_i = 1, \qquad \sum_{i=1}^{N} k_{\perp i} = 0 \tag{2.1}$$

and longitudinal momentum fractions bounded by $0 \leq x_i \leq 1$, since all partons propagate along the hadron's direction of motion. Backward-moving partons are suppressed in the infinite-momentum frame, as first emphasized by [Weinberg, 1966]. The probability distribution for the longitudinal momentum fraction, or parton distribution function (PDF), became a central object of high-energy phenomenology. Global fits to experimental data, such as those produced by the CTEQ collaboration [Hou et al., 2021a], continue to refine these distributions.

The relation between Weinberg's time-ordered perturbation theory in the infinite-momentum frame [Weinberg, 1966] and Dirac's front-form quantization [Dirac, 1949] was first exploited by [Chang and Ma, 1969] in their analysis of QED in the large-momentum limit . The front-form formulation identifies time and space with the light-cone coordinates $x^\pm = (x^0 \pm x^3)/\sqrt{2}$, with the corresponding Hamiltonian and momentum given by $p^\mp = (p^0 \mp p^3)/\sqrt{2}$. For a free massive particle the front-form Hamiltonian is

$$p^- = \frac{p^0 - p^z}{\sqrt{2}} = \frac{p_\perp^2 + m^2}{2p^+} \tag{2.2}$$

which avoids sign ambiguities and eliminates the need for antiparticles, but introduces an infrared singularity at $p^+ = 0$. The Hamiltonian is non-local in the conjugate light-cone coordinate x^-, endowing the initial quantization surface with an infinite correlation length; this raises questions about the consistency of the front form in perturbative field theory.

Despite these challenges, the front form provides a natural pathway to the parton model. Consider the quantization of a free Dirac field by introducing the light-cone gamma matrices

$$\gamma^\pm = \frac{\gamma^0 + \gamma^z}{\sqrt{2}} \qquad \gamma^{+2} = \gamma^{-2} = 0 \qquad \mathbb{P}_\pm = \frac{1}{2}\gamma^\mp \gamma^\pm \qquad \mathbb{P}_+ + \mathbb{P}_- = 1 \tag{2.3}$$

and decomposing the Dirac field into $\psi = \psi_+ + \psi_- = \mathbb{P}_+\psi + \mathbb{P}_-\psi$. The component ψ_- is a constrained variable, as follows from

$$\mathbb{P}_+(i\slashed{D} - m)\psi = iD^+\gamma^-\psi_- + (i\slashed{D}^\perp - m)\psi_+ = 0. \tag{2.4}$$

Since $D^+ = \partial^+ + igA^+$ does not have derivative over time ∂^- , ψ_- can be eliminated:

$$\psi_- = -\frac{(i\slashed{D}^\perp - m)\psi_+}{iD^+\gamma^-} = -\frac{\gamma^+}{iD^+}(i\slashed{D}^\perp - m)\psi_+ \tag{2.5}$$

up to infrared poles at $D^+ = 0$. In light-cone gauge $A^+ = 0$, the field A^- is also constrained and can be removed.

2.5 The *bridge* strategy and the resolution scales

Before constructing a bridge, one must understand the shores it aims to connect. We therefore begin by briefly reviewing the theoretical situations at the two extremes. Since the 1970s it has been clear that hard processes at large momentum transfers, $Q^2 \gg 1\,\mathrm{GeV}^2$, can be described in terms of nearly free partons: gluons, quarks, and antiquarks. The probabilities to find these partons in a hadron are encoded in the PDFs $q(x, Q^2)$. At sufficiently high resolution the pointlike constituents emit each other according to splitting functions derived directly from the QCD Lagrangian, and PDFs defined at different Q^2 are connected by perturbative DGLAP evolution. The combination of perturbative QCD and global fits to hard-scattering data has grown into a vast program; see, for example, CTEQ's recent review [Hou et al., 2021b].
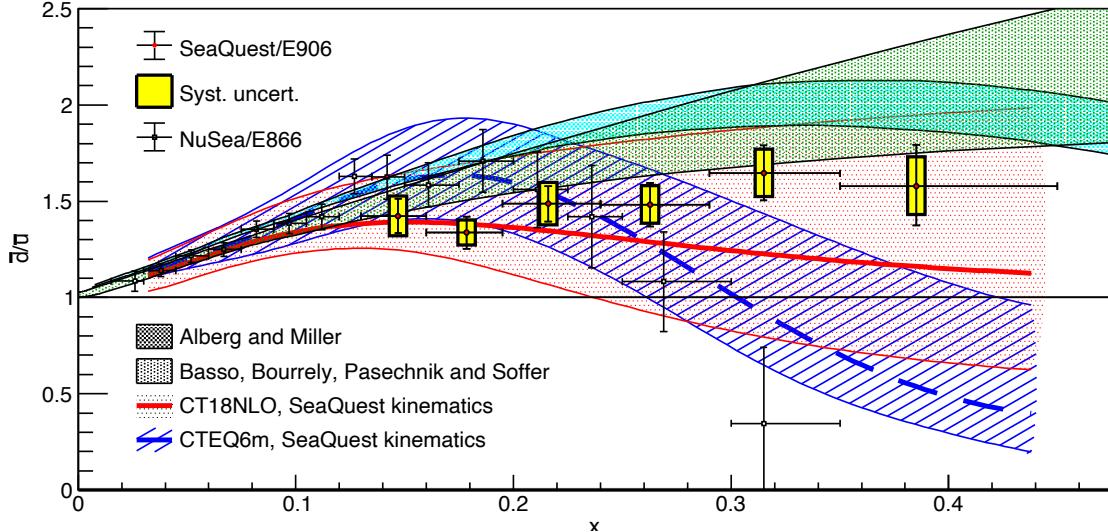
Fig. 2.4 Flavor asymmetry of the antiquark sea as the ratio $\bar{d}/\bar{u}$ versus momentum fraction x, from [Dove et al., 2021].

While the partonic description is a robust endpoint of the bridge, it does rely on certain approximations. In particular, the incoherence assumption underlying DGLAP evolution renders the equations probabilistic kinetic equations. As emphasized by [Kharzeev and Levin, 2017], this assumption leads to an entanglement entropy. Yet hadrons are pure quantum states, and a fully consistent description requires their complete light-front wave functions, without such entanglement and entropy.

Evolving PDFs downward in Q^2 reveals a scale at which gluon emission effectively ceases. The lightest glueballs have masses around $M_{\mathrm{glueball}} \sim 2\,\mathrm{GeV}$, suggesting a gluon effective mass of order $M_{\mathrm{eff}}(\mathrm{gluon}) \sim 1\,\mathrm{GeV}$ and placing the lower threshold of perturbative evolution at $Q^2 \sim M_{\mathrm{eff}}^2$.

At lower Q^2 the dynamics are governed not by quarks and gluons but by the phenomena of chiral symmetry breaking, which foreground the Nambu-Goldstone pions and the scalar condensate σ. In this domain, the QCD Lagrangian is replaced by a chiral effective Lagrangian with an upper cutoff scale associated with the original NJL model, $\Lambda_\chi \sim 1\,\mathrm{GeV}$. The mechanism was later related to instantons [Shuryak, 1982g], with the cutoff scale tied to the typical instanton size $\rho \sim 1/3\,\mathrm{fm}$.

Thus we are led to a natural strategy: the two arcs of the bridge, the chiral and perturbative domains, might meet smoothly at common $1\,\mathrm{GeV}$ scale. In this section we examine whether PDFs computed from both sides indeed join at that point. Of course many observables require more refined approaches than an abrupt transition between effective theories. We note, for instance, various efforts to combine perturbative and nonperturbative contributions, including our own analyses of meson form factors [Shuryak and Zahed, 2021g] and spin-dependent forces [Shuryak and Zahed, 2021a].

It is not a place to discuss the whole set of well known standard PDFs, so let us jump now to one of them we will be discussing most: the PDFs of the antiquark "sea". Before addressing the data at Fig.2.4, consider processes which may add additional $\bar{q}q$ pair to a nucleon. Pairs which arise through gluon splitting would have $\bar{u}u$ and $\bar{d}d$ in equal amounts, since gluons are "flavor blind". By contrast, the instanton-induced 't Hooft four-fermion interaction generates sea quarks in a maximally flavor-antisymmetric pattern due to the Pauli principle governing instanton zero modes. The predicted processes are $u \to u\bar{d}d$ and $d \to d\bar{u}u$, but not $u \to u\bar{u}u$. Because the proton contains two valence u quarks and one valence d quark, the simplest first-order estimate based on instanton vertex predicts the ratio

$$\frac{\bar{d}}{\bar{u}} \to 2, \tag{2.6}$$

while for the Δ^{++}, which has valence content uuu, the sea should consist solely of $\bar{d}$ quarks, with no $\bar{u}$ component at all. Last but not least, one may think of virtual process $N \to N + \pi$ creating a "pion cloud" around a nucleon. Here one may have several flavor options.

The experimental data for the ratio $\bar{d}/\bar{u}$ PDFs are shown in Fig.2.4. The data points indicate this ratio to be $\sim 3/2$, somewhat below pion-based predictions (dark and light gray regions, from authors mentions). It is just in between one and two (as instanton vertices would predict.) The flavor asymmetry of the sea is thus a powerful diagnostic for disentangling the contributions of chiral dynamics (step 2) and perturbative QCD (step 3) to the pentaquark sector of the light-front wave function of the nucleon. Only the former can generate full coherent description, the LF wave functions, from which PDFs and much more would consistently follow.

2.6 Overview of Related Approaches to Hadron Structure

The problem of connecting hadronic spectroscopy at low energies with partonic descriptions at high resolution has been a central theme of strong-interaction physics since the inception of QCD. Over the past several decades, a variety of theoretical frameworks have been developed to address different aspects of this "hadron-parton duality", often emphasizing complementary limits, degrees of freedom, and organizing principles.

Historically, early insights were provided by current algebra and the parton model, culminating in the operator product expansion and perturbative QCD evolution equations for deep inelastic scattering [Wilson, 1969, Altarelli and Parisi, 1977, Dokshitzer, 1977]. At the same time, constituent quark models and potential models successfully accounted for large portions of the hadron spectrum [Isgur and Karl, 1978, Godfrey and Isgur, 1985], albeit without a direct link to partonic observables.

More recent developments have focused on building explicit bridges between these descriptions. These include lattice QCD calculations of hadron structure, continuum functional methods, holographic approaches inspired by gauge/gravity duality, and Hamiltonian light-front formulations. The framework developed in this work belongs to this broader effort, sharing goals with these approaches while differing in methodology and underlying assumptions.

In the following, we briefly summarize the main complementary lines of research, highlighting commonality and distinction. For completeness, we will refer to some reviews and their detailed references, where parts of these complementary lines of research are developed.

2.6.1 Nonperturbative QCD Frameworks

Lattice QCD

Lattice QCD provides a systematically improvable, first-principles framework for studying the nonperturbative regime of QCD by formulating the theory on an Euclidean spacetime lattice. By discretizing spacetime and evaluating the QCD path integral numerically, lattice methods enable controlled calculations of hadron masses, decay constants, and matrix elements of local operators, with quantifiable uncertainties arising from finite lattice spacing, finite volume, and unphysical quark masses [Aoki, 2020].

Over the past decade, lattice simulations have reached a level of maturity where precision calculations of hadron spectroscopy and low-energy structure observables are routinely performed at or near the physical pion mass. In addition to static quantities, lattice QCD has provided essential input for effective field theories and phenomenological models, helping to constrain low-energy constants and validate assumptions about confinement and chiral dynamics.

A major conceptual challenge for lattice QCD has been the extraction of light-cone dominated observables, such as parton distribution functions, which are intrinsically Minkowskian and defined through real-time

correlations. Recent methodological advances have addressed this limitation by relating Euclidean correlation functions to light-cone observables through factorization and matching procedures. Prominent among these is Large-Momentum Effective Theory (LaMET), which enables the computation of quasi-parton distribution functions (quasi-PDFs) from hadrons boosted to large spatial momenta [Ji, 2013]. Closely related approaches include pseudo-PDFs and lattice cross-section methods, which exploit short-distance operator expansions [Radyushkin, 2017, Lin, 2018].

These developments have opened a new avenue for direct comparison between lattice QCD, phenomenological extractions, and model-based calculations at low renormalization scales. At the same time, they highlight important practical and conceptual limitations. Large hadron momenta amplify discretization effects and statistical noise, while the interpretation of quasi-distributions requires perturbative matching and careful control of higher-twist corrections.

From a broader perspective, lattice QCD excels at providing numerically reliable results for well-defined observables, but offers limited transparency regarding the underlying dynamical mechanisms responsible for confinement and dynamical chiral symmetry breaking. In particular, the effective degrees of freedom that emerge at low energies are encoded implicitly in the gauge-field ensembles rather than appearing explicitly in a Hamiltonian description.

The approach pursued in the present work is complementary in spirit. Rather than sampling the full gauge-field path integral numerically, it emphasizes explicit nonperturbative vacuum structures and their effects on hadronic wave functions. This allows for a more direct connection between confinement dynamics, chiral effective interactions, and the structure of light-front wave functions at a defined low scale, while retaining compatibility with lattice results through matching and evolution.

Dyson-Schwinger and Bethe-Salpeter Approaches

Continuum functional approaches based on Dyson-Schwinger equations (DSEs) and Bethe-Salpeter equations (BSEs) provide a nonperturbative framework for QCD that retains full Poincaré covariance and is formulated directly in Minkowski or Euclidean momentum space. In this approach, hadrons emerge as bound states of dressed quarks and gluons whose propagators and interaction vertices are obtained from an infinite tower of coupled integral equations [Roberts and Williams, 1994].

A key achievement of the DSE/BSE program is its unified description of dynamical chiral symmetry breaking and hadron structure. The momentum-dependent quark mass function generated by the quark DSE encodes dynamical mass generation, linking the infrared behavior of QCD to the emergence of constituent-like degrees of freedom at low energies. When combined with Bethe-Salpeter equations for mesons and covariant Faddeev equations for baryons, this framework yields quantitative descriptions of hadron spectra, decay constants, and electromagnetic form factors [Maris and Roberts, 2003, Eichmann, 2016].

Beyond spectroscopy, DSE/BSE methods have been extended to partonic observables, including parton distribution amplitudes, generalized parton distributions, and PDFs. These quantities are obtained by projecting covariant bound-state amplitudes onto light-front kinematics, thereby establishing a connection between Euclidean correlation functions and light-cone physics [Chang et al., 2014, Gao et al., 2017]. Such studies have provided valuable insight into the role of dynamical chiral symmetry breaking in shaping valence-quark distributions and distribution amplitudes.

Despite these successes, the DSE/BSE framework relies on truncation schemes whose systematic improvement is challenging. While symmetry-preserving truncations exist and are well understood in certain channels, the treatment of multi-parton correlations and higher Fock components remains indirect. Moreover, confinement is implemented through analytic properties of propagators rather than through an explicit Hamiltonian or potential. In addition, the spontaneous breaking of chiral in this approach has yet to be related to the topological character of the gauge fields, a key insight from lattice QCD.

Conceptually, the DSE/BSE program shares important common ground with the present work, particularly in its emphasis on dynamical mass generation and the central role of nonperturbative quark interactions. However, it differs in its treatment by ignoring the central role played by the QCD vacuum, and the importance played by its topological constituents in setting up the emergent effective interactions. In addition, the formulation lacks an explicit Hamiltonian formulation. The present approach instead constructs effective light-front Hamiltonians with explicit interactions that encode nonperturbative vacuum physics directly, facilitating a transparent connection between bound-state dynamics, Fock-space structure, and partonic observables.

Instantons and Topological Models

As we noted earlier, topological gauge-field configurations play a fundamental role in the nonperturbative dynamics of QCD. Among these, instantons-finite-action solutions of the classical Yang-Mills equations in Euclidean spacetime-have long been recognized as essential for understanding anomalous symmetries and chiral dynamics ['t Hooft, 1976b]. Instantons generate effective multi-fermion interactions that explicitly break the $U(1)_A$ symmetry and provide a microscopic mechanism for strong correlations among light quarks.

Building on these insights, instanton-based models have been developed to describe a wide range of hadronic phenomena. In the Instanton Liquid Model, the QCD vacuum is approximated as an ensemble of instantons and anti-instantons with a characteristic density and size distribution [Shuryak, 1982a, Diakonov et al., 1997, Schäfer and Shuryak, 1998, Nowak et al., 1996]. This picture naturally accounts for dynamical chiral symmetry breaking through the delocalization of quark zero modes, leading to the emergence of a momentum-dependent constituent quark mass and a nontrivial quark condensate.

Instanton models have been successfully applied to hadron spectroscopy, two-point and three-point correlation functions, and static properties such as magnetic moments and axial charges. Extensions of these ideas have also been used to study parton distribution functions and transverse-momentum dependent distributions, particularly at low normalization scales where nonperturbative effects dominate [Kock et al., 2020].

While instantons provide a compelling mechanism for chiral symmetry breaking, their role in confinement remains less direct. Dilute instanton ensembles do not generate a linearly rising potential, although dense instanton ensembles generate a considerable part of the confining and spin forces [Shuryak and Zahed, 2021a].

The present work builds explicitly on the Instanton Liquid Model as a starting point for constructing hadronic wave functions. Its distinctive feature is the use of these wave functions as input for a light-front Hamiltonian formulation, thereby translating topological vacuum structure into partonic degrees of freedom. In this way, instanton-induced dynamics are not confined to static or Euclidean observables, but are directly linked to light-front wave functions, Fock-space structure, and parton distributions at a well-defined low scale.

2.6.2 Light-Front Hamiltonian Approaches

Light-front (LF) quantization offers a Hamiltonian formulation of relativistic quantum field theory in which boosts along the longitudinal direction are kinematical and hadronic states admit a Fock-space expansion in terms of partonic degrees of freedom. This feature makes LF dynamics particularly well suited for describing parton distribution functions, generalized parton distributions, and distribution amplitudes, while simultaneously retaining a connection to bound-state spectroscopy.

Early applications of light-front dynamics to QCD emphasized conceptual foundations and formal developments, including the structure of LF wave functions, vacuum triviality, and factorization [Dirac, 1949, Brodsky et al., 1998a]. These studies established the basic language used in modern partonic analyses, but

left open the problem of constructing realistic, renormalized LF Hamiltonians capable of describing both low-energy spectroscopy and high-energy observables. More importantly, their relationship to the QCD vacuum as revealed by lattice QCD remains elusive.

Effective Light-Front Potentials and Semiclassical Models

A major line of development has focused on constructing effective LF Hamiltonians using phenomenological or semiclassical inputs. Light-front holography, inspired by gauge/gravity duality, provides an effective Schrodinger equation in a transverse variable that reproduces Regge trajectories and captures aspects of confinement [Brodsky and de Teramond, 2006, Brodsky, 2015].

These models yield analytic or semi-analytic LF wave functions that have been widely used to compute meson and baryon form factors, PDFs, and distribution amplitudes. While highly economical and successful phenomenologically, such approaches rely on guessed effective potentials whose relation to the microscopic QCD vacuum remains indirect.

In contrast, the present framework constructs LF Hamiltonians by explicitly boosting hadronic wave functions derived from nonperturbative vacuum dynamics, thereby preserving a direct link between confinement, chiral symmetry breaking, and partonic observables at a defined low scale.

Discretized Light-Cone Quantization

Discretized light-cone quantization (DLCQ) represents one of the earliest systematic numerical approaches to LF Hamiltonian field theory [Pauli and Brodsky, 1985]. By imposing periodic boundary conditions in the longitudinal direction, DLCQ renders the LF momentum spectrum discrete and allows for numerical diagonalization of truncated Hamiltonians.

DLCQ has been applied successfully in lower-dimensional gauge theories and as a testing ground for nonperturbative renormalization ideas. However, its extension to realistic (3+1)-dimensional QCD is hindered by severe truncation effects and the complexity of renormalization in a discrete momentum basis.

Basis Light-Front Quantization (BLFQ)

Basis Light-Front Quantization (BLFQ) represents a significant evolution of the LF Hamiltonian program [Vary, 2010, Li, 2015]. Instead of discretizing momentum space directly, BLFQ expands LF wave functions in a particular basis, typically combining longitudinal momentum modes with two-dimensional harmonic oscillator functions in the transverse plane.

This choice is motivated both by mathematical convenience and by its close connection to confinement-inspired dynamics. The resulting Hamiltonian matrix can be systematically improved by enlarging the basis, enabling controlled studies of convergence and truncation effects.

BLFQ has been applied to a wide range of systems, including positronium, heavy quarkonia, light mesons, and baryons [Zhao, 2014, Wiecki, 2015, Li, 2017]. Extensions to time-dependent BLFQ have further enabled studies of scattering and real-time evolution in strong external fields [Zhao, 2013].

Renormalization and Fock-Space Truncation

A central challenge in all LF Hamiltonian approaches is renormalization in the presence of Fock-space truncation. Several strategies have been developed, including sector-dependent renormalization, similarity renormalization group methods, and Hamiltonian flow equations [Perry and Wilson, 1993, Głazek and Wilson, 1993].

In BLFQ, renormalization is typically implemented through effective interactions matched to known physical observables or perturbative limits. While systematic and increasingly sophisticated, these procedures highlight the tension between maintaining a manageable Fock space and preserving the full dynamics of QCD.

The approach developed in this book addresses this issue from a complementary angle: rather than relying solely on basis truncation, it incorporates nonperturbative vacuum effects into the effective LF Hamiltonian itself. This reduces the burden placed on higher Fock components at the matching scale and clarifies the division of roles between nonperturbative input and perturbative evolution.

Parton Distributions from Light-Front Wave Functions

A major strength of LF Hamiltonian methods lies in the direct relation between LF wave functions and partonic observables. PDFs, GPDs, and transverse-momentum dependent distributions can be expressed as overlaps of LF wave functions, making the connection between hadron structure and parton dynamics explicit [Diehl, 2003].

BLFQ and related approaches have produced explicit predictions for PDFs and distribution amplitudes, particularly for heavy quarkonia and mesons [Li, 2016]. These results provide valuable benchmarks for lattice QCD and phenomenological fits, especially in kinematic regions where experimental constraints are limited.

In the present framework, LF wave functions are not postulated or fitted but derived by boosting rest-frame wave functions obtained from a dynamical model of the QCD vacuum. This ensures internal consistency between spectroscopy, form factors, and partonic observables. Indeed, the results to be developed in the present work show that the partonic distribution functions at low resolution, are profiling of the emergent constituents from the QCD vacuum, e.g. quark zero modes and constitutive gluons as they emerge from the underlying instanton and anti-instanton dynamics.

Reviews of Light-Cone and Light-Front QCD

A more comprehensive presentation of light-cone and light-front QCD and their applications to hadronic structure, can be found in a number of classic reviews of which we now cite a few and refer to their detailed references for a more complete list of references.

An early and influential synthesis of light-cone quantization and its application to relativistic bound states is provided by Brodsky, Pauli, and Pinsky [Brodsky et al., 1998a]. This review established the conceptual foundations of light-front wave functions, vacuum structure, and factorization, and remains a standard reference.

A complementary pedagogical treatment emphasizing both formal aspects and applications to parton physics is given by Heinzl [Heinzl, 2001], which clarifies the role of constrained fields, zero modes, and renormalization in light-front dynamics.

The extensive review by Carbonell et al. [Carbonell, 1998] focuses on relativistic few-body systems and bound-state equations on the light front, providing a detailed discussion of practical implementations and numerical methods.

For generalized parton distributions and their representation in terms of light-front wave-function overlaps, the reviews by Diehl [Diehl, 2003] and by Belitski and Radyushkin [Belitsky and Radyushkin, 2005] offer a comprehensive and widely used references.

Finally, Brodsky et al. [Brodsky, 2015] review modern developments in light-front dynamics, including holographic approaches and connections to conformal symmetry, illustrating how semiclassical light-front methods can be postulated to organize hadron spectroscopy and structure.

Relation to the Present Work

The developments summarized above underline the breadth and diversity of light-front Hamiltonian approaches to QCD. Basis-based methods such as BLFQ offer systematic numerical control, while semiclassical and holographic models provide analytic insight and phenomenological efficiency.

The framework developed in this book is aligned with these efforts in its use of LF dynamics and Hamiltonian methods, but differs fundamentally in its starting point. By anchoring the LF description in a nonperturbative model of the QCD vacuum and hadronic wave functions, it seeks to unify spectroscopy and parton physics within a single dynamical picture, rather than treating them as separate regimes connected only by evolution equations.

Last but not least is different choice of coordinates for Hamiltonian quantization. We always use Jacobi coordinates, in CM spectroscopy and on the LF, eliminating spurious problem of center-of-mass motion.

2.7 Light-front criticality and Wilsonian resolution.

Before closing this section, we would like to stress a key conceptual point that deserves explicit emphasis in reviewing light-front (LF) Hamiltonian approaches, and that is the infrared (IR) nature of LF QCD itself. Canonical LF formulations correspond to quantizing QCD directly at a critical point, where the LF vacuum is trivial but long-distance dynamics are encoded in constrained fields and zero modes. As a consequence, LF QCD at infinite resolution is intrinsically afflicted by severe IR singularities. A canonical example is the appearance of inverse longitudinal derivatives in constrained fields, such as $\psi_- \sim 1/D^-$, as well as instantaneous gluon interactions proportional to $1/(k^+)^2$, which diverge in the $k^+ \to 0$ limit. These singularities are not accidental; they reflect the fact that the LF formulation, taken literally, has no intrinsic IR scale and therefore sits precisely at a critical point.

Many LF Hamiltonian approaches discussed in Sec. 2.6.2 attempt to manage this problem through explicit regulators, zero-mode subtractions, or basis truncations. While practically useful, such procedures obscure the separation between genuine nonperturbative physics and artifacts of the LF critical formulation. The approach developed in this work is conceptually different and explicitly Wilsonian. As detailed in Secs. 14.4 and 14.5, the LF theory is constructed at a low but finite resolution scale, where the relevant gauge fields are smooth and infrared-safe. This is achieved by defining effective LF degrees of freedom through gauge-covariant gradient flow, which suppresses short-distance fluctuations and introduces a natural separation of scales. At this stage, the LF Hamiltonian and wave functions are well-defined and free of spurious LF IR divergences.

The connection to perturbative QCD is then established by matching gradient-flow-renormalized operators and LF wave functions to the $\overline{\text{MS}}$ scheme at a fixed scale μ_0, followed by perturbative evolution, as discussed in Secs. 14.5 and 14.7. In this way, the LF formulation is treated as an effective theory at low resolution rather than as a fundamental critical description, allowing for a controlled bridge between hadronic spectroscopy and partonic observables.

We emphasize that the Wilsonian viewpoint advocated here does not preclude practical light-front Hamiltonian constructions. Rather, it implies that infrared-sensitive sectors associated with longitudinal zero modes or light-cone criticality must be treated nonperturbatively and absorbed into effective interactions. In concrete implementations, this may take the form of resumming classes of light-front-enhanced diagrams, identified by power counting, into dressed vertices or operators that encode the relevant vacuum structure, as detailed for example in section 20.B.

Later sections provide explicit examples of how such reorganizations arise in practice. Although the resulting Hamiltonians are written in light-front variables, they should be understood as effective descriptions in which the dominant infrared physics has already been accounted for, consistent with the Wilsonian philosophy outlined above.

2.8 Comparison to the lattice LaMET approach

It is instructive to parallel
our strategy
with the Large Momentum Effective Theory (LaMET) approach. In LaMET, partonic physics is accessed through equal-time correlation functions evaluated at large but finite hadron momentum. Crucially, these calculations are performed away from the LF critical point: the finite hadron momentum provides an intrinsic IR regulator, and the theory does not suffer from the singular $k^+ \to 0$ structure characteristic of canonical LF quantization. The matching to light-cone PDFs is achieved only after taking the large-momentum limit through a systematic factorization and perturbative matching procedure.

From this perspective, LaMET and the present LF formulation share an important conceptual similarity. In both cases, one deliberately avoids formulating QCD directly at the critical LF point. Instead, one works with an effective theory defined at a finite momentum in LaMET, finite gradient flow scale in our approach are connecting to the light cone theory through perturbative matching and evolution. This shared Wilsonian logic clarifies why both approaches yield well defined nonperturbative inputs for parton physics, while bypassing the intrinsic IR pathologies of LF QCD formulated at infinite resolution.

The conceptual parallel between the present formulation and the LaMET can be sharpened by identifying explicitly how each framework avoids the light-front (LF) critical point. In canonical LF quantization, the criticality arises from enforcing exact light-like kinematics at the operator level, which removes any intrinsic longitudinal scale and leads to singular structures such as $1/D^-$ and $1/(k^+)^2$. Both LaMET and the present approach bypass this problem by introducing a finite control parameter that measures the distance from the LF critical point and by restoring the light-cone limit only through controlled perturbative matching.

In LaMET, the regulating parameter is the hadron momentum P^z. Equal-time correlation functions are computed at finite but large P^z, where the theory is infrared safe and free of LF zero-mode singularities. The limit $P^z \to \infty$ is never taken at the nonperturbative level; instead, quasi-distributions are factorized and matched to light-cone PDFs in the $\overline{\text{MS}}$ scheme through an expansion in powers of $1/P^z$. In this sense, P^z plays the role of a Wilsonian control scale that keeps the theory away from the LF critical surface.[4]

In the present formulation, the analogous control parameter is the gradient-flow scale $\sqrt{t}$, or equivalently the matching scale $\mu_0 \sim 1/\sqrt{t}$, as developed in Secs. 14.5-14.7. The LF Hamiltonian and wave functions are constructed at finite resolution using flowed gauge fields, for which constrained LF components are smooth and infrared safe. The LF critical point is not imposed as a starting point but is approached only indirectly, through perturbative matching and renormalization-group evolution.

This parallel may be summarized schematically as

---

[4] As in any Wilsonian construction, power-suppressed corrections in $1/P^z$ encode genuine long-distance physics and may exhibit ambiguities analogous to renormalons, which are systematically absorbed into higher-twist matrix elements rather than signaling a breakdown of the formalism.

$$\text{LaMET:} \qquad P^z < \infty \;\; \implies \;\; \text{matching} \;\; \implies \;\; P^z \to \infty,$$

$$\text{This work:} \qquad \sqrt{t} > 0 \;\; \implies \;\; \text{matching} \;\; \implies \;\; \sqrt{t} \to 0.$$

In both cases, it is essential that the limits $P^z \to \infty$ and $\sqrt{t} \to 0$ are *never* taken at the nonperturbative level. The light-cone theory is instead viewed as an emergent description reached only after perturbative matching. This shared Wilsonian logic explains why both LaMET and the present LF formulation yield controlled nonperturbative inputs for parton physics, while bypassing the intrinsic infrared pathologies of canonical LF QCD formulated directly at the critical point.

2.9 Perspective and Scope

The approach developed in this book should be viewed as complementary to the frameworks summarized above. Its distinctive feature is the explicit dynamical continuity it establishes between the QCD vacuum, hadronic bound states, and partonic observables at a common low matching scale. By emphasizing mechanisms rather than parametrizations, it aims to provide both quantitative predictions and qualitative insight into the multiscale structure of hadrons.

Part I
The QCD vacuum

Chapter 3
The QCD vacuum, chiral symmetries and confinement

3.1 Modern theory of tunneling in quantum mechanics

One of the fundamental differences between classical and quantum mechanics (QM) is that QM allows for the phenomenon of *tunneling* between regions where classical motion is permitted, separated by *potential barriers*. If the particle energy is smaller than the potential $E < V(x)$ the kinetic energy is negative,

$$K = E - V(x) < 0,$$

and therefore the momentum becomes imaginary. Motion under the barrier can therefore be described using "Euclidean" (imaginary) time $\tau = it$.

In the language of path integrals, tunneling corresponds to paths defined on the complex time plane, consisting of segments running along real and imaginary directions, separated by specific "turning points."

Perhaps the most spectacular example of tunneling is the α *decay of heavy nuclei* (Gamow 1928), in which an $\alpha = p^2 n^2$ cluster tunnels from the interior of the nucleus to the outside world through the Coulomb barrier. We will not discuss this celebrated example here; instead, we illustrate the main ideas using a simpler setting, the *double-well potential* (DWP).

We consider the nonrelativistic Hamiltonian with the potential

$$V_{DWP} = \lambda(x^2 - f^2)^2, \tag{3.1}$$

which has two minima at $x = \pm f$, often referred to as "classical vacua." Ignoring tunneling, one would expect the motion near each minimum to be independent, leading to a doubly degenerate spectrum. In particular, one expects two ground states with energy

$$E = \omega/2 = f\sqrt{2\lambda}.$$

To make contact with QCD-inspired notation, we express all dimensional quantities in terms of the frequency ω and a dimensionless coupling

$$\alpha = \lambda/\omega^3.$$

For example, the height of the barrier is

$$V_{max} = V(x=0) = \omega\frac{\omega^3}{64\lambda} = \omega\frac{1}{64\alpha}. \tag{3.2}$$

We define the "weak coupling" regime as $\alpha \ll 1$, in which the barrier is very high, $V_{max} \gg \omega$. In this regime, one can develop a *perturbative theory* and compute the vacuum energy as a series

$$E_{pert} = \frac{\omega}{2}\Big[1 + \sum_n C_n \alpha^n\Big], \tag{3.3}$$

using Feynman diagrams.[1]

The double degeneracy of the vacuum (and of other states) is lifted by tunneling. The true eigenstates are symmetric and antisymmetric combinations of the classical vacua, with energies

$$E_{\pm} = E_{pert}\Big[1 \mp \sqrt{\frac{2}{\pi\alpha}}\,\exp\Big(-\frac{1}{12\alpha}\Big) + \dots\Big], \tag{3.4}$$

separated by an exponentially small tunneling contribution.

Using Euclidean time τ, one introduces the Euclidean action[2]

$$S_E = \int d\tau\Big[\frac{1}{2}\dot{x}^2 + V(x)\Big]. \tag{3.5}$$

Tunneling amplitudes are determined by minimizing this action over paths connecting the two vacua. The solution is easy to find: motion in the inverted potential $-V$ turns minima into maxima, and the trajectory "slides" from one to the other,

$$x_{inst}(\tau)/f = \tanh\Big[\omega(\tau - \tau_0)/2\Big]. \tag{3.6}$$

This trajectory is called the *instanton*. Its action,

$$S_{inst} = \omega^3/12\lambda,$$

is precisely the exponent appearing in Eq. (3.4). The existence of instanton-like paths removes the classical degeneracy and makes the quantum vacuum unique.

So, quantum paths in vacuum can be considered a superposition of "zero-point" perturbative oscillations near one of the minima, and nonperturbative tunneling events, the instantons. The same general idea we will discuss below for the QCD vacuum as well.

For an in-depth presentation of modern semiclassical theory, one may consult, for example, the book [Shuryak, 2020]. The traditional WKB method discussed in QM textbooks can be replaced by the *flucton* calculus, in which the wave function is systematically constructed as a semiclassical series to arbitrary order. The perturbative and semiclassical expansions mentioned above are unified into a single **transseries**, which cures the defects of each series individually.[3]

In general, a transseries takes the form of a triple sum over integers p, k, l,

$$\sum C_{pkl}\,\alpha^{2p}\,\big[\exp(-\text{const}/\alpha)\big]^k\,\big[\log(\pm 1/\alpha)\big]^l.$$

The coefficients C_{pkl} satisfy highly nontrivial relations due to the phenomenon known as *resurgence*; for a pedagogical review see, for example, [Behtash et al., 2017]. Flucton and instanton contributions have been computed diagrammatically up to three loops.

To demonstrate that semiclassical theory is not merely a collection of complicated formulae, let us examine how well it works in practice. We focus on the *gap* (splitting of negative-to-positive parity states) [4]

$$gap = E_- - E_+,$$

---

[1] Here one must use diagrams without external legs, whose combinatorial coefficients are more subtle than those of standard diagrams with external lines.

[2] Note that the potential appears with a plus sign here, unlike in Minkowski time. The dot denotes differentiation with respect to τ, not real time.

[3] Divergent series can often be summed using methods such as Borel regularization. These methods relate the ambiguities of the perturbative series to those arising in instanton calculus.

[4] In this sense, it is analogous to a pion mass though for the double-well potential.

which can be computed numerically as a function of the instanton action S. The numerical results are shown as data points in Fig. 3.1 and are compared with the one-, two-, and three-loop semiclassical predictions.

The one-loop result is based on evaluating the determinant of the fluctuation operator (see, for example, the pedagogical review [Vainshtein et al., 1982]). The two-loop correction was computed in [Wohler and Shuryak, 1994]; at this order, new diagrams appear that originate not from the action itself but from enforcing orthogonality to the zero mode. The three-loop correction was obtained in [Escobar-Ruiz et al., 2015], where many diagrams are involved, some evaluated analytically and others numerically. The explicit expressions are shown in the figure.

As the plot demonstrates, even for actions in the range $S = 3 \ldots 6$,[5] the three-loop approximation works remarkably well. The (unshown) residual discrepancy is consistent with an $O(S^{-3})$ correction, as expected from the yet-unknown four-loop contribution.

Looking ahead, QCD instantons have actions $S_{inst} \sim 10\text{-}12$, larger than those shown in the figure. Instanton constituents, known as instanton-dyons, have actions $S_{inst}/N_c \sim 4$, corresponding roughly to the middle of the plotted range. One might therefore expect semiclassical theory to work with comparable accuracy in this context. Unfortunately, for gauge theories the only explicit result currently available is the one-loop instanton density computed by 't Hooft in the 1970. Despite half a century of effort higher-loop results have not yet been obtained.[6]

Instantons correspond to extrema of the path integral, as they minimize the action. Another obvious extremum is the "lazy path" $x(\tau) = 0$. One may also search for complex paths with finite action, motivated by the principles of complex analysis, which suggest that all nearby extrema should be included.

Paths describing "incomplete tunneling" can be represented by instanton-anti-instanton pairs, or "molecules." In the DWP, these configurations were first studied in [Shuryak, 1982d] using numerical simulations of the path ensemble. The instanton-anti-instanton set was defined via "gradient flow"; in complex analysis, the corresponding objects are known as *Lefschetz thimbles*. For a pedagogical introduction, see [Witten, 2010].

The basic idea, dating back to Cauchy, is to deform the integration contour from the real axis into the complex plane. This deformation is most naturally achieved by decomposing the integration domain into a

---

[5] The action is measured in units of $\hbar$, which is set to unity here and throughout.

[6] As the dates of the cited references suggest, each step in this program has taken on the order of two decades.
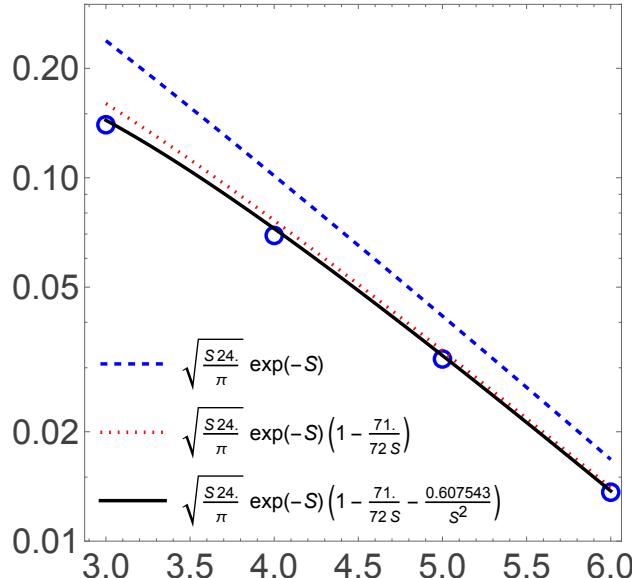
Fig. 3.1 The splitting of the negative-parity state from the vacuum, $gap = E_- - E_+$, shown as data points. The three curves correspond to one-, two-, and three-loop semiclassical approximations.

set of thimbles connecting different extrema. On each thimble the phase of the integrand is constant, allowing the original complex integral to be rewritten as a sum of real integrals (with complex coefficients) that may be separately amenable to standard numerical methods, like Monte-Carlo sampling.

This opens an intriguing possibility for the *complexification* of path integrals, both in quantum mechanics and in quantum field theory. While this approach is not yet fully developed, it may ultimately provide a nontrivial bridge between perturbative and nonperturbative physics. Here, however, we stop and move on to instantons in quantum field theory, and in particular in QCD.

3.2 The topological landscape of gauge fields

The *landscape* refers to the set of *minimal-energy* gauge-field configurations as a function of two main variables. The first is the topological Chern-Simons number,

$$N_{CS} \equiv \frac{\epsilon^{\alpha\beta\gamma}}{16\pi^2} \int d^3x \left(A_\alpha^a \partial_\beta A_\gamma^a + \frac{1}{3}\epsilon^{abc} A_\alpha^a A_\beta^b A_\gamma^c \right), \tag{3.7}$$

while the second variable is the r.m.s. size of the configuration, related to the spatial distribution of the squared field strength,

$$\rho_{r.m.s.} = \frac{\int r^2 G_{\mu\nu}^2 d^3r}{\int G_{\mu\nu}^2 d^3r}. \tag{3.8}$$

For fixed ρ, the landscape is shown in Fig. 3.2. It was defined in [Ostrovsky et al., 2002] in the parametric form

$$U_{\min}(k, \rho) = (1 - k^2)^2 \frac{3\pi^2}{g^2\rho}, \tag{3.9}$$

$$N_{CS}(k) = \frac{1}{4}\text{sign}(k)(1 - |k|)^2(2 + |k|),$$

with parameter k. At $k = \pm 1$ the minimal energy vanishes, while $k = 0$ corresponds to a maximum of the energy. This point was called sphaleron in electroweak theory [Klinkhamer and Manton, 1984].

The set of configurations at arbitrary k is known as the *sphaleron path*. These are static three-dimensional magnetic field configurations, also referred to as *turning points* (by analogy with quantum mechanics, where the semiclassical momentum vanishes). Such configurations are local energy minima in all directions except the size and N_{CS} directions, which are held fixed.

The (anti)instanton corresponds to a tunneling path (blue arrow) connecting the bottoms of two neighboring valleys at zero energy. Since these configurations carry topological charge $Q = \pm 1$, they induce a change in the Chern-Simons number $\Delta N_{CS} = \pm 1$.

However, instanton paths are *not the only form of topological fluctuations* that may occur in this landscape. Indeed, we will discuss two additional classes of paths: (i) those that move along the landscape following the sphaleron path (or *streamline*); (ii) those that traverse the landscape at fixed energy, including tunneling. All of these are illustrated in Fig. 3.2.

The first class is described by a constrained Yang-Mills equation with a nonzero right-hand side, interpreted as an external current that drags the configuration up (or down) the potential along its gradient. In the mathematical literature, it is known as Lefschetz timble, a special path connecting two extrema of a function by following its gradient.

The second class is described by the Yang-Mills equations with a *zero* right-hand side and therefore occurs at fixed energy. The history of such a path passes through the turning points twice, with a Euclidean-time solution in between, a process known as *tunneling at nonzero energy*. In general, these paths should be
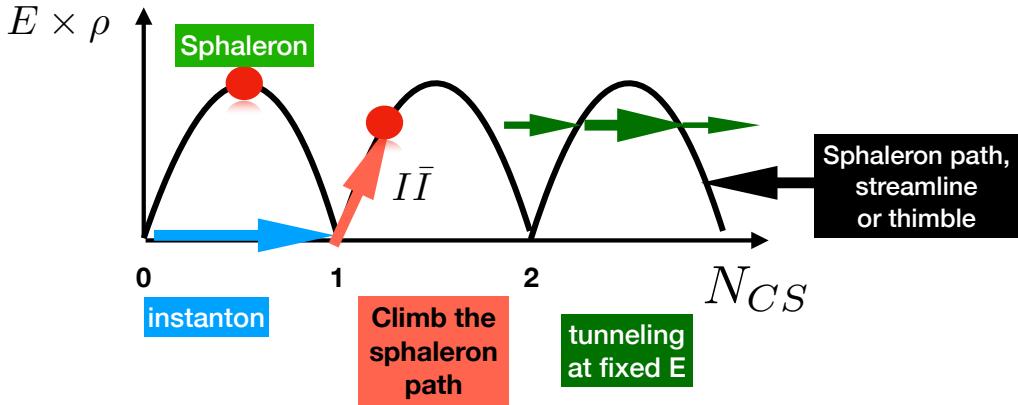
Fig. 3.2 Topological landscape, shown as the gauge-field energy multiplied by the r.m.s. size versus the Chern-Simons number.

supplemented by Minkowski-time solutions before and after the turning points. The technical term for this construction is a *zigzag path*, indicating a transition from real to imaginary time and back again.

3.3 Chiral symmetries of QCD and their breaking

The study of nonperturbative physics in strong interactions began even before the advent of QCD or the introduction of quarks. Already in the early 1960s, Nambu and Jona-Lasinio (NJL) [Nambu and Jona-Lasinio, 1961a], inspired by the BCS theory of superconductivity, investigated the vacuum structure of a theory with *massless* (but strongly interacting) fermions. They showed that an attractive interaction can lead to the formation of a gap at the surface of the Dirac sea. In other words, fermions can acquire a mass dynamically, rather than through an explicit mass term in the Lagrangian.

A key difference from the case of superconductivity is that this phenomenon does not occur in the weak-coupling limit, but instead requires strong coupling.

It is instructive to compare perturbative and nonperturbative forces, using the NJL model as an example of the latter. The first parameter is the coupling constant. The second important parameter is the ultraviolet cutoff $\Lambda_{NJL} \sim 1\,\mathrm{GeV}$, below which the hypothetical attractive four-fermion interaction operates. Typical values used in NJL phenomenology are

$$G_{NJL} = 19\,\mathrm{GeV}^{-2}, \qquad \Lambda_{IR} = 0.24\,\mathrm{GeV}, \qquad \Lambda_{UV} = 0.645\,\mathrm{GeV}, \tag{3.10}$$

for which the constituent quark mass is found to be $M \approx 0.4\,\mathrm{GeV}$.

Let us compare this to the force arising from one-gluon exchange, $F_{\mathrm{gluon}}(k^2) = g^2/k^2$. For a typical momentum exchange inside a meson,

$$k^2 = x\bar{x}\,Q^2 \approx Q^2/4. \tag{3.11}$$

The ratio of the NJL interaction to the gluon-exchange force can then be estimated as

$$\frac{G_{NJL}}{F_{\mathrm{gluon}}} \exp\left(-\frac{k^2}{\Lambda_{UV}^2}\right). \tag{3.12}$$

This ratio is shown in Fig. 3.3. While it decreases at large momenta due to the form factor, it remains larger than unity over a wide range of momentum transfers.
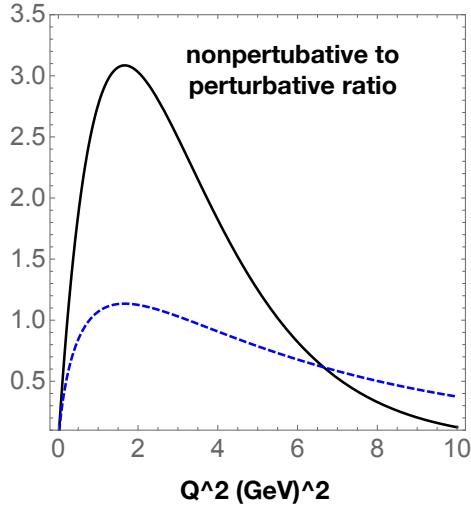
Fig. 3.3 The ratio of the nonperturbative-to-perturbative four-fermion effective vertex (3.12), shown for a Gaussian form factor (solid) and an exponential form factor (dashed), as a function of the momentum transfer squared Q^2 (GeV^2).

Thus, at a qualitative level, the puzzlingly large values of hadronic form factors at intermediate momenta, $Q^2 \sim$ 1-7 GeV^2, may be understood if nonperturbative contributions are added to the perturbative diagrams.

An important consequence of the NJL construction was the introduction of *chiral symmetries*, their *spontaneous breaking* (specifically of the $SU(N_f)_A$ subgroup), the emergence of a nonzero quark condensate $\langle \bar{q}q \rangle \neq 0$, and the appearance of the *Nambu-Goldstone modes*: pions, kaons, and related mesons. NJL suggested that the interquark interaction can be modeled by an attractive local four-fermion operator of the form[7]

$$L_{NJL} = G_{NJL}(\boldsymbol{\pi}^2 + \sigma^2), \tag{3.13}$$

where $\boldsymbol{\pi} = i\bar{q}\gamma_5\boldsymbol{\tau}q$ and $\sigma = \bar{q}q$. It is implicitly assumed that the NJL interaction is restricted to momentum transfers $Q^2 < \Lambda^2_{NJL} \sim 1$ GeV^2. Thus, the NJL model contains two parameters: the coupling G_{NJL} and the cutoff Λ_{NJL}.

Many major developments of the 1960s and 1970s, such as the rise of perturbative QCD and its phenomenological applications, temporarily shifted attention away from these issues. Practical discussions of the nonperturbative QCD vacuum structure resumed with the introduction of the *QCD sum rule* approach by [Shifman et al., 1979]. In this framework, perturbative short-distance descriptions of Euclidean point-to-point correlation functions were complemented by the *operator product expansion* (OPE), which introduced vacuum condensates such as the quark condensate $\langle \bar{q}q \rangle \neq 0$, the *gluon condensate* $\langle G^2 \rangle$, and many higher-dimensional operators.

By matching the long-distance behavior of correlators, expressed in terms of the lightest hadronic states, with their OPE expansions at short distances, it became possible to extract the values of these condensates and to observe a remarkable consistency between the two regimes. Only several spin-zero (scalar and pseudoscalar) quark and gluon channels resisted such a description, indicating much stronger nonperturbative effects [Novikov et al., 1981b].

Extensive phenomenological studies of Euclidean point-to-point correlation functions in many hadronic and glueball channels have confirmed that correlators of operators with different quantum numbers behave strikingly differently (see the review [Shuryak, 1993]). While correlators of vector currents $j_\mu = \bar{q}\gamma_\mu q$, built from light quarks $q = u, d, s$, show only minor deviations from free-quark propagation over distances from zero to about 1 fm, the correlators of spin-zero scalar and pseudoscalar operators ($\gamma_\mu \to 1, \gamma_5$) exhibit strong

---

[7] Boldface denotes isovectors.

deviations from perturbative QCD already at relatively short distances, $x \gtrsim 0.2$ fm. These observations demonstrate that the dominant quark interactions at short distances cannot be reduced to perturbative gluon exchange alone. (Attempts to explain these effects using, for example, rainbow diagrams at strong coupling continue (see e.g. [Raya et al., 2024]). While such approaches may generate a nonzero quark condensate, they do not explain why some correlation functions remain essentially unaffected while others like the π and $\eta - prime$ channels exhibit strong effects of opposite sign. In particular, it is difficult to understand how gluon exchange could produce repulsive forces in a meson channel.)

An alternative picture, developed since the early 1980s and summarized in [Shuryak, 1993], attributes the strong nonperturbative forces responsible for splittings in spin-zero channels to the **collectivization** of instanton zero modes. Equivalently, one may say that nonperturbative interquark interactions are described by the multi-fermion 't Hooft Lagrangian ['t Hooft, 1976b]. These effects are induced by topological fluctuations of the gluon fields, which can be described semiclassically by topological solitons known as *instantons* [Belavin et al., 1975].

For two quark flavors (u, d), the interaction has the schematic four-fermion form[8]

$$L_{'t\,Hooft} \sim \left(\boldsymbol{\pi}^2 + \sigma^2 - \eta'^2 - \mathbf{s}^2 \right), \tag{3.14}$$

where the first two terms reproduce the NJL structure, while the latter two correspond to repulsion in the channels $\eta' = \bar{q}i\gamma_5 q$ and $\mathbf{s} = \bar{q}\boldsymbol{\tau}q$. The negative sign in front of these terms reflects the explicit breaking of $U(1)_A$ symmetry by instantons, a key consequence of the axial anomaly.

3.4 The QCD vacuum as an *instanton liquid* (ILM)

Models of the QCD vacuum that view it as an ensemble of semiclassical solitons -instantons and anti-instantons - are collectively known as instanton liquid models (ILM)[9]. Depending on the theoretical tools and assumptions employed, these models can be classified into the following categories:

(i) In the original model [Shuryak, 1982b], instanton parameters were inferred from empirical values of vacuum observables, such as the *quark and gluon condensates* and the *topological susceptibility*.

(ii) Mean-field analyses of the instanton partition function based on the sum ansatz [Diakonov and Petrov, 1986, Nowak et al., 1996].

(iii) Numerical simulations of the partition function, based on the common quark zero-mode determinant; see [Shuryak and Verbaarschot, 1993a] and the review [Schäfer and Shuryak, 1998].

(iv) The "dense ensemble" (DILM), which includes both isolated instantons and *instanton-anti-instanton molecules* [Shuryak, 2019].

Here we cannot discuss these approaches in detail and instead limit ourselves to comments on their main assumptions and results. For illustrative figures and quantitative lattice results, see Section 3.C.

The typical instanton size and density in ILM are

$$\rho_{ILM} \sim \frac{1}{3}\,\text{fm}, \ \ n_{ILM} \approx 1\,\text{fm}^{-4}. \tag{3.15}$$

Because ρ is relatively small compared to the sizes of most hadrons[10], it is often convenient to employ a *quasi-local approximation*, in which ρ is taken to zero. In this limit, the ILM density appears as a coupling constant multiplying the local 't Hooft Lagrangian. Such "quasi-local" multi-quark vertices are reminiscent of those proposed earlier by Nambu and Jona-Lasinio.

---

[8] Letters in boldface are isovectors.

[9] The key word here is *liquid*, as opposed to an *ideal gas*. It emphasizes that while solitons retain their individual identity, their interactions are strong.

[10] With the exception of the lowest Υ states and the pions.

Indeed, the two NJL parameters, the coupling G_{NJL} and the cutoff $\Lambda_{NJL} \sim 1\,\mathrm{GeV}$, can be directly related to the two ILM parameters quoted above. One can then calculate various diagrams involving these vertices. In contrast to the NJL model, the ILM contains no ultraviolet divergences, since instanton zero modes are not truly pointlike.

The most important property shared by all versions of the ILM is the *spontaneous breaking of the $SU(N_f)_a$ chiral symmetry*. In particular, this mechanism leads to massless pions as Nambu-Goldstone modes.

The well-known *axial anomaly* states that, unlike the vector isoscalar current, the axial current is not conserved. Its divergence is proportional to $\tilde{G}G$, the topological charge density. Tunneling events contribute to this quantity with properly normalized positive or negative integers, and therefore must also change the chirality of each sufficiently light fermion. The microscopic mechanism underlying this phenomenon was discovered in ['t Hooft, 1978]: massless fermions (quarks in QCD, and quarks and leptons in the electroweak theory) possess zero modes in the instanton background. As a result, instantons induce novel fermionic interactions described by the *'t Hooft effective Lagrangian L_{tHooft}*, an operator with $2N_f$ fermion legs. In QCD with u and d quarks, this reduces to a four-fermion operator resembling the hypothetical NJL Lagrangian [Nambu and Jona-Lasinio, 1961b]. Unlike the NJL interaction, however, it explicitly violates the $U(1)_a$ chiral symmetry.

Returning to the ILM in the early 1980s, the central question was whether the instanton density and sizes are *large enough* to generate spontaneous breaking of the $SU(N_f)_a$ chiral symmetry. In other words, can L_{tHooft} play the same dynamical role as the NJL Lagrangian proposed two decades earlier? If so, does it quantitatively reproduce the parameters of chiral perturbation theory, such as the pion mass and couplings? In [Shuryak, 1982g] and subsequent work, it was shown that this is indeed the case. The most direct way to understand this result is through a mean-field analysis, discussed in Section 3.A.

An important qualitative feature of the instanton vacuum is the prediction that vacuum gauge fields are extremely inhomogeneous. Near instanton centers ($r \to 0$), the fields are very strong,

$$G_{a\mu\nu}^2(r) = \frac{192\rho^4}{(\rho^2 + r^2)^4}, \tag{3.16}$$

reaching scales of several GeV^2. These strong fields can capture quarks and confine them into quasi-bound states, the zero modes. At the same time, the fields are nearly zero in the regions between instantons. Clearly, quark propagators behave very differently in these two extreme environments[11].

An *alternative view of chiral symmetry breaking* emphasizes quark *hopping* between instantons, which is possible because their zero modes form degenerate bound states. The resulting quark loops can be either short or long (infinite in the thermodynamic limit $V_4 \to \infty$). The latter are responsible for the accumulation of Dirac eigenvalues near zero, $\lambda \sim 1/V_4$. If *collectivization* of instanton zero modes into the so-called *zero mode zone* (ZMZ) occurs, no gap appears in the Dirac eigenvalue spectrum. The near-zero Dirac eigenvalues are confined to a narrow strip,

$$|\lambda| \sim \mathrm{width}\,(\mathrm{ZMZ}) \sim \frac{\rho^2}{R^3} \sim 20\,\mathrm{MeV}, \tag{3.17}$$

as predicted by the original ILM using the parameters quoted above. In [Glozman et al., 2012], meson and baryon spectroscopy was studied after removing all Dirac eigenstates within a given strip $|\lambda| < \Delta$. A strong restructuring of the light-hadron spectrum was observed when $\Delta > \mathrm{width}\,(\mathrm{ZMZ})$. In particular, the Nambu-Goldstone modes (pions) disappeared entirely from the spectrum, as expected. It would be interesting to extend this analysis to heavy-light systems and to investigate more generally the fate of various spin-dependent forces.

Further statistical descriptions of interacting instanton ensembles were developed using mean-field techniques and numerical simulations; for reviews see [Diakonov et al., 1997, Schäfer and Shuryak, 1998,

---

[11] As an analogy, consider a town experiencing a storm with multiple tornadoes. The behavior of people far from the tornadoes and those caught inside them would be drastically different. Consequently, a *mean propagator* averaged over the entire vacuum (as often used, for example, in the Schwinger Dyson community [Raya et al., 2024]) has limited physical meaning.

Nowak et al., 1996]. Related lattice studies include [Chu et al., 1994, Faccioli and DeGrand, 2003]. Effective models employing the quasi-local approximation or direct numerical simulations of instanton ensembles were actively developed throughout the 1990s.

3.5 Hadrons in the instanton vacuum

The important role of topology and instantons is technically understood through the inclusion of the so-called 't Hooft effective Lagrangian. Since its explicit form is rather technical, we discuss it in the Appendix to this chapter and here only summarize its main properties.

The 't Hooft effective Lagrangian generally includes all fermion flavors in a single nonlocal vertex. In QCD, these are only the light quarks (u, d, s), so the interaction takes the form of a six-fermion operator[12].

The chiralities of quark and antiquark lines are always opposite, so any attempt to close these lines into loops vanishes for massless quarks. This interaction explicitly violates the $U_A(1)$ chiral symmetry, since it changes the chiral charge Q_5 of a state[13].

For temperatures $T < T_c$, the $SU(N_f)$ chiral symmetry is spontaneously broken, and therefore one (or more) quark-antiquark pairs can be replaced by their condensate. This leads to effective four- (or two-) quark operators. Both are extremely important for understanding hadronic physics. The two-quark operator generates a nonzero constituent quark mass, while the resulting four-fermion operators lead to a variety of effects that we discuss below.

As already mentioned, the instanton liquid model (ILM) provides not only qualitative insights, but also a rather good quantitative description of *chiral physics*. Without going into technical details, let us enumerate some of its implications for hadronic spectroscopy. First, it establishes a quantitative connection between the quark condensate and the instanton density. Furthermore, the lightest chiral multiplet, the σ and π mesons, is dominated by the so-called "instanton chain" diagrams involving the 't Hooft interaction. These diagrams can be summed using the Bethe-Salpeter equation, allowing one to relate all chiral parameters[14] to the key vacuum properties given in Eq. (3.15).

Unlike superconductors or the Fermi surface in metals, the surface of the massless Dirac sea can be *gapped* only if the attractive interaction exceeds a critical strength. This was already observed by Nambu and Jona-Lasinio and also applies to the 't Hooft interaction. In Fig. 3.4 we show representative results for the quark constituent mass (left panel) and the chiral condensate (right panel) for different values of the coupling indicated in the figure.

Other mesons-such as vector mesons ρ, ω, tensor mesons, and higher-spin states-do not couple directly to instantons, as already indicated by analyses of empirical correlation functions [Shuryak, 1993]. Chiral channels of the $LL + RR$ type, however, are sensitive to forces induced by $\bar{I}I$ molecules. We will discuss these effects in the next section.

The simplest baryons in the flavor $SU(3)_f$ decuplet are $\Delta(qqq), \ldots, \Omega$. These states can be viewed as three constituent quarks bound together primarily by confinement. The corresponding nonrelativistic potentials, generated by averaging three Wilson lines in the background field of $\bar{I}I$ molecules, have been used extensively[15].

---

[12] In electroweak theory, the instanton-induced Lagrangian involves 12 fermions: 9 quarks and 3 leptons. Which fermions appear depends on the $SU(2)$ gauge orientation of the instanton. An extreme possibility is all up-type fermions: u, c, t (each with three colors) together with e, μ, τ. As required in electroweak theory, all of them must be left-handed.

[13] Instanton-induced production of axial charge is, of course, a specific example of a sphaleron process : whether the motion in the topological landscape proceeds via real or virtual fields is irrelevant, and the general relation between the Chern-Simons number N_{CS} and Q_5 holds for any such process.

[14] These include $\langle \bar{q}q \rangle$, f_π, m_π^2, as well as higher-order couplings of the effective chiral Lagrangian.

[15] Unfortunately, purely heavy states such as ccc or bbb have not yet been observed. However, the same methods can be applied to $cc\bar{c}\bar{c}$ tetraquarks, as discussed below.
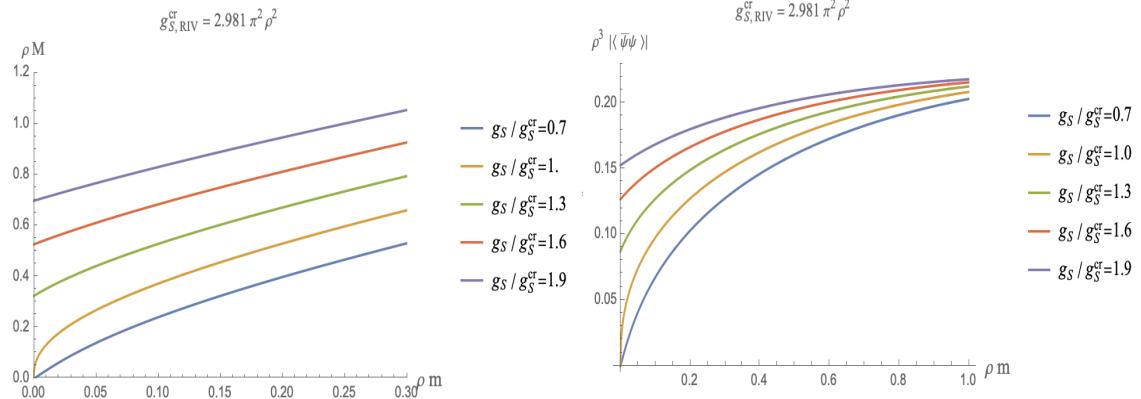
Fig. 3.4 (a) Quark constituent mass M versus the current quark mass m in the ILM, for increasing strength of the 't Hooft coupling g_S (from bottom to top), with the critical coupling $g_{S,\mathrm{RIV}}^{\mathrm{cr}} = 2.981\,\pi^2\rho^2$ and fixed instanton size ρ. (b) Quark condensate $\langle \bar{\psi}\psi \rangle$ versus the current quark mass in the ILM [Liu et al., 2023b].

Finally, nucleons p, n (and the other members of the $SU(3)_f$ octet) differ from the decuplet baryons because the ud pairs in this case are in the so-called *good* diquark. These constitute attractive channels, both through perturbative Coulomb forces [Jaffe and Wilczek, 2003] and through instanton-induced interactions[16] In Section 17.2, we will show how accounting for such pairing effects leads to the observed differences between the nucleon and Δ baryons.

---

[16] In a sense, diquarks are *half-brothers of the pions* and can also be described by instanton-induced loop diagrams. In fact, in two-color QCD ($N_c = 2$), they are true twins and become massless in the chiral limit [Rapp et al., 1998].

Appendix

3.A Chiral symmetry breaking: brief derivations

Historically, the concept of effective quark masses generated by dynamical chiral symmetry breaking was introduced by Nambu and Jona-Lasinio [Nambu and Jona-Lasinio, 1961b]. The central idea is that an attractive interaction between a quark and an antiquark can be sufficiently strong to open a gap at the surface of the massless Dirac sea, in close analogy with electron-electron attraction producing a spectral gap at the Fermi surface in superconductors. As discussed in the Introduction and in the chapter on the QCD vacuum, the modern formulation [Shuryak, 1982e, Diakonov and Petrov, 1986] of the NJL four-fermion operator is nothing but the instanton-induced 't Hooft vertex.

The mechanism can be demonstrated most simply in the mean-field approximation, following the NJL approach. The emergent constituent quark mass in the rest frame appears as a solution of the *gap equation* (14.34),

$$M(k) = m + 2g_S \mathcal{F}(k) \int \frac{d^4q}{(2\pi)^4} \frac{4M(q)}{q^2 + M^2(q)} \mathcal{F}(q). \tag{3.18}$$

The last term represents a dressed quark loop generated by the four-fermion interaction, with $g_S = G_S/N_c$ denoting the rescaled 't Hooft coupling. In contrast to the local NJL model, instanton semiclassical theory introduces the form factor $\mathcal{F}(q)$, which reflects the finite size of instantons.

A formal solution of Eq. (3.18) can be written as

$$M(k) = m\left[1 - \mathcal{F}(k)\right] + M\,\mathcal{F}(k) \sim M\,\mathcal{F}(k), \tag{3.19}$$

which reduces Eq. (3.18) to the standard *gap equation* for the constituent mass M,

$$\frac{m}{M} = 1 - 8g_S \int \frac{d^4k}{(2\pi)^4} \frac{\mathcal{F}^2(k)}{k^2 + M^2}. \tag{3.20}$$

After neglecting the momentum dependence of the running mass in the denominator of Eq. (3.20), as discussed in [Kock and Zahed, 2021], one finds that solutions for M exist only for couplings exceeding a critical value. In the instanton liquid model (ILM), this critical coupling is determined by the instanton-antiinstanton density.

The chiral condensate is obtained in a similar manner,

$$\langle \bar{\psi}\psi \rangle = -\int \frac{d^4k}{(2\pi)^4} \mathrm{Tr}\, S(k) = -8N_c M \int \frac{d^4k}{(2\pi)^4} \frac{\mathcal{F}(k)}{k^2 + M^2}. \tag{3.21}$$

Note that this expression reduces to the scalar mean-field expectation value $\langle \sigma \rangle = \langle \bar{\psi}\psi \rangle / N_c$ only in the local limit of *vanishing* instanton size. In that limit, both Eqs. (3.20) and (3.21) diverge logarithmically in the

infrared and ultraviolet. This problem is resolved in the instanton vacuum, where the quark zero modes generate the form factor $\mathcal{F}(k)$, which is essential for obtaining finite results.

In Fig. 3.4a we show the dependence of the constituent quark mass M on the current quark mass for different values of the multi-fermion coupling g_S in the ILM of the QCD vacuum. In Fig. 3.4b we show the corresponding dependence of the scalar quark condensate on these parameters.

3.B Condensate on the light front

On the light front, the gap equation is modified; we now explain how this occurs. After eliminating the bad fermionic component in the mean-field approximation, only the physical modes of the good component ψ_+ remain. The running quark mass on the light front behaves as $M(k^-) \sim M\mathcal{F}(k^-)$, together with the on-shell condition $2k^-k^+ = k_\perp^2 + M^2$, where M is determined by the scalar gap equation (3.20). Expressed in terms of the physical modes of ψ_+, Eq. (3.20) can be rewritten as

$$\frac{m}{M} = 1 - 2g_S \int \frac{dk^+ d^2 k_\perp}{(2\pi)^3} \frac{\epsilon(k^+)}{k^+} \mathcal{F}^2(k) \bigg|_{k^- = \frac{k_\perp^2 + M^2}{2k^+}} . \tag{3.22}$$

Here we assume that $\mathcal{F}(k^2)$ is free of physical poles. This is the case for (3.38) after analytic continuation, up to spurious branch points whose contributions can be neglected at leading order in the diluteness factor [Kock and Zahed, 2021].

To express the chiral condensate on the light front, we first note that the quark propagator takes the form

$$S(k) \to \left[\frac{i[\slashed{k} + M(k^2)]}{k^2 - M(k^2)^2} - \frac{i\gamma^+}{2k^+} \right] \to \left[\frac{i[\slashed{k} + M(k^2)]}{k^2 - M^2} - \frac{i\gamma^+}{2k^+} \right] , \tag{3.23}$$

following the elimination of the bad component in favor of the good one. The condensate is then given by

$$\langle \bar{\psi}\psi \rangle = -2N_c M \int \frac{dk^+ d^2 k_\perp}{(2\pi)^3} \frac{\epsilon(k^+)}{k^+} \mathcal{F}(k^-) . \tag{3.24}$$

Using the explicit form of the instanton-induced form factor $\mathcal{F}(k)$, the gap equation becomes

$$\frac{m}{M} = 1 - \frac{4g_S}{\pi^2 \rho^2} \int_0^\infty dz\, z \frac{z^3}{z^2 + \frac{\rho^2 M^2}{4}} |z(I_0(z)K_0(z) - I_1(z)K_1(z))'|^4 , \tag{3.25}$$

and similarly the quark condensate reads

$$\rho^3 \langle \bar{\psi}\psi \rangle = -\frac{4N_c}{\pi^2} \rho M \int_0^\infty dz \frac{z^3}{z^2 + \frac{\rho^2 M^2}{4}} |z(I_0(z)K_0(z) - I_1(z)K_1(z))'|^2 . \tag{3.26}$$

In the chiral limit, the constituent mass is nonzero only when the 't Hooft coupling exceeds a critical value $g_{S,\mathrm{RIV}}^{\mathrm{cr}}$, defined by

$$g_{S,\mathrm{RIV}}^{\mathrm{cr}} = 2\pi^2 \rho^2 \left[8 \int_0^\infty dz\, z |z(I_0(z)K_0(z) - I_1(z)K_1(z))'|^4 \right]^{-1} \approx 2.981\pi^2 \rho^2 . \tag{3.27}$$

We note that in the limit $\mathcal{F} \to 1$ the above expressions become divergent, clearly demonstrating the essential role of the instanton-induced zero-mode profile $\mathcal{F}(k)$. In the absence of this structure, ad hoc cutoffs are required. For vacuum loops (the 0-body sector), such a cutoff must apply to on-shell momenta satisfying $k^2 = 2k^+k^- + k_\perp^2$ and should preserve both boost and parity invariance, for example $|\sqrt{2}k^\pm| \leq \Lambda \sim 1/\rho$. Further discussion of this issue can be found in Ref. [Liu et al., 2024d].
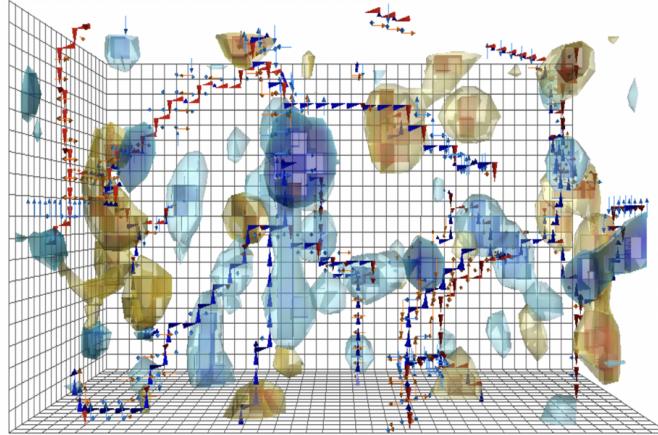
Fig. 3.C.1 Instantons (yellow) and anti-instantons (blue) in the *deep-cooled Yang-Mills vacuum*. After center projection, they are threaded by center P-vortices [Biddle et al., 2020b, Biddle et al., 2020a]. These configurations constitute the primordial gluon epoxy (hard glue) at the origin of light hadron masses [Zahed, 2021]. The center P-vortices are responsible for confinement. See text for details.

3.C QCD topological objects observed on the lattice

Over the last decades, lattice gauge theory has developed into a large and mature field, eventually reaching the capability to perform numerical simulations with (near-)realistic quark masses. As a result, the main features of the hadronic spectrum have been successfully reproduced. One may therefore ask why further efforts to derive and understand many aspects of hadronic structure, as described in this review, are still justified.

There are essentially two reasons. The first, discussed in the first half of this review, concerns a deeper understanding of the confining and spin-dependent forces between quarks. The second is the goal of *bridging the gap between spectroscopy and light-cone observables.* Lattice results, used to the fullest extent possible, guide attempts to explain these phenomena in terms of models that are significantly simpler than full-scale numerical simulations of Euclidean gauge fields.

Proceeding in this spirit, we present two relatively recent examples of visualizations of vacuum fields in QCD. The Instanton Liquid Model discussed above describes these fields as highly inhomogeneous: localized regions of very strong gauge fields at instanton centers are surrounded by "empty" space-time largely free of nonperturbative fields. Since the mid-1990s, such field distributions have been extracted from lattice configurations using various "cooling" methods. Since a picture is worth many words, we refer the reader to the visualization shown in Fig. 3.C.1, which displays a representative topological charge distribution from Refs. [Leinweber, 1999, Biddle et al., 2020b, Biddle et al., 2020a]. It reveals a number of instantons and anti-instantons populating the QCD vacuum.

Note that the topological clusters are also threaded by thin center vortices, or Z_3-flux strings, which span world-sheet surfaces in four dimensions. While center vortices are essential for enforcing confinement at long distances, Fig. 3.C.1 shows that they are, on average, largely decoupled from the strong and inhomogeneous topological fields, except at the branching points of P-vortices. Moreover, the field strength associated with these vortices in the vicinity of topological objects is approximately $\sigma_T \bar{\rho} \approx 0.3\,\text{GeV}$. This is weaker than the typical chromo-electric or chromo-magnetic field strength at an instanton center, $\sqrt{E} = \sqrt{B} \approx 2.5/\bar{\rho} \approx 1.5\,\text{GeV}$, yet it is crucial for long-distance color correlations.

Many years later, lattice simulations have quantified instanton parameters in a systematic way, see for example the size distribution shown in Fig. 3.C.2. Technically, this is obtained from lattice gauge fields that
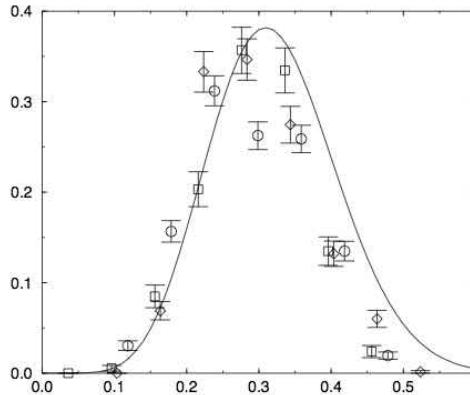
Fig. 3.C.2 Left: Size distribution of instantons from lattice configurations [Hasenfratz, 2000]. The curve represents the theoretical prediction in Eq. (3.28). Right: Schematic paths of quarks and antiquarks for pions and nucleons. Instantons are depicted as small hills with tunnels. Note that chirality flips $L \leftrightarrow R$, as well as at blue dots indicating quark mass insertions.

have been *deeply cooled,* meaning that the action is minimized in a way that removes perturbative gluons while preserving the gauge topology. The curve shown corresponds to the distribution

$$\frac{dn}{d\rho} = \frac{dn}{d\rho}\bigg|_{semiclassical} \cdot e^{-2\pi\sigma\rho^2} , \tag{3.28}$$

proposed in Ref. [Shuryak, 1999], where the suppression of large instanton sizes arises from a dual monopole condensate inferred from the flux-tube tension σ. The semiclassical contribution is known only to one-loop order ['t Hooft, 1976a]; unfortunately, higher-loop corrections, analogous to those studied in quantum mechanics, have not yet been calculated.

Note that the four-dimensional ball volume is $\pi^2\rho^4/2$, and the diluteness parameter $n_{I+\bar{I}}\pi^2\rho^4/2 \sim 1/20 \ll 1$ is indeed small. Nevertheless, instantons interact strongly with each other, which motivates the term *liquid* in the Instanton Liquid Model. The theoretical description began with a mean-field approximation [Diakonov and Petrov, 1986], followed by statistical numerical simulations; for a review, see Ref. [Schäfer and Shuryak, 1998]. An important qualitative feature is that the QCD vacuum is highly inhomogeneous[17], with most regions essentially free of strong fields, while at instanton centers the field strengths are large, $G \sim 2$-$5\,\mathrm{GeV}^2$.

The broader implication of this analysis is that the topological structure of the QCD vacuum is not merely a theoretical curiosity but the organizing principle behind hadron formation. Instantons break chiral symmetry, generate dynamical masses, produce multiplet structures in the diquark sector, and ultimately give rise to the bound-state structure of the low-lying baryons. The instanton liquid model therefore provides a unified, predictive, and physically transparent framework for understanding low-energy hadron physics.

Confinement is not as essential for ground state hadrons, as it is for the high lying ones and their manifest Reggeization. In the Euclidean formulation, the pion and nucleon worldlines are kept bunched by the 't Hooft interactions, which makes them less sensitive to flux piercing by P-vortices in the dual description. This is not the case for the Delta and high-lying hadrons, where the worldlines are wider and more prone to flux piercing.

---

[17] Attempts to describe the vacuum using *averaged* propagators or vertices are therefore doomed to fail. Instead, one should compute entire processes (such as form factors or scattering amplitudes) in the background of a single instanton and subsequently average over the ensemble.

In the LF description (to which we turn in the last part of this review) the Hamiltonian actually produces square masses of hadrons, and Regge trajectories would naturally appear.

3.D The *gradient cooling* hunting for the $I\bar{I}$ molecules

The general notion of the renormalization group (RG) is arguably the most important concept in quantum field theory. In partonic physics it appears in the form of DGLAP evolution: as the resolution scale μ changes, one must add or subtract gluonic degrees of freedom.

Nowadays, *cooling* via the gradient flow can be consistently related to the renormalization group flow [Luscher and Weisz, 2011], placing the scale dependence of the "molecular component" on a firm theoretical footing. Skipping several decades of developments, we consider as an example the recent work of Ref. [Athenodorou et al., 2018], which studied three- and four-point gluon field correlators and related their evolution under cooling to topology. The original motivation was to extract the gluon coupling $\alpha_s(k)$, leading to the definition of the observable

$$\alpha_{MOM}(k) = \frac{k^6}{4\pi} \frac{\langle G^{(3)}(k^2)\rangle^2}{\langle G^{(2)}(k^2)\rangle^3} \,, \tag{3.29}$$

given by the ratio of three-point to two-point Green functions.

In the uncooled quantum vacuum, where perturbative gluons are present, the effective coupling decreases at large momenta $k > 1\,\mathrm{GeV}$, as expected from asymptotic freedom. However, in the low-momentum limit $k \to 0$, a positive power-law behavior persists, with a slope that exactly matches the prediction from an instanton ensemble [Boucaud et al., 2003],

$$\alpha_{MOM}(k) \to \frac{k^4}{18\pi n_{I+\bar{I}}} \,. \tag{3.30}$$

Furthermore, it was observed that as the cooling time τ increases, this same power-law behavior extends to higher momenta, $k > 1\,\mathrm{GeV}$. Cooling was found to eliminate not only perturbative gluons, but also closely bound instanton-anti-instanton pairs.
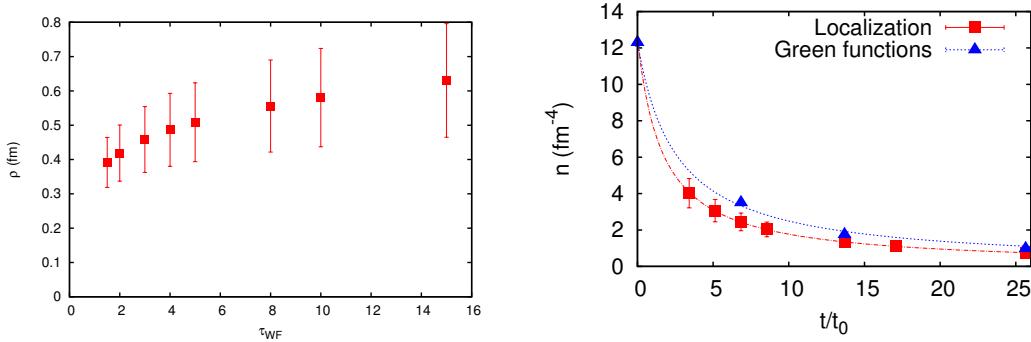
Fig. 3.D.1 Dependence of the mean instanton size (upper panel) and density (lower panel) on the gradient-flow cooling time (τ or t/t_0, arbitrary units). The quantum vacuum corresponds to the extrapolation $\tau \to 0$.

The dependence of the mean instanton size and density on the gradient-flow cooling time is shown in Fig. 3.D.1, taken from Ref. [Athenodorou et al., 2018]. The main conclusion of that analysis is that, when extrapolated to zero cooling time ($\tau \to 0$), the characteristic values are

$$\rho \to \frac{1}{3}\,\text{fm}, \qquad n \to 10\,\text{fm}^{-4}\,. \tag{3.31}$$

Thus, the density of nonperturbative fields is significantly larger than previously estimated in the Instanton Liquid Model. While the results agree with the ILM in the deep-cooling limit (large τ), where $n \sim 1\,\text{fm}^{-4}$, in the physically relevant limit $\tau \to 0$ the density is larger by roughly an order of magnitude[18]. We will use these values as inputs for a *dense instanton liquid model*, which explicitly includes instanton-anti-instanton molecules.

3.E Poisson duality: instantons versus monopoles

Among the various nonperturbative mechanisms proposed to explain infrared QCD phenomena, instantons-topologically nontrivial tunneling configurations of the gauge field-occupy a central role. The instantons induce chirality-changing fermionic zero modes and generate 't Hooft multi-fermion interaction, explaining the mechanism of spontaneous chiral symmetry breaking, the $U_A(1)$ anomaly, and the mass splitting in the pseudoscalar meson sector. When embedded into an ensemble of instantons and anti-instantons, this mechanism forms the basis of the instanton liquid model (ILM), which captures the dominant infrared degrees of freedom of the gluonic vacuum. Lattice gauge theory, particularly with the aid of gradient flow, now provides strong evidence that cooled gauge configurations reveal a dilute but strongly correlated ensemble of instantons and anti-instantons, supporting the ILM picture.

The same gradient flow techniques using the P-vortex projection as we have discussed earlier, have also shown a direct correlation between the location of the emergent branching points, sources of monopoles and anti-monopoles and the location of the instantons and anti-instantons. This is not surprising, given the geometrical origin of both configurations, and their intimate relationship at finite temperature [Kraan and van Baal, 1998b, Lee and Lu, 1998]. What emerges is the intimate relationship between chiral symmetry and confinement, where the instantons and anti-instantons are dominant in the former and in particular in the low-lying hadrons (relatively bunched worldlines not prone to flux piercing), and where monopoles and anti-monopoles through center vortices are dominant for the latter, especially for the high-lying hadrons (relatively broad worldlines prone to flux piercing). The two descriptions are likely dual in the vacuum, extending the initial observation in the thermal state [Ramamurti et al., 2018].

3.F More on $I\bar{I}$ molecules

In Euclidean field ensembles generated on the lattice, an analogous procedure is known as *gradient cooling*. As a function of the cooling time τ, hard gluons above a certain scale are eliminated, rendering gauge field configurations progressively less noisy. Eventually, this procedure leads to a dilute ensemble of instantons. While gluons (small-amplitude fluctuations) are removed, the "topological glue" in the form of instantons remains. Because instantons are local minima of the action, they remain stable under further action reduction.

What we wish to emphasize in this section is that strong gauge-field fluctuations also exist between these two limits: the full quantum vacuum with gluons and the dilute instanton ensemble. These configurations are neither self-dual nor do they possess (near-)zero Dirac eigenvalues. As a result, they do not contribute to chiral symmetry breaking and were therefore not included in the original Instanton Liquid Model (ILM). Nevertheless, they represent genuine fluctuations of the vacuum gauge fields and do contribute to certain observables, most notably Wilson lines. Accordingly, we will investigate their contributions to central and

---

[18] The density may in fact be even larger, since the instanton definition employed in Ref. [Athenodorou et al., 2018] excludes closely bound instanton-anti-instanton pairs (*molecules*).

spin-dependent forces between quarks. The inclusion of such *molecules* is the novel element of the vacuum model developed here.

Close instanton-anti-instanton pairs are, of course, well known and have been observed on the lattice. However, they are not visible in Fig. 3.C.1, which was obtained using so-called deep cooling of gauge configurations. During this process, closely spaced instanton-anti-instanton pairs are already annihilated. The role of the *molecular component* of the vacuum was previously explored in connection with phase transitions in hot and dense matter. Indeed, neglecting quark masses, this component is the only one that survives at temperatures $T > T_c$, where chiral symmetry is restored. The combined treatment of "atomic" and "molecular" components dates back to Ref. [Ilgenfritz and Shuryak, 1989]. The molecular component was also shown to be important at high baryon density, where it contributes to quark pairing and color superconductivity [Rapp et al., 1998]. More recently, we have explored its role through nonperturbative contributions to mesonic form factors [Shuryak and Zahed, 2021g] and matching kernels [Liu and Zahed, 2021].

The theory of sphaleron processes (schematically illustrated in the middle of Fig. 3.2) is closely related to the issue of $I\bar{I}$ interactions. The numerical calculation of the *streamline* along the action gradient was first performed for quantum-mechanical instantons in Ref. [Shuryak, 1988]. For gauge theories, the streamline equation was derived in Ref. [Balitsky and Yung, 1986], solved approximately in Ref. [Yung, 1988], and computed numerically in Ref. [Verbaarschot, 1991]. A surprising finding of the latter work was that the Yung ansatz is remarkably accurate not only at large separations $R \gg \rho$, where it was originally derived, but in fact down to zero separation. Note that the last two works employed conformal inversion about the instanton center, rendering the instanton and anti-instanton co-central.

Consider an instanton I and an anti-instanton $\bar{I}$ of equal size ρ and identical color orientation, with their four-dimensional separation R serving as the parameter of the configuration. Their centers are located at $x_{1\mu} = (0, 0, 0, R/2)$ and $x_{2\mu} = (0, 0, 0, -R/2)$. In the mathematical literature, such a family of configurations is known as a *Lefschetz thimble*. It interpolates between one extremum at $R \to \infty$, corresponding to independent I and $\bar{I}$, and the perturbative vacuum with vanishing mean field at $R = 0$. For $y_4 < 0$, the gauge fields are approximately anti-self-dual, $\mathbf{E} \approx -\mathbf{B}$, while for $y_4 > 0$ they are approximately self-dual, $\mathbf{E} \approx \mathbf{B}$. At $y_4 = 0$, the electric field vanishes. As shown in Ref. [Ostrovsky et al., 2002], the three-dimensional magnetic objects obtained using the Yung ansatz closely resemble sphaleron-path configurations obtained via constrained energy minimization.

The instanton-anti-instanton streamline thus provides a semiclassical description of sphaleron production. In the context of electroweak theory, it was first applied in Refs. [Khoze and Ringwald, 1991, Shuryak and Verbaarschot, 1992] more than three decades ago. Recent interest in the production of QCD sphalerons at the LHC and RHIC is discussed in our work [Shuryak and Zahed, 2021d].

We now turn to lattice observables to which the molecular component of the instanton ensemble contributes. The simplest example is the gluon condensate $\langle G^2_{\mu\nu} \rangle$, introduced within the framework of QCD sum rules [Shifman et al., 1979]. The numerical value of this condensate has been subject to significant revisions, with later studies suggesting a substantially larger magnitude. Additional discrepancies were identified in lattice attempts to extract local or nonlocal observables involving powers of the gauge-field strength $G_{\mu\nu}$.

As already mentioned, instantons (I) are solutions of the Yang-Mills equations in Euclidean time $\tau = ix(4)$ [Belavin et al., 1975], semiclassically describing tunneling between gauge-field configurations with different topology (Chern-Simons number). Anti-instantons ($\bar{I}$) describe tunneling in the opposite direction. By *molecules* we mean strongly overlapping $I\bar{I}$ configurations, corresponding to incomplete tunneling events.

Historically, overlapping $I\bar{I}$ configurations were first studied in the context of the well-known quantum-mechanical double-well potential. As discussed, for example, in Ref. [Shuryak, 1988], one can fix certain points along the path and minimize the action, leading to the concept of *conditional minima*. Action minimization along the direction of its gradient (known as gradient flow) produces *streamline* configurations. (The analogous objects in complex analysis are known as Lefschetz thimbles.)

In gauge theory, the first derivations of such configurations were performed in Refs. [Balitsky and Yung, 1986, Yung, 1988] for large $I\bar{I}$ separations, and in full generality in Ref. [Verbaarschot, 1991], using conformal trans-

formations to render I and $\bar{I}$ co-central. These configurations were later applied to finite-temperature QCD in Ref. [Ilgenfritz and Shuryak, 1989], and to the semiclassical theory of sphalerons at high-energy colliders in Ref. [Shuryak and Verbaarschot, 1992], although such objects have not yet been observed experimentally in either QCD or the electroweak sector.

Gauge-field configurations obtained from lattice simulations, after gradient-flow filtering of gluons, reveal a rather dense ensemble of $I\bar{I}$ molecules. With continued gradient flow, these molecules annihilate, leaving behind a dilute ensemble of isolated instantons and anti-instantons that is stable under action minimization. This ensemble is what is traditionally referred to as the Instanton Liquid Model [Shuryak, 1982b]. Examples of recent lattice studies investigating molecular configurations and their annihilation under gradient flow can be found in Ref. [Athenodorou et al., 2018].

In later work, however, we did not employ either Verbaarschot's or Yung's streamline configurations. Instead, we adopted a variant of the so-called ratio ansatz

$$A^{\mu a}(x) = \frac{\bar{\eta}^{a\mu\nu} y_I^\nu \rho^2 / Y_I^2 + \eta^{a\mu\nu} y_A^\nu \rho^2 / Y_A^2}{1 + \rho^2/Y_A + \rho^2/Y_I}, \tag{3.32}$$

where I and A denote the instanton and anti-instanton, respectively. The centers are located at $y_{I,A}^m = x^m$ for $m = 1, 2, 3$, with $y_I^4 = x^4 - R/2$ and $y_A^4 = x^4 + R/2$. Capital Y denotes the squared distances, for example $Y_A = y_A^\mu y_A^\mu$. Near one of the centers (e.g. Y_I small and Y_A large), the first term dominates, and cancellation of Y_A between numerator and denominator yields the usual singular-gauge fields of an instanton or anti-instanton.
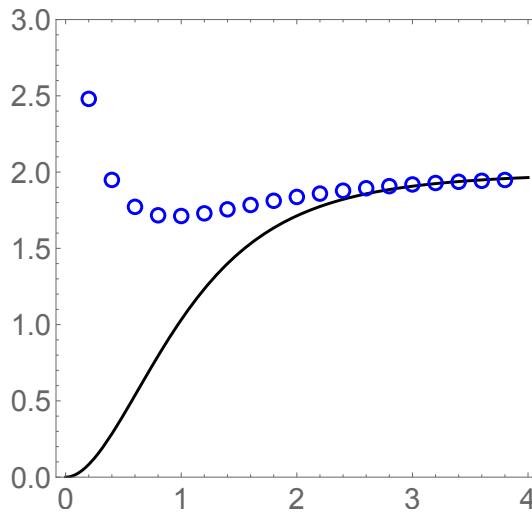
Fig. 3.F.1 Action of the $I\bar{I}$ configurations (in units of the single-instanton action $8\pi^2$) as a function of the separation R/ρ. The solid line corresponds to the streamline configuration [Verbaarschot, 1991], while the points show the result obtained using the ansatz (3.32).

It is straightforward for symbolic programs such as MATHEMATICA to generate explicit (though lengthy) expressions for the field strengths and their squares. The distribution of the gauge-invariant scalar combination $[G_{\mu\nu}^a]^2$ (the action density) is shown in Fig. 3.F.2. The integrated action, measured in units of the single-instanton action $S_0 = 8\pi^2/g^2$, approaches 2 at large separation $R \to \infty$. At small R, however, it does not vanish but instead exhibits a repulsive core for $R \lesssim 0.5$. This feature is unimportant for our purposes, since in subsequent calculations we take $I\bar{I}$ molecules with $R = \rho$ as representative of the vacuum.

The behavior of the gauge fields is illustrated in the right panel of Fig. 3.F.2. The electric field is odd under $x^4 \to -x^4$, while the magnetic field is even. Similarly, A^4 is odd, implying that the configuration restricted
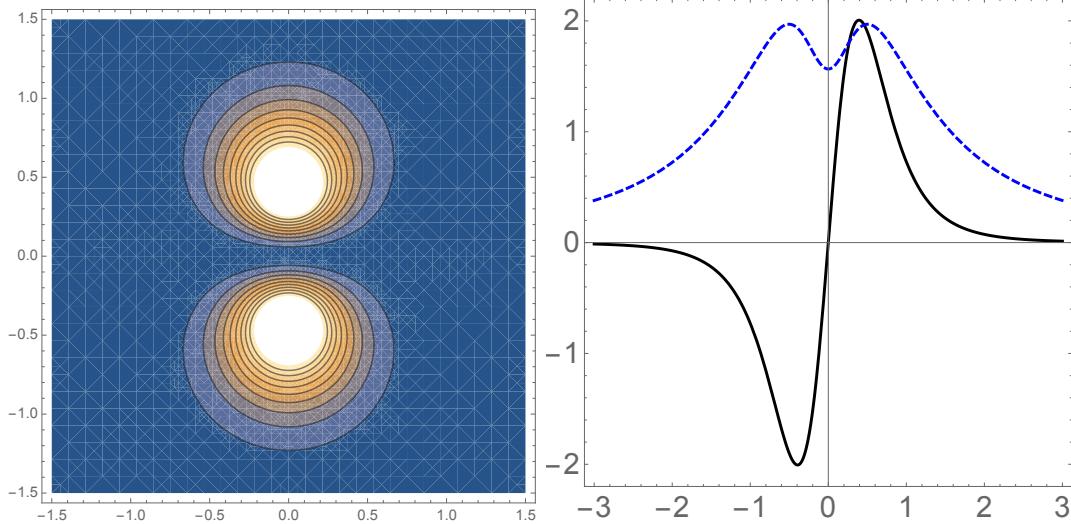
Fig. 3.F.2 Left: Contour plot of the action density as a function of x^1 and x^4, in units of the instanton size ρ. The separation between the centers is $R = \rho$, oriented along the Euclidean time direction $\tau = x^4$. Right: Electric (black solid) and magnetic (blue dashed) field components with $\mu = 3, a = 3$ as functions of x^4/ρ.

to the three-dimensional subspace at $x^4 = 0$ is purely magnetic and belongs to the so-called sphaleron path. The molecular configurations can therefore be interpreted as tunneling amplitudes and anti-amplitudes, separated by the analogue of a quantum-mechanical turning point, at which the electric field (and hence the momentum) vanishes.

Individual instantons (anti-instantons) are self-dual (anti-self-dual), and as a result all components of the stress tensor vanish. This is not the case for molecular configurations. In particular, the Poynting vector $\mathbf{P} = [\mathbf{E}^a \times \mathbf{B}^a]$, which characterizes the direction and magnitude of energy flow, is nonzero. Since the configuration is localized, the energy flow must form closed loops, which turn out to be circular.

3.G 't Hooft effective Lagrangian

The derivation is based on the zero-mode contribution to the quark propagator,

$$S(x,y) = \frac{\psi_0(x)\psi_0^+(y)}{im} + \sum_{\lambda \neq 0} \frac{\psi_\lambda(x)\psi_\lambda^+(y)}{\lambda + im} \,. \tag{3.33}$$

At large distances, the zero mode ψ_0 behaves as $x_\mu \gamma_\mu / x^4$, corresponding to a free propagator in empty space. Amputating these external legs leads to an effective quasi-local vertex with $2N_f$ fermion legs, known as the 't Hooft effective Lagrangian ['t Hooft, 1976b]. It includes the zero modes of all light quark flavors (u, d, s) and therefore induces flavor-mixing interactions,

$$\bar{u}u \leftrightarrow \bar{d}d \leftrightarrow \bar{s}s \,.$$

For $N_f = 3$, in the local (zero-size instanton) approximation and in the chiral limit $(m_q = 0)$, the interaction takes the form of determinantal interactions among the u, d, s quarks [Chernyshev et al., 1996],

$$\mathcal{V}_{qqq}^{L+R} = \frac{G}{N_c(N_c^2 - 1)} \left[\left(\frac{2N_c + 1}{2(N_c + 2)} \right) \det(UDS) + \frac{1}{2(N_c + 1)} \left(\det(U_{\mu\nu}D_{\mu\nu}S) + \text{cyclic} \right) \right] + (L \leftrightarrow R) \tag{3.34}$$

where $U = \bar{u}_R u_L$ and $U_{\mu\nu} = \bar{u}_R \sigma_{\mu\nu} u_L$, with analogous definitions for D and S. For a single instanton within the instanton liquid model, the coupling constant G is related to the instanton density as

$$G = \frac{n_{I+\bar{I}}}{2}\left(4\pi^2\rho^3\right)^3 \left(\frac{1}{m_u^*\rho}\right)\left(\frac{1}{m_d^*\rho}\right)\left(\frac{1}{m_s^*\rho}\right), \tag{3.35}$$

with the so-called *determinantal mass*

$$m_f^* = m_f + \frac{n_{I+\bar{I}}}{2N_c}\frac{4\pi^2\rho^2}{m_f^*}, \tag{3.36}$$

where m_f is the Higgs-induced quark mass appearing in the fundamental QCD Lagrangian.

For most of the analyses in this work, we will specialize to $N_f = 2$, with u and d quarks of nearly degenerate masses. Strangeness will also be addressed in a similar spirit, using U- and V-spin. The interaction (3.34) explicitly breaks the $U_A(1)$ axial symmetry, while preserving flavor and left-right symmetry. This structure becomes more transparent after a Fierz transformation,

$$\frac{G}{8(N_c^2-1)}\left(\frac{2N_c-1}{2N_c}\left[(\bar{\Psi}\Psi)^2 - (\bar{\Psi}\tau^a\Psi)^2 - (\bar{\Psi}i\gamma^5\Psi)^2 + (\bar{\Psi}i\gamma^5\tau^a\Psi)^2\right] - \frac{1}{4N_c}\left[(\bar{\Psi}\sigma_{\mu\nu}\Psi)^2 - (\bar{\Psi}\sigma_{\mu\nu}\tau^a\Psi)^2\right]\right). \tag{3.37}$$

This interaction is strongly attractive in the σ and pion channels and repulsive in the η' channel, thereby resolving the $U_A(1)$ problem. Equation (3.37) is the QCD realization of the interaction originally proposed in the pre-QCD era [Nambu and Jona-Lasinio, 1961a]. Finite instanton-size effects can be restored by the replacement $\psi(x) \to \sqrt{\mathcal{F}(i\partial)}\psi(x)$ in (3.37), with the universal profile $\mathcal{F}(k)$ in momentum space ($k = \sqrt{k^2}$),

$$\mathcal{F}(k) = \left[(zF'(z))^2\right]\bigg|_{z=\frac{k\rho}{2}}, \qquad F(z) = I_0(z)K_0(z) - I_1(z)K_1(z). \tag{3.38}$$

In addition to changing quark flavors, this Lagrangian also induces chirality flips[19].

This Lagrangian can be written in several equivalent forms, which may initially appear confusing. Any multi-fermion operator can be identically rewritten using Fierz identities, which regroup fermions into different pairs. For four-fermion operators there are three possible pairings, corresponding to pairing a given fermion with any of the remaining three. As a result, the $N_f = 2$ 't Hooft Lagrangian admits three equivalent representations. Different forms may be more convenient for different applications, but their coexistence in the literature can lead to confusion. Following Ref. [Rapp et al., 2000], we present all three forms here. In what follows, t^a denote color generators (Gell-Mann matrices for $N_c = 3$), $\tau^- = (\boldsymbol{\tau}, i)$ with $\boldsymbol{\tau}$ the isospin matrices, and the momentum-dependent form factor $F(k)$ (a Dirac matrix) is related to the zero-mode solution.

$$\begin{aligned}
L_1 &= \frac{G}{4(N_c^2-1)}\left[\frac{2N_c-1}{2N_c}(\bar{q}F^+\tau_\alpha^- Fq)^2 + \frac{2N_c-1}{2N_c}(\bar{q}F^+\gamma_5\tau_\alpha^- Fq)^2 + \frac{1}{4N_c}(\bar{q}F^+\sigma_{\mu\nu}\tau_\alpha^- Fq)^2\right] \\
L_2 &= \frac{G}{8N_c^2}\left[(\bar{q}F^+\tau_\alpha^- Fq)^2 + (\bar{q}F^+\gamma_5\tau_\alpha^- Fq)^2 + \frac{N_c-2}{2(N_c^2-1)}\left((\bar{q}F^+\tau_\alpha^- t^a Fq)^2 + (\bar{q}F^+\gamma_5\tau_\alpha^- t^a Fq)^2\right)\right. \\
&\quad \left. - \frac{N_c}{4(N_c^2-1)}(\bar{q}F^+\sigma_{\mu\nu}\tau_\alpha^- t^a Fq)^2\right]
\end{aligned} \tag{3.39}$$

---

[19] In a talk, T. D. Lee once compared instanton tunneling to driving from Queens to Manhattan. Shuryak remarked that a better analogy is tunneling from Britain to France, since it naturally incorporates the interchange of left- and right-handed fermions.

$$L_3 = \frac{G}{8N_c^2}\left[-\frac{1}{N_c - 1}(q^T F^T C \tau_2 t_A^a F q)(\bar{q} F^+ \tau_2 t_A^a C F^* \bar{q}^T) \right.$$
$$\left. -\frac{1}{N_c - 1}(q^T F^T C \tau_2 \gamma_5 t_A^a F q)(\bar{q} F^+ \tau_2 \gamma_5 t_A^a C F^* \bar{q}^T) + \frac{1}{2(N_c + 1)}(q^T F^T C \tau_2 \sigma_{\mu\nu} t_A^a F q)(\bar{q} F^+ \tau_2 \sigma_{\mu\nu} t_A^a C F^* \bar{q}^T) \right].$$
$$(3.40)$$

The first two forms, L_1 and L_2, are often referred to as the mesonic form, since they involve squares of colorless bilinears $(\bar{q} \ldots q)$, which can be interpreted as mesonic currents. These include four species: scalar and pseudoscalar mesons with isospin zero (σ, η') and one (π, δ). To first order in L_i, the masses of these mesons are shifted upward or downward according to the signs of the corresponding terms: the π and σ masses decrease, while those of the δ and η' increase.

The Lagrangian L_3 is known as the *diquark form,* since it contains (qq) and $(\bar{q}\bar{q})$ pairs. Here T denotes transposition, C is the charge-conjugation matrix (equivalent here to the antisymmetric isospin matrix τ_2), and the color generators t_A^a are restricted to those antisymmetric in color indices, as indicated by the subscript A. As in the mesonic case, the first two terms have a sign opposite to that of the last one, implying that, to first order, scalar diquarks receive attractive mass corrections while vector diquarks are repelled (spin-0 down, spin-1 up).

Part II
Hadronic spectroscopy

Chapter 4
Quarkonia

4.1 Quarkonia and tetraquarks

Quarkonia is the collective name for mesons composed of heavy quarks, namely charmonia $\bar{c}c$ and bottomonia $\bar{b}b$. Discovered in the 1970s, they immediately became central pillars of hadronic spectroscopy. Hundreds of experimental and theoretical studies have been devoted to their properties, regularly summarized in the Reviews of Particle Properties (RPP). This review is not the place to recount the historical developments or enter into detailed discussions; it suffices to recall that the mean (spin-averaged) spectra of quarkonia are well reproduced by the nonrelativistic Schrodinger equation with a simple Cornell potential[1].

Beyond their foundational role half a century ago, quarkonium spectroscopy has also played a key role in the recent revolution in hadronic spectroscopy over the past decade. To set the stage, let us briefly explain what has emerged from a closer scrutiny of charmonium states. A plot that clearly illustrates the current situation is shown in Fig. 4.1.1, which displays the *gaps* $gap_n = M_{n+1} - M_1$, i.e. quarkonium masses measured relative to the ground state. This representation allows one to compare charmonium and bottomonium data on a single plot[2].

The first observation concerns a well-known but striking fact: the lowest gaps $gap_1 = M_2 - M_1$ for $\bar{s}s$, $\bar{c}c$, and $\bar{b}b$ quarkonia are nearly identical, even though the corresponding quark masses span more than an order of magnitude[3].

Calculations using the Cornell potential are shown as multiple curves corresponding to different quark masses, spanning the range from $\bar{s}s$ to $\bar{b}b$ systems. However, if one naively plots all ψ states listed in the RPP, the charmonium data appear to deviate strongly from these curves (and from the small red circles indicating theoretical expectations). The reason is well known: out of the nine listed states, only five (the ground state, the first excitation, and three additional states lying near the horizontal dashed lines) are genuine $\bar{c}c$ quarkonia. The remaining four states are the **tetraquarks** of the composition $\bar{c}c\bar{q}q$. This striking difference between charmonium and bottomonium arises from the very different locations of two-meson thresholds in the two systems.

We emphasize these points at the outset because they illustrate dramatic changes taken place in the field. For nearly 50 years, hadrons were classified almost exclusively as mesons or baryons, while all other candidates were relegated to the category of *exotics*, mostly with questionable experimental status. Today, it is evident that roughly half of the observed states in the vector ($J^P = 1^-$) and axial-vector ($J^P = 1^+$) charmonium channels are in fact tetraquarks $\bar{c}c\bar{q}q$.

While their experimental status is excellent, let us add a brief comment on nomenclature further highlights the fluid state of the field. Axial tetraquarks have now acquired their own designation in the RPP, $T_{\bar{c}c}$, whereas

---

[1] We use this as an exercise in Appendix 4.A, where we show how to solve it using Wolfram Mathematica.

[2] It also removes the ambiguity associated with an additive constant in the interquark potential and quark masses.

[3] Remarkably, the higher gaps also show only a weak dependence on the quark mass. This behavior is a consequence of specific features of the Cornell potential, in which the Coulombic $1/r$ and confining r terms partially cancel.
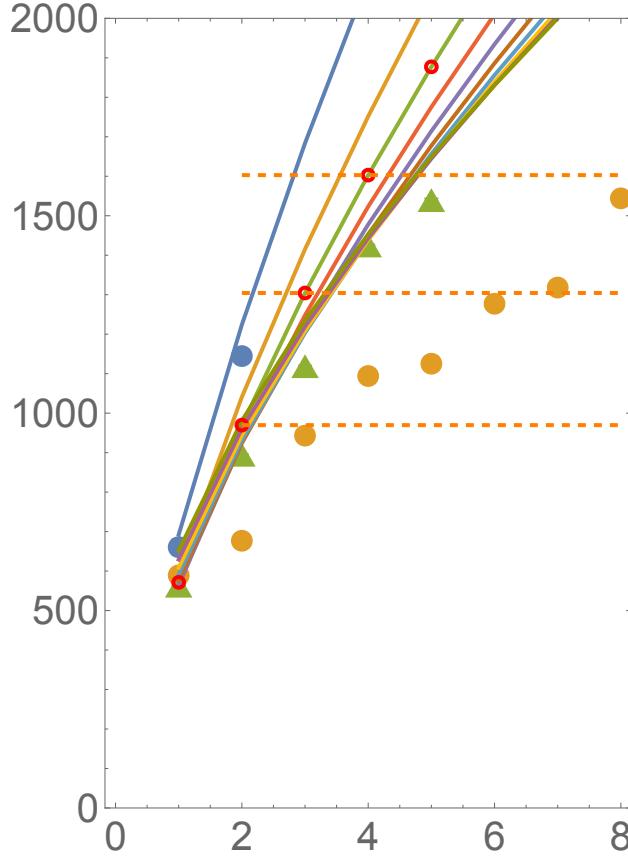
Fig. 4.1.1 Gaps between levels $gap_n = M_{n+1} - M_1$ versus n. Blue disks, orange disks, and green triangles correspond to $\bar{s}s$, $\bar{c}c$, and $\bar{b}b$ quarkonia (ϕ, ψ, and Υ families, $J^{PC} = 1^-$), respectively. The curves show gaps calculated using the Cornell potential for quark masses $0.5, 1.0, 1.5, \ldots, 5\,\mathrm{GeV}$ from left to right. Horizontal dashed lines and small red circles indicate calculated values for successive charmonium states.

vector states are still commonly labeled as ψ, η_c, and so on. This reflects the fact that in the axial channel the $\bar{q}q$ pair forms an isovector ($I = 1$, with quantum numbers analogous to the pion), whereas in the vector channel it corresponds to its chiral partner, the σ.

The theoretical literature on tetraquark structure suggests several possible interpretations: (i) deuteron-like states, bound weakly near threshold; (ii) diquark-antidiquark configurations with two characteristic spatial scales; or (iii) genuinely compact tetraquarks. We will not review these possibilities in detail here, as our primary interest lies in compact multiquark states composed of quarks with equal masses, such as compact tetraquarks, pentaquarks, and hexaquarks. In such systems, there are good reasons to expect that the lowest states are spherically symmetric in the corresponding multidimensional configuration spaces. Accordingly, the only charm-related tetraquark we will discuss explicitly is $T_{\bar{c}\bar{c}cc}$, for which there are strong indications that it belongs to the compact tetraquark category.

4.2 From Wilson lines to effective potentials

Static potentials, introduced by K. Wilson, are defined via the so-called Wilson loops, constructed from Wilson lines

$$W \equiv P \exp\left[i \int A_4^a(\lambda^a/2)\,dx^4\right] \tag{4.1}$$

of the gauge field taken along the Euclidean time direction $\tau = x^4$. Here λ^a are the Gell-Mann matrices, and the factor $1/2$ reflects the fact that quarks transform in the fundamental[4] representation of $SU(3)$. Provided the gauge fields are periodic in τ, W is a gauge-invariant holonomy operator[5]. By construction, W is a unitary matrix describing the rotation of the quark color degree of freedom.

The static potential for a quark-antiquark pair is obtained from the correlator of two Wilson lines, one of them Hermitian conjugated, separated by a spatial distance r,

$$\exp[-V(r)\tau] = \left\langle 1 - \frac{1}{N_c} \operatorname{Tr} W(0)\, W^\dagger(r) \right\rangle. \tag{4.2}$$

Expressions for the static potentials involving three quarks will be discussed in Sec. 6, and for tetraquarks in Sec. 7.

At lowest order in perturbation theory, the two Wilson lines are connected by a single gluon propagator, leading to the Coulomb interaction. Unlike in QED, higher-order diagrams in QCD include gluon self-interactions, which generate the running coupling in the Coulomb potential,

$$V_C(r) = -\frac{4}{3} \frac{\alpha_s(r)}{r}, \tag{4.3}$$

dominant at short distances.

Nonperturbative calculations of the static potential have been the subject of extensive lattice studies since the 1980s. These works established that at large distances the potential exhibits *linear confinement*,

$$V_{\text{string}}(r) = \sigma\, r, \tag{4.4}$$

generated by a flux tube (or confining QCD string) composed predominantly of longitudinal electric field, stabilized by circulating magnetic currents.

By combining the short-distance Coulomb interaction with the long-distance linear term, one arrives at the so-called Cornell potential. Solving the nonrelativistic Schrodinger equation with this potential yields spectra for charmonium and bottomonium that are already in qualitative agreement with experimental data.

While these results are well known, a more detailed examination reveals several open issues. One of them concerns the degree to which the effective potential is known at intermediate distances.

The first issue is that a quantum QCD string can vibrate, implying that the linear potential must be supplemented by so-called Lüscher terms, which scale as $\sim 1/r$ and $1/r^3$ [Luscher, 1981]. Disentangling the Lüscher term from the Coulomb contribution is nontrivial. Moreover, the Nambu-Goto geometric string action leads to the Arvis potential [Arvis, 1983],

$$V_A = \sigma\, r \sqrt{1 - \frac{\pi}{6} \frac{1}{\sigma r^2}}, \tag{4.5}$$

which reproduces the universal Lüscher term but cannot be extended to small r.

(Effective models that reproduce confinement, and the QCD string structure in particular, are often based on variants of dual superconductor models. Unfortunately, these rely on effective Lagrangians containing scalar fields that do not appear in the fundamental QCD Lagrangian.)

A second issue arises in QCD with light quarks, where QCD strings can break through the creation of light quark-antiquark pairs. As a result, the static linear potential should eventually saturate to an r-independent constant related to the $\bar{D}D$ or $\bar{B}B$ thresholds, typically for $r \gtrsim 1\,\text{fm}$. Dynamical level-crossing arguments suggest that the effective potential in this regime is a superposition of linear and constant contributions.

---

[4] In the chapter discussing glueballs those will be substituted by adjoint color generators.

[5] The average of W, known as the Polyakov line, plays an important role in finite-temperature field theory, which will not be discussed in this review.

We approach these issues from two complementary perspectives. First, quarkonium spectroscopy can be used to extract more precise information about effective potentials. Second, we consider explicit models of vacuum gauge fields, substitute them into the definition of the static potential, and test whether the resulting potentials are consistent with spectroscopic data (or lattice results). Guided by visualizations such as Fig. 3.C.1, we explored in Ref. [Shuryak and Zahed, 2021a] the consequences of modeling the vacuum as a gas of instantons or as a gas of closely bound instanton-anti-instanton pairs (molecules). Below, we extend this analysis to systems of three and four quarks, and proceed to calculate the associated spin-dependent potentials. As the reader will see, in nearly all cases the resulting potentials are in reasonable agreement with known phenomenology.

4.2.1 Central potential and instanton-anti-instanton molecules

The definition of the Wilson line (4.1) involves a path-ordered exponential because gauge fields at different points generally correspond to color rotations that do not commute. Fortunately[6], for instanton gauge fields of the form

$$A_\mu^a = \frac{2}{g} \frac{\bar{\eta}_{\mu\nu}^a \rho^2 x^\nu}{x^2(x^2 + \rho^2)} \,, \tag{4.6}$$

the color rotations $A_4^a \, d\tau$ along a straight line $x^\mu = (\mathbf{z}, \tau)$ occur around a fixed direction in color space, namely $z^a/|\mathbf{z}|$, for all τ. This property eliminates the need to explicitly evaluate the path ordering in W and allows for an analytic expression. (In singular gauge, the angle of color rotation is $\theta = \pi - \pi z/\sqrt{z^2 + \rho^2}$.)[7]

Assuming an ensemble of uncorrelated instantons with fixed density N/V_4, the Wilson lines exponentiate, and the static potential reduces to a correlator over a single instanton,

$$V_{\text{inst}} = \frac{N\rho^3}{V_4} \int \frac{d^3 z}{\rho^3} \big[1 - \cos(\theta_1)\cos(\theta_2) - \sin(\theta_1)\sin(\theta_2)(\mathbf{n}_1 \cdot \mathbf{n}_2)\big]. \tag{4.7}$$

The integral over the instanton position converges because at large distances both angles vanish and the integrand tends to zero. In Fig. 4.2.1 we compare the resulting potential with the linear part of the Cornell potential. The instanton-induced contribution to $V_C(r)$ is shown as the solid line for the density

$$n \equiv n_{\text{mol}} + n_{\text{ILM}} = 7 \, \text{fm}^{-4} \,. \tag{4.8}$$

This density is approximately a factor of two smaller than that suggested by the triangles and extrapolation lines in Fig. 3.D.1(b).

The instanton-induced central potential comes remarkably close to the phenomenological potential in the phenomenologically important intermediate region $r \lesssim 3 \, \text{GeV}^{-1}$. Assuming this agreement is meaningful, we proceed below to compute spin-dependent effects, and will show that these results are likewise reasonable.

Note that for this choice of parameters the diluteness parameter is $\kappa \approx 1$. In other words, the ensemble of $I\bar{I}$ molecules is rather dense, with a mean interparticle spacing

$$R_{\text{dense}} \equiv n^{-1/4} = 0.61 \, \text{fm} \approx 2\rho \,.$$

While this may appear surprisingly dense, one should recall that an $I\bar{I}$ molecule does not consist of two independent instantons. Their gauge fields and actions partially cancel, and it is precisely this cancellation that allows for a relatively large density.

---

[6] As already noted in 1978 by the Princeton group [Callan et al., 1978].

[7] Owing to the *hedgehog* structure of the instanton field, this property also holds for lines not aligned with the Euclidean time direction, a fact we will later exploit when approaching the light cone.
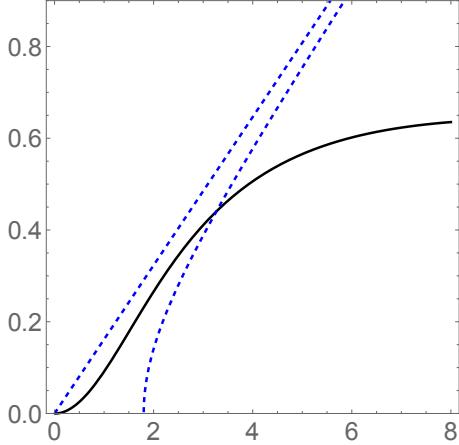
Fig. 4.2.1 Comparison of the central potentials $V_C(r)$ as a function of the interquark distance r in GeV^{-1} (with $1\,\mathrm{fm} \approx 5\,\mathrm{GeV}^{-1}$). The solid line shows the potential derived from the dense instanton ensemble. The confining flux-tube contribution is illustrated by two blue dashed lines: the upper line corresponds to the classical linear string, while the lower line represents the Arvis potential, which accounts for quantum string vibrations [Arvis, 1983].

Before proceeding further, let us consider a well-studied example, the bottomonium system, to assess how differences between the linear and instanton-induced potentials at $r \gtrsim 1\,\mathrm{fm}$ are reflected in the mass spectrum.

The levels of $\bar{b}b$ states obtained using the two potentials are shown in Fig. 4.2.2. We display the nonrelativistic energies of four radial excitations in the S-wave ($L = 0$) channel. Since spin-dependent interactions are not included at this stage (they will be discussed in the next subsections), the calculation corresponds to spin-averaged combinations of the $J = 1$ Υ and $J = 0$ η_b states. The difference between the two potentials at large distances, $r \gtrsim 5\,\mathrm{GeV}^{-1} \approx 1\,\mathrm{fm}$, indeed leads to distinct predictions for highly excited radial states. At large n, the instanton-induced potential does not reproduce the expected Regge behavior $m_n^2 \sim n$. However, for the specific bottomonium states considered here, the practical difference between the two potentials is small. (In the matrix elements for lighter quark systems discussed below, we will nevertheless continue to use wave functions obtained with the standard Cornell potential.)

4.2.2 Spin-dependent potentials

Spin-dependent interactions of heavy quarks, formulated using temporal Wilson lines with additional field insertions, were first derived in Ref. [Eichten and Feinberg, 1981]. They can be expressed in terms of five a priori independent potentials (see Appendix A for definitions), which contribute as

$$
\begin{aligned}
V_{SD} =\ & \left(\frac{S_Q \cdot L_Q}{2m_Q^2} - \frac{S_{\bar{Q}} \cdot L_{\bar{Q}}}{2m_{\bar{Q}}^2} \right) \left(\frac{1}{r} \frac{d}{dr} \big(V(r) + 2V_1(r) \big) \right) \\
& + \left(\frac{S_{\bar{Q}} \cdot L_Q}{m_Q m_{\bar{Q}}} - \frac{S_Q \cdot L_{\bar{Q}}}{m_{\bar{Q}} m_{\bar{Q}}} \right) \left(\frac{1}{r} \frac{d}{dr} V_2(r) \right) \\
& + \frac{(3 S_Q \cdot \hat{r}\, S_{\bar{Q}} \cdot \hat{r} - S_Q \cdot S_{\bar{Q}})}{3 m_Q m_{\bar{Q}}} V_3(r) + \frac{1}{3} \frac{S_Q \cdot S_{\bar{Q}}}{m_Q m_{\bar{Q}}} V_4(r)\,.
\end{aligned}
\tag{4.9}
$$

Here $\mathbf{S}_{Q,\bar{Q}}$ and $\mathbf{L}_{Q,\bar{Q}}$ denote the spin and orbital angular momenta of the $\bar{Q}Q$ pair. $V(r)$ is the central static potential, while $V_1(r)$ and $V_2(r)$ arise from inserting a chromo-electric or chromo-magnetic field, respectively,
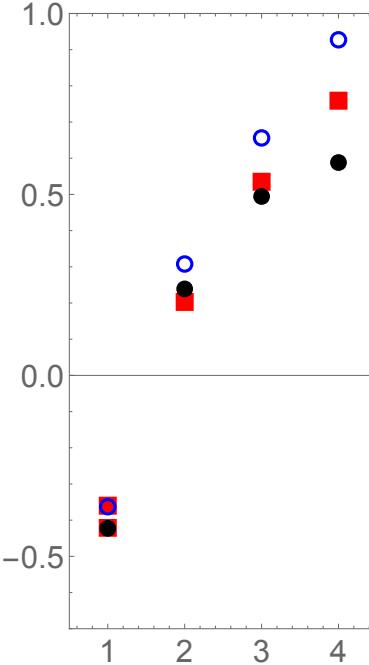
Fig. 4.2.2 Nonrelativistic energies $M_i - 2M_b$ for spin-averaged $\bar{b}b$ states as a function of the principal quantum number n. The five red squares indicate the experimentally measured masses of $\Upsilon(1S)$, $\eta_b(1S)$, $\Upsilon(2S)$, $\Upsilon(3S)$, and $\Upsilon(4S)$. Blue circles correspond to the standard Cornell potential, while black filled circles are obtained using the instanton-induced potential shown in Fig. 4.2.1.

into the temporal Wilson loop. The spinspin and tensor contributions, $V_3(r)$ and $V_4(r)$, follow from the insertion of two chromo-magnetic fields. Equation (4.9) is exact up to order $1/m_Q^2$. The spinspin potential is further constrained by $V_4(r) = 2\nabla^2 V_2(r)$ [Eichten and Feinberg, 1981].

Lorentz invariance relates the central potential $V(r)$ to the spinorbit potentials $V_1(r)$ and $V_2(r)$ through the Gromes relation [Gromes, 1984],

$$V(r) = V_2(r) - V_1(r). \tag{4.10}$$

Spin-dependent contributions generated by the confining string were discussed by Buchmüller [Buchmuller, 1982] and others [Pisarski and Stack, 1987, Gromes, 1984]. Since spinspin interactions are short-ranged, only the spinorbit terms survive at large transverse separation $b_\perp$. This is evident from Eq. (4.10), where asymptotically $V_2(r) \to 0$ and $V(r) \to -V_1(r)$. Consequently [Buchmuller, 1982, Pisarski and Stack, 1987, Gromes, 1984],

$$V_{SL,\text{string}}(b_\perp) = -\left(\frac{S_Q \cdot L_Q}{2m_Q^2} - \frac{S_{\bar{Q}} \cdot L_{\bar{Q}}}{2m_{\bar{Q}}^2}\right)\frac{\sigma_T}{b_\perp} \to -\frac{\sigma_T}{2m_Q^2 b_\perp}\, S \cdot L, \tag{4.11}$$

where $V(r) = \sigma_T r$, $\mathbf{S} = \mathbf{S}_Q + \mathbf{S}_{\bar{Q}}$, and $\mathbf{L} = \mathbf{L}_Q = -\mathbf{L}_{\bar{Q}}$. Because the electric flux tube is confined within the string, the spinorbit interaction arises solely from Thomas precession. Its sign is opposite and its magnitude is half that of the spinorbit contribution generated by the central potential. This behavior follows directly from Eqs. (4.9) and (4.10) if one assumes that $V_2(r)$ is short-ranged, implying $V(r) = -V_1(r)$. The resulting string-induced spinorbit interaction is therefore termed *scalar-like*, in contrast to the *vector-like* Coulomb-induced spinorbit interaction.

Four decades after the discovery of quarkonia and the formulation of perturbative quarkonium theory, static spinspin potentials were evaluated on the lattice using correlators of Wilson lines with explicit field-strength insertions. As shown in Ref. [Koma and Koma, 2007], while V_{SS} is indeed short-ranged, it does not fit the simple vector-plus-scalar exchange paradigm. Instead, pseudoscalar glueball exchange was proposed as
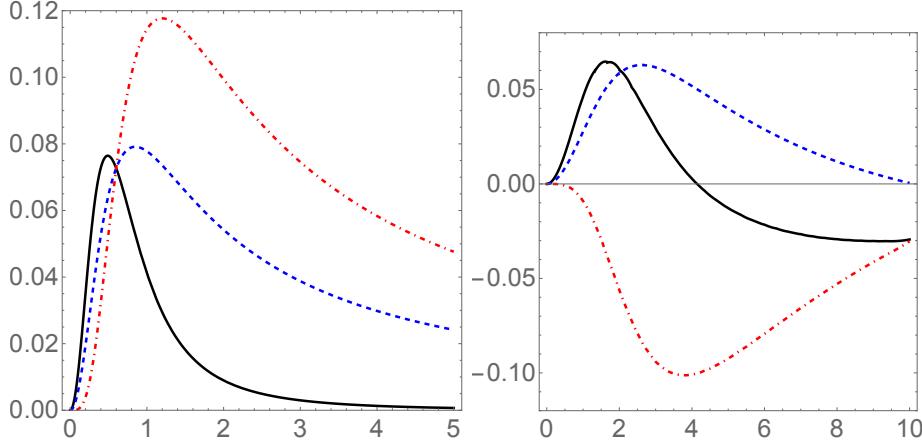
Fig. 4.2.3 Perturbative (left) and instanton-induced (right) spin-dependent potentials for charmonium. The black solid, blue dashed, and red dash-dotted curves correspond to $r^2 V_{SS}$, $r^2 V_{SL}$, and $r^2 V_T$ (in GeV^{-1}), respectively, plotted as functions of r in GeV^{-1}.

an explanation. A decade later, Ref. [Kawanai and Sasaki, 2015] not only extracted the central and spinspin potentials for the $\bar{c}c$ and $\bar{c}s$ systems with high precision, but also employed them in effective Schrodinger equations, achieving good agreement with spectroscopic data. In Fig. 4.2.3, we display (as a solid line) their exponential fit for $\bar{c}c$,

$$V_{SS}^{\bar{c}c} \equiv \alpha e^{-\beta r}, \qquad \alpha = 2.15\,\text{GeV}, \quad \beta = 2.93\,\text{GeV}\,. \tag{4.12}$$

In the instanton vacuum, all potentials appearing in Eq. (4.9) are directly related to the central potential $V(r) = V_C(r)$ [Callan et al., 1978, Eichten and Feinberg, 1981, Yakhshiev et al., 2017],

$$V_C(r) + 2V_1(r) \to 0, \qquad V_2(r) \to \frac{1}{2}V_C(r), \qquad V_3(r) \to -\left(\frac{1}{r}V_C' - V_C''\right). \tag{4.13}$$

These relations lead to the simplified spinorbit interaction

$$\left[\frac{1}{2m_Q^2}\frac{1}{r}\frac{d}{dr}V_C(r)\right](S_Q + S_{\bar{Q}}) \cdot L_Q \equiv \left[\frac{1}{2m_Q^2}\frac{1}{r}\frac{d}{dr}V_C(r)\right]S \cdot L\,. \tag{4.14}$$

This simplification follows from the self-duality of the gauge fields, $\mathbf{E}^a = \pm\mathbf{B}^a$, in Euclidean space. Schematically, the central electric correlator $\langle E_i^a(x)[x,0]^{ab}E_i^b(0)\rangle$ is then directly related to the spinorbit correlator $\langle E_i^a(x)[x,0]^{ab}B_i^b(0)\rangle$ and to the spinspin correlator $\langle B_i^a(x)[x,0]^{ab}B_i^b(0)\rangle$.

The derivation of the corresponding potentials for a sloped Wilson loop on the light front follows the same reasoning as in Refs. [Callan et al., 1978, Yakhshiev et al., 2017]. The only difference is that the relevant integration becomes cylindrical rather than spherical. The resulting central potential carries over to the light cone as

$$V_C(r \to b_\perp) = \left(\frac{4\kappa}{N_c\rho}\right)\mathbf{I}\left(\frac{b_\perp}{\rho}\right)\,. \tag{4.15}$$

We note the sign flip of the spinorbit contribution between the confining (string-induced) potential and the instanton-induced potential, as well as the sign flip of the instanton tensor interaction relative to the perturbative one-gluon spintensor contribution.

4.3 Bridging together the worlds of heavy and light quarks

Let us begin by introducing the concept through the notion of approximate universality of heavy-quark spectra, namely their *unexpectedly weak* dependence on the quark mass.

For purely Coulombic systems, such as the hydrogen atom, the Coulomb potential α/r contains no intrinsic dimensional parameter. As a result, the bound-state energies E_n scale linearly with the electron mass m. In the asymptotic heavy-quark limit, quarkonia are expected to be dominated by an approximately Coulombic interaction, and one would therefore anticipate a similar scaling, $E_n \sim m$.

This expectation is not borne out by real-world $\bar{c}c$ and $\bar{b}b$ quarkonia. In Fig. 8.A.1 we show the (spin-weighted) spectra of charmonia and bottomonia, *counted from their respective ground states*, J/ψ and Υ. Despite the quark masses differing by roughly a factor of three, the excitation spectra are nearly coincident. In particular, the $2S - 1S$ gaps are 0.605 and 0.572 GeV, respectively, differing by only a few percent. Why should this be the case?

A traditional explanation invokes the Cornell potential, which combines a Coulombic $-1/r$ term with a confining $\sim r$ contribution. One might speculate that their effects push the level spacings in opposite directions, leading to an accidental cancellation. This possibility is easy to test[8]. Adopting the Cornell potential

$$V = -\frac{0.641}{r} + 0.113\, r\,, \tag{4.16}$$

(with all energies in GeV and r measured in GeV^{-1}), we computed the $1S$, $2S$, $3S$, and $4S$ masses and the corresponding gaps, shown as open blue points in Fig. 8.A.1. One finds that the higher gaps actually agree even better than the first. Thus, the observed universality is not the result of a single accidental cancellation; it persists and even improves for higher excitations.

This observation naturally raises the question: what form of potential would lead to exact universality? If the quark mass is rescaled by a factor ξ and distances are rescaled by $\xi^{-1/2}$, the kinetic energy remains unchanged. For a power-law potential $V \sim r^\alpha$, the potential energy rescales as $\xi^{-\alpha/2}$. The so-called *Martin potential*, introduced for charmonium,

$$V_{\mathrm{Martin}} = -9.054 + 6.870\, r^{0.1}\,, \tag{4.17}$$

rescales as $\xi^{-0.05}$. Does this explain the observed universality? Our calculations show that it does not: the agreement is far less accurate than the empirical universality of the spectra.

For a logarithmic potential, $V \sim \log r$, a rescaling of the mass simply shifts all energy levels by an additive constant, $-(1/2)\log \xi$, while leaving the level spacings invariant. Thus, the quarkonium spectra suggest that the effective interquark potential is, to a good approximation, logarithmic. Why should this be so?

To address this point, we recalculated the dependence of the spectra on the quark mass and present the results in Fig. 4.3.1. The left panel shows the results for the Cornell potential (4.16), while the right panel corresponds to the instanton-induced potential. In both cases, as the quark mass varies by more than an order of magnitude, from 1 to 15 GeV, the gaps between the spherical S-wave states change only modestly, by about 0.1 GeV in the Cornell case.

The key point illustrated by these plots is that the universality between charmonium and bottomonium arises because the spectral gaps depend only weakly on the quark mass. However, the detailed behavior differs qualitatively: for the Cornell potential the mass dependence exhibits a minimum, whereas for the instanton-induced potential it exhibits a maximum. The true interaction law must therefore lie somewhere in between.

In principle, hadronic spectroscopy can thus provide information about rather subtle features of the interquark potential. In practice, however, the available data are limited: for bottomonia we know the masses of four S states, while for charmonia only the $1S$ and $2S$ states (and hence a single gap) are well established.

---

[8] Note that in doing so we remove relativistic corrections present in the experimental masses.

We have not overlaid the experimental points on Fig. 4.3.1 to avoid cluttering the plot. Doing so would not allow one to discriminate between the two cases, and we are therefore forced to conclude that present data do not reveal whether the observed universality corresponds to a minimum or a maximum in the mass dependence. At present, we cannot decisively determine which potential is favored.
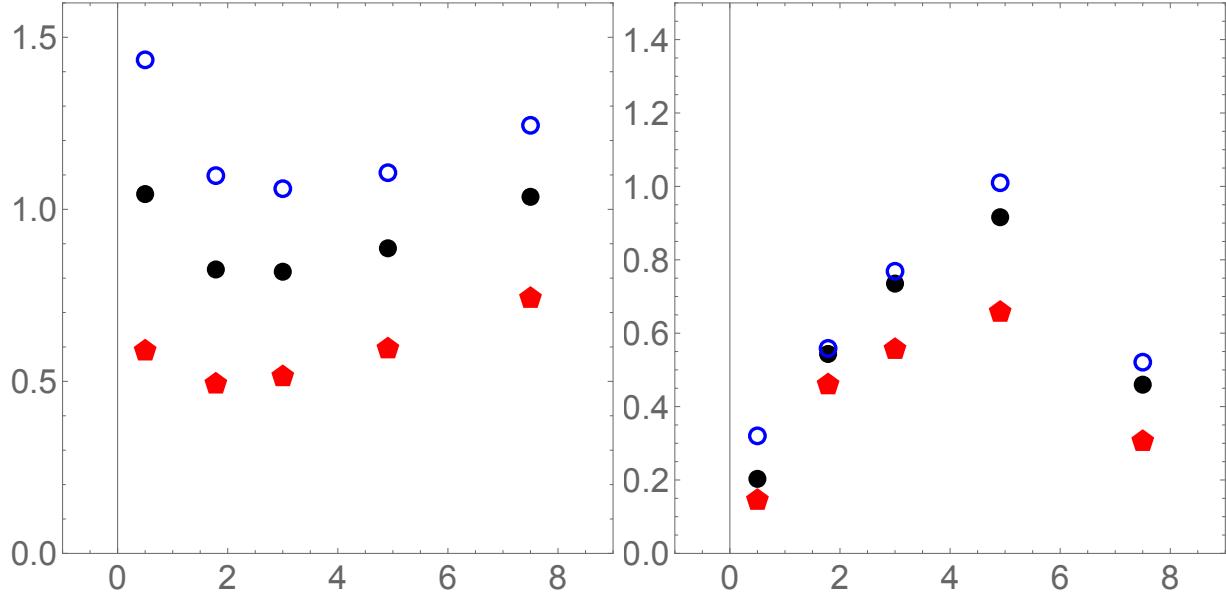
Fig. 4.3.1 Spectral gaps $E(2S) - E(1S)$, $E(3S) - E(1S)$, and $E(4S) - E(1S)$ (in GeV, from bottom to top) as functions of the quark mass m_q (in GeV). The chosen values are 0.5 (strange), 1.7 (charm), 3, 4.7 (bottom), and 7.5 GeV. The left panel corresponds to the Cornell potential (4.16), while the right panel shows the instanton-induced potential.

Finally, let us address the broader idea of *bridging the worlds of light and heavy quarks.* The vacuum paths of heavy quarks are well approximated by straight lines along the time direction, namely Wilson lines. In contrast, the vacuum paths of nearly massless quarks are completely different: instanton zero modes correspond to relativistic motion of light quarks bound within instantons. At first sight, these two pictures appear impossible to reconcile.

However, suppose we are not interested in the detailed dynamics of quarks inside instantons, but only in how they propagate *between* them. After appropriate resummations, one arrives at the notion of constituent quarks with effective masses $M_{u,d} \sim 400$ MeV, generated by the chiral condensate.

Now imagine temporarily setting aside chiral dynamics and using the $\bar{Q}Q$ potential derived from Wilson lines in an $I\bar{I}$ background. At large distances the potential saturates, $V(r \gtrsim 0.8 \, \text{fm}) \sim 800$ MeV. Per quark, this corresponds to a mass shift $\Delta M \sim V/2 \approx 400$ MeV. Thus, somewhat unexpectedly, two frameworks that appear radically different merge in a rather smooth way.

This *bridging* idea is particularly appealing in the strange sector. The effective strange constituent quark mass is $M_s \sim 500$ MeV, roughly three times smaller than for charm and an order of magnitude smaller than for bottom. Yet the spectral gap for the $\phi = \bar{s}s$ vector mesons shown in Fig. 4.1.1 is quite similar to those of heavier quarkonia. Once again, quarkonium-like nonrelativistic Schrodinger equations and chiral BetheSalpeter equations yield nearly identical results in this case.

Appendix

4.A Solving Schrodinger equations in Wolfram Mathematica

Standard quantum mechanics courses include well-known examples of analytic solutions, such as the harmonic oscillator and the hydrogen atom. In practice, however, one often has to solve the Schrodinger equation numerically, in a variety of dimensions and physical settings. In one dimension, several numerical solvers are available that start from a prescribed value of the wave function and its first derivative at one end of the domain, and then tune the energy eigenvalue to obtain acceptable behavior at the other end. In higher dimensions, variational methods have traditionally been used most often.

Recent versions of WOLFRAM MATHEMATICA have significantly simplified such calculations. There is no longer a need to rely on numerical PDE solvers that propagate solutions from one side of the domain to the other. Instead, the command `NDEigensystem` provides a much more convenient approach, directly yielding eigenvalues and eigenfunctions of a given differential operator. In this way, one can obtain wave functions and energies for as many states as required. Below we present an example that computes seven bottomonium states. Note that `u[x]` corresponds to the radial wave function $\psi(r)$, energies and masses are expressed in GeV, and the radial coordinate r is measured in inverse GeV units.

```
In: VCornell[r_] := -(4/3)*0.4/r + (.4^2)*r;
Mb = 4.8;
\[ScriptCapitalL]b = (-u''[x] - 2/x*u'[x])/Mb + (2*Mb + VCornell[x])*
    u[x];
{valb, funb} =
  NDEigensystem[\[ScriptCapitalL]b, u[x], {x, 0, 40}, 7,
    Method -> {"Eigensystem" -> "Arnoldi",
      "SpatialDiscretization" -> {"FiniteElement", {"MeshOptions" -> \
{MaxCellMeasure -> 0.001}}}}];
valb

Out: {9.42516, 9.98909, 10.315, 10.5758, 10.8034, 11.01, 11.2015}

In: Plot[{-funb[[1]], -funb[[2]]}, {x, 0, 10}, PlotRange -> {-1, 3}]
```

The experimentally measured masses are $9.4604, 10.0234, 10.3551, 10.5794, 10.8852$, and $11.$ GeV.

The final line of the code illustrates how to plot the wave functions; the resulting smooth curves are shown in Fig. 4.B.1. Plotting wave functions is particularly useful, as it allows one to verify that the number of nodes matches the expected ordering of the states.

In the present example this issue does not arise, but it is worth noting that the states returned by `NDEigensystem` are not necessarily ordered from lowest to highest energy, as one might expect. Instead,

they are listed according to the magnitude of the *modulus* of the eigenvalues, which can sometimes lead to confusion in their ordering.

This method also works in two dimensions (we will use it for the forward part of baryon wave functions defined on a triangular domain) and in three dimensions. Unfortunately, it does not extend to four dimensions, which will be required for the pentaquark applications discussed below.

4.B Ritz variational method: simple examples

Here we compare direct numerical solutions with the widely used variational method, e.g. employed nowadays in multidimensional applications such as tetraquarks.

The method, proposed by W. Ritz in 1909 for general elliptic partial differential equations, consists of minimizing the energy using a chosen set of basis functions. These basis functions need not form an orthogonal set, although orthogonality can simplify the calculations. In the example below, we compare the variational approach with numerically obtained solutions for a linear potential in the bottomonium problem. We use ten variational coefficients c_i as parameters and minimize the ratio of the expectation value of the Hamiltonian to the norm of the wave function.

```
In: nmax = 10; Radii = Table[0.1*n, {n, 1, nmax}];
Cset = Array[c, nmax]
uMin[x_] := Sum[c[n]*Exp[-x^2/2/Radii[[n]]^2], {n, 1, nmax}];
(* select WF as a set of Gaussians *)
\[Psi]H\[Psi] = Expand[uMin[x]*((-D[uMin[x], {x, 2}] - (2/x)*D[uMin[x], x])/Mc +  VcK[x]*uMin[x])];
\[Psi]H\[Psi]av = Integrate[\[Psi]H\[Psi]*x^2, {x, 0., Infinity}];
norm = Integrate[uMin[x]^2*x^2, {x, 0., Infinity}];
cond := c[1]^2 < 1 && c[2]^2 < 1 && c[3]^2 < 1 && c[4]^2 < 1 &&
  c[5]^2 < 1 && c[6]^2 < 1 && c[7]^2 < 1 && c[8]^2 < 1 && c[9]^2 < 1 &&
   c[10]^2 < 1
In: NMinimize[{\[Psi]H\[Psi]av/norm, cond},
 {c[1], c[2], c[3], c[4], c[5], c[6], c[7], c[8], c[9], c[10]}]
Out: {0.415895, {c[1] -> 2.30567*10^-8, c[2] -> -1.53966*10^-7,  c[3] -> 9.77366*10^-7,
c[4] -> -4.90733*10^-6, c[5] -> 0.0000181519, c[6] -> -0.0000475488, c[7] -> 0.0000847055, c[8] -> -0
Show[Plot[(-uMin[x]/Sqrt[norm]) /. {c[1] -> 2.3056657172291844`*^-8, c[2] -> -1.5396634565426175`*^-7
c[4] -> -4.907333728277542`*^-6, c[5] -> 0.000018151944935911747`,c[6] -> -0.00004754881284624645`, c
```

The upper figure compares smooth curve obtained via *NDEigensystem* to (slightly wiggling) variational result. The error in WF and energy is about 1%.

In order to repeat it for the next level, one has to calculate scalar product of the ground state to the next, and put it as a condition into *NMinimize*: in this case it generates the lower plot. Note that the agreement between curves is fair, but accuracy is significantly degraded, already for the second state it is about 10%. Perhaps playing more with radii can get a bit more accurate results.

In general, NMinimize is not very stable and in some cases it get confused, working only if the number of parameters is reduced. Also restricting the minimization domain by extra conditions sometimes helps to get to the right minimum.
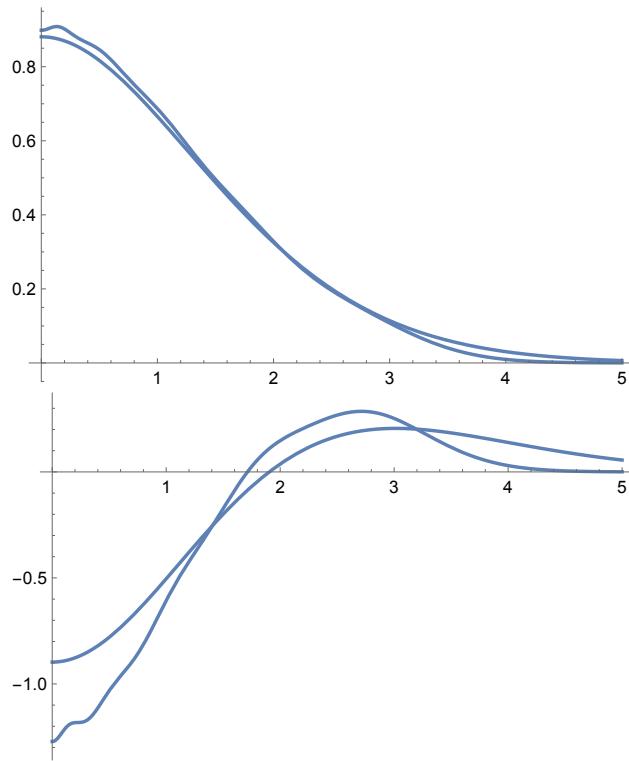
Fig. 4.B.1 Comparison of the first and second WFs, between numerical and variational solutions.

Chapter 5
Glueballs

5.1 Introduction

Glueballs are the simplest color-singlet bound states of non-Abelian gauge theory, composed entirely of gluonic degrees of freedom. As such, they provide a unique window into confinement, dynamical mass generation, and the role of topology in quantum chromodynamics (QCD). In the pure Yang-Mills theory, where quark degrees of freedom are absent, the glueball spectrum is well defined and has been studied extensively using lattice gauge theory, which remains the most reliable nonperturbative approach to this problem.

One of the most obvious question in QCD is why the observed hadrons are made of quarks and not of gluons. It appears that glueballs are much heavier than typical quark-made hadrons, and therefore they have large widths and/or complicated decay patterns in the real world, making them difficult to identify. But why are glueballs heavier? What are their masses, radii and other parameters in a purely gluonic world, and how do they change if one includes light quarks?

Three decades ago [Schäfer and Shuryak, 1995] have shown that instantons lead to a strong attractive force in the $J^{PC} = 0^{++}$ channel, which results in the scalar glueball being much smaller in size than other hadrons (including the pions). In the pseudoscalar 0^{-+} channel the corresponding force is repulsive, and in the 2^{++} case the instanton effect is absent. Furthermore, due to the strong classical field of the instantons, these forces are even stronger as compared to the ones for mesons made of light quarks.

Early high-precision lattice calculations, particularly those employing anisotropic lattices, established the ordering of the lowest-lying glueball states and set quantitative benchmarks for their masses. These studies identified the scalar 0^{++} glueball as the lightest state, followed by the tensor 2^{++}, with the pseudoscalar 0^{-+} and higher-spin excitations appearing at significantly larger masses [Morningstar and Peardon, 1999, Chen et al., 2006]. Subsequent work with improved actions, larger operator bases, and careful continuum extrapolations has refined this picture and confirmed its stability across lattice spacings and volumes. In particular, recent high-statistics calculations have provided a reference spectrum for pure SU(3) Yang-Mills theory, covering a wide range of J^{PC} channels [Athenodorou and Teper, 2020].

While the quenched glueball spectrum is now comparatively well established, several important questions have gained renewed attention in recent years. One concerns the *internal structure* of glueballs in hadrons, including their spatial extent and form factors. Lattice studies of energy-momentum tensor matrix elements and related gravitational form factors have begun to probe the size and mass distribution of glueballs, with emerging evidence that the scalar 0^{++} state may be unusually compact compared to higher-spin excitations. Such results provide new, nontrivial constraints on phenomenological and microscopic models of glueballs. A recent review summarizes the current status of lattice calculations, experimental searches, and theoretical interpretations [Morningstar, 2025].

Another major direction concerns the fate of glueballs in full QCD. When light quarks are dynamical, pure-glue operators can mix with flavor-singlet $q\bar{q}$ states, particularly in the scalar and pseudoscalar channels. This mixing complicates the identification of experimental candidates and blurs the connection between

quenched lattice spectra and observed isoscalar mesons. Lattice calculations incorporating dynamical quarks have begun to address these issues directly, including studies of pseudoscalar glueball-η and η' mixing, highlighting the importance of gluonic components even in channels traditionally associated with quark model states [Jiang et al., 2023].

In parallel with lattice developments, a variety of theoretical approaches have been pursued. Functional methods based on Dyson-Schwinger and Bethe-Salpeter equations reproduce many qualitative features of the glueball spectrum and offer insight into the role of gluon mass generation and effective interaction kernels. Phenomenological models, including constituent-gluon Hamiltonians, flux-tube and bag models, and holographic constructions, provide intuitive pictures for the organization of glueball states and their Regge behavior. Among these, instanton-based approaches are particularly suggestive: topological fluctuations of the gauge field generate a momentum-dependent dynamical gluon mass and induce channel-dependent short-range interactions that are strongest in the scalar channel. Calculations in the instanton vacuum yield a dynamical gluon mass of a few hundred MeV in the infrared and motivate enhanced attraction for the 0^{++} glueball at distances comparable to the instanton size [Musakhanov and Egamberdiev, 2018, Shuryak and Zahed, 2021e].

Motivated by these developments, we construct a constituent two-gluon description of the glueball states in pure Yang-Mills theory. Our framework combines adjoint Coulomb interactions fixed by group theory, Casimir-scaled confinement with gluonic screening, and instanton-induced central and spin-dependent forces.

J= 0	1.475	(30)	(65)
0	2.755	(70)	(120)
0	3.370	(100)	(150)
0	3.990	(210)	(180)
2	2.150	(30)	(100)
2	2.880	(100)	(130)
3	3.385	(90)	(150)
4	3.640	(90)	(160)
6	4.360	(260)	(200)

Table 5.1.1 Masses (GeV) with their error bars of glueballs, for all $P = C = +$ glueballs, from [Meyer, 2004]

A popular point of view among spectroscopists (which we also shared until recently) was that, unlike hadrons made of quarks, glueballs cannot be described by *additive-type* models, in which glueball masses are built predominantly from some effective gluons, with interactions playing only a secondary role. This view was largely shaped by the traditional focus on the lowest states in the scalar, pseudoscalar, and tensor sectors.

In this paper we reverse this logic, and instead consider first a broader set of *normal* states, including radial excitations in the scalar channel and states with higher angular momentum, up to $J = 6$. As a basis we use the lattice study [Meyer, 2004], which, although not recent, addresses the largest number of states; from it we retain only the $P = C = +$ subset listed in Table 5.1.1.

What we find is that these states can in fact be described by a Schrodinger equation, without invoking any extreme assumptions. Moreover, the spectrum of *normal* glueballs turns out to resemble that of strange $\bar{s}s$ and charmed $\bar{c}c$ mesons, although it is true that the role of potential is enhanced, roughly by the factor $9/4$ expected from color algebra.

Particular emphasis is placed on the scalar and tensor channels. While the lowest 0^{++} state is dominated by the short-distance dynamics and is very compact, the other 0^{++} states are not. The J^{++} glueballs with larger angular momentum are affected by angular momentum barriers and significant S-D wave mixing. We solve the resulting coupled-channel problem and discuss the mass hierarchies and spatial structure.

This chapter is organized as follows. We introduce the constituent two-gluon Hamiltonian and specify the confining, Coulomb, instanton-induced, and spin-dependent interactions that define the model. In Sec. 5.3

we solve the resulting Schrodinger equation and present the glueball spectrum in the $C = +$ sector, including radial excitations in the scalar channel and higher-J states up to $J = 6$, together with the corresponding wave functions and radii. The lowest 0^{++} state, whose short-distance dynamics is not captured reliably in the nonrelativistic treatment, is discussed separately and motivates the relativistic Bethe-Salpeter treatment . We complement the numerical spectrum with a semiclassical WKB analysis in appendix, which clarifies the systematics of excitations and the emergence of Regge behavior, and motivates a smooth J-dependent parametrization of short-distance mass shifts. Vector glueball channels and the implications of Bose symmetry and the Landau-Yang selection rule. A number of appendices provide technical details, including the density scaling of the gluon mass, the construction and numerical evaluation of the effective potentials, the formalism and explicit calculations for tensor mixing, analytic expressions for radial integrals, parameter choices, and additional semiclassical and instanton-based derivations supporting the main text.

5.2 The Hamiltonian

5.2.1 Confining potential

We model glueballs as two effective constituent gluons in their center-of-mass frame. The relative motion Hamiltonian is

$$H = 2m_g(\eta) + \frac{\boldsymbol{p}^2}{m_g(\eta)} + V_0 + V_{\mathrm{conf}}(r) + V_C(r) + V_{\mathrm{inst}}(r) + V_{SS}(r) + V_T(r).$$

(5.1)

The confining term is taken as a screened adjoint (double) string,

$$V_{\mathrm{conf}}(r) = \sigma_8\, r\, e^{-r/r_{\mathrm{scr}}} + V_0, \quad \sigma_8 = \frac{C_A}{C_F}\sigma_3 = \frac{9}{4}\sigma_3, \quad \sigma_3 = 0.18~\mathrm{GeV}^2,$$

(5.2)

The overall shift by a constant V_0 is not known *a priori*, but fits to the spectrum yield a rather modest negative value. This shift can be avoided altogether if only level spacings, rather than absolute masses, are used in the fits.

The choice of the adjoint screening length r_{scr} is a rather delicate issue. If r_{scr} is smaller than the typical size of the states, the potential acts merely as a barrier and is unable to support bound states of larger spatial extent, producing at most a few quasibound states. To avoid this situation we place the states in a box of radius $R = 2\,\mathrm{fm}$ and take $r_{\mathrm{scr}} \sim R$, so that the potential inside the box does not decrease but instead saturates, as illustrated in Fig. 5.2.1. A more detailed discussion, as well as the relation of this potential shape to our Monte-Carlo calculations with a single instanton or $\bar{I}I$ molecule using numerically generated Wilson lines, is given in Appendix 5.C.

5.2.2 The short-distance effects

The Coulomb term follows from one-gluon exchange. Using

$$V_C(r) = \frac{\alpha_s}{r}\, T_1 \cdot T_2, \qquad T_1 \cdot T_2 = \frac{1}{2}\big(C_R - C_{R_1} - C_{R_2}\big),$$

(5.3)

one obtains the Casimir form

$$V_C(r) = -\frac{\alpha_s}{2r}\big(C_{R_1} + C_{R_2} - C_R\big).$$

(5.4)
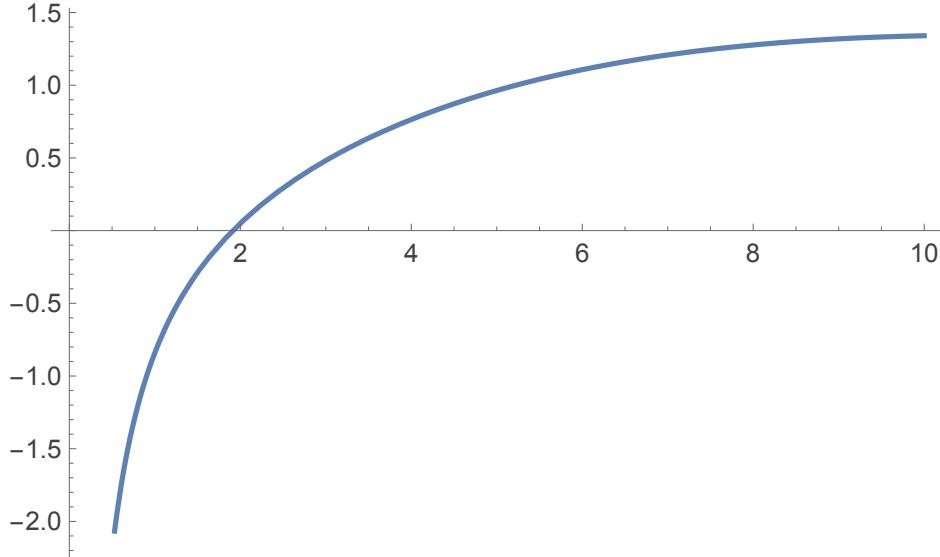
Fig. 5.2.1 Central potential $V_{conf}(r)\,(GeV)$ used versus $r\,(GeV^{-1})$

For two gluons $R_1 = R_2 = A$ with $C_A = 3$ coupled to a singlet $R = 1$ with $C_R = 0$,

$$V_C^{(gg,1)}(r) = -\frac{3\alpha_s^{\text{eff}}}{r}, \tag{5.5}$$

which is attractive and 9/4 times stronger than the $q\bar{q}$ singlet Coulomb coefficient at the same α_s^{eff}.

The instanton-induced interactions are large, but *not* parametrically larger than that for quarks. Naively, writing the field as a sum $A_{class} + A_{gluon}$ one can get their product O(1/g) which however vanishes due to random instanton orientation. Correct interaction estimate comes e.g. from the quartic term

$$g^2 A_{class}^2 A_{gluon}^2 \sim O(g^0) A_{gluon}^2$$

contributing to effective gluon mass. Note that for light quarks the instanton-induced Lagrangian is built from fermion zero modes which also do not have g. Yet numerically it is large and that is why the scalar glueball's size is only $\sim 0.2\,fm$, while the smallest of all mesons - the pion - have radius $\sim 0.5\,fm$.

Correlation functions of scalar, pseudoscalar and tensor operators calculated in [Schäfer and Shuryak, 1995] in ILM are reproduced in Fig.5.2.2. They clearly show that interaction in these three channels are attractive, repulsive, and small, respectively.

Predicted values of the lowest glueball masses and radii (from Bethe-Salpeter amplitudes) are given in the Table 5.2.1.

	scalar	pseudoscalar	tensor
$M(GeV)$	1.4 ± 0.2	$> 3.$	?
$r_{r.m.s}$ (fm)	0.21	?	0.61

Table 5.2.1 Masses and sizes of glueballs from fits to correlation functions and Bethe-Salpeter amplitudes, predicted by [Schäfer and Shuryak, 1995].

The main modification which these old calculations now would require would be in the tensor channel. True, instantons have zero stress tensor. Yet instanton-antiinstanton molecules have comparable electric and magnetic fields, and nonzero stress tensor. Therefore the effects in the tensor channel is expected to be enhanced by the ratio of their density to that of dilute instantons, denoted by parameter $\eta \sim 7$.
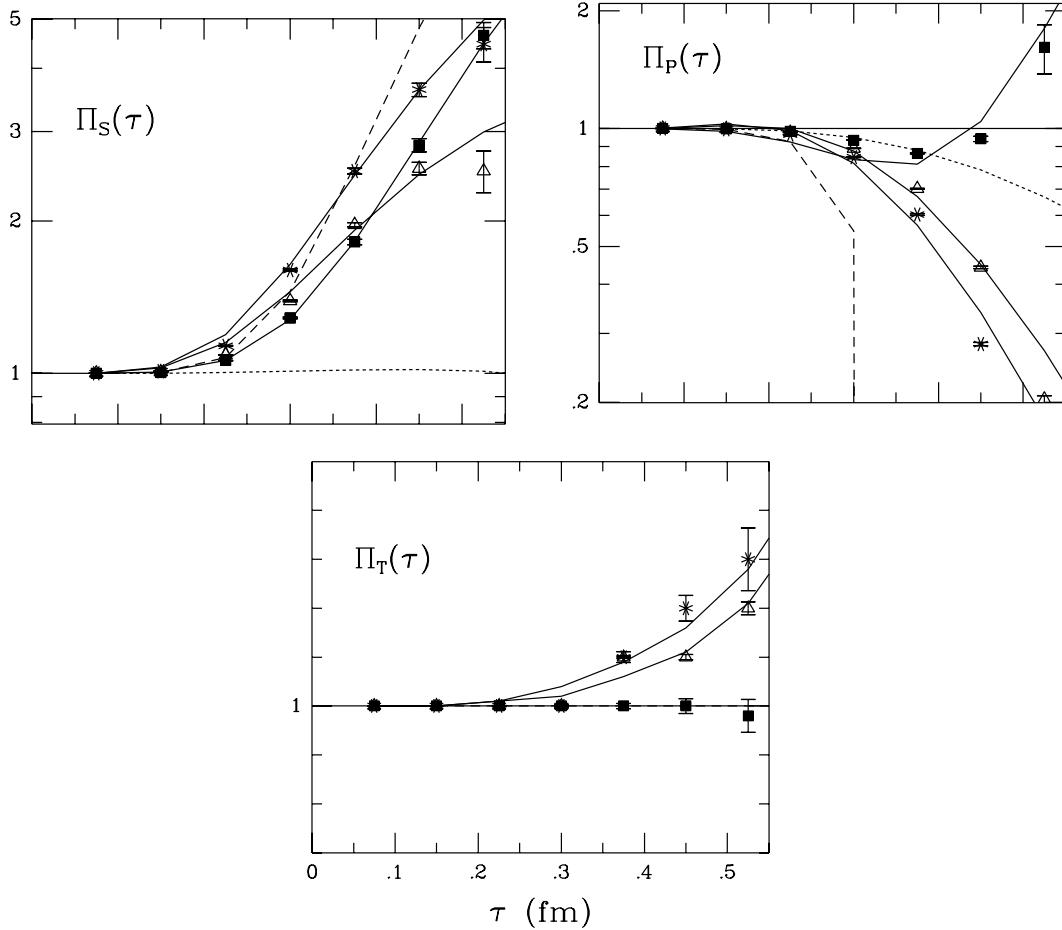
Fig. 5.2.2 Scalar, pseudoscalar and tensor glueball vacuum correlation functions normalized to the corresponding free correlators, as a function of Euclidean time between operators, from [Schäfer and Shuryak, 1995]. The results in the random, quenched and full ensembles are denoted by stars, open triangles and solid squares, respectively. The solid lines show the parametrization described in the text, the dashed line the dilute instanton gas approximation, and the dotted line the QCD sum rule calculation. The horizontal line in the second figure was added to guide the eye, the vertical scale in the third figure is 10^{-4}.

The perturbative spin-spin interaction is local $\sim \delta^3(r)$. The instanton-induced attraction is introduced as a Gaussian centered at the origin, with range ρ,

$$V_{\mathrm{inst}}(r) = -G(\eta)\, e^{-r^2/2\rho^2}, \qquad G(\eta) = G_0\, \eta, \tag{5.6}$$

with $\rho \simeq \frac{1}{3}$ fm, and is assumed to act dominantly in the scalar channel, encoding the strong instanton enhancement of 0^{++}. Because the (anti)instanton field is (anti)self-dual, the induced coupling in [Liu et al., 2024b] (see Eq. (45)) carries the 't Hooft symbols $\eta, \bar{\eta}$ and therefore projects most strongly onto the parity-even scalar combination $G^a_{\mu\nu} G^a_{\mu\nu}$ (enhancing the 0^{++} channel) while the Levi-Civita piece controls the pseudoscalar $G\tilde{G}$ channel.

The spin-dependent terms are taken in the standard form

$$V_{SS}(r) = \frac{C_{SS}(\eta)}{m_g^2(\eta)}\, \delta^{(3)}_\Lambda(\boldsymbol{r})\, \boldsymbol{S}_1 \cdot \boldsymbol{S}_2,$$

$$V_T(r) = \frac{C_T(\eta)}{m_g^2(\eta)}\, \frac{1 - e^{-r^2/\rho^2}}{r^3}\, S_{12}, \tag{5.7}$$

with $S_{12} = 3(\boldsymbol{S}_1 \cdot \hat{\boldsymbol{r}})(\boldsymbol{S}_2 \cdot \hat{\boldsymbol{r}}) - \boldsymbol{S}_1 \cdot \boldsymbol{S}_2$, and a Gaussian-smeared contact regulator

$$\delta_\Lambda^{(3)}(\boldsymbol{r}) = \left(\frac{\Lambda^2}{\pi}\right)^{3/2} e^{-\Lambda^2 r^2}, \qquad \Lambda \sim \rho^{-1}. \tag{5.8}$$

The dense-ILM scaling is implemented by

$$C_{SS}(\eta) = C_{SS}^{(0)}\eta, \qquad C_T(\eta) = C_T^{(0)}\eta, \tag{5.9}$$

with $C_T^{(0)}$ allowed to be negative, consistent with the ILM result in [Shuryak and Zahed, 2021a]. The dynamical constituent gluon mass is parametrized as

$$m_g(\eta) = m_{g0}\sqrt{\eta}, \qquad m_{g0} \simeq 0.36 \text{ GeV}, \tag{5.10}$$

5.3 Glueball spectrum from the Schrodinger equation

5.3.1 The $S = 0$, $J = L$ sector

Since the expected effective gluon mass is $O(1\,\text{GeV})$, general validity of the nonrelativistic approximation is expected to be comparable to that for charmonium. Of course, there are important differences in accuracy arising from larger potentials etc.

We begin with the simplest case, with total spin $S = 0$, so that the total and orbital angular momenta coincide, $J = L$. The calculated spectrum of several $J^{PC} = J^{++}$ channels is shown in Fig. 5.3.1. At this stage only the Coulomb and confining potentials are included, with no spin-dependent forces, as is commonly done, for example, in charmonium studies. The model parameters are chosen to reproduce the three higher states in the scalar channel, which, unlike the lowest $n = 0$ state, have normal hadronic sizes (see the table of r.m.s. radii) and are therefore less sensitive to short-distance forces. The most important parameter obtained in this way is the effective gluon mass, fitted to be [1]

$$m_g = 0.90\,\text{GeV}. \tag{5.11}$$

This implies a value of the parameter η (the enhancement of the gluon mass relative to the dilute ILM value due to instanton-antiinstanton molecules) of $\eta = 6.25$. This is close to the value $\eta \approx 7$ used in [Shuryak and Zahed, 2021a] to reproduce the central charmonium potential. That value was originally motivated by *gradient flow cooling* of lattice gauge configurations [Athenodorou et al., 2018].

To quantify the sizes and shapes of these states, we display the corresponding wave functions in Fig. 5.3.2 and list the root-mean-square radii,

$$r_{\text{r.m.s.}} = \left[\frac{\int dr\, \psi_n^2(r)\, r^4}{\int dr\, \psi_n^2(r)\, r^2}\right]^{1/2}, \tag{5.12}$$

in Table 5.3.1.

E_n (GeV)	1.92	2.79	3.29	4.0
$r_{\text{r.m.s.}}$ (GeV^{-1})	2.03	5.0	6.26	6.25

Table 5.3.1 Energies and r.m.s. radii of scalar glueballs obtained from the Schrodinger equation with the parameters defined in the text.

---

[1] For comparison, the effective masses of the strange and charmed quarks are $m_s \approx 0.5\,\text{GeV}$ and $m_c \approx 1.5\,\text{GeV}$, respectively.
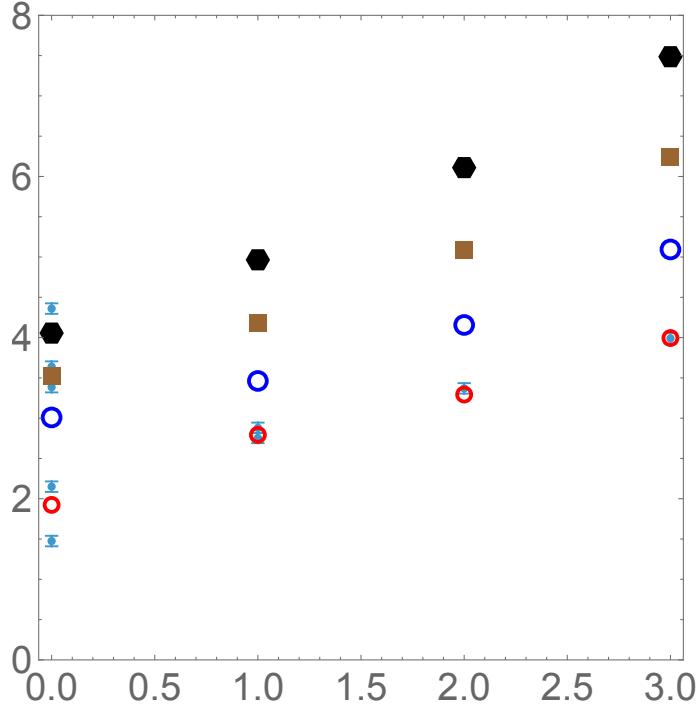
Fig. 5.3.1 The colored points show the calculated energies E_n (GeV) of the four lowest states 0^{++}, 2^{++}, 4^{++}, and 6^{++} (from bottom to top) as a function of the principal quantum number n. The smaller points with error bars are from lattice simulations in pure SU(3) gauge theory [Meyer, 2004].
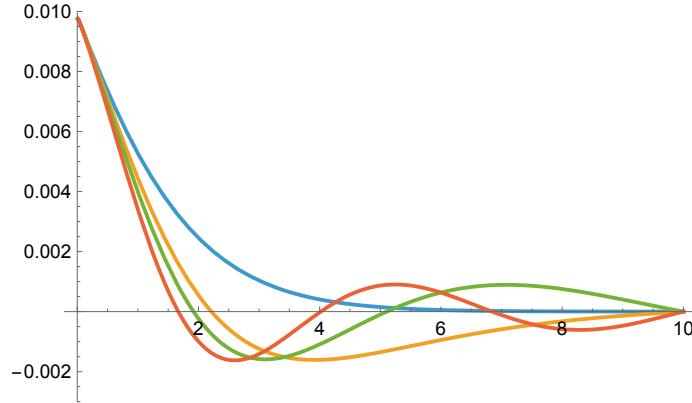
Fig. 5.3.2 Wave functions (unnormalized) $\psi_n(r)$ for $n = 0, 1, 2, 3$ as functions of r (GeV^{-1}).

Fixing the model parameters from the masses of the *normal* 0^{++} states with $n = 1, 2, 3$, which have sizes $r_{\text{r.m.s.}} \sim 5\,\text{GeV}^{-1} \sim 1\,\text{fm}$, we can then consider other channels. The predicted masses for the higher-J states with $J = 4, 6$ turn out to be close to the lattice values. This is expected, since the large centrifugal barrier increases their spatial extent and further suppresses sensitivity to short-distance forces. When discussing these states one should keep in mind that, unlike for mesons, the confining potential for glueballs is expected to be screened at large distances, rendering sufficiently large states unstable, formally corresponding to complex energies. This issue is avoided here by placing the system inside a spherical cavity: in our calculations we take a radius $R = 10\,\text{GeV}^{-1} \approx 2\,\text{fm}$ and impose Dirichlet boundary conditions.

5.3.2 The lowest 0^{++} scalar glueball

Finally, we turn to the lowest 0^{++} state with $n = 0$. As discussed in the Introduction, this state has a long history, with an r.m.s. radius predicted in [Schäfer and Shuryak, 1995] to be $r_{\text{r.m.s.}}(0^{++}, n = 0) \approx 1\,\text{GeV}^{-1} \approx 0.2\,\text{fm}$, a result confirmed three decades later in [Abbott et al., 2025]. As is clear from Table 5.3.1, neither the calculated mass nor the size of this state agrees with the lattice results. This discrepancy is not unexpected, since the present calculation does not yet include short-distance attractive spin-spin forces, whether perturbative or instanton-induced. To estimate their effect, we add a local interaction

$$V_{\text{local}}(r) = G\,\delta^3(r). \tag{5.13}$$

After doing so, we find that reproducing Meyer's value $M_{0^{++}} = 1.475\,\text{GeV}$ requires

$$G \approx 38\,\text{GeV}^{-2}.$$

The corresponding r.m.s. radius is reduced, but only to $r_{\text{r.m.s.}}(0^{++}, n = 0) \approx 1.6\,\text{GeV}^{-1}$, which is still significantly larger than expected. We therefore conclude that the lowest scalar glueball is unlikely to be described reliably within the Schrodinger framework, and we will instead treat it below using a relativistic Bethe-Salpeter approach.

5.3.3 0^{-+} glueballs

The pseudoscalar glueball channel requires separate discussion, since its quantum numbers forbid a direct continuation of the leading even-J adjoint-string-like trajectories. In the constituent-gluon picture, $C = +$ glueballs are composed of two transverse gluons bound by an adjoint flux tube. Parity and charge conjugation are determined by the orbital angular momentum L and total gluon spin S according to

$$P = (-1)^{L+1}, \qquad C = (-1)^{L+S}. \tag{5.14}$$

For $J = 0$ and $C = +$, the pseudoscalar quantum numbers 0^{-+} require $L = 1$ and $S = 1$, corresponding to a $^3P_0$ configuration. Thus, unlike the scalar 0^{++} glueball, the 0^{-+} state is intrinsically an orbital excitation and cannot lie on the same trajectory as the 0^{++}, 2^{++}, and higher even-J states.

According to [Meyer, 2004], the masses of the two lowest 0^{-+} states are

$$M_{0^{-+}}^0 = 2.250\,(60)(100), \qquad M_{0^{-+}}^1 = 3.370\,(150)(150).$$

Solving the Schrodinger equation with $L = 1$ and the shifted potential $V_{\text{conf}} + V_0$ (as done for the 0^{++} channel), we obtain

$$M_{0^{-+}}^0 = 2.65, \qquad M_{0^{-+}}^1 = 3.13.$$

Once again, the excited state is reproduced reasonably well, while the lowest state shows a noticeable discrepancy which should originate from short-distance effects. The situation in this channel is quite subtle. The perturbative spin-spin interaction in the $S_{\text{tot}} = 1$ channel is attractive, since $(\mathbf{S}_1 \cdot \mathbf{S}_2) = -1$, unlike the value $(\mathbf{S}_1 \cdot \mathbf{S}_2) = +1/2$ in $L = S = 1$ charmonium. In contrast, the instanton-induced interaction is repulsive (see, for example, Fig. 5.2.2). Moreover, for nonzero L one has $\psi(0) = 0$, so the perturbative contribution depends sensitively on the smearing of the delta function. For these reasons, we leave this issue unresolved.

5.4 Relativistic treatment of short-distance dynamics

5.4.1 Emergent 4-gluon interaction

At fixed pseudoparticle moduli, the low-mode fermion determinant generates the one-(anti)instanton induced vertices (for each instanton I and anti-instanton A) dressed with perturbative gluons of the form [Liu et al., 2024b]

$$
\Theta_I = \prod_f \left[\frac{m_f}{4\pi^2\rho^2} + i\,\psi_f^\dagger(x)\,U_I\,\frac{1}{2}\Big(1 + \frac{1}{4}\tau^a\,\bar\eta_{\mu\nu}^a\sigma_{\mu\nu}\Big)\,U_I^\dagger\,\frac{1-\gamma_5}{2}\,\psi_f(x) \right]\exp\Big[-\kappa\,\rho^2\,R^{ab}(U_I)\,\bar\eta_{\mu\nu}^b\,G_{\mu\nu}^a(x)\Big],
$$

$$
\Theta_A = \prod_f \left[\frac{m_f}{4\pi^2\rho^2} + i\,\psi_f^\dagger(x)\,U_A\,\frac{1}{2}\Big(1 + \frac{1}{4}\tau^a\,\eta_{\mu\nu}^a\sigma_{\mu\nu}\Big)\,U_A^\dagger\,\frac{1+\gamma_5}{2}\,\psi_f(x) \right]\exp\Big[-\kappa\,\rho^2\,R^{ab}(U_A)\,\eta_{\mu\nu}^b\,G_{\mu\nu}^a(x)\Big],
$$

$$(5.15)$$

in the local (zero size) approximation, with $\kappa \equiv 2\pi^2/g$, and

$$
R^{ab}(U) = \frac{1}{2}\mathrm{Tr}\,(\tau^a U \tau^b U^\dagger)
$$

. The exponential is the (LSZ-reduced) gluonic emission from the pseudoparticle, written compactly as a coupling to the field strength $G_{\mu\nu}^a$.

For the present purpose we isolate the purely gluonic source factor in (5.15), and restaure the finite size form factor

$$
\mathcal{E}_I[G] = \exp\left[-\kappa\rho^2 \int \frac{d^4q}{(2\pi)^4} e^{iq\cdot x}\beta_{2g}(\rho|q|)R^{ab}(U)\bar\eta_{\mu\nu}^b G_{\mu\nu}^a(q)\right],
$$

$$
\mathcal{E}_A[G] = \exp\left[-\kappa\rho^2 \int \frac{d^4q}{(2\pi)^4} e^{iq\cdot x}\beta_{2g}(\rho|q|)R^{ab}(U)\eta_{\mu\nu}^b G_{\mu\nu}^a(q)\right].
$$

$$(5.16)$$

For a single (anti)-instanton of size ρ centered at the origin, the field strength is

$$
\mathbb{G}_{\mu\nu}^a(x) = \frac{4}{g}\,\bar\eta_{\mu\nu}^a\,\frac{\rho^2}{(x^2+\rho^2)^2}
$$

$$(5.17)$$

and the field-strength Fourier transform or form factor, is

$$
\mathbb{G}_{\mu\nu}^a(q) = \frac{4\pi^2\rho^2}{g}\bar\eta_{\mu\nu}^a\,\beta_{2g}(t) \equiv \frac{4\pi^2\rho^2}{g}\bar\eta_{\mu\nu}^a\left(\frac{t^2}{2}K_2(t)\right).
$$

$$(5.18)$$

It is gauge invariant, satisfies $\beta_{2g}(0) = 1$ and decays exponentially for $t \gg 1$. An analogous expression holds for anti-instantons with $\bar\eta \to \eta$. The extra $\frac{1}{2}$ that appears in the exponential arises from the coupling to the background field

$$
\frac{1}{4}\int d^4x\,2\,\mathbb{G}_{\mu\nu}^a(x)G_{\mu\nu}^a(x) \to \frac{1}{2}G_{\mu\nu}^a(q)\int d^4x\,\mathbb{G}_{\mu\nu}^a(x)e^{-iq\cdot x}
$$

$$(5.19)$$

where the rightmost equation follows by LSZ reduction of the perturbative gluon. Note that this reconstruction of the exponent is fully gauge invariant.

The instanton-induced four-gluon operator arises from the fourth-order term in the expansion of the tail-emission functional. Writing

$$X_I[G] = \kappa \rho^2 \int \frac{d^4q}{(2\pi)^4} e^{iq \cdot x} \beta_{2g}(\rho|q|) R^{ab}(U) \bar{\eta}^b_{\mu\nu} G^a_{\mu\nu}(q), \tag{5.20}$$

and similarly for $X_A[G]$, the quartic contribution is proportional to

$$n \left\langle \frac{X_I^4}{4!} + \frac{X_A^4}{4!} \right\rangle_U, \tag{5.21}$$

where n is the instanton density and $\langle \cdots \rangle_U$ denotes averaging over color orientations. Averaging over color orientation with the Haar measure projects onto singlets. For the adjoint dimension $d_A = N_c^2 - 1$, the fourth group average yields the standard contraction structure

$$\left\langle R_{a_1 b_1} R_{a_2 b_2} R_{a_3 b_3} R_{a_4 b_4} \right\rangle_U \Rightarrow \frac{3}{d_A(d_A + 1)} \left(\delta_{a_1 a_2} \delta_{b_1 b_2} \right) \left(\delta_{a_3 a_4} \delta_{b_3 b_4} \right) + \text{perm.}, \tag{5.22}$$

To proceed, we recall the identity

$$\bar{\eta}^b_{\mu\nu} \bar{\eta}^b_{\rho\sigma} = \delta_{\mu\rho}\delta_{\nu\sigma} - \delta_{\mu\sigma}\delta_{\nu\rho} - \epsilon_{\mu\nu\rho\sigma}, \tag{5.23}$$

which yields to the contractions

$$\bar{\eta}^b_{\mu\nu} \bar{\eta}^b_{\rho\sigma} G^a_{\mu\nu} G^a_{\rho\sigma} = 2\, G^a_{\mu\nu} G^a_{\mu\nu} - 2\, G^a_{\mu\nu} \tilde{G}^a_{\mu\nu}. \tag{5.24}$$

Projecting onto the parity-even scalar channel retains only the $(G^a_{\mu\nu} G^a_{\mu\nu})^2$ part, leading the induced and non-local scalar four gluon interaction

$$\Delta\mathcal{L}_{4g} = n \frac{\kappa^4 \rho^8}{2\, d_A(d_A + 1)} \int \prod_{i=1}^{4} \frac{d^4 q_i}{(2\pi)^4} \beta_{2g}(\rho|q_i|)(2\pi)^4 \delta^{(4)}\left(\sum_i q_i\right) \left[G^a_{\mu\nu}(q_1) G^a_{\mu\nu}(q_2)\right] \left[G^c_{\rho\sigma}(q_3) G^c_{\rho\sigma}(q_4)\right] + \text{perm.} \tag{5.25}$$

Each external gluon momentum carries its own form factor $\beta_{2g}(\rho|q_i|)$. Note the leg-by-leg factorization which will be key for the bound state equation to follow. In the local approximation (zero size) the 4-gluon vertex is

$$\Delta\mathcal{L}_{4g}^{(0^{++})}(x) = n \frac{\kappa^4 \rho^8}{2\, d_A(d_A + 1)} \left(G^a_{\mu\nu}(x) G^a_{\mu\nu}(x)\right)^2. \tag{5.26}$$

Eq. (5.25) is the microscopic one-(anti)instanton contact vertex in the 0^{++} channel that we now reduce to an instantaneous two-gluon potential.

5.4.2 Emergent 2-gluon 0^{++}-potential

To extract the gluon two-body potential in the scalar 0^{++} channel, we will use on-shell in-out gluonic external states and the non-local operator (5.25). This procedure parallels the one discussed by us [Shuryak and Zahed, 2021a] for the constituent quark pair interactions.

For the on-shell one-gluon states in the CM frame, we use the normalization

$$\langle \mathbf{k}, \lambda, a | \mathbf{k}', \lambda', a' \rangle = (2\pi)^3 \, 2\omega \, \delta^{(3)}(\mathbf{k} - \mathbf{k}') \, \delta_{\lambda\lambda'} \, \delta_{aa'}. \tag{5.27}$$

For a physical transverse polarization vector $\epsilon^\mu(k, \lambda)$, the field-strength matrix element is

$$\langle 0| G^a_{\mu\nu}(0) |g^b(k, \lambda)\rangle = i\, \delta^{ab} \left(k_\mu \epsilon_\nu(k, \lambda) - k_\nu \epsilon_\mu(k, \lambda)\right), \tag{5.28}$$

and similarly for outgoing legs with $\epsilon \to \epsilon^*$. Define the gauge-invariant two-gluon contraction induced by $G^a_{\mu\nu} G^a_{\mu\nu}$,

$$\mathcal{F}(i,j) \equiv G^a_{\mu\nu}(i)\, G^a_{\mu\nu}(j) \;\Rightarrow\; -2\,\delta^{a_i a_j}\Big[(k_i \cdot k_j)(\epsilon_i \cdot \epsilon_j) - (k_i \cdot \epsilon_j)(k_j \cdot \epsilon_i)\Big]. \tag{5.29}$$

At Born level, (5.26) yields

$$i\mathcal{M}^{(4)}(1,2 \to 3,4) = i\,n\,\frac{\kappa^4 \rho^8}{2\,d_A(d_A+1)}\prod_{i=1}^{4}\beta_{2g}(\rho|k_i|)\Big[\mathcal{F}(1,3)\mathcal{F}(2,4) + \mathcal{F}(1,4)\mathcal{F}(2,3)\Big]. \tag{5.30}$$

Projecting onto the two-gluon color singlet state $|1\rangle_{\rm color} = \delta^{ab}|ab\rangle/\sqrt{d_A}$ sets the color factors in (5.30) to unity for both exchange structures.

The scalar 0^{++} projection is implemented by taking the $J_z = 0$ helicity combination of two transverse gluons,

$$|0^{++}\rangle_{\rm pol} = \frac{1}{\sqrt{2}}\Big(|\lambda_1{=}+, \lambda_2{=}-\rangle + |\lambda_1{=}-, \lambda_2{=}+\rangle\Big), \tag{5.31}$$

and similarly for the outgoing state. In CM kinematics with scattering angle θ between $\mathbf{k}_1$ and $\mathbf{k}_3$, the detail contractions of the transverse helicities for massive on-shell gluons yield

$$\langle 0^{++}|\Big[\mathcal{F}(1,3)\mathcal{F}(2,4) + \mathcal{F}(1,4)\mathcal{F}(2,3)\Big]|0^{++}\rangle = 2\,(\omega^2 + k^2)^2\left(1 + \cos^2\theta\right), \tag{5.32}$$

Using the Legendre polynomials,

$$1 + \cos^2\theta = \frac{4}{3}\,P_0(\cos\theta) + \frac{2}{3}\,P_2(\cos\theta), \tag{5.33}$$

the decomposition apparently shows both $J = 0, 2$. If we regard (5.32) as a helicity-0 object and performs a spinless partial-wave projection,

$$\mathcal{M}^{(4)}_J = \frac{2J+1}{2}\int_{-1}^{1}dx\,P_J(x)\,\mathcal{M}^{(4)}(x), \qquad x = \cos\theta, \tag{5.34}$$

then (5.33) implies the weights and ratio

$$\mathcal{K}_{0^{++}} = \frac{4}{3}, \qquad \mathcal{K}_{2^{++}} = \frac{2}{3}, \quad \frac{\mathcal{K}_{2^{++}}}{\mathcal{K}_{0^{++}}} = \frac{1}{2}. \tag{5.35}$$

However, this ratio reflects only the relative size of the P_2 and P_0 components in (5.33), with the latter essentially an S-channel amplitude. While $\mathcal{K}_{0^{++}}$ is the proper weight in the iteration of the 0^{++}, $\mathcal{K}_{2^{++}}$ does not carry the correct weight in the 2^{++}. Although the emergent instanton vertex contains a P_2 component with relative weight $1/2$ in the helicity-0 decomposition, the *physical* 2^{++} interaction built from transverse gluons follows from helicity projection.

With this in mind, the in-out legs form factors in the S-channel can be restored as follows. In the glueball rest frame, the incoming legs carry relative momentum $\boldsymbol{p}$ and the outgoing legs carry $\boldsymbol{k}$. The four form factors combine as

$$\prod_{i=1}^{4}\beta_{2g}(\rho|k_i|) = \beta_{2g}^2(\rho p)\beta_{2g}^2(\rho k). \tag{5.36}$$

Since the exchange is taking place inside an instanton (anti-instanton) this is appropriately described by an *instantaneous* scalar potential, hence

$$V(\boldsymbol{p}, \boldsymbol{k}) = -V_0\,\beta_{2g}^2(\rho p)\,\beta_{2g}^2(\rho k). \tag{5.37}$$

which is separable. The strength V_0 is obtained by combining the quartic coefficient, the scalar projection factor, and the normalization required to convert an invariant amplitude into a three-dimensional potential.

The latter introduces reduced-state factors $(2\omega)^{-1/2}$ per external leg. Matching these factors at the dominant instanton scale $p, k \sim \rho^{-1}$ yields

$$\omega_\rho = \sqrt{\rho^{-2} + m_g^2}, \tag{5.38}$$

and produces a factor $(2\omega_\rho)^{-2} = 1/(4\omega_\rho^2)$ in the effective coupling. Collecting all contributions gives

$$V_0 = n \, \frac{\kappa^4}{2 \, d_A(d_A + 1)} \, \frac{16\mathcal{K}_{0^{++}}}{4\omega_\rho^2} \, \rho^4. \tag{5.39}$$

5.4.3 Reduced Bethe-Salpeter equation

Let $\Gamma(p; P)$ be the amputated Bethe-Salpeter (BS) vertex for two equal-mass constituent gluons of mass m_g, with total four-momentum P and relative four-momentum p. In the ladder approximation with an instantaneous kernel $V(\boldsymbol{p}, \boldsymbol{k})$, the reduced BS (Salpeter) equation for the scalar 0^{++} glueball is

$$\Gamma(p; P) = \int \frac{d^4k}{(2\pi)^4} \, V(\boldsymbol{p}, \boldsymbol{k}) \, D\left(k + \frac{P}{2}\right) \, D\left(-k + \frac{P}{2}\right) \, \Gamma(k; P), \tag{5.40}$$

where $-iD = 1/(q^2 - m_g^2 + i0)$ is the constituent-gluon propagator. .

In Eq. (5.40) the interaction kernel is constructed using on-shell transverse gluons. This reflects the instantaneous (Salpeter) reduction to follow: after integrating over the relative energy, the dominant contributions arise from the poles of the gluon propagators, and the bound state below threshold is governed by physical transverse degrees of freedom. Off-shell and gauge components are usually implicitly encoded in the effective kernel of the Salpeter reduction, and do not affect the mass eigenvalue. In our case the instanton induced pair interaction is gauge invariant by construction.

With this in mind and in the glueball rest frame

$$P^\mu = (M, \boldsymbol{0}), \qquad p^\mu = (p_0, \boldsymbol{p}), \qquad k^\mu = (k_0, \boldsymbol{k}), \tag{5.41}$$

we define the equal-time Salpeter amplitude

$$\phi(\boldsymbol{p}) \equiv \int \frac{dp_0}{2\pi} \, D\left(p + \frac{P}{2}\right) \, D\left(-p + \frac{P}{2}\right) \, \Gamma(p; P). \tag{5.42}$$

Since $V(\boldsymbol{p}, \boldsymbol{k})$ does not depend on p_0 or k_0, we can multiply both sides of (5.40) by the product of propagators and integrate over p_0 as in (5.42). This yields

$$\phi(\boldsymbol{p}) = \int \frac{d^3k}{(2\pi)^3} \, V(\boldsymbol{p}, \boldsymbol{k}) \, \left[\int \frac{dp_0}{2\pi} \, D\left(p + \frac{P}{2}\right) \, D\left(-p + \frac{P}{2}\right)\right] \, \phi(\boldsymbol{k}) \tag{5.43}$$

The remaining p_0 integral is elementary,

$$\int \frac{dp_0}{2\pi} \, D\left(p + \frac{P}{2}\right) D\left(-p + \frac{P}{2}\right) = \int \frac{dp_0}{2\pi} \, \prod_{s=\pm} \frac{i}{(p_0 + sM/2)^2 - \omega_p^2 + i0} = \frac{1}{2\omega_p} \, \frac{1}{M^2 - 4\omega_p^2 + i0}, \tag{5.44}$$

by contour integration, hence the reduced Bethe-Salpeter integral equation

$$\phi(\boldsymbol{p}) = \frac{1}{2\omega_p} \, \frac{1}{M^2 - 4\omega_p^2} \, \int \frac{d^3k}{(2\pi)^3} \, V(\boldsymbol{p}, \boldsymbol{k}) \, \phi(\boldsymbol{k}), \tag{5.45}$$

5.4.4 0^{++} mass equation

Substituting the separable kernel yields the rank-1 integral equation for the scalar glueball 0^{++} wavefunction in the CM frame

$$\phi(\boldsymbol{p}) = -V_0 \frac{\beta_{2g}^2(\rho p)}{2\omega_p(M^2 - 4\omega_p^2 + i0)} \int \frac{d^3k}{(2\pi)^3} \beta_{2g}^2(\rho k)\phi(\boldsymbol{k}). \tag{5.46}$$

Eliminating the normalization constant, leads to the root equation

$$1 = V_0 \, \mathbf{PP} \int_0^\infty \frac{p^2 \, dp}{(2\pi)^2} \frac{\beta_{2g}^4(\rho p)}{2\omega_p(4\omega_p^2 - M^2)}. \tag{5.47}$$

with the Principal Part ($\mathbf{PP}$) retained for a bound state. Introducing $x = \rho p$, $\mu = m_g \rho$, and $\mathcal{M} = M\rho$ yields the dimensionless form

$$1 = \lambda_M \, \mathbf{PP} \int_0^\infty dx \frac{x^2}{\sqrt{x^2 + \mu^2}} \frac{\left[\frac{x^2}{2} K_2(x)\right]^4}{4(x^2 + \mu^2) - \mathcal{M}^2}, \tag{5.48}$$

with

$$\lambda_M = \frac{V_0 \rho^2}{(2\pi)^2}.$$

Eq. (5.48) is the explicit rank-1 root mass equation for the 0^{++} glueball rescaled mass.

Finally, note that the bound-state mass is fixed by the pole condition of the two-body Green function, $1 - V_0\Pi(P^2) = 0$, which is analytic below threshold. Hence, the Minkowski equation evaluated at $P^2 = M^2$ and the Euclidean equation evaluated at $P_E^2 = -M^2$, yield the same root mass (5.48) by analytical continuation, which in Euclidean signature reads

$$1 = \lambda_M \int_0^\infty dx \frac{x^2}{\sqrt{x^2 + \mu^2}} \frac{\left[\frac{x^2}{2} K_2(x)\right]^4}{4(x^2 + \mu^2) + \mathcal{M}^2}, \tag{5.49}$$

5.4.5 0^{++} wavefunction

In contrast, the reduced momentum-space wavefunctions in Minkowski and Euclidean space are different, yet related to each other. Indeed, in the equal-time (Minkowski) reduction the wavefunction in momentum space is explicitly given by

$$\phi_M(\mathbf{p}) = \mathcal{N}_M \frac{\beta_{2g}^2(\rho p)}{2\omega_p \left(M^2 - 4\omega_p^2 + i0\right)}, \tag{5.50}$$

In contrast, the Euclidean reduced Bethe-Salpeter amplitude is a 4-dimensional function of the form

$$\chi_E(p_4, \mathbf{p}) \sim \frac{\beta_{2g}^2(\rho p)}{\left[(p_4 + \frac{P_4}{2})^2 + \omega_p^2\right]\left[(p_4 - \frac{P_4}{2})^2 + \omega_p^2\right]}, \tag{5.51}$$

originating from the product of the two Euclidean propagators in the iterating kernel, with no additional factor $1/(2\omega_p)$. The equal-time (Salpeter) wavefunction follows by slicing over the relative energy,

$$\phi_M(\mathbf{p}) = \int_{-\infty}^\infty \frac{dp_4}{2\pi} \chi_E(p_4, \mathbf{p}) \propto \frac{\beta_{2g}^2(\rho p)}{2\omega_p \left(M^2 - 4\omega_p^2 + i0\right)}. \tag{5.52}$$

The extra factor of $1/(2\omega_p)$ arises from the relative-energy integration, and is absent in the 4-dimensional Euclidean amplitude.

5.4.6 Numerical results

For sufficiently strong (anti)instanton coupling λ_M a bound state below 2-constitutive gluon treshold can form. Since $\lambda_M \sim \rho^{p+2}$ with $p + 2 \gtrsim 6$, this coupling is very sensitive to the (anti)instanton size ρ, e.g.

$$\left(\frac{\rho}{0.32 \text{ fm}}\right)^6 \sim 10\text{-}15 \tag{5.53}$$

for $\rho \simeq 0.36\text{-}0.38$ fm. With this in mind, for a dense ILM, with $\eta = 6 - 7$ and

$$m_g(\eta) = m_{g0}\sqrt{\eta}, \quad m_{g0} = 0.36 \text{ GeV}, \quad \alpha = \frac{g^2}{4\pi} = 0.3\text{-}0.5, \tag{5.54}$$

the scalar 0^{++} glueball mass is

$$M_{0^{++}} \simeq 1.4\text{-}1.5 \text{ GeV}, \tag{5.55}$$

well below the two-gluon threshold $2m_g(\eta) = 1.8\text{-}1.9$ GeV. The 0^{++} rms radius follows from the exact momentum-space eigenstate (5.50), using

$$\langle r^2 \rangle = \int \frac{d^3p}{(2\pi)^3} \, \phi_M^*(\mathbf{p}) \left(-\nabla_{\mathbf{p}}^2\right) \phi_M(\mathbf{p}). \tag{5.56}$$

with the result

$$\langle r^2 \rangle_{0^{++}}^{1/2} \simeq 0.25\text{-}0.32 \text{ fm}, \tag{5.57}$$

This shows a low-lying and compact scalar glueball, dominated by instanton-scale dynamics, as illusttrated by the radial probability distribution shown in Fig. 5.4.1
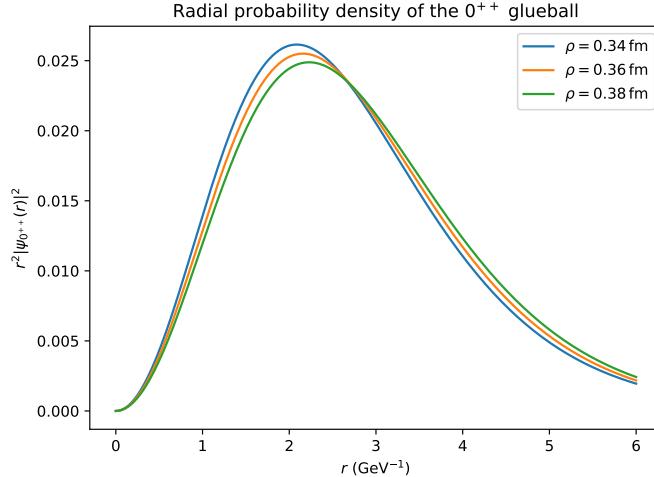
Fig. 5.4.1 0^{++} Glueball radial probability $r^2|\psi_{0^{++}}(r)|^2$ versus $r(\text{GeV}^{-1})$ from the reduced Bethe-Salpeter equation, for different (anti)instanton size $\rho = 0.34, 0.36, 0.38$ fm.

5.5 Glueball summary

The constituent two-gluon Hamiltonian organizes the glueball spectrum naturally into radial and orbital families, closely mirroring the familiar structure of quarkonium spectroscopy. This separation becomes particularly transparent when the instanton density parameter is fixed at $\eta = 1$, or within the instanton liquid model (ILM), where the scalar and tensor ground states are fitted to their lattice values.

Radial excitations correspond to states with fixed total spin and parity but an increasing number of nodes in the relative wavefunction. In the scalar channel, the ground state 0_0^{++} is strongly shifted downward by the combined effects of Coulomb and instanton-induced attraction. As a result, it is a compact state with a characteristic size of order the instanton radius. The first radial excitation, 0_1^{++}, is far less sensitive to short-distance dynamics: its wavefunction extends to larger radii, reducing its overlap with the instanton core. Consequently, its mass lies much closer to the confinement-dominated WKB prediction. This hierarchy illustrates the rapid decoupling of instanton physics with increasing radial quantum number.

Orbital excitations, by contrast, form Regge-like towers at fixed radial quantum number. The tensor family $2^{++}, 4^{++}, 6^{++}, \ldots$ provides the clearest example. In this case, the centrifugal barrier already suppresses short-distance overlap at the ground state, and $^5S_2$-$^5D_2$ mixing further shifts probability density toward larger radii. As a result, the tensor ground state is only moderately displaced from the WKB baseline, while higher-J states align along an approximately linear Regge trajectory with a slope determined by the adjoint string tension.

Figure 5.5.1 displays the resulting glueball spectrum organized by parity and charge conjugation, following the standard layout used in lattice spectroscopy. The comparison emphasizes the selective impact of instanton-induced dynamics. In the $C = +$ scalar channel, coherent Coulomb and instanton attraction generate a deeply bound and compact 0^{++} ground state, well below the confinement baseline. The tensor 2^{++} channel, on the other hand, exemplifies a Reggeized orbital sequence. The residual discrepancy in its lowest state arises from treating it purely as a D-wave; in reality, it is better described as an S-wave dominated state with a significant D-wave admixture, as discussed in the semiclassical analysis. By contrast, vector channels appear only at substantially higher masses and do not support compact two-gluon configurations, in agreement with symmetry constraints and lattice results [Morningstar and Peardon, 1999, Morningstar, 2025].
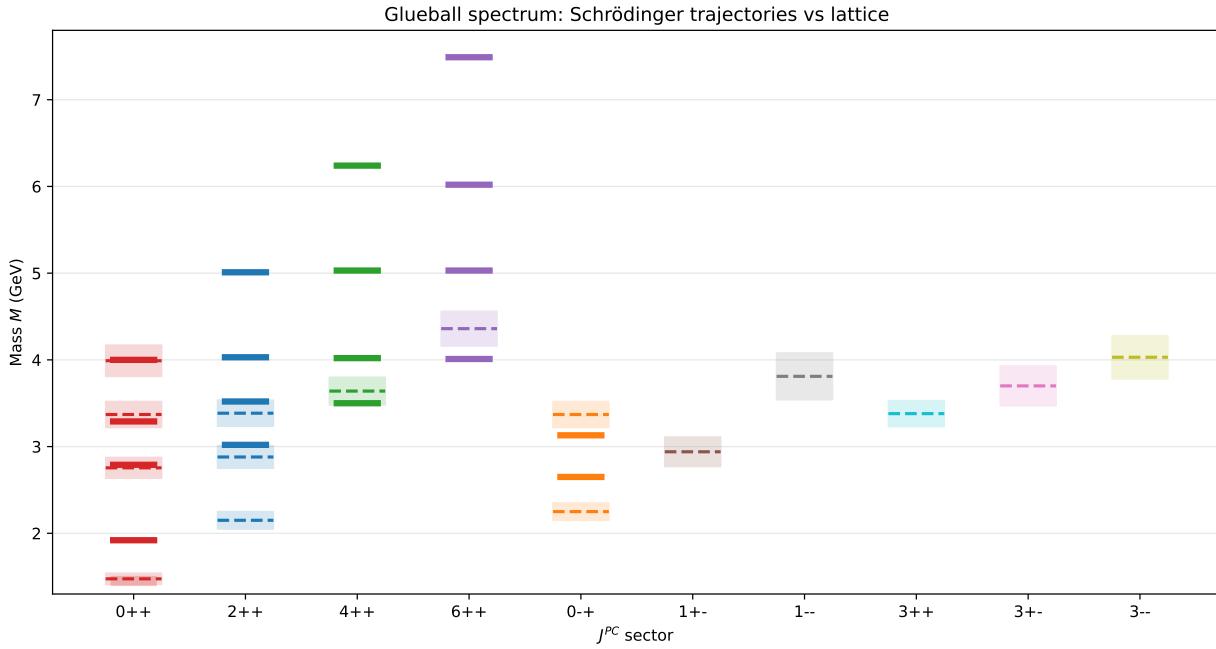
Fig. 5.5.1 Glueball mass spectrum organized by J^{PC} sectors, as listed in Table 5.5.1. Solid markers (this work) and dashed (mean) and spread (uncertainty) markers from quenched SU(3) lattice [Meyer, 2004, Morningstar and Peardon, 1999].

J^{PC}	This work		Lattice [Meyer, 2004, Morningstar and Peardon, 1999]
0^{++}	1.92	(BS: 1.4-1.5)	1.475(30)(65)
0^{++}		2.79	2.755(70)(120)
0^{++}		3.29	3.370(100)(150)
0^{++}		4.00	3.990(210)(180)
2^{++}		3.01	2.150(30)(100)
2^{++}		3.46	2.880(100)(130)
2^{++}		4.16	3.385(90)(150)
2^{++}		5.10	
4^{++}		3.52	3.640(90)(160)
4^{++}		4.18	
4^{++}		5.10	
4^{++}		6.24	
6^{++}		4.06	4.360(260)(200)
6^{++}		4.97	
6^{++}		6.11	
6^{++}		7.49	
0^{-+}		2.65	2.250(60)(100)
0^{-+}		3.13	3.370(150)(150)
1^{+-}			2.94(17)
1			3.81(27)
3^{++}			3.38(15)
3^{+-}			3.70(23)
3			4.03(25)

Table 5.5.1 Glueball masses in pure SU(3) gauge theory: comparison of this work as in Fig. 5.3.1, with lattice results from Refs. [Morningstar and Peardon, 1999, Meyer, 2004].

Appendix

5.A WKB spectrum

A complementary analytic description follows from the semiclassical quantization. For the linear potential $V(r) = \sigma_8 r$ with reduced mass $\mu = m_g/2$, the WKB spectrum with the Langer modification yields

$$E_{nL}^{\mathrm{WKB}}(\eta) = \left[\frac{3\pi}{2} \left(n + \frac{L}{2} + \frac{3}{4} \right) \right]^{2/3} \frac{\sigma_8^{2/3}}{m_g^{1/3}(\eta)},$$
$$M_{nL}^{\mathrm{WKB}}(\eta) = 2m_g(\eta) + E_{nL}^{\mathrm{WKB}}(\eta), \tag{5.58}$$

which captures the universal scaling

$$M - 2m_g \propto \sigma_8^{2/3} m_g^{-1/3}$$

.

A convenient WKB size measure is the outer turning point $r_+ = E/\sigma_8$. For $L = 0$, the WKB radial probability density implies closed expressions for moments. With $p(r) = \sqrt{2\mu(E - \sigma_8 r)}$ and

$$|\psi|^2 d^3 r \propto dr/p(r) \,,$$

we have

$$\langle r \rangle_{L=0}^{\mathrm{WKB}} = \frac{2}{3} r_+, \quad \langle r^2 \rangle_{L=0}^{\mathrm{WKB}} = \frac{8}{15} r_+^2, \quad r_{\mathrm{rms},\, L=0}^{\mathrm{WKB}} = \sqrt{\frac{8}{15}} \, r_+. \tag{5.59}$$

For $L > 0$ we quote r_+ and use $r_{\mathrm{rms}} \approx \sqrt{8/15} \, r_+$ as a uniform semiclassical estimate, which is adequate for trajectory comparisons.

Table 5.B.1 provides the WKB masses and radii at $\eta = 1$ for low-lying $L = 0$ (scalar-like) and $L = 2$ (tensor-like orbital) levels, including the first few excitations. The conversion $1 \ \mathrm{GeV}^{-1} = 0.197$ fm is used.

5.B Gluon mass and density scaling

Musakhanov and Egamberdiev [Musakhanov and Egamberdiev, 2018] derived the gluon polarization operator in the instanton medium and extracted a momentum-dependent dynamical mass. In their ILM setup the *scalar gluon mass* $M_s(q)$ is generated by rescattering on instantons, and the physical transverse gluon mass satisfies $M_g^2(q) = 2M_s^2(q)$, implying at $q = 0$ the standard-ILM value $M_g(0) \simeq 0.36$ GeV [Musakhanov and Egamberdiev, 2018]. The key scaling with density follows from the structure of the self-energy in a random instanton background: to leading order in the density expansion the polarization operator

is proportional to the instanton density n, and the mass is obtained from the infrared limit of the propagator denominator, schematically $D^{-1}(q) \sim q^2 + \Pi(q)$ with $\Pi(0) \propto n$. This implies $m_g^2 \propto n$ and therefore

$$m_g(\eta) = m_{g0}\sqrt{\eta}, \qquad \eta \equiv \frac{n_{\text{eff}}}{n_0}, \tag{5.60}$$

where $n_0 \simeq 1\,\text{fm}^{-4}$ is the traditional ILM density used to define m_{g0}. In the dense-ILM-ensemble [Shuryak, 1982c], η is naturally taken as a flow- or resolution-dependent effective density, rather than a fixed vacuum number [Schäfer and Shuryak, 1998].

n L J	M_{nL}^{WKB} (GeV)	r_+ (fm)	$r_{\text{rms}}^{\text{WKB}}$ (fm)
0 0 0	3.196	0.628	0.459
1 0 0	4.176	1.105	0.807
2 0 0	4.974	1.493	1.090
0 2 2	4.176	1.105	0.807
1 2 2	4.974	1.493	1.090
0 4 4	4.974	1.493	1.090
0 6 6	5.680	1.836	1.341

Table 5.B.1 WKB masses and radii at $\eta = 7$ for the linear adjoint potential. Here J is identified with L for Regge-trajectory purposes. These semiclassical radii are larger than the variational scalar radius because Coulomb and instanton attractions are not included in the baseline WKB table; they can be incorporated as short-distance energy shifts.

5.C Static potentials for fundamental and adjoint charges from instantons and $I\bar{I}$ molecules

Wilson loops involve path-ordered exponents

$$W_C = P \exp\left[i \sum \Delta x_\mu A_\mu^a T^a\right], \tag{5.61}$$

taken over closed contours C, usually of rectangular shape. The sum runs over infinitesimal elements Δx_μ along the loop, and A_μ^a are vacuum gauge fields. Since the contour is closed, W_C is gauge invariant.

For static color charges corresponding to quarks, the color generators are in the fundamental $SU(N_c)$ representation, $T^a = \lambda^a/2$, with Pauli or Gell-Mann matrices. In several of our earlier publications we have numerically calculated the corresponding static confining potentials from ensembles of instantons or $I\bar{I}$ molecules, and applied them to quarkonia, baryons, and tetraquarks [Miesch et al., 2024]. The upper panel of Fig. 5.C.1 shows an example of such a Monte-Carlo simulation. (The Wilson line locations and orientations are randomized.)

Since a *constituent gluon* belongs to the adjoint color representation, the only modification in the Wilson loop is that the generators are now adjoint,

$$(T^a)_{bc} = -i\,\epsilon^a_{\ bc}. \tag{5.62}$$

Unlike the case of Pauli matrices, for which a compact closed form for the exponent exists, no such expression is available here. The practical method we employ is based on a Taylor expansion of the exponent to second order in Δx_μ, assumed to be small. The adjoint potential shown in the lower panel of Fig. 5.C.1 was calculated in this way, using the same gauge-field configurations and the same set of Wilson lines as in the upper panel.

First, note that the vertical scales of the two plots are different, and that, crudely, the ratio of the two potentials is approximately 9/4, as suggested by the ratio of the corresponding color Casimir operators.
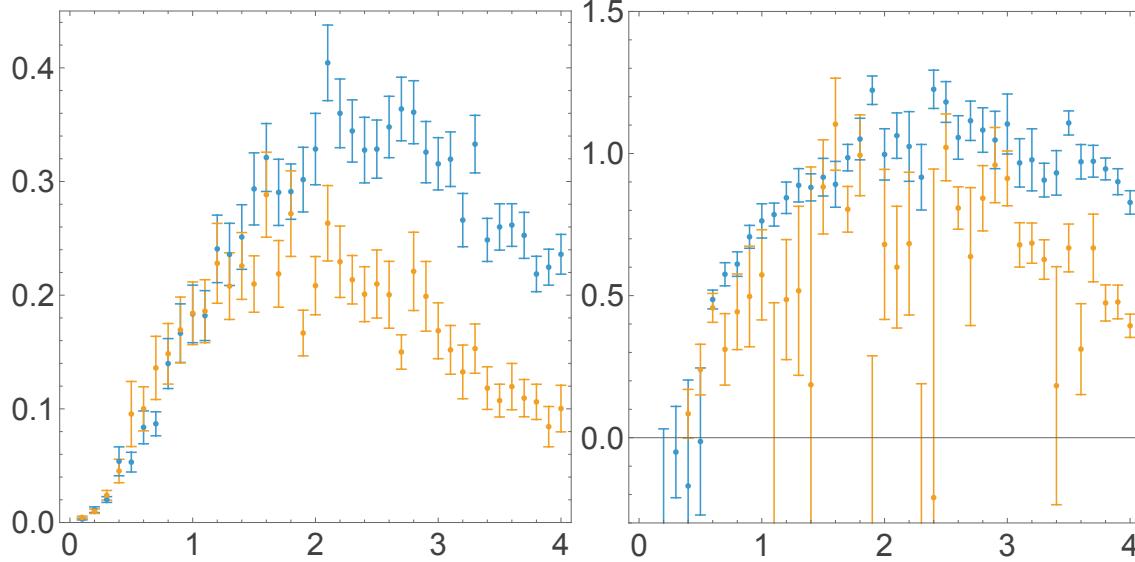
Fig. 5.C.1 Static potentials $V_{conf}(r)\,(GeV)$ versus $r\,(GeV^{-1})$ calculated from fundamental (left) and adjoint (right) Wilson lines. Blue dots are for a $\bar{I}I$ molecule, red are for a single instanton. Potentials still needs to be rescaled proportional to their density.

Second, since the Wilson lines and the resulting potentials contain nonlinear terms (higher powers of the gauge field), such scaling is not expected to hold exactly. Indeed, the shapes of the two potentials differ somewhat. Nevertheless, all potentials reach a maximum at $r \sim 2.5\,\mathrm{GeV}^{-1} \sim 0.5\,\mathrm{fm}$ and then decrease slightly. This feature is likely an artifact of the setup used here, in which a single instanton (or molecule) is surrounded by a Wilson loop. In an ensemble of such objects, the potential is expected to saturate at large r to a constant, equal to twice the effective mass of the static charges.

For heavy quarks interacting via instantons, this asymptotic value is

$$V_{\mathrm{conf}}(r \to \infty) \approx 2\,\eta \times (0.070\,\mathrm{GeV}) \approx 1\,\mathrm{GeV}, \tag{5.63}$$

for $\eta \sim 7$, corresponding to a rescaling from the dilute instanton liquid model to a dense ensemble of molecules. In physical QCD such an energy is sufficient to produce an additional $\bar{q}q$ pair and split quarkonium $\bar{Q}Q$ into two $\bar{Q}q$ mesons.

For *constituent gluons* in pure gauge theory, the large-distance splitting instead corresponds to $gg \to (gg)(gg)$, so that $V_{\mathrm{conf}}(r \to \infty)$ must be at least of order $M_{0^{++}} \sim 1.5\,\mathrm{GeV}$. Guided by these considerations, we model our potential in the form shown in Fig. 5.2.1.

Chapter 6
Baryons

6.1 Brief history

Before starting our brief historical account, let us note that baryon spectroscopy has long been at the center of hadronic physics, both theoretically and experimentally. Consequently, there is no shortage of extensive reviews on the subject. One comprehensive recent source is the collection *50 years of QCD* [Gross et al., 2023]. The particular approximation we will employ is known as the *hypercentral* approximation; for a comprehensive review of its use in baryon studies, see [Giannini and Santopinto, 2015].

The nonrelativistic quark model originated in the 1960s. With the underlying spin-flavor $SU(6)$ symmetry, researchers were able to fix baryon wave functions and calculate important properties, such as magnetic moments. After the discovery of QCD, significant progress followed in the 1970s. Using quadratic (oscillatory) confinement and perturbative spin-dependent forces, Isgur and Karl derived the wave functions of positive-parity baryons [Isgur and Karl, 1979b, Isgur and Karl, 1979a] and of P-wave baryons [Isgur and Karl, 1978], achieving considerable success for the lowest-lying states.

Further refinements, including in particular the introduction of relativized quarks, were made by Capstick and Isgur [Capstick and Isgur, 1985]. With time, the issue of missing resonances faded away, as states in the second and third shells were nearly all observed, leading to the impression that most of the outstanding problems in this field had been resolved.

The extension of this framework to excited baryons, especially to the negative-parity P-shell [Isgur and Karl, 1978], nevertheless revealed a number of conceptual and technical issues. To simplify some of the symmetry aspects for three-light-quark states qqq, the authors focused instead on mixed qqs states (Σ, Λ), and then discussed the light-quark limit $m_s \to m_{u,d}$.

They showed that perturbative predictions based on one-gluon exchange worked qualitatively well for spin-spin and tensor forces, whereas the spin-orbit interaction, calculated within the same approximation, was essentially absent. A major shortcoming at the time was the prediction of D-shell states that were not observed experimentally, giving rise to the so-called *missing resonances problem.* As already mentioned, later refinements, particularly the inclusion of relativized quarks by Capstick and Isgur [Capstick and Isgur, 1985], and subsequent experimental progress largely alleviated this issue.

In our (mostly methodological) paper [Miesch et al., 2023b], we elaborated on several technical aspects of baryon spectroscopy, taking as an example excited nucleon states with negative parity. Some of the novel features of that work will be presented in this section.

Textbook discussions of baryons usually begin with the observation that, since the color wave function $\sim \epsilon_{ijk}$ is antisymmetric, Fermi statistics require the remaining part of the wave function-coordinates $\times$ spins $\times$ isospins-to be symmetric under quark interchange. Isgur and Karl [Isgur and Karl, 1979b, Isgur and Karl, 1979a] avoided constructing such fully symmetric wave functions explicitly for negative-parity baryons by focusing on strange baryons Λ, Σ, where 1-2 quark symmetry is enforced, followed by a
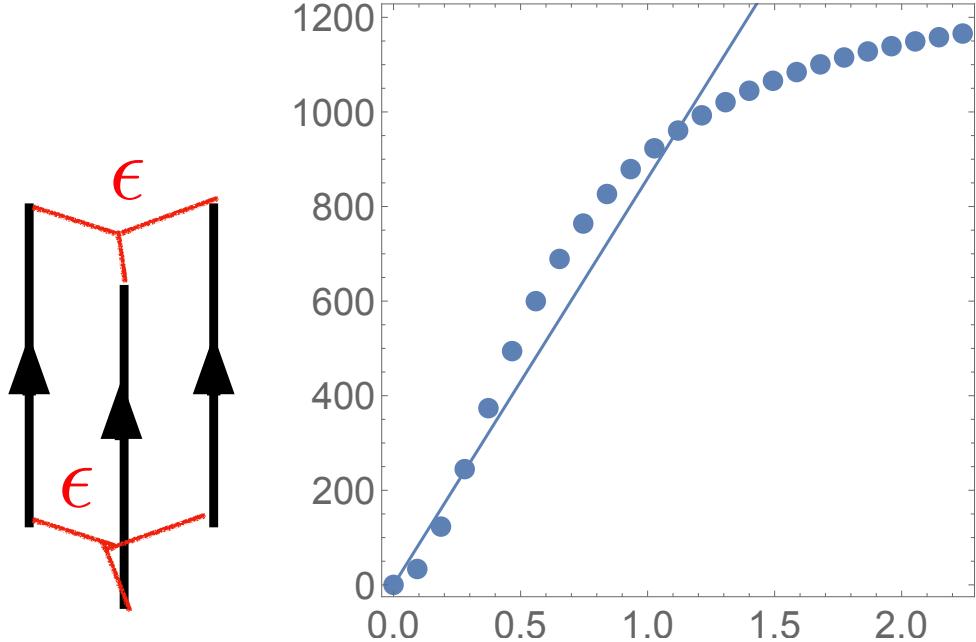
Fig. 6.1.1 Left: a sketch of three Wilson lines connected with Levi-Civita symbols. Right: Effective QQ potential (MeV) versus distance (fm), calculated from instanton-antiinstanton molecules, from [Miesch et al., 2024] (points). The solid line shows the slope of the standard quarkonium potential for comparison.

limiting procedure $m_s \to m_d$. However, there is no fundamental reason to retrace this route repeatedly: the issue can be addressed directly, and the required symmetric wave functions can be constructed explicitly.

Mesons, as two-body systems, have two obvious coordinates: the relative distance $r_{12} = |\mathbf{x}_2 - \mathbf{x}_1|$ and the center-of-mass (CM) position $\mathbf{X}_{CM} = M_1\mathbf{x}_1 + M_2\mathbf{x}_2$. Only the former is physically relevant, while the latter is set to zero.

When dealing with few-body problems, one must proceed analogously and employ variables in which the center-of-mass motion is removed[1]. While this may appear to be an obvious first step, it is worth emphasizing that the complete elimination of center-of-mass motion is essential. The general procedure for an N-body system was developed by Jacobi in the mid-19th century, defining each new coordinate as the displacement between the center of mass of a subsystem and the next particle.

For a three-body system with equal masses, the standard Jacobi coordinates are

$$\boldsymbol{\rho} = (\mathbf{r}_1 - \mathbf{r}_2)/\sqrt{2}, \quad \boldsymbol{\lambda} = (\mathbf{r}_1 + \mathbf{r}_2 - 2\mathbf{r}_3)/\sqrt{6} \tag{6.1}$$

and have been traditionally used in baryon studies since the 1970s, for example in [Isgur and Karl, 1978].

It is instructive to contrast this with alternative approaches in which the center-of-mass motion is not removed. In nuclear physics, for instance, oscillator-type mean-field potentials have often been employed. On the one hand, oscillator-based algebras of a, a^+ operators provide a convenient way to enforce Fermi statistics. On the other hand, the center-of-mass coordinate remains dynamical and introduces spurious degrees of freedom. While this may be relatively harmless for large particle numbers $N \gg 1$, it becomes problematic for small systems. Attempts to *subtract center-of-mass effects (such as the CM energy)* are fundamentally flawed, since quantum entanglement between physical and spurious degrees of freedom persists and contaminates the calculation[2].

---

[1] If calculations are performed in momentum space, this corresponds to setting the total momentum to zero, $\mathbf{P} = 0$.

[2] This is an important distinction between our approach and that of J. Vary and collaborators, who employed such methods even for baryons with $N = 3$.

6.2 Interquark forces in baryons

6.2.1 The central qq potential

For static (infinitely heavy) quarks, interquark forces are described by Wilson lines, either without or with additional gauge-field insertions. The same logic applies to systems with any number of quarks (and anti-quarks), where N Wilson lines are contracted with the appropriate color indices of the color wave functions. For baryons, this structure is schematically shown in Fig. 6.1.1 (left), with the red ϵ denoting the three-index Levi-Civita symbol.

The simplest case arises when the interaction is generated by gluon exchanges between Wilson lines. At lowest order, one readily finds that the binary QQ Coulomb interaction is $2\pi\alpha_s/(3r)$, i.e. one half of the corresponding $Q\bar{Q}$ force [3].

Empirical observations discussed in [Karliner et al., 2017] suggest that the same ratio, $V_{QQ}/V_{Q\bar{Q}} = 1/2$, persists also for nonperturbative effects. A fully nonperturbative derivation can be carried out on the lattice; as an example we mention [de Forcrand and Jahn, 2005].

6.2.2 Flavor dependence of spin forces

As is well known, perturbative spin-spin forces are proportional to Dirac magnetic moments, which involve effective quark masses,

$$\mu_q \sim e/m_q^{\mathrm{eff}}.$$

This immediately implies that the magnetic moment of the strange quark is smaller than that of light quarks by the ratio $m_q^{\mathrm{eff}}/m_s^{\mathrm{eff}}$. Indeed, empirical sq and ss spin-spin forces follow this pattern, which has often been taken as evidence for the validity of the perturbative description.

An alternative perspective is provided by nonperturbative QCD vacuum models, such as instanton-based approaches. Here we recall the early work [Shuryak, 1989] on instanton-induced spin forces. It was observed that two-body forces arise from the reduction of the six-fermion 't Hooft interaction by contracting two of its legs with vacuum condensates. For a light-quark pair qq, the resulting interaction is proportional to $\langle\bar{s}s\rangle$, whereas for a strange-quark pair it is proportional to $\langle\bar{q}q\rangle$. The ratio of these condensates coincides precisely with the ratio of effective constituent masses. As a result, both perturbative and instanton-induced spin-spin forces exhibit the same flavor dependence.

Instanton-induced spin forces were applied to baryon spectroscopy in [Loring et al., 2001][4]. Further contributions to this topic are presented in [Miesch et al., 2024], from which the right panel of Fig. 6.1.1 is taken. A key conceptual issue addressed there is that, for N Wilson lines piercing an instanton field, it is not *a priori* obvious that the resulting interaction can be reduced to a sum of binary forces. Nevertheless, for the baryon case ($N = 3$), this reduction turns out to be valid; see the explicit derivation in [Miesch et al., 2024].

A second, more recently appreciated issue is that strongly correlated instanton-antiinstanton pairs (*molecules*) are more abundant and generate stronger effects than the dilute instanton ensemble of the original instanton liquid model. Their contributions to various Wilson-line correlators were calculated in the same work.

---

[3] A natural explanation is geometric: the color vectors form angles of $2\pi/3 = 120°$, with $\cos(2\pi/3) = 1/2$.

[4] This paper and subsequent works are commonly referred to as the *Bonn baryon model*. It is formulated with relativistic quarks and includes not only binary but also three-body forces.

6.3 The orbital-color-spin-flavor wave function and the permutation group S_3

The wave function of spherical ($L = 0$) light-quark baryons contains color, spin, and flavor indices. The total number of monoms is

$$N_{\text{monoms}} = 3^3 \times 2^3 \times 2^3,$$

so the full wave function must be expressed as a linear combination of these basis elements with appropriate coefficients.

The simplest example is the $\Delta^{3/2,3/2}$ state. Its spin and isospin structure, e.g. $\uparrow\uparrow\uparrow$, is fully symmetric under particle permutations. Consequently, the color wave function must be antisymmetric, $\sim \epsilon_{c_1 c_2 c_3}$. In this case, the construction is straightforward.

Next come the nucleons, for which the color part factorizes in the same antisymmetric form. One must then construct a symmetric spin-isospin wave function. As an example, consider the proton with spin and isospin $S = 1/2$, $I = 1/2$, and projections $S_z = 1/2$, $I_z = 1/2$. A simple preliminary observation is that one of the three spins (and one of the three isospins) must be *down*, while the other two are *up*. One therefore expects $3 \times 3 = 9$ terms in the spin-isospin wave function. Since the total number of spin-isospin monoms is $2^3 \times 2^3 = 64$, the proton wave function occupies a nine-dimensional subspace of this 64-dimensional monom space.

In the literature, this wave function is often written in two equivalent forms: a symmetric representation and an explicit expansion in spin-flavor monoms,

$$
\left| 0\frac{1}{2}\frac{1}{2}\frac{1}{2} \right\rangle_{p_M^+} = \frac{1}{\sqrt{18}} \left[(\uparrow\downarrow\uparrow - \downarrow\uparrow\uparrow)(udu - duu) + (\uparrow\uparrow\downarrow - \uparrow\downarrow\uparrow)(uud - udu) + (\uparrow\uparrow\downarrow - \downarrow\uparrow\uparrow)(uud - duu) \right]
$$

$$
= \frac{1}{\sqrt{18}} \left[2(u^\uparrow d^\downarrow u^\uparrow) + 2(d^\downarrow u^\uparrow u^\uparrow) + 2(u^\uparrow u^\uparrow d^\downarrow) - (d^\uparrow u^\downarrow u^\uparrow) - (u^\downarrow d^\uparrow u^\uparrow) \right.
$$

$$
\left. - (u^\uparrow d^\uparrow u^\downarrow) - (d^\uparrow u^\uparrow u^\downarrow) - (u^\downarrow u^\uparrow d^\uparrow) - (u^\uparrow u^\downarrow d^\uparrow) \right] \tag{6.2}
$$

After combining the terms that appear twice in the first expression, one indeed obtains nine distinct monoms.

To gain a deeper understanding of how this structure arises, let us start by adding three spin-1/2 representations:

$$(1/2) \otimes (1/2) \otimes (1/2) = (3/2) \oplus (1/2) \oplus (1/2).$$

Counting states on both sides confirms this decomposition,

$$2 \times 2 \times 2 = 8 = 4 + 2 + 2.$$

The key lesson is that there are *two* inequivalent ways to combine three spins into a total spin $S_{\text{total}} = 1/2$. When additional quantum numbers (orbital, color, flavor) are included, the number of possible combinations grows rapidly, and only a small subset is compatible with Fermi statistics.

A systematic tool for organizing these representations is provided by Young tableaux. Horizontal rows correspond to symmetrization, while vertical columns correspond to antisymmetrization. Although one might naively expect three possibilities for placing the lowest box, Young tableau rules exclude one of them, leaving precisely two allowed configurations-in agreement with the above counting. These two states form what we shall call a *good basis* for the three-spin problem.

We fix these two basis states as

$$
S_{\frac{1}{2}}^\rho = \frac{1}{\sqrt{2}}(\uparrow\downarrow - \downarrow\uparrow) \uparrow
$$

$$
S_{\frac{1}{2}}^\lambda = -\frac{1}{\sqrt{6}}(\uparrow\downarrow\uparrow + \downarrow\uparrow\uparrow - 2\uparrow\uparrow\downarrow) \tag{6.3}
$$

and define analogous isospin-1/2 states,

$$F_{\frac{1}{2}}^{\rho} = \frac{1}{\sqrt{2}}(ud - du)u$$

$$F_{\frac{1}{2}}^{\lambda} = -\frac{1}{\sqrt{6}}(udu + duu - 2uud) \tag{6.4}$$

The totally symmetric spin-3/2 states are

$$S_{\frac{3}{2}m}^{S} = \left(\uparrow\uparrow\uparrow, \frac{1}{\sqrt{3}}(\uparrow\uparrow\downarrow + \text{perm.}), \frac{1}{\sqrt{3}}(\uparrow\downarrow\downarrow + \text{perm.}), \downarrow\downarrow\downarrow \right). \tag{6.5}$$

Note that these definitions parallel those of the Jacobi coordinates ρ, λ for three-body systems. At this stage, we know that the proton wave function must be constructed as a specific combination of these components, and that it must be orthogonal to all Δ states built from the spin-3/2 wave functions.

To determine the correct combination, we use the fact that quarks are fermions, and therefore the full spin-isospin wave function must be symmetric under *all* permutations of quark labels. The relevant symmetry group is the permutation group of three elements, S_3, which consists of $3! = 6$ elements,

$$\hat{P}_{i=1,\dots,6} = I, \ (12), \ (13), \ (23), \ (123), \ (132). \tag{6.6}$$

Consider first the transposition (12). The ρ-type wave functions are antisymmetric under (12), while the λ-type are symmetric. Consequently, a fully symmetric spin-isospin wave function must be constructed as a combination of $S^{\rho}F^{\rho}$ and $S^{\lambda}F^{\lambda}$. The original four-dimensional space spanned by

$$X^{\rho}X^{\rho}, \ X^{\rho}X^{\lambda}, \ X^{\lambda}X^{\rho}, \ X^{\lambda}X^{\lambda}$$

is reduced to a two-dimensional subspace, since the mixed combinations $S^{\rho}F^{\lambda}$ and $S^{\lambda}F^{\rho}$ are antisymmetric under (12) and must be discarded.

Remarkably, to enforce symmetry under *all* permutations, it is sufficient to check only one additional transposition, e.g. (23). Using Jacobi coordinates, the action of (12) and (23) can be written in matrix form,

$$[\hat{P}_2 = (12)] \begin{pmatrix} \rho \\ \lambda \end{pmatrix} = \begin{pmatrix} -1 & 0 \\ 0 & 1 \end{pmatrix} \begin{pmatrix} \rho \\ \lambda \end{pmatrix}$$

$$[\hat{P}_4 = (23)] \begin{pmatrix} \rho \\ \lambda \end{pmatrix} = \begin{pmatrix} \frac{1}{2} & \frac{\sqrt{3}}{2} \\ \frac{\sqrt{3}}{2} & -\frac{1}{2} \end{pmatrix} \begin{pmatrix} \rho \\ \lambda \end{pmatrix}. \tag{6.7}$$

The central idea is that spin and isospin indices must be combined using a tensor product. In MATHEMATICA, this is implemented by the command `KroneckerProduct`, which combines two matrices of dimensions M and N into a single matrix of dimension MN. Applying this operation to the two $\hat{P}(23)$ matrices yields

$$\hat{P}(23) \bigotimes \hat{P}(23) = \begin{bmatrix} 1/4 & \sqrt{3}/4 & \sqrt{3}/4 & 3/4 \\ \sqrt{3}/4 & 3/4 & -1/4 & -\sqrt{3}/4 \\ \sqrt{3}/4 & -1/4 & 3/4 & -\sqrt{3}/4 \\ 3/4 & -\sqrt{3}/4 & -\sqrt{3}/4 & 1/4 \end{bmatrix}, \tag{6.8}$$

which acts in the four-dimensional *good basis* of spin-isospin space.

Diagonalizing this matrix (using the `Eigensystem` command) yields three eigenvalues equal to 1 and a single eigenvalue equal to -1. Performing the same analysis for $\hat{P}(12) \bigotimes \hat{P}(12)$, which is diagonal, gives two eigenvalues $+1$ and two eigenvalues -1.

The final step is to identify the *common eigenvector* with eigenvalue $+1$ for both operators. There is one and only one such vector, $(1, 0, 0, 1)$, corresponding to

$$\psi_{\text{sym}} = (S^{\rho}I^{\rho} + S^{\lambda}I^{\lambda})/\sqrt{2}.$$

Thus, the symmetric proton spin-isospin wave function is

$$\left|0\frac{1}{2}\frac{1}{2}m\right\rangle_{p_M^+} \sim \frac{1}{\sqrt{2}}(S^\rho_{\frac{1}{2}m}F^\rho_{\frac{1}{2}} + S^\lambda_{\frac{1}{2}m}F^\lambda_{\frac{1}{2}}). \tag{6.9}$$

The conversion of expressions of this type into vectors in the standard monom basis is explained in Appendix 6.C.

The reader may feel that this derivation of a well-known result is unnecessarily complicated. However, following this procedure allows one to construct wave functions of multiquark hadrons that have eluded theorists for decades. In the problems discussed below, we will encounter matrices in the *good basis* with dimensions of hundreds or even thousands-large, but still manageable. The corresponding operators in the monom basis often have dimensions of millions by millions. As we will show, even in such cases one can perform practical calculations while preserving the familiar quantum-mechanical notation.

6.4 Hyperspherical approximation for single-flavor baryons

We now turn to the discussion of complicated wave functions of states containing 3, 4, 5, 6, or even 12 quarks, starting with states that possess the *highest symmetries*. In the quantum mechanics of atoms, the discussion begins with the S shell, and the principal quantum number n is introduced. Only afterward are states with nonzero orbital angular momentum $L \neq 0$ considered. Subsequently, the electron spin S is included and the total angular momentum $\mathbf{J} = \mathbf{L} + \mathbf{S}$ is defined.

Similarly, we will start with *spherically symmetric states*, for which there exists a single (hyper-radial) wave function obtained from a single radial Schrodinger equation.

Few-body systems composed of quarks with different flavors generally have nontrivial kinetic energy operators, with coefficients depending on the corresponding quark masses. However, if all quarks are identical, then in modified Jacobi coordinates (see Appendix 6.A) the kinetic energy operator $\hat{K}$ takes a *spherically symmetric form of a Laplacian*, multiplied by the universal coefficient $1/2m$. After removing the motion of the center of mass, one finds a six-dimensional hyperspace for baryons, a nine-dimensional one for tetraquarks, and so on, reaching fifteen dimensions for hexaquarks ($n = 6$). The details for these cases are described in Appendices 6.A and 6.B.

The Laplacian in these higher dimensions differs from the familiar $d = 3$ case because of the appearance of a quasi-centrifugal term $\sim 1/mr^2$. Nevertheless, its scaling behavior remains the same as that of the ordinary Laplacian. As we have checked, this universality appears to persist across different systems.

The *hyperspherical approximation* has been successfully used in nuclear physics since the 1970s. One of us (ES) has also applied this method to the ^{4}He wave function in Ref. [Shuryak and Torres-Rincon, 2020], not only reproducing the ground 1S-state binding energy $B \approx 28$ MeV, but also discovering a second, shallow 2S bound state, which is known experimentally. This success naturally increased our confidence in the method.

The next issue is that binary interactions $\sum_{i>j} V(\mathbf{r}_{ij})$ depend on the interparticle distances r_{ij} and therefore are *not* spherically symmetric in hyperdimensional coordinates. Nevertheless, one can always define their spherical projection by averaging over the solid angle (with 5, 8, etc., angular variables):

$$V \rightarrow \bar{V} \equiv \frac{1}{\Omega}\int V \, d\Omega. \tag{6.10}$$

The difference $\Delta V \equiv (V - \bar{V})$ can affect a spherically symmetric state only starting at second order, and is therefore expected to be small.

If the flavors of all three quarks are the same, the flavor wave function is symmetric. Since the color wave function is necessarily antisymmetric, the spin wave function must also be symmetric for an S-wave state, implying $J = S = 3/2$. Examples of such states are the $uuu = \Delta^{++}$ and $sss = \Omega^-$ baryons. Unfortunately,

analogous ccc or bbb baryons have not yet been observed experimentally, so for these systems we can only make predictions and compare them with lattice results.

The radial Schrodinger equation we use for the reduced wave function $u(R_6)$ is related to the full radial wave function by

$$\psi(R_6) = u(R_6)/R_6^{5/2}\,. \tag{6.11}$$

Note that the factor R_6^5 is absorbed into the volume element, so that $u(R_6)$ has the usual one-dimensional normalization, $\sim \int dR_6 \, |u(R_6)|^2$. This reduction removes the first-derivative term from the Laplacian, but introduces an additional quasi-centrifugal term. The resulting equation has the form

$$\left(-u'' + \frac{15}{4R_6^2}u \right)\frac{1}{2M} + (V_6 - E_{Ns})u = 0\,. \tag{6.12}$$

The radial projection of the potential onto R_6 is defined in Appendix 6.B and is worked out explicitly for a Cornell-type binary potential.

The mass splittings of the lowest s- and p-states for ccc and uuu baryons, obtained numerically from Eq. (6.12), are shown in Fig. 6.4.1. The binary QQ potential is taken to be one half of the Cornell potential (used above for the Υ family). We do not show the absolute masses, but instead focus on the level splittings.

Experience shows that these splittings depend only weakly on the choice of quark mass and are primarily controlled by the interaction potential. Indeed, as shown in Fig. 6.4.1, the spectra of ccc and uuu baryons appear nearly identical, despite the quark masses differing by more than a factor of three. This mirrors the well-known similarity of splittings in the charmonium and bottomonium families emphasized earlier, where the absolute mass scales also differ by a comparable factor.

More specifically, for the s-shell ccc baryons we find

$$M_{ccc}^{2S} - M_{ccc}^{1S} \approx 391,\ \ M_{ccc}^{3S} - M_{ccc}^{1S} \approx 685\,\text{MeV}$$

while for the $uuu = \Delta^{++}$ states we obtain

$$M_{uuu}^{2S} - M_{uuu}^{1S} \approx 438,\ \ M_{uuu}^{3S} - M_{uuu}^{1S} \approx 804\,\text{MeV}$$

These should be compared with the experimental values

$$M_{uuu}^{2S} - M_{uuu}^{1S} \approx 278,\ \ M_{uuu}^{3S} - M_{uuu}^{1S} \approx 688\,\text{MeV}$$

(from the 2022 Particle Data Tables, using masses from Breit-Wigner fits).

The deviations between the calculated and experimental splittings are comparable to the shifts expected from spin-spin and 't Hooft interactions, which have so far been neglected. However, their sign would be opposite, shifting the $1S$ state downward more strongly than the excited states. These effects are also relativistic corrections of order $\sim 1/M^2$, and thus should be much less important for charm quarks. We therefore conclude that the effective baryonic potential used here (Ansatz A) is somewhat stronger than in reality. We will return to this point in the next section.

The corresponding wave functions are shown in Fig. 6.4.2. Unlike the splittings, they exhibit dramatic differences between the uuu and ccc baryons. This reflects the fact that these hadrons have very different spatial sizes, with the ccc baryons being much more compact. Moreover, even the ground states display somewhat unusual behavior: despite the enhanced Coulomb forces in six-dimensional systems, the quasi-centrifugal potential leads to wave functions that are strongly suppressed at small hyper-radial distances.

These wave functions can be used to compute matrix elements of various operators. For example, the root-mean-square radii of the three s-states of the Δ are

$$\sqrt{\langle R_6^2 \rangle} = 4.97,\ 7.53,\ 9.72\,\text{GeV}^{-1}\,. \tag{6.13}$$
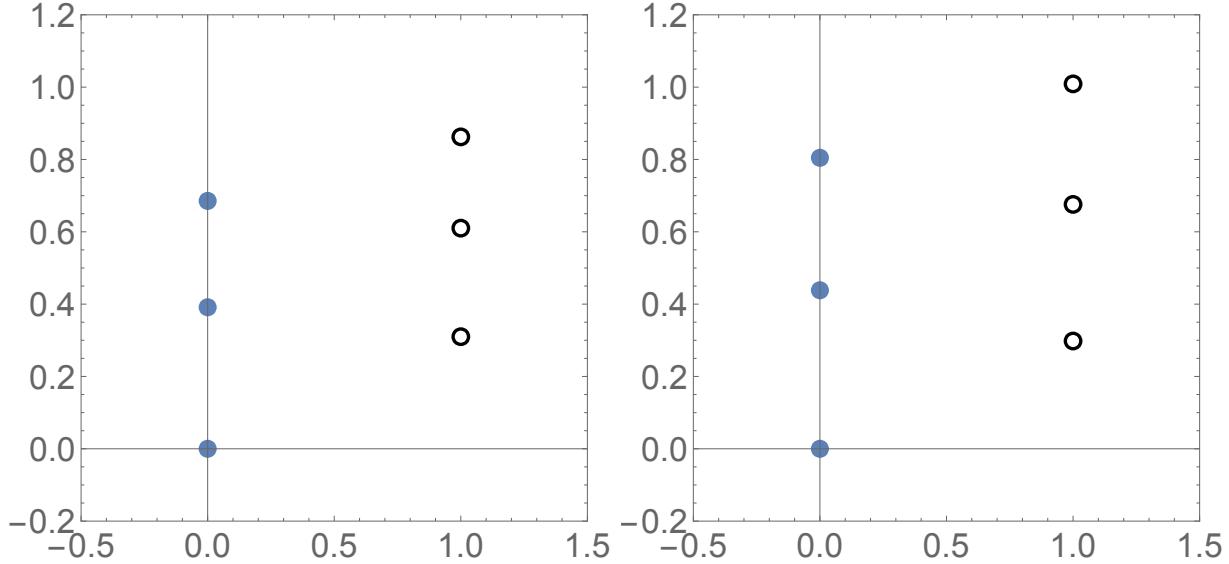
Fig. 6.4.1 Masses of ccc baryons (upper plot) and $uuu = \Delta^{++}$ (lower plot) $M(N, L)$ for $L = 0$ and $L = 1$ shells, measured relative to the corresponding ground states.
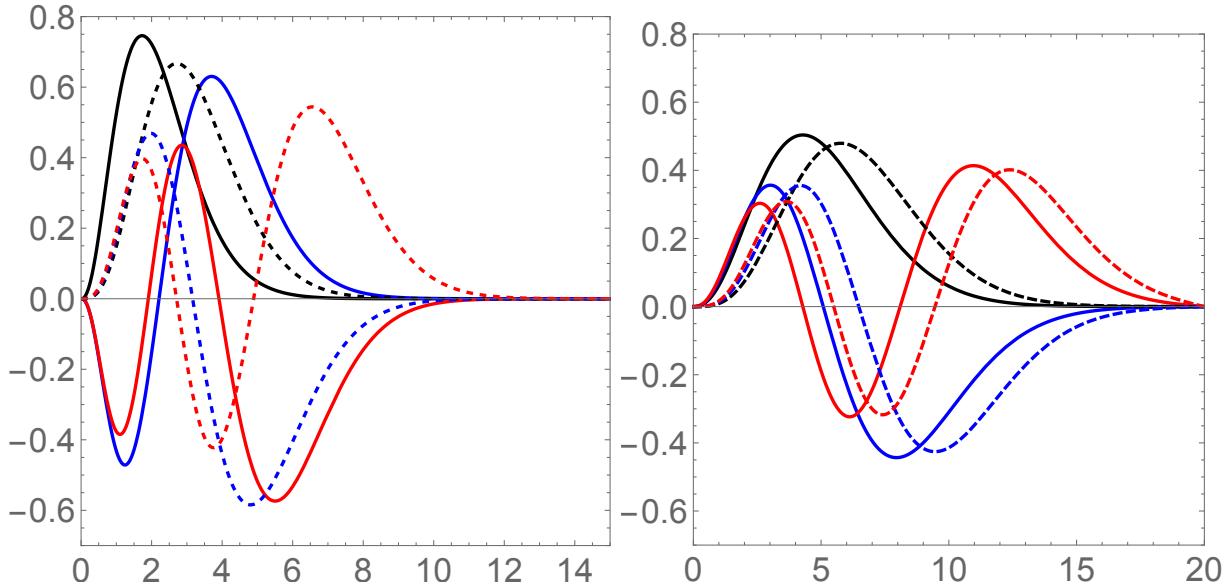
Fig. 6.4.2 Wave functions $u(R_6)$ of ccc (upper) and uuu baryons (lower) for $L = 0$ (solid lines) and $L = 1$ (dashed lines), shown as functions of the hyper-radial distance R_6 (GeV^{-1}).

To summarize, in this section we have tested the assumption that the approximate universality of spectra observed for S- and P-shell states of c and b quarkonia can also extend to baryons. Our results indicate that this is indeed the case.

Specifically, we modeled the nonperturbative forces between quarks in baryons as a sum of Cornell-style binary interactions, reduced by the same factor of $1/2$ (as for perturbative forces) relative to the mesonic $\bar{Q}Q$ potential. We find that this leads to s-p shell splittings that are somewhat larger than those observed in the $uuu = \Delta^{++}$ baryon, indicating that the effective baryonic potential is slightly too strong.

6.5 Electric, magnetic and transitional formfactors

6.5.1 Brief history

The most direct observables related to the spin structure are the hadronic magnetic moments. Already in the 1960s it was shown that the proton and neutron magnetic moments are reasonably well described by nonrelativistic qqq models, without any additional admixtures or orbital motion. If admixtures of states with $L \neq 0$ in excited qqq configurations, or of pentaquark $qqqq\bar{q}$ sectors, are included, one must examine whether mechanisms exist that lead to cancellations between spin and orbital contributions.

The next class of sensitive observables are transitional matrix elements between on-shell states of relevant operators (such as electromagnetic currents), either at zero or finite momentum transfer Q. In the latter case, the corresponding quantities are referred to as (transitional) form factors. The diagonal pp and nn form factors are further decomposed into electric and magnetic Sachs form factors. The electromagnetic current itself contains contributions proportional to the quark charges (Dirac term) and to the quark spins (Pauli term). There is no need to reproduce the well-known standard formulae here.

For many decades it was widely accepted that the ratio of electric to magnetic form factors is independent of the momentum transfer Q. This belief was based on the assumption that the spin and radial parts of the nucleon wave function factorize. In addition, it was expected that the neutron electric form factor vanishes, $G_E^n = 0$.

However, experiments at JLAB [Jones et al., 2000, Gayou et al., 2002, Puckett et al., 2012] have demonstrated that neither of these expectations is supported by data. The ratio G_E^p/G_M^p decreases with increasing Q, with a possible sign change at the upper end of the measured range, $Q^2 \sim 8.5 \, \text{GeV}^2$. Moreover, the electric form factor of the neutron is clearly nonzero, $G_E^n \neq 0$.

Before turning to theory, it is worth noting that the JLAB data lie in the range $Q^2 \leq 9 \, \text{GeV}^2$, corresponding to $Q/2 \approx 1.5 \, \text{GeV}$. Thus, these experiments probe neither the small-Q regime, where a soft chiral cloud is expected to dominate, nor the asymptotically large-Q region, where hard perturbative predictions should apply. Instead, they belong to an intermediate, or *semi-hard*, regime in which form factors must be computed nonperturbatively[5].

Clearly, any mixing between states will affect the form factors. As one example from the literature, the mixing of ground-state nucleons (proton and neutron) with D-shell states was studied in Ref. [Simonov, 2021]. In that work, a schematic model was shown to reproduce the JLAB data for the electric and magnetic form factors of both the proton and neutron, but only at the price of rather strong and specific mixing. This study inspired our work [Miesch et al., 2025b], in which we analyzed the D-shell states, their mixing, and their possible admixture into the nucleon wave function in detail. Some of these results will be presented below in the chapter on the D-shell. Our analysis indicates that the admixture of D-wave components can indeed be large enough to explain the observed behavior of the electric form factors.

6.5.2 Theoretical approaches and some results

Before evaluating form factors explicitly, let us comment on several general issues. At medium and large momentum transfer, $Q \sim \text{few GeV} > M_N$, relativistic effects are clearly essential. It is therefore natural to formulate the problem using light-front (LF) dynamics, as discussed in the later parts of this review. At the very least, one should attempt to boost wave functions from the center-of-mass frame to momenta of order $Q/2$. Examples for the nucleon and the Δ are given in Ref. [Shuryak and Zahed, 2023b], where the corresponding form factors are also analyzed.

---

[5] See, for example, the discussion and calculations in [Shuryak and Zahed, 2021g].

At small Q, one might naively attempt to use Fourier transforms of nonrelativistic center-of-mass wave functions, as is common in atomic physics. However, this approach fails. One reason is that constituent quarks, unlike electrons, are not pointlike. In addition, baryon radii are affected by their *chiral clouds.*

At intermediate Q, nonrelativistic wave functions may still be employed, provided a *boost prescription* is used (following e.g. [Simonov, 2021]),

$$\psi(\mathbf{p}_\perp, p_l) \rightarrow \frac{1}{\gamma}\, \psi(\mathbf{p}_\perp, p_l/\gamma),$$

which amounts to a Lorentz contraction of the longitudinal size by the gamma factor $1/\gamma = \sqrt{1 - v^2}$. Below, we will discuss to what extent this procedure can be used to describe form factors in the intermediate "semi-hard" region.

In addition to elastic observables, *transitional form factors* from the nucleon to N^* and Δ resonances provide a rich set of probes of internal structure. In particular, the Roper resonance $N^*(1440)$ exhibits a transitional form factor that is in clear disagreement with a *minimal scenario* in which it is interpreted as a simple radial $2S$ excitation. This provides further motivation for future studies.

Having completed this general discussion, we now turn to explicit calculations. In the nonrelativistic limit, form factors are evaluated directly from the wave functions. More specifically, in the commonly used Breit frame[6], elastic scattering corresponds to a transition from an initial hadron with momentum $\mathbf{Q}/2$ to a final hadron with momentum $-\mathbf{Q}/2$ along the z axis, induced by the electromagnetic current operator $\langle j | J_\mu^{em} | i \rangle$.

The first step in evaluating form factors is the computation of Fourier transforms of the wave functions, followed by their convolution. In the nonrelativistic approximation, the electric form factor can be inverted to obtain the charge distribution, which in turn determines the wave function and the underlying Schrodinger potential[7]. The resulting potential is finite at infinity, suggesting an apparent "no confinement" behavior. In particular, the hypercoulomb potential leads to an analytic form factor of the form $\sim 1/(1 + Q^2/\Lambda^2)^{7/2}$.

We found this situation rather confusing and therefore repeated these calculations ourselves. The outcome was unambiguous: the form factors obtained within the hypercentral approach do *not* agree[8] with experimental data.

As noted earlier, relativistic effects can be partially included through Lorentz contraction in the Fourier transforms. In the upper panel of Fig. 6.5.1 we show the form factors calculated using the 1S (blue dots) and 1D (orange dots) wave functions obtained in the hyperdistance approximation. As expected, the 1D state is significantly softer than the 1S state, since the 1S wave function is finite at the origin, while the 1D wave function is quadratically suppressed by the centrifugal barrier.

These results should be compared with the empirical dipole fit to the proton magnetic form factor (dashed line). Clearly, the 1S form factor obtained from the hypercentral wave function (blue dots) fails to reproduce the data, even at small Q^2. Nevertheless, its behavior at larger $Q^2 \gtrsim 0.5\,\mathrm{GeV}^2$ is qualitatively similar.

The fact that hypercentral wave functions significantly underestimate the nucleon radius has been noted previously; see, for example, [Gallimore and Liao, 2024]. Indeed, standard radial wave functions are expected to describe the spatial distributions of constituent quark *centers*, rather than the distributions of charge, mass, or energy. We now briefly discuss two ideas that may help explain this discrepancy.

First, constituent quarks are not pointlike objects; they possess intrinsic spatial extent and internal charge and mass distributions, which introduce additional form factors.

Second, the three-quark ground-state wave function represents only part of the full nucleon wave function. There is mixing with excited states (to be discussed in the chapter on the D-shell) and with higher Fock components (to be discussed in the chapter on pentaquarks). In a different language, the nucleon is

---

[6] Also known as the *brick-wall frame*, in which the momentum reverses sign after the collision.

[7] For details, see, for example, [Giannini and Santopinto, 2015].

[8] Recall, however, that this model reproduces the energy spectrum quite well.
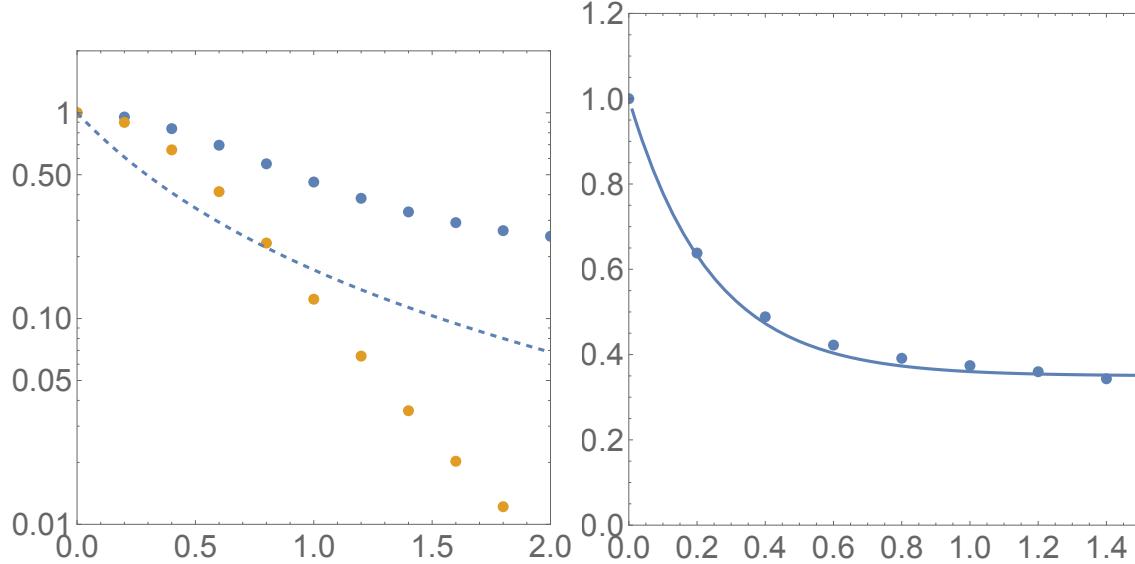
Fig. 6.5.1 The left plot shows the $\frac{1}{2}^+$ form factor obtained from the 1S (blue dots) and 1D (orange dots) wave functions as a function of $Q^2\,(\mathrm{GeV}^2)$. The dashed blue line represents the nucleon dipole fit $FF_{dipole} = 1/(1 + Q^2/0.71)^2$. The right plot shows the constituent quark or *pion cloud* form factor versus $Q^2\,(\mathrm{GeV}^2)$. The points correspond to the ratio of the calculated form factor to the fitted experimental curve in the left panel. The solid line is $0.35 + 0.65\,\exp(-Q^2 R_{\mathrm{cloud}}^2/6)$ with $R_{\mathrm{cloud}} = 1\,\mathrm{fm} \approx 5\,\mathrm{GeV}^{-1}$.

surrounded by a pion cloud, as described, for example, in the *little bag model* [Brown and Rho, 1979] or in *chiral soliton* models [Diakonov et al., 1996].

To make this discussion more quantitative, let us assume that the experimental form factor can be written as the *product* of two contributions: one associated with the global wave function described by the hyperradius, and one associated with the constituent quark structure,

$$FF_N(Q^2) = FF_{\mathrm{WF}}(Q^2) \cdot FF_{\mathrm{cloud}}(Q^2). \tag{6.14}$$

The right panel of Fig. 6.5.1 shows the extracted form factor $FF_{\mathrm{cloud}}(Q^2)$. A pointlike contribution from the constituent quarks is present, accounting for approximately one third of the total form factor.

At small momentum transfer, this contribution can be parametrized by a Gaussian $\exp(-Q^2 R^2/6)$ with a large radius $R \approx 5\,\mathrm{GeV}^{-1} \approx 1\,\mathrm{fm}$. Such a form factor is well described by instanton-based semiclassical theories of chiral symmetry breaking. In order to generate a nonzero quark condensate, virtual quarks bound to an instanton (zero modes) must propagate to neighboring (anti)instantons in the ensemble, which are typically separated by distances of order $R \sim n_{\mathrm{inst}}^{-1/4} \sim 1\,\mathrm{fm}$. In other words, constituent quarks carry a substantial chiral cloud.

We now briefly outline the calculations underlying the discussion above. The radial (hyperdistance) wave functions and their six-dimensional Fourier transforms were evaluated numerically. For analytical parametrizations, it is useful to recall the exact Fourier transforms of Gaussian and exponential wave functions,

$$\exp\left(-\frac{\mathrm{Y}^2}{2\Lambda^2}\right) \rightarrow \exp\left(-\frac{\mathrm{P}^2\Lambda^2}{2}\right),$$

$$\exp\left(-\mathrm{Y}\cdot\mathrm{A}\right) \rightarrow \frac{1}{(1 + \mathrm{P}^2/A^2)^{7/2}}. \tag{6.15}$$

With this in mind, the numerical form factors shown in Fig. 6.5.2 for the 1S (blue dots) and 1D (orange dots) states are well fitted by simple analytical expressions.
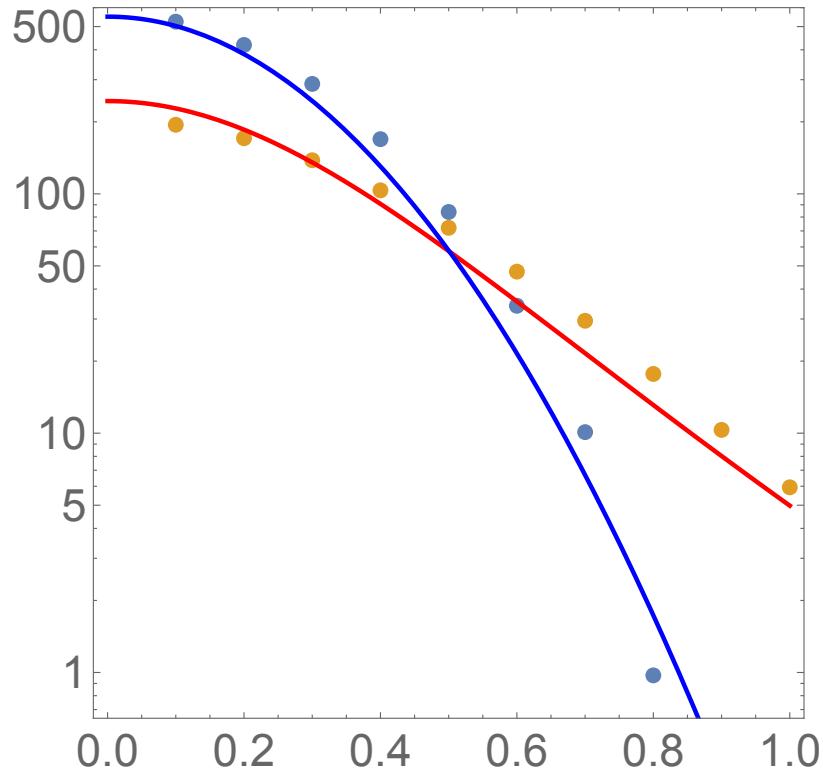
Fig. 6.5.2 Blue and red points show the Fourier transforms of the 1S and 1D radial wave functions as functions of momentum p (GeV). The solid lines represent the analytical fits given in the text.

In the Breit frame, the form factor is given by a convolution of wave functions corresponding to total momenta $\mathbf{Q}/2$ and $-\mathbf{Q}/2$. The boost amounts to dividing the longitudinal momentum components by the gamma factor

$$1/\gamma = \sqrt{1 - v^2} = \sqrt{1/(1 + Q^2/4M^2)},$$

so that the Lorentz-contracted wave functions are $\phi = \psi(\mathbf{p}_\perp, p_{\text{long}}/\gamma)$. The form factor includes scattering off all three quarks, labeled by $i = 1, 2, 3$, weighted by their charges e_i,

$$G_E(Q) = \sum_i \frac{e_i}{e\gamma} \int \frac{d^3 p_\rho d^3 p_\lambda}{(2\pi)^6}$$
$$\times \phi(p_\rho, p_\lambda)\phi(\mathbf{p}_\rho + \nu_\rho^i \mathbf{Q}, \mathbf{p}_\Lambda + \nu_\lambda^i \mathbf{Q}), \tag{6.16}$$

where for the proton $e_i = (2/3, 2/3, -1/3)$, and ν_ρ, ν_λ denote the fractions of the total momentum $\mathbf{Q}$ carried by the corresponding Jacobi coordinates.

The form factors obtained from relativized versions of the hyperdistance model[9] show better agreement with experimental data. Rather than pursuing these models further, we will instead turn, in the later parts of this review, to a derivation of form factors directly from light-front wave functions.

---

[9] See Fig. 24 of [Giannini and Santopinto, 2015].

Appendix

6.A Schrodinger equations in d dimensions

The nonrelativistic kinetic energy of A particles of identical mass m, written in terms of $N = A - 1$ modified Jacobi coordinates, takes the simple form of a Laplacian (multiplied by $1/m$) [Fabre de la Ripelle and Navarro, 1979],

$$-\frac{1}{2} \sum_{i=1}^{A} \nabla_i^2 = -\frac{1}{2} \left(\partial_\rho^2 + \frac{3N-1}{\rho} \partial_\rho - \frac{1}{\rho^2} K_N^2 \right). \tag{6.17}$$

The particular cases of three and four particles will be discussed below.

The hyperspherical harmonics (HHs) are eigenstates of the grand-angular momentum operator,

$$K_N^2 \, \mathcal{Y}_{[K]}^{KLM_L}(\Omega_N) = (K(K + 3N - 2)) \, \mathcal{Y}_{[K]}^{KLM_L}(\Omega_N). \tag{6.18}$$

The $2^N + N$ angular variables $\Omega_N = (\hat{\xi}_1, \ldots, \hat{\xi}_N; \varphi_1, \ldots, \varphi_N)$ consist of the directions of the individual Jacobi coordinates $\hat{\xi}_i$ and the hyperangles defined by $\cos \varphi_j = \xi_j / \rho$. The quantum numbers L, M_L are the usual eigenvalues of the total orbital angular momentum operators L^2 and L_z. The explicit form of the HHs follows from recoupling the individual angular momenta l_i.

The hyperspherical harmonics are normalized according to

$$\int d\Omega_N \, \mathcal{Y}_{[K]}^{KLM_L \, *}(\Omega_N) \, \mathcal{Y}_{[K']}^{K'L'M_L'}(\Omega_N) = \delta_{[K],[K']}, \tag{6.19}$$

and their total degeneracy is given by [Fabre de la Ripelle and Navarro, 1979]

$$d_K = (2K + 3N - 2) \frac{(K + 3N - 3)!}{K!(3N - 2)!}. \tag{6.20}$$

For example, for $A = 4$ particles ($N = 3$), the $K = 0$ HH has degeneracy $d_0 = 1$, while the $K = 1$ HHs have degeneracy $d_1 = 9$.

For the applications relevant to this paper, however, we mostly employ different sets of angular coordinates. For instance, in the case of pentaquarks, the original $5 \times 3 = 15$ coordinates are reduced to four Jacobi vectors $\boldsymbol{\alpha}, \boldsymbol{\beta}, \boldsymbol{\gamma}, \boldsymbol{\delta}$, corresponding to 12 coordinates after fixing the center of mass at the origin. In this parametrization, there are $4 \times 2 = 8$ angles θ_i, ϕ_i $(i = 1, \ldots, 4)$ specifying directions in four three-dimensional subspaces, and three additional angles, denoted $\chi_2, \chi_1, \phi_\chi$, which parametrize directions in the four-dimensional space spanned by the vector lengths $\alpha, \beta, \gamma, \delta$.

Using any such coordinate system, we follow the same general procedure. One starts by computing the metric tensor $g_{\mu\nu}$ as the coefficients of the differentials in the quadratic form $ds^2 = g_{\mu\nu} dx^\mu dx^\nu$. All geometric quantities then follow from standard expressions. In particular, the volume element is given by $\sqrt{\det g}$. For

the 12-dimensional example discussed above, it takes the form

$$\sqrt{\det g} \prod dx^i = Y^{11} dY \left[\prod_{i=1..4} \sin(\theta_i)\, d\theta_i\, d\phi_i \right] \left[\sin^2(\chi_2)\, \sin(\chi_1)\, d\chi_2\, d\chi_1\, d\phi_\chi \right].$$

If all quarks have the same mass, the kinetic energy operator is proportional to the Laplace-Beltrami operator,

$$-L = \frac{1}{\sqrt{\det g}} \frac{\partial}{\partial x^\mu} \sqrt{\det g}\, g^{\mu\nu} \frac{\partial}{\partial x^\nu}, \tag{6.21}$$

where $g^{\mu\nu}$ is the inverse metric tensor.

6.B Baryons in hyperspherical coordinates

To describe the specifics of the hyperspherical approximation, we first consider three quarks forming a baryon. The three coordinate vectors of the quarks are compressed into two Jacobi vectors,

$$\boldsymbol{\rho} = \frac{1}{\sqrt{2}} \mathbf{r}_{12}, \qquad \boldsymbol{\lambda} = \frac{1}{\sqrt{6}} (\mathbf{r}_{13} + \mathbf{r}_{23}), \tag{6.22}$$

where $\mathbf{r}_{ij} = \mathbf{r}_i - \mathbf{r}_j$ are three-dimensional vectors. The square root factors define the so-called modified Jacobi coordinates, which ensure that the kinetic energy takes the form of a sum of second derivatives with the same coefficient $1/2m$. As a result, the kinetic energy becomes spherically symmetric in six dimensions.

The hyperdistance is the six-dimensional radial coordinate, denoted by R_6, and is defined as

$$R_6^2 \equiv \boldsymbol{\rho}^2 + \boldsymbol{\lambda}^2 = \frac{1}{3} \left[(\mathbf{r}_1 - \mathbf{r}_2)^2 + (\mathbf{r}_1 - \mathbf{r}_3)^2 + (\mathbf{r}_3 - \mathbf{r}_2)^2 \right]. \tag{6.23}$$

It is naturally related, in a fully symmetric manner, to the sum of all squared interparticle distances.

In its most symmetric form, the hyperspherical approximation does not distinguish between $\boldsymbol{\rho}$ and $\boldsymbol{\lambda}$, but instead treats all six coordinates on an equal footing. Standard spherical coordinates can be introduced using five angular variables $\theta_1, \theta_2, \theta_3, \theta_4 \in [0, \pi]$ and $\phi \in [0, 2\pi]$, leading to the six-dimensional solid angle

$$\Omega_6 = \int d\theta_1\, d\theta_2\, d\theta_3\, d\theta_4\, d\phi\, \sin^4(\theta_1)\, \sin^3(\theta_2)\, \sin^2(\theta_3)\, \sin(\theta_4) = \pi^3. \tag{6.24}$$

Alternatively, a six-dimensional coordinate parametrization with five angular variables can be defined as

$$\boldsymbol{\rho} = R_6 \cos(\Phi)\, \hat{\mathbf{n}}_1, \qquad \boldsymbol{\lambda} = R_6 \sin(\Phi)\, \hat{\mathbf{n}}_2,$$

where $\hat{\mathbf{n}}_1$ and $\hat{\mathbf{n}}_2$ are unit vectors with independent solid-angle integrations.

The numerical coefficients in the definitions of these coordinates ensure that the kinetic energy operator takes the form of a Laplacian in the six-dimensional space $\{\boldsymbol{\rho}, \boldsymbol{\lambda}\}$, divided by $2m$. (The total center-of-mass momentum carries a different coefficient, but it is assumed to vanish.) We defer the explicit derivation to the section devoted to four-particle systems.

In general, the effective potential V_6 depends on all six coordinates. It can, however, be projected onto the six-dimensional radial coordinate R_6 by performing an angular average. If the binary interactions are of Cornell type, consisting of linear and Coulomb-like terms, for example $V_{12} = \kappa_2/r_{12} + \sigma_2 r_{12}$, their projections are obtained through the solid-angle integrals

$$\langle r_{12} \rangle = \sqrt{2}\, \langle |\boldsymbol{\rho}| \rangle = \sqrt{2} R_6 \frac{\int d\Omega_6\, d_{12}}{\Omega_6} \approx 0.960\, R_6, \tag{6.25}$$

where

$$d_{12} = \sqrt{C_1^2 + S_1^2 C_2^2 + S_1^2 S_2^2 C_3^2} = \sqrt{1 - S_1 S_2 S_3}, \tag{6.26}$$

and we have introduced the shorthand notations $C_i = \cos(\theta_i)$ and $S_i = \sin(\theta_i)$.

Dimensional considerations also imply that the Coulomb term $1/r$ in the binary potential must generate a contribution $\sim 1/R_6$ in hyperspherical coordinates. The angular averaging of the Coulomb interaction involves the factor $1/(\sqrt{2}d_{12})$, leading to

$$\left\langle \frac{1}{r_{12}} \right\rangle = \frac{1}{\Omega_6} \int d\Omega_6 \, \frac{1}{\sqrt{2}\, d_{12}} \approx \frac{1.20}{R_6}. \tag{6.27}$$

The convergence of this integral follows from the fact that d_{12} can vanish only if all three angles $\theta_1, \theta_2, \theta_3 \approx \pi/2$.

As a result, the effective potential in the hyperspherical coordinate R_6 takes the form

$$V(R_6) = 3\left[0.96\, R_6\,(0.113/2) - \frac{1.2}{R_6}\,(0.64/2)\right], \tag{6.28}$$

where the factor of 3 accounts for the interactions of the three quark pairs 12, 13, and 23. The numerical values 0.113 and 0.64 (in GeV^2 units) are taken from our version of the Cornell potential.

6.C The spin-tensor and vector representations of the multi-index WFs

Nucleon-like baryons have color×spin×flavor wave functions derived earlier in this chapter, for example the spin-flavor part of the proton wave function in Eq. (6.9). Multiquark hadrons possess much more complicated wave functions of the form (orbital)×color×spin×flavor, often containing thousands of components in the monomial space and, in some cases, even millions. Clearly, an automatic procedure is required to record such wave functions in a form that allows for efficient manipulation.

The procedure consists of two main steps. The first is to define the wave functions as spin tensors. We illustrate this for the proton wave function (6.9), written schematically as $S_\rho I_\rho + S_\lambda I_\lambda$.

We begin by specifying the basis states. For both spin and isospin, these are

$$up = \{1, 0\}, \qquad down = \{0, 1\}.$$

The spin-isospin wave function in spin-tensor form is then represented as a 2^6-dimensional table, defined by the Mathematica command

$$
\begin{aligned}
SIproton = \text{Table}\Big[&(up[[s1]] * down[[s2]] - up[[s2]] * down[[s1]])up[[s3]] \\
&\times (up[[i1]] * down[[i2]] - up[[i2]] * down[[i1]])up[[i3]])/2 \\
&+ (up[[s1]]down[[s2]]up[[s3]] + down[[s1]]up[[s2]]up[[s3]] - 2up[[s1]]up[[s2]]down[[s3]]) \\
&\times (up[[i1]]down[[i2]]up[[i3]] + down[[i1]]up[[i2]]up[[i3]] - 2up[[i1]]up[[i2]]down[[i3]])/6 \\
&, \{s1, 1, 2\}, \{s2, 1, 2\}, \{s3, 1, 2\}, \{i1, 1, 2\}, \{i2, 1, 2\}, \{i3, 1, 2\}\Big]
\end{aligned}
\tag{6.29}
$$

The output is

$$= \{\{\{\{\{\{0, 0\}, \{0, 0\}\}, \{\{0, 0\}, \{0, 0\}\}\}, \{\{\{0, \sqrt{2}/3\}, \{-1/(3\sqrt{2}), 0\}\}, \{\{-1/(3\sqrt{2}), 0\},$$

$$\{0, 0\}\}\}\}, \{\{\{\{0, -1/(3\sqrt{2})\}, \{\sqrt{2}/3, 0\}\}, \{\{-1/(3\sqrt{2}), 0\}, \{0, 0\}\}\}, \{\{\{0, 0\}, \{0, 0\}\},$$

$$\{\{0, 0\}, \{0, 0\}\}\}\}\}, \{\{\{\{\{0, -1/(3\sqrt{2})\}, \{-1/(3\sqrt{2}), 0\}\}, \{\{\sqrt{2}/3, 0\}, \{0, 0\}\}\}, \{\{\{0, 0\}, \{0, 0\}\}, \{\{0, 0\},$$

$$\{0,0\}\}\}\}, \{\{\{\{0,0\}, \{0,0\}\}, \{\{0,0\}, \{0,0\}\}\}, \{\{\{0,0\}, \{0,0\}\}, \{\{0,0\}, \{0,0\}\}\}\}\}\}$$

In the second step, a single 64-dimensional vector representation is obtained by applying the `Flatten` command, which removes all internal brackets. In this form, only nine of the 64 components of the proton wave function are nonzero.

The normalization can be verified straightforwardly by computing the scalar product $SIproton \cdot SIproton = 1$. Expectation values of any operator $\hat{O}$ (for example, the magnetic moment) can then be obtained as $SIproton \cdot \hat{O} \cdot SIproton$, and similarly for other observables.

Chapter 7
Tetraquarks

Historically, the first in-depth study of tetraquarks dates back to Ref. [Jaffe, 1977], where it was argued that tetraquarks composed of light quarks could be rather light, form specific $SU(3)_f$ multiplets, and in particular provide an explanation for some known scalar mesons. These calculations were performed within the framework of the MIT bag model and were received with considerable skepticism at the time, largely because of the well-known limitations of that particular model.

It took roughly four decades for the community's attitude to shift from skeptical to enthusiastic, following the discovery of $\bar{c}c\bar{q}q$ tetraquark candidates, already mentioned in the charmonium chapter. In this chapter, we begin with the kinematics of the general case involving four different quark flavors, and then turn to special limiting cases, in particular the single-flavor $cc\bar{c}\bar{c}$ systems.

7.1 Four-flavor tetraquarks

When all four quark flavors are different, the identification of exotic states is relatively straightforward. For example, in the D^-K^+ channel, any resonance must have the minimal valence quark content $\bar{c}d\bar{s}u$, and is therefore manifestly exotic. Resonances observed by LHCb in this channel include

$$X_0(2900): \quad M = 2.866 \pm 0.007 \pm 0.002 \,\text{GeV}, \qquad \Gamma = 57 \pm 12 \pm 4 \,\text{MeV},$$

$$X_1(2900): \quad M = 2.904 \pm 0.005 \pm 0.001 \,\text{GeV}, \qquad \Gamma = 110 \pm 11 \pm 4 \,\text{MeV}.$$

At present, the exact quantum numbers of these states are not yet firmly established, nor is it clear whether they represent the lowest-lying states in this channel.

Among the early theoretical studies of these resonances, we focus here on Ref. [Karliner and Rosner, 2020]. In that work, the authors describe the states as two diquarks connected by a QCD string stretched between two string junctions. Using a schematic additive mass model, combined with earlier results for baryons obtained within the same framework, they note that part of such a tetraquark configuration (a ud diquark bound to a c quark) resembles the structure of the Λ_c baryon. The remaining contributions arise from the sc binding and from the additional mass associated with the string junction, for which previous studies suggested a value $S \approx 165 \,\text{MeV}$.

It should be emphasized that in such string-based models only the ud and cs pairwise interactions are included, while all other quark pairs are assumed to be noninteracting. Clearly, more comprehensive approaches, incorporating realistic interquark forces and fully quantum-mechanical treatments, are required in order to obtain reliable wave functions and a complete spectroscopy.

In four-flavor tetraquarks, all quarks are distinguishable, and therefore no antisymmetrization of the wave function is required. As a result, such systems can, in principle, be studied using direct numerical

methods, such as path integral techniques[1]. A closely related first-principles approach is the solution of the Schrodinger equation in imaginary (Euclidean) time, also known as diffusion Monte Carlo; see, for example, Ref. [Gordillo and Segovia, 2025].

In that work, the Hamiltonian includes $(\lambda\lambda)(\sigma\sigma)$ operators and is represented as a matrix in an appropriate monomial basis. The operator $\exp(-\hat{H}\tau)$ is then implemented numerically as a relaxation from an initial Ansatz toward the true ground state. The results indicate that the experimentally observed resonances are close to isospin $I = 1$ states, while the corresponding $I = 0$ states (not yet observed) are predicted to lie roughly $400\,\mathrm{MeV}$ lower in mass.

An important feature of the resulting wave functions is that the distributions of interparticle distances for all quark pairs are very similar in shape and are quite compact, with $r^2|\psi|^2$ peaking at $r \sim 0.5\,\mathrm{fm}$. If confirmed, this behavior would strongly disfavor interpretations, whether in terms of two mesons or two loosely bound diquarks.

7.2 Color-spin-flavor structure of tetraquarks in terms of diquarks

Tetraquarks consist of two quarks and two antiquarks. The constraints imposed by Fermi statistics are therefore even simpler than in the baryonic case discussed above, and they can be analyzed without any special techniques.

We begin with diquarks, qq. For light quarks (uu, ud, dd), the combined color-spin-flavor wave function must be antisymmetric under permutation of the two quarks. The same applies to a pair of antiquarks. The relevant permutation group is S_2, which is particularly simple, so all possibilities can be enumerated explicitly.

Color admits an antisymmetric $\underline{3}$ and a symmetric 6 representation. **Spin** admits an antisymmetric singlet (spin 0) and a symmetric triplet (spin 1), and the same structure applies to $SU(2)$ isospin.

Altogether, there are four possible diquark configurations,

$$d_1 = \underline{3} \otimes 1 \otimes 1, \qquad d_2 = \underline{3} \otimes 3 \otimes 3, \qquad d_3 = 6 \otimes 3 \otimes 1, \qquad d_4 = 6 \otimes 1 \otimes 3.$$

Combining a diquark with an antidiquark is only possible if their color representations match, ensuring that the resulting tetraquark is a color singlet. This leads to eight possible combinations,

$$d_1\bar{d}_1, \; d_1\bar{d}_2, \; d_2\bar{d}_1, \; d_2\bar{d}_2, \; d_3\bar{d}_3, \; d_3\bar{d}_4, \; d_4\bar{d}_3, \; d_4\bar{d}_4.$$

As usual, we start with the extreme cases, which are the simplest. Suppose the total spin and isospin of the tetraquark are maximal,

$$S_{\mathrm{tet}} = I_{\mathrm{tet}} = 2.$$

As an explicit example, consider $T^{++} = u \uparrow u \uparrow \bar{d} \uparrow \bar{d} \uparrow$. In this case, the only remaining degree of freedom is color, which must be antisymmetric, $\underline{3}$. Consequently, only a single structure is allowed, schematically $d_2\bar{d}_2 = (333) - (333)$.

Next, suppose that S_{tet} is arbitrary, while $I_{\mathrm{tet}} = 2$ remains fixed. In this situation, both color and spin degrees of freedom contribute, and the diquarks d_2 and d_4 are allowed. This leads to four possible tetraquark configurations, and so on. As we shall see, these states can mix through various interactions.

The first interaction we consider is the "relative color" force,

---

[1] One of us employed such methods more than forty years ago to study two electrons in the helium atom and four nucleons in the helium nucleus; see E. V. Shuryak and O. V. Zhirov, Testing Monte Carlo methods for path integrals in some quantum mechanical problems, Nucl. Phys. B **242**, 393 (1984).

$$H_{\lambda\lambda} = \sum_{i>j} w_{ij}(\boldsymbol{\lambda}_i\boldsymbol{\lambda}_j), \tag{7.1}$$

where the sum runs over all six quark-quark and quark-antiquark pairs. The explicit Mathematica implementation of this operator is given in Appendix 7.B.

The color wave function can be written as a superposition of two components,

$$|\psi\rangle = F_1\,|\underline{3}\rangle + F_2\,|6\rangle.$$

Sandwiching the operator V_0 defined above between diquark-antidiquark states and performing the summation over all color indices yields

$$H_{\lambda\lambda}^{66} = \frac{2}{3}\left(2w_{12} - 5w_{13} - 5w_{14} - 5w_{24} - 5w_{32} + 2w_{34}\right), \tag{7.2}$$

$$H_{\lambda\lambda}^{33} = -\frac{4}{3}\left(2w_{12} + w_{13} + w_{14} + w_{24} + w_{32} + 2w_{34}\right). \tag{7.3}$$

In the 66 case, the contributions from qq and $\bar{q}\bar{q}$ pairs are repulsive, whereas in the $\underline{33}$ case all terms are attractive. A naive application of the diquark model would therefore suggest that the $\underline{33}$ configuration should have a lower energy than the 66 one. However, this conclusion is incorrect. If all interaction strengths are equal, $w_{ij} = w$, both expressions reduce to the same value, $-(32w/3)$.

This remarkable result is well known [Badalian, 2023, Miesch et al., 2024]. We emphasize it here because it contradicts a widespread intuition: starting from "good diquarks" (F_1) rather than "bad" ones (F_2) does *not* automatically lead to lower tetraquark energies. In this case, the repulsion within the diquarks is exactly compensated by stronger attraction between them.

Further splittings and mixings arise once more complicated interactions are included, such as the color-spin Hamiltonian,

$$H_{\lambda\lambda\sigma\sigma} = V\sum_{ij}(\boldsymbol{\lambda}_i\boldsymbol{\lambda}_j)(\boldsymbol{\sigma}_i\boldsymbol{\sigma}_j). \tag{7.4}$$

Since this operator does not change isospin, there are four states that split into two pairs, $(311311, 311631)$ and $(333333, 333613)$. The corresponding Hamiltonian matrices are

$$H(311311 - 311631) = V\begin{pmatrix} 44/3 & -6\sqrt{2} \\ -6\sqrt{2} & -2/3 \end{pmatrix}, \tag{7.5}$$

with eigenvalues after mixing $V(18.43, -4.44)$, and

$$H(613613 - 311631) = V\begin{pmatrix} 20/3 & -6\sqrt{2} \\ -6\sqrt{2} & -34/3 \end{pmatrix}, \tag{7.6}$$

with eigenvalues after mixing $V(-17.80, -0.20)$.

Another possible interaction is pion exchange, proposed by Ripka and Glozman,

$$H_{\sigma\sigma\tau\tau} = V_{\sigma\sigma\tau\tau}\sum_{i>j}(\boldsymbol{\sigma}_i\boldsymbol{\sigma}_j)(\boldsymbol{\tau}_i\boldsymbol{\tau}_j), \tag{7.7}$$

where $\boldsymbol{\tau}$ are Pauli matrices for $SU(2)$ flavor (or Gell-Mann matrices for $SU(3)$). In this case, the color structure remains unchanged, while the isospin is affected. The Hamiltonian then takes the form

$$H(311311 - 311333) = V_2\begin{pmatrix} 18 & 3 \\ 3 & 2 \end{pmatrix}, \tag{7.8}$$

with eigenvalues after mixing $V_2(18.544, 1.456)$. The color-sextet pair splits in an analogous manner.

We conclude this technical subsection by explaining why we have chosen to discuss tetraquarks in a somewhat old-fashioned way, using spin tensors and explicit summation over all indices. In principle, all states can be represented as vectors in a universal *monom basis* of dimension $N_{\text{monoms}} = 3^4 \cdot 2^4 \cdot 2^4 = 20736$. In *Wolfram Mathematica*, this is easily implemented using the `TensorProduct` command. For example, the first $d_1 \bar{d}_1$ wave function can be written as

$$\Psi_1 = \text{Flatten}\big[\text{SparseArray}[\text{TensorProduct}(color33, spin0, spin0, spin0, spin0)]\big], \tag{7.9}$$

which produces a vector of length N_{monoms}, with only 192 nonzero components[2]. The individual factors can be prepared as spin tensors; for example,

$$spin0 = \text{Flatten}\big[\text{Table}[(up[[s1]] * down[[s2]] - up[[s2]] * down[[s1]])/\sqrt{2}, \{s1, 1, 2\}, \{s2, 1, 2\}]\big],$$

which returns the spin-zero diquark wave function $\{0, 1/\sqrt{2}, -1/\sqrt{2}, 0\}$.

For the present discussion, where only eight wave functions are needed, this formalism may appear excessive. Its real advantage becomes clear when various Hamiltonians are represented as universal matrices of dimension $N_{\text{monoms}} \times N_{\text{monoms}}$, enabling systematic and automated calculations.

7.3 Quantum mechanics of four quarks in hyper-spherical coordinates

The modified Jacobi coordinates for four particles are defined by

$$\boldsymbol{\xi}_1 = \sqrt{\frac{1}{2}}(\mathbf{r}_1 - \mathbf{r}_2) \tag{7.10}$$

$$\boldsymbol{\xi}_2 = \sqrt{\frac{1}{6}}(\mathbf{r}_1 + \mathbf{r}_2 - 2\mathbf{r}_3)$$

$$\boldsymbol{\xi}_3 = \frac{1}{2\sqrt{3}}(\mathbf{r}_1 + \mathbf{r}_2 + \mathbf{r}_3 - 3\mathbf{r}_4)$$

plus the CM coordinate $\mathbf{X} = (\mathbf{r}_1 + \mathbf{r}_2 + \mathbf{r}_3 + \mathbf{r}_4)/4$, complleting it to 12 coordinates. In this case the *hyperdistance* is defined as

$$\begin{aligned} R_9^2 &\equiv \boldsymbol{\xi}_1^2 + \boldsymbol{\xi}_2^2 + \boldsymbol{\xi}_3^2 \\ &= \frac{1}{4}[(\mathbf{r}_1 - \mathbf{r}_2)^2 + (\mathbf{r}_1 - \mathbf{r}_3)^2 + (\mathbf{r}_1 - \mathbf{r}_4)^2 \\ &+ (\mathbf{r}_3 - \mathbf{r}_2)^2 + (\mathbf{r}_4 - \mathbf{r}_2)^2 + (\mathbf{r}_3 - \mathbf{r}_4)^2] \end{aligned} \tag{7.11}$$

is connected to the sum of the squared distances of all six pairs of quarks. When supplemented by 8 angles, it describes the 9-dimensional space in which quantum mechanics is performed.

Calculating from (7.10) the Jacobian matrix $\partial \xi_i / \partial r_j$ and using it twice, one can transform the kinetic energy into new coordinates.

$$-2mK = \frac{\partial^2}{\partial \boldsymbol{\xi}_1^2} + \frac{\partial^2}{\partial \boldsymbol{\xi}_2^2} + \frac{\partial^2}{\partial \boldsymbol{\xi}_3^2} + \frac{1}{4}\frac{\partial^2}{\partial \mathbf{X}^2} \tag{7.12}$$

Keeping the CM coordinate $\mathbf{X} = 0$ and ignoring the last term, we can use the kinetic energy proportional to the 9-dimensional Laplacian.

The dependence on the wave function on the hyper-distance *only* select the lowest spherically symmetric S-shell. Only the radial Schrodinger equation needs to be solved. Note that after changing to the reduced wave-function, it differs from the familiar 3-dimensional case, by only the quasi-centrifugal term $12/R_9^2$.

---

[2] This is why the `SparseArray` format is convenient, though optional.

The angular averaging is performed as in the previous section, except now there is a different volume element, namely

$$\Omega_9 = \int (\prod_{i=1}^{7} d\theta_i) d\phi \, sin(\theta_1)^7 * sin(\theta_2)^6 * sin(\theta_3)^5 * sin(\theta_4)^4 \, sin(\theta_5)^3 * sin(\theta_6)^2 * sin(\theta_7) = \frac{32\pi^4}{105}$$

(7.13)

The angular integrations when averaging using the Cornell potential, are done as in the previous section, with obvious changes

$$\langle r_{12} \rangle = \sqrt{2}\langle|\boldsymbol{\rho}|\rangle = \frac{\sqrt{2}R_9}{\Omega_9} \int d\Omega_9 d_{12} \approx 0.773 R_9$$

(7.14)

$$\left\langle \frac{1}{r_{12}} \right\rangle = \frac{1}{R_9 \Omega_9} \int \frac{d\Omega_9}{\sqrt{2}d_{12}} \approx 1.55/R_9$$

(7.15)

7.4 Single-flavor tetraquarks

The $cc\bar{c}\bar{c}$ tetraquarks were first observed by the LHCb Collaboration, and subsequently by the CMS and ATLAS collaborations, in $J/\psi \, J/\psi$ (and related) decay channels. Three interfering states have been reported, all with the same quantum numbers, most likely 2^{++}. The current LHCb values (in MeV) are

$$\begin{aligned} M_1 &= 6593^{+15}_{-14}, & \Gamma_1 &= 446^{+66}_{-54}, \\ M_2 &= 6847 \pm 10, & \Gamma_2 &= 135^{+16}_{-14}, \\ M_3 &= 7173^{+9}_{-10}, & \Gamma_3 &= 73^{+18}_{-15}, \end{aligned}$$

(7.16)

and these states are observed both in the $J/\psi \, J/\psi$ and $J/\psi \, \psi'$ channels.

Theoretical investigations on the lattice began with studies of charmonium scattering lengths, such as η_c-η_c and J/ψ-J/ψ scattering, reported in Ref. [Meng et al., 2025]. While the lowest-order diagrams naively suggest an attractive interaction between the two quarkonia, the lattice calculations instead indicate that the low-energy interaction is in fact *repulsive*. The corresponding scattering lengths are

$$a^{0+}_{\eta_c - \eta_c} = -0.104(09)\,\text{fm}, \qquad a^{2+}_{J/\psi - J/\psi} = -0.165(16)\,\text{fm}.$$

(7.17)

Since the absolute masses of the tetraquark states are sensitive to additive constants in the potential (or, equivalently, to the quark mass), we will focus instead on the mass splittings, or gaps

$$M_2 - M_1, \qquad M_3 - M_1,$$

(7.18)

which should be compared with the gaps between successive radial excitations.

Appendix

7.A Kinematics of four bodies with different masses

The kinematics of four bodies with equal masses were discussed above in Section 7.3. In this Appendix, we consider the more general case of four bodies with different masses, as well as alternative choices of coordinates that are sometimes used in the literature.

We begin with the original Jacobi construction, defining coordinates for four objects with unequal masses. These coordinates are obtained through the following transformation from the original particle coordinates $x[[i]]$,

$$\alpha = -x[[1]] + x[[2]], \tag{7.19}$$
$$\beta = (M_1 x[[1]] + M_2 x[[2]])/(M_1 + M_2) - x[[3]],$$
$$\gamma = (M_1 x[[1]] + M_2 x[[2]] + M_3 x[[3]])/(M_1 + M_2 + M_3) - x[[4]],$$
$$\delta = (M_1 x[[1]] + M_2 x[[2]] + M_3 x[[3]] + M_4 x[[4]])/(M_1 + M_2 + M_3 + M_4).$$

The coordinate δ corresponds to the center-of-mass (CM) position and, as usual, is set to zero.

By computing the inverse transformation, one can express the original coordinates $x[[i]]$ in terms of $\alpha, \beta, \gamma, \delta$ and then determine the metric in the new coordinate system from the line element. The resulting expression is

$$
\begin{aligned}
dl^2 =& \frac{(M_1^2 + M_2^2)}{(M_1 + M_2)^2}\, d\alpha^2 + \frac{(M_1^2 + 2M_1 M_2 + M_2^2 + 2M_3^2)}{(M_1 + M_2 + M_3)^2}\, d\beta^2 \\
&- \frac{2(M_1 + M_2 - 2M_3)\, d\beta(M_4 d\gamma + (M_1 + M_2 + M_3 + M_4)d\delta)}{(M_1 + M_2 + M_3)(M_1 + M_2 + M_3 + M_4)} \\
&+ \frac{1}{(M_1 + M_2 + M_3 + M_4)^2}\Big[(M_1^2 + M_2^2 + 2M_2 M_3 + M_3^2 + 2M_1(M_2 + M_3) + 3M_4^2)\, d\gamma^2 \\
&- 2(M_1^2 + M_2^2 + M_3^2 + 2M_2(M_3 - M_4) + 2M_1(M_2 + M_3 - M_4) - 2M_3 M_4 - 3M_4^2)\, d\gamma\, d\delta \\
&+ 4(M_1 + M_2 + M_3 + M_4)^2\, d\delta^2\Big] \\
&+ \frac{2(M_1 - M_2)\, d\alpha}{(M_1 + M_2)(M_1 + M_2 + M_3)(M_1 + M_2 + M_3 + M_4)} \\
&\times \Big[M_3(M_1 + M_2 + M_3 + M_4)\, d\beta + (M_1 + M_2 + M_3)(M_4 d\gamma + (M_1 + M_2 + M_3 + M_4)\, d\delta)\Big]. \tag{7.20}
\end{aligned}
$$

From this metric one can derive the Laplacian involving the inverse metric $g^{\mu\nu}\partial_\mu\partial_\nu$, which is likewise non-diagonal.

In the special case of equal masses, $M = M_1 = M_2 = M_3 = M_4$, both the metric and the Laplacian become diagonal,

$$dl^2 = (6\,d\alpha^2 + 8\,d\beta^2 + 9\,d\gamma^2 + 48\,d\delta^2)/12. \tag{7.21}$$

By rescaling the coordinates (denoted by bars) with appropriate factors and neglecting the CM motion ($d\delta \to 0$), the line element reduces to

$$d\bar{\alpha}^2 + d\bar{\beta}^2 + d\bar{\gamma}^2, \tag{7.22}$$

which exhibits manifest spherical symmetry.

In some studies of four-body systems (including tetraquarks), an alternative set of coordinates is employed[3],

$$a = x[[2]] - x[[1]], \tag{7.23}$$
$$b = x[[3]] - x[[4]],$$
$$c = (M_1 x[[1]] + M_2 x[[2]])/(M_1 + M_2) - (M_3 x[[3]] + M_4 x[[4]])/(M_3 + M_4),$$
$$d = (M_1 x[[1]] + M_2 x[[2]] + M_3 x[[3]] + M_4 x[[4]])/(M_1 + M_2 + M_3 + M_4).$$

Here again, d represents the center-of-mass coordinate and is set to zero. The corresponding metric is, in general, non-diagonal,

$$
\begin{aligned}
dl^2 = &\; \frac{(M_1^2 + M_2^2)}{(M_1 + M_2)^2}\,da^2 + \frac{(M_3^2 + M_4^2)}{(M_3 + M_4)^2}\,db^2 \\
&- \frac{2(M_3 - M_4)\,db\big[-(M_1 + M_2)dc + (M_1 + M_2 + M_3 + M_4)dd\big]}{(M_3 M_4)(M_1 + M_2 + M_3 + M_4)} \\
&+ \frac{2(M_1 - M_2)\,da\big[(M_3 + M_4)dc + (M_1 + M_2 + M_3 + M_4)dd\big]}{(M_1 + M_2)(M_1 + M_2 + M_3 + M_4)} \\
&+ \frac{1}{(M_1 + M_2 + M_3 + M_4)^2}\Big[2(M_1^2 + 2M_1 M_2 + M_2^2 + (M_3 + M_4)^2)\,dc^2 \\
&- 4(M_1^2 + 2M_1 M_2 + M_2^2 - (M_3 + M_4)^2)\,dc\,dd + 4(M_1 + M_2 + M_3 + M_4)^2\,dd^2\Big]. \tag{7.24}
\end{aligned}
$$

A non-diagonal metric again implies a non-diagonal Laplacian. However, when all masses are equal ($M = M_1 = M_2 = M_3 = M_4$), the metric simplifies to

$$dl^2 = (da^2 + db^2 + 2\,dc^2 + 8\,dd^2)/2, \tag{7.25}$$

which is diagonal.

Is there any preference between these two coordinate choices? We find that there is. For tetraquarks of the type $qQ\bar{q}\bar{Q}$, with masses chosen as $m = M_1 = M_3$ and $M = M_2 = M_4$, the alternative coordinates lead to a diagonal Laplacian,

$$L = \frac{\partial}{\partial a^2} + \frac{(m + M)^2}{(m^2 + M^2)}\frac{\partial}{\partial b^2} + \frac{\partial}{\partial c^2} + \frac{1}{4}\frac{\partial}{\partial d^2}. \tag{7.26}$$

For convenience, the main features of the two coordinate choices discussed above are summarized in the appended table. It compares the original Jacobi construction and the alternative pair-based coordinates for different mass patterns, focusing on whether the resulting metric (and hence the Laplacian) is diagonal after removal of the center-of-mass motion. In the generic case of four unequal masses, both choices lead to non-diagonal kinetic terms and offer no particular advantage. For equal masses, the two constructions become equivalent and reduce to a spherically symmetric form. The most important case for applications, however, is the $qQ\bar{q}\bar{Q}$ tetraquark with $m = M_1 = M_3$ and $M = M_2 = M_4$, where the alternative coordinates yield a

---

[3] These are also often referred to as Jacobi coordinates, although this terminology is somewhat misleading. The original idea of Jacobi was to define relative coordinates between the center of mass of a subset of particles and the next particle.

diagonal Laplacian even for unequal masses. This makes them the optimal choice for practical calculations of tetraquark spectra and wave functions.

Mass pattern	Coordinates	Laplacian	Comment
$M_1 \neq M_2 \neq M_3 \neq M_4$	Jacobi (α, β, γ)	Non-diagonal	Fully general, but algebraically cumbersome
$M_1 \neq M_2 \neq M_3 \neq M_4$	Alternative (a, b, c)	Non-diagonal	No practical simplification
$M_1 = M_2 = M_3 = M_4$	Jacobi	Diagonal	Spherical symmetry after CM removal
$M_1 = M_2 = M_3 = M_4$	Alternative	Diagonal	Equivalent to Jacobi choice
$q Q \bar{q} \bar{Q} m = M_1 = M_3 M = M_2 = M_4$	Alternative	Diagonal	Optimal choice for tetraquarks
$q Q \bar{q} \bar{Q} m = M_1 = M_3 M = M_2 = M_4$	Jacobi	Non-diagonal	Less convenient

7.B Color matrices for quarks and antiquarks

Here 8 λ matrices are Gell-Mann generators of $SU(3)$ for quarks, given in Mathematica notations[4]. Matrices $\lambda b = -\lambda^*$ are appropriate for antiquarks

```
\[Lambda][1] = {{0, 1, 0}, {1, 0, 0}, {0, 0, 0}}; \[Lambda][
  2] = {{0, -I, 0}, {I, 0, 0}, {0, 0, 0}};
 \[Lambda][3] = {{1, 0, 0}, {0, -1, 0}, {0, 0, 0}};
\[Lambda][4] = {{0, 0, 1}, {0, 0, 0}, {1, 0, 0}};
\[Lambda][5] = {{0, 0, -I}, {0, 0, 0}, {I, 0, 0}};
\[Lambda][6] = {{0, 0, 0}, {0, 0, 1}, {0, 1, 0}}; \[Lambda][
  7] = {{0, 0, 0}, {0, 0, -I}, {0, I, 0}};
 \[Lambda][8] = {{1, 0, 0}, {0, 1, 0}, {0, 0, -2}}/Sqrt[3];
 \[Lambda]b[1] = -{{0, 1, 0}, {1, 0, 0}, {0, 0, 0}}; \[Lambda]b[
  2] = {{0, -I, 0}, {I, 0, 0}, {0, 0, 0}};
 \[Lambda]b[3] = -{{1, 0, 0}, {0, -1, 0}, {0, 0, 0}};
\[Lambda]b[4] = -{{0, 0, 1}, {0, 0, 0}, {1, 0, 0}};
\[Lambda]b[5] = {{0, 0, -I}, {0, 0, 0}, {I, 0, 0}};
\[Lambda]b[6] = -{{0, 0, 0}, {0, 0, 1}, {0, 1, 0}}; \[Lambda]b[
  7] = {{0, 0, 0}, {0, 0, -I}, {0, I, 0}};
 \[Lambda]b[8] = -{{1, 0, 0}, {0, 1, 0}, {0, 0, -2}}/Sqrt[3];


V0 :=w12* Sum[\[Lambda][A][[c1p, c1]]*\[Lambda][A][[c2p, c2]],{A, 1, 8}]*\[Delta]3[[c3p, c3]]*\[Delt
  w34*Sum[\[Lambda]b[A][[c3p, c3]]*\[Lambda]b[A][[c4p, c4]], {A, 1, 8}]*\[Delta]3[[c1p, c1]]*\[Delta]3
  w24*Sum[\[Lambda][A][[c2p, c2]]*\[Lambda]b[A][[c4p, c4]], {A, 1, 8}]*\[Delta]3[[c3p, c3]]*[Delta]3[
  w14*Sum[\[Lambda][A][[c1p, c1]]*\[Lambda]b[A][[c4p, c4]], {A, 1, 8}]*\[Delta]3[[c3p, c3]]*\[Delta]3
  w32*Sum[\[Lambda]b[A][[c3p, c3]]*\[Lambda][A][[c2p, c2]], {A, 1, 8}]*\[Delta]3[[c1p, c1]]*\[Delta]3
```

---

[4] Note however that in order to use it one has to rewrite it to their Mathematica: direct copy would lead to font problems, as they are different in Wolfram and PDF.

Chapter 8
Excited baryons

8.1 The negative-parity P-shell baryons

To reveal the role of various spin-dependent forces between quarks, it is *not* sufficient to consider only the lowest S-shell baryons. Spin-spin interactions generate essentially a single mass splitting between the N and Δ. In contrast, spin-orbit and tensor forces become operative only in higher baryonic shells, where the spectrum is richer and the phenomenology more informative.

The pioneering study by Isgur and Karl (IK) [Isgur and Karl, 1979b] focused on the negative-parity P-shell baryons. Their analysis concentrated primarily on hyperons containing a strange quark, for which wave functions with 12-symmetry were sufficient. The light-quark baryons were then obtained as appropriate limits of these hyperon states, by reducing the strange-quark mass to that of the light quarks.

IK employed two Jacobi vectors, $\boldsymbol{\rho}$ and $\boldsymbol{\lambda}$, which naturally separate structures that are antisymmetric or symmetric under permutation of quarks 1 and 2, $\hat{P}(12)$. In the P-shell, the wave functions factorize into three parts: orbital, spin, and isospin. Using three building blocks with the same ρ, λ structure, one obtains a $2^3 = 8$-dimensional space, within which the states symmetric under *all* permutations can be identified. This observation played a central role in the work of IK and their successors.

A systematic treatment, without relying on educated guessing and with a clear path toward generalization to multiquark systems, requires the explicit construction of representations of the relevant permutation groups. We present these constructions in the appendix to this chapter.

In contrast to the Isgur-Karl approach, we choose not to introduce additional parameters associated with strangeness, and instead focus exclusively on light-quark states. As is well known, the negative-parity $L = 1$ (P-shell) baryons consist of seven states: five N^* and two Δ^*. Restricting attention to the N^* sector, the five masses together with two mixing matrix elements (for the $J = 3/2$ and $J = 1/2$ pairs) provide seven independent inputs. In Table 8.1.1 we list the current experimental masses of the P-shell states and compare them with the original Isgur-Karl predictions [Isgur and Karl, 1979b].

We adopt here a strategy that inverts the usual logic of spectroscopy. Rather than postulating a specific model and comparing its predictions with data, we first extract *phenomenological values* of the matrix elements of the relevant operators directly from experiment. Given the known structure of the wave functions and the spin-orbit-isospin structure of the operators, the masses can be expressed as linear combinations of these matrix elements. The seven experimental inputs are sufficient to determine them uniquely.

The mixing angles of the $S = 3/2$ and $S = 1/2$ states are determined from decay data and are listed in the RPP reviews,

$$\theta_{S1/2} = -32^\circ, \qquad \theta_{S3/2} = 6^\circ.$$

The relation between the energies of the mixed states and the unmixed ones is

$$M_\pm = \frac{1}{2}\left(M_1 + M_2 \pm \sqrt{4H_{mix}^2 + (M_1 - M_2)^2} \right), \tag{8.1}$$

and the corresponding mixing angle is

$$\tan\theta = \frac{2H_{mix}}{M_1 - M_2 - \sqrt{4H_{mix}^2 + (M_1 - M_2)^2}}. \tag{8.2}$$

Using the observed masses $M_\pm$ and mixing angles, we extract the unmixed masses $M_{1,2}$, which are listed in the final column of Table 8.1.1. The resulting mixing matrix elements are

$$\begin{aligned} H_{mix}(J = 1/2) &= 51.7\,\text{MeV}, \\ H_{mix}(J = 3/2) &= -18.7\,\text{MeV}. \end{aligned} \tag{8.3}$$

Below, we will use the five masses to determine five matrix elements and compare the value of the tensor matrix element with these two mixing matrix elements.

In the P-shell with $L = 1$, one has either $L_\rho = 1, L_\lambda = 0$ or $L_\lambda = 1, L_\rho = 0$. Accordingly, for the orbital wave functions $\varphi_{LM}^{\rho,\lambda}$ we define

$$\begin{aligned} \varphi_{1m}^\rho &= (\rho_-, \sqrt{2}\rho_z, -\rho_+)\varphi_{00} \equiv z_m^\rho \varphi_{00}, \\ \varphi_{1m}^\lambda &= (\lambda_-, \sqrt{2}\lambda_z, -\lambda_+)\varphi_{00} \equiv z_m^\lambda \varphi_{00}, \end{aligned} \tag{8.4}$$

with $\rho_\pm = (\rho_1 \pm i\rho_2)$ and $\lambda_\pm = (\lambda_1 \pm i\lambda_2)$. Up to the overall radial dependence, these are the standard angular functions Y_1^m with $m = -1, 0, +1$.

Combining these orbital states with all possible spin configurations yields five excited nucleon states,

$$J^P = L^P \oplus S^P = 1^- \otimes \left(\frac{1}{2}^+, \frac{3}{2}^+ \right) \to 2 \times \left(\frac{1}{2}^-, \frac{3}{2}^- \right), \frac{5}{2}^-. \tag{8.5}$$

That is, two $\frac{1}{2}^-$ states, two $\frac{3}{2}^-$ states, and one $\frac{5}{2}^-$ state. Standard Clebsch-Gordan coefficients specify how to combine the orbital and spin parts into states of definite J, J_z. However, to construct fully antisymmetric baryon wave functions consistent with Fermi statistics, the isospin structure must also be incorporated properly. The construction of symmetric wave functions from the three ρ, λ structures is described in the appendix to this chapter; see Eq. (8.23).

We now present the explicit results, beginning with the case $S = \frac{3}{2}$ and the corresponding $J = \frac{5}{2}, \frac{3}{2}, \frac{1}{2}$ states. Starting from the maximal spin state, one may use the familiar two-structure combination,

$$\left| 1\frac{3}{2}\frac{5}{2}\frac{5}{2} \right\rangle_{p_M^-} = C_A S_{\frac{3}{2}\frac{3}{2}}^S \frac{1}{\sqrt{2}} \left(F_{\frac{1}{2}}^\rho \varphi_{11}^\rho + F_{\frac{1}{2}}^\lambda \varphi_{11}^\lambda \right),$$

while the remaining states require combinations involving all three ρ, λ structures,

Table 8.1.1 The P-shell baryons composed of light quarks. The original Isgur-Karl predictions [Isgur and Karl, 1979b] are compared with experimental masses from the RPP. The last column lists the masses after unmixing (see text).

states J^P	Isgur-Karl	experiment	unmixed
$N_{1/2^-}^*$	1490	1535	1567.3, $S = 1/2$
$N_{1/2^-}^*$	1655	1650	1617.7, $S = 3/2$
$N_{3/2^-}^*$	1535	1520	1521.97, $S = 1/2$
$N_{3/2^-}^*$	1745	1700	1698.0, $S = 3/2$
$N_{5/2^-}^*$	1670	1675	$S = 3/2$

$$\left|1\frac{3}{2}\frac{3}{2}\frac{3}{2}\right\rangle_{p_M^-} = C_A\left(\sqrt{\frac{3}{5}}\,S^S_{\frac{3}{2}\frac{3}{2}}\frac{1}{\sqrt{2}}\big(F^\rho_{\frac{1}{2}}\varphi^\rho_{10} + F^\lambda_{\frac{1}{2}}\varphi^\lambda_{10}\big)\right.$$

$$\left.-\sqrt{\frac{2}{5}}\,S^S_{\frac{3}{2}\frac{1}{2}}\frac{1}{\sqrt{2}}\big(F^\rho_{\frac{1}{2}}\varphi^\rho_{11} + F^\lambda_{\frac{1}{2}}\varphi^\lambda_{11}\big)\right),$$

$$\left|1\frac{3}{2}\frac{1}{2}\frac{1}{2}\right\rangle_{p_M^-} = C_A\left(-\frac{1}{\sqrt{2}}\,S^S_{\frac{3}{2}\frac{3}{2}}\frac{1}{\sqrt{2}}\big(F^\rho_{\frac{1}{2}}\varphi^\rho_{1-1} + F^\lambda_{\frac{1}{2}}\varphi^\lambda_{1-1}\big)\right.$$

$$+\frac{1}{\sqrt{3}}\,S^S_{\frac{3}{2}\frac{1}{2}}\frac{1}{\sqrt{2}}\big(F^\rho_{\frac{1}{2}}\varphi^\rho_{10} + F^\lambda_{\frac{1}{2}}\varphi^\lambda_{10}\big)$$

$$\left.-\frac{1}{\sqrt{6}}\,S^S_{\frac{3}{2}-\frac{1}{2}}\frac{1}{\sqrt{2}}\big(F^\rho_{\frac{1}{2}}\varphi^\rho_{11} + F^\lambda_{\frac{1}{2}}\varphi^\lambda_{11}\big)\right). \tag{8.6}$$

Here $S^S_{\frac{3}{2}\frac{3}{2}} = \uparrow\uparrow\uparrow$ denotes the totally symmetric three-quark spin-$\frac{3}{2}$ state.

In general, constructing a state of definite J from orbital angular momentum L and spin S requires summing over all kinematically allowed combinations $m = J_z = m_L + m_S$, weighted by the standard Clebsch-Gordan coefficients,

$$\left|1\frac{3}{2}Jm\right\rangle_{p_M^-} = \sum_{m_S} \mathbf{C}^{Jm}_{1m_L\,\frac{3}{2}m_S}\left[C_A\, S^S_{\frac{3}{2}m_S}\frac{1}{\sqrt{2}}\big(F^\rho_{\frac{1}{2}}\varphi^\rho_{1m_L} + F^\lambda_{\frac{1}{2}}\varphi^\lambda_{1m_L}\big)\right]. \tag{8.7}$$

We use the convention

$$\mathbf{C}^{Jm}_{Lm_L Sm_S} = (-1)^{S-L-m}\sqrt{2J+1}\begin{pmatrix} L & S & J \\ m_L & m_S & -m \end{pmatrix}. \tag{8.8}$$

The expressions for spin $\frac{1}{2}$ states with $J = \frac{3}{2}, \frac{1}{2}$ are more involved. The maximal-J states for fixed L, S are

$$\left|1\frac{1}{2}\frac{3}{2}\frac{3}{2}\right\rangle_{p_M^-} = C_A\frac{1}{\sqrt{2}}\left(F^\rho_{\frac{1}{2}}\frac{1}{\sqrt{2}}\big(\varphi^\rho_{11}S^\lambda_{\frac{1}{2}\frac{1}{2}} + \varphi^\lambda_{11}S^\rho_{\frac{1}{2}\frac{1}{2}}\big)\right.$$

$$\left.+F^\lambda_{\frac{1}{2}}\frac{1}{\sqrt{2}}\big(\varphi^\rho_{11}S^\rho_{\frac{1}{2}\frac{1}{2}} - \varphi^\lambda_{11}S^\lambda_{\frac{1}{2}\frac{1}{2}}\big)\right),$$

$$\left|1\frac{1}{2}\frac{1}{2}\frac{1}{2}\right\rangle_{p_M^-} = C_A\left(\sqrt{\frac{2}{3}}\frac{1}{\sqrt{2}}\left(F^\rho_{\frac{1}{2}}\frac{1}{\sqrt{2}}\big(\varphi^\rho_{11}S^\lambda_{\frac{1}{2}-\frac{1}{2}} + \varphi^\lambda_{11}S^\rho_{\frac{1}{2}-\frac{1}{2}}\big)\right.\right.$$

$$\left.+F^\lambda_{\frac{1}{2}}\frac{1}{\sqrt{2}}\big(\varphi^\rho_{11}S^\rho_{\frac{1}{2}-\frac{1}{2}} - \varphi^\lambda_{11}S^\lambda_{\frac{1}{2}-\frac{1}{2}}\big)\right)$$

$$-\sqrt{\frac{1}{3}}\frac{1}{\sqrt{2}}\left(F^\rho_{\frac{1}{2}}\frac{1}{\sqrt{2}}\big(\varphi^\rho_{10}S^\lambda_{\frac{1}{2}-\frac{1}{2}} + \varphi^\lambda_{10}S^\rho_{\frac{1}{2}-\frac{1}{2}}\big)\right.$$

$$\left.\left.+F^\lambda_{\frac{1}{2}}\frac{1}{\sqrt{2}}\big(\varphi^\rho_{10}S^\rho_{\frac{1}{2}-\frac{1}{2}} - \varphi^\lambda_{10}S^\lambda_{\frac{1}{2}-\frac{1}{2}}\big)\right)\right). \tag{8.9}$$

For the isobar one finds

$$\left|1\frac{1}{2}\frac{3}{2}\frac{3}{2}\right\rangle_{\Delta_M^-} = C_A\, F^S_{\frac{3}{2}}\frac{1}{\sqrt{2}}\big(S^\rho_{\frac{1}{2}\frac{1}{2}}\varphi^\rho_{11} + S^\lambda_{\frac{1}{2}\frac{1}{2}}\varphi^\lambda_{11}\big). \tag{8.10}$$

The lower-J states for fixed L, S follow by standard Clebsch-Gordan construction,

$$\left|1\frac{1}{2}Jm\right\rangle_{p_M^-} = \sum_{m_S} \mathbf{C}^{Jm}_{1m_L\ \frac{1}{2}m_S} \left[C_A \frac{1}{\sqrt{2}} \left(F^\rho_{\frac{1}{2}} \frac{1}{\sqrt{2}} (\varphi^\rho_{1m_L} S^\lambda_{\frac{1}{2}m_S} + \varphi^\lambda_{1m_L} S^\rho_{\frac{1}{2}m_S}) \right.\right.$$

$$\left.\left. + F^\lambda_{\frac{1}{2}} \frac{1}{\sqrt{2}} (\varphi^\rho_{1m_L} S^\rho_{\frac{1}{2}m_S} - \varphi^\lambda_{1m_L} S^\lambda_{\frac{1}{2}m_S}) \right) \right], \tag{8.11}$$

and similarly for the odd-parity Δ states,

$$\left|1\frac{1}{2}Jm\right\rangle_{\Delta_M^-} = \sum_{m_S} \mathbf{C}^{Jm}_{1m_L\ \frac{1}{2}m_S} \left[C_A\, F^S_{\frac{3}{2}} \frac{1}{\sqrt{2}} \left(S^\rho_{\frac{1}{2}m_S} \varphi^\rho_{1m_L} + S^\lambda_{\frac{1}{2}m_S} \varphi^\lambda_{1m_L} \right) \right]. \tag{8.12}$$

8.1.1 Spin forces from P-shell states

Knowledge of the coefficients of the relevant operators for the five (unmixed) negative-parity N^* masses allows one to determine the corresponding matrix elements of the spin-spin, spin-orbit, and tensor forces.

Without going into technical details, let us recall one striking feature first noted by Isgur and Karl [Isgur and Karl, 1979a]: the contribution of the spin-orbit force is strongly suppressed relative to the spin-spin and tensor forces, and its matrix elements are consistent with zero within errors. Our fit fully confirms this observation. We therefore adopt what we refer to as the *optimized IK model,* in which the spin-orbit interaction is neglected and only the spin-spin and tensor forces (considered to be more reliable) are retained,

$$\langle H_0 \rangle = 1607\,\text{MeV},$$
$$\frac{\langle \rho^2 V_{SS} \rangle}{\langle \rho^2 + \lambda^2 \rangle} = 83.2\,\text{MeV},$$
$$\frac{\langle \rho^4 V_{\text{tensor}} \rangle}{\langle \rho^2 + \lambda^2 \rangle} = 43.7\,\text{MeV}. \tag{8.13}$$

Here H_0 denotes the spin-independent part of the Hamiltonian, which is common to all five resonances. Our only assumptions are that the spin-dependent forces are treated to first order, and that near-threshold effects are neglected[1].

The overall quality of the description of the masses is illustrated in Fig. 8.1.1. In all cases, the deviations are significantly smaller than the typical half-widths of the resonances[2].

As independent "external tests" of the accuracy of the model, we use the empirical mixing matrix elements in Eq. (8.3). The observed ratio of the magnitudes of the mixing matrix elements in the tensor channel is

$$\frac{H_{mix}(J = 1/2)}{H_{mix}(J = 3/2)} \approx -2.76. \tag{8.14}$$

If only the tensor operator is retained, the ratio of the corresponding coefficients is $-\sqrt{10} = -3.16$, which is reasonably close.

Using the fitted tensor matrix element extracted from the splittings shown in Fig. 8.1.1, we obtain the value given in Eq. (8.13), namely 43.7 MeV. This should be compared with 51.6 MeV inferred from the mixing matrix element in the $J = \frac{1}{2}$ P-shell pair discussed above.

In summary, the spectra of P-shell baryons are well described by the combined effects of spin-spin and tensor forces. Any additional contributions not explicitly included here can affect the masses only at the level of ~ 8 MeV. This uncertainty is small compared both to the typical splittings, ~ 100 MeV, and to the characteristic scale $\Gamma/2 \sim 50$ MeV, which we use as an estimate of the maximal possible shifts due to threshold effects.

---

[1] Isgur and Karl made additional assumptions, such as adopting a Gaussian radial wave function.

[2] These half-widths provide a natural scale for the threshold effects that are ignored in the present analysis.
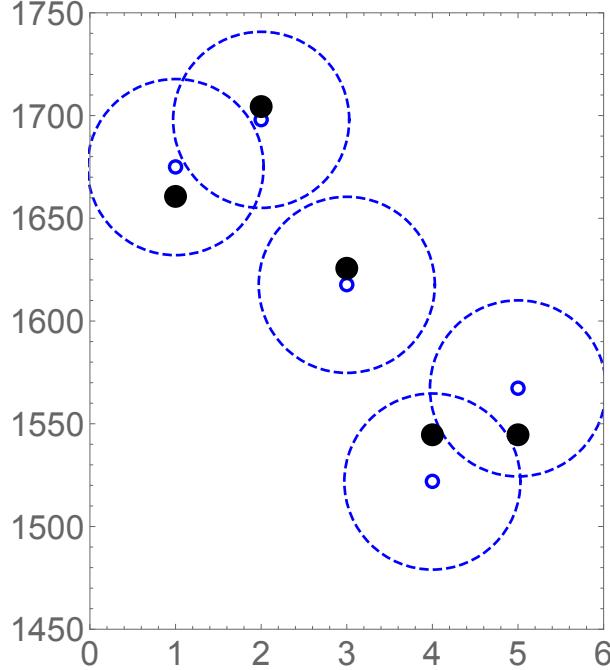
Fig. 8.1.1 The black dots show the masses of the negative-parity P-shell baryons obtained from the optimized IK model with fitted radial matrix elements (8.13), ordered as $|J = \frac{5}{2}\rangle$, $|J = \frac{3}{2}, S = \frac{3}{2}\rangle$, $|J = \frac{1}{2}, S = \frac{3}{2}\rangle$, $|J = \frac{3}{2}, S = \frac{1}{2}\rangle$, $|J = \frac{1}{2}, S = \frac{1}{2}\rangle$. The small blue circles indicate the experimental pole positions. They are surrounded by large dashed blue circles whose radii are of order the typical half-width $\Gamma/2$.

8.2 The wave functions and splittings of negative-parity N^*

Having extracted empirical values of the matrix elements of the spin-dependent forces, we now compare them with the corresponding theoretical values obtained within the hyperdistance approximation. We begin by outlining the general structure of the calculation.

All matrix elements involve six-dimensional integrals over the Jacobi coordinates $\boldsymbol{\rho}$ and $\boldsymbol{\lambda}$, which can be separated into four angular and two radial integrations,

$$\int \left(\frac{d\Omega_\rho}{4\pi} \frac{d\Omega_\lambda}{4\pi} \right) (\rho^2 d\rho \, \lambda^2 d\lambda) \dots . \tag{8.15}$$

The wave functions consist of a common six-dimensional spherically symmetric radial function $\phi_{00}(R)$, with $R^2 = \rho^2 + \lambda^2$, multiplied by appropriate orbital factors. For the P-wave baryons considered here, the orbital parts are linear in $\boldsymbol{\rho}$ and $\boldsymbol{\lambda}$. The matrix elements receive multiple contributions from different components of the fully symmetrized wave functions, as detailed in the Appendix.

In the expressions below, all angular integrations are performed explicitly, while the integrals over the moduli ρ and λ are left unevaluated, since no specific assumption about the functional form of $\phi_{00}(R)$ is made. We therefore introduce the shorthand notation

$$\langle \hat{V}(\rho, \lambda) \rangle \equiv \int \int d\rho \, d\lambda \, \rho^2 \lambda^2 |\phi_{00}|^2 \, V(\rho, \lambda), \tag{8.16}$$

for such radial integrals. For example, the normalization integral ($\hat{V} = \hat{1}$) averages the squared orbital wave function,

$$\langle \rho^2 + \lambda^2 \rangle = \int \int d\rho \, d\lambda \, \rho^2 \lambda^2 |\phi_{00}|^2 (\rho^2 + \lambda^2). \tag{8.17}$$

This quantity appears in the denominators of all subsequent expressions.

The masses of the excited nucleon states N_J^* contain an overall constant (not written explicitly below), supplemented by contributions from four spin-dependent operators: spin-spin, spin-orbit, tensor, and 't Hooft terms. The resulting mixing matrices in the P-shell subspaces are

$$\mathbb{M}'_{\frac{5}{2}} = \frac{3}{4} \frac{\langle (\rho^2 + \lambda^2) V_S(\sqrt{2}\rho) \rangle}{\langle (\rho^2 + \lambda^2) \rangle} + 3 \frac{\langle \rho^2 V_{LS}(\sqrt{2}\rho) \rangle}{\langle (\rho^2 + \lambda^2) \rangle} - \frac{1}{5} \frac{\langle \rho^4 V_T(\sqrt{2}\rho) \rangle}{\langle (\rho^2 + \lambda^2) \rangle}, \tag{8.18}$$

$$
\begin{aligned}
\mathbb{M}'_{\frac{3}{2}} = & \begin{pmatrix} 3/4 & 0 \\ 0 & -3/4 \end{pmatrix} \frac{\langle (\rho^2 + \lambda^2) V_S(\sqrt{2}\rho) \rangle}{\langle (\rho^2 + \lambda^2) \rangle} - \begin{pmatrix} 2 & -\sqrt{5/2} \\ -\sqrt{5/2} & -1 \end{pmatrix} \frac{\langle \rho^2 V_{SL}(\sqrt{2}\rho) \rangle}{\langle (\rho^2 + \lambda^2) \rangle} \\
& + \begin{pmatrix} 4/5 & 1/\sqrt{10} \\ 1/\sqrt{10} & 0 \end{pmatrix} \frac{\langle \rho^4 V_T(\sqrt{2}\rho) \rangle}{\langle (\rho^2 + \lambda^2) \rangle} + \begin{pmatrix} 0 & 0 \\ 0 & 1 + 3a \end{pmatrix} \frac{G_{tH}\langle \lambda^2 \rangle}{8\sqrt{2}\pi \langle (\rho^2 + \lambda^2) \rangle},
\end{aligned} \tag{8.19}
$$

$$
\begin{aligned}
\mathbb{M}'_{\frac{1}{2}} = & \begin{pmatrix} 3/4 & 0 \\ 0 & -3/4 \end{pmatrix} \frac{\langle (\rho^2 + \lambda^2) V_S(\sqrt{2}\rho) \rangle}{\langle (\rho^2 + \lambda^2) \rangle} - \begin{pmatrix} 5 & 1 \\ 1 & -2 \end{pmatrix} \frac{\langle \rho^2 V_{SL}(\sqrt{2}\rho) \rangle}{\langle (\rho^2 + \lambda^2) \rangle} \\
& + \begin{pmatrix} -1 & -1 \\ -1 & 0 \end{pmatrix} \frac{\langle \rho^4 V_T(\sqrt{2}\rho) \rangle}{\langle (\rho^2 + \lambda^2) \rangle} + \begin{pmatrix} 0 & 0 \\ 0 & 1 + 3a \end{pmatrix} \frac{G_{tH}\langle \lambda^2 \rangle}{8\sqrt{2}\pi \langle (\rho^2 + \lambda^2) \rangle}.
\end{aligned} \tag{8.20}
$$

The rows and columns of the 2×2 matrices correspond to states with $S = \frac{3}{2}$ and $S = \frac{1}{2}$, respectively,

$$\mathbb{M}_J = \begin{pmatrix} \langle S = \frac{3}{2} | \mathbb{V}_{S+T+SL+V_{TH}} | S = \frac{3}{2} \rangle & \langle S = \frac{3}{2} | \mathbb{V}_{S+T+SL+V_{TH}} | S = \frac{1}{2} \rangle \\ \langle S = \frac{1}{2} | \mathbb{V}_{S+T+SL+V_{TH}} | S = \frac{3}{2} \rangle & \langle S = \frac{1}{2} | \mathbb{V}_{S+T+SL+V_{TH}} | S = \frac{1}{2} \rangle \end{pmatrix}_J. \tag{8.21}$$

Some of these matrices contain non-diagonal elements, implying that the total spin S is not, in general, a good quantum number for the observed states.

8.2.1 The shape of P-wave states

The explicit wave functions for all P-wave states are derived in spin-tensor form in the Appendix to this section. Once these expressions are available, it is straightforward to evaluate matrix elements of arbitrary spin-isospin-angular operators[3].

Although we do not present the detailed derivations here, it is instructive to discuss the *shape* of the P-wave states. Except for the total $J = \frac{1}{2}$ case, these shapes are expected to be nontrivial.

The coordinate-space densities $|\psi|^2$, summed over all spin and isospin indices, for the five negative-parity N^* states with $J_z = \frac{1}{2}$ are

---

[3] Note, for example, that the orbital angular-momentum operator involves derivatives with respect to angles or coordinates. MATHEMATICA can perform such operations directly on tables of functions, such as our orbital-spin-tensor wave functions.

$$|N^*_{J=5/2, J_z=1/2, S=3/2}|^2 \sim \frac{2}{5}\left(\lambda_1^2 + \lambda_2^2 + 3\lambda_3^2 + \rho_1^2 + \rho_2^2 + 3\rho_3^2\right),$$

$$|N^*_{J=3/2, J_z=1/2, S=3/2}|^2 \sim \frac{2}{15}\left(7\lambda_1^2 + 7\lambda_2^2 + \lambda_3^2 + 7\rho_1^2 + 7\rho_2^2 + \rho_3^2\right),$$

$$|N^*_{J=1/2, J_z=1/2, S=3/2}|^2 \sim \frac{2}{3}\left(\lambda_1^2 + \lambda_2^2 + \lambda_3^2 + \rho_1^2 + \rho_2^2 + \rho_3^2\right),$$

$$|N^*_{J=3/2, J_z=1/2, S=1/2}|^2 \sim \frac{2}{15}\left(7\lambda_1^2 + 7\lambda_2^2 + \lambda_3^2 + 7\rho_1^2 + 7\rho_2^2 + \rho_3^2\right),$$

$$|N^*_{J=1/2, J_z=1/2, S=1/2}|^2 \sim \frac{2}{3}\left(\lambda_1^2 + \lambda_2^2 + \lambda_3^2 + \rho_1^2 + \rho_2^2 + \rho_3^2\right).$$

We note that the $J = \frac{5}{2}$ and $J = \frac{3}{2}$ states exhibit elliptic deformations of opposite sign, while both $J = \frac{1}{2}$ states remain spherically symmetric in this sense.

Appendix

8.A Enforcing Fermi statistics by representations of the permutation group S_3

Negative-parity baryons possess nontrivial *orbital* wave functions in addition to spin and isospin. The orbital part can be constructed from either the ρ or the λ Jacobi vector, so one must understand the action of permutations on three objects of ρ, λ type. There are $2^3 = 8$ such possibilities, namely $X_1^\rho X_2^\rho X_3^\rho, \ldots$, forming an eight-dimensional space.

Symmetry under the transposition (12) is straightforward to analyze: of the eight combinations, four containing an even number of X^ρ factors are symmetric, while the remaining four are antisymmetric. To proceed further, one must determine how these basis states transform under the permutation $\hat{P}(23)$. We follow the same strategy as before and evaluate this transformation explicitly using MATHEMATICA[4].

The resulting matrix representation of $\hat{P}(23)$ in this basis is

$$M_{23} \bigotimes M_{23} \bigotimes M_{23} = \tag{8.22}$$

$$= \begin{bmatrix} -1/8 & \sqrt{3}/8 & \sqrt{3}/8 & -3/8 & \sqrt{3}/8 & -3/8 & -3/8 & 3\sqrt{3}/8 \\ \sqrt{3}/8 & 1/8 & -3/8 & -\sqrt{3}/8 & -3/8 & -\sqrt{3}/8 & 3\sqrt{3}/8 & 3/8 \\ \sqrt{3}/8 & -3/8 & 1/8 & -\sqrt{3}/8 & -3/8 & 3\sqrt{3}/8 & -\sqrt{3}/8 & 3/8 \\ -3/8 & -\sqrt{3}/8 & -\sqrt{3}/8 & -1/8 & 3\sqrt{3}/8 & 3/8 & 3/8 & \sqrt{3}/8 \\ \sqrt{3}/8 & -3/8 & -3/8 & 3\sqrt{3}/8 & 1/8 & -\sqrt{3}/8 & -\sqrt{3}/8 & 3/8 \\ -3/8 & -\sqrt{3}/8 & 3\sqrt{3}/8 & 3/8 & -\sqrt{3}/8 & -1/8 & 3/8 & \sqrt{3}/8 \\ -3/8 & 3\sqrt{3}/8 & -\sqrt{3}/8 & 3/8 & -\sqrt{3}/8 & 3/8 & -1/8 & \sqrt{3}/8 \\ 3\sqrt{3}/8 & 3/8 & 3/8 & \sqrt{3}/8 & 3/8 & \sqrt{3}/8 & \sqrt{3}/8 & 1/8 \end{bmatrix}$$

written in the basis of the following eight monomials:

$$X_1^\lambda X_2^\lambda X_3^\lambda, \ X_1^\rho X_2^\lambda X_3^\lambda, \ X_1^\lambda X_2^\rho X_3^\lambda, \ X_1^\rho X_2^\rho X_3^\lambda, \ X_1^\lambda X_2^\lambda X_3^\rho, \ X_1^\rho X_2^\lambda X_3^\rho, \ X_1^\lambda X_2^\rho X_3^\rho, \ X_1^\rho X_2^\rho X_3^\rho.$$

The determinant of this matrix is unity, with four eigenvalues equal to -1 and four equal to $+1$. This spectrum is the same as for the (diagonal) matrix representing the permutation $\hat{P}(12)$, although the corresponding eigenvectors are different. One can then readily verify that the two symmetric subspaces have *only one common* symmetric vector,

$$(-1, 0, 0, 1, 0, 1, 1, 0),$$

in this basis. This vector corresponds to the unique orbital-spin-isospin structure compatible with full S_3 symmetry,

$$-X^\lambda X^\lambda X^\lambda + X^\rho X^\rho X^\lambda + X^\rho X^\lambda X^\rho + X^\lambda X^\rho X^\rho. \tag{8.23}$$

---

[4] The command used is `KroneckerProduct` with three arguments.

Proceeding to the next excitation, the D-shell with $L = 2$, the orbital wave function is a tensor constructed from *two* coordinates. One convenient approach is therefore to consider permutations of four objects of ρ, λ type. In a suitable basis of $2^4 = 16$ combinations, eight are symmetric under $\hat{P}(12)$ and eight are symmetric under $\hat{P}(23)$. Examining their intersection, one finds two independent combinations that are symmetric under both permutations. These will be discussed in the section devoted to the $L = 2$ D-shell baryons.

Finally, converting these symbolic expressions in the *good basis* into explicit wave functions (including orbital dependence, spin, and flavor indices) proceeds in a standard way; see Ref. [Miesch et al., 2023a]. From a mathematical perspective, this amounts to mapping the 8- (or 16-)dimensional good-basis space back to the full monomial space. This is accomplished by systematic use of the spin-tensor representation of the orbital-spin-isospin wave functions. The symbolic objects S_ρ, S_λ are replaced by their explicit forms in coordinate, spin, and isospin variables, after which MATHEMATICA generates a table with indices $s_1, s_2, s_3, i_1, i_2, i_3$. The resulting coefficients are linear functions of the $\boldsymbol{\rho}$ and $\boldsymbol{\lambda}$ coordinates; examples are shown in Fig. 8.A.1 and Fig. 8.A.2.

$$\left\{\left\{\left\{\{\{0, 0\}, \{0, 0\}\}, \{\{0, 0\}, \{0, 0\}\}\right\}, \left\{\left\{\left\{0, -\frac{2\,(\lambda[1] - i\,\lambda[2] + 2\,\lambda[3])}{3\,\sqrt{3}}\right\},\right.\right.\right.\right.$$

$$\left\{\frac{1}{9}\left(\sqrt{3}\,\lambda[1] - i\,\sqrt{3}\,\lambda[2] + 2\,\sqrt{3}\,\lambda[3] + 3\,\rho[1] - 3\,i\,\rho[2] + 6\,\rho[3]\right), 0\right\}\right\},$$

$$\left\{\left\{\frac{1}{9}\left(\sqrt{3}\,\lambda[1] - i\,\sqrt{3}\,\lambda[2] + 2\,\sqrt{3}\,\lambda[3] - 3\,\rho[1] + 3\,i\,\rho[2] - 6\,\rho[3]\right), 0\right\}, \{0, 0\}\right\}\right\},$$

$$\left\{\left\{\left\{0, \frac{1}{9}\left(\sqrt{3}\,(\lambda[1] - i\,\lambda[2]) + 3\,(\rho[1] - i\,\rho[2])\right)\right\},\right.\right.$$

$$\left\{\frac{1}{9}\left(\sqrt{3}\,\lambda[1] - i\,\sqrt{3}\,\lambda[2] - 3\,\rho[1] + 3\,i\,\rho[2]\right), 0\right\}\right\}, \left\{\left\{-\frac{2\,(\lambda[1] - i\,\lambda[2])}{3\,\sqrt{3}}, 0\right\}, \{0, 0\}\right\}\right\},$$

$$\left\{\left\{\left\{0, \frac{2}{9}\left(\sqrt{3}\,\lambda[3] - 3\,\rho[3]\right)\right\}, \left\{-\frac{4\,\lambda[3]}{3\,\sqrt{3}}, 0\right\}\right\}, \left\{\left\{\frac{2}{9}\left(\sqrt{3}\,\lambda[3] + 3\,\rho[3]\right), 0\right\}, \{0, 0\}\right\}\right\}\right\},$$

$$\left\{\left\{\left\{\left\{0, \frac{1}{9}\left(\sqrt{3}\,\lambda[1] - i\,\sqrt{3}\,\lambda[2] - 3\,\rho[1] + 3\,i\,\rho[2]\right)\right\}, \left\{-\frac{2\,(\lambda[1] - i\,\lambda[2])}{3\,\sqrt{3}}, 0\right\}\right\},\right.\right.$$

$$\left\{\left\{\frac{1}{9}\left(\sqrt{3}\,(\lambda[1] - i\,\lambda[2]) + 3\,(\rho[1] - i\,\rho[2])\right), 0\right\}, \{0, 0\}\right\}\right\},$$

$$\left\{\left\{\left\{0, \frac{2}{9}\left(\sqrt{3}\,\lambda[3] + 3\,\rho[3]\right)\right\}, \left\{\frac{2}{9}\left(\sqrt{3}\,\lambda[3] - 3\,\rho[3]\right), 0\right\}\right\}, \left\{\left\{-\frac{4\,\lambda[3]}{3\,\sqrt{3}}, 0\right\}, \{0, 0\}\right\}\right\}\right\},$$

$$\left\{\{\{0, 0\}, \{0, 0\}\}, \{\{0, 0\}, \{0, 0\}\}\}, \{\{\{0, 0\}, \{0, 0\}\}, \{\{0, 0\}, \{0, 0\}\}\}\right\}\right\}$$

Fig. 8.A.1 Spin-tensor wave function for $|N^*, J = 3/2, Jz = 1/2, S = 1/2 >$.

8.B The D-shell ($L = 2$) baryons

Representation theory of angular momentum tells us that one can construct positive-parity excited nucleon states with the following J^P assignments,

$$L^\pi \otimes S = 2^+ \otimes \frac{1}{2}, \frac{3}{2} = \left(\frac{3^+}{2}, \frac{5^+}{2}\right), \ \left(\frac{1^+}{2}, \frac{3^+}{2}, \frac{5^+}{2}, \frac{7^+}{2}\right).$$

However, the explicit construction of wave functions that are symmetric under quark permutations requires additional care. Such wave functions have been discussed, for example, in Ref. [Capstick and Roberts, 2000].

$$\left\{\left\{\left\{\left\{\{\{0, 0\}, \{0, 0\}\}, \{\{0, 0\}, \{0, 0\}\}\right\}, \left\{\left\{0, \frac{2}{3} \sqrt{\frac{2}{3}} \ (\lambda[1] - \mathtt{i} \ \lambda[2] - \lambda[3])\right\},\right.\right.\right.\right.$$

$$\left\{\frac{1}{9} \ \sqrt{2} \ \left(- \sqrt{3} \ \lambda[1] + \mathtt{i} \ \sqrt{3} \ \lambda[2] + \sqrt{3} \ \lambda[3] - 3 \ \rho[1] + 3 \ \mathtt{i} \ \rho[2] + 3 \ \rho[3]\right), 0\right\}\right\},$$

$$\left\{\left\{\frac{1}{9} \ \sqrt{2} \ \left(- \sqrt{3} \ \lambda[1] + \mathtt{i} \ \sqrt{3} \ \lambda[2] + \sqrt{3} \ \lambda[3] + 3 \ \rho[1] - 3 \ \mathtt{i} \ \rho[2] - 3 \ \rho[3]\right), 0\right\}, \{0, 0\}\right\}\right\}\right\},$$

$$\left\{\left\{\left\{\left\{0, -\frac{1}{9} \ \sqrt{2} \ \left(\sqrt{3} \ \lambda[1] - \mathtt{i} \ \sqrt{3} \ \lambda[2] + 3 \ \rho[1] - 3 \ \mathtt{i} \ \rho[2]\right)\right\},\right.\right.\right.$$

$$\left\{\frac{1}{9} \ \sqrt{2} \ \left(- \sqrt{3} \ (\lambda[1] - \mathtt{i} \ \lambda[2]) + 3 \ (\rho[1] - \mathtt{i} \ \rho[2])\right), 0\right\}\right\},$$

$$\left\{\left\{\frac{2}{3} \ \sqrt{\frac{2}{3}} \ (\lambda[1] - \mathtt{i} \ \lambda[2]), 0\right\}, \{0, 0\}\right\}\right\},$$

$$\left\{\left\{\left\{0, \frac{1}{9} \ \left(\sqrt{6} \ \lambda[3] - 3 \ \sqrt{2} \ \rho[3]\right)\right\}, \left\{-\frac{2}{3} \ \sqrt{\frac{2}{3}} \ \lambda[3], 0\right\}\right\},$$

$$\left\{\left\{\frac{1}{9} \ \left(\sqrt{6} \ \lambda[3] + 3 \ \sqrt{2} \ \rho[3]\right), 0\right\}, \{0, 0\}\right\}\right\}\right\}\right\},$$

$$\left\{\left\{\left\{\left\{\left\{0, \frac{1}{9} \ \sqrt{2} \ \left(- \sqrt{3} \ (\lambda[1] - \mathtt{i} \ \lambda[2]) + 3 \ (\rho[1] - \mathtt{i} \ \rho[2])\right)\right\}, \left\{\frac{2}{3} \ \sqrt{\frac{2}{3}} \ (\lambda[1] - \mathtt{i} \ \lambda[2]), 0\right\}\right\},\right.\right.\right.$$

$$\left\{\left\{-\frac{1}{9} \ \sqrt{2} \ \left(\sqrt{3} \ \lambda[1] - \mathtt{i} \ \sqrt{3} \ \lambda[2] + 3 \ \rho[1] - 3 \ \mathtt{i} \ \rho[2]\right), 0\right\}, \{0, 0\}\right\}\right\},$$

$$\left\{\left\{0, \frac{1}{9} \ \left(\sqrt{6} \ \lambda[3] + 3 \ \sqrt{2} \ \rho[3]\right)\right\}, \left\{\frac{1}{9} \ \left(\sqrt{6} \ \lambda[3] - 3 \ \sqrt{2} \ \rho[3]\right), 0\right\}\right\},$$

$$\left\{\left\{-\frac{2}{3} \ \sqrt{\frac{2}{3}} \ \lambda[3], 0\right\}, \{0, 0\}\right\}\right\}\right\},$$

$$\left\{\{\{0, 0\}, \{0, 0\}\}, \{\{0, 0\}, \{0, 0\}\}\right\}, \left\{\{\{0, 0\}, \{0, 0\}\}, \{\{0, 0\}, \{0, 0\}\}\right\}\right\}\right\}\right\}$$

Fig. 8.A.2 Spin-tensor wave function for $|N^*, J = 1/2, Jz = 1/2, S = 1/2 >$

A fully systematic treatment is most naturally achieved using representations of the permutation group S_3 [Miesch et al., 2023a].

Since the orbital part of the wave function for $L = 2$ consists of symmetric tensors constructed from the coordinate vectors ρ^i and λ^i, there are three independent tensor structures,

$$\rho^i \rho^j, \qquad \lambda^i \lambda^j, \qquad (\rho^i \lambda^j + \lambda^i \rho^j).$$

The first two are symmetric under the transposition (12), while the last is antisymmetric. Under the permutation (23) these structures mix according to a nontrivial matrix. To construct fully symmetric (physical) wave functions, these orbital tensors must therefore be combined with spin and isospin wave functions of appropriate symmetry.

For total spin $S = \frac{3}{2}$, the spin wave functions are fully symmetric (for example $\uparrow\uparrow\uparrow$). In this case one must construct the S_3 representation from three objects (two coordinates and one isospin factor) which we denote symbolically as $X^{A1} X^{A2} X^{A3}$ with binary indices $A = \{\rho, \lambda\}$. As shown earlier, this procedure yields a single fully symmetric combination, given in Eq. (8.23).

For total spin $S = \frac{1}{2}$, there are two independent spin structures, S^ρ and S^λ. The most direct way to construct the corresponding wave functions is to build symmetric representations of *four* spinor-like objects,

$$X^{A1} X^{A2} X^{A3} X^{A4},$$

again with binary indices $A = \rho, \lambda$. There are $2^4 = 16$ such combinations, half of which are symmetric and half antisymmetric under the permutation (12). The 16×16 matrix representing the permutation (23) (not shown) has eight symmetric and eight antisymmetric eigenvectors. As demonstrated in the Appendix, there are precisely two combinations that are symmetric under *all* permutations. These can be written as

$$\lambda^i \lambda^j S_\lambda I_\lambda + \rho^i \lambda^j S_\lambda I_\rho + \lambda^i \rho^j S_\rho I_\lambda + \rho^i \rho^j S_\rho I_\rho, \tag{8.24}$$

$$\lambda^i \lambda^j S_\rho I_\rho - \rho^i \lambda^j S_\lambda I_\rho - \lambda^i \rho^j S_\rho I_\lambda + \rho^i \rho^j S_\lambda I_\lambda. \tag{8.25}$$

Linear combinations of these two structures generate the tensor-excited states with total spin $S = \frac{1}{2}$. For states with definite J and J_z, one then proceeds in the standard way by evaluating the appropriate Clebsch-Gordan coefficients.

Chapter 9
Pentaquarks

9.1 Why are pentaquarks important?

In the Introduction we mentioned the origins of the recent revolution in hadronic spectroscopy, triggered by the discovery of $c\bar{c}q\bar{q}$ tetraquarks hiding among charmonium states. Today, such tetraquark states listed in the PDG are nearly *as numerous as* the genuine charmonium levels themselves. These states may be viewed as the addition of a $\bar{q}q$ pair (with σ- or π-like quantum numbers) to a compact $\bar{c}c$ core. In close analogy, adding an extra $\bar{q}q$ pair to a baryon naturally leads to a rich spectrum of pentaquark states. The experimental and theoretical history of pentaquarks is full of puzzles, which we will not attempt to review exhaustively here.

Although this may not be immediately apparent, there exists a substantial "theoretical barrier" between the spectroscopy of mesons, baryons, and tetraquarks on the one hand, and that of pentaquarks on the other. In the former cases, color indices can be factorized in the wave function, whereas in pentaquarks (and larger multiquark systems) this is no longer possible. As a result, the construction of color-spin-flavor wave functions leads to a much larger monom space, and enforcing Fermi statistics becomes significantly more challenging. Developing systematic tools to address this problem is a central goal of the present work.

In our recent paper [Miesch et al., 2025c], we studied light-quark pentaquarks in detail and derived explicit antisymmetric wave functions for their S- and P-shell states. The latter are essential for investigating baryon-pentaquark mixing, a phenomenon that may help resolve several long-standing puzzles, including the flavor asymmetry of the antiquark sea and the unexpectedly strong orbital motion observed in nucleons. The latter issue emerged prominently in connection with the so-called "spin puzzle." The naive expectation that the nucleon spin is carried entirely by valence quarks was disproved by experiment, and orbital angular momentum is now believed to provide a major contribution.

In a recent study [Miesch et al., 2025b], we investigated whether such orbital motion could be induced by a deuteron-like mechanism through mixing with D-shell baryons. We concluded that this scenario is highly unlikely, even when assuming unrealistically strong tensor forces. In contrast, in the present work devoted to admixtures of pentaquark states, the available data on orbital motion appear to be reproduced successfully.

A broader lesson is that pentaquarks are perhaps less important as isolated states than as admixtures to ordinary baryons. Already forty years ago, Isgur and collaborators [Kokoski and Isgur, 1987, Geiger and Isgur, 1990] argued that adding an extra $\bar{q}q$ pair with σ (vacuum) quantum numbers requires it to be in a $^3P_0$ state ($J = 0$, $S = 1$, $L = 1$), following earlier ideas such as those in Ref. [Le Yaouanc et al., 1973]. This insight highlighted why some amount of orbital motion in nucleons may be unavoidable.

In those early studies, pentaquarks were modeled effectively as multiple baryon-meson states. Subsequent developments along these lines were pursued in Refs. [Santopinto and Bijker, 2007, Bijker et al., 2009] and others, leading to what is now known as the *unquenched constituent quark model* (UCQM). These works led to the realization that all baryons, including the nucleon, contain a significant admixture (of order $\sim 40\%$) of five-quark components. Remarkably, many textbook results from the three-quark constituent model (such as

magnetic moments) remain intact due to cancellations within the five-quark sector, while new phenomena, such as orbital angular momentum, can be naturally explained.

A different line of thought pursued the inclusion of a "pion cloud" around the nucleon. An extreme realization of this idea is the Skyrmion model, in which the qqq core is eliminated altogether and baryons emerge as solitons of semiclassical pion fields. Less radical approaches introduce pions through diagrams derived from effective chiral Lagrangians.

In the present work, we treat the addition of σ-like and π-like quark pairs on equal footing, as required by chiral symmetry. The relations between the corresponding admixture operators date back to the 1950s, such as the Goldberger-Treiman relation and the Gell-Mann-Levy linear sigma model [Gell-Mann and Levy, 1960].

For completeness, we note that several other groups continue to study the five-quark Fock component of the nucleon with similar goals. Perhaps the closest in spirit to our approach is Ref. [An and Saghai, 2019], where states of the $L = 1$ pentaquark shell are analyzed, including their mixing with the nucleon via the $^3P_0$ model. As the reader will see, our construction is technically quite different: we derive pentaquark wave functions directly from the requirements of Fermi statistics, rather than from combinations of color-spin-flavor group representations. The latter approach is nevertheless discussed in the Appendices for comparison and completeness. More importantly, in contrast to Ref. [An and Saghai, 2019], our treatment of nucleon-pentaquark mixing explicitly enforces chiral symmetry.

Experimental searches for light pentaquarks have been carried out for decades, but so far no universally accepted signals have emerged. A notable attempt was the 2003 report by the LEPS collaboration [Nakano et al., 2003] of a $\Theta = uudd\bar{s}$ resonance with

$$M_\Theta = 1.54 \pm 0.01 \text{ GeV}, \qquad \Gamma_\Theta < 25 \text{ MeV}.$$

Although this signal was observed in a few other experiments, it was not confirmed by subsequent measurements with higher statistics. For a recent review of the experimental situation and future prospects, see for example Ref. [Amaryan, 2025]. The chiral soliton model [Diakonov et al., 2012] predicted such a light Θ as a member of an antidecuplet multiplet, and many alternative models were proposed; see Ref. [Praszalowicz, 2024] for a recent discussion.

At that time, we proposed a schematic quark-diquark symmetry [Shuryak and Zahed, 2004a], in which the pentaquark was approximated as a three-body system composed of two *good* diquarks, $(ud)^2\bar{s}$, rotating in a P-wave. Such a picture suggested near-degeneracy with P-wave excited decuplet baryons, implying a higher mass scale, $M \sim 1.9$ GeV.

Needless to say, our present approach is far removed from such simplified models. We now work with a complete set of wave functions derived explicitly below. Although at present no firm identification of the resulting states with known resonances can be made, we place confidence in the underlying principles: Fermi statistics and the hyperdistance approximation. In this sense, we follow the same strategy as in our previous studies of excited baryons, tetraquarks, and hexaquarks.

The results obtained here serve as intermediate stepping stones toward a quantitative understanding of five-quark Fock components in the nucleon. As usual, the analysis of complicated multiquark wave functions begins with states of extreme quantum numbers, such as the channel with maximal spin, $J^P = 5/2^+$. Before turning to its theoretical description, let us note that it may correspond to the resonance $N^*(2000)\,5/2^+$, observed in channels such as $N\pi$, $N\sigma$, $\Delta\pi$, and ΛK^*; see the multichannel analysis of Ref. [Anisovich et al., 2012]. This state is the second resonance with these quantum numbers, lying well above the first $5/2^+$ state, $N^*(1680)$, which is traditionally identified as a qqq, $L = 2$ D-shell excitation. Moreover, it lies close to the negative-parity state $N^*(2060)\,5/2^-$, which may be interpreted as its chiral partner.

Finally, we comment briefly on pentaquarks containing charm quarks. Our use of the hyperdistance approximation for fully charmed tetraquarks [Miesch et al., 2025a] successfully reproduces the observed level splittings. Unfortunately, this approach cannot be straightforwardly extended to the $uudc\bar{c}$ pentaquarks observed by LHCb, and such states will therefore not be discussed here.

9.2 The five-body kinematics

The coordinates of five bodies, with the center-of-mass (CM) motion removed, are described by four three-dimensional Jacobi coordinates[1], denoted $\boldsymbol{\alpha}, \boldsymbol{\beta}, \boldsymbol{\gamma}, \boldsymbol{\delta}$:

$$
\begin{aligned}
\mathbf{X}_1 &= (15\sqrt{2}\boldsymbol{\alpha} + 5\sqrt{6}\boldsymbol{\beta} + 5\sqrt{3}\boldsymbol{\gamma} + 3\sqrt{5}\boldsymbol{\delta})/30, \\
\mathbf{X}_2 &= (-15\sqrt{2}\boldsymbol{\alpha} + 5\sqrt{6}\boldsymbol{\beta} + 5\sqrt{3}\boldsymbol{\gamma} + 3\sqrt{5}\boldsymbol{\delta})/30, \\
\mathbf{X}_3 &= (-10\sqrt{6}\boldsymbol{\beta} + 5\sqrt{3}\boldsymbol{\gamma} + 3\sqrt{5}\boldsymbol{\delta})/30, \\
\mathbf{X}_4 &= (-5\sqrt{3}\boldsymbol{\gamma} + \sqrt{5}\boldsymbol{\delta})/10, \\
\mathbf{X}_5 &= -(2/\sqrt{5})\boldsymbol{\delta}
\end{aligned}
\tag{9.1}
$$

with the inverse relations

$$
\begin{aligned}
\boldsymbol{\alpha} &= (\mathbf{X}_1 - \mathbf{X}_2)/\sqrt{2}, \\
\boldsymbol{\beta} &= (\mathbf{X}_1 + \mathbf{X}_2 - 2\mathbf{X}_3)/\sqrt{6}, \\
\boldsymbol{\gamma} &= \sqrt{3}/6(\mathbf{X}_1 + \mathbf{X}_2 + \mathbf{X}_3 - 3\mathbf{X}_4), \\
\boldsymbol{\delta} &= \sqrt{5}/2(\mathbf{X}_1 + \mathbf{X}_2 + \mathbf{X}_3 + \mathbf{X}_4)
\end{aligned}
\tag{9.2}
$$

The Jacobi coordinates are defined sequentially, with the first two coinciding with the $\boldsymbol{\rho}$ and $\boldsymbol{\lambda}$ coordinates used in baryon spectroscopy. Since the CM is placed at the origin, $\sum_{i=1}^{5} \mathbf{X}_i = 0$, the last coordinate $\boldsymbol{\delta}$ can be re-expressed solely in terms of $\mathbf{X}_5$, which we identify with the antiquark coordinate.

Each three-dimensional vector can be parameterized by its magnitude and two polar angles θ_i, ϕ_i, with $i = 1, 2, 3, 4$. The four-dimensional space of their magnitudes $|\alpha|, |\beta|, |\gamma|, |\delta|$ is described by the hyperdistance in 12 dimensions,

$$
Y^2 = \boldsymbol{\alpha}^2 + \boldsymbol{\beta}^2 + \boldsymbol{\gamma}^2 + \boldsymbol{\delta}^2,
\tag{9.3}
$$

together with three additional angular variables $\theta 1_\chi, \theta 2_\chi, \phi_\chi$. In total, the configuration space is parameterized by Y, eight ordinary angles, and three *extraordinary* ones.

The integration measure factorizes into a product of four three-dimensional and one four-dimensional solid angles,

$$
d\Omega_{11} = d\Omega_\alpha d\Omega_\beta d\Omega_\gamma d\Omega_\delta d\Omega_\chi,
\tag{9.4}
$$

where $d\Omega_\chi = \sin^2(\theta 2_\chi) \sin(\theta 1_\chi)\, d\theta 2_\chi\, d\theta 1_\chi\, d\phi_\chi$, and the usual $d\Omega_i = \sin(\theta_i) d\theta_i d\phi_i$. The generic wave functions may then be written in a factorized form,

$$
\Psi = R_n(Y)\, F(\theta 1_\chi, \theta 2_\chi, \phi_\chi) \prod_{i=1}^{4} Y_{l_i, m_i}(\theta_i, \phi_i).
\tag{9.5}
$$

9.3 Building the pentaquark wave functions

9.3.1 Pentaquarks with maximal spin $S = 5/2$

Before discussing the pentaquark case $q^4\bar{q}$, let us briefly recall the logic used in Ref. [Miesch and Shuryak, 2024] for the related system of hexaquarks (q^6). As usual, one starts from the simplest configurations, namely those with maximal possible spin: $S = 3$ for hexaquarks and $S = 5/2$ for pentaquarks.

---

[1] A general Mathematica statement generating Jacobi coordinates for arbitrary n is given in the Appendix to this chapter.

Recall that the $S = 3$ hexaquark is the only case for which a fully antisymmetric wave function has been derived analytically [Kim et al., 2020]. This construction used traditional group-theoretical methods, combining available color and flavor representations, and resulted in an explicit expression as a sum of five terms with different color-flavor structures. This state is widely believed to have been observed experimentally [Adlarson et al., 2011] as the resonance $d^*(2380)$ in the reaction

$$p + n \rightarrow d + \pi^0 + \pi^0. \tag{9.6}$$

Its width, $\Gamma_{d^*} \approx 70 \, \text{MeV}$, is significantly smaller than that of the Δ baryon, $\Gamma_\Delta \approx 115 \, \text{MeV}$, which was one of the arguments against interpreting it as a loosely bound $\Delta\Delta$ state. Moreover, a deuteron-like $\Delta\Delta$ interpretation would require a binding energy of order $\approx 84 \, \text{MeV}$, which appears uncomfortably large.

By analogy, the simplest pentaquark configurations are those with maximal spin $S = 5/2$. If the isospin is also maximal, the only remaining nontrivial structure is the color wave function, which cannot be fully antisymmetric because the height of the color Young tableau is limited to $N_c = 3$. Nevertheless, antisymmetric pentaquark states with $S = 5/2$ and $I = 3/2$ or $I = 1/2$ can still be constructed, even using the conventional procedure of combining color and flavor representations [Miesch et al., 2023a].

The wave function for the $S = 5/2$, $I = 1/2$ state is given explicitly in [Miesch et al., 2023a] using a monom basis using Wolfram Mathematica, and also obtaining a wave function with 144 nonzero components. Comparing permutation-group methods, with good agreement. Several properties of the maximal-spin $S = 5/2$ states, such as

$$\langle \sum_{i>j} \boldsymbol{\lambda}_i \boldsymbol{\lambda}_j \rangle = -40/3 \tag{9.7}$$

and

$$\langle \sum_{i>j} (\boldsymbol{\lambda}_i \boldsymbol{\lambda}_j)(\mathbf{S}_i \mathbf{S}_J) \rangle = -10/3, \tag{9.8}$$

can be obtained analytically. Remarkably, these relations continue to hold for other, much more complicated pentaquark states discussed below. Such numerical checks proved to be very useful throughout our analysis.

The distributions of flavor and color between the four-quark core and the antiquark are highly nontrivial. For example, for the $S = 5/2$, $I = 1/2$ state the mean values of the isospin projections are

$$\langle I_z(q) \rangle = 1/4, \qquad \langle I_z(\bar{q}) \rangle = -1/2. \tag{9.9}$$

Note that the sum rule $4\langle I_z(q) \rangle + \langle I_z(\bar{q}) \rangle = 1/2$ is satisfied, as expected.

9.3.2 Color-spin-flavor wave functions for S-shell ($L = 0$) pentaquarks from the permutation group S_4

A significant technical difficulty in constructing the theory of multiquark hadrons is the requirement to enforce complete antisymmetry of the quark wave functions dictated by Fermi statistics. The traditional approach proceeds by successively adding quarks (or quark pairs) in all possible representations of the relevant symmetry groups ($SU(3)$ for color and $SU(2)$ for spin and flavor) and combining them step by step. A systematic description of this procedure is given in the Appendix to this chapter.

The wave functions derived here are based on the novel technique developed in Ref. [Miesch and Shuryak, 2024]. For pentaquarks, this method relies on constructing antisymmetric representations of the four-quark core using the permutation group S_4. We begin with Table 9.3.1, which lists the number of core states as a function of total isospin I and spin S. As expected, the table is symmetric under interchange of I and S.

After adding the antiquark via the standard procedure, one obtains the full set of pentaquark states summarized in Table 9.3.2. Because the antiquark is not subject to exchange symmetry with the quarks

and may carry either spin or isospin projection, the number of available states increases substantially. The antisymmetric representations of the permutation group S_4 for four light quarks are constructed following the procedure of Ref. [Miesch and Shuryak, 2024].

The standard monom spacefor S-shell ($L = 0$) pentaquarks has color-spin-flavor dimension

$$d_{monoms} = 3^6 \times 2^5 \times 2^5 = 746496, \tag{9.10}$$

where the antiquark corresponds to two boxes in the color Young tableau, giving rise to the factor 3^6. For P-shell ($L = 1$) states (which will be needed below for the study of baryon-pentaquark mixing) this dimension is multiplied by four, reflecting the number of Jacobi coordinates that enter linearly. As a result, the monom space dimension exceeds one million.

At first sight, writing operators as matrices in such a large space may appear prohibitive, even with the aid of Mathematica. Fortunately, this is not the case, for two reasons. First, in each of the four subspaces (orbital, color, flavor, and spin) one can define a *good basis* based on the corresponding Young tableaux. In practice, this allows one to work with permutation matrices of dimension much smaller than d_{monoms},

$$N_{GB} = N_{GB}^{\text{color}} \times N_{GB}^{\text{spin}} \times N_{GB}^{\text{flavor}}.$$

The two basic generators of the permutation group are constructed using the *KroneckerProduct* operation in Mathematica and subsequently diagonalized. The desired wave functions correspond to antisymmetric eigenvectors that are common to both generators. Since all $n!$ elements of S_n can be generated from these two, such eigenvectors are antisymmetric under all permutations.

For spherically symmetric S-shell ($L = 0$) states, the relevant antisymmetric color-spin-flavor subspaces are listed in Table 9.3.2. The integers give the multiplicities of the states, while the numbers in parentheses indicate the dimensions of the corresponding good basis used in each (S, I) sector. Although the resulting permutation matrices are still too large to display explicitly, their dimensions are far smaller than that of the full monom space (9.10), making their manipulation straightforward.

As an illustrative example, consider the pentaquarks with maximal spin $S = 5/2$. In this case, the only nontrivial Young tableaux are those associated with color and isospin. Using standard $SU(2)$ spin addition, one finds five distinct ways to combine the quarks into total isospin $I = 1/2$, implying a "good basis" of dimension five in isospin space. The color Young tableau that yields a color singlet consists of two closed columns, $\epsilon_{abc}\epsilon_{def}$, as in the hexaquark case. Unlike the latter, however, permutations act only on the four quarks, with indices a, b, c, d. This leads to a color "good basis" of dimension three, and hence a total dimension of $3 \times 5 = 15$.

The two generators of S_4 are then constructed and diagonalized within this space. A single common eigenvector with eigenvalue -1 is found, corresponding to the fully antisymmetric state. Thus, there exists a unique pentaquark state with $S = 5/2$ and $I = 1/2$, mirroring the situation encountered for maximal-spin hexaquarks.

Once all relevant antisymmetric states have been identified, the most efficient strategy is to return to the universal description in the full monom basis of dimension (9.10). Although vectors and operators in this

I \ S	0	1	2
0	0	1	0
1	1	1	1
2	0	1	0

Table 9.3.1 Number of states (per choice of I_z and S_z) for each combination of total spin and isospin for four quarks. Adding an antiquark shifts each state's spin up or down by 1/2.

I/S	1/2	3/2	5/2
1/2	3 (75)	3 (60)	1 (15)
3/2	3 (60)	3 (48)	1 (12)
5/2	1 (15)	1 (12)	0

Table 9.3.2 Spin-isospin table of antisymmetric S-shell ($L = 0$) pentaquark states. The integers denote state multiplicities, while the numbers in parentheses give the dimensions of the corresponding good basis.

space formally involve matrices of size $d_{monoms} \times d_{monoms}$, *Wolfram Mathematica* allows one to handle them efficiently using standard expressions such as $vector^* \cdot matrix \cdot vector^2$.

In practice, the number of nonzero components in the wave functions is much smaller than d_{monoms}, so these objects are highly sparse. While it is clearly impractical to publish the full wave functions, it is nevertheless instructive to compare the number of nonzero terms in their monom representations. As anticipated, the smallest numbers occur for maximal spin $S = 5/2$: the state with $I = 3/2$ has only 252 nonzero components, while the $I = 1/2$ state has 708. Moving to lower spin and then to P-shell ($L = 1$) states leads to a dramatic increase. For example, the 13 states with $L = 1$, $S = 1/2$, $I = 1/2$ used below for mixing with nucleons together contain 187 200 nonzero components.

For $I = 1/2$ and $S = 1/2, 3/2$, we find two triplets of states in each case, in agreement with expectations based on Young tableaux. These triplet states are not uniquely defined; only the eigenstates of specific physical operators are physically meaningful. The sums over all ten quark-quark and quark-antiquark pairs, $(\lambda\lambda) = \sum_{i>j} \boldsymbol{\lambda}_i\boldsymbol{\lambda}_j$ and $SS = \sum_{i>j} \boldsymbol{\sigma}_i\boldsymbol{\sigma}_j$, are related to the Casimir operators of color and spin and are therefore diagonal in this basis.

To lift the remaining degeneracies, one needs a Hamiltonian. As an example, we consider the one-gluon-exchange color-spin interaction summed over all ten pairs,

$$H_{\lambda\sigma} = -C_{\lambda\sigma} \sum_{i>j} (\boldsymbol{\lambda}_i\boldsymbol{\lambda}_j)(\mathbf{S}_i\mathbf{S}_j). \tag{9.11}$$

We evaluated the full Hamiltonian matrix between all states and diagonalized it. The resulting eigenvalues for the seven states with $I = 1/2$ (the $S = 1/2$ triplet, the $S = 3/2$ triplet, and the $S = 5/2$ singlet) are listed in Table 9.3.3. As expected, the maximal-spin state $S = 5/2$ has the highest energy. If the resonance $N^*(2000)\,5/2^+$ is indeed identified with this pentaquark, the remaining states should lie somewhat below 2 GeV.

(An alternative Hamiltonian, used for example in Ref. [An and Saghai, 2019], is the flavor-spin interaction associated with pion exchange, following Ripka and Glozman,

$$H_{\tau\sigma} = -C_{\tau\sigma} \sum_{i>j} (\boldsymbol{\tau}_i\boldsymbol{\tau}_j)(\mathbf{S}_i\mathbf{S}_j). \tag{9.12}$$

Here $\mathbf{S} = \boldsymbol{\sigma}/2$, whereas for color and flavor we use Gell-Mann and Pauli matrices without the factor $1/2$. Using the same wave functions, we also constructed and diagonalized this Hamiltonian. Since its spectrum is not qualitatively different from that of the color-spin Hamiltonian, we do not display it explicitly.)

By symmetry, the mean value of the S_z component is the same for all four quarks, but differs for the antiquark. By construction, the expectation values satisfy the sum rule

$$\sum_{i=1..5} \langle S_z(i) \rangle = 4\langle S_z^1 \rangle + \langle S_z^5 \rangle = S_z^{\text{total}}. \tag{9.13}$$

---

[2] While the `SparseArray` format can accelerate computations for large vectors and matrices, some general commands (such as `Expand`, `Conjugate`, and `ComplexExpand`) do not function correctly in this format in version 14.1. For this reason, we found it safer to work in the `Normal` format for algebraic manipulations.

S	1/2	1/2	1/2	3/2	3/2	3/2	5/2
$\lambda\lambda$	-40/3	-40/3	-40/3	-40/3	-40/3	-40/3	-40/3
SS	-3/2	-3/2	-3/2	0	0	0	5/2
$H_{\lambda\sigma}/C_{\lambda\sigma}$	-4.66	-1.44	2.77	-3	1/3	10/3	10/3

Table 9.3.3 Properties of the seven antisymmetric $L = 0$, $I = 1/2$ pentaquark states: three $S = 1/2$, three $S = 3/2$, and one $S = 5/2$.

The mean spin and isospin values of the quarks and the antiquark can be compared with expectations from naive models. For instance, in the diquark-based picture of Ref. [Shuryak and Zahed, 2004a], two spin-isospin zero diquarks imply $\langle S_z^q \rangle \approx \langle I_z^q \rangle \approx 0$, with all spin and isospin carried by the antiquark, $\langle S_z^{\bar{q}} \rangle \approx \langle I_z^{\bar{q}} \rangle \approx 1/2$. Inspection of Table 9.3.3 shows that while some states exhibit either vanishing quark spin or vanishing quark isospin, both never vanish simultaneously. This provides yet another illustration of how oversimplified such naive models can be.

An alternative naive picture, in which spin and isospin are shared equally among all five constituents, is likewise not supported by the present, more detailed analysis.

In summary, the explicit construction of fully antisymmetric S-shell pentaquark wave functions reveals a spectrum and internal structure that are considerably richer than suggested by simple diquark-based or equal-sharing models. Even in the most constrained case of maximal spin, the allowed states are unique and highly nontrivial, while for lower spins multiple states appear whose physical distinction only emerges after diagonalization of realistic interaction Hamiltonians. The resulting distributions of spin and isospin between the quark core and the antiquark demonstrate that neither extreme localization on the antiquark nor uniform sharing among constituents is realized. This underscores the necessity of enforcing Fermi statistics exactly and treating color, spin, and flavor dynamics on equal footing when analyzing pentaquark structure.

9.3.3 Pentaquarks of the $L = 1$ shell

Because the σ and π operators that introduce the corresponding mesons (to be used below for *unquenching* of the nucleon) necessarily carry nonzero orbital angular momentum, P-shell pentaquark states can mix with the nucleon.

For $L = 1$ pentaquarks, the dimension of the good basis is increases by a factor of four relative to the S-shell case. This factor simply reflects the number of Jacobi coordinate vectors $\boldsymbol{\alpha}, \boldsymbol{\beta}, \boldsymbol{\gamma}, \boldsymbol{\delta}$ that can appear linearly in the orbital wave function. Correspondingly, one finds approximately four times as many fully antisymmetric states; these are listed in Table 9.3.4.

The pentaquark states that can mix with the nucleon must have isospin $I = 1/2$ and spin $S = 1/2$ or $S = 3/2$. The complete list of states compatible with Fermi statistics is given in Table 9.3.4, amounting to 24 states in total[3].

Even the largest good basis encountered here, of dimension 300, is still many orders of magnitude smaller than the full monom basis of dimension 746496. The corresponding vectors are sparse, though not extremely so: the 13 states with $S = 1/2$ contain 187 200 nonzero components, while the 11 states with $S = 3/2$ contain 198 000 nonzero components. P-shell wave functions are therefore substantially more complicated than their $L = 0$ counterparts. In particular, the amplitudes are no longer simple numbers but explicit functions of 12 variables: eight angles θ_i, ϕ_i ($i = 1, 2, 3, 4$) and four radial coordinates. The angular-momentum operators involve derivatives with respect to these angles, which can nevertheless be applied directly to our sparse vectors of very large dimension.

Some operators, such as the color operator

---

[3] In Ref. [An and Saghai, 2019] the number of $L = 1$ compatible states is quoted as 17, and they are not organized into fully Fermi-statistics-compliant combinations. We also disagree with the way their energies are derived from the Hamiltonian.

I/S	1/2	3/2	5/2
1/2	13 (300)	11 (240)	3 (60)
3/2	11 (240)	10 (192)	3 (48)
5/2	3 (60)	3 (48)	1 (12)

Table 9.3.4 Antisymmetric pentaquark states with $L = 1$, total spin S and isospin I. As in Table 9.3.2, the first numbers indicate the number of states, while the numbers in parentheses give the dimension of the corresponding good basis.

$$\Big\langle \sum_{i>j} \boldsymbol{\lambda}_i \boldsymbol{\lambda}_j \Big\rangle = -\frac{40}{3},$$

have identical expectation values for all states. This follows from the fact that the four-quark core always transforms according to the [211] color Young tableau.

The eigenvalues of the 13×13 color-spin Hamiltonian for the $L = 1$ pentaquark shell with $S = 1/2$ are shown in Fig. 9.3.1. Although the resulting spectra are rather similar, the underlying states themselves can differ substantially. While it is unlikely that individual pentaquark states can be experimentally resolved due to their overlapping widths, we will show below that specific linear combinations of these states constitute the five-quark Fock component of the nucleon.
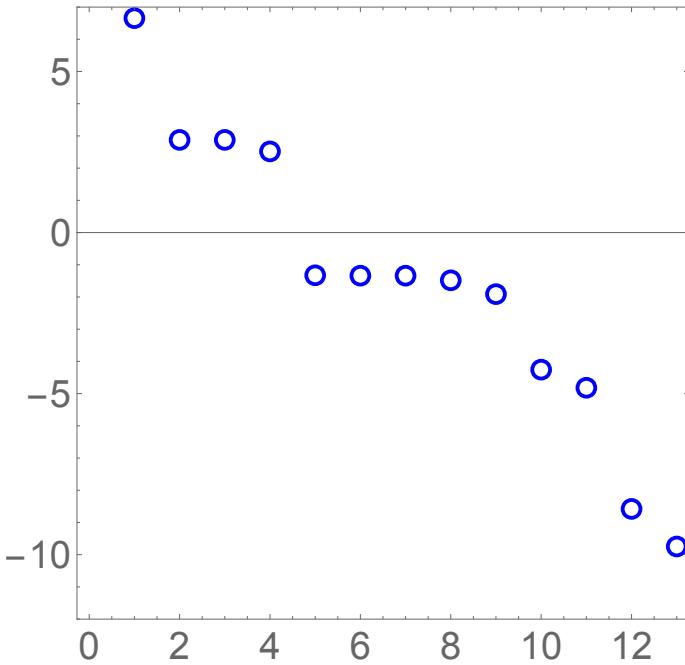
Fig. 9.3.1 Eigenvalues of the color-spin Hamiltonian for $L = 1$, $S = 1/2$ pentaquark states, normalized to the matrix element $H_{\lambda\sigma}/C_{\lambda\sigma}$.

As for the $L = 0$ pentaquark shell, we evaluated the distributions of various physical quantities over the four Jacobi solid angles and among the five constituents. To avoid excessive clutter, we present results only for three representative states (1, 7, and 13 of the $S = 1/2$ set) listed in Table 9.3.5.

The four Jacobi coordinates are associated with four pairs of angles θ_i, ϕ_i, and we computed the expectation values of the squared orbital angular momenta in each corresponding solid angle,

$$L_i^2 f = -\frac{1}{\sin\theta_i} \frac{\partial}{\partial\theta_i}\Big(\sin\theta_i \frac{\partial f}{\partial\theta_i}\Big) - \frac{1}{\sin^2\theta_i} \frac{\partial^2 f}{\partial\phi_i^2}, \tag{9.14}$$

with $i = 1, 2, 3, 4$. Symmetry among the quarks in the core implies $\langle L^2(1)\rangle = \langle L^2(2)\rangle = \langle L^2(3)\rangle$, while the corresponding value associated with the antiquark (the fourth angle) is different. As shown in Table 9.3.5, the three selected states exhibit markedly different distributions. The lowest-energy state (state 1) carries almost no orbital angular momentum on the antiquark and almost no spin on the quarks.

We also computed expectation values of the z-components $L_z(i)$ for $i = 1, \ldots, 4$. All results satisfy the expected sum rules,

$$\sum_{i=1..4} \langle L^2(i)\rangle = 3L^2(1) + L^2(4) = 2, \tag{9.15}$$

$$\sum_{i=1..4} \langle L_z(i)\rangle = 3L_z(1) + L_z(4) = -1, \tag{9.16}$$

as required for the $L = 1$ shell. For completeness, we recall that the spin and isospin components satisfy the analogous relations

$$\sum_{i=1..5} \langle S_z(i)\rangle = 4S_z(1) + S_z(5) = \frac{1}{2}, \qquad \sum_{i=1..5} \langle I_z(i)\rangle = 4T_z(1) + T_z(5) = \frac{1}{2}.$$

state number	1	7	13
$L^2(1)$	0.4965	0.6652	0.6547
$L^2(4)$	0.0258	0.0043	0.0358
$S_z(1)$	0.0963	0.0562	0.0931
$S_z(5)$	0.1146	0.2748	0.1272
$I_z(1)$	0.1523	0.0516	0.0545
$I_z(5)$	-0.1094	0.2934	0.2817

Table 9.3.5 Distribution of selected observables over Fermi-antisymmetric pentaquark states with $L = 1$, $S = 1/2$, and $I = 1/2$. The operator $L^2(i)$ denotes the squared orbital angular momentum associated with the ith Jacobi solid angle. Mean z-components of spin and isospin are shown for a representative quark ($i = 1$) and for the antiquark ($i = 5$).

9.3.4 Where pentaquarks become chaotic?

Quantum few-body systems are known to undergo a transition to the so-called *quantum chaos* regime; see, for example, Ref. [Zelevinsky, 1996] for a review. This phenomenon is well documented in atomic and nuclear systems with several particles or holes near closed shells. A historically important example is the cerium atom, which has four valence electrons and thus 12 effective coordinates. It was shown in Ref. [Flambaum et al., 1997] that even its lowest-energy states display chaotic behavior.

Since this phenomenon is generic, it is natural to expect it to arise in multiquark systems as well. Pentaquarks (the subject of this section) also involve 12 Jacobi coordinates, the same number as the cerium atom. One may therefore anticipate a similar transition to chaos in these systems. One of us has previously discussed this issue for baryons, pentaquarks, and their admixture within a light-cone framework, using different wave functions and basis states [Shuryak, 2019].

The simplest signature of quantum chaos is a random (Gaussian-like) Porter-Thomas distribution of amplitudes of exact Hamiltonian eigenstates when expanded in a natural basis, such as that of the single-particle Hamiltonian. In Fig. 9.3.2 we show two such distributions for fixed-energy states, plotted in terms of their monom coefficients.

The upper histogram corresponds to the S-shell state with $L = 0$, $S = 5/2$, $I = 1/2$, which we obtained both analytically and numerically. Its wave function consists of three distinct structural terms, multiplied by permutations. The histogram confirms that only two amplitude values (up to an overall sign) appear,
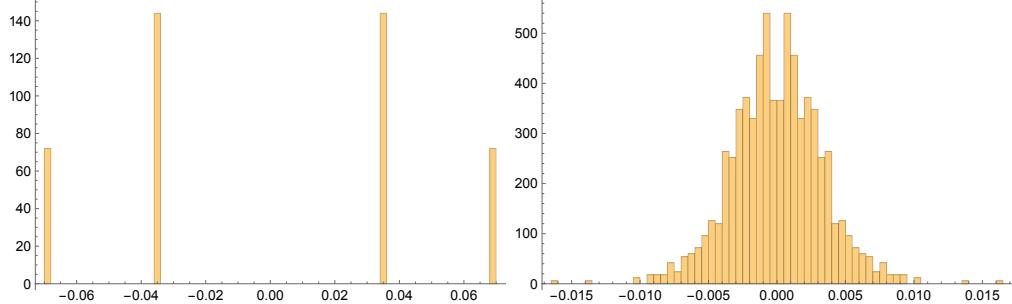
Fig. 9.3.2 Distribution of monom coefficients for an S-shell state with $L = 0$, $S = 5/2$, $I = 1/2$ (upper panel) and for a P-shell state with $L = 1$, $S = 1/2$, $I = 1/2$ (lower panel).

each repeated many times. Since there are $4! = 24$ quark permutations and three structural terms, the total occupancy of the histogram is $72 = 24 \times 3$. This state is therefore highly regular and far from chaotic.

The lower histogram corresponds to one of the P-shell $L = 1$ pentaquark states. Its overall shape is indeed close to a Gaussian, although systematic deviations are clearly visible. The most prominent feature is a dip near zero amplitude. Such dips are often associated with finite-size effects. (For example in the Dirac eigenvalue spectrum of lattice or instanton studies of the QCD vacuum.) In the present case, however, the dip is well understood in chiral random-matrix models [Shuryak and Verbaarschot, 1993b, Verbaarschot and Zahed, 1993] in terms of finite volume and finite matrix size, and has been confirmed in numerous lattice simulations. The precise origin of the dip in the present histogram remains unclear. We only note that the total number of nonzero coefficients is about 14 400 in a monom basis of dimension 746 496, so the wave function is still relatively sparse.

Another notable feature of the lower histogram is the presence of regularly spaced peaks. This may signal a quantum system whose phase space supports both regular and chaotic motion, with the chaotic component being dominant.

Quasi-random expansion coefficients in a given basis constitute only one of many possible indicators of chaos. One may also examine probability distributions of single-particle observables, such as spatial densities or distributions over single-particle energies, and compare them with predictions of statistical models (for instance, a Fermi gas characterized by an effective temperature and entropy). Indeed, even a single many-body eigenstate can admit an effective thermal description at the level of single-particle observables. We defer such investigations to future work.

In summary, we have presented evidence that a transition toward quantum chaos may occur in pentaquarks already at the second excitation level, namely in the $L = 1$ shell.

The onset of chaotic behavior in the $L = 1$ pentaquark sector has direct consequences for baryon-pentaquark mixing. As the density of antisymmetric five-quark states increases and their wave functions become broadly delocalized in the underlying basis, the coupling of a three-quark baryon to the five-quark sector ceases to be dominated by a small number of well-defined configurations. Instead, the mixing proceeds through a large set of near-degenerate pentaquark states with statistically distributed amplitudes. In this regime, individual mixing matrix elements lose predictive power, while their ensemble-averaged properties constrained by symmetry, sum rules, and the structure of the interaction operators, become the relevant quantities. Consequently, sizable baryon-pentaquark admixtures arise naturally, even in the absence of narrow pentaquark resonances, providing a dynamical mechanism for enhanced five-quark Fock components in low-lying baryons.

9.4 Nucleon-pentaquark mixing

The *unquenching* of mesons and baryons (namely, attempts to quantify the four-quark sector of mesons and the five-quark sector of baryons) has a long history and remains an open problem. For several decades, from the 1960s until relatively recently, multiquark hadrons were largely regarded as "exotica", a category viewed with skepticism due to the lack of firmly established experimental evidence. This situation has changed dramatically in the last decade.

Although this shift has not yet fully permeated the broader community, its impact can be clearly illustrated by examining one of the central pillars of QCD spectroscopy: heavy quarkonia. While bottomonium spectroscopy remains fully consistent with a simple $\bar{b}b$ interpretation well described by a Cornell-type potential, states of charmonium already deviates significantly from this picture. The first state unambiguously inconsistent with a pure $\bar{c}c$ assignment was the $X(3872)$ with $J^P = 1^+$. Originally grouped under the generic X, Y, Z labels reflecting their unknown structure, such states are now separated in the PDG into distinct categories.

In particular, axial-vector states with quantum numbers $I = 1$, $J^P = 1^+$, which necessarily carry isospin, are interpreted as pion-added systems and are classified as tetraquarks, denoted $T_{\bar{c}c1}$ in the 2024 PDG. In contrast, vector ($J^P = 1^-$) and pseudoscalar ($J^P = 0^-$) states with $I = 0$ (which may be interpreted as "σ-added) continue to be listed under the traditional ψ and η_c labels. This asymmetric treatment is unfortunate, particularly in view of the empirical observation that axial and vector states often appear as near-degenerate pairs, suggestive of chiral partner relationships.

(Some charmed tetraquarks are often interpreted as molecular, deuteron-like two-meson bound states located near threshold, such as DD^*. However, this description does not apply universally. In recent years, a large number of tetraquark states have been observed, including systems with cc pairs and even fully charmed $\bar{c}\bar{c}cc$ tetraquarks at the LHC. For details on such states and their mixing patterns we refer to Ref. [Ferretti et al., 2013] and references therein.)

The key point of this detour is the following: the number of known pion-admixed and sigma-admixed charmonium-like states appears to be roughly equal. With four $T_{\bar{c}c1}$ states and four additional ψ-like states that cannot be accommodated within the $\bar{c}c$ spectrum, the observed pattern suggests an approximate π-σ symmetry, reminiscent of the original chiral symmetry. Chiral doubling in heavy-light systems was first discussed in Refs. [Nowak et al., 1993, Bardeen and Hill, 1994, Nowak et al., 2004] and later confirmed experimentally by the BaBar [Aubert et al., 2003] and CLEO [Besson et al., 2003] collaborations.

Turning now to baryons, a similar pattern emerges. Historically, the appearance of the $\sigma = f_0$ meson in hadronic reactions has been systematically underestimated. To emphasize the relevance of chiral mixing in the baryon sector, we list in Table 9.4.1 the branching ratios of well-established nucleon resonances into $N\pi$ and $N\sigma$ final states. Although the pion channels generally dominate, this primarily reflects the larger available phase space for $N\pi$ decays. When translated into coupling constants, the values of $g_{NN^*\pi}$ and $g_{NN^*\sigma}$ turn out to be comparable within uncertainties, precisely as expected from naive chiral symmetry considerations.

After these phenomenological detours, we return to the theoretical framework. The traditional strategy for estimating the five-quark admixture in baryons proceeds in two steps: (i) the formulation of *meson-admixture operators* that add a $\bar{q}q$ pair to a baryon, followed by (ii) the projection of the resulting states onto good pentaquark configurations consistent with Fermi statistics and other symmetry constraints.

Although we have carried out a detailed calculation of nucleon-pentaquark mixing in Ref. [Miesch et al., 2025c], we do not reproduce those results here. The reason is that a subsequent study reformulated the same physics on the light front, yielding results that are more directly connected to experimental observables such as antiquark parton distribution functions. Readers interested in these applications are therefore referred to the final part of this book, where this subject is discussed in detail.

Before turning to the explicit mechanisms of nucleon-pentaquark mixing, it is useful to place the discussion in the broader dynamical context established in the previous section. The appearance of a dense spectrum

state	$N\pi$	$N\sigma$
$N^*(1440)\,1/2^+$	0.55-0.75	0.11-0.23
$N^*(1520)\,3/2^+$	0.55-0.65	< 0.1
$N^*(1535)\,1/2^-$	0.32-0.52	$0.02 - 0.1$
$N^*(1650)\,1/2^-$	0.5-0.7	$0.02 - 0.18$
$N^*(1675)\,5/2^-$	0.38-0.42	$0.03 - 0.07$
$N^*(1675)\,5/2^-$	0.38-0.42	$0.03 - 0.07$
$N^*(1680)\,5/2^+$	0.6-0.7	$0.09 - 0.19$
$N^*(1700)\,3/2^-$	0.07-0.17	$0.02 - 0.14$
$N^*(1710)\,1/2^+$	0.05-0.20	< 0.16
$N^*(1720)\,3/2^+$	0.08-0.14	$0.02 - 0.14$
$N^*(1875)\,3/2^-$	0.03-0.11	$0.02 - 0.08$
$N^*(1880)\,1/2^+$	0.03-0.31	$0.08 - 0.40$
$N^*(1895)\,1/2^-$	0.02-0.18	< 0.13
$N^*(1900)\,3/2^+$	0.01-0.20	$0.01 - 0.07$
$N^*(2060)\,5/2^-$	0.07-0.12	$0.03 - 0.09$
$N^*(2100)\,1/2^+$	0.08-0.32	$0.14 - 0.35$
$N^*(2120)\,3/2^-$	0.05-0.15	$0.04 - 0.14$
$N^*(2190)\,7/2^-$	0.1-0.2	$0.03 - 0.09$

Table 9.4.1 Branching ratios of $N\pi$ and $N\sigma$ decays of $N^*(mass)J^P$ resonances (left column), from PDG24

and quasi-chaotic wave functions in the $L = 1$ pentaquark shell implies that five-quark states form a highly entangled many-body sector rather than a small set of isolated configurations. In such a regime, mixing between three-quark baryons and five-quark states is not governed by proximity to individual resonances, but instead by collective properties of the pentaquark spectrum and by symmetry-driven selection rules. This perspective motivates treating baryon-pentaquark mixing as a generic and robust feature of low-energy QCD, closely tied to chiral dynamics and the ubiquity of $\bar{q}q$ excitations in hadronic wave functions.

Chapter 10
Hadrons made of six, nine, or twelve quarks
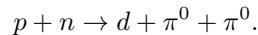
10.1 Some evidences for multiquark states

In this chapter we consider quantum states composed of more quarks. Dibaryons may be viewed as hexaquarks (q^6), three-baryon systems as q^9, and four-baryon systems as q^{12} objects.

The central issue is not merely one of nomenclature. Rather, the key question is whether such multiquark configurations are *compact enough* to exist as objects qualitatively distinct from ordinary nuclear states, either as bound states or as resonances. An alternative possibility is that compact multiquark configurations appear only as *admixtures* to conventional nuclear wave functions, in close analogy with the baryon-pentaquark mixing discussed earlier.

Phenomenological indications

We begin with several phenomenological examples. The experiment WASA-at-COSY [Adlarson et al., 2011] observed a dibaryon resonance $d^*(2380)$ with spin $J = 3$ in the reaction

$$p + n \to d + \pi^0 + \pi^0.$$

This state lies approximately $84\,\mathrm{MeV}$ below the $\Delta\Delta$ threshold. From a nonrelativistic perspective, the spin assignment $J = 3$ could arise from the vector addition $3/2 + 3/2$ of two Δ baryons, suggesting a molecular, deuteron-like interpretation.[1] Equally well, the state may correspond to an S-shell hexaquark with maximal spin $6 \times \frac{1}{2}$. In general, the physical state may be a mixture of both configurations.

Additional hints for multiquark components arise from hadron-nucleus scattering. While the standard Glauber-type description based on multiple pN scatterings is highly successful in many applications, it fails for scattering on ^{4}He. As noted in [Dakhno and Nikolaev, 1985], the total cross section, the diffraction slope, and the position of the diffractive minimum all deviate from standard expectations. The inclusion of a compact 12-quark component was shown to resolve all three discrepancies [Dakhno and Nikolaev, 1985, Mosallem and Uzhinskii, 2002]. The parameters extracted in these studies are mutually consistent and indicate that the 12-quark configuration is not extremely small in size.

---

[1] If this were the case, one would expect the width to be dominated by the Δ width, $\Gamma_\Delta \approx 115\,\mathrm{MeV}$. The observed width, $\Gamma_{d^*} \approx 70\,\mathrm{MeV}$, is significantly smaller, which may indicate a more compact structure.

Relation to nuclear structure

From a theoretical standpoint, three- and four-baryon systems naturally include light nuclei, which have been extensively studied in nuclear physics. Particular attention has long been paid to the α particle, $^4\mathrm{He} = ppnn$, which is a "double-magic" system with closed $1S$ shells for both protons and neutrons. Its exceptional binding and compactness have motivated decades of discussion on whether heavier nuclei such as ^{12}C or ^{16}O exhibit α-cluster substructure. In the same spirit, one may ask whether the α particle itself should be described as containing a compact 12-quark $1S$ component (3 colors $\times$ 2 spins $\times$ 2 isospins).

Even at the nucleon level, achieving an accurate description of the α particle is challenging. A naive sum of pairwise nuclear potentials yields a very deep minimum, approximately $6 \times 50 \sim 300\,\mathrm{MeV}$, but only for a small fraction of the available four-body configurations. One way to resolve this tension is through the hyperdistance approximation, which successfully reproduces the physical binding energy, $B \approx 28\,\mathrm{MeV}$. Another approach employs first-principles simulations based on path-integral Monte Carlo methods.[2] These studies indicate that four-nucleon preclusters can survive at temperatures $T \sim 100\,\mathrm{MeV}$, characteristic of hadronic freeze-out.

Limitations of nucleon-based descriptions

The deeper conceptual issue, however, is not technical. While modern renormalization-group methods allow low-energy nuclear forces to be fixed uniquely from nucleon scattering data, this is not yet true for the short-distance repulsive core. Different potential models fitted to spectra and phase shifts exhibit a wide spread in their short-range behavior. Naively summing six such cores in a multi-nucleon system leads to repulsions of order several GeV, an outcome that is both unrealistic and highly uncertain. As has been emphasized repeatedly in the literature, this problem is more naturally addressed at the quark level.

Beyond diquark models

A related theoretical issue concerns "good diquark" models. As argued already in the Introduction, singling out a small subset of pairwise interactions (six diquarks in a 12-quark system) while neglecting the remaining pairs (66 in total) is logically inconsistent and leads to unobserved phenomena. At the perturbative level, this can be demonstrated explicitly.

At the nonperturbative level, one must explain the origin of strong diquark binding. For light u, d, s quarks, such binding is largely attributed to the instanton-induced 't Hooft interaction [Rapp et al., 1998, Alford et al., 1998]. Achieving a binding of order $6 \cdot B_{qq}$ in a 12-quark cluster would require six instantons within the same spatial region, which is problematic given the diluteness of instantons in the QCD vacuum. Thus, for light-quark 12-quark systems, the problem is naturally elevated to one of instanton correlations in the nonperturbative vacuum, a topic well beyond the scope of the present work.

Lattice and symmetry considerations

An alternative approach is provided by lattice QCD. Although progress remains limited, recent studies of strange and charmed dibaryons have yielded encouraging results [Dhindsa et al., 2025].

---

[2] One of us pioneered numerical path-integral techniques over forty years ago [Shuryak and Zhirov, 1984]. Recently, this approach has been revived to study α preclustering in heavy-ion collisions [DeMartini and Shuryak, 2021].

Finally, for light u, d quarks, spin and isospin share the same $SU(2)$ structure and can be interchanged. One therefore expects "mirror" multiquark states– for example, hexaquarks with $S = 3, I = 0$ and $S = 0, I = 3$.[3]

Practical construction of multiquark wave functions

Although the "monom space" and spin-tensor notation are conceptually natural, their size grows rapidly with the number of quarks. Color, flavor, and spin spaces scale as 3^n, 2^n, and 2^n, respectively, yielding a total dimension 12^n. For hexaquarks ($n = 6$), this already reaches the millions, making direct matrix manipulations impractical.

Fortunately, these dimensions can be drastically reduced using the "best basis" approach introduced in [Miesch and Shuryak, 2024]. This method constructs orthonormal bases corresponding to the required Young tableaux in each monom subspace, rendering explicit calculations feasible even for large multiquark systems.

In summary, existing experimental indications and theoretical considerations suggest that multiquark configurations with six or more quarks cannot be dismissed as purely academic constructs. While in some cases they may appear as distinct resonances, in others they are more naturally interpreted as compact components admixed into conventional nuclear wave functions. The limitations of nucleon-based descriptions at short distances, together with symmetry arguments and nonperturbative dynamics at the quark level, motivate a systematic construction of multiquark wave functions consistent with Fermi statistics. In the following sections we therefore turn to explicit realizations of hexaquark, nonaquark, and dodecaquark states, using permutation-group methods and reduced bases that make such analyses tractable.

10.2 Building of the multi-quark wave functions

We will not present Jacobi coordinates explicitly here. Instead, in Appendix 10.A we provide a Mathematica script that generates Jacobi coordinates for an arbitrary number of particles N. When all quark masses are equal, the kinetic energy is proportional to the Laplacian, allowing one to employ the same hyperdistance approximation used in previous chapters.

The general strategy for constructing multiquark wave functions was already introduced in earlier chapters and is based on representations of the permutation group S_n. The corresponding Mathematica implementation and additional technical details are described in Ref. [Miesch and Shuryak, 2024]. Here we briefly summarize the main elements of the procedure.

A single light quark carries $3 \times 2 \times 2 = 12$ color-spin-flavor states. Consequently, an N-quark state[4] can be expanded in a "monom" basis of dimension $N_{\mathrm{monoms}} = 12^N$. In spin-tensor notation, implemented as Mathematica `Tables`[5], a generic wave function takes the form

$$\psi = \sum_{\text{all indices}} C_{\text{indices}} \, |c_1 \ldots c_N \, s_1 \ldots s_N \, i_1 \ldots i_N\rangle,$$

with explicit color, spin, and isospin indices.

The procedure for constructing wave functions consistent with Fermi statistics can be summarized as follows:

---

[3] These mirror states need not be degenerate if the Hamiltonian is of color-spin type, but they would be nearly so in flavor-spin models of the Riska-Glozman type, dominated by pion exchange.

[4] In contrast to the pentaquark case, antiquarks are absent here, so the counting of color states is simpler.

[5] Since these tables are often used in flattened form, the ordering of indices (color, spin, isospin) must be chosen consistently at construction time.

1. Identify the **allowed tensor structures** in each sector (color, spin, flavor, orbital), corresponding to the required Young tableaux. For example, in the color sector a baryon is described by the antisymmetric tensor $\epsilon_{c_1 c_2 c_3}$, while for hexaquarks the color structure generalizes to $\epsilon_{c_1 c_2 c_3} \epsilon_{c_4 c_5 c_6}$ together with all index permutations. In the presence of antiquarks, Kronecker symbols $\delta_{\bar{c}}^{c}$ may also appear.
2. Generate **all permutations** of the n indices under the generators of S_n, and express the resulting $n!$ tensors as vectors in the monom space $\mathbb{C}^{N^n}$.
3. **Orthogonalize** this set of vectors, for example using the Gram-Schmidt procedure. This produces a significantly reduced orthonormal "good basis". The expected dimension of this basis can be estimated [Miesch and Shuryak, 2024].
4. Construct the matrices representing the two independent **permutation-group generators** acting on the original monom space, and project them onto the reduced basis obtained in the previous step. This yields two matrices of dimension $n' \times n'$.
5. After performing steps 1-4 for each sector (color, spin, flavor, orbital, etc.), take the **Kronecker product**[6] of the corresponding permutation generators. This produces two matrices acting in the full reduced Hilbert space, of total dimension $n'_{\text{total}} = n'_{\text{color}} \cdot n'_{\text{spin}} \cdot n'_{\text{flavor}} \cdots$.
6. **Diagonalize** the two generators simultaneously, searching for common eigenvectors with the required symmetry (eigenvalues ± 1, depending on the fermionic or bosonic character of the sector). These eigenvectors are the desired wave functions, which may be projected back to the full monom basis if needed.

10.2.1 The simplest case of maximal spin $S = 3$

We already used these procedures for baryons and pentaquarks, so now let us proceed directly to $N = 6$ Hexaquark case. As usual, we start with the simplest case of maximal spin[7].

Simplification in this case comes from the total spin being at its maximal value $S = 3$, so that all quark spins $\uparrow\uparrow\uparrow\uparrow\uparrow\uparrow$ point in the same direction. Thus the spin part of the WF is trivially symmetric and factorizes. What remains to deal with are the intermixed *color* and *flavor* WFs. The former make representations of the $SU(3)$ group, and the latter either $SU(2), u, d$ or $SU(3), u, d, s$ flavor groups.

SU(3) color   SU(2) flavor
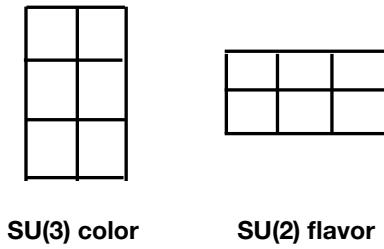
Fig. 10.2.1 Color and flavor Young tableax for hexaquarks

The space of all color states have 3^6 monoms. Color Young tableaux shown in Fig.10.2.1 should look like two complete vertical sets of squares. Those are antisymmetrized, or represented by 3-index Levi-Civita symbol. In our notations they correspond to all permutations of two of those

```
TensorProduct[LeviCivitaTensor[3], LeviCivitaTensor[3]]
```

---

[6] Recall that the Kronecker product combines matrices into a single matrix acting on the product space, whereas the tensor product combines vectors into a higher-rank tensor.

[7] Or maximal isospin, but not both

For step 2, we considered every possible one of these rearrangements and wrote them in as vectors in $\mathbb{C}^{3^6}$, using Mathematica's *Flatten* function. There are 6! permutations in symmetric S_6 group, so that is the number of 3^6-dimensional vectors in our list. (By a coincidence 6! = 720 happens to be close to 3^6 = 729 .)

Orthogonalization of this set of vectors was accomplished through Mathematica's *Orthogonalize* procedure, which by default uses Gram-Schmidt method and generates a set of independent orthonormal vectors. From dimension 720 that reduces to "good basis" of only 5 linearly independent combinations. The notations below use $k = 1$ is P_{12}, $k = 2$ is P_{cycle} permutation generators, defined in this basis $\{\mathbf{b}_i\}_{i=1}^5$ were then found by taking

$$(P_{color}^k)_{ij} = \mathbf{b}_i^T \cdot P_{\mathbb{C}^{729}}^k \cdot \mathbf{b}_j,$$

where $P_{\mathbb{C}^{729}}^k$ was generated as we did in smaller dimensions for baryons.

For the flavor sector we select *uuuddd* quark composition, so the necessary tensor structure is three diquarks or three columns each being 2d Levi-Civita

```
TensorProduct[LeviCivitaTensor[2], LeviCivitaTensor[2],LeviCivitaTensor[2]]
```

Just like for color, there are 6! quark permutations of the flavor indices f_i's, also leading to just 5 unique linearly independent combinations. We then compute two P_{flavor}^k 5×5 matrices for generators of S_6.

The next step is to perform *KronekerProduct* of color and spin (or flavor) spaces[8], and representing two generators of the S_6 group, P_{12} and P_{cycle}. Their diagonalization allows to search for common eigenstates with total eigenvalue -1 (antisymmetry for Fermions). There is indeed one such state found.

Most of the wavefunctions we obtained are too large to list here, but for instance the color-flavor 25-dimensional wavefunction can be written in the ("flattened") basis $\{\mathbf{b}_{color}\} \otimes \{\mathbf{b}_{flavor}\}$

$$(0,0,0,0,\frac{1}{\sqrt{5}},0,0,0,-\frac{1}{\sqrt{5}},0,0,0,\frac{1}{\sqrt{5}},0,0,0,\frac{1}{\sqrt{5}},0,0,0,-\frac{1}{\sqrt{5}},0,0,0,0) \tag{10.1}$$

Note that there are 3 positive terms and 2 negative terms with otherwise equal coefficient: we checked that they are exactly those found by Kim, Kim, and Oka in [Kim et al., 2020].

10.2.2 Generic spin cases

$S \backslash S_z$	0	1	2	3
0	0			
1	$\{1, 5 \times 5 \times 9\}$	$\{1, 5 \times 5 \times 9\}$		
2	0	0		
3	$\{1, 5 \times 5 \times 1\}$	$\{1, 5 \times 5 \times 1\}$	$\{1, 5 \times 5 \times 1\}$	$\{1, 5 \times 5 \times 1\}$

Table 10.2.1 Hexaquarks with *uuuddd* flavor content, with different values of spin S (rows) and its projections S_z (columns). When the number of states is 0, as it is for $S = 0$ and 2, the row is all zeroes. When the number of antiperiodic wave functions found is one, we give the dimension of the orthogonalized basis for tensor product of color-flavor-spin states.

Using the power of the proposed method, we apply it for hexaquarks with other quantum numbers.

For spins smaller than 3, the spin WF is no longer trivial. For $S = 1, S_z = 0$, the general symmetry structure can be obtained from Young tableaux. It is antisymmetry in 2 pairs of indices and symmetry in the other two. The tensor structure to be permuted is therefore $[\uparrow\downarrow][\uparrow\downarrow]\{\uparrow\downarrow\}$, where symmetric and antisymmetric combinations are

$$[\uparrow\downarrow] = (\uparrow\downarrow - \downarrow\uparrow)/\sqrt{2}$$

---

[8] Perhaps it is useful to remind here the difference between *KronekerProduct* and *TensorProduct* commands. The former convert any number of matrices into one big matrix. The latter convert product of vectors into a large vector.

$$\{\uparrow\downarrow\} = (\uparrow\downarrow + \downarrow\uparrow)/\sqrt{2}$$

with large number of permutations of indices. Yet, after *orthogonalization* the basis of independent states possesses only 9 linearly independent vectors. Therefore, two S_6 generators σ_{spin}^1 and σ_{spin}^2 in this basis are 9×9 matrices, given as examples in equation 10.2.

$$P_{spin}^1 = \begin{pmatrix} -1 & 0 & 0 & 0 & 0 & 0 & 0 & 0 & 0 \\ 0 & -1 & 0 & 0 & 0 & 0 & 0 & 0 & 0 \\ 0 & 0 & -1 & 0 & 0 & 0 & 0 & 0 & 0 \\ 0 & 0 & 0 & 1 & 0 & 0 & 0 & 0 & 0 \\ 0 & 0 & 0 & 0 & 1 & 0 & 0 & 0 & 0 \\ 0 & 0 & 0 & 0 & 0 & 1 & 0 & 0 & 0 \\ 0 & 0 & 0 & 0 & 0 & 0 & 1 & 0 & 0 \\ 0 & 0 & 0 & 0 & 0 & 0 & 0 & 1 & 0 \\ 0 & 0 & 0 & 0 & 0 & 0 & 0 & 0 & 1 \end{pmatrix},$$

$$P_{spin}^2 = \begin{pmatrix}
\frac{1}{4} & \frac{1}{4\sqrt{3}} & \frac{1}{\sqrt{6}} & -\frac{\sqrt{3}}{4} & -\frac{1}{4} & -\frac{1}{\sqrt{2}} & 0 & 0 & 0 \\
-\frac{\sqrt{3}}{4} & \frac{1}{12} & \frac{1}{3\sqrt{2}} & -\frac{1}{4} & \frac{1}{12\sqrt{3}} & \frac{1}{3\sqrt{6}} & -\frac{\sqrt{2}}{3} & -\frac{4}{3\sqrt{3}} & 0 \\
0 & -\frac{\sqrt{2}}{3} & \frac{1}{6} & 0 & -\frac{\sqrt{\frac{2}{3}}}{3} & \frac{1}{6\sqrt{3}} & -\frac{1}{3\sqrt{3}} & \frac{1}{6\sqrt{6}} & -\frac{\sqrt{\frac{5}{2}}}{2} \\
-\frac{\sqrt{3}}{4} & -\frac{1}{4} & -\frac{1}{\sqrt{2}} & -\frac{1}{4} & -\frac{1}{4\sqrt{3}} & -\frac{1}{\sqrt{6}} & 0 & 0 & 0 \\
\frac{3}{4} & -\frac{1}{4\sqrt{3}} & -\frac{1}{\sqrt{6}} & -\frac{1}{4\sqrt{3}} & \frac{1}{36} & \frac{1}{9\sqrt{2}} & -\frac{\sqrt{2}}{9} & -\frac{4}{9} & 0 \\
0 & \sqrt{\frac{2}{3}} & -\frac{1}{2\sqrt{3}} & 0 & -\frac{\sqrt{2}}{9} & \frac{1}{18} & -\frac{1}{9} & \frac{1}{18\sqrt{2}} & -\frac{\sqrt{\frac{5}{6}}}{2} \\
0 & 0 & 0 & \sqrt{\frac{2}{3}} & -\frac{\sqrt{2}}{9} & -\frac{4}{9} & -\frac{1}{9} & -\frac{2\sqrt{2}}{9} & 0 \\
0 & 0 & 0 & 0 & \frac{8}{9} & -\frac{2\sqrt{2}}{9} & -\frac{1}{9\sqrt{2}} & \frac{1}{36} & -\frac{\sqrt{\frac{5}{3}}}{4} \\
0 & 0 & 0 & 0 & 0 & 0 & \frac{\sqrt{\frac{3}{10}}}{2} + \frac{7}{2\sqrt{30}} & \frac{\sqrt{\frac{3}{5}}}{4} - \frac{2}{\sqrt{15}} & -\frac{1}{4}
\end{pmatrix} \qquad (10.2)$$

The next step is to define these two generators ($k = 1,2$ for P_{12} and P_{cycle}) written as tensor product incorporating every sector of the WF, e.g.

$$P_{total}^k = P_{color}^k \otimes P_{spin}^k \otimes P_{flavor}^k. \qquad (10.3)$$

In the previous subsection - hexaquarks with maximal spin $S = 3$ - these were matrices (in "good basis") of dimension $5 \cdot 5 \cdot 1 = 25$. For other spin values and *uuuddd* quarks, those we found to be matrices in the following minimal dimensions: for $S = 2$ they are in 125-d space, for $S = 1$ in 225-d, and for spin 0 they are matrices in 125-dimensions again.

While all of them are too large to be given in press, we still emphasize that these dimensions are many times smaller than that of the full space of monoms, 12^6. Furthermore, in practice there is absolutely no problem to operate with them inside Mathematica. In particularly, all are generated in a second, and diagonalized as quickly.

A procedure to find common antisymmetric eigenstates one can e.g. add two matrices with coefficients being some random numbers, e.g. e and π, and then look for eigenvalues $-e - \pi$.

The particular number of solutions for each spin depends only on the spin value S, and of course not on its projection S_z, as follows from rotational symmetry. Yet the calculation themselves are not technically identical, so we did it for *all* values of S_z to check for their mutual consistency. Some of the results are shown in Table 10.2.1.

At $S = 0$ and $S = 2$ we found no solutions were possible with the permutation antisymmetry desired. At $S = 1$ and $S = 3$ however, we found a *single* antiperiodic wave function for each value of S_z.

$I=0$					$I=1$						$I=2$				
L \ S	0	1	2	3	L \ S	0	1	2	3		L \ S	0	1	2	3
0	0	1	0	1	0	1	0	1	0		0	0	1	0	0
1	1	1	2	0	1	1	4	2	1		1	2	2	1	0
2	4	9	5	2	2	9	15	10	2		2	5	10	5	1

Table 10.2.2 Number of antisymmetric $6\,q$ states (per choice of m_s and m_l) at each combination of total orbital and spin angular momentum for the light quark hexaquark. For example, last in row 1 of the $I=0$ plot is the KKO state with S=3, L=0. At $L=0$ there are 3 possible combinations of S and I, with the ability to swap them identically as they are both $SU(2)$: (1,0), (3,0), and (2,1). It is worth noting that these exactly match the allowed quantum number combinations for dibaryons made from nucleons and Δ's first calculated in 1964 by Dyson and Xuong [Dyson and Xuong, 1964].

L \ S	0	1	2	3
0	0	1	0	0
1	0	2	1	0
2	5	7	4	1

Table 10.2.3 Number of *udsuds* antisymmetric states (per choice of m_s and m_l) at each combination of total orbital and spin angular momentum for *udsuds* hexaquark. -

Let us now change the flavor content, adding two strange quarks to *uuddss* hexaquark. The flavor becomes $SU(3)$ and its treatment is similar to that of color, if total adds to zero. The resulting antisymmetric states are reported in Table 10.2.3.

Completing the hexaquark discussion, let us consider another simplified case, of same-flavor quarks (e.g. *ccccc*). The number of good states is in the Table 10.2.4.

Let us explain some cases without solutions first. If both flavor and spin is flat-symmetric, then Fermi statistics requirement falls on color WF, which cannot be fulfilled for 6 quarks.

L \ S	0	1	2	3
0	1	0	0	0
1	0	1	0	0
2	2	2	1	0

Table 10.2.4 Number of antisymmetric states (per choice of m_s and m_l) at each combination of total orbital and spin angular momentum for *ccccc* hexaquark.

10.3 Matrix Elements of basic operators and hexaquark masses

With the color-flavor-spin wave functions available, one can attempt to calculate the average values of pertinent operators. The obvious step one is to do that perturbatively, for a gluon exchanges. The lowest order gluon exchange generates potentials proportional to "relative color" operators made out of color generators $\langle \lambda_i^A \lambda_j^A/4 \rangle$ where $A = 1..8$ and $i,j = 1..n$. Relativistic corrections lead to spin-spin, spin-orbit and tensor forces, as usual. Perturbative one-gluon exchange require that those also are proportional to colors, e.g. spin-spin is proportional to

$$\langle \sum_{i>j} (\frac{1}{4}\lambda_i^A \lambda_j^A)(\mathbf{S}_i \mathbf{S}_j) \rangle$$

For $S-shell, L=0$ hadrons the spin-spin forces are the only relativistic corrections.

The resulting masses are shown for light hexaquarks in table 10.3.1 and for all other $L=0$ states in table 10.3.2. Note that the ordering of the compact hexaquark states in 10.3.1 (fourth column) is rather different from the ordering of the dibaryon molecules with the same quantum numbers (fifth column). The (0,3) state

uniquely breaks the pattern: not only it is degenerate with the (1,2) state and lighter than the (2,1) state, it is lighter than (or at least close to) the dibaron molecule state with spin 3 and isospin 0, which was predicted to have a mass of 2350 MeV. Every other channel show that a molecule is lighter than compact hexaquark. Perhaps this is the only hexaquark state that has been experimentally observed.

Higher order gluon exchanges lead to operators with higher orders of Gell-Mann matrices. Those diagrams can best be obtained from an expansion of the set of Wilson lines convoluted with color wave functions, see e.g. Fig.10.3.1 for hexaquarks. For example, for hexaquarks one can either put two color epsilons with all 6! permutations or simplify it to just 5 "good basis" color convolutions. As far as we know, next order gluon exchanges were not yet used in spectroscopy.

(I, S)	$\langle\lambda\lambda\rangle$	$\langle\lambda\lambda SS\rangle$	$6q$ mass	Molec.model	Experiment
$(0, 1)$	-16	-2/3	2098	1876	1876
$(1, 0)$	-16	-2	2196	1876	1878
$(1, 2)$	-16	-4	2342	2160	2160
$(2, 1)$	-16	-20/3	2536	2160	2160
$(0, 3)$	-16	-4	2342	2350	2380
$(3, 0)$	-16	-12	2926	2350	2464

Table 10.3.1 $6q$ matrix elements of color and color-spin operators for all of the $L = 0$ light hexaquark states. The resulting masses (in MeV) obtained from simple additive model [Kim et al., 2020] are in the 4-th column (using $m_q = 330$ MeV, $m_s = 500$ MeV, and $m_c = 1270$ MeV). The fifth column show prediction of molecular dibaryons model [Dyson and Xuong, 1964]. The 6-th column show experimentally measured values of the resonances with corresponding quantum numbers (taken from compilation [Clement, 2017]).

State	$\langle\lambda\lambda\rangle$	$\langle\lambda\lambda SS\rangle$	Mass (MeV)
$udsuds$, $S = 0$	-16	6	1611
$cccccc$, $S = 0$	-16	-12	7819
$udud\bar{q}$, $S = \frac{3}{2}$	$-\frac{20}{3}$	7/4	1623
$udud\bar{q}$, $S = \frac{1}{2}$	$-\frac{20}{3}$	1/2	1714
$udud\bar{c}$, $S = \frac{3}{2}$	-7.654	1.117	2607
$udud\bar{c}$, $S = \frac{1}{2}$	-7.654	1.442	2582
$udud\bar{Q}$, $m_Q \to \infty$, $S = \frac{3}{2}$	-8	4/3	$1319 + m_Q$

Table 10.3.2 Matrix elements and masses for all other $L = 0$ states found in this paper, using the same fit from [Kim et al., 2020].

The nonperturbative confining potentials are defined via correlators of n Wilson lines,

$$\langle\Psi|\left(\delta_{c1}^{c1'}...\delta_{cn}^{cn'} - W_{c1}^{c1'}...W_{cn}^{c1n'}\right)|\Psi'\rangle \tag{10.4}$$

with path-ordered exponential of color generators

$$W = Pexp[i(\lambda^a/2)\int gA_0^a dt]_{c1}^{c1'}$$

The setting is shown schematically in Fig.10.3.1

Note that while total wave functions Ψ is a spin-tensor with many different indices (color, flavor, spin etc) the main perturbative $\lambda\lambda$ operator has only color indices. So, if Ψ consists of several factorizable parts

$$W = \sum_A C^A \psi_{color}^A \psi_{flavor}^A \psi_{spin}^A$$
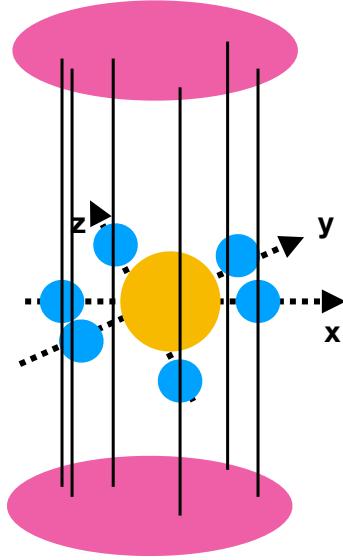
Fig. 10.3.1 The setting for calculation of the effective potential for $n = 6$ quarks, located at (blue) points in three dimensions. The vertical direction is Euclidean time, six vertical lines are Wilson lines. Red ovals above and below indicate color wave functions to which Wilson lines are traced. Yellow circle indicate gauge fields of an instanton.

one can sum over non-color indices using normalization of those wave functions and put this operator as "sums of squares" of the color wave functions

$$\sum_A C_A^2 \psi_{color}^A(c) \big(\delta_{c1}^{c1'} ... \delta_{cn}^{cn'} - W_{c1}^{c1'} ... W_{cn}^{c1n'} \big) \psi_{color}^A(c')$$

We have calculated it explicitly for variouse states. For hexaquarks, their five color wave functions are explicitly given in Appendix of the original paper. We also of course convoluted those with Wilson lines to get color potentials, but the expression is too long to be given here (can be obtained from the authors upon request). This expression can be directly evaluated on the lattice, or by any vacuum model (e.g., in the instanton model), producing forces among quarks in all hexaquarks.

10.4 Nine and twelve-quark S-shell states

Light u, d quarks form an isospin-1/2 doublet and carry three color and two spin degrees of freedom, resulting in a total of $2 \times 3 \times 2 = 12$ internal states. This number therefore plays the role of a "magic number", completing the $1S$ ($L = 0$) quark shell.

The corresponding quantum numbers naturally bring to mind the α particle, $^4\text{He} = ppnn$, the classic example of a "double magic" nucleus, known to be deeply bound and compact. A substantial nuclear-physics literature discusses the extent to which heavier nuclei such as ^{12}C and ^{16}O may exhibit α-cluster correlations. Indeed, nucleons in the α particle do not strongly overlap, making a four-body nuclear description well justified. Nevertheless, it remains a legitimate question whether the α-particle wave function may contain a sufficiently compact component that is more naturally described in terms of twelve quarks.

The theoretical description of the ^4He wave function has a long history, dating back to the 1930s, and played a key role in the development of the hyperdistance approximation that we employ for multiquark systems. Alternatively, one may avoid approximations altogether and perform numerical Path

Integral Monte Carlo calculations [Shuryak and Zhirov, 1984]. This approach has recently been revived in Ref. [DeMartini and Shuryak, 2021], where evidence for α preclustering was reported at temperatures $T \sim 100$ MeV, relevant for hadronic freezeout in heavy-ion collisions.

Before turning to explicit calculations, it is useful to comment on diquark-based approaches to multiquark systems. Such models often argue that the 12-quark problem can be reduced to a system of six diquarks, thereby transforming a fermionic many-body problem into a bosonic one. As already discussed in the Introduction, this line of reasoning is fundamentally flawed. There is no justification for singling out six pairs out of the total 66 possible quark-quark pairs, even if those six are assumed to experience the strongest attraction[9]. All pairwise interactions must be treated on equal footing[10].

The origin of strong diquark correlations is commonly traced to the instanton-induced 't Hooft interaction, see Refs. [Rapp et al., 1998, Alford et al., 1998]. To obtain a binding energy of $6\,B_{qq}$ from six diquarks would require six instantons to be localized within a single 12-quark cluster. This scenario is highly implausible, given the dilute nature of instantons in the QCD vacuum.

As a theoretical starting point, one may instead consider a toy model in which the quarks are sufficiently heavy to justify a nonrelativistic Schrodinger description with perturbative Coulomb interactions. We begin with the most symmetric case, involving two heavy flavors (e.g. c and b) with a common mass M.

As shown above for systems of three, four, five, and six quarks, one can construct wave functions obeying Fermi statistics by explicit construction of color-spin-flavor tensor products and subsequent diagonalization of the Hamiltonian within this space. For 12-quark systems (and even for nine quarks), this approach rapidly becomes intractable. The full monom space has dimension $N_{\text{monoms}} = 12^{12} \approx 8.9 \times 10^{12}$, and even the initial reduction to a "good basis" poses severe difficulties. Although the color space alone has dimension $3^{12} \sim 10^6$, the number of permutations of open-index tensors constructed from four Levi-Civita symbols is prohibitively large, even with the aid of Wolfram Mathematica.

Nevertheless, by restricting to a reduced set of permutations and starting with nine quarks, we were able to identify partial "good basis" structures. For $N = 9$, the color basis has dimension 33, and the flavor basis dimension 42. If the total spin is maximal, $S = 9/2$, the spin sector factorizes, and the combined color-flavor basis has dimension $33 \times 42 = 1386$. The two generators of the permutation group S_9 can be constructed as matrices in this space. Diagonalizing them leads to the negative result that no common eigenvectors with eigenvalue -1 (corresponding to full antisymmetry) exist. Extending the analysis to non-maximal spin introduces an additional factor of 42 from the spin sector, yielding matrices of dimension $33 \times 42 \times 42$, which are beyond our current computational reach.

Although the explicit construction of wave functions becomes prohibitively difficult for $N = 9$ and $N = 12$, it remains possible to determine whether Fermi-statistics-compliant states exist at all. This can be achieved by consulting tables of Kronecker coefficients available in the mathematical literature. For the lowest spin and isospin values ($S, I = 0$ for even N, and $S, I = 1/2$ for odd N), such analyses indicate the existence of a single state for $N = 9$, $N = 12$, and $N = 24$, with no corresponding states for $N = 15$, 18, or 21.

The possibility that such compact quark clusters exist as admixtures to conventional nuclear states has been discussed for decades and remains an important direction for future investigation.

Concluding remarks.

In summary, the analysis of nine- and twelve-quark systems highlights both the conceptual importance and the technical difficulty of extending multiquark spectroscopy beyond the few-body domain. While the explicit construction of fully antisymmetric wave functions becomes rapidly impractical as the number of quarks increases, group-theoretical considerations indicate that such states do exist at selected quark numbers, including $N = 9$ and $N = 12$. This strongly suggests that compact multiquark configurations may arise not

---

[9] We have already seen explicitly that the "good diquark" ideology fails for tetraquarks.

[10] This can be demonstrated already at the perturbative level.

as isolated exotic resonances, but rather as well-defined components admixed into ordinary nuclear wave functions. Clarifying the dynamical role of these components, and their interplay with conventional nuclear forces, remains a key challenge for future theoretical and lattice studies.

Appendix

10.A Modified Jacobi coordinates for N bodies

The general idea is to compute location of the CM of the first n bodies and then define coordinate as distance to $n+1$th. For bodies of the same mass, let us give compact Mathematica commands generating those

```
In:   Jacobi[n_] := Inverse[DiagonalMatrix[
    Table[Sqrt[i + 1]/Sqrt[i], {i, 1, n}]]] . (Table[
     Join[Table[1/i, i], Table[0, n - i]], {i, 1, n}] +
    DiagonalMatrix[Table[-1, n - 1], 1])
```

Let us check what it will produce for 3,4 and 5 bodies, baryons, tetraquarks and pentaquarks as we have defined those coordinates above:

```
  In:   Jacobi[3]
Out: {{1/Sqrt[2], -(1/Sqrt[2]), 0},
{1/Sqrt[6], 1/Sqrt[ 6], -Sqrt[(2/3)]},
{1/(2 Sqrt[3]), 1/(2 Sqrt[3]), 1/(2 Sqrt[3])}}

In: Jacobi[4]
Out: {{1/Sqrt[2], -(1/Sqrt[2]), 0, 0},
{1/Sqrt[6], 1/Sqrt[6], -Sqrt[(2/3)], 0},
   {1/(2 Sqrt[3]), 1/(2 Sqrt[3]), 1/( 2 Sqrt[3]), -(Sqrt[3]/2)},
  {1/(2 Sqrt[5]), 1/(2 Sqrt[5]), 1/(2 Sqrt[5]), 1/(2 Sqrt[5])}}

In: Jacobi[5]
Out: {{1/Sqrt[2], -(1/Sqrt[2]), 0, 0, 0},
{1/Sqrt[6], 1/Sqrt[6], -Sqrt[(2/3)], 0, 0},
{1/(2 Sqrt[3]), 1/(2 Sqrt[3]), 1/(2 Sqrt[3]),-(Sqrt[3]/2), 0},
{1/(2 Sqrt[5]), 1/(2 Sqrt[5]), 1/(2 Sqrt[5]), 1/(2 Sqrt[5]), -(2/Sqrt[5])},
{1/Sqrt[30], 1/Sqrt[30],  1/Sqrt[30], 1/Sqrt[30], 1/Sqrt[30]}}
```

The Jacobi coordinates we call $\alpha, \beta...$ are given as combination of actual body coordinates x_i, $i = 1..n$ with coefficients just obtained. For example $\boldsymbol{\alpha} = (\mathbf{x}_1 - \mathbf{x}_2)/\sqrt{2}$ etc. Note that the last bracket always gives the location of the Center of Mass, to be put to zero. Thus the number of Jacobi coordinates is not n but $n-1$.

Note that for baryons (n=3), the traditional names of Jacobi coordinates are $\boldsymbol{\rho}, \boldsymbol{\lambda}$ rather than $\boldsymbol{\alpha}, \boldsymbol{\beta}$, and in this case we will use traditional ones.

Note that in order to calculate the metric tensor in new coordinates it is convenient to start with the Cartesian form for old coordinates $ds^2 = \sum dx_i^2$, and then, using the matrix *inverse* to that obtained above, rewrite it as $ds^2 = g_{11}d\alpha^2 + ...$. Note further that the Laplacian includes g^{ij}, the inverse of the metric g_{ij} obtained. The volume element is given by $\sqrt{det(g)}$. In Mathematica use *Inverse* and *Det* commands.

For the cases of bodies with different masses we discuss in tetraquark chapter.

Parton model and the light front properties of hadrons

Chapter 11
Deep Inelastic scattering, PDF moments and DGLAP evolution

This part is partly introductory in context. We start with parton distributions (PDFs) and related theory. The Distribution Amplitudes (DAs) will be introduced in connection with pion in 19.3. Generalizations of PDFs are discussed in chapters on GPDs and TMDs later in this part.

11.1 Light front quantization

We are not going to repeat here the standard lore related to Deep Inelastic scattering and other hard processes: there is no shortage of literature for that. And still, a number of basic definitions (with commentaries) are perhaps needed for non-experts.

To introduce the notations, we start with free fermions on the light front. The Hamiltonian is obtained from the expanded relativistic kinetic energy, assuming the longitudinal momentum is the largest [Brodsky, 1994]

$$P^- = \int dx^- d^2x_\perp \; T^{+-} = \int [d^3k]_+ \int [d^3q]_+ \frac{k_\perp^2 + M^2}{2k^+} \bar\psi_+(k)\gamma^+ \psi_+(q)(2\pi)^3 \delta_+^3(k-q) \qquad (11.1)$$

What we call a Hamiltonian gives the spectrum of mass squared $M^2 = P^+ P^-$. The LF form of quantized fermionic field in momentum space is defined by

$$\psi_+(x^-, x_\perp) = \int [d^3k]_+ \psi(k) e^{-ik^+ x^- + ik_\perp \cdot x_\perp} \qquad (11.2)$$

with the free LF spinors for the quarks and anti-quarks

$$u_s(p) = \frac{1}{\sqrt{\sqrt{2}p^+}} \left(\not p + M\right) \begin{pmatrix} \chi_s \\ \chi_s \end{pmatrix} \qquad v_s(p) = \frac{1}{\sqrt{\sqrt{2}p^+}} \left(\not p - M\right) \begin{pmatrix} 2s\chi_s \\ -2s\chi_s \end{pmatrix} \qquad (11.3)$$

respectively. Here χ_s a 2-spinor with a spin pointing in the z-direction. Slashed momentum vectors mean, as usual, their convolution with gamma matrices. $\psi(k)$ annihilates a particle in a $u_s(k)$ mode, or creates an antiparticle in a $v_s(k)$ mode, i.e.

$$\psi_+(k) = \sum_s u_s(k)b_s(k)\theta(k^+) + v_s(-k)c_s^\dagger(-k)\theta(-k^+)$$

$$(11.4)$$

The measure in momentum space is defined as

$$[d^3k]_+ = \frac{dk^+ d^2k_\perp}{(2\pi)^3 2k^+} \epsilon(k^+) \qquad (11.5)$$

which sums over the positive k^+ region for particle modes, and over the negative k^+ region for antiparticle modes.

11.2 Partons at the light front and PDFs

The mass spectrum diagonalizes the light front Hamiltonian

$$P^-|X,P\rangle = \frac{m_X^2}{2P^+}|X,P\rangle \tag{11.6}$$

with the states expanded in multi-component Fock representations. For example, a meson in the lowest Fock representation reads

$$|\text{Meson } X,P\rangle = \frac{1}{\sqrt{N_c}}\int_0^1 \frac{dx}{\sqrt{2x\bar{x}}}\int \frac{d^2k_\perp}{(2\pi)^3}\sum_{s_1,s_2}\Phi_X(x,k_\perp,s_1,s_2)b_{s_1}^\dagger(k)c_{s_2}^\dagger(P-k)|0\rangle \tag{11.7}$$

with the light front normalization $\langle P|P'\rangle = (2\pi)^3 2P^+\delta^3(P-P')$ and

$$\int_0^1 dx \int \frac{d^2k_\perp}{(2\pi)^3}\sum_{s_1,s_2}|\Phi_X(x,k_\perp,s_1,s_2)|^2 = 1 \tag{11.8}$$

The parton distribution functions (PDFs) are pertinent matrix elements of the light front quark and gluon operators organized in a twist expansion (the twist of an operator is the dimension minus spin). In the large momentum limit $[D^+]$ factors out, with the space-time dimensions reduced by 1, e.g. $[\psi_+] = 1, [\psi_-] = 2$. The twist-2 and twist-4 unpolarized PDF for a meson are respectively,

$$\langle X,P|\bar{\psi}_+\frac{1}{2}\gamma^+\psi_+|X,P\rangle \qquad \langle X,P|\bar{\psi}_-\frac{1}{2}\gamma^+\psi_-|X,P\rangle \tag{11.9}$$

in the light cone gauge. They count the number of partons in the hadron state, in the infinite momentum frame.

11.2.1 Partons from leading pQCD factorization

The light front form of the leading twist unpolarized hadron PDFs, follow from the factorization of the inclusive photon-hadron cross section as illustrated by the hand-bag diagram with $d\sigma \sim l^{\mu\nu}(q)\,W_{\mu\nu}(k)$. The hadronic kernel

$$M_{\alpha\beta}(k) = \int d^4x\, e^{ik\cdot x}\,\langle P|T^*(\bar{\psi}_\beta(0)\psi_\alpha(x)|P\rangle \tag{11.10}$$

which corresponds to removing a quark of momentum-k and spin-α from the hadron at x, and returning as a a quark of momentum-k but spin-β at point 0, factors out in the hand-bag diagram, defines the hadronic tensor

$$W^{\mu\nu}(k) = \int d^4k\,\text{Tr}\left(M(k)\gamma^\mu\frac{i(\not{k}+\not{q})}{(k+q)^2+i0}\gamma^\nu\right) + [\text{cross}] \tag{11.11}$$

which is frame covariant. Note that the leading contribution to the hadronic matrix element is from the photon transverse polarizations $\mu,\nu = \perp,\perp$. In the nucleon rest frame, $P^\mu = (m_N, 0^\perp, 0)$ and $q^\mu = (\nu, 0^\perp, -\sqrt{\nu^2+Q^2})$. In the Bjorken limit with $\nu, Q^2 \to \infty$ but fixed $x_B = Q^2/2\nu m_N$, the photon 4-

momentum simplifies $q^\mu \approx (\nu, 0^\perp, -(\nu + m_N x_B))$, hence $q^- \approx \nu \gg q^+ \approx m_N x_B$ and (11.11) reduces to

$$W^{\mu\nu}(k) = -g_\perp^{\mu\nu} \int d^4k \, \text{Tr}\left(M(k) \frac{i\gamma^+}{2(k^+ + p^+) + i0} \right) + [\text{cross}] \tag{11.12}$$

which simplifies to

$$W^{\mu\nu}(k) = -ig_\perp^{\mu\nu} \int \frac{dx}{2\pi} \left(\frac{q(x)}{x - x_B + i0} + \frac{\bar{q}(\bar{x})}{\bar{x} + x_B + i0} \right) = -g_\perp^{\mu\nu} \frac{1}{2} \big(q(x_B) + \bar{q}(-x_B) \big) \tag{11.13}$$

The light cone quark PDF is

$$q(x) = \int_{-\infty}^{\infty} \frac{dx^-}{2P^+} e^{ixP^+ x^-} \langle P|\bar{\psi}(0)\gamma^+ W(0, x^-)\psi(x^-)|P\rangle \rightarrow \int \frac{d^2k_\perp}{(2\pi)^3} |\Phi_X(x, k, s, s')|^2 \tag{11.14}$$

and the anti-quark PDF is

$$\bar{q}(x) = \int_{-\infty}^{\infty} \frac{dx^-}{2P^+} e^{-ixP^+ x^-} \langle P|\bar{\psi}(0)\gamma^+ W(0, x^-)\psi(x^-)|P\rangle \rightarrow \int \frac{d^2k_\perp}{(2\pi)^3} |\Phi_X(\bar{x}, k, s, s')|^2 \tag{11.15}$$

We have restored the gauge link

$$W(x^-, 0) = \exp\left[-ig \int_0^{x^-} d\eta^- A^+(\eta^-) \right] \rightarrow 1$$

which is 1 in the light cone gauge $A^+ = 0$. The unpolarized inclusive cross section counts the number of partonic quarks in a hadron, in the leading twist aproximation at parton $x = x_B$ in the Bjorken limit. In the hadron rest frame, the twist-2 PDFs probe the quark correlation function along the x^- light front direction. They are inherently non-perturbative.

11.3 Operators and Twist classification

11.3.1 Operators of the leading twist

"Twist" is defined as operator's dimension minus its spin. Quark operators of spin n contain symmetrized product of covariant derivatives, and thus twist 2

$$O_n^q(x) \equiv \bar{\psi} \nabla_{\{\alpha 1} ... \nabla_{\alpha n-1} \gamma_{\beta\}} \psi, \tag{11.16}$$

Similar definitions hold for gluonic operators. For example, the gluonic stress tensor

$$O_{\alpha\beta}^g(x) \equiv G_{\alpha\mu}^a G_{\mu\beta}^a - \text{trace}, \tag{11.17}$$

has dimension 4 and spin 2, so its twist is dimension-spin 4-2=2. Let us recall that the instanton field, although strong, has zero stress tensor, and so there is no instanton contributions to it. The $I\bar{I}$ molecules however, do contribute. The gluonic PDF's second moment is related to its average in a hadron: it is known both from data and lattice.

The correlator of the gluonic stress tensors in *vacuum*

$$\Pi^{qg}(|x|) \sim \langle O_{\alpha\beta}^q(x) O_{\alpha\beta}^g(0) \rangle \tag{11.18}$$

describes the propagation of tensor glueballs. And indeed, unlike the scalar and pseudoscalar ones, it is enhanced by instantons, but remains relatively small. (Perhaps it can be used to see the contribution of the $I\bar{I}$ molecules .)

11.3.2 Anomalous dimensions of operators

Generally, perturbative renormalization of operators yields mixing of quark and gluon operators. The ensuing expressions are unwieldy and we will not cover them here. For twist 3 and 4 one can find these expressions in the original work in [Shuryak and Vainshtein, 1982a]. Instead, we will give an example of the use of the anomalous dimensions relevant to the "spin crisis" as discussed in [Thomas, 2008]. It is based on the RG form preserving chiral symmetry. Using standard (one-loop) notations

$$t = ln(Q^2/\Lambda_{QCD}^2), \;\; \alpha_s = \frac{4\pi}{\beta_0 ln(Q^2/\Lambda_{QCD}^2)}, \;\; \beta_0 = 11 - \frac{2}{3} N_f \tag{11.19}$$

one can derive the RG evolution for the orbital momentum contributions in closed forms. For the flavor-singlet and isovector combinations they are given by

$$L^{u+d+s}(t) + \Sigma = (\frac{1}{2})\frac{3N_f}{16+3N_f} + (\frac{t}{t_0})^{-\frac{32+6N_f}{9\beta_0}} \left(L^{u+d}(t_0) + \Sigma/2 - \frac{3N_f}{16+3N_f} \right) \tag{11.20}$$

$$L^{u-d}(t) = -(\Delta u - \Delta d)/2 + (\frac{t}{t_0})^{-\frac{32}{9\beta_0}} \left(L^{u-d}(t_0) + (\Delta u - \Delta d)/2 \right) \tag{11.21}$$

From which one can obtain the orbital momenta for each flavor separately. At large Q the values of $L_u \approx -0.36, L_d \approx 0.28$ are of opposite sign, but evolve to lower scale $1\,\text{GeV}$ to be about the same. Further evolution down to the initial model scale [1], yields vanishing $L_d \approx 0$ and a larger $L_u \approx 0.3$. These results support the idea of a d quark always bound into a scalar ud diquark and is decoupled from the nucleon's spin, while the u quark is free with most of the nucleon spin.

11.3.3 Examples of DGLAP evolution

Using anomalous dimensions in practice is not very convenient, because the operator averages are *moments* of the PDFs, that is their convolution with powers of x. Those naturally require knowledge of the PDFs over all $x \in (0,1)$, which is not available in practice.

Dokshitzer-Gribov-Lipatov, and Altarelli-Parisi (DGLAP) worked out convenient "evolution equations" describing parton splitting reactions, such as $q \to qg, g \to gg$ and so on. Those equations allows to "evolve" PDFs in resolution, in any direction

$$PDF(x, Q_1^2) \leftrightarrow PDF(x, Q_2^2)$$

In particular, the standard normalization point used by the lattice community is $Q^2 = 2\,\text{GeV}^2$, to which results from different lattices are evolved for comparison.

The experiments are done at much larger resolutions, in a wide range $Q^2 = 10 - 1000\,\text{GeV}^2$, so a practical tool allowing simultaneous fit to many different experiments was badly needed. Large collaborations have been created for performing this task, such as CTEQ collaboration. Its web page provides a lot of textbook-like material and useful practical tools.

---

[1] In [Thomas, 2008] the low scale was set to $0.4\,\text{GeV}$, perhaps too low for the use of pQCD. Yet the results seem to make sense.

While there is no need to reproduce most of it here, let us still mention a particularly useful source we used, for the purposes of this book. We suggest ManeParse [2] providing directly the $PDF(x, Q)$ functions in Mathematica notebook form.

We now provide three examples of DGLAP evolution from this source. One is the evolution of the density of (relatively soft) gluons. It shows a rapid disappearance of the soft gluons at resolution at or below $Q \to 1\,\text{GeV}$. So, at lower resolution one can assume that gluons are absent[3].
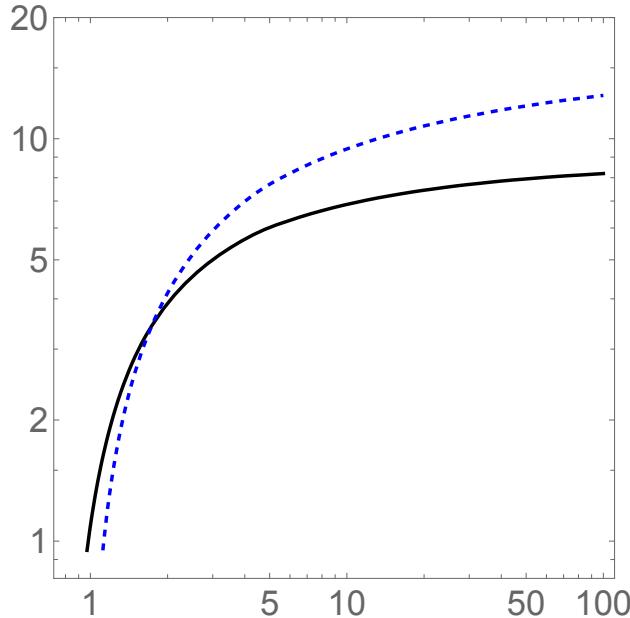
Fig. 11.3.1 Plot of the gluon PDF $xg(x, Q)$ versus $Q(GeV)$ at $x = 0.01$ (black solid) and $x = 0.005$ (blue dashed).

Two more plots in Fig.11.3.2 show the evolution of the u, d distributions in the proton, as well as that of the antiquark "sea" $\bar{u}, \bar{d}$. The low-resolution ones (dashed) lack perturbative small-x partons and thus turn down at the left sides of the plots. The "evolved" ones (solid) move to the left and have a different form.

These PDFs are believed to be dominated by the qqq and the $qqqq\bar{q}$ Fock components of the proton wave functions, which we discuss in the pentaquark chapters. One may use the empirical PDF plots like this and compare them to the PDFs derived from the "theoretical wave functions", e.g. for our $L = 1$ pentaquark admixture to the nucleons. Those are supposed to be defined at the boundary of DGLAP desciption, namely at the "boundary scale" $Q = 1\,\text{GeV}$ between the chiral and gluonic evolutions.

11.4 The force acting on a quark and twist-3 operators

This section follows our paper [Liu et al., 2025].

Higher twist operators are of higher dimensions, including higher powers of quark and gluon fields. They carry information about the partonic correlations. Their general theory has been carried out in the early 1980's in [Shuryak and Vainshtein, 1982a] for unpolarized targets, and in [Shuryak and Vainshtein, 1982b]

---

[2] A Mathematica reader for Parton Distribution Functions D.B.Clark, E.Godat, F.I.Olness Published in : Comput.Phys.Commun .216 (2017) 126 - 137 e - Print : 1605.08012[hep - ph]

[3] Once again, we remind the reader that "gluons" (as small amplitude waves) are different from the *glue* which include e.g. semiclassical glue in the form of instantons.
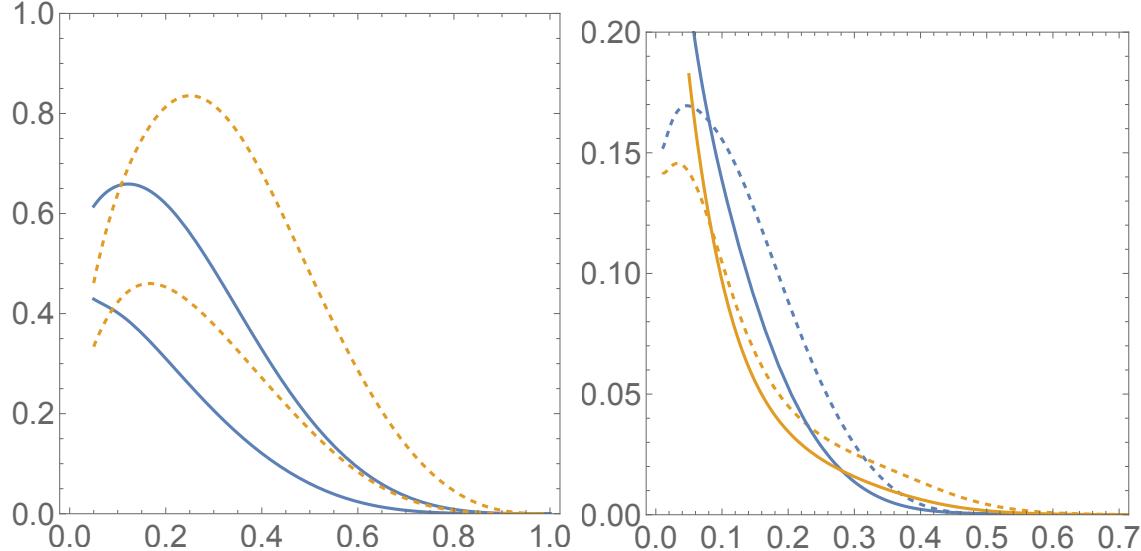
Fig. 11.3.2   the $xu(x), xd(x)$ distributions, and the other of antiquarks $x\bar{u}(x), x\bar{d}(x)$, upper and lower curves [Miesch et al., 2025c]. Those are evolving from resolution $Q^2 = 50\,\text{GeV}^2$ (solid lines) to $Q^2 = 1\,GeV^2$ (dashed). It is this lower one at which the bridging to spectroscopy is supposed to take place.
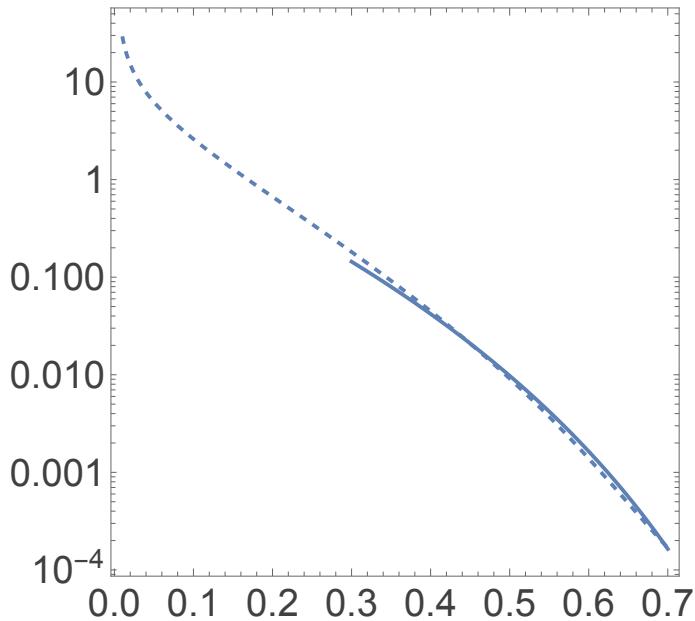
Fig. 11.3.3 Left:The PDFs of antiquarks $u(x,1) + d(x,1)$ at scale $Q = 1\,GeV$ (no x prefactor), from ManeParse, compared to the fit $\sim (1-x)^8$ shown by the solid line [Miesch et al., 2025c]

for polarized ones. They provide the QCD corrections to the partonic sum rules, such as the Bjorken and the Ellis-Jaffe sum rule.

   The most interesting correlation between partons are those stemming from a polarized target. While the structure function $g_1(x, Q^2)$ starts with the usual twist-2 operators, the structure function $g_2(x, Q^2)$ starts with twist-3. Since in experiments the structure functions can be separated *kinematically*, this fact offers the most direct access to the higher twist physics. For a transversely polarized nucleon, at 90^0 to the incoming momentum, $g_1(x, Q^2)$ vanishes and the remaining DIS amplitude is purely twist-3. The pertinent physics is

related with the local operator[4]

$$O_{\bar{q}Gq} = ig\big(\bar{q}\gamma^\rho G^{\mu\nu}q\big) \tag{11.22}$$

given by the value of the gauge field strength on the struck quark. (The color indices are not explicitly shown but assumed, here and below.)

The magnitude of this effect has been discussed in [Burkardt, 2013]. It was pointed out that in the large-N_c limit, the forces on the u and d quarks in the proton should be equal in magnitude but opposite in sign. The suggested magnitude was of the order of

$$F_u = -F_d \sim 0.1\,\text{GeV}/\text{fm} \tag{11.23}$$

Note that it is an order of magnitude smaller than the confining "string tension" force

$$F_{\bar{Q}Q} = \sigma \approx 1\,\text{GeV}/\text{fm} \approx 0.2\,\text{GeV}^2 \tag{11.24}$$

11.4.1 Twist-3 force in the Instanton Liquid Model (ILM)

In the late 1970's to early 1980's studies of semiclassical pseudoparticles - instantons and anti-instantons - had led to view the QCD vacuum as an "instanton liquid" [Shuryak, 1982e]. The vacuum is very inhomogeneous, with 4-quark operators of the type $LR + RL$ (here left-handed current means $L = \bar{q}(1 + \gamma_5)q$, and right-handed with the opposite sine on front of γ_5) strongly enhanced through fermionic zero modes, of a single pseudoparticle . Unfortunately, the operator (11.22) is of different type, $LL + RR$, therefore it *not* enhanced in a single pseudoparticle, and thus it does not appear in the leading order in the pseudoparticle density. The evaluation of matrix elements of such operators has been postponed in earlier literature, in favor of discussion of the "most enhanced" effects.

A single instanton has a probability proportional to very small product of light quark "Lagrangian" (Higgs-induced) masses $m_u m_d m_s / \Lambda_{QCD}^3 \sim 10^{-4}$. Therefore an ideal gas of independent pseudoparticles would be extremely dilute and thus irrelevant. Fortunately [Shuryak, 1982e], the QCD vacuum is not an ideal gas but rather a "liquid", with strong correlations mediated by light quark exchanges. As a result, small "Lagrangian" masses are substituted by much larger effective quark masses, the $SU(N_f)$ chiral symmetry is broken by a nonzero quark condensate. In the ILM the density and typical size of the pseudoparticles are

$$\frac{N}{V_4} = n_{I+\bar{I}} \approx 1\text{fm}^{-4}, \quad \rho \sim \frac{1}{3}\text{fm} \tag{11.25}$$

In spite of smallness of the diluteness parameter

$$\frac{N\rho^4}{V_4 N_c} \approx (\frac{1}{3})^5 \ll 1 \tag{11.26}$$

properties of instanton ensemble are not expandable in simple Taylor series in diluteness. For example, (for two light quark flavors) a constituent quark mass scales as a *root* of diluteness

$$M\rho \sim \sqrt{\frac{N\rho^4}{V_4}} \tag{11.27}$$

as it follows from Bethe-Salpeter equation summing infinite number of quark loop diagrams.

Derivation of effective action S_{eff} for constituent quarks in the mean field approach [Diakonov and Petrov, 1986] complemented this mass by a specific form factor $\mathcal{F}(k)$

---

[4] Although the operator carries three open indices ρ, μ, ν, the last pair is antisymmetrized, and the total spin is 2 and not 3.

$$S_{eff} = \int \frac{d^4 k}{(2\pi)^4} \psi^\dagger(k)[\not{k} - iM\mathcal{F}(k)]\psi(k) \tag{11.28}$$

related to quark zero mode. The form factor describes dependence of the constituent quark mass on the momentum scale under investigation. Further studies of quark propagators were done using numerical simulations of the instanton ensembles, see review [Schäfer and Shuryak, 1998].

To our knowledge, the first attempts to theoretically quantify twist-3 and twist-4 matrix elements have been carried in [Balla et al., 1998]. They have used a version of the ILM for vacuum structure, and chiral soliton version (following from it at large number of colors) for the nucleon. Without going into great details, their main conclusion is that the twist-3 matrix elements are non-zero but still suppressed by a power of the diluteness parameter. Let us also mention the recent study in [Hatta and Schoenleber, 2024] devoted to the twist-3 contributions for other (e.g. momentum) sum rules.

11.4.2 Lattice studies

We would not go into the technicalities and long history of lattice gauge field simulations, and the number of key achievements. It is sufficient to note that current lattice simulations are able to work with fermions as light as the quarks in the real world, reproducing major parts of hadronic phenomenology rather well. This includes the nucleon mass, form factors, PDFs and even GPDs.

Recently, there have been new attempts to quantify the values of higher twist operators. In particular the recent work by the Adelaide group [Crawford et al., 2025], where numerical evaluation of the twist-3 operators in the nucleon, were quoted well inside the (statistical) error bars. Remarkably, their results

$$F_u \approx 3\,\text{GeV/fm}, \quad F_d = 0. \pm 0.05\,\text{GeV/fm} \tag{11.29}$$

are much larger than the one suggested earlier in (11.23). The force on u and d are surprisingly different. Furthermore, as is clear from Fig. 5 of that paper, it is normal both to the directions of motion (z) and the nucleon's spin (x), being localized inside a small sphere of radius only $0.2 - 0.3$ fm. The vanishing force on the d quark brings in a (perhaps simplistic) explanation: if d quark is always locked into the spin-zero ud "good diquark", there would be no polarization-sensitive effects associated with it.

In DIS scattering, the twis-3 PDF measures the average Lorentz force in the nucleon. While it is not amenable to partonic densities, it describes the colored force interaction on a struck parton. For a polarized nucleon along the x-direction with light cone momentum P^+ along the z=direction, the average Lorentz force force

$$d_2 = -\frac{\langle PS_x|\bar{q}(0)\gamma^+ gG^{+y}(0)q(0)|P, S_x\rangle}{2m_N(P^{+2})S_x} = \frac{F^y(0)}{\sqrt{2}m_N S_x} \tag{11.30}$$

is related to the second Mellin moment of the quark intrinsic $\bar{g}_2(x)$ (after subtraction of the twis-2 contribution) [Aslan et al., 2019]

$$\frac{d_2}{3} = \int_0^1 dx\, x^2\, \bar{g}_2(x) \tag{11.31}$$

On the light front, the color valued field strength is

$$G^{+y} = \frac{1}{\sqrt{2}}(-E^y + B^x) = -\frac{1}{\sqrt{2}}(\mathbf{E} + \mathbf{v} \times \mathbf{B})^y \tag{11.32}$$

for a struck parton along the negative z-direction.

At low resolution, the Lorentz force (11.30) can be evaluated using the ILM. For that we first note that in Euclidean signature, the contribution from a single instanton or anti-instanton vanishes because of self-duality, i.e. $E = \pm B$. Vacuum tunneling configurations carry zero energy-momentum tensor. Second we also note that the force involves the quark charge which is chiral even. In the ILM the contribution to (11.30) stems from IA molecules which induce chirally even flips, and is therefore of second order in the packing fraction.

Its evaluation is rather technical, so one should consult the original work [Liu et al., 2025]. The force is different for different hadrons (pions, nucleons, rho mesons), which is not surprising since even their sizes are different. As an example of the results see Figs.11.4.1,11.4.2,11.4.3
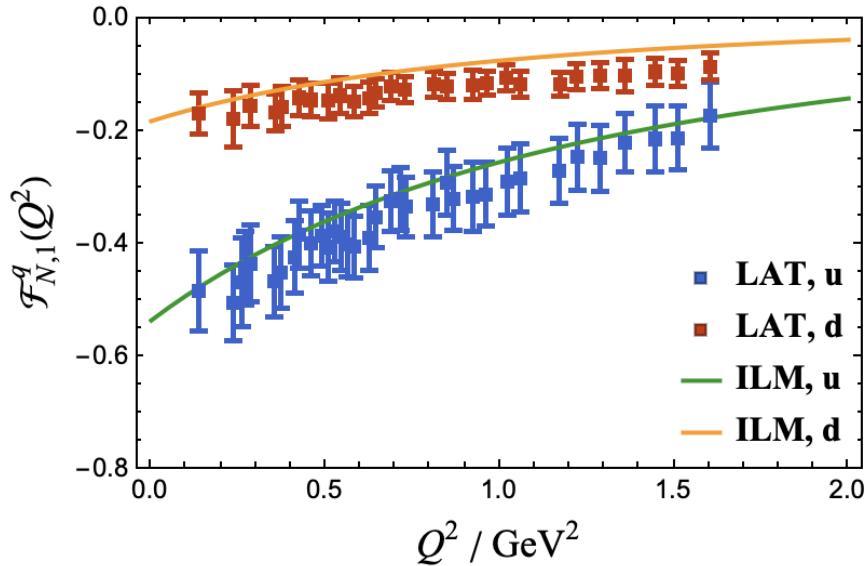
Fig. 11.4.1 Color force form factors $\mathcal{F}_{N,1}^q(Q^2)$ from ILM [Liu et al., 2025] with parameters $n_{mol} = 7.248$ fm^{-4}, $\gamma_{I\bar{I}} = 24.22$ fm^4, and determinantal quark mass $m^* = 82.6$ MeV evolved to 2 GeV compared to the lattice calculation with pion mass 450 MeV in [Crawford et al., 2025].

The color Lorentz force arises naturally from the non-perturbative QCD vacuum fluctuations of the gauge field, including correlated instanton-anti-instanton pairs. By combining semiclassical strength and spatial structure of these fields with the operator structure of higher-twist quark-gluon correlators, we have shown that molecular correlations provide an important mechanism behind the large higher-twist effects observed in polarized deep inelastic scattering, and confirmed in recent lattice simulations. This agrees with our previous derivation of the confining potential in quarkonia, from the same setting.

One new result of this study is the explicit construction and analysis of the gauge field structure of the molecular ensemble, and its role in the quark-colored force. By employing the "ratio ansatz" for the correlated instanton-anti-instanton pair, we derived explicit expressions for the color-electric and color-magnetic field components and computed their spatial profiles. The overlap of the quark zero modes across the molecular pair was analyzed in detail, revealing a strong delocalization effect that enhances the color force. Using Monte Carlo sampling over molecular orientations and separations, we obtained a robust estimate of the average color Lorentz force, $F \approx 2\text{-}3$ GeV/fm, acting on a single quark. This result indicates that the nonperturbative color forces are comparable to, or can even exceed the magnitude of the confining string tension.

Our analysis shows a direct connection between these microscopic nonperturbative fields and the experimentally accessible twist-3 observables. The color Lorentz force operator $\bar{q}gG^{+i}\gamma^+q$ whose expectation value defines the twist-3 matrix element d_2 is shown to acquire contributions from the molecular component of the instanton liquid. The induced form factors encode the nonlocal structure of this coupling and provide a uni-
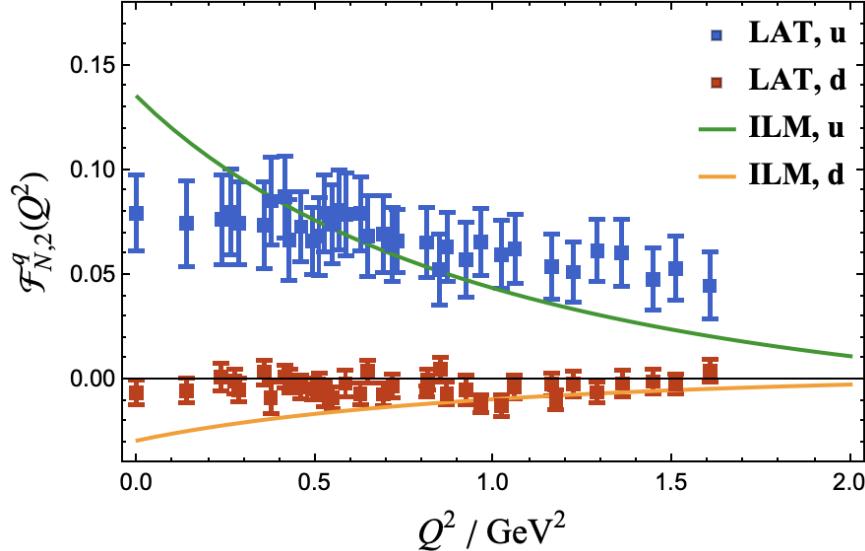
Fig. 11.4.2 Color Lorentz force form factors $\mathcal{F}^q_{N,2}(Q^2)$ using the ILM [Liu et al., 2025] with parameters $n_{\mathrm{mol}} = 7.248 \ \mathrm{fm}^{-4}$, $\gamma_{I\bar{I}} = 24.22 \ \mathrm{fm}^4$, and a determinantal quark mass $m^* = 82.6$ MeV, evolved to 2 GeV and compared to the lattice calculation with pion mass 450 MeV in [Crawford et al., 2025].
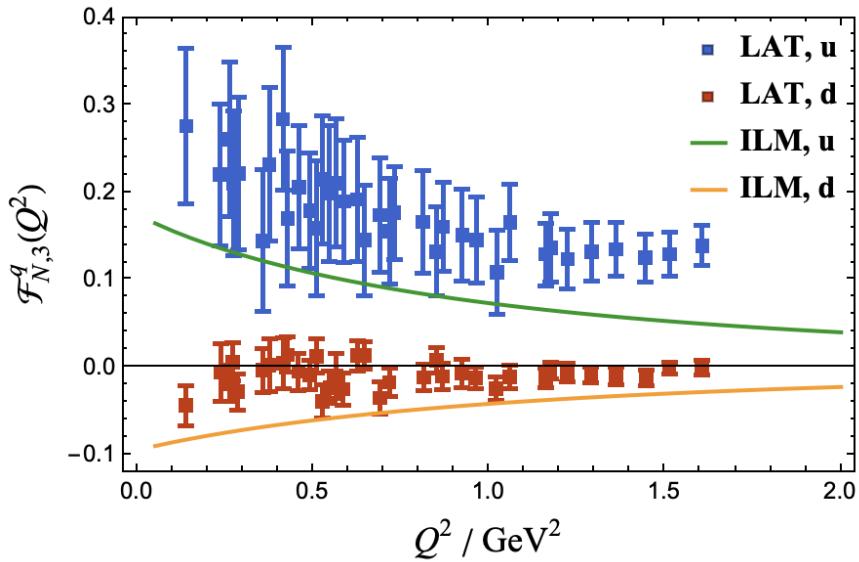
Fig. 11.4.3 Color Lorentz force form factors $\mathcal{F}^q_{N,3}(Q^2)$ from the ILM [Liu et al., 2025] with parameters $n_{\mathrm{mol}} = 7.248 \ \mathrm{fm}^{-4}$, $\gamma_{I\bar{I}} = 24.22 \ \mathrm{fm}^4$, and a determinantal quark mass $m^* = 82.6$ MeV, evolved to 2 GeV and compared to the lattice calculation with pion mass 450 MeV in [Crawford et al., 2025].

fied description of the quark-gluon interaction over a broad range of momentum transfers. In particular, the molecular contributions dominate at low Q^2, leading to enhanced color forces consistent with phenomenological extractions from polarized structure functions. These findings confirm that the twist-3 sector is direct manifestation of the underlying topological fields in the QCD vacuum. Remarkably, the emergent color Lorentz force form factors are shown to be intimately related to the hadronic gravitational and transversity form factors, offering additional insights to the nature of the mass and force distributions in hadrons.

Chapter 12
The origin of hadronic mass and spin

12.1 Introduction

In general, one may relate hadronic masses $O(\Lambda_{QCD})$ to quantum breaking of the scale (conformal) symmetry, induced by the running coupling and captured by the trace anomaly. Even in the chiral limit, the trace of the QCD energy-momentum tensor (EMT) is nonzero due to a quantum (scale) anomaly [Vainshtein et al., 1982, Nowak et al., 1996]. The nucleon mass M_N can be related to the change of the gluon field (trace anomaly) in the nucleon state relative to the vacuum

$$M_N \sim \frac{1}{2M_N} \bigg(\langle N|F^2|N \rangle - \langle 0|F^2|0 \rangle \bigg) \approx \chi \tag{12.1}$$

As we already discussed, most hadronic masses emerge from "constituent" effective quark masses described within the *instanton vacuum* picture. As we detailed earlier, the QCD vacuum at low resolution is a dilute ensemble of instantons and anti-instantons whose density and size set a nonperturbative hadronic scale. The delocalization of the quark zero modes across the ensemble generates spontaneous chiral symmetry breaking with the emergence of a constituent-like quark mass. Quark hopping in the QCD vacuum, from one instanton to the next, induces a momentum-dependent dynamical mass $M(p) \approx M_0\, F^2(p\rho)$ with $M_0 \approx 380\,\text{MeV}$, with $F(p\rho)$ a profiling of the zero mode. The gluon condensate measures the instanton plus anti-instanton density n or $\langle 0|F^2/32\pi^2|0 \rangle \approx n$.

The nucleon matrix element of F^2 in the trace anomaly, is tied to the variance of instanton-number fluctuations in a grand-canonical treatment of the ensemble with the instanton-liquid "compressibility" $\chi = \partial^2 \ln Z/\partial n^2$ (Z referring to the grand-canonical ensemble) [Zahed, 2021]. This remarkable identity shows that most hadrons scoop their mass from the non-perturbative glue in the QCD vacuum. For the pion (as a Goldstone boson) this contribution vanishes in the chiral limit.

To quantify the budgeting of the mass at low resolution, Ji's gauge-invariant energy decomposition is useful [Ji, 1995, Ji, 2021]. In particular, at a hadronic ("soft") renormalization scale tied to the instanton size, a *hierarchy* of contributions emerge: a dominant M_q (quark kinetic/potential from zero-mode hopping) contribution, plus a sizeable anomalous piece M_a stemming from the displaced gluon condensate ("epoxy"), with a comparatively small valence-gluon piece M_g

More specifically, in QCD the stress tensor includes quark fields q and gluon field strength $F^a_{\mu\nu}$,

$$T^{\mu\nu} = -F^{a\mu\lambda}F^{a\nu}{}_{\lambda} + \frac{1}{4}g^{\mu\nu}F^a_{\alpha\beta}F^{a\,\alpha\beta} + \frac{i}{4}\bar{q}\gamma^{\{\mu}\overset{\leftrightarrow}{D^{\nu\}}}q, \tag{12.2}$$

is "anomalous" [1], with a nonzero trace

---
[1] All heavy quark mass effects are contained in the running beta function
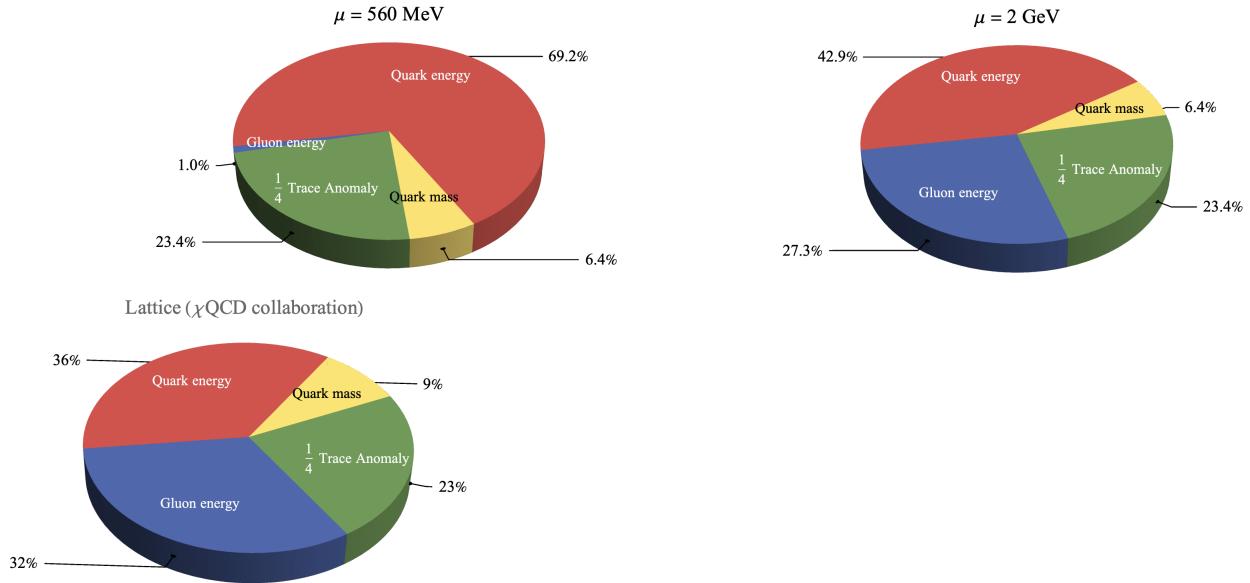
Fig. 12.1.1 Mass decomposition using Ji's nucleon mass sum rule, in the QCD instanton vacuum at the resolution $\mu = 560$ MeV $\sim 1/\rho$ [Liu et al., 2024c] (a), and after DGLAP evolution at a resolution $\mu = 2$ GeV (b); (c) Mass decomposition using Ji's nucleon mass sum rule, at a resolution of $\mu = 2$ GeV from the lattice collaboration [Yang et al., 2018].

$$T^\mu{}_\mu = \frac{\beta(g)}{2g} F^a_{\alpha\beta} F^{a\,\alpha\beta} + (1+\gamma_m)\, m\, \bar{q}q, \tag{12.3}$$

so scale symmetry is broken by quantum effects (trace anomaly), even for $m \to 0$. For a nucleon state $|N\rangle$ in its rest frame, Ji's mass decomposition is given by [Ji, 1995, Ji, 2021]

$$M_N = \frac{1}{2M_N} \langle N|T^{00}|N\rangle = M_q + M_g + M_m + M_a, \tag{12.4}$$

with M_q (quark kinetic/potential), M_g (gluon field energy), M_m (explicit quark-mass term), and M_a (anomalous/trace part). At a scale $\mu \sim 1/\rho$ fixed by the instanton mean size [Zahed, 2021]

$$M_q : M_a : M_g \approx 0.70 : 023 : 0.07 \tag{12.5}$$

So about 70% of the nucleon mass originates from the quark zero mode dynamics, 25% from the displaced gluon condensate (anomaly), and 7% from valence gluons. In contrast and since the pion is a Goldstone mode, its mass vanishes in the chiral limit, as per the Gell-Mann-Oakes-Renner relation

$$f_\pi^2 M_\pi^2 = -2m\langle 0|\bar{q}q|0\rangle \tag{12.6}$$

The pion mass budget is still of similar structure as the nucleon but shifted at finite quark mass [Zahed, 2021]

$$M_\pi : M_q : M_g \approx 0.85 : 0.12 : 0.03 \tag{12.7}$$

Under RG evolution to higher μ, the relative gluon contribution increases and the quark (kinetic/potential) piece decreases/mixes, bringing the composition closer to current lattice results quoted at $\mu = 2$ GeV [Yang et al., 2018]

$$M_q : M_g : M_a : M_m = 0.33(4)(4) : 0.37(5)(4) : 0.23(1)(1) : 0.09(2)(1). \tag{12.8}$$

A qualitative comparison between the lattice results at high resolution and the instanton vacuum model is shown in Table.

Framework	M_q	M_g	M_a	M_m
Lattice QCD (PRL'18, $\mu = 2$ GeV)	0.33(4)(4)	0.37(5)(4)	0.23(1)(1)	0.09(2)(1)
Inst. vacuum (soft scale, qualitative)	dominant	small	sizeable	small

In summary, the instanton-vacuum picture provides a clear physical mechanism for mass generation and a soft-scale hierarchy (M_q dominant, M_g small). The current lattice results at $\mu = 2$ GeV quantify the decomposition with a larger gluon share. The two viewpoints are consistent once renormalization-scale dependencce, operator mixing and evolution are taken into account.

12.2 The quenching of the intrinsic spin

The decomposition of the nucleon spin is a central question in hadronic physics. Deep inelastic scattering experiments (e.g., EMC, COMPASS, HERMES) show that the intrinsic quark spin accounts for only $\sim 30\%$ of the nucleon spin, leading to the so-called "proton spin puzzle." Lattice QCD calculations confirm this trend, but the precise mechanisms remain debated.

The QCD instanton vacuum offers a simple mechanism for why the nucleon intrinsic spin gets quenched. This mechanism once combined with the observation that the non-perturbative glue in this vacuum carries almost no angular momentum, a simple understanding of the nucleon spin decomposition emerges.

A simple budgeting of the nucleon spin is given by Ji's decomposition [Ji, 1995]

$$\frac{1}{2} = S_q + L_q + J_g \,, \tag{12.9}$$

where S_q is the intrinsic quark spin contribution, L_q is the quark orbital angular momentum, and J_g is the total gluon angular momentum (spin + orbital). More specifically, the quark intrinsic spin operator is

$$\boldsymbol{S}_q = \int d^3x \, q^\dagger \frac{\boldsymbol{\Sigma}}{2} \, q \,, \qquad \Sigma^i = \gamma^5 \gamma^0 \gamma^i \,, \tag{12.10}$$

so that the flavor-singlet axial charge is

$$\Sigma = \frac{1}{2m_N} \langle P, S | \bar{q} \gamma^\mu \gamma_5 q | P, S \rangle \, s_\mu \,, \tag{12.11}$$

where s_μ is the nucleon spin vector. The gauge-invariant quark orbital angular momentum operator is

$$\boldsymbol{L}_q = \int d^3x \, q^\dagger \left(\boldsymbol{x} \times i\boldsymbol{D} \right) q \,, \tag{12.12}$$

where $\boldsymbol{D} = \boldsymbol{\nabla} - ig\boldsymbol{A}$ is the covariant derivative. The total gluon angular momentum operator is

$$\boldsymbol{J}_g = \int d^3x \, \boldsymbol{x} \times \left(\boldsymbol{E}^a \times \boldsymbol{B}^a \right) \,, \tag{12.13}$$

with $\boldsymbol{E}^a$ and $\boldsymbol{B}^a$ the chromo-electric and chromo-magnetic fields. This gauge-invariant form includes both gluon spin and orbital contributions together. This spin decomposition is gauge invariant and provides a basis for connecting theory with experiment and lattice QCD.

The $U(1)$ axial anomaly provides a key relation between the divergence of the singlet axial current and the topological charge density

$$\partial^\mu J_\mu^5 = 2im\bar{\psi}\gamma_5\psi + \frac{g^2}{16\pi^2} F\tilde{F} \,, \tag{12.14}$$

where $F\tilde{F}$ is the dual field strength tensor. In the chiral limit, the divergence of the singlet axial current is sourced completely by the topological charge density. At low resolution, the major observation is that

the quark intrinsic spin is not conserved separately, but mixes with topological charge fluctuations, in the instanton vacuum

$$\Sigma \;\approx\; \frac{N_f}{3}\,\frac{1}{32\pi^2}\int d^4x\,\frac{\langle 0|\,F\tilde{F}(x)\,F\tilde{F}(0)\,|0\rangle}{\langle 0|\,F^2(0)\,|0\rangle}\,, \tag{12.15}$$

This highlights the role of vacuum topology in reducing the observable quark spin contribution, through the scooping of the topological susceptibility. In pure Yang-Mills with no light quark screening, the topological fluctuations per 4-volume, are given by the Witten-Veneziano relation [Veneziano, 1979, Witten, 1979]

$$\left(\frac{1}{32\pi^2}\right)^2\int \frac{d^4x}{V_4}\,\langle 0|\,F\tilde{F}(x)\,F\tilde{F}(0)\,|0\rangle = \frac{f_\pi^2 M_1^2}{2N_f} \tag{12.16}$$

with M_1 related to the "bare" eta-prime mass. In QCD with light quarks, screening of the topological fluctuations maybe substantial, leading to a quenching of the intrinsic spin

$$\Sigma = \frac{N_f}{3}\left[\frac{M_1^2\,\langle\bar{q}q\rangle}{n}\left(\frac{2N_f\langle\bar{q}q\rangle}{f_\pi^2}\;-\;\frac{M_1^2}{N_f}\sum_{f=1}^{N_f}\frac{1}{m_f}\right)^{-1}\right]\xrightarrow[m_f\to m]{}\;\frac{1}{3}\left[\frac{f_\pi^2\,M_1^2}{2\,n}\right]\left[1+\frac{M_1^2}{m_\pi^2}\right]^{-1}. \tag{12.17}$$

In the chiral limit one effectively trades $M_1 \to m_\pi$, causing a total depletion of the intrinsic nucleon spin!

At low resolution or "soft" renormalization scale with $\mu \sim 1/\rho$, the QCD instanton vacuum suggests the following partition of the nucleon spin

$$S_q \approx 0.60, \qquad L_q \approx 0.36, \qquad J_g \approx 0.04\,. \tag{12.18}$$

Hence, the majority of the spin arises from quarks, primarily through their intrinsic spin, while gluons contribute only a few percent. The chief reason is that at low resolution the glue is dominated by tunneling self-dual gauge fields that carry neither energy nor angular momentum This contrasts with high-scale lattice QCD results, which show a comparable S_q but a larger J_g. The difference is attributed to QCD scale evolution. The gluon contributions grow at higher resolution at the expense of the quark orbital contribution, since the intrinsic spin is fixed by the topological susceptibility which is RG invariant.

In summary, the instanton vacuum explains how topological charge fluctuations "absorb" part of the quark spin through the anomaly, leaving a reduced observable intrinsic spin Σ. The relation to the topological susceptibility suggests that in the chiral limit, the light quark masses vanish and screening becomes perfect, an indication that Σ could approach zero. At finite quark masses, the screening is partial, so a sizable quark intrinsic spin fraction survives, consistent with phenomenology. The small gluon contribution at the instanton scale shows that the glue is "soft", but evolves to larger values at higher renormalization scales.

These observations provide a natural explanation for the observed suppression of the quark intrinsic spin in the nucleon at low resolution. The decomposition [Zahed, 2022]

$$\frac{1}{2} \approx 0.60 + 0.36 + 0.04 \tag{12.19}$$

illustrates the dominance of the quark degrees of freedom at the non-perturbative scale, with gluonic contributions emerging at higher resolution. This framework connects the proton spin puzzle with the topological structure of the QCD vacuum.
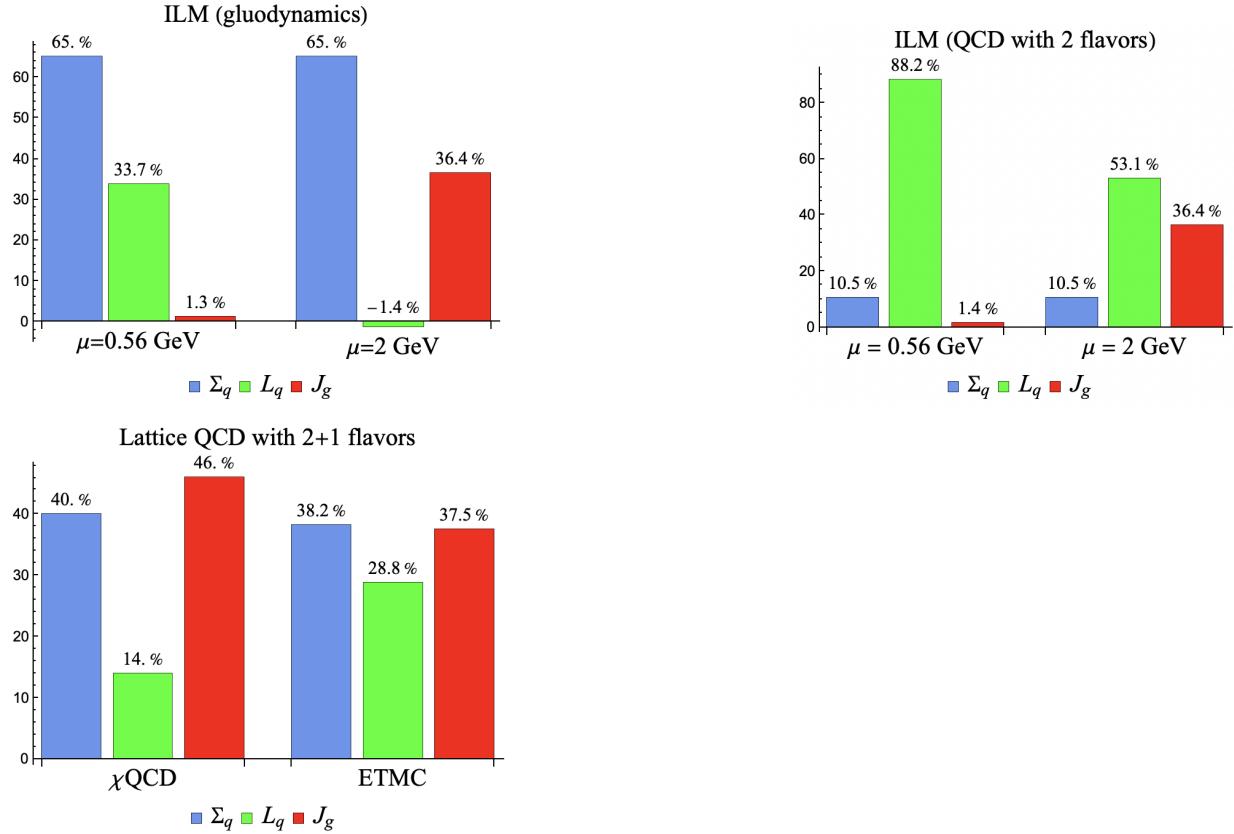
Fig. 12.2.1 a: Spin decomposition using Ji's sum rule, in the quenched QCD instanton vacuum at $\mu = 0.56$ GeV (left), and $\mu = 2$ GeV (right); b: Spin decomposition using Ji's sum rule, in the $N_f = 2$ QCD instanton vacuum at $\mu = 0.56$ GeV (left) and $\mu = 2$ GeV (right); c: Spin decomposition using Ji's sum rule at a resolution of $\mu = 2$ GeV, from the lattice collaboration χQCD [Wang et al., 2022] (left) and the ETMC [Alexandrou et al., 2020] (right). All the results from the ILM are from [Liu et al., 2024c].

Chapter 13
Generalized parton distributions (GPDs)

13.1 Introduction and Physical Motivation

Parton distributions (PDFs) were generalized to GPDs, which provide a unified light-front framework for describing the internal structure of hadrons [Ji, 1997a, Belitsky and Radyushkin, 2005]. They interpolate between parton distribution functions (PDFs) in the forward limit and electromagnetic as well as gravitational form factors when integrated over the parton momentum fraction. Because the defining matrix elements are off-forward, GPDs encode transverse spatial information in addition to longitudinal momentum flow, giving access to a genuine (2+1)-dimensional tomography of hadrons.

GPDs arise as off-forward matrix elements of twist-2 quark and gluon operators on the light front. Their phenomenological importance is underscored by deeply virtual Compton scattering (DVCS) and deeply virtual meson production [Ji, 1997a, Radyushkin, 1997], both of which probe specific combinations of quark GPDs over a controlled range of momentum transfer. Experimental programs at JLab, COMPASS, and future EIC facilities [Abdul Khalek et al., 2022, Anderle et al., 2021] aim to map these functions with increasing precision.

The Instanton Liquid Model (ILM) [Shuryak and Zahed, 2021b, Shuryak and Zahed, 2021c] provides an analytically tractable description of nonperturbative QCD at the low-resolution scale $\mu_0 \sim 1$ GeV. Instantons induce nonlocal interactions that generate a momentum-dependent dynamical mass and nonlocal vertex functions. These structures naturally feed into the corresponding light-front wave functions (LFWFs), providing characteristic $k_\perp$-dependent shapes for GPDs that differ from purely phenomenological parametrizations or perturbative constructions.

This section presents a complete ILM-based construction of mesonic and baryonic GPDs in the DGLAP region $\xi \leq x \leq 1$. Since particle number is preserved in this interval, GPDs reduce to overlaps of initial and final LFWFs (an approach particularly well suited to the nonlocal ILM structure). The resulting GPDs define low-scale boundary conditions that may be evolved perturbatively to higher scales relevant for lattice QCD or phenomenology.

13.2 Twist-2 Definitions and Kinematics

The unpolarized meson GPD is defined through the standard light-front bilinear [Ji, 1997a, Belitsky and Radyushkin, 2005]

$$H(x, \xi, t) = \int \frac{dz^-}{4\pi} \, e^{i\frac{x}{2}P^+ z^-} \, \langle M(p^+)|\bar{q}(0)\gamma^+[0, z^-] \, q(z^-)|M(p^-)\rangle, \qquad (13.1)$$

with Wilson line $[0, z^-] = 1$ in light-cone gauge. The polarized analogue is obtained by replacing $\gamma^+ \to \gamma^+\gamma_5$. The symmetric-frame kinematics follow the standard GPD conventions

$$p^{\pm} = P^{\pm} \pm \frac{\Delta^{\pm}}{2}, \qquad t = -\Delta^2, \qquad x = \frac{k^+}{P^+}, \qquad \xi = -\frac{\Delta^+}{2P^+}, \tag{13.2}$$

as summarized in Eq. (3). We adopt the mostly-plus metric so that $p^2 = -m^2$ and $t < 0$.

Because ILM LFWFs contain only the lowest Fock sector, they cannot describe the ERBL domain $0 < x < \xi$, which involves parton-number-changing transitions. As emphasized in Refs. [Ji, 1997a, Belitsky and Radyushkin, 2005], full polynomiality requires both DGLAP and ERBL regions, so only DGLAP-sector polynomiality constraints apply here.

13.3 Mesonic GPDs from ILM Light-Front Wave Functions

Mesons in the ILM possess three leading LFWF components labeled by orbital projection $\Lambda = 0, \pm 1$ [Ji et al., 2004a]. At zero skewness the unpolarized GPD reduces to the overlap integral

$$H(x, 0, t) = \sum_{\Lambda = 0, \pm 1} \int \frac{d^2 k_{\perp}}{(2\pi)^3} \, \psi^*_{P,\Lambda}(x, k'_{\perp}) \, \psi_{P,\Lambda}(x, k_{\perp}), \tag{13.3}$$

with the momentum shift

$$k'_{\perp} = k_{\perp} + (1 - x)\Delta_{\perp}. \tag{13.4}$$

Earlier ILM studies demonstrate that mesonic LFWFs are well approximated by Gaussians [Shuryak and Zahed, 2021b, Shuryak and Zahed, 2021c],

$$\psi(x, k_{\perp}) \sim e^{-A(x) k_{\perp}^2}, \tag{13.5}$$

leading to the analytic expression

$$H(x, 0, -\Delta_{\perp}^2) \sim e^{-A(x)\left(\frac{3}{4} - x(1-x)\right)\Delta_{\perp}^2}, \tag{13.6}$$

consistent with Eq. (9). This yields an x-dependent transverse radius,

$$\langle b_{\perp}^2(x) \rangle = 4A(x) \left(\frac{3}{4} - x(1-x) \right),$$

which narrows at large x as expected from the localization of high-momentum constituents.

13.4 Nucleon and Δ GPDs in the ILM

The nucleon and Δ LFWFs follow from solving ILM-inspired constituent Hamiltonians [Shuryak and Zahed, 2022a, Shuryak and Zahed, 2022b]. For baryons the twist-2 quark GPDs are defined by [Ji, 1997a, Belitsky and Radyushkin, 2005]

$$\int \frac{dz^- P^+}{4\pi} \, e^{\frac{i}{2} x P^+ z^-} \langle p', \Lambda' | \bar{q}(0)\gamma^+ q(z^-) | p, \Lambda \rangle = \bar{N}(p', \Lambda') \left[H(x, \xi, t)\gamma^+ + E(x, \xi, t)\frac{i\sigma^{+j}\Delta_j}{2m_N} \right] N(p, \Lambda), \tag{13.7}$$

$$\int \frac{dz^- P^+}{4\pi} \, e^{\frac{i}{2} x P^+ z^-} \langle p', \Lambda' | \bar{q}(0)\gamma^+ \gamma_5 q(z^-) | p, \Lambda \rangle = \bar{N}(p', \Lambda') \left[\tilde{H}(x, \xi, t)\gamma^+ \gamma_5 + \tilde{E}(x, \xi, t)\frac{\Delta^+ \gamma_5}{2m_N} \right] N(p, \Lambda), \tag{13.8}$$

with conventions matching Eq. (12).

At $\xi = 0$ the unpolarized GPDs reduce to LFWF overlaps [Shuryak and Zahed, 2022a]:

$$H(x,0,t) = \int \mathcal{D}[x_i, k_{i\perp}]\, \delta(x - x_1)\, \psi_+^*(x_i, k_{i\perp}', \lambda_i)\psi_+(x_i, k_{i\perp}, \lambda_i), \tag{13.9}$$

$$E(x,0,t) = -2m_N\, q_L \int \mathcal{D}[x_i, k_{i\perp}]\, \delta(x - x_1)\, \psi_+^*\psi_-. \tag{13.10}$$

Numerical ILM LFWFs yield GPDs well described by the Gaussian ansatz [Guidal et al., 2005]

$$\mathrm{GPD}(x, Q^2) \approx f_1(x)\exp[-Q^2 f_2(x)],$$

with a pronounced x-dependent width. As Q^2 increases the peak of $H(x,0,Q^2)$ shifts to larger x, confirming that high-Q^2 probes select compact, high-momentum configurations, in agreement with the trends shown in Fig. 1 of [Shuryak and Zahed, 2022a].

13.5 GPD Slopes and Transverse Tomography

The slope

$$-d(\ln H)/dQ^2$$

evaluated near $Q^2 \simeq 1$ GeV^2 shows a maximum near $x \approx 1/3$ [Shuryak and Zahed, 2022b], see Fig. 2. The corresponding transverse radius

$$R_{\mathrm{rms}}(x) = \sqrt{2 f_2(x)}$$

is typically around 0.6 fm.

Using the Gaussian form, the impact-parameter density at zero skewness is

$$q(x, b_\perp) = \int \frac{d^2\Delta_\perp}{(2\pi)^2}\, e^{-i\Delta_\perp \cdot b_\perp}\, H(x, 0, -\Delta_\perp^2), \tag{13.11}$$

which yields the analytic expressions noted in [Shuryak and Zahed, 2022b]. These describe a narrowing of the profile at large x and a broadening at small x, completing the intuitive 3D tomographic picture.

13.6 Electromagnetic and Gravitational Form Factors

Integrating GPDs over x at zero skewness gives the standard form factors [Belitsky and Radyushkin, 2005]

$$F_1(t) = \int dx\, H(x,0,t), \qquad F_2(t) = \int dx\, E(x,0,t), \qquad G_A(t) = \int dx\, \tilde{H}(x,0,t), \tag{13.12}$$

as stated in Eq. (21). ILM results for $Q^4 F_1^d(Q^2)$ match dipole-like behavior at low Q^2 and approach the perturbative scaling limit at high Q^2 [Shuryak and Zahed, 2022b].

The first moment yields the gravitational form factors [Polyakov and Schweitzer, 2018a]

$$A(t) = \int dx\, x H(x,0,t), \qquad B(t) = \int dx\, x E(x,0,t),$$

Eq. (22). ILM predictions show $A(t)$ falling more slowly than $F_1(t)$, implying a more compact mass distribution than charge distribution, consistent with the trends in Fig. 4 of [Shuryak and Zahed, 2022b].

13.7 Comparison to Lattice QCD and Global Picture

Lattice-determined ratios such as $A_2(0, |t|)/A_1(0, |t|)$ agree well in slope with ILM predictions [Hägler et al., 2008]. Normalization differences reflect the lower ILM scale where valence quarks carry most of the momentum.

Recent LaMET-based extractions of quasi-GPDs [Bhattacharya et al., 2022] show good agreement with ILM results for $x > 0.4$ at fixed $t = -0.69$ GeV^2, despite strong t-dependence. This reinforces the interpretation of ILM predictions as physically realistic low-scale inputs for DGLAP evolution.

13.8 Summary

GPDs in the Instanton Liquid Model arise from the nonlocal structure of instanton-induced interactions and retain full analytic control in the DGLAP region. ILM LFWFs produce transparent predictions for the x- and t-dependence of GPDs, transverse tomography, and associated form factors. Comparison with lattice QCD and LaMET reconstructions shows good agreement at moderate and large x, highlighting the physical relevance of instanton-induced constituent dynamics at low resolution.

Appendix

13.A Operator Structure and Kinematic Conventions for GPDs

Generalized parton distributions are defined through nonlocal quark bilinears on the light front. For a quark field q in a meson or baryon state, the leading twist-2 unpolarized operator reads

$$\mathcal{O}^+(z^-) = \bar{q}(0)\gamma^+[0, z^-]q(z^-), \tag{13.13}$$

where $[0, z^-]$ is the straight-line Wilson link along the light-cone direction. In light-cone gauge the Wilson line reduces to unity, but it is important to keep track of it formally when defining gauge-invariant GPDs. The matrix element of this operator between hadron states of four-momenta p^μ and p'^μ defines the unpolarized GPD $H(x, \xi, t)$ [Belitsky and Radyushkin, 2005].

The GPD kinematic variables are introduced through the symmetric frame:

$$p^\pm = P^\pm \pm \frac{\Delta^\pm}{2}, \qquad \xi = -\frac{\Delta^+}{2P^+}, \qquad t = -\Delta^2, \qquad x = \frac{k^+}{P^+}. \tag{13.14}$$

Here $P = (p + p')/2$ is the average hadron momentum, $\Delta = p' - p$ is the momentum transfer, and x measures the average plus-momentum carried by the struck quark. These conventions agree with the standard treatments in Refs. [Belitsky and Radyushkin, 2005, Ji, 1997b] and ensure that the forward limit $t \to 0$, $\xi \to 0$ reproduces the usual parton distributions.

Because light-front quantization breaks manifest Lorentz symmetry, the evaluation of matrix elements must follow precise kinematic restrictions. In particular, the overlap representation of GPDs in terms of LFWFs applies only in the DGLAP region $\xi \leq x \leq 1$, where parton number is conserved. The ERBL region $0 < x < \xi$ requires LFWFs with an additional quark-antiquark pair. Since the ILM truncation includes only the lowest Fock component, the ERBL region is beyond its scope, and the full polynomiality constraints cannot be enforced [Belitsky and Radyushkin, 2005]. The analysis presented throughout the paper and in these appendices therefore adheres strictly to the DGLAP region.

13.B Light-Front Reduction of Nonlocal Instanton Dynamics

Instantons generate nonlocal interactions through the presence of fermionic zero modes, giving rise to a momentum-dependent constituent mass and nonlocal vertex factors [Shuryak and Zahed, 2021b, Shuryak and Zahed, 2021c]. The quark propagator in momentum space acquires the structure

$$S^{-1}(k) = \slashed{k} - M(k), \qquad M(k) = M\,F(k), \tag{13.15}$$

where $F(k)$ is the instanton zero-mode form factor. The detailed expression involves Bessel functions and decays for $k_\perp^2 \gtrsim 1/\rho^2$, with ρ the average instanton size.

For constructing LFWFs in the ILM, one performs a light-front reduction of the Bethe-Salpeter amplitude. Schematically, for the twist-2 operator matrix element one obtains

$$\langle p'|\mathcal{O}^+(z^-)|p\rangle = \int \frac{dk^-}{2\pi} \mathrm{Tr}\big[\Psi^\dagger(k';P')\,\gamma^+\,\Psi(k;P)\big], \tag{13.16}$$

where $\Psi(k;P)$ is the Bethe-Salpeter amplitude of the nonlocal ILM interaction. Only the poles corresponding to forward propagation in light-front time contribute at leading order, consistent with the truncation to the valence Fock sector. The transverse-momentum nonlocality contained in the instanton form factors is inherited by the LFWFs, which are found to have approximately Gaussian dependence on $k_\perp$ in both mesonic and baryonic channels [Shuryak and Zahed, 2021b, Shuryak and Zahed, 2021c].

13.C Gaussian Overlap and Emergence of Transverse Radii

ILM meson wave functions are well approximated by Gaussian profiles in transverse momentum:

$$\psi(x, k_\perp) = \mathcal{N}(x)\exp[-A(x)k_\perp^2], \tag{13.17}$$

as supported by explicit ILM LFWF calculations [Shuryak and Zahed, 2021b]. Under a transverse momentum transfer $\Delta_\perp$, the struck quark momentum shifts as

$$k'_\perp = k_\perp + (1-x)\Delta_\perp. \tag{13.18}$$

Substituting this into the overlap representation yields

$$H(x, 0, -\Delta_\perp^2) \propto \exp\big[-A(x)\left(\tfrac{3}{4} - x(1-x)\right)\Delta_\perp^2\big], \tag{13.19}$$

identical to Eq. (9). The Gaussian form provides a direct analytic link between the transverse probe $\Delta_\perp$ and the spatial width of the partonic distribution. Fourier transformation produces

$$q(x, b_\perp) = \int \frac{d^2\Delta_\perp}{(2\pi)^2}\, e^{-i\Delta_\perp \cdot b_\perp}\, H(x, 0, -\Delta_\perp^2), \tag{13.20}$$

resulting in analytic impact-parameter densities exhibiting the characteristic narrowing for large x and broadening for small x. This behavior is consistent with the partonic interpretation of transverse localization [Guidal et al., 2005].

13.D Spinor Algebra for Nucleon Twist-2 GPDs

The twist-2 quark operators for the nucleon couple to the Dirac bilinears γ^+ and $i\sigma^{+j}\Delta_j$, whose matrix elements between light-front helicity spinors are well documented [Belitsky and Radyushkin, 2005]. For helicity-conserving transitions one obtains

$$\bar{N}(p')\gamma^+ N(p) = 2P^+\sqrt{1-\xi^2}\,\delta_{\Lambda'\Lambda}, \tag{13.21}$$

while the Pauli term mediates helicity flip through

$$\bar{N}(p')\frac{i\sigma^{+j}\Delta_j}{2m_N}N(p),\tag{13.22}$$

linking opposite helicities. The overlap formula for $E(x,0,t)$ therefore depends on interference between LFWF components with opposite nucleon helicity.

In ILM baryons, instanton-induced diquark correlations enhance mixing between scalar- and axial-vector-diquark components, increasing the magnitude of the helicity-flip amplitude and producing a nonvanishing $E(x,0,t)$ [Shuryak and Zahed, 2022a, Shuryak and Zahed, 2022b]. This feature is evident in the d-quark GPDs displayed in Fig. 1 of the main text and reflects the rich orbital-spin structure of ILM nucleon wave functions.

13.E GPD Slopes and Extraction of Transverse Radii

For a Gaussian t-dependence of the form

$$H(x,0,-Q^2) \sim \exp[-Q^2 f_2(x)],$$

the logarithmic slope at $Q^2=0$ determines the transverse radius:

$$B(x) = -\left.\frac{\partial}{\partial Q^2}\ln H(x,0,-Q^2)\right|_{Q^2=0}, \qquad R^2_{\rm rms}(x) = 4B(x) = 2f_2(x),\tag{13.23}$$

as in Eq. (19). The ILM results show a clear maximum of $B(x)$ near $x \simeq 1/3$ for both the nucleon and the Δ [Shuryak and Zahed, 2022b]. This corresponds to a configuration in which the three quarks share momentum symmetrically and are most extended spatially. The radius decreases toward both small and large x, reflecting the collapse of the spectator system for $x \to 1$ and the absence of a Regge-enhanced small-x rise due to the valence truncation.

13.F Moments and Gravitational Form Factors

The first moments of the unpolarized GPDs give the quark contributions to the gravitational form factors of the energy-momentum tensor [Polyakov and Schweitzer, 2018a]:

$$A(t) = \int dx\, xH(x,0,t), \qquad B(t) = \int dx\, xE(x,0,t).\tag{13.24}$$

$A(t)$ determines the quark momentum distribution inside the hadron, while $B(t)$ enters the Ji spin sum rule

$$J = \tfrac{1}{2} = A(0) + B(0),\tag{13.25}$$

valid when gluonic contributions are included implicitly in the constituent description [Ji, 1997b]. In the present ILM analysis, only $A(t)$ can be reliably extracted because $E(x,0,t)$ requires both helicity components of the nucleon wave function.

The ILM predicts that $A(t)$ falls more slowly than $F_1(t)$, indicating that the mass distribution is more compact than the charge distribution. This trend is visible in Fig. 4 of the main text and is consistent with lattice QCD extractions [Hägler et al., 2008]. The ILM relation

$$\frac{3A_d(Q^2)}{F_1^d(Q^2)} = C_0 + \frac{Q^2}{M_{\rm fit}^2},\tag{13.26}$$

matches the approximate linear behavior seen in baryonic form factor ratios.

13.G Comparison to Lattice QCD and Quasi-GPDs

Two types of lattice comparisons are relevant. The first concerns form-factor moments. Lattice studies of $A_1(0,t)$ and $A_2(0,t)$ show that the gravitational form factor decreases more slowly with $|t|$ than the Dirac form factor [Hägler et al., 2008]. The ILM reproduces the same qualitative behavior and a comparable slope, though normalization differences arise because the ILM corresponds to a much lower renormalization scale where quarks carry nearly all the hadron momentum.

The second comparison involves full GPDs extracted using LaMET from boosted nucleon matrix elements [Bhattacharya et al., 2022]. At $t = -0.69$ GeV^2 the ILM result for $H(x,0,t)$ agrees with the lattice determination for $x \gtrsim 0.4$, reflecting the dominance of valence dynamics in that region. The discrepancy at small x is expected, since the ILM contains no explicit gluons or sea quarks. Despite these differences, the qualitative t-dependence and x-shape are consistent with the lattice trends, supporting the interpretation of ILM GPDs as reliable low-scale boundary conditions.

Chapter 14
Light front Hamiltonians in pQCD and the instanton ensemble

14.1 Basic definitions

The symmetric energy momentum tensor following from (14.38) for free fermions is

$$T^{\mu\nu} = \frac{1}{2}\left[\bar{\psi}i\gamma^\mu\partial^\nu\psi + \bar{\psi}i\gamma^\nu\partial^\mu\psi\right] - g^{\mu\nu}\mathcal{L} \tag{14.1}$$

with the corresponding LF Hamiltonian

$$P^- = \int dx^- d^2x_\perp \; T^{+-} = \int dx^- d^2x_\perp \frac{1}{2}\left[\bar{\psi}i\gamma^+\partial_+\psi + \bar{\psi}i\gamma^-\partial_-\psi\right] - \mathcal{L} \tag{14.2}$$

More specifically, including the gauge field in long derivatives, and including instanton-induced 4-fermion 't Hooft Lagrangian, one gets (14.2) in coordinate space as

$$
\begin{aligned}
P^- = & \int dx^- d^2x_\perp \bar{\psi}\frac{\left(-\partial_\perp^2 + M^2\right)}{2i\partial_-}\gamma^+\psi \\
& -\frac{G_S}{2}\int dx^- d^2x_\perp \left[\bar{\psi}\psi\hat{D}_+^{-1}\bar{\psi}\psi - \bar{\psi}\tau^a\psi\hat{D}_-^{-1}\bar{\psi}\tau^a\psi - \bar{\psi}i\gamma^5\psi\hat{D}_+^{-1}\bar{\psi}i\gamma^5\psi + \bar{\psi}i\gamma^5\tau^a\psi\hat{D}_+^{-1}\bar{\psi}i\gamma^5\tau^a\psi\right]
\end{aligned}
\tag{14.3}
$$

and in momentum space

$$
\begin{aligned}
P^- = & \int [d^3k]_+ \int [d^3q]_+ \frac{k_\perp^2 + M^2}{2k^+}\bar{\psi}(k)\gamma^+\psi(q)(2\pi)^3\delta_+^3(k-q) \\
& + \int [d^3k]_+ \int [d^3q]_+ \int [d^3p]_+ \int [d^3l]_+ (2\pi)^3\delta_+^3(p+k-q-l)V(k,q,p,l)
\end{aligned}
\tag{14.4}
$$

The interaction kernel $V(k,q,p,l)$ is given in terms of the good component of the fermionic bilinears. In the scalar and pseudoscakar channels, it is explicitly

$$
\begin{aligned}
V(k,q,p,l) = &-\frac{G_S}{2}\alpha_+(k^+ - q^+)\bar{\psi}_+(k)\left(\frac{\boldsymbol{\gamma}_\perp \cdot \mathbf{k} + M}{2k^+}\gamma^+ + \gamma^+\frac{\boldsymbol{\gamma}_\perp \cdot \mathbf{q} + M}{2q^+}\right)\psi_+(q) \\
&\times \bar{\psi}_+(p)\left(\frac{\boldsymbol{\gamma}_\perp \cdot \mathbf{p} + M}{2p^+}\gamma^+ + \gamma^+\frac{\boldsymbol{\gamma}_\perp \cdot \mathbf{l} + M}{2l^+}\right)\psi_+(l) \\
&+\frac{G_S}{2}\alpha_-(k^+ - q^+)\bar{\psi}_+(k)\left(\frac{\boldsymbol{\gamma}_\perp \cdot \mathbf{k} + M}{2k^+}i\gamma^+\gamma^5 + i\gamma^5\gamma^+\frac{\boldsymbol{\gamma}_\perp \cdot \mathbf{q} + M}{2q^+}\right)\psi_+(q) \\
&\times \bar{\psi}_+(p)\left(\frac{\boldsymbol{\gamma}_\perp \cdot \mathbf{p} + M}{2p^+}i\gamma^+\gamma^5 + i\gamma^5\gamma^+\frac{\boldsymbol{\gamma}_\perp \cdot \mathbf{l} + M}{2l^+}\right)\psi_+(l) \\
&+\frac{G_S}{2}\alpha_-(k^+ - q^+)\bar{\psi}_+(k)\left(\frac{\boldsymbol{\gamma}_\perp \cdot \mathbf{k} + M}{2k^+}\gamma^+\tau^a + \tau^a\gamma^+\frac{\boldsymbol{\gamma}_\perp \cdot \mathbf{q} + M}{2q^+}\right)\psi_+(q) \\
&\times \bar{\psi}_+(p)\left(\frac{\boldsymbol{\gamma}_\perp \cdot \mathbf{p} + M}{2p^+}\gamma^+\tau^a + \gamma^+\tau^a\frac{\boldsymbol{\gamma}_\perp \cdot \mathbf{l} + M}{2l^+}\right)\psi_+(l) \\
&-\frac{G_S}{2}\alpha_+(k^+ - q^+)\bar{\psi}_+(k)\left(\frac{\boldsymbol{\gamma}_\perp \cdot \mathbf{k} + M}{2k^+}i\gamma^+\gamma^5\tau^a + \tau^a i\gamma^5\gamma^+\frac{\boldsymbol{\gamma}_\perp \cdot \mathbf{q} + M}{2q^+}\right)\psi_+(q) \\
&\times \bar{\psi}_+(p)\left(\frac{\boldsymbol{\gamma}_\perp \cdot \mathbf{p} + M}{2p^+}i\gamma^+\gamma^5\tau^a + i\gamma^5\gamma^+\tau^a\frac{\boldsymbol{\gamma}_\perp \cdot \mathbf{l} + M}{2l^+}\right)\psi_+(l)
\end{aligned}
\tag{14.5}
$$

The fermionic field in momentum space is defined as

$$
\psi(x^-, x_\perp) = \int [d^3 k]_+ \psi(k) e^{-ik^+ x^- + ik_\perp \cdot x_\perp}
\tag{14.6}
$$

It annihilates a particle ina $u_s(k)$ mode, or creates an antiparticle in a $v_s(k)$ mode, i.e.

$$
\psi(k) = \sum_s u_s(k) b_s(k)\theta(k^+) + v_s(-k)c_s^\dagger(-k)\theta(-k^+)
\tag{14.7}
$$

The measure in momentum space is

$$
[d^3 k]_+ = \frac{dk^+ d^2 k_\perp}{(2\pi)^3 2k^+}\epsilon(k^+)
\tag{14.8}
$$

which sums over the positive k^+ region for particle modes, and over the negative k^+ region for antiparticle modes.

Note that each 't Hooft vertex is renormalized in the mean-field or large N_c approximation, with the momentum dependent normalization factors

$$
\alpha_\pm(P^+) = \left[1 \pm 2g_S \int \frac{dl^+ d^2 l_\perp}{(2\pi)^3}\frac{\epsilon(l^+)}{P^+ - l^+}\right]^{-1}
\tag{14.9}
$$

which precisely resums the longitudinal tadpole contributions after the elimination of the bad fermionic component. These tadpole contributions are the vacuum contributions on the LF. For the t'Hooft interaction in the zero size limit, the interaction is generically of the form

$$
\begin{aligned}
V(k,q,p,l) = & \\
\sum_{s_1, s_1', s_2, s_2'} & \mathcal{V}_{s_1, s_2, s_1', s_2'}(k,q,p,l) b_{s_1}^\dagger(k) c_{s_2}^\dagger(q) c_{s_2'}(p) b_{s_1'}(l)
\end{aligned}
\tag{14.10}
$$

with

$$\mathcal{V}_{s_1,s_2,s_1',s_2'}(k,q,p,l) = -g_S\alpha_+(k^+ + q^+)\bar{u}_{s_1}(k)v_{s_2}(q)\bar{v}_{s_2'}(p)u_{s_1'}(l)$$
$$+ g_S\alpha_-(k^+ + q^+)\bar{u}_{s_1}(k)i\gamma^5 v_{s_2}(q)\bar{v}_{s_2'}(p)i\gamma^5 u_{s_1'}(l)$$
$$+ g_S\alpha_-(k^+ + q^+)\bar{u}_{s_1}(k)\tau^a i\gamma^5 v_{s_2}(q)\bar{v}_{s_2'}(p)\tau^a i\gamma^5 u_{s_1'}(l)$$
$$- g_S\alpha_+(k^+ + q^+)\bar{u}_{s_1}(k)\tau^a i\gamma^5 v_{s_2}(q)\bar{v}_{s_2'}(p)\tau^a i\gamma^5 u_{s_1'}(l) \tag{14.11}$$

In the large N_c limit, only the s-channel contribution of the $'$t Hooft interaction dominates. These arguments carry to the mean field Lagrangian (14.39) through the substitutions

$$V(k,q,p,l) \to \sqrt{\mathcal{F}(k)\mathcal{F}(k)\mathcal{F}(k)\mathcal{F}(l)}V(k,q,p,l) \tag{14.12}$$

and

$$\alpha_\pm(P^+) \to \left[1 \pm 2g_S \int \frac{dl^+ d^2 l_\perp}{(2\pi)^3} \frac{\epsilon(l^+)}{P^+ - l^+}\mathcal{F}(l)\mathcal{F}(P-l)\right]^{-1} \tag{14.13}$$

so that

$$P^- = \int [d^3 k]_+ \int [d^3 q]_+ \frac{k_\perp^2 + M^2}{2k^+}\bar{\psi}(k)\gamma^+\psi(q)(2\pi)^3\delta_+^3(k-q) \tag{14.14}$$

$$+ \int [d^3 k]_+ \int [d^3 q]_+ \int [d^3 p]_+ \int [d^3 l]_+(2\pi)^3\delta_+^3(p+k-q-l)\sqrt{\mathcal{F}(k)\mathcal{F}(q)\mathcal{F}(p)\mathcal{F}(l)}V(k,q,p,l)$$

The interaction kernel is now

$$V(k,q,p,l) = -\frac{G_S}{2}\left[\alpha_+(k^+ - q^+)\bar{\psi}(k)\psi(q)\bar{\psi}(p)\psi(l) - \alpha^-(k^+ - q^+)\bar{\psi}(k)i\gamma^5\psi(q)\bar{\psi}(p)i\gamma^5\psi(l)\right.$$

$$\left. - \alpha^-(k^+ - q^+)\bar{\psi}(k)\tau^a\psi(q)\bar{\psi}(p)\tau^a\psi(l) + \alpha^+(k^+ - q^+)\bar{\psi}(k)i\tau^a\gamma^5\psi(q)\bar{\psi}(p)i\tau^a\gamma^5\psi(l)\right] \tag{14.15}$$

where the tadpole resummed vertices

$$\alpha_\pm(P^+) = \left[1 \pm 2g_S \int \frac{dl^+ d^2 l_\perp}{(2\pi)^3}\frac{\epsilon(l^+)}{P^+ - l^+}\mathcal{F}(l)\mathcal{F}(P-l)\right]^{-1}$$

The reader may have noticed that for the Lagrangian (14.39) in non-local form, the symmetric form of the energy momentum tensor may require further amendment in the presence of the non-local form factors. This is not the case, as we now explain. Indeed, boost invariance and parity suggests the substitution the substitution

$$\lim_{P^+ \to \infty} \sqrt{\mathcal{F}(k)\mathcal{F}(P-k)} \to \mathcal{F}\left(\frac{2P^+ P^-}{\lambda_S^2} = \frac{k_\perp^2 + M^2}{\lambda_S^2 x\bar{x}}\right) \tag{14.16}$$

The same substitution was developed in the analysis of the ILM using the large momentum effective theory(LaMET) [Kock et al., 2020, Kock and Zahed, 2021]. The substitution (14.16) garentees the consistency of the two approaches. λ_S is a parameter of order 1. Remarkably, the same boost invariant substitution with $\lambda_S = 1$ was argued long ago by Lepage and Brodsky in [Lepage and Brodsky, 1980], in their analysis of 2-body bound states on the light front using Bethe-Salpeter vertices. Note that the substitution (14.16) eliminates the metric component g_{-+} from the non-local form factors, with consequently no change in the symmetric energy-momentum tensor component T^{+-}.

Finally, we note that it is straightforward to generalize the Hamiltonian formalism to consider meson bound states in the U-spin or V-spin sectors relevant for kaons. In the case of kaons, the coupling constant will be replaced by $g_K = N_c G_K$, with a constituent mass matrix $M = \text{diag}(M_u, M_d)$ in the flavor basis, as the s quark is significantly heavier than u, d quarks. This construction will be detailed below.

14.2 Quasi-parton distributions

For a long time, the PDFs defined as light-cone correlations have been only accessible phenomenologically, or through their (power-x) moments from lattice simulations on Euclidean lattices. Empirically, moments is hard to get precisely, as this would need data at all values of momentum fractions x.

Yet relatively recently, Ji and his collaborators [Ji et al., 2021, Ji, 2024] (see references therein) have suggested how PDFs can be extracted from "quasi-PDFs" defined from the large momentum limit of equal-Euclidean-time and high momentum correlations, by proper matching. In short time, reserach in this direction became very active field.

Parton distributions extracted from equal-time momentum distributions in hadrons of increasing rapidities, are readily obtained from the light cone distributions (11.14-11.15). For illustration, consider the rapidity regulated light cone quark distribution (11.14)

$$q(x,v) = -\frac{2}{1+v} \int_{-\infty}^{\infty} \frac{dx_v^-}{4\pi} e^{ik \cdot x_v} \langle P|\bar{\psi}(0)\gamma_v^+ W(0,x_v^-)\psi(x_v^-)|P\rangle \tag{14.17}$$

in a proton at rest $P^\mu = (m_N, 0^\perp, 0)$ with $k^\mu = xP^\mu$, and

$$x_v = (-vz, 0^\perp, z) \qquad x_v^- = \frac{x_v^0 - x_v^3}{\sqrt{2}} \qquad \gamma_v^+ = \frac{\gamma^0 + v\gamma^3}{\sqrt{2}}$$

which can also be rewritten as

$$q(x,v) = \int_{-\infty}^{\infty} \frac{dz}{4\pi} e^{-ixm_N vz} \langle P|\bar{\psi}(0)(\gamma^0 + v\gamma^3)W(0,x_v^-)\psi(x_v^-)|P\rangle \tag{14.18}$$

The quark correlation along the regulated rapidity direction x_v^- reduces to the light cone direction for $v \to 1$. It is related to the quark equal-time quark correlation function by a boost transformation. For that we first shift $z \to \gamma z$ with the Lorentz factor $\gamma = 1/\sqrt{1-v^2}$ in (14.17)

$$q(x,v) = \int_{-\infty}^{\infty} \frac{dz}{4\pi} e^{-ix\gamma m_N vz} \langle P|\bar{\psi}(0)\gamma(\gamma^0 + v\gamma^3)W(0,x_v)\psi(x_v)|P\rangle \tag{14.19}$$

with now $x_v = (-\gamma vz, 0^\perp, \gamma z)$. We now note that under a boost transformation with rapidity $\chi = 2\tanh^{-1} v$, the bilocal fermionic operator transforms as

$$e^{-i\chi\mathbb{K}}\psi(t_1,x_1)\overline{\psi}(t_2,x_2)e^{i\chi\mathbb{K}} = S[v]\psi(\tilde{t}_1,\tilde{x}_1)\overline{\psi}(\tilde{t}_2,\tilde{x}_2)S^{-1}[v] \tag{14.20}$$

We have omitted the gauge link and the transverse coordinates for convenience. The former will be reintroduced by inspection since gauge invariance is frame invariant. The field valued boost operator $\mathbb{K}$ in the 3-direction is (physical gauge)

$$\mathbb{K} = \int d^3x\, x^3 \left(\frac{1}{2}(E^2 + B^2) + \psi^\dagger(i\alpha \cdot D + m\gamma^0)\psi\right) \tag{14.21}$$

The Lorentz transformed coordinates are $\tilde{t} = \gamma(t - vx^3)$, $\tilde{x}^3 = \gamma(x^3 - vt)$, and the spin valued boost operator is $S[v] = e^{\frac{i}{2}\sigma_{03}\chi}$ with the spin matrix $\sigma_{\mu\nu} = \frac{i}{2}[\gamma_\mu, \gamma_\nu]$. Inserting (14.20) in (14.17) and noting that

$$S^{-1}[v]\gamma^0 S[v] = \gamma(\gamma^0 + v\gamma^3) \qquad\qquad S^{-1}[v]\gamma^3 S[v] = \gamma(\gamma^3 - v\gamma^0) \tag{14.22}$$

it follows that the Lorentz transformation $S[v]$ cancels out between the boosted operator (14.20) and (14.22), with the result

$$q(x,v) = \int_{-\infty}^{\infty} \frac{dz}{4\pi} e^{-ix\gamma m_N vz} \langle P|e^{-i\chi\mathbb{K}}\bar{\psi}(0)\gamma^0 W(0,z)\psi(z)e^{i\chi\mathbb{K}}|P\rangle$$
$$= \int_{-\infty}^{\infty} \frac{dz}{4\pi} e^{-ix\gamma m_N vz} \langle P(v)|\bar{\psi}(0)\gamma^0 W(0,z)\psi(z)|P(v)\rangle \tag{14.23}$$

after reinstating the gauge link by gauge invariance. (14.23) is the equal-0-time invariant quark propagator in a boosted hadron state. It is the quasi-PDF introduced by Ji and his collaborators [Ji et al., 2021]. Note that the argument we have presented shows the equivalence beyond perturbation theory.

(14.23) follows from (14.17) and vice versa through boost transformations, modulo renormalization. It is this last issue that makes the quasi-PDFs more UV friendly [Ji, 2024]. PDFs are defined from the get go on the light front with the limit $v \to 1$ assumed before the UV limit. The result is a non-local theory with induced perturbative IR divergences as noted earlier. The quasi-PDFs are velocity regulated and free from IR divergences, with the UV limit carried before the light front limit $v \to 1$. The PDFs follow from the quasi-PDFs by matching, with generically in leading twist [Ji et al., 2021]

$$q(x, v \to 1) = \int_{-\infty}^{\infty} \frac{dy}{y} C\left(\frac{y}{x}, \frac{P(v)}{\mu}\right) q(y,v) + \mathcal{O}\left(\frac{\Lambda^2}{P(v)^2}\right) \tag{14.24}$$

14.3 ′T Hooft effective Lagrangian on the light front

It is usually argued that the QCD vacuum is trivial on the LF, owing to the vanishing of the the backward diagrams in perturbation theory [Lepage and Brodsky, 1980]. However, this is not true as the vacuum physics is carried by the longitudinal zero modes on the LF [Ji et al., 2020b, Ji et al., 2020a]. For the emergent effective interaction (3.37), this physics is explicitly carried by the constrained part of the fermionic field as initially noted in [Bentz et al., 1999, Itakura and Maedan, 2000, Naito et al., 2004]. More specifically, the projection of the fermion field along the light front, splits the field into a good plus bad component, with the latter non-propagating or constraint. The elimination of the constaint, induces multifermion interactions in terms of the good component. In the mean-field approximation using $\frac{1}{N_c}$ counting rules, these interactions account for the spontaneous breaking of chiral symmetry on the light front through tadpoles [Bentz et al., 1999, Itakura and Maedan, 2000, Naito et al., 2004].

For simplicity, consider the local form of Lagrangian associated to (3.37) in the large N_c and flavor symmetric approximation,

$$\mathcal{L} = \bar{\Psi}(i\slashed{\partial} - m)\Psi + \frac{G_S}{2}\left[(\bar{\Psi}\Psi)^2 - (\bar{\Psi}\tau^a\Psi)^2 - (\bar{\Psi}i\gamma^5\Psi)^2 + (\bar{\Psi}i\gamma^5\tau^a\Psi)^2\right] \tag{14.25}$$

with $G_S = G/4N_c^2$. The modifications for the finite instanton sizes will be quoted at the end. To carry the mean-field or $\frac{1}{N_c}$ analysis, it is more transparent to use the semi-bosonized form of (14.25)

$$\bar{\Psi}(i\slashed{\partial} - m)\Psi + G_S\bar{\Psi}\left(\sigma - \sigma^a\tau^a - i\pi\gamma^5 + i\pi^a\tau^a\gamma^5\right)\Psi - \frac{G_S}{2}\left[\sigma^2 - (\sigma^a)^2 - \pi^2 + (\pi^a)^2\right] \tag{14.26}$$

using the auxillary fields σ, σ^a, π, and π^a. To proceed, we now split the fermionic field Ψ into a good component Ψ_+ and a bad component Ψ_-

$$\Psi = \Psi_+ + \Psi_- \equiv \frac{1}{2}\gamma^-\gamma^+\Psi + \frac{1}{2}\gamma^+\gamma^-\Psi \tag{14.27}$$

The bad component does not propagate along the light front x^+-direction, and therefore can be eliminated from (14.25) using the equation of motion,

$$\Psi_- = \frac{\gamma^+}{2} \frac{1}{i\partial_-} \left(-i\gamma_\perp^i \partial_i + \hat{M} \right) \Psi_+ \tag{14.28}$$

where $\hat{M}$ denotes

$$\hat{M} = m - G_S \left(\sigma - \sigma^a \tau^a - i\pi\gamma^5 + i\pi^a \tau^a \gamma^5 \right) \tag{14.29}$$

with $m = m_{u,d}$ and the propagator for the longitudinal modes

$$\langle x^- | \frac{1}{i\partial_-} | y^- \rangle = G(x^-, y^-) = \int_{-\infty}^{\infty} \frac{dk^+}{2\pi} \frac{1}{k^+} e^{-ik^+(x-y)^-} = \frac{-i}{2}\epsilon(x^- y^-) \tag{14.30}$$

In terms of (14.28), the semi-bosonized Lagrangian (14.26) can be solely rewritten in terms of the good component

$$\mathcal{L} = \bar{\Psi}_+ i\gamma^+ \partial_+ \Psi_+ - \frac{G_S}{2} \left[\sigma^2 - (\sigma^a)^2 - \pi^2 + (\pi^a)^2 \right] - \bar{\Psi}_+ \left(i\gamma_\perp^i \partial_i - \hat{M} \right) \frac{\gamma^+}{2} \frac{1}{i\partial_-} \left(i\gamma_\perp^i \partial_i - \hat{M} \right) \Psi_+ \tag{14.31}$$

It is now clear that the elimination of the auxillary interactions induce non-local multi-fermion interactions. In leading order in $1/N_c$ they contribute mostly through tadpoles and renormalize the initial 4-fermi interactions. For that, we shift the scalar field by $\sigma = N_c \sigma_0 + \delta\sigma$ in (14.31) with a finite vev $\sigma_0 \sim N_c^0$, as all other vevs are excluded by isospin symmetry and parity, hence $\sigma^a, \pi, \pi^a, \delta\sigma \sim \mathcal{O}(\sqrt{N_c})$, with $g_S = N_c G_S \sim N_c^0$. To resum all the leading tadpole diagrams, we set the coefficient of $\delta\sigma$ to zero,

$$\langle \bar{\psi}\psi \rangle - N_c \sigma_0 = 0 \tag{14.32}$$

with now the effective fermionic field

$$\psi = \Psi_+ + \frac{\gamma^+}{2} \frac{-i}{\partial_-} (i\gamma_\perp^i \partial_i - M)\Psi_+ \tag{14.33}$$

As a result, the good component of the quark field acquires a constituent mass of order N_c^0

$$M = m - G_S \langle \bar{\psi}\psi \rangle \tag{14.34}$$

This is how the spontaneous breaking of chiral symmetry takes place on the light front. To proceed, we note that σ^a, π, π^a, and $\delta\sigma = \sigma - N_c\sigma_0$ are of order $\mathcal{O}(\sqrt{N_c})$, while the 't-Hooft coupling $G_S = g_S/N_c$, so that to leading order in $1/N_c$ the semi-bosonized Lagrangian is quadratic in the boson fields

$$\begin{aligned}
\mathcal{L} \sim \ & \bar{\psi}(i\slashed{\partial} - M)\psi \\
& -\frac{1}{2}G_S \left[\delta\sigma \hat{D}_+ \delta\sigma - \sigma^a \hat{D}_- \sigma^a - \pi \hat{D}_- \pi + \pi^a \hat{D}_+ \pi^a \right] \\
& +G_S \left[\bar{\psi}\psi\hat{\sigma} - \bar{\psi}\tau^a \psi\sigma^a - \bar{\psi}i\gamma^5 \psi\pi + \bar{\psi}i\gamma^5 \tau^a \psi\pi^a \right]
\end{aligned} \tag{14.35}$$

with

$$\hat{D}_\pm = 1 \pm G_S \left\langle \bar{\psi}\gamma^+ \frac{-i}{\overleftrightarrow{\partial_-}} \psi \right\rangle \tag{14.36}$$

where $1/i\overleftrightarrow{\partial_-}$ in (14.36), is defined such that for any fields $\chi(x)$ and $\psi(x)$,

$$\chi(x) \frac{-i}{\overleftrightarrow{\partial_-}} \psi(x) = \frac{i}{\partial_-} \left[\chi(x) \right] \psi(x) + \chi(x) \frac{-i}{\partial_-} [\psi(x)] \tag{14.37}$$

$\hat{D}_\pm$ follows from the resummation of the tadpole diagrams in mean-field, or leading order in $1/N_c$. Indeed, each virtual quark tadpole is of order $\mathcal{O}(N_c)$, thereby compensating the 't Hooft coupling $G_S \sim \mathcal{O}(1/N_c)$, with a net factor of $\mathcal{O}(N_c^0)$. Note that the fermionic contributions $\bar{\psi}\psi$, $\bar{\psi}\tau^a\psi$, $\bar{\psi}i\gamma^5\psi$, and $\bar{\psi}i\gamma^5\tau^a\psi$ in (14.35), are all of the same order as the remnant quantum fluctuations or $\mathcal{O}(\sqrt{N_c})$. With this in mind, we can now eliminate the auxillary bosonic fields, to obtain the light front Lagrangian

$$\mathcal{L} \sim \bar{\psi}(i\partial\!\!\!/ - M)\psi + \frac{G_S}{2}\left[\bar{\psi}\psi\hat{D}_+^{-1}\bar{\psi}\psi - \bar{\psi}\tau^a\psi\hat{D}_-^{-1}\bar{\psi}\tau^a\psi - \bar{\psi}i\gamma^5\psi\hat{D}_+^{-1}\bar{\psi}i\gamma^5\psi + \bar{\psi}i\gamma^5\tau^a\psi\hat{D}_+^{-1}\bar{\psi}i\gamma^5\tau^a\psi\right] \quad (14.38)$$

In the mean-field or leading order in $1/N_c$ approximation, the light front Lagrangian can be solely written in terms of the good fermionic component. The elimination of the bad component, generates a constituent mass, introduces an effective quark field (14.33) and renormalizes by $\hat{D}_\pm^{-1}$ (tadpole resummation) each of the original multi-fermion interaction in the ILM in the zero size limit.

Most of the arguments presented above, carry for the non-local effective Lagrangian in the ILM. More specifically, the mean-field version of (14.35) is now

$$\mathcal{L} \sim \bar{\psi}(i\partial\!\!\!/ - M)\psi - \frac{1}{2}G_S\left[\delta\sigma\hat{D}_+\delta\sigma - \sigma^a\hat{D}_-\sigma^a - \pi\hat{D}_-\pi + \pi^a\hat{D}_+\pi^a\right]$$

$$+G_S\left(\bar{\psi}\sqrt{\mathcal{F}(i\partial)}\delta\sigma\sqrt{\mathcal{F}(i\partial)}\psi - \bar{\psi}\sqrt{\mathcal{F}(i\partial)}\sigma^a\tau^a\sqrt{\mathcal{F}(i\partial)}\psi - \bar{\psi}\sqrt{\mathcal{F}(i\partial)}i\gamma^5\pi\sqrt{\mathcal{F}(i\partial)}\psi + \bar{\psi}\sqrt{\mathcal{F}(i\partial)}i\gamma^5\tau^a\pi^a\sqrt{\mathcal{F}(i\partial)}\psi\right)$$

$$(14.39)$$

Here $\sqrt{\mathcal{F}}(i\partial)$ is a derivative operator acting on all of the field on its right-hand side. In momentum space, it generates the pertinent form factors inherited from the underlying quark zero modes. Also,

$$\hat{D}_\pm \to 1 \pm G_S\left\langle \bar{\psi}\gamma^+\mathcal{F}(i\partial)\frac{-i}{\overleftrightarrow{\partial_-}}[\mathcal{F}(i\partial)\psi]\right\rangle \quad (14.40)$$

following from the mean-field resummation of the leading tadpoles. The auxillary bosonic fields can be eliminated by carrying explicitly the Gaussian integration, as in the zero size limit.

14.4 Effective theory of partons on the LF

Some of the formal objections to the LF formulation are: 1/ The apparent non-commutativity of the LF and large cut-off limits; 2/ The LF non-locality following from the removal of the constraint fields; 3/ The lack of rotational symmetry on the LF. While some of these objections maybe difficult to overcome in a perturbative framework [Ji, 2024], they are readily addressed in the non-perturbative QCD ILM that we will develop below. In short, in [Liu et al., 2024d] it was explicitly shown that all IR problems are resolved in the ILM on the LF, and that rotational symmetry is achieved dynamically when power counting in the instanton packing fraction is enforced.

14.5 Light front wave functions from gradient flow

Regarding the order of the limits, we note that the ILM is a well defined non-perturbative framework of the QCD vacuum and its excitations, at a fixed resolution or gradient flow (GF) time (Luscher gradient flow). The LFWFs in the ILM are obtained by taking the infinite momentum limit *at fixed resolution in*

the continuum limit. This limit is safe, since the underlying cooled gauge configurations are UV free. The resulting LFWFs are to be understood in the Wilsonian sense.

More specifically, in the ILM the LFWFs are built from cooled gauge configurations with fixed size and density, $\rho \simeq \frac{1}{3}$ fm$\,$, $n \simeq \frac{1}{\text{fm}^4}$. These parameters define an effective resolution scale $\mu_0 \sim \frac{1}{\rho} \simeq 0.6-1$ GeV, interpreted as a gradient-flow cutoff through $\mu_0 = \frac{1}{\sqrt{8t}}$, where t is the flow time. The gradient flow smooths gauge fields over a radius $\sqrt{8t}$, removing ultraviolet fluctuations above this scale.

In QCD, the definition of a renormalized parton distribution function (PDF)

$$q(x,\mu) = \int \frac{dz^-}{4\pi} e^{ixP^+z^-} \langle P|\bar{\psi}(0)\gamma^+\psi(z^-)|P\rangle_\mu \tag{14.41}$$

requires that the ultraviolet cutoff Λ (or renormalization scale μ) be removed before taking the infinite-momentum limit

$$\lim_{P^+\to\infty} \lim_{\Lambda\to\infty} q(x,\Lambda,P^+). \tag{14.42}$$

This ensures proper factorization and regulator independence. QCD is critical in the $P \to \infty$ limit; correlation functions become singular unless the continuum limit is taken first.

In the ILM approach, however, one first fixes a finite smoothing scale via gradient flow and then takes $P^+ \to \infty$

$$\lim_{P^+\to\infty} q(x,\mu_0,P^+;t), \qquad \mu_0 = 1/\sqrt{8t} \text{ finite.} \tag{14.43}$$

Thus the LFWFs correspond to an *effective hadronic resolution* μ_0, not to a continuum limit. The apparent inversion of limits is harmless provided the ILM wavefunctions are interpreted as effective low-scale inputs

$$\text{ILM LFWF}(P^+\to\infty,\mu_0) \equiv \Psi_{\text{eff}}(x_i,\boldsymbol{k}_{\perp i};\mu_0). \tag{14.44}$$

Because gradient flow suppresses UV modes, the resulting effective theory has no critical behavior and allows a finite, well-defined $P \to \infty$ limit. Thus, the LFWFs are meaningful only at the finite resolution μ_0; they are not continuum QCD LFWFs. These wavefunctions encode nonperturbative physics at the scale μ_0 and are used to construct operator-defined quantities such as PDFs, GPDs, and distribution amplitudes (DAs)

$$q(x,\mu_0) = \sum_n \int [dx_i][d^2k_{\perp i}] \,|\Psi_n(x_i,\boldsymbol{k}_{\perp i};\mu_0)|^2\, \delta(x - x_i), \tag{14.45}$$

$$\phi(x,\mu_0) = \int [d^2k_\perp]\, \Psi_{\text{val}}(x,\boldsymbol{k}_\perp;\mu_0). \tag{14.46}$$

To connect these to continuum QCD parton distributions in the $\overline{\text{MS}}$ scheme, we:

1. Treat the outputs as *flow-scheme* objects at scale μ_0.
2. Perform a short-distance (small flow-time) *matching* GF$\to \overline{\text{MS}}$ at the *same* scale μ_0.
3. Evolve to higher μ with standard DGLAP (or ERBL for DAs).

The potentially dangerous infinite momentum frame limit at fixed cutoff *never occurs in the ILM*: the $P \to \infty$ taken in the ILM is within the flowed theory QCD$_{\text{GF}}(t)$, which is UV-finite. The only interface with renormalized QCD is the short-distance matching at μ_0, where continuum perturbation theory applies and the order of limits is respected.

14.6 Matching gradient flow (GF) to perturbative renormalization with $\overline{\text{MS}}$

Let $O_\Gamma(zv)$ denote the gauge-invariant quark bilocal with a straight Wilson line of length z along direction v (Euclidean notation) and $\Gamma = \gamma \cdot v$ ($\parallel$ projector). Denote by $O_{\Gamma,R}(zv,t)$ the flowed operator renormalized in the GF scheme at flow time t, and by $O_\Gamma^{\overline{\text{MS}}}(zv;\mu)$ the renormalized operator in $\overline{\text{MS}}$ at scale μ. In the small flow-time limit [Brambilla and Wang, 2024, Hieda and Suzuki, 2016, Mereghetti et al., 2022]

$$O_{\Gamma,R}(zv,t) \;=\; C_\psi(t,\mu)\, e^{\delta m\, z}\, O_\Gamma^{\overline{\text{MS}}}(zv;\mu) \;+\; \mathcal{O}(t), \qquad C_\psi(t,\mu) = \big[c_{\psi h_v}(t,\mu)\big]^2, \tag{14.47}$$

where $c_{\psi h_v}$ is the matching coefficient of the local current $\bar\psi h_v$ in the auxiliary-field formalism and δm is the (subtracted) Wilson-line mass term. Since C_ψ is z-independent at this order, its Fourier transform to x-space yields a *diagonal* kernel. At one loop (NLO) in α_s, we have [Mereghetti et al., 2022]

$$c_{\psi h_v}(t,\mu) = 1 - \frac{\alpha_s(\mu)}{4\pi}\, C_F \left[\frac{3}{2}\, L_t + \frac{1}{2}\ln(432) + 1\right] + \mathcal{O}(\alpha_s^2), \tag{14.48}$$

$$C_\psi(t,\mu) = \big[c_{\psi h_v}(t,\mu)\big]^2 = 1 - \frac{\alpha_s(\mu)}{4\pi}\, 2C_F \left[\frac{3}{2}\, L_t + \frac{1}{2}\ln(432) + 1\right] + \mathcal{O}(\alpha_s^2). \tag{14.49}$$

with

$$L_t \equiv \ln\big(2\,\mu^2 t\, e^{\gamma_E}\big), \qquad C_F = \frac{N_c^2 - 1}{2N_c}. \tag{14.50}$$

Therefore, the matching of quark PDFs from GF to $\overline{\text{MS}}$ at the same scale $\mu = \mu_0$ reads

$$q^{\overline{\text{MS}}}(x,\mu_0) = \big[C_{qq}^{\text{GF}\to\overline{\text{MS}}} \otimes q^{\text{GF}}\big](x,\mu_0) + \big[C_{qg}^{\text{GF}\to\overline{\text{MS}}} \otimes g^{\text{GF}}\big](x,\mu_0) + \mathcal{O}\!\left(\frac{\Lambda_{\text{QCD}}^2}{\mu_0^2}\right),$$

$$g^{\overline{\text{MS}}}(x,\mu_0) = \big[C_{gq}^{\text{GF}\to\overline{\text{MS}}} \otimes q^{\text{GF}}\big](x,\mu_0) + \big[C_{gg}^{\text{GF}\to\overline{\text{MS}}} \otimes g^{\text{GF}}\big](x,\mu_0) + \mathcal{O}\!\left(\frac{\Lambda_{\text{QCD}}^2}{\mu_0^2}\right). \tag{14.51}$$

At leading order, one may set $C_{ij} = \delta_{ij}\,\delta(1-x)$. At next-to-leading order,

$$C_{ij}(x;\mu_0) = \delta_{ij}\,\delta(1-x) + \frac{\alpha_s(\mu_0)}{2\pi}\, c_{ij}^{(1)}(x) + \cdots, \tag{14.52}$$

where $c_{ij}^{(1)}(x)$ are finite and computable from the small-flow-time expansion. Once matched, the evolution to higher μ follows from the the DGLAP equations in $\overline{\text{MS}}$. The matching between the gradient-flow (GF) scheme and the $\overline{\text{MS}}$ scheme at fixed μ_0 is a short-distance renormalization, not a dynamical evolution. Because the gradient flow acts as a uniform Gaussian smearing of the quark fields, the one-loop coefficient is proportional to $\delta(1-x)$: the renormalization is *multiplicative and x-independent*. The x-shape of the distribution is entirely set by the LFWFs themselves.

14.6.1 Remarks

- Eq. (14.51) is *diagonal in x* at this order (no plus-distributions): the small-flow-time matching is entirely multiplicative for the quark bilocal at one loop. Non-singlet flavors do not mix with gluons; in the singlet channel, $C_{qg}^{(1)} = 0$ at this order within the same approximation.
- The linearly divergent Wilson-line mass δm cancels between schemes by construction once the *same* subtraction is used; it does not introduce x-dependence in the kernel.

- For gluonic Wilson-line operators (relevant to gluon quasi-PDFs), analogous one-loop coefficients exist; they are not needed for quark PDFs here.

14.6.2 Size of corrections

Two (families of) power corrections bound the accuracy of the matching-and-evolve procedure:

1. **Higher-twist corrections in QCD at the matching point:**

$$\delta_{\mathrm{HT}} \; \sim \; \mathcal{O}\!\left(\frac{\Lambda_{\mathrm{QCD}}^2}{\mu_0^2}\right). \tag{14.53}$$

   In the ILM $\rho \simeq 0.33$ fm, one has $\mu_0 \sim 1/\rho \approx 0.6\text{-}1.0$ GeV. With $\Lambda_{\mathrm{QCD}} \approx 0.3$ GeV, the estimate ranges from $\sim 25\%$ (for $\mu_0 = 0.6$ GeV) down to $\sim 9\%$ (for $\mu_0 = 1.0$ GeV).

2. **Small-flow-time expansion (SFTE) remainders in** $\mathrm{QCD}_{\mathrm{GF}}(t)$:

$$\delta_{\mathrm{SFTE}} \; \sim \; \mathcal{O}\!\left(t\,Q^2\right) \; + \; \mathcal{O}\!\left((z^2/t)\times\cdots\right), \tag{14.54}$$

   where Q is the *short* distance probed in the matching (here $Q \sim \mu_0$) and z is the Wilson-line length entering the bilocal. Choosing $\mu_0 \simeq 1/\sqrt{8t}$ minimizes large logs, but implies $\mu_0^2 t = 1/8$; numerically this is ~ 0.125, i.e. a $\mathcal{O}(10\%)$ effect as a rule-of-thumb. Keeping $|z| \lesssim \sqrt{8t}$ controls the (z^2/t) sector.

14.6.3 The role of higher Fock components

The nucleon light front wave function (LFWF) is constructed as a sequence of Fock sectors

$$|N\rangle = |qqq\rangle + |qqqq\bar{q}\rangle + \cdots, \tag{14.55}$$

where the five-quark component arises from extra quark pairs (e.g. generated by the instanton-induced 't Hooft interaction). This term encodes quark-antiquark pair creation through instanton zero modes, providing a nonperturbative *sea-quark* structure already at the resolution $\mu_0 \sim 1/\rho \sim 1$ GeV. Hence, the LFWFs naturally include low-x support without invoking perturbative evolution.

The $qqqq\bar{q}$ Fock component effectively incorporates nonperturbative sea quarks that, in conventional QCD analyses, would appear only through perturbative evolution. Thus, at the hadronic scale $\mu_0 \sim 1$ GeV, the LFWFS in the ILM already captures part of the small-x content. The gradient-flow to $\overline{\mathrm{MS}}$ conversion simply redefines the operator normalization at that scale; it does not alter the internal x-distribution. This situation is analogous to modern global fits where the initial condition at μ_0 already contains an intrinsic sea

$$q_{\mathrm{fit}}(x,\mu_0) = q_{\mathrm{val}}(x,\mu_0) + q_{\mathrm{sea}}^{\mathrm{intr}}(x,\mu_0). \tag{14.56}$$

DGLAP evolution then builds upon this input, rather than generating the sea from scratch. The inclusion of the $qqqq\bar{q}$ sector in the ILM provides an intrinsic, nonperturbative sea that extends the LFWFs to small x. The GF $\to \overline{\mathrm{MS}}$ matching at μ_0 is x-independent because it merely rescales the flowed operator normalization. DGLAP evolution from μ_0 upward adds further perturbative, logarithmic x-dependence, completing the connection to high-scale QCD PDFs.

14.6.4 Division of roles at fixed μ_0

Step	Effect	x-dependence
LFWFs	Nonperturbative valence and sea structure	Strong, dynamical
GF $\to \overline{\text{MS}}$ matching	Short-distance field renormalization	None (multiplicative)
DGLAP evolution ($\mu > \mu_0$)	Perturbative radiation, logarithmic scaling	Generated perturbatively

Procedure summary for matching and evolution:

1. Fix $\mu_0 = 1/\sqrt{8t}$ from the ILM flow time (equivalently, from ρ).
2. Compute $q^{\text{GF}}(x, \mu_0)$ from the ILM LFWFs (include the $qqqqq$ sector to seed the sea).
3. Apply Eq. (14.51) to obtain $q^{\overline{\text{MS}}}(x, \mu_0)$, $g^{\overline{\text{MS}}}(x, \mu_0)$.
4. Evolve with NLO/NNLO DGLAP to a larger μ.

14.7 Hamiltonian renormalization

Consider the LF Hamiltonian developed in a basis function. After the einbein method of linearizing the confining potential, a longitudinal σ_L and transverse σ_T confining tensions arise. The basis LF truncation at the level of the transverse and longitudinal modes introduce two cutoffs

$$\sum_{i=1}(2n_i + |m_i|) \le N_{\text{max}}, \qquad \sum_{i=1} j_i = K_{\text{max}}. \tag{14.57}$$

Now assume that we increase the size of the Fock space from qqq to $qqqq\bar{q}$ and introduce a sigma coupling g_σ and a pion coupling g_π to mix the S- and P-waves in the nucleon state. The dimensionality increase in size of the Fock space will be denoted by N_{Fock}.

To proceed, we denote by

$$\boldsymbol{g} \equiv \begin{pmatrix} \sigma_T \\ \sigma_L \\ g_\sigma \\ g_\pi \end{pmatrix},$$

the vector of all running couplings. We now discuss how these couplings run with the inherent Hamiltonian cutoffs, and the increase dimensionality of the Fock space and evaluate the pertinent beta functions. Throughout, the CM is separated, with only intrinsic states. Let $(\mathcal{O}_1, \mathcal{O}_2, \mathcal{O}_3, \mathcal{O}_4)$ be four renormalization conditions (observables) that we hold fixed as the regulators $(N_{\text{max}}, K_{\text{max}}, N_{\text{Fock}})$ are varied. Typical choices are, for example, the three lowest intrinsic eigenvalues (or a combination of eigenvalues and transition matrix elements).

14.7.1 Renormalization conditions as implicit equations

Define

$$\boldsymbol{\mathcal{F}}(\boldsymbol{g}; N_{\text{max}}, K_{\text{max}}, N_{\text{Fock}}) \equiv \begin{pmatrix} \mathcal{O}_1(\boldsymbol{g}; N_{\text{max}}, K_{\text{max}}, N_{\text{Fock}}) - \mathcal{O}_1^{\text{phys}} \\ \mathcal{O}_2(\boldsymbol{g}; N_{\text{max}}, K_{\text{max}}, N_{\text{Fock}}) - \mathcal{O}_2^{\text{phys}} \\ \mathcal{O}_3(\boldsymbol{g}; N_{\text{max}}, K_{\text{max}}, N_{\text{Fock}}) - \mathcal{O}_3^{\text{phys}} \\ \mathcal{O}_4(\boldsymbol{g}; N_{\text{max}}, K_{\text{max}}, N_{\text{Fock}}) - \mathcal{O}_3^{\text{phys}} \end{pmatrix} = \boldsymbol{0}. \tag{14.58}$$

Each observable depends on each of the four couplings $(\sigma_T, \sigma_L, g_\sigma, g_\pi)$ and on the three cutoffs $(N_{\text{max}}, K_{\text{max}}, N_{\text{Fock}})$.

Denote the 4×4 Jacobian with respect to the couplings by

$$\boldsymbol{J}(\boldsymbol{g}; N_{\max}, K_{\max}, N_{\text{Fock}}) \equiv \frac{\partial \boldsymbol{\mathcal{F}}}{\partial \boldsymbol{g}} = \begin{pmatrix} \partial_{\sigma_T} \mathcal{O}_1 & \partial_{\sigma_L} \mathcal{O}_1 & \partial_{g_\sigma} \mathcal{O}_1 & \partial_{g_\pi} \mathcal{O}_1 \\ \partial_{\sigma_T} \mathcal{O}_2 & \partial_{\sigma_L} \mathcal{O}_2 & \partial_{g_\sigma} \mathcal{O}_2 & \partial_{g_\pi} \mathcal{O}_2 \\ \partial_{\sigma_T} \mathcal{O}_3 & \partial_{\sigma_L} \mathcal{O}_3 & \partial_{g_\sigma} \mathcal{O}_3 & \partial_{g_\pi} \mathcal{O}_3 \\ \partial_{\sigma_T} \mathcal{O}_4 & \partial_{\sigma_L} \mathcal{O}_4 & \partial_{g_\sigma} \mathcal{O}_4 & \partial_{g_\pi} \mathcal{O}_4 \end{pmatrix}. \tag{14.59}$$

Assuming $\det \boldsymbol{J} \neq 0$ at the renormalization point, then $\boldsymbol{g}$ can be expressed as functions of $(N_{\max}, K_{\max}, N_{\text{Fock}})$ in a neighborhood of that point.

14.7.2 Differential RG and beta functions

Taking a total differential of (14.58) at fixed physical targets and varying all three regulators give

$$\boldsymbol{J} \, d\boldsymbol{g} + \frac{\partial \boldsymbol{\mathcal{F}}}{\partial \ln N_{\max}} d\ln N_{\max} + \frac{\partial \boldsymbol{\mathcal{F}}}{\partial \ln K_{\max}} d\ln K_{\max} + \frac{\partial \boldsymbol{\mathcal{F}}}{\partial \ln N_{\text{Fock}}} d\ln N_{\text{Fock}} = \boldsymbol{0}. \tag{14.60}$$

Define the beta vector field in coupling space as the response to changes in the logarithms of the cutoffs:

$$\boldsymbol{\beta}^{(N)}(\boldsymbol{g}; N_{\max}, K_{\max}, N_{\text{Fock}}) \equiv \left. \frac{d\boldsymbol{g}}{d\ln N_{\max}} \right|_{K_{\max}, N_{\text{Fock}}} = -\boldsymbol{J}^{-1} \frac{\partial \boldsymbol{\mathcal{F}}}{\partial \ln N_{\max}}, \tag{14.61}$$

$$\boldsymbol{\beta}^{(K)}(\boldsymbol{g}; N_{\max}, K_{\max}, N_{\text{Fock}}) \equiv \left. \frac{d\boldsymbol{g}}{d\ln K_{\max}} \right|_{N_{\max}, N_{\text{Fock}}} = -\boldsymbol{J}^{-1} \frac{\partial \boldsymbol{\mathcal{F}}}{\partial \ln K_{\max}}, \tag{14.62}$$

$$\boldsymbol{\beta}^{(F)}(\boldsymbol{g}; N_{\max}, K_{\max}, N_{\text{Fock}}) \equiv \left. \frac{d\boldsymbol{g}}{d\ln N_{\text{Fock}}} \right|_{N_{\max}, K_{\max}} = -\boldsymbol{J}^{-1} \frac{\partial \boldsymbol{\mathcal{F}}}{\partial \ln N_{\text{Fock}}}, \tag{14.63}$$

$$\tag{14.64}$$

Thus the full flow along an arbitrary path $(\ln N_{\max}(t), \ln K_{\max}(t), \ln N_{\text{Fock}}$ is

$$\frac{d\boldsymbol{g}}{dt} = \boldsymbol{\beta}^{(N)} \frac{d\ln N_{\max}}{dt} + \boldsymbol{\beta}^{(K)} \frac{d\ln K_{\max}}{dt} + \boldsymbol{\beta}^{(F)} \frac{d\ln N_{\text{Fock}}}{dt}. \tag{14.65}$$

The beta functions depend on the three regulators because $\boldsymbol{J}$ and the regulator-derivative vectors depend on $(\boldsymbol{g}; N_{\max}, K_{\max}, N_{\text{Fock}})$, and running in one direction mixes into the other through $\boldsymbol{J}^{-1}$.

14.7.3 Concrete asymptotics from basis LF truncation

Asymptotically, regulator effects enter as inverse powers with possible cross terms. A generic local ansatz for the observables near a renormalization point is

$$\mathcal{O}_a(\boldsymbol{g}; N_{\max}, K_{\max}, N_{\text{Fock}}) = \mathcal{O}_a^{(\infty)} + \sum_{i \in \mathbf{g}} A_{ai}(\ln N_{\max}, \ln K_{\max}), N_{\text{Fock}}) \, g_i$$

$$+ \frac{C_a}{N_{\max}^p} + \frac{D_a}{K_{\max}^q} + \frac{E_a}{N_{\text{Fock}}^r} + \frac{F_a}{N_{\max}^p K_{\max}^q} + \cdots, \tag{14.66}$$

where $p, q, r > 0$ are determined by basis selection rules and level spacing, and A_{ai} may have mild logarithmic dependence. Then

$$\partial_{\sigma_T}\mathcal{O}_a = A_{a,\sigma_T} + \mathcal{O}(g), \qquad \partial_{\sigma_L}\mathcal{O}_a = A_{a,\sigma_L} + \mathcal{O}(g),$$

$$\partial_{g_\sigma}\mathcal{O}_a = A_{a,g_\sigma} + \mathcal{O}(g), \qquad \partial_{g_\pi}\mathcal{O}_a = A_{a,g_\pi} + \mathcal{O}(g), \tag{14.67}$$

$$\partial_{\ln N_{\max}}\mathcal{O}_a = \partial_{\ln N_{\max}} A_{ai}\, g_i - p\,\frac{C_a}{N_{\max}^p} - p\,\frac{F_a}{N_{\max}^p K^q} + \cdots, \tag{14.68}$$

$$\partial_{\ln K_{\max}}\mathcal{O}_a = \partial_{\ln K_{\max}} A_{ai}\, g_i - q\,\frac{D_a}{K_{\max}^q} - q\,\frac{F_a}{N_{\max}^p K^q} + \cdots. \tag{14.69}$$

$$\cdots = \cdots \tag{14.70}$$

Substituting into (14.61)-(14.62) yields explicit leading-order beta functions.

14.7.4 Explicit example for a 2x2 evolution

To illustrate explicitly how this works, let us switch the couplings $g_{\sigma,\pi}$ to the Fock states, and quantify the evolution in the three Fock space for a finite dimensional curt-off Hamiltonian. With this in mind, and if A_{ai} are treated as constants locally, then

$$\boldsymbol{J} \approx \begin{pmatrix} A_{1,\sigma_T} & A_{1,\sigma_L} \\ A_{2,\sigma_T} & A_{2,\sigma_L} \end{pmatrix} \tag{14.71}$$

and

$$\boldsymbol{\beta}^{(N)} \simeq \frac{1}{\det \boldsymbol{J}} \begin{pmatrix} A_{2,\beta^2} & -A_{1,\beta^2} \\ -A_{2,\kappa^2} & A_{1,\kappa^2} \end{pmatrix} \begin{pmatrix} p\,C_1 N_{\max}^{-p} + p\,F_1(N_{\max}^{-p} K_{\max}^{-q}) \\ p\,C_2 N_{\max}^{-p} + p\,F_2(N_{\max}^{-p} K_{\max}^{-q}) \end{pmatrix} + \cdots, \tag{14.72}$$

$$\boldsymbol{\beta}^{(K)} \simeq \frac{1}{\det \boldsymbol{J}} \begin{pmatrix} A_{2,\beta^2} & -A_{1,\beta^2} \\ -A_{2,\kappa^2} & A_{1,\kappa^2} \end{pmatrix} \begin{pmatrix} q\,D_1 K_{\max}^{-q} + q\,F_1(N_{\max}^{-p} K_{\max}^{-q}) \\ q\,D_2 K_{\max}^{-q} + q\,F_2(N_{\max}^{-p} K_{\max}^{-q}) \end{pmatrix} + \cdots. \tag{14.73}$$

which show the power-law suppression in the regulators, and how the transverse and longitudinal cutoffs $N_{\max}$ and $K_{\max}$ enter each component via $\boldsymbol{J}^{-1}$.

If only one renormalization condition is imposed in this simplified case, (14.60) gives one equation for two unknowns in $d\boldsymbol{g}$, so the flow is underdetermined. Two independent observables are required to determine the joint running of (σ_T, σ_L). More specifically for this case, choose $\mathcal{O}_1$ as the lowest intrinsic eigenvalue dominated by transverse dynamics, and $\mathcal{O}_2$ as the lowest longitudinal excitation energy. In general, we expect $\partial_{\sigma_{T,L}}\mathcal{O}_{1,2} > 0$, (with magnitudes given by expectation values of the corresponding operators). Compute these derivatives numerically at a reference point, estimate (p,q) from convergence rates, and plug into (14.72)-(14.73) to obtain numerical beta functions.

14.7.5 Summary for 2x2 evolution

- Each observable depends on both couplings (σ_T, σ_L) and both regulators $(N_{\max}, K_{\max})$.
- Beta functions follow by differentiating the vector renormalization conditions and solving a 2×2 linear system with Jacobian $\boldsymbol{J}$; see Eqs. (14.61)-(14.62).
- The resulting $\boldsymbol{\beta}$ depend on $(N_{\max}, K_{\max})$ through explicit regulator terms and the inverse Jacobian.

Part IV
Hadronic spectroscopy on the light front

Chapter 15
Quarkonia and "normal" mesons on light front

Before we start this chapter, let us explain its title. By *"normal hadrons"* we mean those which can be described well by including only confining forces : examples include vector and tensor mesons, decuplet baryons, etc. Their typical r.m.s. sizes are $\langle r \rangle \sim 1\,fm$. Obviously, there are spin-dependent forces, but those are subleading.

Quarkonia are made of quarks c, b which are much heavier than effective light quark masses ($M_q \approx 0.35\,GeV, M_s \approx 0.5\,GeV$). Respectively, their sizes and quark velocities are smaller, and perturbative Coulomb-like potential $\sim 1/r$ needs to be included.

Furthermore, if these masses be *parametrically large*, they should be oulomb and be similar to positronium. This is true, but however is not the case for real-world c, b quarks. In fact the balance between Coulombic and confining forces remains delicate. For example, *"the main spectral gap"* between the 2s and the 1s states remains about the same, for quarkonia with $\bar{s}s, \bar{c}c$ and even $\bar{b}b$ flavors.

Yet there exist some "unusual" hadrons with sizes significantly smaller than 1 fm. This happens because strong attraction between their constituents can also neither be the Coulombic nor confining forces, but the instanton-induced ones responsible for chiral symmetry breaking. The smallest one is the "scalar glueballs", and their unusually small size $\sim 0.2\,fm$ was predicted in [Schäfer and Shuryak, 1995] and later confirmed by lattice studies such as [Abbott et al., 2025]. However, glueballs are not discussed in this work.

Examples of "unusual" mesons we do discuss are σ and π mesons: their properties are defined mostly by instanton-induced 't Hooft Lagrangian rather than confining forces [1]

15.1 Boosting quarkonia WFs

Heavy quark bound states are the pillars of hadronic spectroscopy. Already in 1970's, after J/ψ and Y families discoveries, it was shown that nonrelativistic approach, with a Cornell and spin-dependent potentials provides quite accurate description of their properties. Naturally, one would think that boosted versions of their WFs have a similar level of accuracy on the LF. Before boosting, it is useful to transfer WFs from spherical to cylindrical coordinates (see e.g. [Adhikari et al., 2019]).

There are some obvious differences between the description in the rest frame, and on the light front. For instance, there are different symmetries: 3-dimensional angular momenta $\mathbf{S}, \mathbf{L}, \mathbf{J}$ are reduced to their 2-dimensional transverse parts, with spin $\mathbf{S}$ and orbital momentum $\mathbf{L}$ projected onto longitudinal momentum $\mathbf{P}$. The projection of J is denoted by "meson helicity" Λ. Obviously, hadron states with different Λ values, are treated differently: say $\rho(\Lambda = 0)$ and $\rho(\Lambda = \pm 1)$ have different wave functions (even more than one: see below). While masses, magnetic and quadrupole moments, etc should turned out to be the same, the

---

[1] It would be interesting to work out their relatives - η' and scalar isovector a_1 - in which t' Hooft Lagrangian is *repulsive*, and therefore with unusually large masses and sizes, but so far it is not done yet.

3-dimensional rotation is some complicated transformation, involving all components of the wave functions, and we will not attempt to explicitly use it.

Our approach to quarkonia at LF were worked out in two papers, [Shuryak and Zahed, 2021a, Shuryak and Zahed, 2021f]. The first question to be addressed is whether the states of heavy quarkonia can be represented by linear Regge trajectories in *squared masses*, as would be natural for LF Hamiltonians?

In Fig.15.1.1 we show the experimental masses of six $(nS), n = 0 - 5$ Upsilon mesons, compared to the standard results from the Schroedinger equation, with the Cornell potential (black triangles) and with only its linear part $V_{conf} = \sigma_T r$ (blue circles). The first observation is that using a linear potential alone (blue circles), we find a nearly-linear Regge trajectory. This observation will be important in the next subsection, as it shows that even for heavy bottomonia, the light-front Hamiltonian can be approximated by an oscillator with good accuracy. Note however, that the slope of the straight line, is here completely different from the $1/\alpha'$ slope of a similar trajectory for light mesons (e.g. for ω mesons we used in [Shuryak and Zahed, 2021a]).
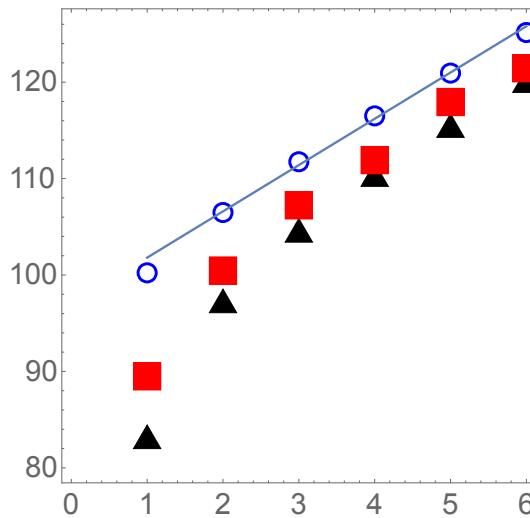
Fig. 15.1.1 $M_{n+1}^2 (GeV)^2$ versus $n + 1, n = 0, ..5$, for the six S zero orbital momentum (L=0) states of bottomonium. The red squares correspond to the experimentally observed Upsilons. The black triangles show the masses obtained from the Schroedinger equation, with the Cornell potential (linear and Coulomb potentials, no spin forces). The blue circles show the masses if the Coulomb potential is switched off, and only the linear potential is used. The straight line is shown for comparison.

The second observation is that the expected contribution from the spin-dependent potential V_{SS} (responsible for splitting between squares and triangles), is positive and decreases with n. The former is due to the positivity of the spin factor $\mathbf{S}_1 \cdot \mathbf{S}_2 = 1/4$, and the second to the fact that $V_{SS}(r)$ is rather short range, in comparison to the size of the lowest Upsilon, but much smaller than the sizes of the excited ones. Another way to anticipate the accuracy of an oscillator approximation in the light front description (discussed in [Shuryak and Zahed, 2021b] and using ω_3 mesons with $L = 2$), is to study the mass dependence of bottomonium on its orbital momentum L. In Fig.15.1.2 we show the calculated 18 squared masses for $n = 0 - 5$ (left-to-right) and $L = 0, 1, 2$ (bottom-to-top). While the Coulomb potential was included, it affects mostly and only $n = 0, L = 0$ Upsilon. The Regge trajectories for nonzero angular momentum $L = 1, 2$, show better linear dependence on n than $L = 0$. The corresponding wave function vanishes at the origin $r = 0$, and is less affected by short-range Coulomb and spin-dependent forces.

We further note, that at larger n (right side of the plot) the dependence on L also becomes linear, as the $L = 0, 1, 2$ points become equidistant. This observation encourages us to think that the oscillator description of the light front Hamiltonian and LFWFs, will need only relatively small corrections.
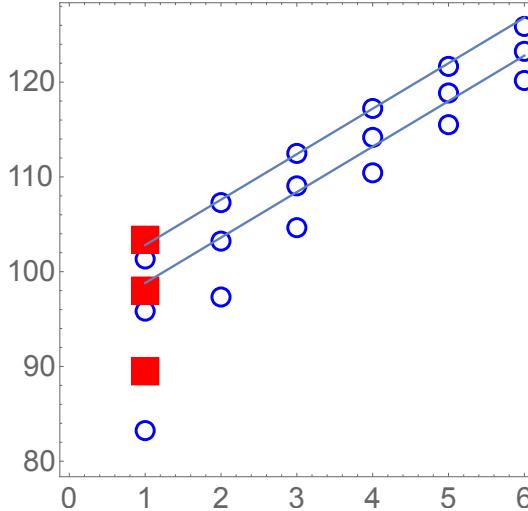
Fig. 15.1.2 $M_{n+1}^2\,(GeV)^2$ versus $n+1, n = 0, 1...$ for three families of bottomonium states, with orbital momentum $L = 0, 1, 2$ (from bottom up). The red squares correspond to the experimentally observed $\Upsilon, h_b, \Upsilon_2$ mesons (from bottom up). The blue circles show masses obtained from the Schroedinger equation, with the Cornell potential (linear and Coulomb potentials, still without spin forces). The straight lines are shown for comparison.

In [Shuryak and Zahed, 2021b], we described how we may include the linear confining term in H_{LF} (instanton induced at intermediate distances), and make it more user friendly, by eliminating the square root using the well-known einbein $e = 1/a$ trick, i.e.

$$2M\mathbb{V}_C(a, b, x, b_\perp) \approx \sigma_T\left(\frac{|id/dx|^2 + b\,b_\perp^2}{a} + a\right) \tag{15.1}$$

Here a, b are variational parameters. The minimization with respect to a is assumed, followed by the substitution $b \to M^2 \approx (2m_Q)^2$ for heavy mesons, and most light ones. (For the pion, this last substitution is not valid, as we have shown in [Shuryak and Zahed, 2021b]).

For a numerical analysis of (15.1), we used in [Shuryak and Zahed, 2021b] a basis set of functions composed of a 2-dimensional transverse oscillator, times longitudinal states $sin(\pi n x)$ with odd n. More specifically, the light front Hamiltonian can be re-arranged as follows

$$H_{LF} = H_0 + \tilde{V} + V_{perp} + V_{spin} \tag{15.2}$$

with the spin-part including both the perturbative and non-perturbative instanton contributions. As we noted earlier, in the dense instanton vacuum, the central part is hardly differentiable from the linear confining potential at intermediate distances.

The first contribution H_0

$$H_0 = \frac{\sigma_T}{a}\left(-\frac{\partial^2}{\partial x^2} - b\frac{\partial^2}{\partial \mathbf{k}_\perp^2}\right) + \sigma_T a + 4(m_Q^2 + k_\perp^2) \tag{15.3}$$

is diagonal in the functional basis used [Shuryak and Zahed, 2021b]. In this form, we make use of the momentum representation, with $\mathbf{k}_\perp$ as variable. Similarly, one can use the coordinate representation with $\mathbf{b}_\perp$ as a variable, and $\mathbf{k}_\perp = i\partial/\partial\mathbf{b}_\perp$. The latter choice is much more convenient when discussing states with nonzero angular momenta, in relation to the azimuthal angle coordinate ϕ in the transverse plane (see more on that in Appendix).

The second contribution $\tilde{V}$
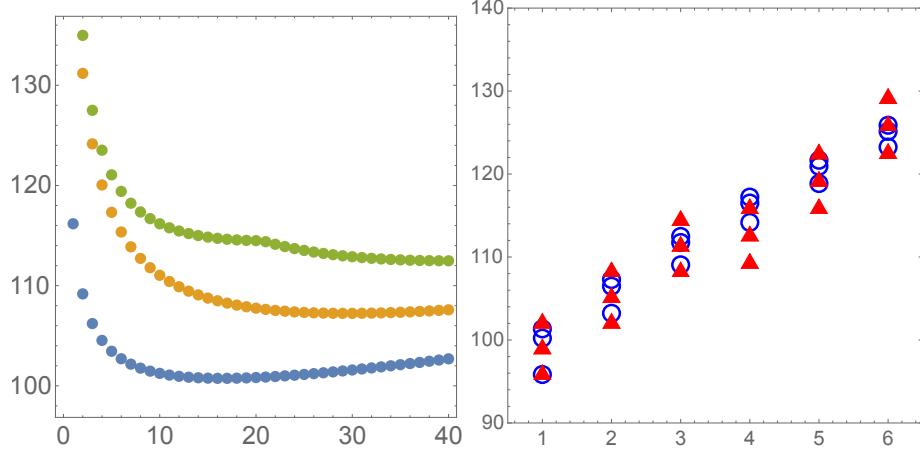
Fig. 15.1.3 Top: Squared masses M_n^2 for $\bar{b}b$ mesons for $n = 1, 2, 3$ versus the variational parameter a. Bottom: Squared masses for $n = 0..5$ (left to right) and orbital momentum $m = 0, 1, 2$ (down to up), calculated from the light front Hamiltonian H_{LF} (red triangles), and shifted by a constant, $M_{n+1}^2 - 5\,GeV^2$. For comparison, the blue-circles show the squared masses M_{n+1}^2 calculated from the Schroedinger equation in the CM frame, with only linear plus centrifugal potentials.

$$\tilde{V}(x, \mathbf{k}_\perp) \equiv (m_Q^2 + k_\perp^2)\left(\frac{1}{x\bar{x}} - 4\right) \tag{15.4}$$

has nonzero matrix elements $\langle n_1 | V(x, \mathbf{k}_\perp) | n_2 \rangle$ for all n_1, n_2 pairs. The perturbative part V_{perp} for heavy quarks is the Coulomb term, with running coupling and other radiative corrections. Finally, the last term V_{spin} contains matrices in spin variables and in orbital momenta, which we will consider later.

The calculated masses (shifted by a constant "mass renormalization", to make $n = 0, m = 0$ states the same) are shown in Fig.15.1.3. The bottom part shows good agreement between the masses obtained solving the Shroedinger equation in the rest frame (blue circles), and the masses following from the light-front frame (red-triangles). The slope is correct, and is determined by the same string tension σ_T. The splittings in orbital momentum are of the same scale, but not identical. This is expected, as we compare the 2-dimensional m-states on the light front, with the 3-dimensional L-states in the center of mass frame.

The irregularity between the third and fourth set of states, is due to our use of a modest basis set, with only three radial functions (altogether 12 functions if one counts them with 4 longitudinal harmonics). This can be eliminated using a larger set.

As a final note in this section, we recall that the chief goal of these calculations is to generate the pertinent LFWFs for all these states, from the light front Hamiltonian H_{LF}. The details about the setting and some of these wavefunctions can be found

As a good picture is better than thousand words, let us present results of two modern approaches following [Cao et al., 2025]. One of them is Dyson-Schwinger (DSE) which is fully relativistic and take interaction from averaged lattice configurations. Another is Basis light front quantization (BLFQ) by Vary et al in which LF Hamiltonian is written as a matrix in some preselected basis, with kinetic energy and interactions. The results for LF WFs are shown in Fig.15.1.4 for Dyson-Schwinger (DSE) and BLFQ wave functions, of $J/\psi, \eta_c$ mesons. It is clear from it that while these two wave functions are in qualitative agreement, they obviously are not yet derived quantitatively. So, unfortunately, the existing methods have not yet converged on say few-percent accuracy, even for the simplest hadrons, the heavy quarkonia.
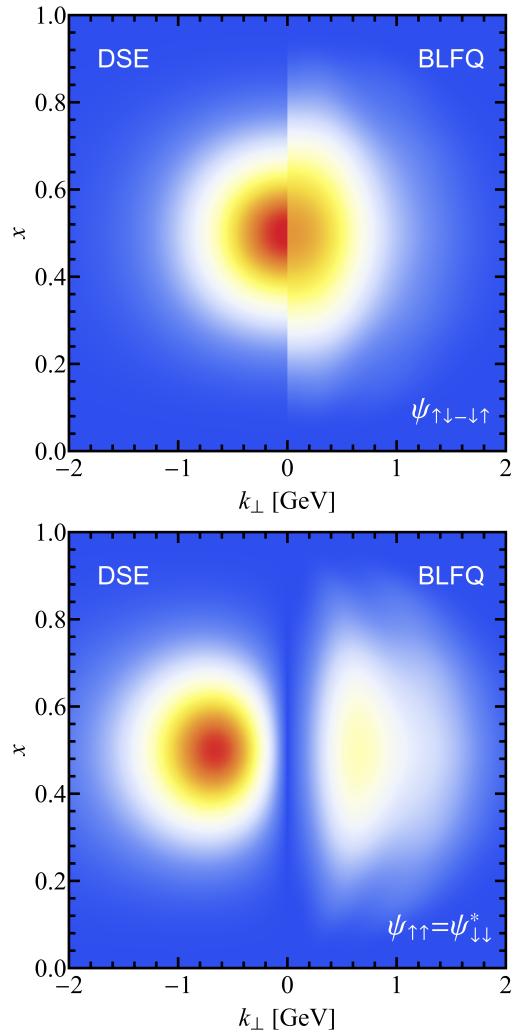
Fig. 15.1.4 The LF wave function of J/ψ and η_c mesons. The left side from Dyson-Schwinger equation, the right from Basis-light-front-quantization.

Appendix

15.A Heavy-quark reduction

The heavy quark expansion of a Dirac fermion of mass m_Q with fixed velocity, in an arbitrary gauge field is best achieved using the Foldy-Wuthuysen transformation on the relativistic fermion propagator,

$$e^{-i\frac{\not{D}_\perp}{2m_Q}}\frac{1}{i\not{D}-m_Q}e^{-i\frac{\not{D}_\perp}{2m_Q}} \tag{15.5}$$

with $i\not{D}=i\not{\partial}+\not{A}$ and $\not{D}_\perp=\not{D}-\not{v}\,v\cdot D$ satisfying $[\not{D}_\perp,\not{v}]_+=0$. We will refer to v_μ the 2-dimensional *light-cone-like* velocity along the 2-dimensional *light-cone-like* coordinate x_+ in Euclidean signature, and to $v_{\perp\mu}$ its orthogonal velocity along the 2-dimensional *light-cone-like* coordinate x_- also in Euclidean signature,

$$v_\mu=(\mathbf{0}_\perp,\sin\theta,\cos\theta),\qquad v_{\perp\mu}=(\mathbf{0}_\perp,-\cos\theta,\sin\theta), \tag{15.6}$$

with $x_+=v\cdot x$ and $x_-=v_\perp\cdot x$. These light-cone-like Euclidean coordinations (lower indices) are not to be confused with the Minkowski light-cone coordinates $x^\pm=x^0\pm x^3$ (upper-indices). With this in mind, and to order $1/m_Q^2$ the heavy quark propagator is

$$\frac{1}{iv\cdot D}-\frac{1}{iv\cdot D}\left(\frac{1}{2m_Q}(i\not{D}_\perp)^2-\frac{1}{4m_Q^2}(i\not{D}_\perp)(iv\cdot D)(i\not{D}_\perp)\right)\frac{1}{iv\cdot D} \tag{15.7}$$

The bracket in (15.7) gives rise to a vertex insertion, which can be re-arranged

$$\frac{1}{2m_Q}\left((iD)^2-\frac{1}{2}\sigma_{\mu\nu}F_{\mu\nu}\right)-\frac{1}{4m_Q^2}\left(i\sigma_{\alpha\nu}iD_\alpha v_\mu F_{\mu\nu}+iD_\nu v_\mu F_{\mu\nu}\right) \tag{15.8}$$

with $\sigma_{\alpha\nu}=\frac{1}{2i}[\gamma_\alpha,\gamma_\nu]$. In (15.8) we have dropped all terms that vanish on-shell, i.e $v\cdot DQ_v=0$ with Q_v the heavy quark field. When inserted on a straight Wilson line, (15.8) produces the spin corrections up to order $1/m_Q^2$. Note that in the Dirac representation σ_{4i} is off-diagonal. The electric contribution mixes particles and anti-particles. It does not contribute when inserted on a straight Wilson line defined as

$$\mathbf{W}(y,x)=\langle y_+|\frac{1}{v\cdot D}|x_+\rangle\,\delta(\mathbf{x}-\mathbf{y})=\mathbf{P}e^{i\int_{x_+}^{y_+}A\cdot dz}\,\theta(y_+-x_+)\delta(\mathbf{x}-\mathbf{y}) \tag{15.9}$$

with the ordering along x_+ and the short hand notation $x_\mu=(\mathbf{x}_\perp,x_-,x_+)\equiv(\mathbf{x},x_+)$.

15.A.1 Slated Wilson loop dressed with fields

The undressed Wilson loop in the resummed instanton vacuum is

$$\langle \mathbf{1}_\theta \rangle = \langle \mathbf{W}(\theta, 0_\perp)\, \mathbf{W}^\dagger(\theta, b_\perp) \rangle_C \approx e^{-Z_+ V_C(\xi_\theta)}$$

(15.10)

with $\xi_\theta = (\cos^2\theta\, b_3^2 + b_\perp^2)^{\frac{1}{2}}$, and where $V_C(\xi_\theta) \to V_C(\xi_x)$ follows by analytical continuation $\theta \to -i\chi$. The spin dressed Wilson loop to order $1/m_Q^2$ follows by inserting the corrections (15.7) on the Wilson lines

$$
\begin{aligned}
\langle \mathbf{1}_\theta \rangle \delta_{12} + \Bigg(&+ \frac{i}{4m_{Q1}^2} \int_{-\frac{1}{2}Z_+}^{+\frac{1}{2}Z_+} dz_+ \Big[\sigma_{1\alpha\nu} v_\mu \langle F_{\mu\nu}(x_1,z_+) i D_\alpha(x_1,z_+) \mathbf{1}_\theta \rangle + 1 \leftrightarrow 2 \Big] \\
&+ \frac{1}{4m_{Q1}^2} \int_{-\frac{1}{2}Z_+}^{+\frac{1}{2}Z_+} dz_+ \int_{-\frac{1}{2}Z_+}^{+\frac{1}{2}Z_+} dz'_+ \Big[\langle \sigma_{1\mu\nu} F_{\mu\nu}(x_1,z_+)(iD)^2(x_1,z'_+) \mathbf{1}_\theta \rangle + 1 \leftrightarrow 2 \Big] \\
&+ \frac{1}{8m_{Q1}m_{Q2}} \int_{-\frac{1}{2}Z_+}^{+\frac{1}{2}Z_+} dz_+ \int_{-\frac{1}{2}Z_+}^{+\frac{1}{2}Z_+} dz'_+ \Big[\langle \sigma_{1\mu\nu} F_{\mu\nu}(x_1,z_+)(iD)^2(x_2,z'_+) \mathbf{1}_\theta \rangle \\
&\qquad\qquad\qquad\qquad\qquad\qquad\qquad\qquad + \langle (iD)^2(x_1,z_+) \sigma_{2\mu\nu} F_{\mu\nu}(x_2,z'_+) \mathbf{1}_\theta \rangle \\
&\qquad\qquad\qquad\qquad\qquad\qquad\qquad\qquad - \frac{1}{2} \langle \sigma_{1\mu\nu} F_{\mu\nu}(x_1,z_+) \sigma_{2\alpha\beta} F_{\alpha\beta}(x_2,z'_+) \mathbf{1}_\theta \rangle \Big] \Bigg) \delta_{12}
\end{aligned}
$$

(15.11)

after dropping the terms that vanish on-shell, the terms that vanish by parity after averaging in the presence of the undressed Wilson loop, and those with no contribution to the spin-dependent potentials. In (15.11) we have labeled the quark masses for a general Wilson loop with unequal masses, and used the short hand notation

$$\delta_{12} = \delta(\mathbf{x}_1 - \mathbf{y}_1)\delta(\mathbf{x}_2 - \mathbf{y}_2)$$

Throughout, the affine integration parameters z_+, z'_+ in (15.11) are proper times. The conversion to ordinary times $(z_+, z'_+) \to (z_+, z'_+)/\gamma_E$ amounts to extra Lorentz contraction factors of $1/\gamma_E = \sqrt{1 + \dot{x}_E^2}$ in Euclidean signature, that will be added at the end by inspection.

15.A.2 Identities

To simplify (15.11) we use the identities with slated Wilson lines (dropping the delta functions)

$$\mathbf{W}(x_+, y_+)\mathbf{W}(y_+, z_+) = \langle x_+ | \frac{1}{v \cdot D} | y_+ \rangle \langle y_+ | \frac{1}{v \cdot D} | z_+ \rangle = \langle x_+ | \frac{1}{v \cdot D} | z_+ \rangle = \mathbf{W}(x_+, z_+)$$

(15.12)

which is a property of the eikonalized and ordered Wilson line. More impotantly, we have the identity

$$
\begin{aligned}
& D_\nu(x_+)\mathbf{W}(x_+, y_+) - \mathbf{W}(x_+, y_+)D_\nu(y_+) \\
&= \langle x_+ | D_\nu \frac{1}{v \cdot D} - \frac{1}{v \cdot D} D_\nu | y_+ \rangle = \langle x_+ | \frac{1}{v \cdot D} [v \cdot D, D_\nu] \frac{1}{v \cdot D} | y_+ \rangle \\
&= \langle x_+ | \frac{1}{v \cdot D} (-iv_\mu F_{\mu\nu}) \frac{1}{v \cdot D} | y_+ \rangle = \int_{-\frac{1}{2}Z_+}^{+\frac{1}{2}Z_+} dz_+ \, \mathbf{W}(x_+, z_+)(-iv_\mu F_{\mu\nu})(z_+)\mathbf{W}(z_+, y_+)
\end{aligned}
$$

(15.13)

The end-point derivative of a Wilson line, amounts to an insertion of a pertinent field strength (plaquette in a lattice form) along the line,

$$v_\mu F_{\mu\nu} = v_4 F_{4\nu} + v_3 F_{3\nu} = \cos\theta F_{4\nu} + \sin\theta F_{3\nu} \tag{15.14}$$

Finally, we have the large $|z_+| \to \infty$ identity

$$\mathbf{W}(y, z_+; x, z_+) D_\alpha(x, z_+) \mathbf{W}(x, z_+; y, z_+) \to \partial_\alpha^y \tag{15.15}$$

as the fields are assumed to vanish at asymptotic z_+. A repeated use of (15.12-15.15) allows to simplify (15.11).

15.A.3 Resulting spectrum

The sum of the spin contributions to the squared mass operator on the light front in the instanton vacuum, is now explicit and of the form

$$
\begin{aligned}
M_{SD,I}^2(\xi_x, b_\perp) = 2M V_{SD,I}(\xi_x, b_\perp) = 2M \ \Bigg(&\left[\frac{\sigma_1 \cdot (b_{12} \times s_1 \hat{3})}{4m_{Q1}} - \frac{\sigma_2 \cdot (b_{21} \times s_2 \hat{3})}{4m_{Q2}} \right] \frac{1}{\xi_x} V_C'(\xi_x) \\
&+ \left[\frac{\sigma_1 \cdot (b_{12} \times s_1 \hat{3})}{2m_{Q1}} - \frac{\sigma_2 \cdot (b_{21} \times s_2 \hat{3})}{2m_{Q2}} \right] \frac{1}{\xi_x} \mathbb{V}_1'(\xi_x) \\
&+ \left[\frac{\sigma_2 \cdot (b_{12} \times s_1 \hat{3})}{2m_{Q2}} - \frac{\sigma_1 \cdot (b_{21} \times s_2 \hat{3})}{2m_{Q1}} \right] \frac{1}{\xi_x} \mathbb{V}_2'(\xi_x) \\
&+ \frac{1}{4m_{Q1}m_{Q2}} \sigma_{1\perp i} \sigma_{2\perp j} \left[\left(\hat{b}_{21i}\hat{b}_{21j} - \frac{1}{2}\delta_{\perp ij} \right) \mathbb{V}_3(\xi_x) \right] \Bigg)
\end{aligned}
\tag{15.16}
$$

with $b_{21} = -b_{12} = b_\perp$ and $s_{1,2}$ the signum of the velocity along the 3-direction (sign of the helicity). All spin potentials $\mathbb{V}_{1,2,3}(\xi_x)$ are tied to the central potential $\mathbb{V}_C(\xi_x)$ in the instanton vacuum,

$$\mathbb{V}_2(\xi_x) = \mathbb{V}_1(\xi_x) + V_C(\xi_x) \to \frac{1}{2}V_C(\xi_x) \qquad \mathbb{V}_3(\xi_x) = \frac{2b_\perp^2}{\xi_x^2}\mathbb{V}_C''(\xi_x) \qquad \mathbb{V}_4(\xi_x) = 0 \tag{15.17}$$

While on the light front $\mathbb{V}_{2,4}(\xi_x)$ are no longer tied by the Bianchi-identity (covariantized Lenz law), we note that the leading contributions match the rest frame contributions at $\theta = 0$. Therefore, the rest frame relation $\mathbb{V}_2(R) = \frac{1}{2}V_C(R)$ in the instanton vacuum [Eichten and Feinberg, 1981] (note the sign convention difference), carries to the light front $\mathbb{V}_2(\xi_x) = \frac{1}{2}V_C(\xi_x)$. This is not the case for $\mathbb{V}_{3,4}(\xi_x)$.

A key feature of the spin orbit contributions in (15.16), is that a flip of a spin say σ_1, can be compensated by a flip in the sign of the helicity say s_1 or s_2. This is reminiscent of the rest frame symmetry of the spin-orbit interactions, that show that a flip in the spin can be compensated by a flip in the angular momentum, thereby preserving the total angular momentum. The light front Hamiltonian in the instanton vacuum, is the squared mass operator for a $Q\bar{Q} \equiv Q_1 Q_2$ pair, that includes the free plus the central contribution (15.17), and the spin contributions (15.16),

$$M^2 = \sum_{i=1,2} \frac{k_\perp^2 + m_{Qi}^2}{x_i} + 2M(V_C(\xi_x) + V_{SD,I}(\xi_x, b_\perp)) \tag{15.18}$$

with Bjorken $x_{i=1,2}$ and satisfying $x_1 + x_2 = 1$. A detailed analyses of the spectrum and light front wave-functions following from (15.18) as applied to heavy and light mesons, with comparative estimates from perturbative one-gluon exchange and confinement, will be detailed in a sequel.

15.B String induced scalar spin-orbit interaction

Most of the spin-orbit interaction mediated by perturbative one-gluon exchange and non-perturbative instanton interactions, at short and intermediate distances respectively is vector-like. In the standard constituent quark model it yields substantial spin-orbit splitting (of the order of 100 MeV and must be omitted to account for the phenomenological success of the constituent quark model in the description of light and heavy-light hadrons. In contrast, the induced spin-orbit coupling from a quantized NG string is scalar-like, with the same magnitude and opposite sign. A large cancellation between the vector and scalar spin-orbit contributions, is usually argued to take place.

To understand the origin of the scalar spin-orbit interaction induced by a confining string, consider the standard NG string with end-points, carrying equal mass and spin,

$$S = \sigma_T \int d\tau \, d\sigma \, \sqrt{h} + \int_B d\tau \left(M\sqrt{\dot{X}^2} - \frac{1}{2}\sigma_{\mu\nu}\frac{\dot{X}^\mu \ddot{X}^\nu}{\dot{X}^2} \right) \tag{15.19}$$

with the determinant

$$h = \det\left(\eta_{\mu\nu}\partial_a X^\mu \partial_b X^\nu \right) \tag{15.20}$$

The boundary spin factor enforces Thomas precession along each of the end-point world lines [Strominger, 1981, Polyakov, 1988]. Recall that 2 infinitesimal boosts are equivalent to 1 infinitesimal boost plus a Thomas precession. It is a Berry phase [Nowak et al., 1991]. Their contribution to the interaction potential is best seen by considering a specific solution to EOM following from (15.19),

$$\partial_\alpha\left(\sqrt{h}h^{\alpha\beta}\partial_\beta X^\mu \right) = 0 \tag{15.21}$$

subject to the spinless boundary conditions at $\sigma = \pm 1$

$$\sigma_T\sqrt{h}\partial_\sigma X^\mu \pm M\partial_\tau\left(\frac{\dot{X}^\mu}{\sqrt{\dot{X}^2}} \right) = 0 \tag{15.22}$$

The rotating string in the 12-plane is such a solution [Sonnenschein and Weissman, 2015] (and references therein), with the embedding

$$X^\mu = (\tau, r\sigma\cos(\omega\tau), r\sigma\sin(\omega\tau), 0) \tag{15.23}$$

which solves the EOM, and for which the boundary condition reduces to

$$\frac{\sigma_T}{\gamma} = \gamma M \frac{v^2}{r} \tag{15.24}$$

The end-point velocity is $v = \omega r$ and the Lorentz contraction factor is fixed by $1/\gamma^2 = 1 - v^2$. In (15.24) the tension in the string balances the centrifugation, with the correct relativistic gamma factors.

From the Noether currents following from Poincare symmetry, the energy is

$$P^0 = 2\gamma M + \frac{\sigma_T 2r}{v} \int_0^v \frac{dx}{\sqrt{1-x^2}} - \frac{1}{2}(\sigma_1^z + \sigma_2^z)\gamma^2 v^2 \omega$$

$$(15.25)$$

and angular momentum

$$J^z = 2\gamma M r^2 + \frac{2\sigma_T \omega}{v^3} \int_0^v \frac{x^2\, dx}{\sqrt{1-x^2}} + \frac{1}{2}(\sigma_1^z + \sigma_2^z)$$

$$(15.26)$$

The spin contribution to the rotating string can be recast using the boundary constraint (15.24)

$$V_{TSL}(r) = -\frac{1}{2}(\sigma_1^z + \sigma_2^z)\gamma^2 v^2 \omega = -\frac{1}{2}\frac{S^z L^z}{M^2 r}\frac{dV_C(2r)}{d2r}$$

$$(15.27)$$

with $L^z = mvr$ and $S^z = \frac{1}{2}(\sigma_1^z + \sigma_2^z)$ and the confining part of the central potential $V_C(r) = \sigma_T r$. It is the scalar spin-orbit coupling arising from Thomas precession, the resultant of successive boosts along the locus of the massive end-points with attached spins. This contribution from the confining string, was originally noted in [Buchmuller, 1982, Gromes, 1984, Pisarski and Stack, 1987].

We now note that the central contribution from the NG string, receives quantum corrections leading to the Arvis potential [Arvis, 1983]

$$V_C(r) = \left(\sigma_T^2 r^2 - \frac{D_\perp}{24\alpha'}\right)^{\frac{1}{2}} = \sigma_T(r^2 - r_c^2)^{\frac{1}{2}} \approx \sigma_T r - \frac{\pi D_\perp}{24r} - \frac{\pi^2}{2\sigma_T r^3}\left(\frac{D_\perp}{24}\right)^{\frac{1}{2}}$$

$$(15.28)$$

with $D_\perp = 2$, $\alpha' = l_S^2 = 1/2\pi\sigma_T$ and the critical string length

$$r_c = \pi\left(\frac{\alpha' D_\perp}{6}\right)^{\frac{1}{2}} \to \frac{\pi l_S}{\sqrt{3}}$$

The large distance expansion yields the linear confining part plus the universal Luscher term [Luscher and Palombi, 2010]. All the three contributions in (15.28) are well reproduced by the high precision QCD analysis of the inter-quark potential. The Arvis potential shows that the string contribution no longer applies for $r < r_c \approx l_S$.

If we regard the Arvis potential as a renormalized string tension $\sigma_T r \to \sigma_T(r)r$ that vanishes as $\sigma_T(r_c) = 0$, then its large distance suggests that the Thomas spin-orbit contribution in (15.27) receives a Luscher correction,

$$V_{TSL}(r) \approx -\frac{1}{2}\frac{S \cdot L}{M^2 r}\left(\sigma_T + \frac{\pi D_\perp}{24r^2}\right)$$

$$(15.29)$$

which is significant at intermediate distances, and similar to the one following from one gluon exchange

$$V_{GSL}(r) = \frac{1}{2}\frac{S \cdot L}{M^2 r}\frac{dV_G(r)}{dr} \approx -\frac{1}{2}\frac{S \cdot L}{M^2 r}\frac{C_{12}\alpha_s}{r^2}$$

$$(15.30)$$

with the color factor

$$C_{12} = \langle T_1^A T_2^A \rangle = -\frac{4}{3}\,(\text{meson}), -\frac{2}{3}\,(\text{baryon})$$

The remarkable phenomenological success of the Isgur and Karl analysis of the even and odd parity baryonic spectra [Isgur and Karl, 1978], made use of only the one-gluon exchange spin-spin and tensor inter-actions. The spin-orbit interaction (15.30) was deemed too strong, and altogether omitted. We have recently confirmed their observations [Miesch et al., 2023a]. This spin-orbit puzzle has been with us for decades.

We now suggest that the Luscher contribution to the spin-orbit emerging from the string through Thomas precession (15.29), may solve part of this puzzle. For $D_\perp = 2$, it is about the right magnitude but opposite sign, to balance the vector spin-orbit interaction originating from one gluon exchange,

$$C_{12}\alpha_s + \frac{\pi}{12} \approx 0 \qquad (15.31)$$

for a Coulomb coupling

$$\alpha_s \approx \frac{\pi}{16} \ \text{(meson)}, \ \ \frac{\pi}{8} \ \text{(baryon)}$$

The remaining long range scalar spin-orbit interaction in (15.29), proportional to the string tension, is also partly compensated by the vector spin-orbit interaction induced by instantons in the intermediate range [Shuryak and Zahed, 2021b]. These two observations explain why the spin-orbit interaction is absent in addressing the hadronic spectroscopy [Isgur and Karl, 1978, Miesch et al., 2023a], solving the puzzle.

15.2.1 QCD strings on the light front

15.3 Confinement in the basic relativistic meson problem

Confinement-one of the defining nonperturbative features of QCD-must be handled relativistically, even for constituent quarks traditionally treated by semiclassical potential models. Before turning to light-front quantization, it is useful to review the simplest relativistic model of meson confinement: two quarks of mass m_Q connected by a classical string with tension σ_T. This setting captures the essential physics of linear confinement and the emergence of Regge trajectories.

15.4 Confinement and rotating strings

Experimentally, excited mesons lie on nearly linear Regge trajectories,

$$J = a_M + \alpha' M_J^2, \qquad \alpha' = \frac{1}{2\pi\sigma_T},$$

with small deviations for heavy quark systems. The classical rotating string with massive endpoints reproduces this structure accurately [Sonnenschein and Weissman, 2014]. The empirical linearity of Regge trajectories for both light and heavy mesons motivates the use of the Nambu-Goto string supplemented with massive quark endpoints.

Working in the rest frame, the quark-string system is represented by a classical Hamiltonian derived from the Nambu-Goto action. For equal-mass quarks separated by r and rotating with angular momentum J, the Hamiltonian reads

$$H(r, p_r, J) = 2\sqrt{p_r^2 + m_Q^2 + \frac{J^2}{4r^2}} + \sigma_T r, \qquad (15.32)$$

where p_r is the radial momentum. The term $\sigma_T r$ represents the energy stored in the stretched flux tube between the quarks. For a fixed total energy E, the radial momentum takes the form

$$p_r^2(E, r) = \frac{1}{4}(E - \sigma_T r)^2 - m_Q^2 - \frac{J^2}{4r^2},$$

and the classical turning points $r_\pm$ are defined by $p_r(r_\pm) = 0$.

The spectrum follows from the WKB quantization rule

$$\int_{r_-}^{r_+} dr\, p_r(E, J) = \pi\left(n + \frac{1}{2}\right),\tag{15.33}$$

which encodes the relativistic dynamics exactly at the semiclassical level. Unlike the nonrelativistic case, the integral cannot be inverted analytically except in special limits. Numerical inversion yields the full radial spectrum $M_{n,J}$. In the limit of light quarks, an analytic approximation emerges:

$$M_{n,J}^2 \approx 4\pi\sigma_T\left(n + \frac{J}{2}\right),$$

which demonstrates simultaneous linear radial and orbital Regge trajectories. The combination $\frac{2m_Q}{/}E_n$ controls mass corrections. These corrections distort the low-lying part of the trajectory while leaving the high-n behavior essentially unchanged. This supports the conclusion that the rotating relativistic string with massive endpoints provides a realistic description of the observed meson spectrum.

15.4.1 Confinement for radial strings

For one half of the quark-string system the classical relativistic energy reads

$$E = \sigma_T r + \sqrt{p^2 + m_Q^2}, \qquad (E - \sigma_T r)^2 = p^2 + m_Q^2.$$

Quantization of this Klein-Gordon-type relation is subtle: for strictly linear $V(r) = \sigma_T r$ the spectrum suffers from the usual Klein paradox and cannot be defined nonperturbatively in terms of fixed particle number. We therefore use the semiclassical WKB approximation, which correctly captures the high-lying spectrum.

The momentum vanishes at a turning point $r = r_*$, and in the massless limit ($m_Q = 0$) $E = \sigma_T r_*$. For $r < r_*$ the motion is classically allowed, and the Bohr-Sommerfeld rule gives

$$n + \frac{1}{2} = \frac{2}{\pi}\int_0^{r_*} dr\, p(r, E_n).$$

For $J = 0$ and $V = \sigma_T r$ the integral can be carried out analytically, yielding

$$n = a_M + \alpha' E_n^2\left[\sqrt{1 - b^2} + b^2\ln\left(\frac{1 - \sqrt{1 - b^2}}{b}\right)\right], \qquad b = \frac{2m_Q}{E_n}.$$

The quantum shift a_M is not universal; following standard WKB practice we take $a_M = 1/2$, which is known to reproduce the light vector meson system satisfactorily. Other channels experience small additional shifts, plausibly due to spin interactions discussed later.

For arbitrary m_Q, this relation cannot be inverted analytically; numerical inversion gives M_n^2 for given n. For light quarks with $m_Q \simeq 0.35\,\text{GeV}$ and $\sigma_T = (0.42\,\text{GeV})^2$, the resulting radial trajectory is nearly linear in M_n^2, closely following the asymptotic massless prediction

$$M_n^2 \approx \frac{n + \frac{1}{2}}{\alpha'}.$$

Heavier quarks introduce curvature, as expected. Comparison with the experimental ω and ω_3 trajectories shows good agreement: the extracted σ_T matches that from heavy quarkonia, and the near-constant vertical shift between the two trajectories is consistent with two units of orbital excitation. The approximate relation $n + l = \text{const}$ often used phenomenologically works reasonably well for light quarks but is not expected to be exact for massive ones.

15.5 Confinement on the light front

Light-front quantization presents well-known challenges: boosting wave functions from the rest frame mixes Hamiltonian and momentum operators. Nevertheless, boost-invariant observables (such as M_n^2 and transverse momentum scales) can be compared directly between formulations.

15.5.1 Confinement in 1+1 dimensions

Chiral symmetry breaking generates an effective constituent mass $m_Q \approx 0.35\,\text{GeV}$. In equal-time quantization the free Hamiltonian is

$$P^0 = \sqrt{\mathbf{p}_q^2 + m_Q^2} + \sqrt{\mathbf{p}_{\bar{q}}^2 + m_Q^2}.$$

In light-front gauge $x^+ = \tau$ the on-shell relation $2p^+ p^- = m_Q^2$ yields the free light-front Hamiltonian,

$$P^- = \frac{m_Q^2 + p_{\perp q}^2}{2p_q^+} + \frac{m_Q^2 + p_{\perp \bar{q}}^2}{2p_{\bar{q}}^+}.$$

Confinement arises from the QCD string with tension $\sigma_T \approx (420\,\text{MeV})^2$. In $1+1$ dimensions the Nambu-Goto action reduces to [Bars, 1976a, Bars, 1976b]

$$P^- = \frac{m_Q^2}{2p_q^+} + \frac{m_Q^2}{2p_{\bar{q}}^+} + \sigma_T |x_{\bar{q}}^- - x_q^-|.$$

Introducing the CM and relative coordinates and momenta gives the meson mass operator

$$M^2 = \frac{m_Q^2}{x(1-x)} + 2\sigma_T\, |i\,\partial_x|,$$

with $x = p_q^+/P^+$ the Bjorken variable. Diagonalizing this operator yields the light-front wave functions $\varphi_n(x)$:

$$\left(\frac{m_Q^2}{x(1-x)} + 2\sigma_T |i\partial_x| \right) \varphi_n(x) = M_n^2 \varphi_n(x).$$

Using the Fourier representation of $|q|$, this becomes the 't Hooft equation,

$$M_n^2 \varphi_n(x) = \frac{m_Q^2}{x(1-x)} \varphi_n(x) - \frac{2\sigma_T}{\pi} \,\text{PV} \int_0^1 dy\, \frac{\varphi_n(y) - \varphi_n(x)}{(x-y)^2}.$$

The nonlocal kernel contains both a confining interaction and an induced self-energy term. Writing the equation as

$$M_n^2 \varphi_n(x) = \frac{m_Q^2 - 2\sigma_T/\pi}{x(1-x)} \varphi_n(x) - \frac{2\sigma_T}{\pi} \,\text{PV} \int_0^1 dy\, \frac{\varphi_n(y)}{(x-y)^2},$$

one sees that the negative induced self-energy cancels the positive string term for $m_Q \to 0$, giving a massless mode $\varphi_0(x)$ in the large-N_c limit, analog of a Nambu-Goldstone boson.

A semiclassical WKB treatment of the 't Hooft equation produces the Regge-like spectrum

$$M_n^2 - m_Q^2 \ln\left(\frac{x_+ \bar{x}_-}{x_- \bar{x}_+} \right) = 2\pi\sigma_T n,$$

with turning points

$$x_\pm = \frac{1}{2}\left(1 \pm \sqrt{1 - \frac{4m_Q^2}{M_n^2}}\right), \qquad M_n \geq 2m_Q.$$

For $m_Q \to 0$ this reduces to the open-string form $M_n^2 = n/\alpha'$, while for large n,

$$\varphi_n(x) \approx \sqrt{2}\,\sin((n+1)\pi x), \qquad M_n^2 \simeq \frac{n}{\alpha'} + 2m_Q^2 \ln n.$$
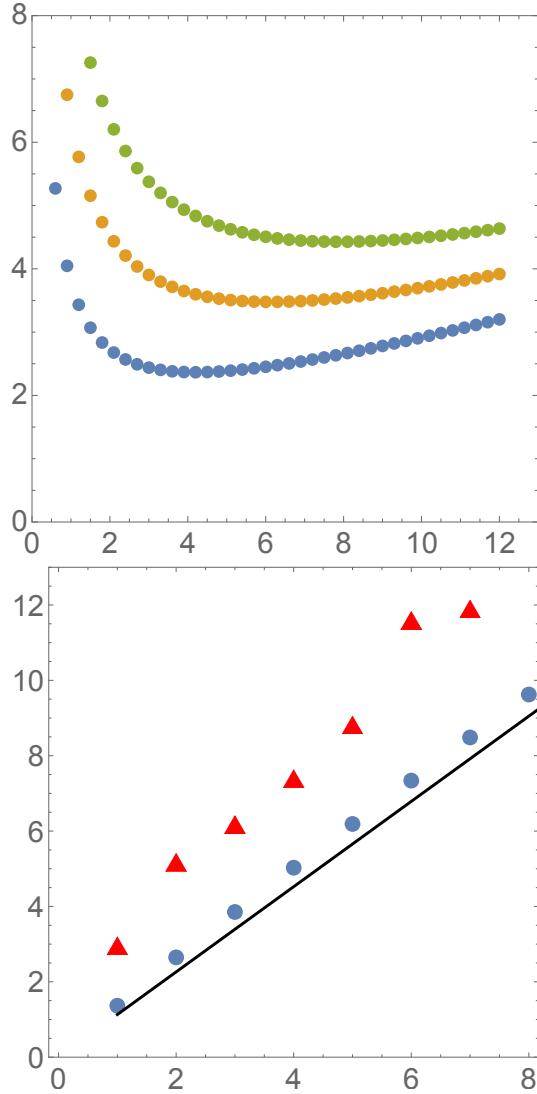
Fig. 15.5.1 The upper plot shows the dependence of the three lowest eigenvalues M_n^2 on the parameter a, in the region around their mimima. The lower plot shows M_{n+1}^2 versus $n+1 = 1..7$. The results obtained from the Hamiltonian diagonalization with fixed $a = 2.36$, are shown by red triangles. The blue disks are the semiclassical results discussed previously, the line is a simple linear expression $M_n^2 = n/\alpha'$, both shown for comparison.
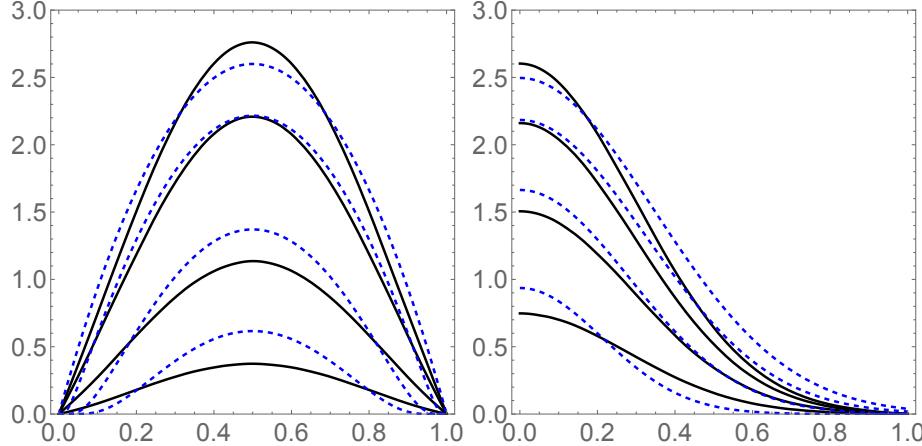
Fig. 15.5.2 The left plot shows the dependence of the ground state wave function $\Psi_0(x, p_\perp)$ versus x ar $p_\perp^2 = 0, 0.2, 0.4, 0.6\, GeV^2$, top to bottom curves. The right plot is versus $p_\perp$ at $x = 0.1, 0, 2, 0.3, 0, 4$. All solid curves are from the exact solution, while all dashed lines are for the simplified form

15.5.2 Eliminating the Square Root in the Light-Front Hamiltonian

To sidestep the nonlocal square root in the light-front Hamiltonian, we introduce an einbein parameter and define

$$M^2(a, b) = \frac{m_Q^2 + k_\perp^2}{x(1-x)} + \sigma_T \left(\frac{|i\partial_x|^2 + b\, x_\perp^2}{a} + a \right), \qquad (15.34)$$

with $a = 1/e$ and b tuned self-consistently so that $b \to M_{nl}^2$. Minimizing in a after diagonalization recovers the original form. To proceed, we decompose

$$M^2 = H_0 + V,$$

where

$$H_0 = \frac{\sigma_T}{a} \left(-\partial_x^2 - b\, \partial_{k_\perp}^2 \right) + \sigma_T a + 4(m_Q^2 + k_\perp^2), \qquad V = (m_Q^2 + k_\perp^2) \left(\frac{1}{x(1-x)} - 4 \right). \qquad (15.35)$$

With $b = (2m_Q)^2$, diagonalization of a truncated basis reveals shallow minima of $M_n^2(a)$; In [Shuryak, 2019] the value $a = 2.36$ yields a spectrum consistent with the expected Regge slope.

Using these fixed parameters, the lowest LFWF is well approximated by

$$\psi_1(\rho, x) \approx e^{-\beta^2 \rho^2/2} \sin(\pi x), \qquad \beta = \left(\frac{4a}{\sigma_T b} \right)^{1/4}, \qquad (15.36)$$

with higher harmonics suppressed at the percent level. The transverse width is

$$\langle p_\perp^2 \rangle = \frac{1}{\beta^2} = \sqrt{\frac{\sigma_T b}{4a}}.$$

A full numerical solution in (x, p_x, p_y) yields $M^2 \simeq 2.58\, \text{GeV}^2$ and a wave function matching the analytic form to high precision. A comparison to the common ansatz

$$\Psi_0(x, \xi) = 4C_2\, x(1-x)\, e^{-C_1 \xi^2}, \qquad \xi^2 = \frac{p_\perp^2}{x(1-x)},$$

shows qualitative agreement but endpoint deviations.

Chapter 16
Light quarks at the light front

16.1 Effective "constituent" quark mass and chiral condensate

Let us start this part, devoted to LF models, with discussion of the chiral condensate (14.32) and constituent quark mass (14.34). The reader may think this discussion is unnecessary, as are both frame invariant scalars. We however think that evaluating them in both frames (in fact, in the mean-field or large N_c approximation) would be still instructive[1].

Discussion of the chiral condensate are needed, as they would directly lead to the LF description of the pion and sigma mesons.

The light-front (LF) formulation of QCD provides a Hamiltonian description of hadronic structure in which observables are defined at fixed light-front time $x^+ = x^0 + x^3$ [Brodsky et al., 1998b] (and references therein). This representation diagonalizes the boosts along the z-axis, making it particularly suited to relativistic bound-state problems. However, the apparent simplicity of the LF vacuum contrasts strongly with the complex instant-form picture, where the ground state hosts condensates, instantons, and other nonperturbative excitations.

The resolution, as discussed in Ref. [Liu et al., 2023a], is that LF dynamics encodes the effects of the vacuum through *zero modes*, i.e. field components with longitudinal momentum $p^+ = 0$. These modes are responsible for reproducing chiral symmetry breaking, condensates, and anomalies, despite the vacuum apparent emptiness. The purpose of this chapter is to present a detailed explanation of how these zero modes generate the effective vacuum condensate $\langle \bar{q}q \rangle_{\text{LF}}$, and ensure equivalence with the instant-form theory.

16.2 Constituent Quark Mass and Chiral Condensate on the Light Front

In the preceding sections we have constructed the effective multi-fermion interactions emerging from the instanton liquid vacuum, projected them onto the light-front, eliminated the constrained ("bad") fermion components, and derived a light-front Hamiltonian expressed solely in terms of the dynamical ("good") fermion degrees of freedom. We now turn to show that this light-front Hamiltonian yields the same non-perturbative signatures of chiral symmetry breaking (namely a constituent quark mass and a nonvanishing chiral condensate) as found in the rest frame. In doing so, we demonstrate the frame-independence (boost invariance) of these emergent quantities, and thereby cement the physical equivalence between the instanton vacuum description in the rest frame and its light-front incarnation.

---

[1] Difficulties in deriving chiral symmetry breaking in LF formulation are well known in literature. An extreme point of view expressed in [Brodsky and Shrock, 2011] was that QCD vacuum is *empty* by itself, with nonperturbative phenomena ocuring only inside hadrons. We, on the other hand, treat LF not as a basis for fundamental theory, but simply a limit, from frame at rest to the large momentum limit. Thus, all Lorentz scalar must simply be preserved in that limit.

The starting point is the rest-frame (Euclidean signature) gap equation for the dynamical quark mass. Denoting by m the current (bare) quark mass, by g_S the effective 't Hooft coupling normalized by the number of colors, and by $F(k)$ the form factor arising from the zero-mode structure of the instanton ensemble, one obtains [Liu et al., 2023b, Liu et al., 2024d]

$$M(k) = m + 2\,g_S\,\int \frac{d^4q}{(2\pi)^4}\,\frac{4\,M(q)}{q^2 + M^2(q)}\,F(q)\,.$$

In the limit of low momenta ($k\rho \ll 1$), the running mass becomes approximately constant, $M(k) \approx M(0) \equiv M$. This nonperturbative constituent mass represents the dynamical breaking of chiral symmetry, induced by the nonlocal multi-fermion interactions mediated by instantons. In that way, the vacuum generates a "mass gap" even when the current mass m is small (or vanishing), characteristic of spontaneous chiral symmetry breaking.

On the light-front, after elimination of the bad components of the fermion fields in the mean-field approximation, only the good components, ψ_+, remain dynamical. The elimination process renormalizes the multi-fermion interactions and yields a dynamical constituent mass function $M(k^2)$ for the good-component quarks. The effective light-front quark propagator takes the form

$$S(k) \;\rightarrow\; \frac{i\left[\slashed{k} + M(k^2)\right]}{k^2 - M^2(k^2)} \;-\; \frac{i\,\gamma^+}{2k^+}\,,$$

where the second term arises from the constrained structure of the original fermion field. Using this propagator, one computes the scalar condensate on the light-front as

$$\langle\bar{\psi}\psi\rangle \;=\; -2\,N_c\,M\,\int \frac{dk^+\,d^2k_\perp}{(2\pi)^3}\,\frac{\epsilon(k^-)\,F(k^-)}{k^+}\bigg|_{k^- \frac{k_\perp^2 + M^2}{2k^+}}\,,$$

where $\epsilon(k^-)$ implements the light-front energy cutoff in the vacuum tadpole loops. In practice, with a suitable boost-invariant sharp cutoff, the integral yields a nonzero condensate, indicating that the vacuum structure on the light front is nontrivial, contrary to naive expectations of a "trivial LF vacuum."

A non-trivial and central result of the analysis is that the values of both the constituent mass M and the chiral condensate computed on the light front are identical to those obtained in the rest frame, within the mean-field approximation the authors employ. This equivalence follows from the fact that both quantities are Lorentz scalars (frame-independent), and that the form factors arising from the instanton zero modes (which encode the nonlocality in the interactions) are handled carefully so as to respect boost invariance. Thus the breaking of chiral symmetry, manifested in a finite mass gap and a nonzero condensate in the rest-frame approach, survives intact in the light-front description.

This equivalence has important physical implications. First, it dispels the common lore that the light-front vacuum must be trivial: rather, the nonperturbative vacuum dynamics (here encoded in instanton-induced multi-fermion interactions) are still present and generate nonzero condensates via tadpole effects of the constrained modes. Second, it establishes that partonic descriptions of hadrons built on the light-front can faithfully capture essential vacuum physics such as spontaneous chiral symmetry breaking. Consequently, light-front wavefunctions and partonic distributions derived from this formalism inherently carry nonperturbative chiral dynamics; e.g., the resulting meson wavefunctions yield the correct constituent mass and condensate values, ensuring consistency with rest-frame phenomenology.

The demonstration that the constituent quark mass and chiral condensate are the same on the light front and in the rest frame underscores the universality of vacuum-induced chiral symmetry breaking in QCD, independent of the quantization frame. It validates the use of the light-front Hamiltonian derived from the instanton liquid model (ILM), as a legitimate starting point for nonperturbative hadron structure. In particular, since this construction is based only on the emergent 't Hooft interactions from the ILM (with form factors determined by the quark zero modes), it brings a concrete and controlled realization of chiral

symmetry breaking into the light-front formalism. This sets the stage for subsequent analyses (as in later sections) of bound states such as pions and kaons, their light-front wavefunctions, distribution amplitudes and parton distributions – all grounded in the same nonperturbative vacuum physics that yields the constituent mass and condensate.

In summary, the core message that the nonperturbative vacuum structure of QCD, realized via instantons, survives the light-front quantization: the emergent constituent quark mass and scalar condensate remain nonzero and coincide with their rest-frame values. This result justifies the use of the light-front formalism for realistic hadron phenomenology in a framework that fully accounts for spontaneous chiral symmetry breaking.
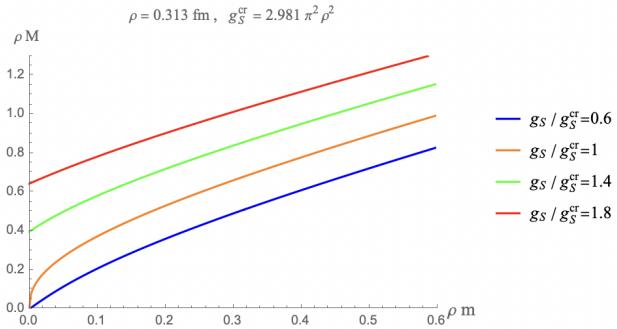
Fig. 16.2.1 Constituent mass as a function of the current mass with different scalar couplings g_S, for a fixed instanton size $\rho = 0.31$ fm.
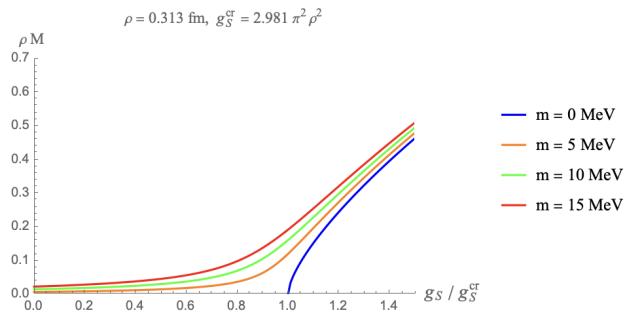
Fig. 16.2.2 Constituent quark mass versus the scalar coupling g_S.

16.3 LF sigma,pion wavefunctions vs those for "generic" mesons

Now, we can use the light front Hamiltonian (14.14) to solve the eigenvalue equation for the LF meson wave functions, in the mean-field or large N_c limit,

$$P^-|X,P\rangle = \frac{m_X^2}{2P^+}|X,P\rangle \tag{16.1}$$

When restricted to the lowest Fock component, the meson LF wavefunctions are of the form
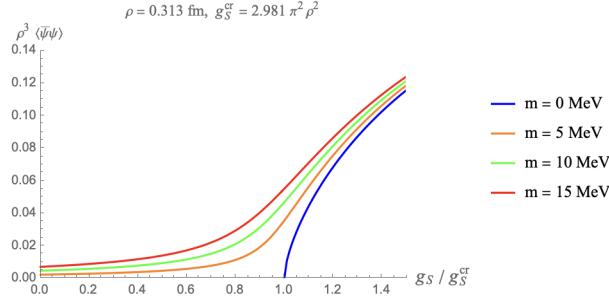
Fig. 16.2.3 Quark condensate as a function of the scalar coupling g_S.

$$|\text{Meson } X, P\rangle = \frac{1}{\sqrt{N_c}} \int_0^1 \frac{dx}{\sqrt{2x\bar{x}}} \int \frac{d^2k_\perp}{(2\pi)^3} \sum_{s_1, s_2} \Phi_X(x, k_\perp, s_1, s_2) b_{s_1}^\dagger(k) c_{s_2}^\dagger(P-k)|0\rangle \tag{16.2}$$

with the LF scattering normalization $\langle P|P'\rangle = (2\pi)^3 2P^+ \delta^3(P - P')$, or

$$\int_0^1 dx \int \frac{d^2k_\perp}{(2\pi)^3} \sum_{s_1, s_2} |\Phi_X(x, k_\perp, s_1, s_2)|^2 = 1 \tag{16.3}$$

In the sigma and pion channels, with the valence quark assignments

$$\sigma = \frac{1}{\sqrt{2}}(u\bar{u} + d\bar{d}) \qquad \pi^{\pm,0} = u\bar{d}, \ d\bar{u}, \ \frac{1}{\sqrt{2}}(u\bar{u} - d\bar{d}) \tag{16.4}$$

the LF vertices Φ_X (16.2) in the 2-particle Fock space take a simple form

$$\Phi_\sigma(x, k_\perp, s_1, s_2) = \phi_\sigma(x, k_\perp)\bar{u}_{s_1}(k)\frac{1}{\sqrt{2}}v_{s_2}(P-k)$$

$$\Phi_\pi^a(x, k_\perp, s_1, s_2) = \phi_\pi(x, k_\perp)\bar{u}_{s_1}(k)\frac{\tau^a}{\sqrt{2}}i\gamma^5 v_{s_2}(P-k) \tag{16.5}$$

The spin-flavor part is carried by the LF spinors $u_s(k)$ (particle) and $v_s(k)$ (anti-particle), with ϕ_X a scalar-isoscalar wavefunction at the origin of the mesonic distribution amplitude (see below). Inserting (16.5) in (16.2) and then in (16.1), and unwinding the various contractions from the 4-Fermi interaction terms, yield the boost invariant eigenvalue equation

$$m_X^2 \Phi_X(x, k_\perp, s_1, s_2) = \frac{k_\perp^2 + M^2}{x\bar{x}} \Phi_X(x, k_\perp, s_1, s_2)$$

$$+ \frac{1}{\sqrt{2x\bar{x}}}\sqrt{\mathcal{F}(k)\mathcal{F}(P-k)} \int_0^1 \frac{dy}{\sqrt{2y\bar{y}}} \int \frac{d^2q_\perp}{(2\pi)^3} \sum_{s,s'} \mathcal{V}_{s_1,s_2,s,s'}(k, P-k, q, P-q)\Phi_X(y, q_\perp, s, s')\sqrt{\mathcal{F}(q)\mathcal{F}(P-q)} \tag{16.6}$$

For the sigma and pion channels, the interaction kernels after contraction on the LF, are

$$\sum_{s,s'} \mathcal{V}_{s,s',s_1,s_2}(q, q', k, k')\Phi_\sigma(y, q_\perp, s, s')$$

$$= -g_S \alpha_+(P^+)\text{Tr}\left[(\slashed{q} + M)(\slashed{q}' - M)\right]\phi_\sigma(y, q_\perp)\bar{u}_{s_1}(k)\mathbf{1}\text{tr}(\mathbf{1})v_{s_2}(k') \tag{16.7}$$

$$= -4g_S\alpha_+(P^+)\left(\frac{q_\perp^2 + (y - \bar{y})^2 M^2}{y\bar{y}}\right)\phi_\sigma(y, q_\perp)\bar{u}_{s_1}(k)v_{s_2}(k')$$

$$\sum_{s,s'} \mathcal{V}_{s,s',s_1,s_2}(q,q',k,k')\Phi_\pi^a(y,q_\perp,s,s')$$

$$= -g_S\alpha_+(P^+)\mathrm{Tr}\left[(\not q + M)(\not q' + M)\right]\phi_\pi(y,q_\perp)\bar{u}_{s_1}(k)i\gamma^5\tau^b\mathrm{tr}(\tau^a\tau^b)v_{s_2}(k') \tag{16.8}$$

$$= -4g_S\alpha_+(P^+)\left(\frac{q_\perp^2 + M^2}{y\bar{y}}\right)\phi_\pi(y,q_\perp)\bar{u}_{s_1}(k)i\gamma^5\tau^a v_{s_2}(k')$$

The corresponding eigenvalue equations for the scalar-isoscalar wavefunctions ϕ_X are

$$m_\sigma^2\phi_\sigma(x,k_\perp) = \frac{k_\perp^2 + M^2}{x\bar{x}}\phi_\sigma(x,k_\perp)$$
$$- \frac{2g_S\alpha_+(P^+)}{\sqrt{x\bar{x}}}\sqrt{\mathcal{F}(k)\mathcal{F}(P-k)}\int\frac{dy}{\sqrt{y\bar{y}}}\int\frac{d^2q_\perp}{(2\pi)^3}\left(\frac{q_\perp^2 + (y-\bar{y})^2M^2}{y\bar{y}}\right)\phi_\sigma(y,q_\perp)\sqrt{\mathcal{F}(q)\mathcal{F}(P-q)} \tag{16.9}$$

$$m_\pi^2\phi_\pi(x,k_\perp) = \frac{k_\perp^2 + M^2}{x\bar{x}}\phi_\pi(x,k_\perp)$$
$$- \frac{2g_S\alpha_+(P^+)}{\sqrt{x\bar{x}}}\sqrt{\mathcal{F}(k)\mathcal{F}(P-k)}\int\frac{dy}{\sqrt{y\bar{y}}}\int\frac{d^2q_\perp}{(2\pi)^3}\left(\frac{q_\perp^2 + M^2}{y\bar{y}}\right)\phi_\pi(y,q_\perp)\sqrt{\mathcal{F}(q)\mathcal{F}(P-q)} \tag{16.10}$$

The solutions are generic,

$$\phi_X(x,k_\perp) = \frac{1}{\sqrt{2x\bar{x}}}\frac{C_X}{m_X^2 - \frac{k_\perp^2 + M^2}{x\bar{x}}}\sqrt{\mathcal{F}(k)\,\mathcal{F}(P-k)} \tag{16.11}$$

with C_X fixed by the normalization (16.3). It characterises the effective quark-meson coupling g_X in in a covariant formulation, i.e. $C_X = -\sqrt{N_c}g_X$ (the minus sign enforces spectral positivity). The pion is found to be strongly bound, and the sigma a threshold state.

16.4 Other light-front Hamiltonians

Jia and Vary [Jia and Vary, 2019] proposed a light-front Hamiltonian treatable via basis diagonalization, in analogy with atomic and nuclear structure methods. Their Hamiltonian contains effective quark masses, longitudinal and transverse confinement, and an NJL four-fermion term (not discussed here):

$$H = H_M + H_\| + H_\perp + H_{NJL}, \qquad H_M = \frac{m_Q^2}{x_1} + \frac{m_{\bar{Q}}^2}{x_2},$$

$$H_\| = \frac{\kappa^4}{(m_Q + m_{\bar{Q}})^2}\frac{1}{J(x)}\partial_x J(x)\partial_x, \qquad H_\perp = k_\perp^2\left(\frac{1}{x_1} + \frac{1}{x_2}\right) + \kappa^4 x_1 x_2 r_\perp^2,$$

where $J(x) = x_1 x_2$. With equal quark masses, $(1/x_1 + 1/x_2) = 1/(x_1 x_2)$.

Because both longitudinal and transverse confinements are quadratic, the Hamiltonian resembles coupled harmonic oscillators. In the basis constructed in [Jia and Vary, 2019], all terms except NJL become diagonal, yielding the analytic spectrum

$$M_{nml}^2 = (m_Q + m_{\bar{Q}})^2 + 2\kappa^2(2n + |m| + l_L + 3/2) + \frac{\kappa^4}{(m_Q + m_{\bar{Q}})^2}l_L(l_L + 1),$$

where n is the transverse oscillator number, m the helicity, and l_L the longitudinal index.

The light-front kinetic structure naturally produces the term $k_\perp^2/(x\bar{x})$, which couples transverse and longitudinal motion. The basis suppresses, but cannot fully remove, this mixing. Introducing the boost-

invariant variable $\zeta = k_\perp/\sqrt{x(1-x)}$ can simplify some expressions, but if performed exactly it generates additional kinetic contributions absent from the model.

Qualitatively, the spectrum grows linearly with the quantum numbers (n, m), consistent with Regge phenomenology. Quantitatively, however, the recommended confinement scale $\kappa = 0.227\,\mathrm{GeV}$ yields slopes far too small. Matching the observed radial and orbital Regge trajectories requires significantly larger κ (e.g. $\sim 0.5\,\mathrm{GeV}$). Spin splittings, such as the $\omega_3 - \omega$ mass gap, are also underestimated by nearly an order of magnitude.

Thus, while the Jia and Vary Hamiltonian captures the structural features of light-front confinement, its parameter tuning reflects the special low-lying π and ρ states (dominated by short-range spin and residual interactions) rather than the generic dynamics of excited mesons governed by confinement.

16.5 Central potential from instantons on the Light Front

Instantons provide localized semiclassical fluctuations of the gauge field. In the dense instanton liquid-including both dilute instantons and correlated $I\bar{I}$ molecules-one can reproduce the central potential at intermediate distances $r \sim 0.5\,\mathrm{fm}$ together with nonperturbative spin-independent forces. Their role on the light front follows from the dominance of instanton-induced magnetic fields in the relevant nonlocal correlators.

To extract the instanton-induced potential on the light front, we evaluate the connected part of the light-cone Wilson loop for a $Q\bar{Q}$ pair separated by a transverse distance $b_\perp$. As in Euclidean $Q\bar{Q}$ scattering, we assign a relative angle θ between Wilson lines, average over the instanton ensemble of density N/V_4, and analytically continue the result to the light front by $\theta \to -i\chi$ where χ is the rapidity difference.

More specifically, the connected loop exponentiates [Shuryak and Zahed, 2021b]

$$\langle W(\theta, 0_\perp)\, W^\dagger(\theta, b_\perp)\rangle_C = \exp\left[-\frac{2N}{2N_c V_4}\int d^4 z\, \mathrm{Tr}_c\left(1 - W_I(\theta, 0_\perp)\, W_I^\dagger(\theta, b_\perp)\right)\right],$$

with W_I the Wilson line evaluated in a single instanton field. For a sloped trajectory in singular gauge,

$$W_I = \cos\left(\pi - \frac{\pi\gamma}{\sqrt{\gamma^2 + \rho^2}}\right) - i\,\hat{n}^a \tau^a \sin\left(\pi - \frac{\pi\gamma}{\sqrt{\gamma^2 + \rho^2}}\right),$$

where

$$\gamma^2 = (z_4 \sin\theta - z_3 \cos\theta)^2 + (z_\perp - b_\perp)^2, \qquad n^a = \eta_{\mu\nu}^a \dot{x}^\mu (z-b)^\nu.$$

After integrating over the instanton position, the remaining dependence is encoded in a universal cylindrical integral,

$$\mathbf{I}(\xi), \qquad \xi = \frac{b_\perp}{\rho},$$

giving the Euclidean loop

$$\langle WW^\dagger\rangle_C = \exp\left[-Z_E^+ \frac{4\kappa}{N_c\rho}\mathbf{I}(\xi)\right], \qquad \kappa = \frac{N\rho^4}{V_4}.$$

Analytic continuation $Z_E^+ \to iZ_M^+$, $\theta \to -i\chi$ yields the LF Hamiltonian contribution

$$P_I^- = \frac{1}{\gamma_\beta}\left(\frac{4\kappa}{N_c\rho}\right)\mathbf{I}(\xi), \qquad \gamma_\beta = \cosh\chi.$$

Thus, the induced contribution to the invariant mass of the $Q\bar{Q}$ system is

$$M^2 = \frac{k_\perp^2}{x(1-x)} + 2P^+ P_I^- \approx \frac{k_\perp^2}{x(1-x)} + 2M\left(\frac{4\kappa}{N_c\rho}\right)\mathbf{I}(\xi),$$

with mass operator

$$M = \frac{|k_\perp|}{\sqrt{x(1-x)}} + \left(\frac{4\kappa}{N_c\rho}\right)\mathbf{I}(\xi) + \mathcal{O}(\kappa^2).$$

For small separations,

$$\mathbf{I}(\xi) \approx \alpha\xi^2, \qquad \xi \ll 1,$$

while for large ξ,

$$\mathbf{I}(\xi) \approx 2\Delta m_Q + \frac{C}{\xi^p}, \qquad p \ll 1.$$

Allowing the separation to include a longitudinal component $b_\mu = (0, b_\perp, b_3)$ modifies the geometry of the line-instanton interaction. After analytic continuation and conversion to dimensionless LF variables, the result is expressed through a generalized function

$$\mathbf{H}(\tilde{\xi}_x), \qquad \tilde{\xi}_x^2 = \frac{1}{(M\rho)^2}\left(\frac{d}{dx}\right)^2 + \frac{b_\perp^2}{\rho^2},$$

so that

$$M^2 \approx \frac{k_\perp^2 + m_Q^2}{x(1-x)} + 2M\left(\frac{4\kappa}{N_c\rho}\right)\mathbf{H}(\tilde{\xi}_x) \equiv \frac{k_\perp^2 + m_Q^2}{x(1-x)} + 2MV_C(\xi_x).$$

Its limiting forms are

$$\mathbf{H}(\tilde{\xi}_x) \approx c_2\tilde{\xi}_x^2 + c_4\tilde{\xi}_x^4 + \cdots, \qquad \tilde{\xi}_x \ll 1,$$

and at large distances,

$$\mathbf{H}(\tilde{\xi}_x) \approx \text{const} + \frac{C}{\tilde{\xi}_x^p}, \qquad p \ll 1.$$

16.5.1 Spin-dependent forces

In the instanton vacuum, spin-dependent interactions on the light front get a bit simpler, if one is using the self-duality of the gauge fields of instantons. Because E and B fields satisfy $BB = EE$ and $BE = \pm EE$, all spin potentials become linked to the central potential $V_C(\xi_x)$. Their construction parallels that detailed for the central potential. Unfortunately, fields of $I\bar{I}$ molecules are not selfdual, and their derivation should follow generic definitions.

16.5.2 Spin-spin interaction

The transverse chromoelectric correlator controls the spin-spin force. Using the rotation relating $v_\mu F_{\mu i}$ to E_i and its analytic continuation [Shuryak and Zahed, 2023a]

$$M_{SS}^2 = 2M\,\frac{\sigma_{1\perp i}\sigma_{2\perp j}}{4m_{Q1}m_{Q2}}R_{im}R_{jn}\,\partial_{1m}\partial_{1n}V_C(\xi_x),$$

showing that instanton-induced spin-spin forces depend entirely on second derivatives of V_C. Thus

$$\mathbb{V}_3(\xi_x) = \frac{2b_\perp^2}{\xi_x^2}V_C''(\xi_x), \qquad \mathbb{V}_4(\xi_x) = 0.$$

16.5.3 Spin-orbit structure

The spin-orbit potentials retain the rest-frame relation

$$\mathbb{V}_2(\xi_x) = \mathbb{V}_1(\xi_x) + V_C(\xi_x) \to \tfrac{1}{2}V_C(\xi_x),$$

valid in the instanton background. Light-front kinematics modifies the tensor structure, but the dependence on V_C persists. A spin flip may be compensated by a helicity flip, mirroring the rest-frame symmetry that preserves total angular momentum.

16.5.4 Light-front Hamiltonian

The squared-mass operator for a $Q\bar{Q}$ pair is

$$M^2 = \sum_{i=1}^{2} \frac{k_\perp^2 + m_{Qi}^2}{x_i} + 2M\big(V_C(\xi_x) + V_{SD,I}(\xi_x, b_\perp)\big),$$

with Bjorken fractions $x_1 + x_2 = 1$. The instanton-induced spin contribution is

$$V_{SD,I} = \frac{\sigma \cdot (b_\perp \times s)}{\xi_x}\left(V_C' + \mathbb{V}_1' + \mathbb{V}_2'\right) + \frac{\sigma_{1\perp i}\sigma_{2\perp j}}{4m_{Q1}m_{Q2}}\left(\hat{b}_i\hat{b}_j - \tfrac{1}{2}\delta_{ij}\right)\mathbb{V}_3,$$

with all $\mathbb{V}_{1,2,3}$ fixed by V_C. This compact structure encodes all instanton-mediated spin effects relevant for meson spectroscopy on the light front.

16.6 Spin interaction from a string on the light front

Spin-dependent forces induced by the confining QCD string have been analyzed extensively in the rest frame [Buchmuller, 1982, Pisarski and Stack, 1987, Gromes, 1984]. At large interquark separation R, the electric flux is localized within the string, so only the *self* spin-orbit (SO) terms survive. These originate mainly from Thomas precession and therefore carry a sign opposite to the familiar Coulombic SO force.

In the rest frame, and in the large-R limit, the surviving SO potential is

$$V_{LS}^{\text{string}}(R) \approx \left(\frac{\boldsymbol{\sigma}_1 \cdot \mathbf{L}_1}{4m_{Q1}^2} - \frac{\boldsymbol{\sigma}_2 \cdot \mathbf{L}_2}{4m_{Q2}^2}\right)\left(\frac{1}{R}V_C'(R) + \frac{2}{R}V_1'(R)\right), \tag{16.12}$$

with the convention $\mathbf{L}_1 = -\mathbf{L}_2 \equiv \mathbf{L}$. For the linear potential $V_C(R) = \sigma_T R$ and using $V_1(R) \approx -V_C(R)$ (the short-range cross-term V_2 vanishes at large R), (16.12) reduces to

$$V_{LS}^{\text{string}}(R) \approx \left(\frac{\boldsymbol{\sigma}_1 \cdot \mathbf{L}}{4m_{Q1}^2} - \frac{\boldsymbol{\sigma}_2 \cdot \mathbf{L}}{4m_{Q2}^2}\right)(1-2)\frac{\sigma_T}{R},$$

which displays the characteristic negative sign of the string-induced SO interaction. On the light front, this result translates to [Shuryak and Zahed, 2023a]

$$M_{LS,\text{string}}^2 \approx 2M\left[\frac{\boldsymbol{\sigma}_1 \cdot (\mathbf{b}_{12} \times s_1\hat{3})}{4m_{Q1}} - \frac{\boldsymbol{\sigma}_2 \cdot (\mathbf{b}_{21} \times s_2\hat{3})}{4m_{Q2}}\right](1-2)\frac{\sigma_T}{\xi_x}, \tag{16.13}$$

where $\mathbf{b}_{ij}$ is the transverse separation and ξ_x the longitudinal x-dependent measure of the string length on the light front.

As already noted in [Shuryak and Zahed, 2023a] (Appendix B), the SO potential following the Eichten-Feinberg analysis [Eichten and Feinberg, 1981] is larger by roughly a factor of two [Pineda and Vairo, 2001]. Importantly, the sign of (16.13) matches that of the string and of instanton effects in the dense regime, and is opposite to the perturbative Coulomb-exchange SO force (consistent with the original rest-frame findings [Buchmuller, 1982, Pisarski and Stack, 1987, Gromes, 1984].)

Chapter 17
Baryons at the light front

17.1 Confined N-quarks in 1+1 dimensions

For simplicity, consider first the dimensionally reduced "longitudinal" LF Hamiltonian for N confined quarks of equal mass,

$$H_{LF,L} = \sum_{i=1}^{N} \left(\frac{m_Q^2}{x_i} + 2\sigma_T \left| \frac{i\partial}{\partial x_i} \right| \right) \tag{17.1}$$

The corresponding WFs for N-quarks are solutions to

$$\sum_{i=1}^{N} \left(\frac{m_Q^2}{x_i} + 2\sigma_T \left| \frac{i\partial}{\partial x_i} \right| \right) \varphi_n[x] = M_n^2 \varphi_n[x] \tag{17.2}$$

giving mass squared of specific states.

Note that this Hamiltonian already includes two main nonperturbative phenomena in QCD. The first term is the kinetic energy, it includes effective "constituent" quark masses stemming from chiral symmetry breaking. The second, proportional to the string tension σ_T, describes quark confinement[1] It will be solved in momentum representation, so coordinates are present as a derivative over momenta.

The variables x_i are Bjorken-Feynman momentum fractions for N identical particles moving in a box $0 \leq x_i \leq 1$ and subject to the momentum constraint

$$X = \sum_{i=1}^{N} x_i = 1 \tag{17.3}$$

The condition (17.3) makes physical support of the problem nontrivial. It is $\tilde{N}$-simplex with one dimension lower $\tilde{N} = N - 1$. For baryons $N = 3$, the domain is an equilateral triangles, see Fig.17.10.1, and our solution for quantum mechanics on it was developed in [Shuryak and Zahed, 2021c]. For larger N the domain is the N-dimensional generalization of an equilateral triangle. For $N = 4$ it is a tetrahedron or 3-simplex, and for pentaquarks $N = 5$ it is the 4-dimensional 5-simplex with 5 corners, 10 edges and 10 triangular faces. The singular kinetic energy term forces the wavefunction to vanish at these boundaries (Dirichlet boundary condition). The shape of effective "cup potential" is shown in Fig.17.1.1 for the baryons.

To solve this problem, we proceed in three steps. First, we unwind the square roots by using the einbein trick

---

[1] For $N = 3$ quarks, it is similar to the baryonic equation derived in 2-dimensional QCD by [Bars, 1976a, Durgut, 1976].

$$\sum_{i=1}^{N} \left| \frac{i\partial}{\partial x_i} \right| = \sum_{i=1}^{N} \frac{1}{2} \left(\frac{1}{e_{iL}} + e_{iL} \left(\frac{i\partial}{\partial x_i} \right)^2 \right)$$

$$\rightarrow \frac{1}{2} \left(\frac{3}{e_L} + e_L \sum_{i=1}^{N} \left(\frac{i\partial}{\partial x_i} \right)^2 \right) \tag{17.4}$$

and assume equal $e_{iL} = e_L$ at the extrema, in the steepest descent approximation. Second, we diagonalize the free Laplacian after isolating the center of mass coordinate, using normal mode coordinates (analogue of Jacobi coordinates) see below. Third, we minimize the energies with respect to e_L.
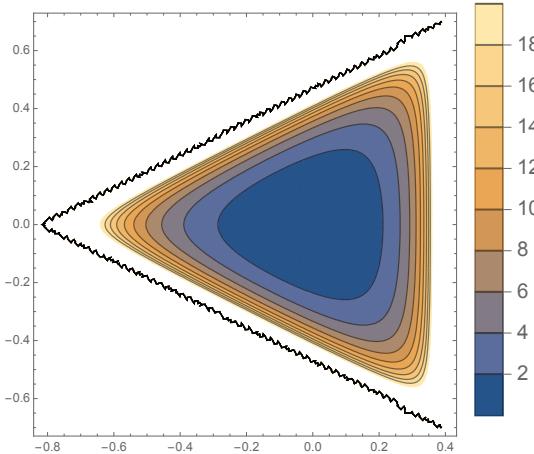
Fig. 17.1.1 Effective potential for equilateral triangular domain for $N = 3$ (three quarks).

The Hamiltonian and wave functions use momentum representation and Jacobi coordinates (so, unlike the group of Vary et al, we do not have issues with center-of-CM motion).

There are two methods to do quantum mechanics for such Hamiltonian:

(i) One is to work out complete set of eigenfunctions for Laplacian (the second term), and then representing the second term as a matrix. In some truncated form it can be diagonalized.

(ii) For a triangle, one can numerically solve Schrodinger equation, with laplacian and cup potential included, see [Shuryak and Zahed, 2022a].

17.2 LFWFs for baryons, including Delta and Nucleons

As an example of results derived in [Shuryak and Zahed, 2022a] let us show Fig.17.2.1 from it, comparing squared baryon masses calculated from LF Hamiltonian with experimental and lattice results, for same flavor baryons qqq, sss, ccc, bbb. Many more details, including explicit wave functions can be found in this paper.

Further study of baryons was done in [Shuryak and Zahed, 2023b]. The principle new element introduced compared to the previous work was quark-quark (or diquark) correlations. Let us remind that for light quarks those appear not only due to spin-spin pQCD attraction, but due to instanton-induced 'tHooft Lagrangian as well. Needless to say, such effects are important for nucleons, our main goal.

Diquark correlations of light quarks in nucleons and hadronic reactions, have been extensively discussed in the literature in the past decades, see e.g. [Carroll et al., 1968, Jaffe and Wilczek, 2003], and more recently in the review [Barabanov et al., 2021].
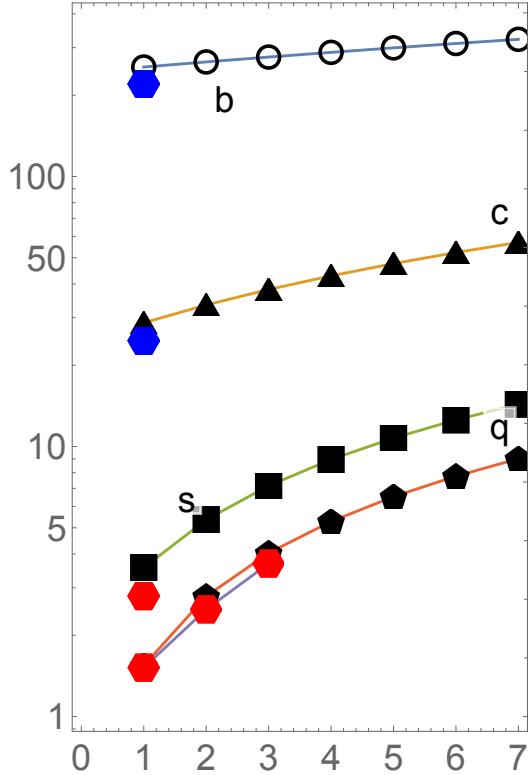
Fig. 17.2.1 Squared masses of baryons $M_{n+1}^2(Q, \frac{3}{2})$ in GeV^2, versus the principal quantum number $n + 1 = 1..7$. The black circles, triangles, squared and pentagons are results of our calculations for the flavors b, c, s, q. The red hexagons are the experimental values of three Δ^{++} and one Ω^- masses, from PDG. The two blue hexagons are model predictions for masses of ccc and bbb baryons.

In two-color QCD with $N_c = 2$, diquarks are baryons. In the chiral limit, QCD with two colors and flavors, admit Pauli-Gursey symmetry, an extended SU(4) symmetry that mixes massless baryons and mesons. In three-color QCD with $N_c = 3$, diquarks play an important role in the light and heavy light baryons.

The simplest way to understand diquark correlations in hadrons, is in single-heavy baryons where the heavy spectator quark compensates for color, without altering the light diquark spin-flavor correlations. A good example are Qud baryons, with Σ_Q composed of a light quark with a flavor symmetric assignment $I = 1, J^P = 1^+$, and Λ_Q composed of a light quark pair with a flavor asymmetric assignment $I = 0, J^P = 0^+$ state, the so called *bad* and *good* diquark states. Note that the latter has no spin, and thus no spin-dependent interaction with the heavy quark Q, while the former does. However, assuming that the standard spin-spin interactions are of the form $(\boldsymbol{\sigma}_1 \boldsymbol{\sigma}_2)$, this spin interaction can be eliminated as follows

$$M(1^+ud) - M(0^+ud) \approx \left((2M(\Sigma_Q^*) + M(\Sigma_Q)/3\right) - M(\Lambda_Q) \approx 0.21\,\text{GeV}$$

with the numerical value thus obtained from experimental masses of cud, bud baryons yields the binding of two types of light quark diquarks. We note tha the mass difference between heavy-light baryon and meson iof $m(Qud) - m(Qu) \approx 329\,MeV$, is close to a constituent quark mass. With antisymmetric color and spin wave function, scalar diquarks must also be antisymmetric in flavor: so those can only be ud, us, sd pairs. Those are called "good" diquarks in the literature, in contrast to the "bad" ones made of same flavor $dd, uu, ...bb$ and, by Fermi statistics, with a symmetric spin $S = 1$ wave functions. With antisymmetric color and spin wave function, scalar diquarks must also be antisymmetric in flavor: so those can only be ud, us, sd pairs. Those
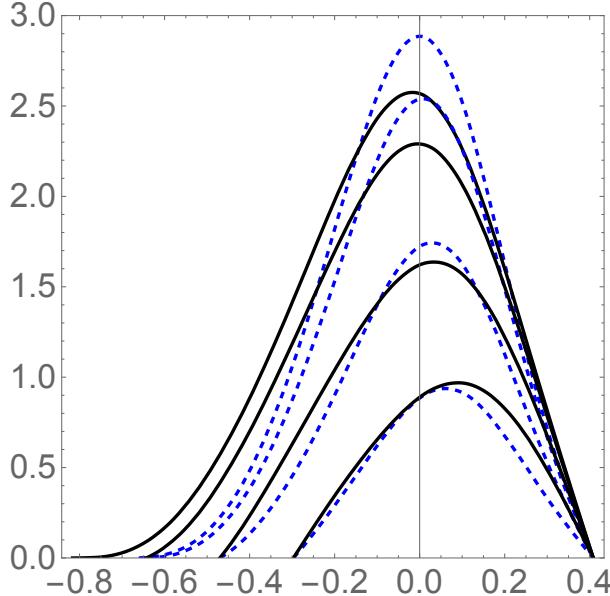
Fig. 17.2.2 LFWFs for the lowest Delta (dashed lines) and N (solid lines). The plots are shown versus the Jacobi coordinate λ, for fixed $\rho = 0, 0.1, 0.2, 0.3$, top to bottom.

are called "good" diquarks in the literature, in contrast to the "bad" ones made of same flavor $dd, uu, ...bb$ and, by Fermi statistics, with a symmetric spin $S = 1$ wave functions[2]

We would not go in detail description of how diquark correlations in LF wave functions were taken into account in [Shuryak and Zahed, 2023b]. Let us just mention that we started from Qqq Λ_c-type baryons with only one light diquark, and proceed to nucleons posessing pairing in both ud channels. The resulting effect of diquark pairing leads to difference between LF WFs for flavor-symmetric Delta baryons and the nucleons, see Fig.17.2.2

17.3 Formfactors and GPDs of Delta and Nucleons

In this section we examplify our main point: the LFWFs (e.g. those defined above) provide full description of the state, directly leading to all kind of formfactors, and distributions (PDFs,GPDs etc).

We start with electromagnetic (virtual photon) formfactors, following from longitudinal wave functions for the Delta and Proton shown in Fig17.3.1. In order to emphaseise better the most interesting region of intermediate q^2, we plot $Q^4 F_1^d(Q^2)$, see Fig.17.3.1.

Experiments are of course done with protons and neutrons, but using them one can extract separate formfactors for u or d quarks. This was done e.g. in [Qattan and Arrington, 2012], and the red circles in Fig.17.3.1 are from Fig.8 of this work. (For clarity we do not show the datapoints in the range $Q^2 < 1\,GeV^2$, as the error bars for these points are ± 0.02 on average.) From the plot, we see that this formfactor does not appear to reach a constant at experimentally available Q^2, and the measured points slowly decreasing towards the right hand side. Old dipole parametrization $Q^4 F = Q^4/(1+Q^2/m_\rho^2)^2$ also asymptotes a constant at large Q^2, but of a completely different magnitude.

---

[2] Realization that diquarks would turn to Cooper pairs in dense quark matter, as pointed out in [Rapp et al., 1998, Alford et al., 1998]. For a pedagogical review on "color superconductivity" see e.g.[Schäfer and Shuryak, 2001].
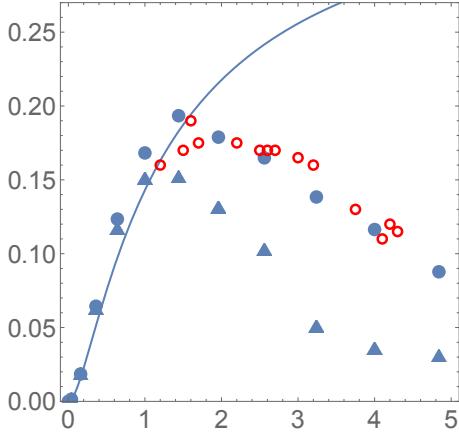
Fig. 17.3.1 $Q^4 F_1^d(Q^2)$, (GeV^4) versus the momentum transfer Q^2 (GeV^2). The triangles and closed points correspond to the Delta and Proton LFWFs, respectively. The red circles are extraction from the experimental data on the p and n formfactors mentioned in the text. The solid line shown for comparison, corresponds to the dipole form factor $Q^4/(1 + Q^2/m_\rho^2)^2$.

Remarkably, our longitudinal proton wave functions reproduces such a trend, and (with the parameter $A = 4\,GeV^{-2}$) they follow the shape indicated by the data rather well. The calculated formfactor for the case when the struck quark is u has a similar shape. Unfortunately, according to [Qattan and Arrington, 2012], the experimental trend is different, the constant at $Q^2 \to \infty$ is approached from below. By the Drell-Yan relation this flavor difference is also seen in the PDFs of u and d at $x \to 1$. Flavor asymmetry must be related with the asymmetry of the spin-orbit part of the wave function, which in our approximations is so far ignored.

Note that the corresponding formfactor for Delta (triangles) is significantly softer, as one would expect from the size of the wave function. Recall that the large difference between the Delta and Proton formfactors (so well seen in this plot) is completely due to the 't Hooft quasi-local pairing ud interaction. We also calculated gravitational formfactors from the same LFWFs, see Fig.17.3.2
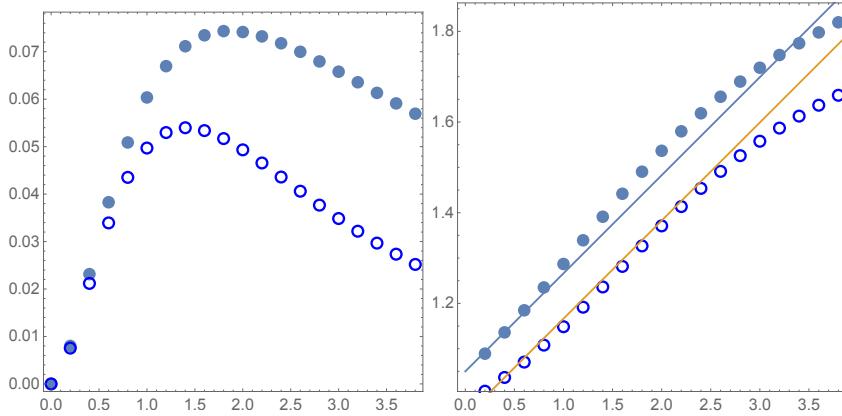
Fig. 17.3.2 Scaled gravitational form factor $Q^4 A_d(Q^2)$ in GeV^4 versus Q^2 in GeV^2 (top), for the struck d-quark in a nucleon (closed-points) and the isobar (open-points). Ratio of the gravitational to electromagnetic formfactors $3A^d(Q^2)/F_1^d(Q^2)$ versus Q^2 in GeV^2 (bottom), for the nucleon (closed-points) and the isobar (open points).

The same LFWFs were used for evaluation of the "gravitational" formfactors. While not experimentally available, we can substitute electromagnetic current to stress tensor $T^{\mu\nu}$[3], as if it was scattering with a graviton. This formfactor described distribution of the energy/momentum inside baryons, rather than electric charge. The first moment of the unpolarized GPDs at zero skewness, is tied to the quark A, B form factors of the energy-momentum tensor [Belitsky and Radyushkin, 2005]

$$A(t) = \int dx\, x H(x, 0, t), \;\; B(t) = \int dx\, x E(x, 0, t) \tag{17.5}$$

They can be used to quantify the distribution of momentum, angular momentum and pressure-like stress, inside the nucleon [Polyakov and Schweitzer, 2018a] (and references therein). More specifically, the total nucleon angular momentum at this low-resolution, is given by Ji's sum rule [Ji, 1997b]

$$J = \frac{1}{2} = A(0) + B(0) \tag{17.6}$$

with the non-perturbative gluons implicit in the balance, as they enter implicitly in the composition of the LF Hamiltonian (mass, string tension, ...) for the constituent quarks. In Fig.17.3.2 (top) we show the numerical results for $Q^4 A^d$ versus Q^2 in GeV^2, for a struck d-quark, following from the integration of the unpolarized d-quark-A GPD, for the nucleon (filled-point) and Δ-isobar (open-point). Again, we observe that the isobar form factor falls faster than the mucleon form factor, an indication that the nucleon is more compact gravitationally than the isobar, with a smaller gravitational radius. In Fig.17.3.2 (top) we plot the ratio of the gravitational formfactor relative to the electromagnetic form factor, for the struck d-quark in the nucleon (filled-points) and isobar (open-points). The decrease in Q^2 of the gravitational form factor, is slower than the electromagnetic form factor for both hadrons. This means that the spatial mass distribution of the struck d-quark, is more compact than the spatial charge distribution.

Generalized Parton Distributions (GPDs) For the proton with quark assignment uud, we assume that the struck quark is d, with longitudinal momentum fraction x_3. In our (modified) Jacobi coordinates, this momentum fraction is directly related to the longitudinal variable λ. For the unpolarized d-quark GPD this amounts to integrating the off-forward LFWFs over 5 variables, the transverse momenta $\mathbf{p}_\rho, \mathbf{p}_\lambda$ and ρ for the nucleon. To proceed, we approximate the dependence on the transverse momenta $\mathbf{p}_\rho, \mathbf{p}_\lambda$ by Gaussians, which is quite accurate, and carry the integrals analytically. The remaining integration over ρ is performed numerically. We recall that the LFWFs are generated at a low renormalization scale, say $\mu_0 = 1$ GeV, with a nucleon composed of three constituent quarks, without constituent gluons.

In Fig.17.3.3 we show the unpolarized nucleon GPD for the struck d-quark, as a function of x, Q^2 and zero skewness. At small Q^2, the dependence on the longitunal parton momentum x, is that expected for a PDF with a maximum at $x = \frac{1}{3}$. At larger Q^2, the maximum of the GPD clearly shifts towards larger values of x. The GDP is not simply factorizable into the PDF times the form factor, which are separable in x and Q^2. The right shift in Fig.17.3.3 shows that the nucleon shape changes with x. This is a key point of interest to us, as we now proceed to detail these shape modifications.

Theoretical considerations [Guidal et al., 2005] have suggested that the GPDs can be approximated generically, by a "Gaussian ansatz" in the momentum transfer Q^2, with a width and a pre-exponent that are x-dependent

$$\mathrm{GPDs}(x, Q^2) \sim f_1(x)\, e^{-Q^2 f_2(x)} \tag{17.7}$$

We recall that the standard nucleon formfactors are dipole-like at low Q^2 (say lower than 10 GeV^2) with $F(Q^2) \sim 1/(m^2 + Q^2)^2$. At very large Q^2 it asymptotes to a constant $Q^4 F(Q^2) \to const$ which is fixed by the perturbative QCD scattering rule. In between, the Q^2 dependence remains an open issue.

---

[3] One more option sometimes discuss is the trace of the stress tensor, as if induced by a Higgs-like scalar. This formfactor gives distribution of the mass.
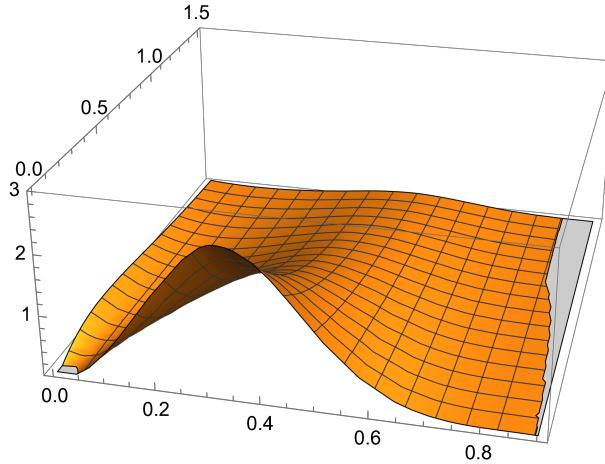
Fig. 17.3.3 The nucleon GPD function $H_d^N(x, \xi = 0, Q^2)$ for a struck d-quark.

Our LF formfactors were found to be consistent with these observations (see below), and our GPDs at fixed x are indeed numerically consistent with the exponent $exp[-\frac{Q^2 f_s(x)}{\sqrt{1-\xi^2}}]$ with no dependence of the pre-expont on the skewness, for $x > \xi$. (We have checked that the x-integration of this exponent with $\xi = 0$, returns the expected formfactor.)

The r.m.s. size $R_{r.m.s.}(x)$ is maximal at $x \sim \frac{1}{3}$, and is numerically about 0.6 fm. It decreases sharply for $x \sim 1$, and moderatly for $x \sim 0$. This can be explained by the fact that for $x \sim \frac{1}{3}$, all three quarks carry about the same longitudinal momentum on the LH, which corresponds to three quarks at rest in the CM or rest frame. Semiclassically, this means a configuration in which a struck quark is near a "turning points" of the wave function, with their QCD strings maximally streched. In contrast, x away from $\frac{1}{3}$, corresponds to a struck quark rapidly moving in the CM frame, which must happen near the hadron center, The corresponding size is therefore small. Note that for $x \to 1$, the distribution of the struck d-quark becomes nearly pointlike, with slopes close to zero. Our LFWFs show that the magnitude of this effect is different for nucleon and Δ-isobar, sensitive to the the diquark substructure of the former.

17.4 Applications to negative parity baryons

The aim of this work is to *derive* the light-front Hamiltonian and the corresponding wave functions (LFWFs), starting with the most basic meson settings and certain nonperturbative dynamics. In this methodical paper we will focus on "the main components" of the wave functions with zero orbital momentum, and ignore different spin structures. Its generalization to full wave functions, with all allowed spin and angular momentum values, will be done in the next papers of the series.

One Hamiltonian leads to an infinite set of wave functions, any of which have infinitely many matrix elements. LFWFs are mutually orthogonal and can be properly normalized. The DAs are normalized only to certain empirical constants, like f_π for a pion. The PDFs of baryons are traced over all quarks but one: tracing mixes together all sectors of the wave function, with different quantum numbers and even the number of partons. Due to quantum entanglement, it leads to an entropy.

It is improved in the LF frame, as the motion of all quarks gets "frozen" (see the right sketch), the distinctions between the heavy and the light quarks basically go away, as both can be "eikonalized" and

treated in fully relativistic formalism. If so, their interactions can be deduced from pertinent Wilson line correlators for any quarks.

17.5 Wilson lines dressed by spin variables

The perturbative contribution to the central potential on the light front, induced by a one-gluon exchange with an effective mass m_G in the RIV, can be constructed using the general technique of a sloped Wilson loop as we detailed in [Shuryak and Zahed, 2021b]. In particular, the one-gluon interaction with spin effects, follows by dressing the Wilson loop, with explicit spin factors

$$
\Big\langle \mathrm{Tr}\mathbf{P}\ \Big[\exp\Big(+g\int d\tau_1 (i\dot{x}(\tau_1)\cdot A(x(\tau_1)) + \frac{1}{4}\sigma_{1\mu\nu}F_{\mu\nu}(x(\tau_1))\Big)
$$
$$
\times \exp\Big(-g\int d\tau_2 (i\dot{x}(\tau_2)\cdot A(x(\tau_2) + \frac{1}{4}\sigma_{2\mu\nu}F_{\mu\nu}(x(\tau_2))\Big) \Big] \Big\rangle \tag{17.8}
$$

with $\sigma_{\mu\nu} = \frac{1}{2i}[\gamma_\mu, \gamma_\nu]$, and $\sigma_{\mu\nu} = \eta_{a\mu\nu}\sigma^a$ using 't Hooft symbol. The averaging is understood using the QCD action. We have made explicit the gauge coupling g, for a perturbative treatment to follow. For massive quarks traveling on straight trajectories, the affine time τ relates to the conventional time t through

$$
\mu = \frac{dt}{d\tau} = \frac{m_Q}{\sqrt{1+\dot{\mathbf{x}}^2}} \to \gamma m_Q \tag{17.9}
$$

in Euclidean signature. We note that the holonomies tracing out the Wilson loop are unaffected by the exchange $\tau \to t$, in contrast to the spin contributions which get rescaled by $1/\mu$. We now proceed to use (17.8) to derive the spin interactions for one-gluon exchange, followed by the ones induced by instantons, all in Euclidean signature. The upshot of this construction will be the derivation of the spin interactions on the light front for both the perturbative and non-perturbative contributions.

17.6 Central Coulomb interaction from one-gluon exchange

The Coulomb interaction between a $Q\bar{Q} \equiv Q_1 Q_2$ pair attached to the Wilson lines, can be obtained in perturbation theory by expanding the holonomies, and averaging the AA correlator in leading order. For that, we parametrize the world-lines by

$$
x_\mu(t_1) = (0, 0, \sin\theta\, t_1, \cos\theta\, t_1) \qquad x_\mu(t_2) = (b_1, b_2, \sin\theta\, t_2 + b_3, \cos\theta\, t_2) \tag{17.10}
$$

The perturbative one-gluon contribution from (17.8) reads

$$
g^2 T_1^A T_2^B \int dt_1 \int dt_2 \Big(\cos^2\theta \langle A_4^A(t_1)A_4^B(t_2)\rangle + \sin^2\theta \langle A_3^A(t_1)A_3^B(t_2)\rangle + 2\sin\theta\cos\theta \langle A_4^A(t_1)A_3^B(t_2)\rangle \Big)
$$
$$
\tag{17.11}
$$

with the gluon correlator in Feynman gauge

$$
\langle A_\mu^A(t_1)A_\nu^B(t_2)\rangle = \frac{1}{2\pi^2} \frac{\delta^{AB}\delta_{\mu\nu}}{|x(t_1)-x(t_2)|^2} \tag{17.12}
$$

Inserting (17.12) into (17.11) and changing variables $T_E = t_1 + t_2$ and $\tau = t_1 - t_2$, yield

$$\frac{g^2 T_1^A T_2^A}{2\pi^2} \int \frac{dT_E}{2} \int dt \frac{1}{t^2 + \cos^2\theta\, b_3^2 + b_\perp^2} = \frac{g^2 T_1^A T_2^A}{4\pi} \frac{T_E}{\sqrt{b_3^2 \cos^2\theta + b_\perp^2}} \tag{17.13}$$

The analytical continuation $\theta \to -i\chi$ and $T_E \to iT_M$ of (17.13), re-exponentiates to the Coulomb contribution

$$\exp\left[-i\gamma T_M \left(-\frac{g^2 T_1^A T_2^A}{4\pi} \frac{1/\gamma}{\sqrt{\gamma^2 b_3^2 + b_\perp^2}} \right) \right] \tag{17.14}$$

with γT_M the dilatated time along the light-like Wilson loop. The Coulomb contribution to the light front $Q\bar{Q}$ Hamiltonian P_{Cg}^- follows, leading the squared invariant mass as

$$2P^+ P_{Cg}^- = 2P^+ \left(-\frac{g^2 T_1^A T_2^A}{4\pi} \frac{1/\gamma}{\sqrt{\gamma^2 b_3^2 + b_\perp^2}} \right) \to 2M \left(-\frac{g^2 T_1^A T_2^A}{4\pi} \frac{1}{\xi_x} \right) = 2M \mathbb{V}_{Cg}(\xi_x) \tag{17.15}$$

with $P^+/M = \gamma$, and $\gamma b_3 \to id/dx/M$ the conjugate of Bjorken-x.

In the random instanton vacuum (RIV), the perturbative gluons acquire a momentum dependent mass from their rescattering through the instanton-anti-instanton ensemble [Musakhanov and Yakhshiev, 2021]

$$m_G(k\rho) = m_G \left(k\rho\, K_1(k\rho) \right) \qquad m_G \rho \approx 2 \left(\frac{6\kappa}{N_c^2 - 1} \right)^{\frac{1}{2}} \approx 0.55 \tag{17.16}$$

using the estimate $\kappa = \pi^2 \rho^4 n_{I+\bar{I}}$ in the right-most result. With this in mind, (17.15) is now

$$\mathbb{V}_{Cg}(\xi_x) = -\frac{g^2 T_1^A T_2^A}{2\pi^2} \frac{1}{\xi_x} \int_0^\infty \frac{dx\, x \sin x}{x^2 + (\xi_x m_G(x\rho/\xi_x))^2} \to -\frac{g^2 T_1^A T_2^A}{4\pi} \frac{e^{-m_G \xi_x}}{\xi_x} \tag{17.17}$$

with the right-most result following for a constant gluon mass.

17.7 Spin-spin interaction from one-gluon exchange

The perturbative spin-spin interaction follows from the cross term in (17.8)

$$-\frac{g^2}{16} \int d\tau_1 d\tau_2 \langle \sigma_{1\mu\nu} F_{\mu\nu}(x(\tau_1)) \sigma_{2\alpha\beta} F_{\alpha\beta}(x(\tau_2)) \rangle \tag{17.18}$$

Note that the perturbative electric field is purely imaginary in Euclidean signature, leading mostly to phases and not potentials in the long time limit. Also, the Dirac representation σ_{4i} is off-diagonal, an indication that the electric contribution mixes particles and anti-particles, which is excluded by the use of straight Wilson lines on the light front. With this in mind and using (17.9), we can reduce (17.18) to

$$-\frac{g^2}{4\mu^2} \int dt_1 dt_2 \langle \sigma_{1ij} F_{ij}(x(t_1)) \sigma_{2kl} F_{kl}(x(t_2)) = -\frac{g^2}{4\mu^2} \sigma_1^a \sigma_2^b \int dt_1 dt_2 \langle B_a(x(t_1)) B_b(x(t_2)) \rangle \tag{17.19}$$

with

$$\langle B_a(x(t_1)) B_b(x(t_2)) \rangle = T_1^A T_2^B \epsilon_{aij} \epsilon_{bkl} \partial_{1i} \partial_{2k} \langle A_j^A(x(t_1)) A_m^B(x(t_2)) \rangle$$
$$= T_1^A T_2^A (\delta_{ab} \delta_{ik} - \delta_{ak} \delta_{bi}) \partial_{1i} \partial_{2k} \times \frac{1}{2\pi^2} \frac{1}{|x(t_1) - x(t_2)|^2} \tag{17.20}$$

Inserting (17.20) into (17.19), and carrying the time integrations along the sloped Wilson loop, give [Shuryak and Zahed, 202

$$-\frac{g^2 T_1^A T_2^A}{4\pi}\frac{T_E}{4\mu^2}\left[\sigma_{1\perp}\cdot\sigma_{2\perp}\left(-3\cos^2\theta\frac{(\cos\theta\,b_3)^2}{\xi_\theta^2}+\cos^2\theta\right)\frac{1}{\xi_\theta^3}\right]\tag{17.21}$$

which is the dominant contribution under the analytical continuation $\theta\to-i\chi$, $\mu\to\gamma m_Q$ and $T_E\to iT_M$, in the ultra-relativistic limit $\gamma\gg1$, and in Minkowski signature. The final spin-spin contribution to the squared mass is in general

$$H_{SS}=2M\left[\frac{\sigma_{1\perp}\cdot\sigma_{2\perp}}{4m_{Q1}m_{Q2}}\left(\nabla_\perp^2\,\mathbb{V}_{Cg}(\xi_x)\right)\right]=2M\mathbb{V}_{SS}(\xi_x,b_\perp)\tag{17.22}$$

17.8 Spin-orbit interaction from one-gluon exchange

The cross spin-orbit interaction is readily obtained from the $12+21$ cross terms

$$-\frac{g^2 T_1^A T_2^B}{2}\,\sigma_2^a\int d\tau_1 d\tau_2\,i\dot{x}_i(\tau_1)\langle A_i^A(x(\tau_1)B_a^B(x(\tau_2)))\rangle+1\leftrightarrow2\tag{17.23}$$

which can be reduced to

$$-\frac{ig^2 T_1^A T_2^B\sin\theta}{2\mu}\sigma_2^a s_1\int dt_1 dt_2\langle A_3^A(x(t_1))B_a^B(x(t_2)))\rangle+1\leftrightarrow2\tag{17.24}$$

with $s_{1,2}=\mathrm{sgn}(v_{1,2}^3)$ the signum of the 3-velocity of particle 1,2 (a more refined definition will be given below). After carrying the integrations, and the analytical continuations, the spin-orbit contribution to the squared mass is

$$H_{SL,12}=2M\left[\left(\frac{\sigma_2\cdot(b_{12}\times s_1\hat{3})}{2m_{Q2}}-\frac{\sigma_1\cdot(b_{21}\times s_2\hat{3})}{2m_{Q1}}\right)\left(\frac{1}{\xi_x}\mathbb{V}'_{Cg}(\xi_x)\right)\right]\tag{17.25}$$

in general, with $b_{21}=-b_{12}\equiv b_\perp$.

The standard self spin-orbit interaction with Thomas precession is more subtle. To unravel it, we note that the insertion of a single spin contribution along the path-ordered Wilson loop amounts to expanding the spin factors in (17.8) to first order, and retaining the holonomies to all orders in $\mathbf{1}_\theta$, namely

$$\frac{1}{4\mu}\sigma_{1\mu\nu}\int dt_1\langle gF_{\mu\nu}(x(t_1))\,\mathbf{1}_\theta\rangle+1\leftrightarrow2\tag{17.26}$$

with the path ordered color-spin trace subsumed. Here $\mathbf{1}_\theta$ refers to the slated Wilson loop without the spin dressing. We now decompose

$$F_{\mu\nu}=v_{1\mu}v_{1\alpha}F_{\alpha\nu}+F_{\mu\nu}^\perp\equiv F_{\mu\nu}^{||}+F_{\mu\nu}^\perp\tag{17.27}$$

into a contribution parallel to $v_1=\dot{x}_1$ and a contribution orthogonal to v_1. The contribution parallel to the worldline when inserted in (17.26) can be undone by the identity (see Eq.71 in [Shuryak and Zahed, 2021b])

$$\int dt_1\langle gv_\alpha F_{\alpha\nu}(x(t_1))\,\mathbf{1}_\theta\rangle=-i\partial_{1\nu}\langle\mathbf{1}_\theta\rangle\equiv-i\partial_{1\nu}\,e^{-T_E\mathbb{V}_C(\xi_\theta)}\tag{17.28}$$

with $\mathbb{V}_C(\xi_\theta)\approx\mathbb{V}_{Cg}(\xi_\theta)$ the central Coulomb potential in perturbation theory. The longitudinal contribution to (17.26)

$$-\frac{1}{4\mu}\sigma_{1\mu\nu}v_{1\mu}i\partial_{1\nu}\,e^{-T_E\mathbb{V}_C(\xi_\theta)}+1\leftrightarrow 2$$

$$(17.29)$$

is gauge-invariant. After carrying the analytical continuation, (17.29) contributes both a real and imaginary part. The latter is an irrelevant phase factor in Euclidean signature. The *real* part contributes to the direct mass squared operator as

$$H_{LS,11}=2M\left[\left(\frac{\sigma_1\cdot(b_{12}\times s_1\hat{3})}{4m_{Q1}}-\frac{\sigma_2\cdot(b_{21}\times s_2\hat{3})}{4m_{Q2}}\right)\left(\frac{1}{\xi_x}\mathbb{V}'_{Cg}(\xi_x)\right)\right]$$

$$(17.30)$$

in leading order in perturbation theory. This is the standard spin-orbit contribution with the correct Thomson correction on the light front, familiar from atomic physics in the rest frame. The total perturbative spin contribution on the light front, is the sum of (17.22), (17.25) and (17.30),

$$H_{LS,g}=2M\left(\frac{l_{1\perp}\cdot S_{1\perp}}{2m_{Q1}^2}-\frac{l_{2\perp}\cdot S_{2\perp}}{2m_{Q2}^2}+\frac{l_{1\perp}\cdot S_{2\perp}}{m_{Q1}m_{Q2}}-\frac{l_{2\perp}\cdot S_{1\perp}}{m_{Q1}m_{Q2}}\right)\frac{1}{\xi_x}\mathbb{V}'_{Cg}(\xi_x)+2M\left(\frac{S_{1\perp}\cdot S_{2\perp}}{m_{Q1}m_{Q2}}\right)\nabla_\perp^2\mathbb{V}_{Cg}(\xi_x)$$

$$(17.31)$$

with the respective spins $\mathbf{S}_{1,2}=\boldsymbol{\sigma}_{1,2}/2$, and transverse orbital momenta

$$l_{1,2\perp}=\pm(b_\perp\times m_{Q1,2}s_{1,2}\hat{3})_\perp \qquad s_{1,2}=\mathrm{sgn}(v_{1,2})\to\frac{Mx_{1,2}}{m_{Q1,2}}$$

$$(17.32)$$

17.9 Instanton-induced spin forces

To construct the spin-dependent interactions in the ILM on the light front, we apply the general construction by Eichten and Feinberg [Eichten and Feinberg, 1981], to the slated Wilson loop in Euclidean signature, followed by the analytical continuation $\theta\to-i\chi$ to Minkowski signature. This construction was detailed earlier.

17.10 LF wave functions of baryons

The variables x_i are Bjorken-Feynman momentum fractions for N identical particles moving in a box $0\le x_i\le 1$ and subject to the momentum constraint

$$X=\sum_{i=1}^{N}x_i=1$$

$$(17.33)$$

The condition (17.33) makes physical support of the problem nontrivial. It is $\tilde{N}$-simplex with one dimension lower $\tilde{N}=N-1$. For baryons $N=3$, the domain is an equilateral triangles, see Fig.17.10.1, and our solution for quantum mechanics on it was developed in [Shuryak and Zahed, 2021c]. For larger N the domain is the N-dimensional generalization of an equilateral triangle. For $N=4$ it is a tetrahedron or 3-simplex, and for pentaquarks $N=5$ it is the 4-dimensional 5-simplex with 5 corners, 10 edges and 10 triangular faces.
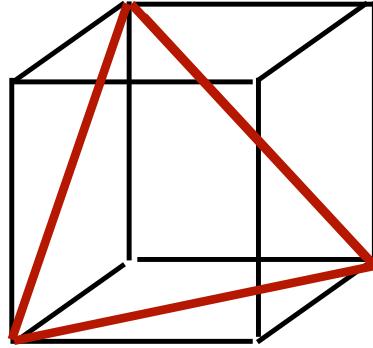
Fig. 17.10.1 equilateral triangle formed by cube $x_1, x_2, x_3 \in [0,1]^3$ cut by momentum normalization condition $x_1 + x_2 + x_3 = 1$

The singular kinetic energy term forces the wavefunction to vanish at these boundaries (Dirichlet boundary condition). The shape of effective "cup potential" is shown in Fig.17.1.1 for the baryons.

To solve this problem, we proceed in three steps. First, we unwind the square roots by using the einbein trick

$$\sum_{i=1}^{N} \left| \frac{i\partial}{\partial x_i} \right| = \sum_{i=1}^{N} \frac{1}{2} \left(\frac{1}{e_{iL}} + e_{iL} \left(\frac{i\partial}{\partial x_i} \right)^2 \right)$$

$$\rightarrow \frac{1}{2} \left(\frac{3}{e_L} + e_L \sum_{i=1}^{N} \left(\frac{i\partial}{\partial x_i} \right)^2 \right) \tag{17.34}$$

and assume equal $e_{iL} = e_L$ at the extrema, in the steepest descent approximation. Second, we diagonalize the free Laplacian after isolating the center of mass coordinate, using normal mode coordinates (analogue of Jacobi coordinates) see below. Third, we minimize the energies with respect to e_L.

The Hamiltonian and wave functions use momentum representation and Jacobi coordinates[4]. There are two methods to do quantum mechanics for such Hamiltonian:
(i) One, documented for triangle in [Shuryak and Zahed, 2021c], is to work out complete set of eigenfunctions for Laplacian (the second term), and then representing the second term as a matrix. In some truncated form it can be diagonalized.
(ii) For a triangle, one can also numerically solve Schrodinger equation, with laplacian and cup potential included[5].

---

[4] Therefore, unlike the group of Vary et al, we do not have issues with center-of-CM motion.

[5] Unfortunately, this way of solving the problem for larger dimensions - tetra, pentaquarks - have not yet been done.

Chapter 18
Pentaquarks on the light front

18.1 The A_4 simplex and the forward wave functions

The theory of hadrons on the light front largely parallels the discussion given above for mesons and baryons. The Hamiltonian is approximately a sum of (oscillator-like) Gaussian terms in transverse momenta, supplemented by a more complicated part depending on longitudinal momenta, or rather on Bjorken momentum fractions x_i, $i = 1, \ldots, 5$.

As usual, the first step is the elimination of the center-of-mass motion. As a result, the five momentum fractions are constrained to lie in the plane

$$\sum_{i=1}^{5} x_i = 1.$$

As in previous cases, this constraint is implemented using (modified) Jacobi coordinates $\alpha, \beta, \gamma, \delta$, which automatically incorporate this condition:

$$
\begin{aligned}
x_1 &= (6 + 15\sqrt{2}\alpha + 5\sqrt{6}\beta + 5\sqrt{3}\gamma + 3\sqrt{5}\delta)/30 \\
x_2 &= (6 - 15\sqrt{2}\alpha + 5\sqrt{6}\beta + 5\sqrt{3}\gamma + 3\sqrt{5}\delta)/30, \\
x_3 &= (6 - 10\sqrt{\beta} + 5\sqrt{3}\gamma + 3\sqrt{5}\delta)/30, \\
x_4 &= 1/10(2 - 5\sqrt{3}\gamma + \sqrt{5}\delta), \\
x_5 &= 1/5 - (2\delta)/\sqrt{5}
\end{aligned}
\tag{18.1}
$$

The corresponding four-dimensional simplex (similar to Fig. 17.10.1, but not plotted for obvious reasons) is known in mathematics as the A_4 simplex[1]. It has five corners, corresponding, as usual, to configurations in which one of the $x_i = 1$ and all others vanish. Their explicit locations in Jacobi coordinates are

$$
\begin{aligned}
a_1 &= \{1/\sqrt{2}, 1/\sqrt{6}, 1/(2\sqrt{3}), 1/(2\sqrt{5})\} \\
a_2 &= \{-(1/\sqrt{2}), 1/\sqrt{6}, 1/(2\sqrt{3}), 1/(2\sqrt{5})\} \\
a_3 &= \{0, -\sqrt{2/3}, 1/(2\sqrt{3}), 1/(2\sqrt{5})\} \\
a_4 &= \{0, 0, -(\sqrt{3}/2), 1/(2\sqrt{5})\} \\
a_5 &= \{0, 0, 0, -(2/\sqrt{5})\}
\end{aligned}
\tag{18.2}
$$

All corners have norm 4/5, and all ten mutual scalar products are equal to $-1/5$. Consequently, all angles between pairs of vectors $\theta_{i>j}$ are equal, with $\cos(\theta_{i>j}) = -1/4$.

---

[1] Our colloquial name for it is a "starfish". In *Wolfram Mathematica* we use the command `starfish = Simplex[a_1, \ldots, a_5]`, which constructs a simplex from a given set of points. This is particularly useful, for example, for defining integrals over this domain.

There are ten line segments connecting pairs of corners a_i, a_j with $i \neq j$, known as "edges". For example, the above expressions show that the edge connecting a_4 and a_5 lies in the $\alpha = \beta = 0$ plane. Associated with these edges are "faces" defined by triples of corners a_i, a_j, a_k $(i \neq j \neq k)$, such as $(1, 2, 3)$. These faces are two-dimensional equilateral triangles. By "across" we mean that the centers of edges, $(a_i + a_j)/2$, and the centers of complementary faces, $(a_i + a_j + a_k)/3$, are connected by straight lines passing through the global center $\alpha = \beta = \gamma = \delta = 0$.

Our task is now to formulate quantum mechanics on this simplex. As in the baryon case, the confining part of the Hamiltonian becomes a quadratic form, which in momentum space turns into a Laplacian:

$$M^2 = 2P^+P^- = H_{conf} + V_{cup} + 25\langle p_{\perp i}^2 + m_i^2 \rangle + H_{\lambda\lambda\sigma\sigma}. \tag{18.3}$$

The "cup potential" is defined as

$$V_{cup} \sim \left(\sum_1^5 \frac{(p_{\perp i}^2 + m_i^2)}{X_i} \right) - 25\langle p_\perp^2 + m^2 \rangle. \tag{18.4}$$

Its name reflects its shape: it rises sharply near all boundaries of the simplex and is near zero in the middle, $\alpha \approx \beta \approx \gamma \approx \delta \approx 0$. The third term is a constant subtracted from the potential for convenience, making it approximately zero at the center; it is correspondingly added to the confining part of the Hamiltonian. The final color-spin term will be discussed later.

To avoid divergences at the boundaries of the simplex, the wave functions must vanish there. More precisely, we restrict ourselves to cases with finite $\psi V \psi$, which requires the wave function to vanish near a boundary as $\psi \sim (A - A_{\text{boundary}})^p$ with power $p > 1/2$.

Using the Ritz variational approach, we start with the simple ansatz

$$\Psi_{faces} = \big(\prod_{i=1..5} x_i(\alpha, \beta, \gamma, \delta \in \text{"starfish"}) \big). \tag{18.5}$$

With the x_i given by Eq. (18.1), this ansatz not only enforces Dirichlet boundary conditions but is in fact close to the true ground state. Using the Ritz method with a correction function consisting of several Gaussians, we found that corrections are at the level of a few percent, which we neglect in what follows.

An alternative approach, also developed earlier for baryons and the Laplacian on a triangle, is based on constructing an appropriate superposition of plane waves. These waves must vanish on all ten faces of the A_4 simplex and be eigenfunctions of the Laplacian. The required number of plane waves is determined by the size of the relevant permutation group S_N: it is $3! = 6$ for baryons and $5! = 120$ for the "starfish". The details of this construction are given in Appendix 18.5.

The results of our study of wave functions on A_4 are summarized in two plots, corresponding to the ground S-shell and the first excited (P-shell) states. In Fig. 18.1.1 we show the shape of the ground-state Laplacian eigenfunction on A_4, and in Fig. 18.1.2 that of the first excited states. While the variational Ritz method successfully reproduces the overall shapes of these wave functions (indeed, these calculations were performed before we discovered the exact eigensystem in the mathematical literature), it does not accurately describe their asymptotic tails.

The pentaquark wave function provides a full description of the state, with all observables. For example, it yields readily the probability momentum fraction $P(x_{\bar{q}})$. This is achieved by integration of the wave function squared over α, β, γ variables , as a function of δ.

$$PDF = \int_{\alpha, \beta, \gamma} |\Psi|^2$$

(We recall that the 4-th Jacobi coordinate δ is directly related to the momentum fraction x_5, see (18.1).)
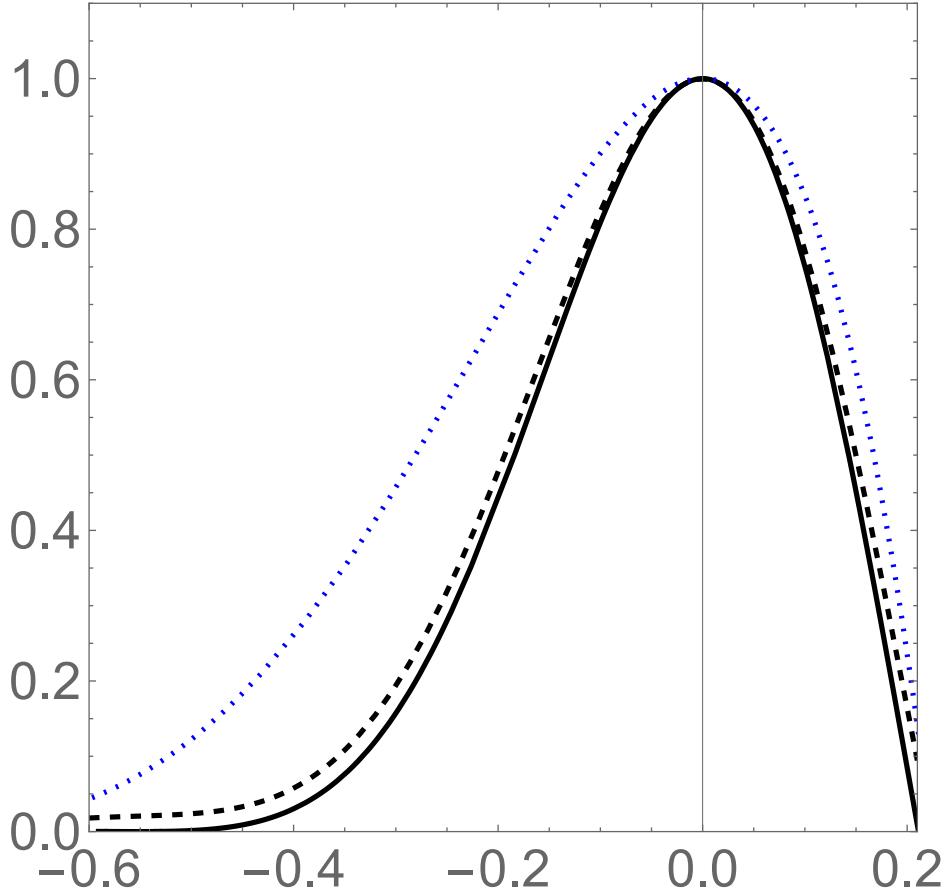
Fig. 18.1.1 The lowest Laplacian eigenfunction $\psi[1,1,1,1]$ at $\alpha = \beta = \gamma = 0$ versus δ (solid line) compared to our simplest variational function (18.5) (dotted line) and its improvement by Ritz variational procedure (dashed line). For a more clear comparison all are normalized to their value at the origin.

18.2 Pentaquark orbital-color-spin-flavor wave functions on the light front

The nontrivial part of the construction concerns the wave functions (WFs) depending on color, spin, and flavor variables. The essential difference from traditional spectroscopy in the center-of-mass (CM) frame is the symmetry structure: in the CM frame there is full spherical $O(3)$ symmetry, while on the light front (LF) only axial $O(2)$ symmetry remains. As a result, the usual classification in terms of J, L, and S is no longer available; instead, only the projections J_z, L_z, and S_z are good quantum numbers. LF wave functions of this type have been considered previously in the literature; see, for example [Ji et al., 2004b, Belitsky and Radyushkin, 2005].

Spectroscopy in the CM and on the LF therefore differs fundamentally due to the absence of spherical symmetry in the latter case. In the CM frame, a wave function with fixed total angular momentum and projection J, J_z (e.g. $J = 1/2$, $J_z = 1/2$) is constructed as a standard sum over orbital projections using Clebsch-Gordon coefficients,

$$\sum_{L_z} \binom{1/2, 1/2}{L, L_z, S, 1/2 - L_z} Y_{L, L_z}(\theta, \phi) |S, S_z\rangle,$$

which describes the addition of angular momenta $\mathbf{L} + \mathbf{S} = \mathbf{J}$. On the LF, however, the quantum numbers L and S are not defined. For example, in the P shell the three possible values $L_z = -1, 0, 1$ and the six possible

values $S_z = -5/2, -3/2, \ldots, 5/2$ can be combined freely, with the only global constraint being their sum J_z. Mixing of states with the same J_z is determined by the spin-dependent part of the Hamiltonian.

These mixing coefficients are to be fixed by diagonalizing the LF Hamiltonian. Components with $L_z = \pm 1$ correspond to adding one quantum of the transverse oscillator, while the $L_z = 0$ component contains an extra linear coordinate

$$z = -i\frac{\partial}{\partial p_z}\,.$$

Since in our previous paper [Miesch et al., 2025c] we derived pentaquark WFs in the S and P shells, all that is required here is to repeat the same procedure on the light front. In the S shell ($L = 0$), the only modification concerns the spin classification. For five quarks there are six possible values of the spin projection, $S_z = -5/2, -3/2, \ldots, 5/2$. The extreme case $S_z = 5/2$ corresponds to the unique fully symmetric spin state $\uparrow\uparrow\uparrow\uparrow\uparrow$. In this case, Fermi statistics is enforced entirely by the (nontrivial) color⊗flavor wave functions already constructed in [Miesch et al., 2025c] for isospin $I = 1/2$ and $I = 3/2$. (No states with $I = 5/2$ exist.)

For convenience, we reproduce a shortened version of the table from that work, which gives the number of antisymmetric states with fixed I and S_z:
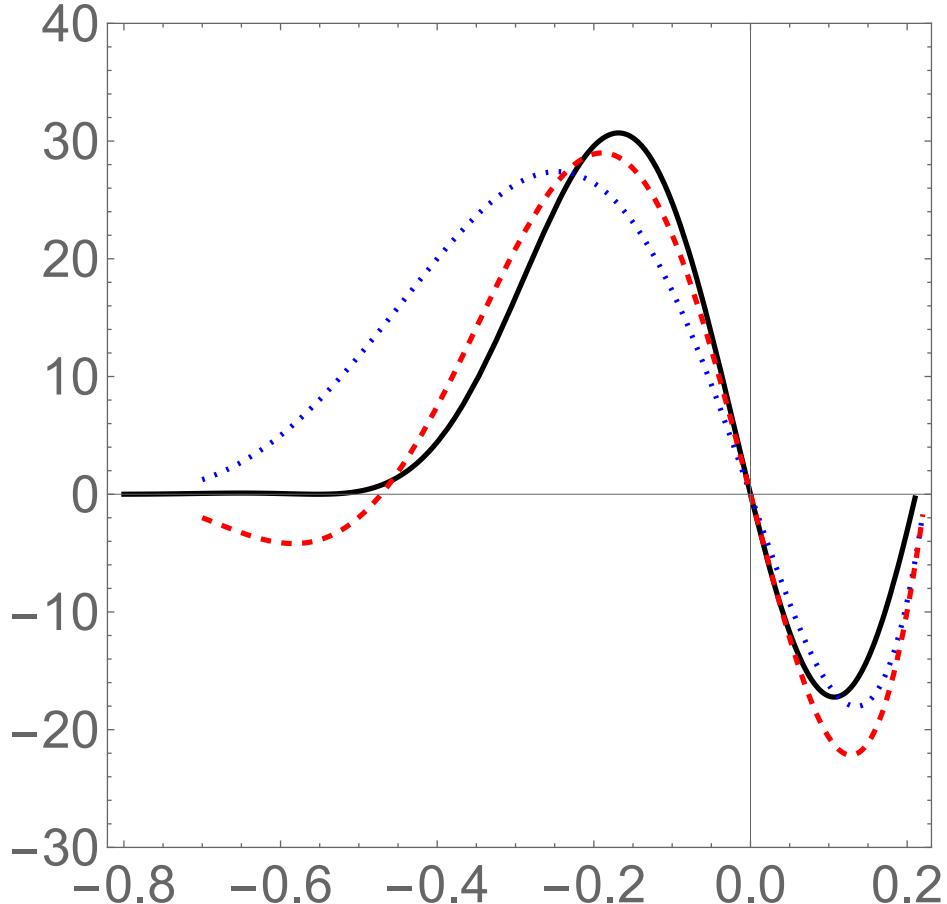
Fig. 18.1.2 Comparison between the shapes of the P-shell ($L = 1$) wave functions (arbitrary units) on 5-simplex A_4, at $\alpha = \beta = \gamma = 0$ as a function of δ. Black solid line is the exact Laplacian eigenstate with $\psi[\{2, 1, 1, 1\}]$, blue dotted is initial trial function (18.23) for $C = 0$, and red dashed is variational function with a single parameter, at value $C = 4.5$.

I/S_z	1/2	3/2	5/2
-5/2	1 (15)	1 (12)	0
-3/2	4 (75)	4 (60)	1 (15)
-1/2	7 (150)	7 (120)	2 (30)
1/2	7 (150)	7 (120)	2 (30)
3/2	4 (75)	4 (60)	1 (15)
5/2	1 (15)	1 (12)	0

Table 18.2.1 Spin projection S_z versus isospin I for antisymmetric pentaquark states with $L = 0$. Numbers in parentheses give the dimensions of the "good basis" used for constructing and diagonalizing permutation matrices.

With the new axially symmetric (I, S_z) classification, both the number of states and the permutation generators are organized differently. Generating the analogous table in the (I, S_z) basis, we find the same total number of states, albeit distributed differently among the spin projections.

It is instructive to explain how this counting is related to the CM-frame classification used in [Miesch et al., 2025c]. Consider, for example, the total number of states with $I = 1/2$. In the CM-frame table of [Miesch et al., 2025c], this number is

$$2 \times 3 + 4 \times 3 + 6 \times 1 = 24,$$

where the first factors are the multiplicities $2S + 1$ for fixed total spin S. On the LF, spherical symmetry is absent and the total spin S is not used. Instead, the same states are counted as

$$2(7 + 4 + 1) = 24,$$

where the factor of 2 accounts for the doubling due to negative values of S_z. Thus the same physical states are present, but organized differently. The different $2S + 1$ orientations of a spin-S multiplet, which are related by rotations in the CM frame, are no longer related on the LF, where only axial rotations preserving S_z remain.

We now introduce the color-spin Hamiltonian,

$$H_{\lambda\lambda\sigma\sigma} = -\sum_{i>j} V_{\lambda\lambda\sigma\sigma}^{ij}(\boldsymbol{\lambda}_i\boldsymbol{\lambda}_j)(\boldsymbol{\sigma}_i\boldsymbol{\sigma}_j), \tag{18.6}$$

and compute the Hamiltonian matrix including all states. Here the potential is replaced by its average value evaluated with the dominant symmetric WF, and back-reaction on the spins is neglected. Although the individual matrix elements are complicated $\mathcal{O}(1)$ numbers, diagonalization yields eigenvalues that reproduce exactly those found in the alternative classification of [Miesch et al., 2025c].

In particular, the seven states with $S_z = 1/2$ and $I = 1/2$ have energies

$$E_n = 4.6667, \ 3.0000, \ 1.4415, \ -2.7749,$$
$$-0.33333, \ -3.3333, \ -3.3333, \tag{18.7}$$

all of which were reported previously. The four states with $S_z = 3/2$ and $I = 1/2$ have energies

$$E_n = 3.000000, \ -0.3333333, \ -3.333333, \ -3.333333.$$

The repetition of eigenvalues between different S_z sectors is a consequence of the (now hidden) $O(3)$ symmetry of the Hamiltonian, which is not imposed explicitly but remains present.

Turning to what were formerly called P-shell states, which involve linear dependence on coordinates, one finds that the construction requires working in a space of monomials of dimension $4 \times 3^6 \times 2^5 \times 2^5$. In the CM frame, one adds angular momenta $\mathbf{L} + \mathbf{S} = \mathbf{J}$ and classifies states by J and J_z using Clebsch-Gordon coefficients. On the LF, this is replaced by the much simpler condition $L_z + S_z = J_z$.

For $I = 1/2$, $S_z = 1/2$, and nominal $L = 1$ states, the resulting energies are

$$E_n = 9.05,\ 9.05,\ -7.33,\ 4.67,\ 4.67,\ -3.33,$$
$$-\ 3.33,\ -3.33,\ -3.33,\ -3.33,\ -3.33,\ -3.33,$$
$$3.00,\ 3.00,\ 3.00,\ -2.77,\ -2.77,\ -2.77,$$
$$1.67,\ 1.67,\ 1.62,\ 1.62,\ 1.44,\ 1.44,$$
$$1.44,\ -0.333,\ -0.333, \tag{18.8}$$

with further repetitions for larger values of S_z due to the presence of multiple components with the same total J.

For baryon-pentaquark mixing, discussed below, one must use negative-parity P-shell ($L = 1$) pentaquark states. In the CM-frame treatment, this was achieved by using wave functions linear in the coordinates (on top of radial functions). As reviewed in [Miesch et al., 2025c], enforcing Fermi statistics leads to nontrivial orbital-color-spin-flavor structures; see Table IV of that work.

On the light front, the same construction applies. Linear dependence on coordinates is replaced by linear dependence on momenta. This change does not affect permutation properties, so the orbital-color-spin-flavor structure of the states remains unchanged. There are again two classes of structures: those with $L_z = \pm 1$, involving transverse momenta, and those with $L_z = 0$, involving longitudinal momenta. While Table IV of [Miesch et al., 2025c] lists antisymmetric $L = 1$ structures with all possible total spins S and isospins I, here we present the analogous classification in terms of spin projections S_z.

I/S_z	$1/2$	$3/2$	$5/2$
-5/2	3 (60)	3 (48)	1 (12)
-3/2	14 (300)	13 (240)	4 (60)
-1/2	27 (600)	24 (480)	7 (120)
1/2	27 (600)	24 (480)	7 (120)
3/2	14 (300)	13 (240)	4 (60)
5/2	3 (60)	3 (48)	1 (12)

Table 18.2.2 Spin projection S_z versus isospin I for antisymmetric pentaquark states with $L = 1$. Numbers in parentheses denote the dimensions of the corresponding "good basis".

For mixing with the nucleon, one must select pentaquark states with $I = 1/2$. We therefore focus on the 27 states with $S_z = 1/2$, corresponding to $J_z = 1/2$ and $L_z = 0$. These 27 P-shell wave functions are all fully antisymmetric under the quark permutation group S_4. The linear combinations of longitudinal momenta are then combined with the color, spin, and isospin structures constructed in our previous work.

18.3 Chiral evolution and flavor asymmetry of the sea

Our *starting point* is the well-known traditional quark model used in hadronic spectroscopy. The key phenomenon incorporated in this model is chiral symmetry breaking, which generates an effective mass for the "constituent quarks." For light quarks this mass is $m_q \sim 1/3\,\mathrm{GeV}$. This scale is much smaller than the induced mass of gluons, and therefore hadronic spectroscopy is traditionally described in terms of bound states of constituent quarks, while gluonic states or excitations are treated as "exotica." The conventional states are two-quark mesons and three-quark baryons, although tetraquarks $q^3\bar{q}$ and pentaquarks $q^4\bar{q}$ have also been observed recently, primarily with heavy-quark content.

The *first ark of the bridge* (described in detail in this series of works) is the transfer of such quark models from the center-of-mass frame to the light front. For the simplest cases-such as heavy quarkonia-this amounts to a change from spherical to cylindrical coordinates, followed by a transformation of longitudinal momenta into the Bjorken-Feynman variable x. In general, however, it is more convenient to start directly from light-

front Hamiltonians H_{LF} and perform their quantization. One important advantage is that no nonrelativistic approximation is required, so that heavy and light quarks are treated on the same footing.

The *second ark of the bridge* is constructed via *chiral dynamics*, which seeds the quark sea through the production of additional quark-antiquark pairs. Below we discuss how this can be implemented, both at first order in the 't Hooft effective action and via intermediate pions.

As the *third ark of the bridge*, we argue that one should employ the well-known DGLAP evolution of parton distribution functions (possibly with modifications), evolving down to a scale at which gluons are absent. At that point, the $q\bar{q}$ sea should be reduced to the component generated purely by chiral dynamics (step two). The antiquark flavor asymmetry $\bar{d} - \bar{u}$ provides a key diagnostic, since it cannot be generated by flavor-blind gluons and therefore cleanly separates gluonic and chiral contributions.

18.4 Properties of the "nucleon sea" and baryon-pentaquark mixing

18.5 Baryon-pentaquark mixing on the light front

In our paper [Shuryak and Zahed, 2023b] we employed a "radiative" (DGLAP-like) description, in which a $\bar{q}q$ pair is produced from one of the quarks. The mixing was attributed to the 't Hooft four-fermion Lagrangian, which allows the transition $u \to ud\bar{d}$ but not $u \to uu\bar{u}$. Another mechanism considered was production via an intermediate pion propagator. The probability, as a function of the momentum fraction of the initial quark, was convoluted with its PDF in the nucleon, e.g. $u_v^{\text{proton}}(x)$. In this approach, any interference between the newly created quark and the spectator quarks in the nucleon was neglected. Finally, these calculations were performed at the level of density matrices (PDFs), rather than using coherent wave functions.

It is worth noting that the observed flavor asymmetry of the antiquark sea, as well as the presence of significant orbital angular momentum, can both be traced to σ- and π-meson clouds in the nucleon. The technical description in [Miesch et al., 2025c] follows earlier literature and projects the baryon wave function, multiplied by mesonic operators T_σ and T_π, onto pentaquark states. The so-called meson-baryon-pentaquark overlap is given by an integral over all coordinates $\mathbf{x}_i$, $i = 1 \ldots 5$:

$$C_n = \int_x \Psi_n^{penta}(\mathbf{x}_i)\,\hat{T}(\mathbf{x}_4 - \mathbf{x}_5)\,B(\mathbf{x}_1, \mathbf{x}_2, \mathbf{x}_3). \tag{18.9}$$

The antiquark is associated with the last coordinate $\mathbf{x}_5$. All coordinates are expressed in terms of four Jacobi coordinates $\boldsymbol{\alpha}, \ldots, \boldsymbol{\delta}$. Each factor consists of a "main" (radial) wave function, depending on the corresponding hyperdistance (Y_5 for the pentaquark and Y_3 for the baryon), and the associated color-spin-flavor structure, represented as vectors in the corresponding "monom" spaces.

The present task is to reformulate all of these ingredients within the light-front framework. The baryon and pentaquark wave functions are modified accordingly.

The nucleon color-spin-flavor structure remains as described in our previous work. The radial wave function $B(Y)$, which depends on the hyperdistance $Y_B^2 = \boldsymbol{\alpha}^2 + \boldsymbol{\beta}^2$, is split into a product of functions depending on transverse and longitudinal momenta:

$$B(\mathbf{x}_i) \to B_\perp(\mathbf{p}_i^\perp)\,B_{\Delta 3}(\alpha, \beta).$$

The function $B_{\Delta 3}(\alpha, \beta)$ represents the ground-state baryon wave function on the triangle and depends on two momentum fractions.[2]

---

[2] For different baryons these fractions differ; for example, we discuss the difference between the Δ and nucleon cases due to the "good diquark" effect in the latter.

The procedure for the pentaquark is analogous, with the wave function factorizing into transverse and longitudinal components:

$$\Psi(\mathbf{x}_i) \to \Psi_\perp(\mathbf{p}_i^\perp)\,\Psi_{\Delta 5}(\alpha, \beta, \gamma, \delta).$$

This factorization reflects the independence of transverse and longitudinal variables in the light-front Hamiltonian employed. The longitudinal wave functions are defined on the 5-simplex $\Delta 5$, as introduced earlier in this paper.

An additional complication arises from the fact that admixtures with nucleon-meson configurations require P-shell pentaquarks. This is a nontrivial issue, since part of the center-of-mass wave function contains terms linear in the coordinates. Because these terms have nontrivial transformation properties under quark permutations, their treatment required extensive calculations of orbital-color-spin-flavor wave functions obeying Fermi statistics [Miesch et al., 2025c]. Upon boosting to the light front, one finds that longitudinal momenta satisfy $p_z \gg p_\perp$. As a result, the components with $L_z = \pm 1$, constructed from transverse momenta, become subleading, and only the $L_z = 0$ component survives. This leads to a significant simplification, since $J_z = S_z$. The longitudinal part is then generalized from the previously constructed orbital-color-spin-flavor wave functions, with the coordinates replaced by longitudinal momentum fractions $\alpha, \beta, \gamma, \delta$.

The mesonic operator $\hat{T}$ contains the $\bar{q}q$ vertex, which in coordinate space is conventionally written as a Gaussian $\exp[(\mathbf{x}_4 - \mathbf{x}_5)^2/2\rho^2]$. In momentum space this becomes the corresponding Gaussian form. We assume that the boost to the light front compresses hadrons longitudinally, leaving only the transverse-momentum dependence.

The operators providing the appropriate quantum numbers in $\hat{T}$ are $(\mathbf{S}\cdot\mathbf{L})$ for T_σ and $(\mathbf{S}\cdot\mathbf{p})$ for T_π. Here $\mathbf{S} = \mathbf{S}_4 + \mathbf{S}_5$ is the total spin of the quark-antiquark pair. Since boosts leave only rotations in the transverse plane, we make the replacement

$$(\mathbf{S}\cdot\mathbf{L}) \to S_z L_z.$$

For the pion-related operator the situation is different: longitudinal momenta dominate, and we therefore use

$$(\mathbf{S}\cdot\mathbf{p}) \to (S_4^z p_4 + S_5^z p_5).$$

The longitudinal momenta of the fourth quark and fifth antiquark are expressed in terms of the Jacobi variables γ and δ.

Finally, we address isospin in the $N+\pi$ and $\Delta+\pi$ channels. Unlike spin S, orbital angular momentum L, and total J, which are not good quantum numbers in the light-front formulation, isospin remains well defined. Adding a σ meson presents no difficulty, but adding a pion with $I_\pi = 1$ to a nucleon or Δ requires that the total isospin match that of the proton, $I = 1/2$, $I_z = 1/2$. This is achieved using standard Clebsch-Gordan coefficients:

$$|N\pi\rangle = \frac{1}{\sqrt{3}}|p\pi^0\rangle - \sqrt{\frac{2}{3}}|n\pi^+\rangle \tag{18.10}$$

$$|\Delta\pi\rangle = \frac{1}{\sqrt{2}}|\Delta^{++}\pi^-\rangle - \sqrt{\frac{1}{3}}|\Delta^+\pi^0\rangle + \frac{1}{\sqrt{6}}|\Delta^-\pi^+\rangle$$

In general, there are three possible admixtures to the nucleon, with overlap coefficients denoted by $C_{p\sigma}$, $C_{N\pi}$, and $C_{\Delta\pi}$. Although their contributions will eventually be summed, we study the three admixtures separately; see Table 18.5.1.

Using the 27 $L = 1$ pentaquark states defined above, we evaluated the projections of $p + \sigma$, $N + \pi$, and $\Delta + \pi$ states onto these configurations. The overlap coefficients C_n in Eq. (18.9) were calculated as described in the previous section, using appropriate combinations of coordinates in $|P_n\rangle$ together with the Ansatz function (18.5). In this calculation we included only functions normalized over momentum fractions $\alpha, \beta, \gamma, \delta \in$ starfish.

The individual 27 pentaquark states are not spherical, and we project onto baryon-plus-meson wave functions in which particles 1-3 form the baryon and particles 4-5 form the meson. Nevertheless, one of the admixtures turns out to be spherical:

$$\Delta\psi_{p\sigma} \cdot \Delta\psi_{p\sigma} \sim (\alpha^2 + \beta^2 + \gamma^2 + \delta^2).$$

This factor changes the shape of the wave function, which is shown in Fig. 18.5.1.
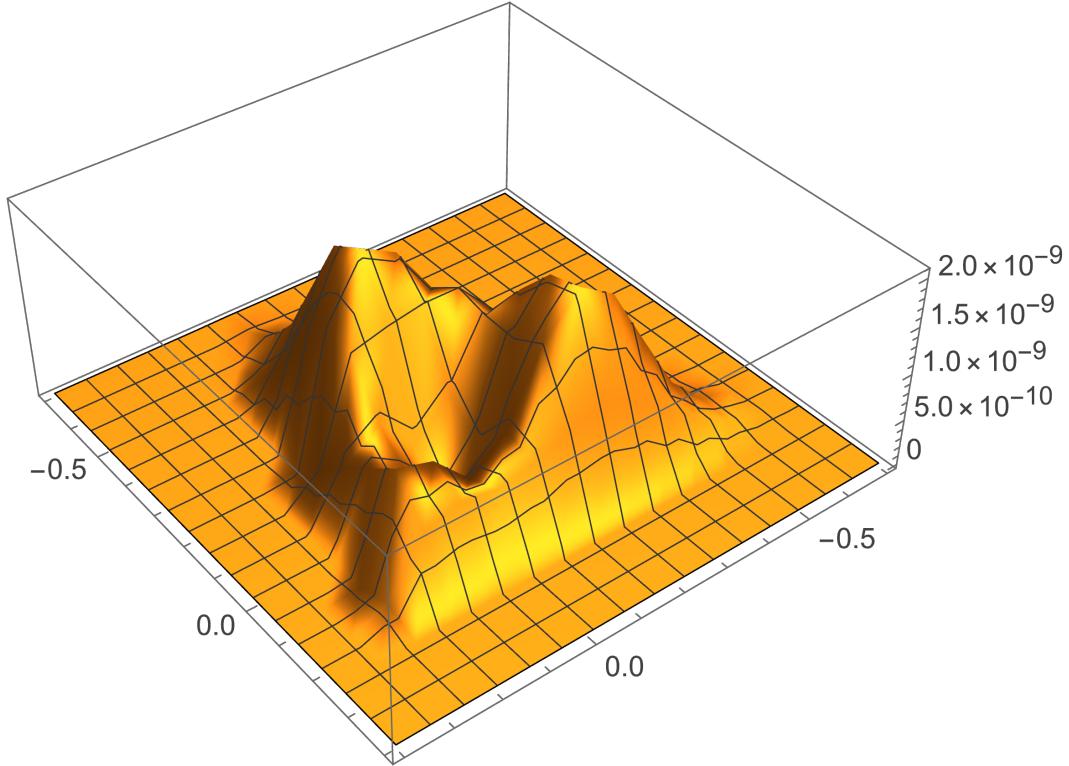
Fig. 18.5.1 The shape of $\Delta\psi^2_{N\sigma}$ on the $\alpha = \beta = 0$ and γ, δ plane.

Accordingly, the antiquark PDF (obtained by integrating $\Delta\psi^2$ over α, β, γ) is modified, as shown in Fig. 18.5.2. Compared to the predictions for the ground $(L = 0)$ shell pentaquarks, the distribution becomes narrower and shifts toward smaller x [Miesch et al., 2025c]. Nevertheless, the large-x behavior (more clearly visible in the lower panel) exhibits the same $\sim (1 - x)^8$ scaling.

Some properties of the three different five-quark admixtures to the proton are listed in Table 18.5.1. We begin with the mean spin of the antiquark (particle 5),

$$\langle S_5 \rangle = \Delta\psi_A \cdot S_5 \cdot \Delta\psi_{p\sigma}, \tag{18.11}$$

where $A = p\sigma, N\pi, \Delta\pi$. All three admixtures yield negative contributions, which should be compared to the total nucleon spin $S_z = +0.5$.

Another important observable is the isospin projection of the antiquarks. We define the operators projecting onto $\bar{d}$ and $\bar{u}$ flavors as

$$I_\pm = (\hat{1} \pm \tau_z)/2, \tag{18.12}$$

applied to particle 5 (the antiquark). Note that the isospin components for antiquarks are inverted. In this case, the $p\sigma$ and $N\pi$ admixtures favor $\bar{d}$, while the $\Delta\pi$ channel favors $\bar{u}$.
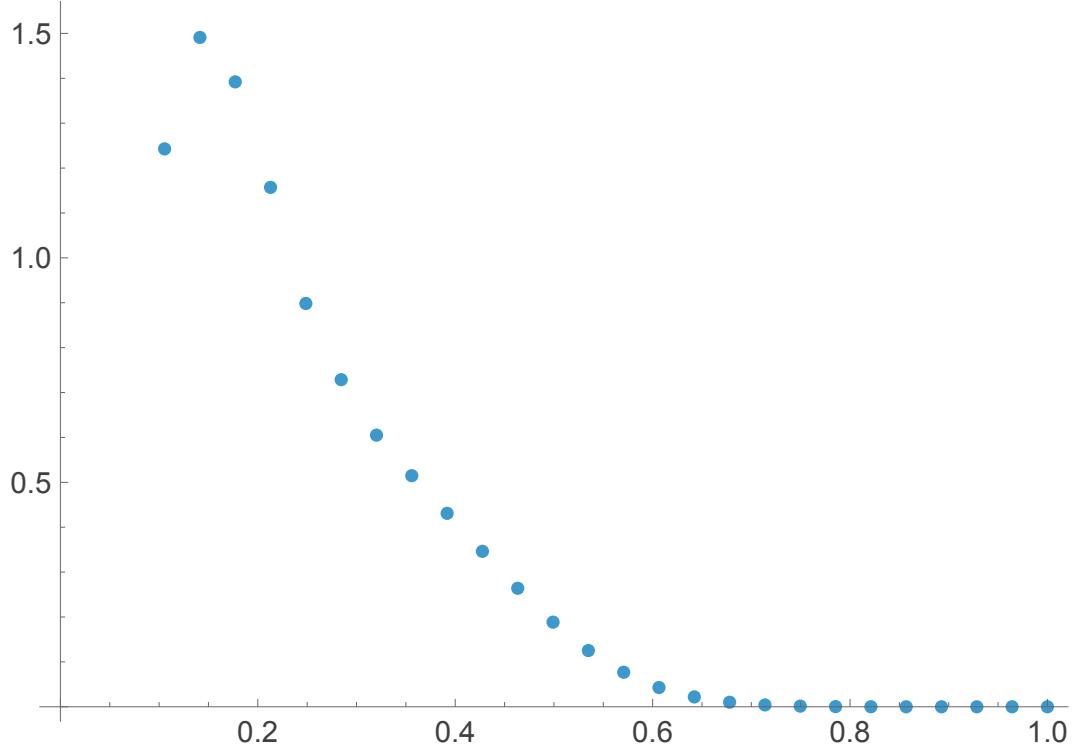
Fig. 18.5.2 Predicted antiquark PDF from $\Delta\psi_{p\sigma}$ (arbitrary units) as a function of the Bjorken momentum fraction x.

operator	$p\sigma$	$N\pi$	$\Delta\pi$
$S_z(5)$	-0.177	-0.112	-0.0338
$\bar{d} = I_+(5)$	0.81	0.858	0.333
$\bar{u} = I_-(5)$	0.19	0.142	0.666

Table 18.5.1 Properties of the three five-quark admixtures to the nucleon [Eq. (18.10)], defined as expectation values of the operators listed in the first column.

Appendix

18.A Pentaquarks on LF: the forward wave function

The longitudinal part of the LF Hamiltonian is not an oscillator, but rather a Laplacian (confining) operator supplemented by an irreducible potential V. For five quarks, the five momentum fractions are conveniently redefined through Jacobi combinations belonging to the pentachoron ("starfish") or A_4 manifold of momentum fractions $\alpha, \beta, \gamma, \delta$. In this appendix we discuss several approaches to quantizing this system.

18.A.1 N fermions on a circle

Since fermions cannot pass each other in one dimension, their coordinates s_i are ordered as $s_1 < s_2 < \cdots < s_N < s_1 + 1$. One may furthermore fix the center-of-mass coordinate by imposing $\sum_i s_i = 0$, in which case the physical domain becomes a four-dimensional simplex. Geometrically, this simplex is similar (though not identical) to our symmetric simplex.

The fermions-on-a-circle problem admits known analytic solutions for the wave functions in the form of Slater determinants [Girardeau, 1960], see Eq. (18.19). These depend on four independent momenta $n_{21}, n_{31}, n_{41}, n_{51}$, which must all be nonzero and distinct in order for the determinant not to vanish. For the ground state one naturally selects an "occupied Fermi sphere" configuration, taking the lowest possible values $-2, -1, 1, 2$ (recall that zero momentum is already included). The corresponding Laplacian eigenvalue is proportional to the sum of squares $0^2 + 2 \times 1^2 + 2 \times 2^2 = 10$.

Expanding the determinant yields a lengthy sum of plane waves. Remarkably, however, this expression can be simplified into a product of ten sinusoidal factors, one for each pair $i \neq j$,

$$\psi_{sin} \sim \prod_{i \neq j} \sin\left(\frac{s_i - s_j}{2}\right). \tag{18.13}$$

Unfortunately, the four-dimensional simplex relevant to this problem is not the same as the one required for pentaquarks. Although a mapping between the two domains exists, under this mapping the Laplacian transforms into a different elliptic operator. As a result, the elegant fermions-on-a-circle solution does not directly solve the problem of interest here.

We now observe that the standard simplex $\Delta_N[x_1, \ldots, x_N]$ is geometrically isomorphic to the ordered simplex $\Delta_N^*[s_1, \ldots, s_N] \subset \mathbb{R}^N$,

$$s_1 \leq s_2 \leq \cdots \leq s_N \leq s_1 + a, \tag{18.14}$$

where the parameter a is fixed by the side length of the simplex. The faces of the ordered simplex correspond to configurations in which two successive coordinates coincide, $s_i = s_{i+1}$. The light-front wave functions defined on this domain are therefore equivalent to those of N bosons interacting via hard-core repulsion on a circle of unit circumference,

$$\varphi[x] \to \varphi[s] \qquad \text{with} \qquad \varphi[s \,|\, s_i = s_j] = 0. \tag{18.15}$$

Such impenetrable bosons are well known to map onto free fermions via the Pauli exclusion principle. The corresponding N-fermion wave functions are Slater determinants built from circular plane waves [Girardeau, 1960],

$$\varphi_n[s] = \frac{1}{N^{4/3}} \begin{vmatrix} e^{i\tilde{n}_1 s_1} & e^{i\tilde{n}_1 s_2} & \dots & e^{i\tilde{n}_1 s_N} \\ e^{i\tilde{n}_2 s_1} & e^{i\tilde{n}_2 s_2} & \dots & e^{i\tilde{n}_2 s_N} \\ \vdots & \vdots & \ddots & \vdots \\ e^{i\tilde{n}_N s_1} & e^{i\tilde{n}_N s_2} & \dots & e^{i\tilde{n}_N s_N} \end{vmatrix}, \tag{18.16}$$

with $\tilde{n}_i = 2\pi n_i$. These wave functions have support on disjoint simplices related by permutation symmetry and possess eigen-energies

$$E[n] = \sum_{i=1}^{N} \tilde{n}_i^2. \tag{18.17}$$

The ordering $s_i \in [0,1]$ suggests an interpretation in terms of equidistant particles on a one-dimensional string of length one, undergoing longitudinal vibrations. To eliminate the center-of-mass coordinate, we perform the shift $s_j = \frac{S}{N} + \tilde{s}_j$. Substituting this into Eq. (18.16), and rearranging rows and columns of the Slater determinant, we obtain [He et al., 2025a]

$$\begin{vmatrix} e^{i\tilde{n}_1 s_1} & e^{i\tilde{n}_1 s_2} & \dots & e^{i\tilde{n}_1 s_N} \\ \vdots & \vdots & \ddots & \vdots \\ e^{i\tilde{n}_N s_1} & e^{i\tilde{n}_N s_2} & \dots & e^{i\tilde{n}_N s_N} \end{vmatrix} = \begin{vmatrix} e^{i\tilde{n}_1 \frac{S}{N}} e^{i\tilde{n}_1 \tilde{s}_1} & \dots & e^{i\tilde{n}_1 \frac{S}{N}} e^{i\tilde{n}_1 \tilde{s}_N} \\ \vdots & \ddots & \vdots \\ e^{i\tilde{n}_N \frac{S}{N}} e^{i\tilde{n}_1 \tilde{s}_1} e^{i\tilde{n}_{N1} \tilde{s}_1} & \dots & e^{i\tilde{n}_N \frac{S}{N}} e^{i\tilde{n}_1 \tilde{s}_N} e^{i\tilde{n}_{N1} \tilde{s}_N} \end{vmatrix}. \tag{18.18}$$

Extracting the common center-of-mass phase,

$$e^{i\frac{S}{N} \sum_{i=1}^{N} \tilde{n}_i}, \tag{18.19}$$

yields

$$\varphi_n[s] = \frac{1}{N^{4/3}} e^{i\frac{S}{N} \sum_{i=1}^{N} \tilde{n}_i} \begin{vmatrix} 1 & 1 & \dots & 1 \\ e^{i\tilde{n}_{21} \tilde{s}_1} & \dots & e^{i\tilde{n}_{21} \tilde{s}_N} \\ \vdots & \ddots & \vdots \\ e^{i\tilde{n}_{N1} \tilde{s}_1} & \dots & e^{i\tilde{n}_{N1} \tilde{s}_N} \end{vmatrix} \equiv e^{i\frac{S}{N} \sum_{i=1}^{N} \tilde{n}_i} \varphi_{\tilde{n}}[\tilde{s}], \tag{18.20}$$

where $\tilde{n}_{i1} = \tilde{n}_i - \tilde{n}_1$ for $i = 2, \dots, N$. The coefficients $\tilde{n}_{i1}$ are ordered as $0 < \tilde{n}_{21} < \tilde{n}_{31} < \tilde{n}_{41} < \dots$ to avoid redundant counting. Eliminating the center-of-mass degree of freedom yields reduced wave functions $\varphi_{\tilde{n}}[\tilde{s}]$ depending only on the $N-1$ relative coordinates, with energies

$$\tilde{E}[\tilde{n}] = \frac{1}{\varphi_n[s]} \left[\left(\frac{\partial}{\partial s_i} \right)^2 - N \left(\frac{\partial}{\partial S} \right)^2 \right] \varphi_n[s]$$

$$= \sum_{i=1}^{N} \tilde{n}_i^2 - \frac{1}{N} \left(\sum_{i=1}^{N} \tilde{n}_i \right)^2$$

$$= \sum_{i=2}^{N} \tilde{n}_{i1}^2 - \frac{1}{N} \left(\sum_{i=2}^{N} \tilde{n}_{i1} \right)^2. \tag{18.21}$$

Since the set of Slater determinants is orthonormal and complete, the functions $\varphi_{\tilde{n}}[\tilde{s}]$ form a complete basis. The normal-mode coordinates may thus be identified with the Jacobi coordinates.

18.A.2 Variational Ritz method for Laplacian eigenfunctions at A_4

For five bodies ($N = 5$), the kinematical domain is a regular pentachoron, a four-dimensional simplex with five vertices, ten edges, ten equilateral faces, and five regular tetrahedra, which we refer to as a "starfish". There are essentially two approaches to solving the Schrodinger equation in this geometry: (i) the variational Ritz method, employed in this work, and (ii) expansion in a complete basis defined on a different pentachoron arising in the N-fermion-on-a-circle problem, which will be discussed elsewhere [He et al., 2025b].

The Ritz method for elliptic partial differential equations is well established and relies on minimizing an energy functional over a finite set of parameters, typically the coefficients of a chosen basis. In the present case we explored several trial forms. For the ground state we ultimately settled on a relatively simple Ansatz involving Gaussian corrections,

$$\Psi_{Ritz} = \Psi_{faces} \left[1 + \sum_{i}^{N} C_i \exp(-Y^2/2R_i^2) \right], \tag{18.22}$$

where the first factor is the linear Ansatz (18.5), and the bracketed term provides a correction function. The expectation value of the Laplacian (with or without the cup potential), normalized by the wave function norm,

$$\langle -\nabla^2 \rangle = \frac{\int_{simplex} \Psi_p (-\nabla^2) \Psi_p}{\int_{simplex} \Psi_p^2},$$

is minimized with respect to the coefficients C_i using the `NMinimize` command. We tested various numbers of correction terms and choices of radii, ultimately returning to a set of three Gaussians. For the Laplacian-to-norm ratio we observed an improvement from the initial value 182 down to 165, corresponding to an improvement of roughly 10%.

We further found that including the cup potential, $V_{cup} \sim (1/x_1 + 1/x_2 + 1/x_3 + 1/x_4 + 1/x_5 - 25)$, reduces the magnitude of the correction function, bringing the ground-state wave function closer to the original linear Ansatz (18.5). Consequently, this Ansatz was used in the calculations that follow.

The P-shell pentaquark states have negative parity, implemented through an additional factor linear in the coordinates. The simplest trial function we found that minimizes the Laplacian takes the form

$$\psi_1(C) \sim \Psi_{faces} \, \delta \left(1 - C(\alpha^2 + \beta^2 + \gamma^2 + \delta^2) \right). \tag{18.23}$$

While the unmodified function $\psi_1(0)$ yields $\langle -\nabla^2 \rangle / \langle 1 \rangle \approx 312.0$, the optimized choice $C = 4.5$ reduces this value by approximately 10%. More elaborate trial functions lead to further, though modest, improvements. The resulting wave functions are compared in Fig. 18.1.2. The change of sign near the origin is a robust feature, whereas a second zero near $\delta \approx -0.5$ in the variational solution is not robust and depends on the

specific Ansatz. In the true P_1 state this second zero should be absent. We have verified that the variational function remains orthogonal to the S-shell ($L = 0$) state within small numerical integration errors. We therefore conclude that the variational solution should not be trusted for $\delta < -0.5$.

18.A.3 Exact Laplacian eigenfunctions at A_4

The "equilateral" (or regular) simplex on which we must solve the LF Schrodinger equation is known in the mathematical literature as the A_4 simplex. It is closely related to representations of the permutation group S_4. Problems involving tilings in arbitrary dimensions are intimately connected with the diagonalization of the Laplacian on such simplices, a connection that became clear to us only after most of this work had been completed.

We follow the derivation presented in Ref. [Doumerc and Moriarty, 2008]. The so-called *fundamental weights* in dim $= 5$ consist of four vectors ω_i embedded in five-dimensional space,

$$\omega = \big\{\{4/5, -1/5, -1/5, -1/5, -1/5\}, \{3/5, 3/5, -2/5, -2/5, -2/5\},$$
$$\{2/5, 2/5, 2/5, -3/5, -3/5\}, \{1/5, 1/5, 1/5, 1/5, -4/5\}\big\}. \tag{18.24}$$

Together with the origin $\{0, 0, 0, 0, 0\}$, these points form the five vertices of a simplex that is similar to, but distinct from, the "starfish" simplex relevant for our problem. In Jacobi coordinates, the vertices of the latter are given by five different points a_i,

$$\{\ 1/\sqrt{2}, 1/\sqrt{6}, 1/(2\sqrt{3}), 1/(2\sqrt{5})\},$$
$$\{\ -(1/\sqrt{2}), 1/\sqrt{6}, 1/(2\sqrt{3}), 1/(2\sqrt{5})\},$$
$$\{\ 0, -\sqrt{2/3}, 1/(2\sqrt{3}), 1/(2\sqrt{5})\},$$
$$\{\ 0, 0, -(\sqrt{3}/2), 1/(2\sqrt{5})\},$$
$$\{\ 0, 0, 0, -(2/\sqrt{5})\}. \tag{18.25}$$

The affine transformation mapping one simplex onto the other was determined numerically using the *Mathematica* command `FindGeometricTransform`. It consists of a rotation combined with translations,

$$\{\ \{0.4 + 0.228825\alpha + 0.213762\beta + 0.237755\gamma + 0.473607\delta\},$$
$$\{\ 0.2 - 0.59907\alpha - 0.0816497\beta + 0.0288675\gamma + 0.111803\delta\},$$
$$\{\ -0.2 + 0.228825\alpha - 0.559635\beta - 0.11547\gamma\},$$
$$\{\ 0.0707107\alpha + 0.305049\beta - 0.518007\gamma - 0.111803\delta\},$$
$$\{\ -0.4 + 0.0707107\alpha + 0.122474\beta + 0.366854\gamma - 0.473607\delta\}\}. \tag{18.26}$$

In arbitrary dimension, the eigenstates of the Laplacian on a simplex can be expressed as a sum over permutations of the full S_{d-1} group. In *Mathematica* notation this can be written compactly as

$$\text{Sum[Signature[w] Exp[2 I*Pi*(Permute[p, w] . y)], \{w, Sn\}]}, \tag{18.27}$$

or equivalently,

$$\sum_{w \in S_d} \text{sign}[w]\, e^{2\pi i(wp)\cdot y}. \tag{18.28}$$

Here the "momenta" are defined as $p = \sum_{i=1}^{4} m_i\omega_i$, with m_i being positive integers, S_n denoting the $(d-1)!$ permutations of the permutation group, and y representing the coordinates, either in the original simplex or

after projection onto the "starfish" simplex as described above. The permutations act on the components of p (not on the ω_i) and are required to enforce the correct boundary conditions on all faces of the simplex.

The ground state corresponds to $m = \{1, 1, 1, 1\}$, or equivalently $p = \{-2, -1, 0, 1, 2\}$, reminiscent of a five-element "Fermi sphere". Owing to its complexity, the explicit expression for the real part of the wave function is given at the end of this section; its imaginary part vanishes identically.

The exact lowest Laplacian eigenvalue for $\psi[1, 1, 1, 1]$ is

$$-\nabla^2 \psi[1, 1, 1, 1]/\psi[1, 1, 1, 1] = 186.972, \tag{18.29}$$

which lies close to the values obtained from variational minimization. It should be emphasized, however, that while the exact value is uniform throughout the simplex, the variational estimates were obtained from ratios of integrals over the full domain.

The general expression for Laplacian eigenvalues on a unit d-simplex is

$$E(m_1, m_2, \ldots, m_{d-1}) \propto \pi^2 |p|^2 = \pi^2 \sum_{i=1}^{d-1} \sum_{j=1}^{d-1} \left(\min(i, j) - \frac{ij}{d} \right) m_i m_j. \tag{18.30}$$

For the present case with four integers, this reduces to

$$E(m_1, m_2, m_3, m_4) \sim (\qquad 2m_1^2 + 3m_2^2 + 3m_3^2 + 3m_3 m_4 + 2m_4^2$$
$$+4m_2 m_3 + 2m_2 m_4 + 3m_1 m_2 + 2m_1 m_3 + m_1 m_4), \tag{18.31}$$

up to an overall scaling factor arising from the coordinate transformation from x to y.

The predicted ratio of P-wave to S-wave eigenvalues is therefore

$$\frac{Pwave}{Swave} = (74/5)/10 = 1.48. \tag{18.32}$$

This is smaller than the ratio obtained from the uncorrected variational Ansatz (18.5),

$$\frac{Pwave}{Swave} = 312./182. = 1.71. \tag{18.33}$$

As expected, variational corrections tend to lower this ratio toward the exact value, reaching approximately 1.6.

The exact eigenfunction vanishes more rapidly than the variational one near the boundary corresponding to $x \to 1$. Computing the corresponding PDF (defined as the integral of the squared wave function over α, β, γ) and plotting it on a logarithmic scale reveals a steeper falloff, consistent with a power-law behavior $\sim (1 - x)^p$ with $p \approx 12$.

The expectation value of the cup potential V_{cup} is significantly smaller for the exact eigenfunctions than for the variational ones, to the extent that it may be neglected at the $\sim 10\%$ level. One may wonder why V_{cup} plays a more important role for baryons (defined on a triangle) than for pentaquarks (defined on a 5-simplex). This may reflect a more general trend as the number of constituents increases.

Finally, for completeness, we present the explicit form of the lowest Laplacian eigenstate $\psi(1, 1, 1, 1)$. Owing to the requirement of Dirichlet boundary conditions on all ten faces of the A_4 simplex, a large number of plane waves is required:

$Re \ \psi[1,1,1,1] =$ (18.34)

$\cos(\ 2.5651\beta + 13.3389\gamma - 1.5708\delta) - \cos(-10.4036\alpha + 4.85939\beta + 7.37354\gamma - 0.868315\delta + 1.25664)$

$- \cos(\ -3.2149\alpha - 12.7221\beta + 3.74594\gamma - 0.868315\delta + 1.25664) + \cos(-8.41672\alpha - 9.71879\beta + 4.65284\gamma - 0.165833\delta + 2.51327)$

$+ \cos(\ -9.41018\alpha - 0.573574\beta + 9.90275\gamma - 0.165833\delta + 2.51327) + \cos(9.41018\alpha + 7.99807\beta + 5.65549\gamma + 1.5708\delta)$

$- \cos(\ -5.20182\alpha + 0.438171\beta - 12.432\gamma + 2.27328\delta + 1.25664) - \cos(-6.19528\alpha + 9.58339\beta - 7.18206\gamma + 2.27328\delta + 1.25664)$

$- \cos(\ 0.993459\alpha - 7.99807\beta - 10.8097\gamma + 2.27328\delta + 1.25664) - \cos(4.20836\alpha + 11.0013\beta + 6.56239\gamma + 2.27328\delta + 1.25664)$

$- \cos(\ 10.4036\alpha + 2.5651\beta + 8.1847\gamma + 2.27328\delta + 1.25664) - \cos(11.3971\alpha - 6.58012\beta + 2.93479\gamma + 2.27328\delta + 1.25664)$

$- \cos(\ 9.41018\alpha + 5.43297\beta - 7.68338\gamma + 3.14159\delta) + \cos(-9.41018\alpha - 1.99153\beta - 8.99585\gamma + 3.67824\delta + 3.76991)$

$+ \cos(\ -10.4036\alpha + 7.15369\beta - 3.74594\gamma + 3.67824\delta + 3.76991) + \cos(-3.2149\alpha - 10.4278\beta - 7.37354\gamma + 3.67824\delta + 3.76991)$

$+ \cos(\ 8.57164\beta + 9.9985\gamma + 3.67824\delta + 3.76991) + \cos(7.18874\alpha - 9.00981\beta + 6.3709\gamma + 3.67824\delta + 3.76991)$

$+ \cos(\ 6.19528\alpha + 0.135402\beta + 11.6208\gamma + 3.67824\delta + 3.76991) - \cos(5.20182\alpha - 0.708976\beta - 12.0264\gamma + 3.84407\delta + 1.25664)$

$- \cos(\ 9.41018\alpha + 9.14522\beta + 0.0957439\gamma + 3.84407\delta + 1.25664) - \cos(-8.41672\alpha - 7.42449\beta - 6.46664\gamma + 4.38072\delta + 5.02655)$

$- \cos(\ 0.993459\alpha + 3.13867\beta + 12.5277\gamma + 4.38072\delta + 5.02655) + \cos(-0.993459\alpha + 11.4395\beta - 5.86958\gamma + 4.54656\delta + 2.51327)$

$+ \cos(\ 6.19528\alpha - 6.14194\beta - 9.49718\gamma + 4.54656\delta + 2.51327) + \cos(4.20836\alpha + 12.1485\beta + 1.00264\gamma + 4.54656\delta + 2.51327)$

$+ \cos(\ 11.3971\alpha - 5.43297\beta - 2.62496\gamma + 4.54656\delta + 2.51327) + \cos(-9.41018\alpha + 5.43297\beta + 6.56239\gamma + 5.0832\delta + 6.28319)$

$+ \cos(\ -2.22144\alpha - 12.1485\beta + 2.93479\gamma + 5.0832\delta + 6.28319) + \cos(-5.20182\alpha + 5.29757\beta - 10.2126\gamma + 5.24904\delta + 3.76991)$

$+ \cos(\ 11.3971\alpha - 1.72072\beta + 5.15417\gamma + 5.24904\delta + 3.76991) - \cos(-7.42326\alpha - 9.14522\beta + 3.84169\gamma + 5.78569\delta + 7.53982)$

$- \cos(\ -8.41672\alpha + 9.0916\gamma + 5.78569\delta + 7.53982) - \cos(-9.41018\alpha + 2.86787\beta - 6.77648\gamma + 6.654\delta + 6.28319)$

$- \cos(\ 7.18874\alpha - 4.15042\beta + 8.59028\gamma + 6.654\delta + 6.28319) + \cos(5.20182\alpha + 4.15042\beta - 9.80701\gamma + 6.81983\delta + 3.76991)$

$+ \cos(\ 10.4036\alpha + 4.85939\beta - 2.93479\gamma + 6.81983\delta + 3.76991) - \cos(-9.41018\alpha + 6.58012\beta + 1.00264\gamma + 7.35648\delta + 7.53982)$

$- \cos(\ -2.22144\alpha - 11.0013\beta - 2.62496\gamma + 7.35648\delta + 7.53982) - \cos(-4.20836\alpha + 7.28909\beta + 7.87487\gamma + 7.35648\delta + 7.53982)$

$- \ \cos \ (2.98038\alpha - 10.2924\beta + 4.24727\gamma + 7.35648\delta + 7.53982) - \cos(7.15369\beta - 8.90011\gamma + 7.52231\delta + 5.02655)$

$- \cos(\ 11.3971\alpha - 0.573574\beta - 0.405578\gamma + 7.52231\delta + 5.02655) + \cos(-7.42326\alpha - 7.99807\beta - 1.71806\gamma + 8.05896\delta + 8.79646)$

$+ \cos(\ -3.2149\alpha + 1.85612\beta + 10.4041\gamma + 8.05896\delta + 8.79646) - \cos(10.8659\beta - 1.12099\gamma + 8.2248\delta + 6.28319)$

$- \cos(\ 7.18874\alpha - 6.71552\beta - 4.74859\gamma + 8.2248\delta + 6.28319) + \cos(-7.42326\alpha - 4.28582\beta + 6.06107\gamma + 8.76144\delta + 10.0531)$

$+ \cos(\ -4.20836\alpha + 8.43624\beta + 2.31512\gamma + 9.62976\delta + 8.79646) + \cos(2.98038\alpha - 9.14522\beta - 1.31248\gamma + 9.62976\delta + 8.79646)$

$+ \cos(\ -8.41672\alpha + 2.29429\beta - 2.02789\gamma + 10.3322\delta + 10.0531) + \cos(2.98038\alpha - 5.43297\beta + 6.46664\gamma + 10.3322\delta + 10.0531)$

$- \cos(\ 6.19528\alpha + 3.57684\beta - 5.05842\gamma + 10.4981\delta + 7.53982) - \cos(-7.42326\alpha - 3.13867\beta + 0.501322\gamma + 11.0347\delta + 11.3097)$

$- \ \cos \ (-2.22144\alpha - 2.4297\beta + 7.37354\gamma + 11.0347\delta + 11.3097) + \cos(0.993459\alpha + 6.58012\beta - 4.15152\gamma + 11.2006\delta + 8.79646)$

$+ \cos(\ 7.18874\alpha - 1.85612\beta - 2.52921\gamma + 11.2006\delta + 8.79646) - \cos(-3.2149\alpha + 4.15042\beta - 0.715412\gamma + 12.6055\delta + 11.3097)$

$- \cos(\ 2.98038\alpha - 4.28582\beta + 0.9069\gamma + 12.6055\delta + 11.3097) + \cos(-2.22144\alpha - 1.28255\beta + 1.8138\gamma + 13.308\delta + 12.5664))$

Chapter 19
Hard exclusive reactions, formfactors

19.1 Pion PDF

In this section we discuss the pion parton distribution function (PDF). At leading twist, the partonic content of any light hadron is encoded in bilocal light-front correlation functions, whose Fourier transforms define the distribution functions. Since the pion is a spin-zero Goldstone mode, its partonic structure at the twist-2 level reduces to a single nontrivial distribution: the unpolarized quark PDF $q_\pi(x)$. In particular, for spin-0 hadrons the helicity and transversity distributions do not contribute at leading twist, leaving the unpolarized PDF as the unique partonic observable [Collins, 2011].

The physical motivation for determining the pion PDF within the instanton-vacuum light-front framework, follows directly from the role of the pion as the fundamental Goldstone excitation of spontaneously broken chiral symmetry. Its partonic content is nonperturbative in origin, yet it must match perturbative factorization descriptions at high resolution. In [Liu et al., 2023b, Liu et al., 2023a] parton distributions are obtained from light-front matrix elements evaluated at low resolution, where the pion is correctly dominated by its lowest quark-antiquark Fock component. The light-front wave function used in the construction of the PDF is therefore the same one obtained from the nonlocal, instanton-induced dynamics; its shape encodes the full nonperturbative structure arising from the instanton vacuum.

The leading-twist parton distributions follow from the Fourier transform of a bilocal fermionic matrix element of the form

$$q_\pi(x) = \frac{1}{4\pi} \int d\xi^- \, e^{-ixP^+\xi^-} \, \langle \pi(P)|\bar{\psi}(0)\gamma^+ W(0,\xi^-)\psi(\xi^-)|\pi(P)\rangle, \tag{19.1}$$

where W is the appropriate light-front Wilson line. Section VI further states that these matrix elements are to be computed using the light-front wave functions determined earlier, and localized entirely in the lowest $q\bar{q}$ component at the resolution scale of the instanton-vacuum Hamiltonian. In the ILM at low resolution, the pion is described solely by its $q\bar{q}$ component, with the unpolarized PDF given as

$$q_\pi(x) = \int \frac{d^2k_\perp}{2(2\pi)^3} \sum_{s_1,s_2} \left|\Phi_\pi(x,k_\perp,s_1,s_2)\right|^2. \tag{19.2}$$

No additional higher-Fock corrections enter at the resolution scale associated with the instanton vacuum. The support is restricted to $0 < x < 1$ because Φ_π is defined only for $k^+ = xP^+$ between 0 and P^+. Normalization of the light-front state ensures the valence sum rule

$$\int_0^1 dx \, q_\pi(x) = 1, \tag{19.3}$$

which follows immediately from the normalization condition of the light-front wave function with no additional assumptions.

In the chiral limit ($m_u = m_d \to 0$), the pion mass $M_\pi \to 0$ but f_π remains finite, ensuring the Goldstone nature of the pion. The PDF is symmetric under $x \leftrightarrow 1 - x$ in this limit, reflecting isospin symmetry. At large x, the counting rules predict $q_v^\pi(x) \sim (1 - x)^{2+\gamma}$, where γ encodes logarithmic QCD corrections [Brodsky and Farrar, 1973, Farrar and Jackson, 1975]. This behavior emerges naturally from the LFWF structure and provides a nontrivial check of consistency with perturbative QCD.
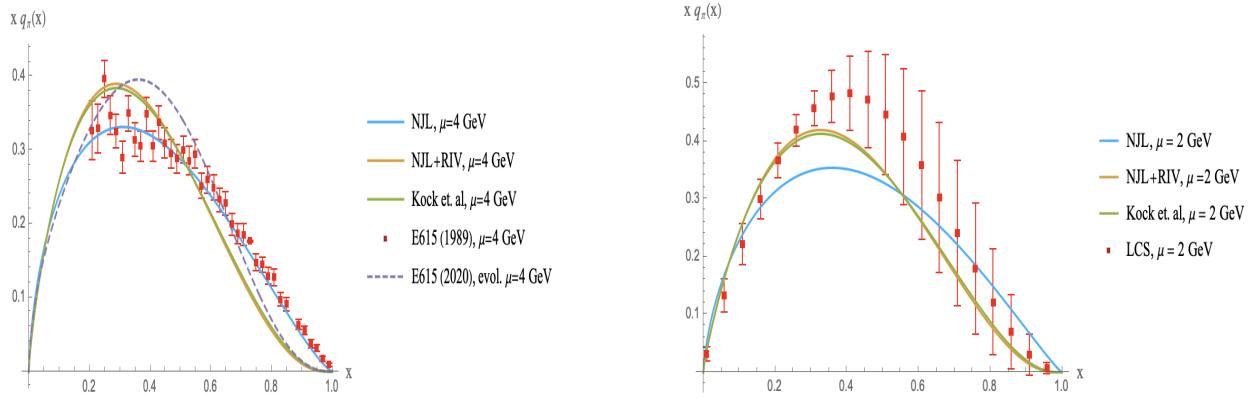
Fig. 19.1.1 a: Pion parton momentum distribution function for zero instanton size (solid-blue) and finite instanton size of $\rho = 0.317$ fm (solid-orange), both of which are evolved to $\mu = 4$ GeV with a pion mass $m_\pi = 135$ MeV. The results are compared to the those extracted from the ILM using the LaMET (solid-green) [Kock et al., 2020, Kock and Zahed, 2021], also evolved to $\mu = 4$ GeV. The E615 data from 1989 (red) are from [Conway et al., 1989], corresponding to a fixed invariant muon pair mass $m_{\mu^+\mu^-} \geq 4.05$ GeV. The improved E615 data from 2010 (dashed-purple) are from [Aicher et al., 2010], using the original E615 experimental data from [Conway et al., 1989].
b: The same pion parton distribution functions as in a, but now evolved to $\mu = 2$ GeV, for comparison with the lattice data using cross sections (LCS) (red) from [Sufian et al., 2020].

19.2 Summary

The leading-twist pion PDF in the instanton-vacuum light-front approach is entirely determined by the valence light-front wave function through Eq. (19.2). All nonperturbative features of the pion - including the momentum asymmetry, endpoint behavior, and the normalization - originate from the instanton-induced nonlocality encoded in the Bethe-Salpeter kernel and inherited by the projected light-front wave function.

The nonlocal instanton model gives a realistic description of f_π, the shape of $\phi_\pi(x, \mu_0)$, and the pion PDF [Diakonov et al., 1997, Liu et al., 2023a]. Quantitatively:

- $f_\pi \approx 92.4$ MeV (input or output of the model),
- $\langle x \rangle_q^\pi \approx 0.5$ at low scale,
- The DA is broad and nearly flat at $\mu_0 \simeq 1$ GeV, evolving toward $6x(1 - x)$ at larger μ.

Lattice QCD and experimental extractions (e.g. from $\pi\gamma$ transition form factors and LaMET computations) support this picture [Zhang et al., 2020, Shi et al., 2015b, Kock et al., 2020, Sufian et al., 2020].

19.3 Pion Distribution Amplitudes on the LF and pion formfactors

The theory of *exclusive QCD reactions* [Brodsky and Farrar, 1973, Chernyak and Zhitnitsky, 1977, Radyushkin, 1977].
is based on two assumptions:
(i) the *separation of scales*, based on the assumption that the momentum transfer Q (the scale in the "hard block"), is large compared to the typical quark mass and transverse momenta inside hadrons; (ii) that the "hard block" can be calculated *perturbatively using gluon exchanges.*

However, the theory based on these two assumptions is insofar not successful phenomenologically. In particular, in the domain of Q in which experimental and lattice results are available, the mesonic form factors, while approximately $\sim 1/Q^2$, are well above the one-gluon exchange predictions. This should not be surprising, as there is an important difference between the scales in DIS and jet physics on one hand, and exclusive processes on the other. The former operates in the range $Q^2 = 10^2 - 10^4 \, \text{GeV}^2$, while exclusive processes we study so far in a different range, $Q^2 = 2 - 10 \, \text{GeV}^2$ (sometimes called semi-hard domain).

In this chapter (based on our paper [Shuryak and Zahed, 2021g]) we will accept the assumption (i) mentioned above: the Q^2 scale is indeed large compared to the typical squared transverse momentum $\langle p_\perp^2 \rangle \sim 0.1 \, \text{GeV}^2$ within a hadron, or the constituent quark mass $M^2 \sim 0.1 - 0.15 \, \text{GeV}^2$. In the Breit frame description of form factors, conventional "collinear" kinematics should still hold. So we still have a notion of a "hard block operator", sandwiched between two wave functions. Yet we do not accept the second assumption (ii), showing that at such momentum transfer Q, the nonperturbative quark interactions are *not* at all negligible in comparison to gluon exchanges. Therefore a purely perturbative treatment of the "hard block" needs to be appended by calculations of *leading nonperturbative contributions*, and this paper makes the first steps in this direction.

Distribution Amplitudes (DAs) are defined by matrix elements different from PDFs: unlike them they are matrix element between vacuum and hadron state. In other words, the hadron is produced by a given operator "out of nothing". Its usage in hard processes (mainly elastic formfactors) is for incoming and outgoing hadrons in relativistic kinematics. Similar to PDFs, the moments of DAs can be related by OPE to local operators. This relation allowed to evaluate DAs numerically, on the Euclidean lattices.

The first pion DA is defined using the forward matrix element of the twist-2 operator on the LF,

$$\phi_\pi(x) = -i \int \frac{d\xi^-}{2\pi} e^{ixP^+\xi^-} \langle 0|\bar{\psi}(0)\gamma^+\gamma^5 \frac{\tau^a}{\sqrt{2}} W(0,\xi^-)\psi(\xi^-)|\pi^a(P)\rangle \tag{19.4}$$

with the normalization fixed by the pion weak decay constant

$$\langle 0|\bar{\psi}\gamma^+\gamma^5 \frac{\tau^a}{\sqrt{2}}\psi|\pi^a(P)\rangle = if_\pi P^+ \tag{19.5}$$

In general, pion is characterized by three DAs

$$\int_{-\infty}^{+\infty} \frac{p^+ dz^-}{2\pi} e^{ixp\cdot z} \left\langle 0 \left| \bar{d}_\beta(0)[0,z]u_\alpha(z) \right| \pi^+(p) \right\rangle$$
$$= \left(+\frac{if_\pi}{4}\gamma^5 \left(\slashed{p}\, \varphi_{\pi^+}^A(x) - \chi_\pi \varphi_\pi^P(x) - i\chi_\pi \sigma_{\mu\nu} \frac{p^\mu n^\nu}{p\cdot n} \frac{\varphi_\pi'^T(x)}{6} \right) \right)_{\alpha\beta} \tag{19.6}$$

Here $[x,y]$ is the shorthand notation for the gauge link between two points on the light front, and $\sigma_{\mu\nu} = \frac{1}{2i}[\gamma_\mu, \gamma_\nu]$. In this example the first term contains momentum, while the other two do not. Therefore the axial A-DA is of leading twist, while the two others P, T-DA are subleading (next twist) at large momentum $p \to \infty$.

The three functions $\varphi^i(x)$ have indices $i = A, P, T$ standing for axial, pseudoscalar and tensor gamma matrices in the operator. They are all normalized to 1. Their explicit definition follows from (19.6) by

inversion

$$\varphi_{\pi^+}^A(x) = \frac{1}{if_\pi} \int_{-\infty}^{+\infty} \frac{dz^-}{2\pi} e^{ixp\cdot z} \left\langle 0 \left| \overline{d}(0)\gamma^+\gamma_5[0,z]u(z) \right| \pi^+(p) \right\rangle$$

$$\varphi_{\pi^+}^P(x) = \frac{1}{f_\pi\chi_\pi} \int_{-\infty}^{+\infty} \frac{p^+ dz^-}{2\pi} e^{ixp\cdot z} \left\langle 0 \left| \overline{d}(0)i\gamma_5[0,z]u(z) \right| \pi^+(p) \right\rangle$$

$$\varphi_{\pi^+}^{T\prime}(x) = \frac{-6}{f_\pi\chi_\pi} \frac{p^\mu n^\nu}{p\cdot n} \int_{-\infty}^{+\infty} \frac{p^+ dz^-}{2\pi} e^{ixp\cdot z} \left\langle 0 \left| \overline{d}(0)\sigma_{\mu\nu}\gamma_5[0,z]u(z) \right| \pi^+(p) \right\rangle \quad (19.7)$$

To relate the tensor pion DA amplitude in (19.7) to the pseudoscalar light front wavefunction with helicity-1, we note that the dominant tensor matrix element on the light cone reads

$$\langle 0|\overline{d}(0)i\sigma^{+i}\gamma_5 u(z^-, z_\perp)|\pi^+(p)\rangle$$
$$= 2p^+ \frac{\partial}{\partial z_\perp^i}\psi_1^P(z^-, z_\perp) \quad (19.8)$$

with $(x = k^+/p^+)$

$$\psi_1^P(x, k_\perp) = \int dz^- dz_\perp e^{i(k^+ z^- - k_\perp \cdot z_\perp)}\psi_1^P(z^-, z_\perp) \quad (19.9)$$

Note the relation $\psi_{\pm 1}^P(x, k_\perp) = k_\perp^\pm \psi_1^P(x, k_\perp)$ with $k_\perp^\pm = k_x \pm ik_y$. A comparison with (19.7) shows that the twist-3 pion distribution amplitude in $\varphi_T(x, k_\perp)$ matches the $m = 1$ contribution through

$$\frac{\partial}{\partial k_\perp^i}\varphi_T(x, k_\perp) = \frac{6}{f_\pi\chi_\pi}k_\perp^i \psi_1^P(x, k_\perp) \quad (19.10)$$

Inserting the LF normalized pion state (16.2) with the corresponding solution (16.11), the pion DA follows

$$\phi_\pi(x) = \frac{\sqrt{N_c}M}{2\sqrt{2}\pi^2} \int_0^\infty dk_\perp^2 \frac{C_\pi}{x\overline{x}m_\pi^2 - (k_\perp^2 + M^2)}\mathcal{F}(k)\mathcal{F}(P - k) \quad (19.11)$$

At asymptotically increasing momentum transfer $\log(Q^2/\Lambda_{QCD}^2) \to \infty$ one should include perturbative processes of gluon radiation. When the light-front functions $\varphi_\pi(\xi)$ are decomposed into Gegenbauer polynomials, each of the polynomial carries as a coefficient a (negative) power of the preceding log with a calculable *anomalous dimension*. Asymptotically, only the leading contribution survives in the form (asymptotic wave function)

$$\varphi_\pi \to \varphi_\pi^{\text{asymptotic}}(\xi) = \frac{3}{4}(1 - \xi^2) = 6x\overline{x} \quad (19.12)$$

Needless to say that this limit is very far from the realistic kinematic range of interest in the present analysis. Heavy nonrelativistic quarks should have values of quark momenta around $x \approx \overline{x} \approx 1/2$. The opposite case of light quarks generate much wider distributions. The ones used can be approximated by the form

$$\varphi_\pi(\xi, p) = \frac{\Gamma(3/2 + p)}{\sqrt{\pi}\Gamma(1 + p)}(1 - \xi^2)^p = \frac{6^p \Gamma(3/2 + p)}{\sqrt{\pi}\Gamma(1 + p)}(x\overline{x})^p \quad (19.13)$$

The case $p = 1$ is the "asymptotic" distribution, while the case $p = 0$ is called "flat". Several authors have used an intermediate case $p = 1/2$ called "semicircular".

The pion is a particular particle, a Nambu-Goldstone mode, and therefore its properties one can calculate in any theory in which chiral symmetry gets spontaneously broken. Historically the NJL model and its non-

local versions (some related with the instanton liquid model) have been used to calculate the pion light-front wave function [Broniowski and Ruiz Arriola, 2017, Petrov and Pobylitsa, 1997, Anikin et al., 2001]. Before we briefly discuss the results of "realistic" models, related to larger set of hadronic wave functions, let us introduce some extreme cases. For example, in [Ruiz Arriola and Broniowski, 2002] a "flat" pion wave function was used as an "initial condition" for radiative evolution. Some typical shapes of the pion and other light meson wave functions are shown in Fig.19.3.1. Note that η' is the channel in which 't Hooft Lagranigian is repulsive, thus quarks are far from each other and have small relative motion.
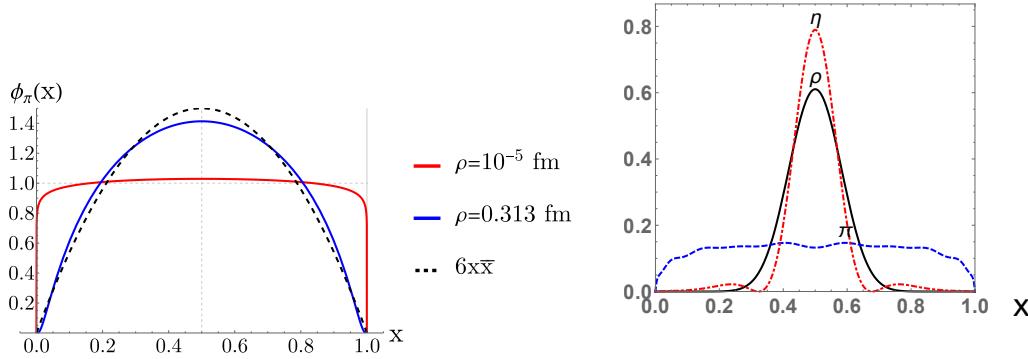
Fig. 19.3.1 Left plot: the pion DA from [Kock et al., 2020] sizes, for different instanton. Right plot: the light mesons - pion,rho and η' light front distribution functions, from [Shuryak, 2019].

In contrast, in 1980's Chernyak and collaborators [Chernyak and Zhitnitsky, 1984] using the QCD sum rules arrived at pion wave function

$$\varphi_{CZ}(x) = 30x(1-x)(2x-1)^2 \tag{19.14}$$

known as "the double-hump" one. But, since then no support for this shape has materialized, and it also does not agree with lattice results on momentum fractions, so we will not discuss it. Let us state once again, that we see phenomenological failure of the pQCD expressions not in the modified shape of the wave function, but in missing nonperturbative part of the hard blocks.

The light pseudoscalar mesons $P = \pi, K, \eta$ are related to chiral symmetry breaking and therefore they exist even in models without confinement, such as the NJL and ILM. Their wave functions and parton distribution amplitudes (PDA) have been calculated in various approximations. The question was addressed originally in the ILM framework in [Petrov et al., 1999], and more recently using the quasi-distribution proposal by one of us in [Kock et al., 2020]. The distribution amplitude for the light P-pseudoscalars was obtained to be [Kock et al., 2020]

$$\varphi_P(x) = \frac{2N_c}{f_P^2} \int \frac{d^2 k_\perp}{(2\pi)^3} \frac{\theta(x\bar{x})}{(k_\perp^2 + M^2(0, m_f) - x\bar{x}m_P^2)} M^2\left(\frac{\sqrt{k_\perp^2 + M^2(0, m_f)}}{\lambda_P \sqrt{x\bar{x}}}\right) \tag{19.15}$$

where the momentum-dependent quark mass is

$$M(k) = M(0)\left(\left|z\left(I_0 K_0 - I_1 K_1\right)'\right|^2\right)_{z=\frac{1}{2}\rho k} \tag{19.16}$$

Here λ_P is a cut-off parameter of order 1, e.g. $\lambda_\pi = 3.41$, and $M(0) = 386$ MeV with an instanton size $\rho = 0.3$ fm. As shown in [Kock et al., 2020], this momentum dependence has been confirmed by lattice studies. For a light current quark mass m_f, the running effective quark mass $M(k, m_f) \approx M(k) + m_f$.

The corresponding shape of the wave function is shown in the upper plot of Fig.19.3.1 as reproduced from [Kock et al., 2020], is in agreement with [Petrov et al., 1999]. Both calculations show a wave functions rather close to the asymptotic one, and very far from the "double-hump" distribution (19.14).

Another approach to light front wave functions is based on some model-dependent Hamiltonians. Jia and Vary [Jia and Vary, 2019] introduced a convenient form of it, including constituent quark masses (that is, chiral symmetry breaking), plus some form of confinement, plus NJL-type residual interactions. This approach was followed by one of us [Shuryak, 2019], who calculated the wave functions for the π, ρ, η' mesons, as shown in the lower plot of Fig.19.3.1. Also, the wave functions for the Δ and nucleon were given in [Shuryak, 2019], even with the inclusion of the 5-light-quark tail, providing the first results for the *anti*quark distribution inside the nucleon.

For a finite instanton size, the pion DA is

$$\phi_\pi(x) = \frac{\sqrt{N_c}M}{\sqrt{2}\pi^2} C_\pi \int_{\frac{\rho M}{2\lambda\sqrt{x\bar{x}}}}^{\infty} dz \frac{z^5}{\frac{\rho^2 m_\pi^2}{4\lambda^2} - z^2} (F'(z))^4 \tag{19.17}$$

In the zero instanton size approximation with a fixed transverse momentum cutoff $|k_\perp| < \Lambda$, the pion DA amplitude is a step function

$$\phi_\pi(x) \xrightarrow{m_\pi \to 0} \frac{\sqrt{N_c}M}{\sqrt{2}\pi} \left[\ln\left(1 + \frac{\Lambda^2}{M^2}\right)\right]^{1/2} \theta(x\bar{x}) \tag{19.18}$$

in agreement with a result established first in the local NJL model [Broniowski and Ruiz Arriola, 2017].
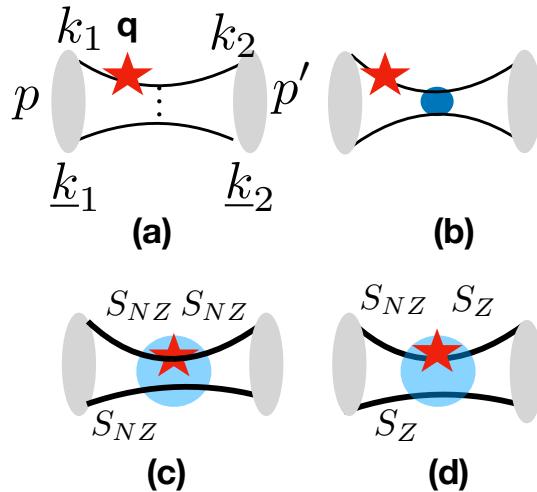
Fig. 19.3.2 The perturbative one-gluon exchange diagrams: (a) explains our notations for momenta of quarks and mesons. The thin solid lines are free quark propagators, the red star indicates the virtual photon (or scalar) vertex, bringing in large momentum q^μ, and the shaded ovals represent the (light-front) mesonic density matrices (distributions). The diagram (b) indicates a "Born-style contribution", in which the gluon propagator is substituted by the Fourier transform of the instanton field. The diagrams (c,d) contain three propagators in the instanton background (thick lines). In (c) all of them are S_{NZ}, made of nonzero Dirac modes, while in (d) two of them are S_Z made of quark zero modes. This last contribution we will refer to as the "'t Hooft-style term".)

19.4 Hard and semi-hard vertices of formfactors

This section is based on paper [Shuryak and Zahed, 2021g], from which our studies of the role of instanton-antiinstanton molecules began.

Out of all formulae in this section, the only part (to our knowledge) derived in literature long ago [Brodsky and Farrar, 1973, Chernyak and Zhitnitsky, 1977, Radyushkin, 1977] is the first term of (19.19), with the chirality-diagonal distribution functions.

We will keep the notations of the contributions as explained in Fig.19.3.2. For example, the (photon-induced) *vector scattering amplitude* on the pion, with perturbative one-gluon exchange will be referred to as V_a^π, and reads explicitly

$$V_a^\pi(Q^2) = \epsilon_\mu(q)(p^\mu + p'^\mu)\,(e_u + e_{\bar d})\left(\frac{2C_F\pi\alpha_s f_\pi^2}{N_c Q^2}\right)\int dx_1 dx_2$$

$$\times\left[\frac{\varphi_\pi(x_1)\varphi_\pi(x_2)}{\bar x_1\bar x_2 + m_{\rm gluon}^2/Q^2} + \frac{\chi_\pi^2}{Q^2}\left(\frac{\tilde\varphi_\pi(x_1)\tilde\varphi_\pi(x_2)}{\bar x_1\bar x_2 + m_{\rm gluon}^2/Q^2}\right)\left(\frac{1}{\bar x_1 + E_\perp^2/Q^2} + \frac{1}{\bar x_2 + E_\perp^2/Q^2} - 2\right)\right]$$

$$(19.19)$$

Here we show explicitly the electromagnetic charges $e_u = 2/3, e_{\bar d} = 1/3$, although of course the total charge of a positive pion is $e_u + e_{\bar d} = 1$. The color matrices give the factor $C_F = (N_c^2 - 1)/2N_c = 4/3$ with $N_c = 3$ number of colors. The large spacelike photon momentum is q^μ and $q_\mu q^\mu = -Q^2 < 0$. The photon polarization vector is $\epsilon_\mu(q)$, with $\epsilon_\mu q^\mu = 0$. The momenta of the initial and final mesons are called p and p'. The pion decay constant is $f_\pi \approx 133\,{\rm MeV}$, it characterizes the wave function at the origin in the transverse plane, $r_\perp = 0$. For the pion distribution we use the expression (19.6) which includes not only the chirally diagonal part of the distribution $\varphi_\pi(x)$ but also the chirally non-diagonal one $\tilde\varphi_\pi(x)$. Both depend only on the longitudinal momentum fraction x of one of the quarks only. They are assumed to correspond to a 2-body sector of the full wave function. Here the bar indicates that the momentum fractions are those of antiquarks, $\bar x_i \equiv 1 - x_i$. In terms of the asymmetry parameters, these variables read as $x_i = (1 + \xi_i)/2, \bar x_i = (1 - \xi_i)/2$. The regulators are the gluon mass and quark "transverse energy".

Note that the first term in (19.19) is well known, but the second term $\sim \chi_\pi^2/Q^2$ is new, to our knowledge in the asymptotic analysis. We will keep it since χ_π is not small, unlike the masses and transverse momenta. We note further that the last bracket in that term averages to a positive contributions, as it will be shown in the summary plot Fig. 19.4.1.

The contribution we call the *Born-like instanton contribution* V_b^π has the same traces and can be obtained by substituting in V_a^π the Fourier transforms of the instanton gauge field instead of the gluon propagator, with

$$\pi\alpha_s(Q/2) \to \kappa\left\langle\mathbb{G}^2(Q\rho\sqrt{\bar x_1\bar x_2})\right\rangle \tag{19.20}$$

and is therefore

$$V_b^\pi(Q^2) = \epsilon_\mu(q)(p^\mu + p'^\mu)\,(e_u + e_{\bar d})\left(\frac{2C_F\kappa f_\pi^2}{N_c Q^2}\right)\int dx_1 dx_2\,\left\langle\mathbb{G}^2(Q\rho\sqrt{\bar x_1\bar x_2})\right\rangle$$

$$\times\left[\frac{\varphi_\pi(x_1)\varphi_\pi(x_2)}{\bar x_1\bar x_2 + m_{\rm gluon}^2/Q^2} + \frac{\chi_\pi^2}{Q^2}\left(\frac{\tilde\varphi_\pi(x_1)\tilde\varphi_\pi(x_2)}{\bar x_1\bar x_2 + m_{\rm gluon}^2/Q^2}\right)\left(\frac{1}{\bar x_1 + E_\perp^2/Q^2} + \frac{1}{\bar x_2 + E_\perp^2/Q^2} - 2\right)\right]$$

$$(19.21)$$

The contribution V_c^π, with three *non*-zero mode propagators is

$$V_c^\pi = \epsilon_\mu(q)(p^\mu + p'^\mu)(e_u + e_{\bar{d}}) \frac{\kappa \pi^2 \rho^2 f_\pi^2 \chi_\pi^2}{N_c M^2} \langle \mathbb{G}_V(Q\rho) \rangle \int dx \tilde{\varphi}_\pi(x) x$$

The instanton induced formfactors $\mathbb{G}$ and $\mathbb{G}_V(Q\rho)$ are derived explicitly in [Shuryak and Zahed, 2021g]. The angular brackets indicate averaging over the instanton size.

The inclusion of instanton-antiinstanton molecules in the hard block of the pion formfactor was the most important step made in [Shuryak and Zahed, 2021g], from which left plot of Fig.19.4.1 is taken. As one can see, their contribution (squares) with gluon exchange (disks) together (dotted line) provides a realistic magnitude of the pion formfactor at intermediate momentum transfers.

For comparison, the right plot of Fig.19.4.1 summarizes current theoretical predictions and experimental projections[1] for coming data of the JLab E12 experiments.
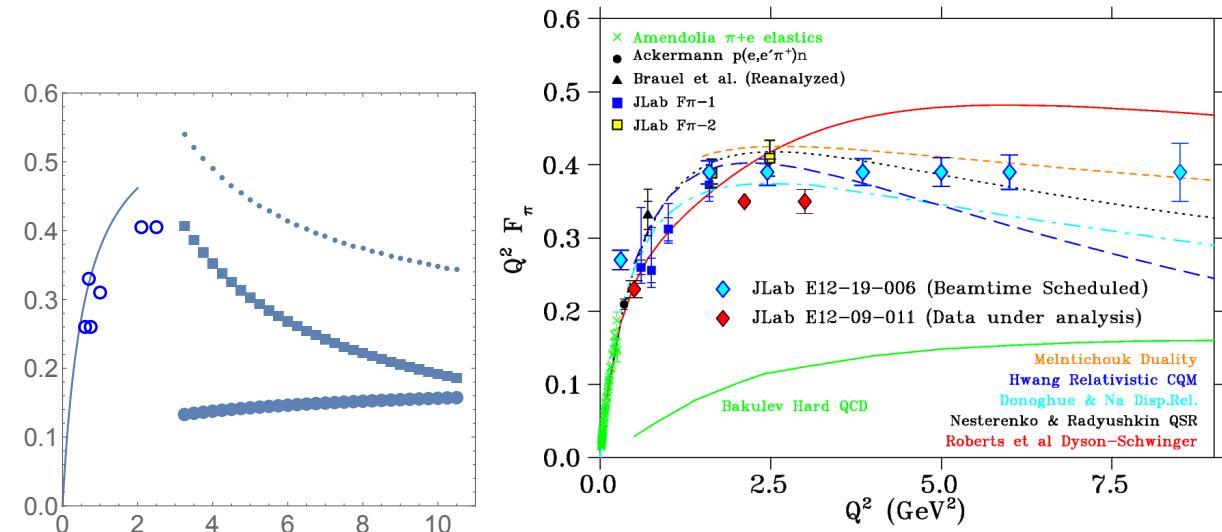
Fig. 19.4.1 The vector form factors of the pion times the squared momentum transfer, $Q^2 F_\pi(Q^2)$ (GeV^2) versus $Q^2(GeV^2)$.
Left: from [Shuryak and Zahed, 2021g]. The closed discs show the perturbative gluon exchange contribution. The squares correspond to the instanton molecule contribution from the nonzero mode propagators. The dotted line above is their sum. The curve in the l.h.s. is the usual dipole formula, and the open points are some experimental data.
Right: Points with symbols indicated in the upper left corner are experimental data, curves are various predictions of theoretical models mentioned in the lower right corner. Light blue and red diamonds are *not* data but location/accuracy projections for JLab E12 experiments (from their documents).

The pion and kaon formfactors were calculated on the lattice many times, for recent results at the largest momentum transfers see Fig.19.4.2. according to them, $Q^2 F(Q) \approx const$ up to rather high Q^2, no expected downward transition to perturbative predictions are so far seen: this is one of the most striking puzzles of the QCD theory.

We will not give here lengthy expressions for other meson formfactors (scalar or Higgs-induced, gravitational or stress-tensor induced): all of them are obtained in the same general setting. Their relative size and Q^2 dependence would perhaps provide better understanding of the origin of the effective hard block. For example, scalar formfactor need extra chirality flip relative to vector ones: perturbative theory thus predict extra penalty in form of extra powers of $1/Q$. Contrary to that, lattice calculations reported by [Davies et al., 2018] observed scalar formfactor for $\bar{c}c$ channel to be several times *larger* than the vector one, also with flat $Q^2 F(Q^2)$: it remains another open puzzle related with meson formfactors.

---

[1] At the time of this writing we could not locate any publications with their results, but perhaps showing projected error bars and Q^2 range in this review is still worth it.
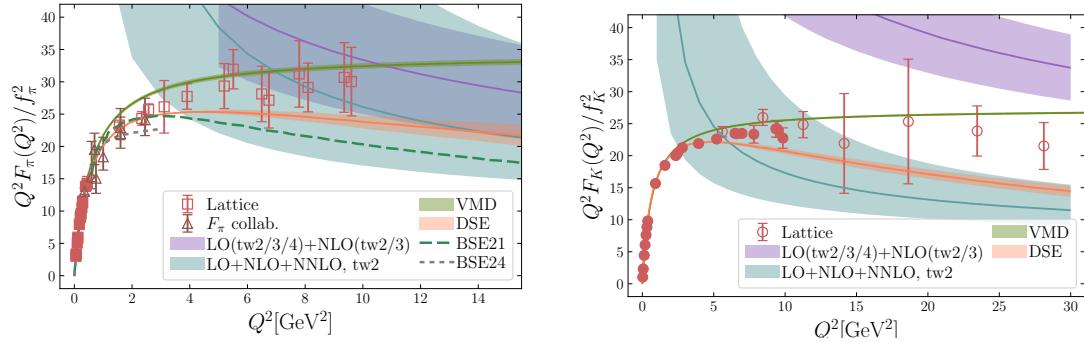
Fig. 19.4.2 Pion and kaon formfactors calculated on the lattice [Ding et al., 2024] at larger momentum transfer values, shown by open squares.

Appendix

19.A Axial Ward Identity, GMOR Relation, and the Zero-Mode Condensate

The axial Ward identity,

$$\partial_\mu J_5^\mu = 2m\, \bar{q}\mathrm{i}\gamma_5 q + 2\mathrm{i}N_f \frac{g^2}{32\pi^2} F\tilde{F}, \qquad (19.22)$$

links explicit mass terms and topological effects. Solving for the constrained component ψ_- in terms of ψ_+ gives

$$\psi_- = \frac{1}{2\mathrm{i}\partial^+}(\boldsymbol{\gamma}_\perp \cdot \boldsymbol{D}_\perp + m)\gamma^+ \psi_+. \qquad (19.23)$$

Substitution yields a zero-mode operator:

$$\mathcal{Z}_{\mathrm{zero}}(x) \equiv \frac{1}{2}\Big[\bar{\psi}_+(x)\frac{1}{\mathrm{i}\partial^+}(\boldsymbol{\gamma}_\perp \cdot \overleftrightarrow{D}_\perp + m)\gamma^+ \psi_+(x) + \mathrm{h.c.}\Big]_0. \qquad (19.24)$$

The projection onto $p^+ = 0$ reads

$$[\mathcal{O}(x)]_0 = \lim_{\eta \to 0^+} \int \frac{\mathrm{d}k^+}{2\pi} e^{-\mathrm{i}k^+ x^-} \tilde{\mathcal{O}}(k^+)\theta(\eta - |k^+|) = \frac{1}{L^-}\int_{-L^-/2}^{L^-/2} \mathrm{d}y^-\, \mathcal{O}(y^-). \qquad (19.25)$$

This operator $\mathcal{Z}_{\mathrm{zero}}$ defines the LF vacuum condensate:

$$\langle \bar{q}q \rangle_{\mathrm{LF}} \equiv \langle 0|\mathcal{Z}_{\mathrm{zero}}|0\rangle \neq 0. \qquad (19.26)$$

Inserting into the axial Ward identity and taking vacuum-pion matrix elements yields the Gell-Mann-Oakes-Renner relation:

$$f_\pi^2 m_\pi^2 = -2\hat{m}\,\langle \bar{q}q \rangle_{\mathrm{LF}} + \mathcal{O}\big(\hat{m}^2\big), \qquad (19.27)$$

demonstrating that the pion mass and decay constant arise consistently from the zero-mode vacuum condensate. Physically, the LF zero-mode condensate plays the same role as the instant-form quark condensate in generating Goldstone bosons.

19.B Relation to Hadronic Matrix Elements

Hadronic observables probe the underlying vacuum through their coupling to zero modes. Light-front wave functions describe Fock states with $p^+ > 0$, while the zero-mode contributions complete the symmetry relations and ensure correct normalization of chiral currents. For instance, the pion distribution amplitude and decay constant f_π require inclusion of $\mathcal{Z}_{\mathrm{zero}}$ to recover low-energy theorems. Thus, experimental quantities

such as m_π, f_π, and form factors reflect the existence of a zero-mode vacuum condensate even though it is invisible in naive Fock space.

19.C Instanton Form Factors and Normalization

The quark zero mode in an instanton background is

$$\psi_0(x) = \frac{\rho}{\pi} \frac{1}{(x^2 + \rho^2)^{3/2}} \frac{1 - \gamma_5 \slashed{x}/\sqrt{x^2}}{2} U, \tag{19.28}$$

where ρ is the instanton size and U a color rotation. Its Fourier transform gives the form factor

$$F(k\rho) = 2z[I_0(z)K_1(z) - I_1(z)K_0(z) - I_1(z)K_1(z)/z], \quad z = k\rho/2. \tag{19.29}$$

The nonlocal kernel is

$$\mathcal{K}(k_1, \ldots, k_{2N_f}) = G \prod_i F(k_i\rho)(2\pi)^4 \delta^{(4)}\left(\sum k_i\right), \tag{19.30}$$

with G determined by the instanton density n and distribution $d(\rho)$. Using $n \simeq 1$ fm^{-4} and $\rho \simeq 0.33$ fm yields $G \sim$ 5-10 GeV^{-2}. These parameters quantitatively reproduce the observed condensate and f_π values.

19.D From Covariant to Light-Front Gap Equation

The Euclidean gap equation

$$M(p_E) = m + \int \frac{\mathrm{d}^4\ell_E}{(2\pi)^4} K(p_E, \ell_E) \frac{M(\ell_E)}{\ell_E^2 + M^2(\ell_E)} \tag{19.31}$$

is transformed to LF variables via $\ell^\pm = \ell^0 \pm \ell^3$:

$$M(x, \boldsymbol{\ell}_\perp) = m + \int_0^1 \mathrm{d}y \int \frac{\mathrm{d}^2\boldsymbol{k}_\perp}{(2\pi)^3} K(x, \boldsymbol{\ell}_\perp; y, \boldsymbol{k}_\perp) \frac{M(y, \boldsymbol{k}_\perp)}{\boldsymbol{k}_\perp^2 + M^2(y, \boldsymbol{k}_\perp) - y(1-y)P^{+2}}. \tag{19.32}$$

Boundary terms at $x = 0, 1$ carry zero-mode contributions that generate $\langle \bar{q}q \rangle_{\mathrm{LF}}$. Numerical solutions show the same critical coupling G_{crit} as covariant approaches, confirming full equivalence when zero modes are retained.

Chapter 20
Pion Distribution Amplitudes and formfactors

20.1 Why distribution amplitudes matter

The pion's distribution amplitudes (DAs) encode how longitudinal momentum is shared by its valence quark and antiquark on the light cone. They are the central nonperturbative inputs in factorized descriptions of hard exclusive processes and enter the hard kernels for the pion's electromagnetic and gravitational form factors (GFFs) [Lepage and Brodsky, 1980, Efremov and Radyushkin, 1980a, Collins and Soper, 1982b, Diehl, 2003, Belitsky and Radyushkin, 2005]. Physically, $\varphi_\pi(x, \mu)$ gives the probability amplitude (at resolution scale μ) to find the $u\bar{d}$ Fock state with the quark carrying the fraction x of the pion's large $+$ momentum.

In this chapter we (i) define the twist-2 and twist-3 pion DAs with gauge links, (ii) summarize their evaluation in the instanton liquid model (ILM) of the QCD vacuum, and (iii) present their Efremov-Radyushkin-Brodsky-Lepage (ERBL) evolution [Efremov and Radyushkin, 1980b, Lepage and Brodsky, 1979].

20.2 Light-cone definitions

Let p^μ denote the pion momentum and $z^\mu = (0, z^-, \mathbf{0}_\perp)$ a lightlike separation. With a straight Wilson line $W[0, z] = \mathcal{P} \exp\left[-ig \int_0^{z^-} A^+(t)\, dt\right]$, the twist-2, 3 DAs are defined by [Shuryak and Zahed, 2021g, Kock et al., 2020]

$$\varphi_\pi^A(x, \mu) = \frac{1}{iF_\pi} \int \frac{dz^-}{2\pi} e^{ixp^+z^-} \langle 0|\bar{d}(0)\gamma^+\gamma_5\, W[0, z]\, u(z)|\pi^+(p)\rangle\bigg|_\mu , \tag{20.1}$$

$$\varphi_\pi^P(x, \mu) = \frac{p^+}{F_\pi \chi_\pi(\mu)} \int \frac{dz^-}{2\pi} e^{ixp^+z^-} \langle 0|\bar{d}(0)i\gamma_5\, W[0, z]\, u(z)|\pi^+(p)\rangle\bigg|_\mu , \tag{20.2}$$

$$\frac{\varphi_\pi^{T\,\prime}(x, \mu)}{6} = \frac{p^\mu p'^\nu p^+}{F_\pi \chi_\pi(\mu)\, p\cdot p'} \int \frac{dz^-}{2\pi} e^{ixp^+z^-} \langle 0|\bar{d}(0)\sigma_{\mu\nu}\gamma_5\, W[0, z]\, u(z)|\pi^+(p)\rangle\bigg|_\mu . \tag{20.3}$$

Here $F_\pi = \sqrt{2}\, f_\pi \approx 133\,\mathrm{MeV}$ and $\chi_\pi(\mu) = m_\pi^2/(\overline{m}_u(\mu) + \overline{m}_d(\mu))$ from PCAC. The prime on φ^T denotes differentiation with respect to x. Eqs. (20.1)-(20.3) obey the normalization $\int_0^1 dx\, \varphi^{A,P}(x, \mu) = 1$ and $\int_0^1 dx\, \varphi^{T\,\prime}(x, \mu) = 0$. We recall that twist counts suppression by powers of the hard scale Q in collinear factorization. The leading-twist axial DA φ^A dominates at asymptotic Q, while $\varphi^{P,T}$ are genuinely twist-3 and enter with $1/Q$ suppression-but can be numerically important at semi-hard scales [Braun et al., 2016, Shuryak and Zahed, 2021g, Liu and Zahed, 2022, Liu et al., 2024d].

At the "instanton scale" $\mu_0 \equiv 1/\bar{\rho} \approx 0.63\,\mathrm{GeV}$, the ILM gives compact integral forms for the DAs [Liu et al., 2023b, Liu et al., 2024d]

$$\varphi_\pi^A(x;\mu_0) = \frac{2N_c M^2}{f_\pi^2}\frac{1}{8\pi^2}\,\theta(x\bar{x})\int_0^\infty dk_\perp^2\,\frac{\mathcal{F}^2\left(\frac{k_\perp}{\lambda_\pi^A\sqrt{x\bar{x}}}\right)}{x\bar{x}\,m_\pi^2 - k_\perp^2 - M^2}, \tag{20.4}$$

$$\varphi_\pi^P(x;\mu_0) = \frac{N_c M}{f_\pi^2\chi_\pi(\mu_0)}\frac{\theta(x\bar{x})}{8\pi^2\,x\bar{x}}\int_0^\infty dk_\perp^2\,\frac{k_\perp^2 + M^2}{x\bar{x}\,m_\pi^2 - k_\perp^2 - M^2}\,\mathcal{F}\left(\frac{k_\perp}{\lambda_\pi^P\sqrt{x\bar{x}}}\right), \tag{20.5}$$

$$\frac{\varphi_\pi^{T\,\prime}(x;\mu_0)}{6} = \frac{N_c M}{f_\pi^2\chi_\pi(\mu_0)}\frac{(x-\bar{x})\,\theta(x\bar{x})}{8\pi^2\,x\bar{x}}\int_0^\infty dk_\perp^2\,\frac{k_\perp^2 + M^2}{x\bar{x}\,m_\pi^2 - k_\perp^2 - M^2}\,\mathcal{F}\left(\frac{k_\perp}{\lambda_\pi^T\sqrt{x\bar{x}}}\right), \tag{20.6}$$

with $\bar{x} \equiv 1-x$. The instantonic profile $\mathcal{F}$ is determined by the zero-mode wavefunction and can be expressed via modified Bessel functions; phenomenological scale parameters $(\lambda_\pi^A, \lambda_\pi^P, \lambda_\pi^T)$ fix the normalization at μ_0. Note that the operator identity

$$\partial_\nu\,\bar{d}(0)\sigma^{\mu\nu}\gamma^5 u(z) = -\partial^\mu\,\bar{d}(0)i\gamma^5 u(z) + m\,\bar{d}(0)\gamma^\mu\gamma^5 u(z)$$

implies that φ^P and φ^T share the same low-energy coupling $\chi_\pi(\mu)$-and hence inherit the quark-mass anomalous dimension.
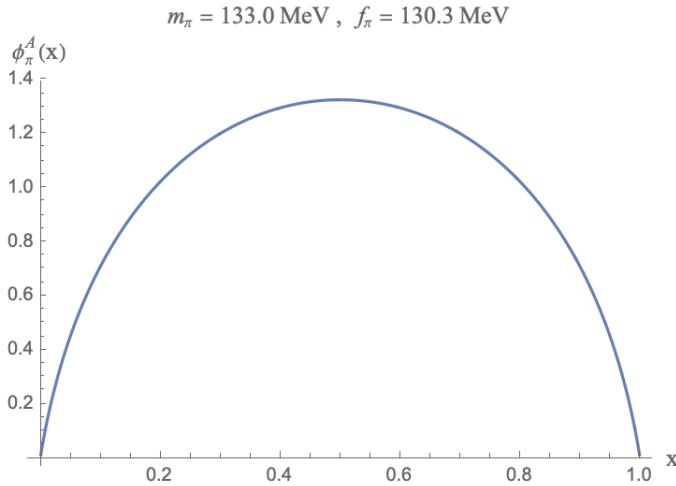
Fig. 20.2.1 The un-evolved pion DA versus parton-x at low resolution, in the the QCD instanton vacuum.

20.3 Asymptotics and ERBL evolution

At large μ the leading-twist DA approaches the conformal limit $\varphi_\pi^A(x,\mu) \to 6x\bar{x}$, while [Efremov and Radyushkin, 1980a]

$$\varphi_\pi^P(x,\mu) \to 1 \times \left[\frac{\alpha_s(\mu)}{\alpha_s(\mu_0)}\right]^{-3C_F/b}, \qquad \varphi_\pi^T(x,\mu) \to 6x\bar{x} \times \left[\frac{\alpha_s(\mu)}{\alpha_s(\mu_0)}\right]^{C_F/b}, \tag{20.7}$$

reflecting their distinct anomalous dimensions. For practical evolution one expands in Gegenbauer polynomials [Diehl, 2003] (and references therein)

$$\varphi^{A,T}(x,\mu) = 6x\bar{x}\sum_{n=0}^\infty a_n^{A,T}(\mu)\,C_n^{(3/2)}(x-\bar{x}), \qquad \varphi^P(x,\mu) = \sum_{n=0}^\infty a_n^P(\mu)\,C_n^{(1/2)}(x-\bar{x}), \tag{20.8}$$

The polynomials are ortho-normal, and satisfy the following properties
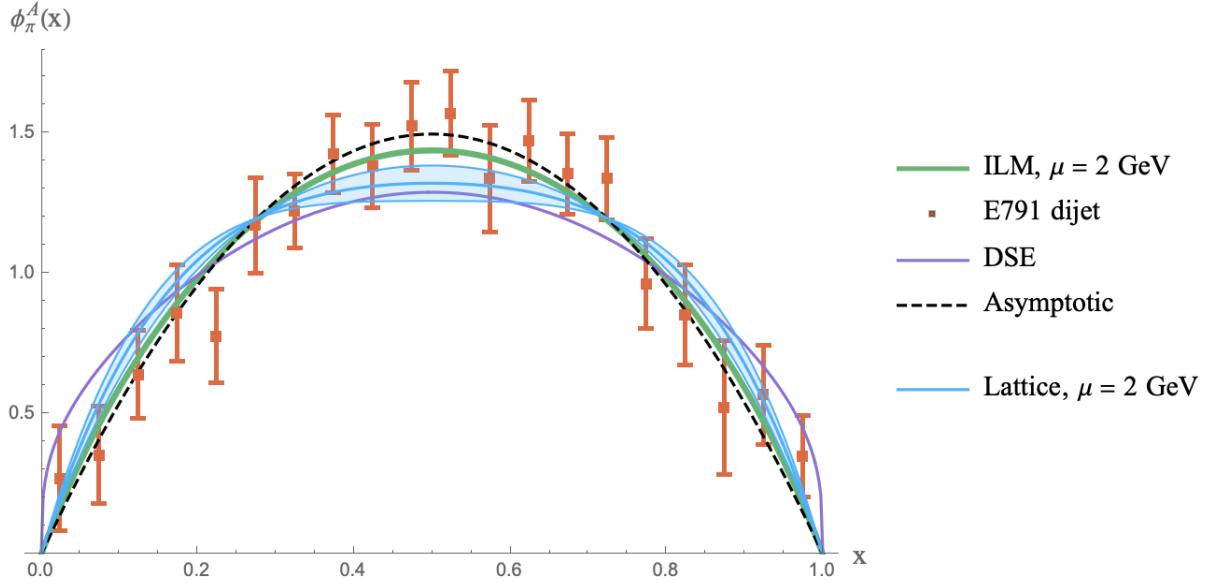
Fig. 20.2.2 The evolved pion DA using the NLO ERBL equation to $\mu = 2$ GeV (solid-green), compared with the lattice calculation (RQCD) (shaded-blue) [Bali et al., 2019] , Dyson-Schwinger result [Shi et al., 2015a] (solid-purple) and the asymptotic QCD result (dashed-black). The experimental data points (red squared points) are extracted from π^- into di-jets via diffractive dissociation with invariant dijet mass 6 GeV [Aitala et al., 2001] and normalized in [Broniowski et al., 2008].

$$\int_0^1 dx \, [x(1-x)]^{\lambda-1/2} \, C_n^{(\lambda)}(2x-1) C_m^{(\lambda)}(2x-1) = \delta_{mn} \frac{\pi 2^{1-2\lambda} \Gamma(n+2\lambda)}{n! \, (n+\lambda) \, \Gamma^2(\lambda)}, \qquad (20.9)$$

$$C_0^{(\lambda)}(z) = 1, \quad C_1^{(\lambda)}(z) = 2\lambda z, \qquad (20.10)$$

$$\frac{d}{dz} C_n^{(\lambda)}(z) = 2\lambda \, C_{n-1}^{(\lambda+1)}(z). \qquad (20.11)$$

With this in mind and using the orthogonality, yield the moments

$$a_n^{A,T}(\mu) = \frac{2(2n+3)}{3(n+1)(n+2)} \int_0^1 dy \, C_n^{(3/2)}(y - \bar{y}) \, \varphi^{A,T}(y, \mu), \qquad (20.12)$$

$$a_n^P(\mu) = (2n+1) \int_0^1 dy \, C_n^{(1/2)}(y - \bar{y}) \, \varphi^P(y, \mu). \qquad (20.13)$$

The leading-log ERBL evolution is diagonal in this basis [Efremov and Radyushkin, 1980a, Lepage and Brodsky, 1979]

$$a_n^X(\mu) = a_n^X(\mu_0) \left[\frac{\alpha_s(\mu)}{\alpha_s(\mu_0)} \right]^{\gamma_n^X/b}, \qquad X \in \{A, P, T\}, \qquad (20.14)$$

with one-loop anomalous dimensions

$$\gamma_n^A = C_F \left[-3 + 4 \sum_{j=1}^{n+1} \frac{1}{j} - \frac{2}{(n+1)(n+2)} \right], \, \gamma_n^P = C_F \left[-3 + 4 \sum_{j=1}^{n+1} \frac{1}{j} - \frac{8}{(n+1)(n+2)} \right], \, \gamma_n^T = C_F \left[-3 + 4 \sum_{j=1}^{n+1} \frac{1}{j} \right], \qquad (20.15)$$

and $b = \frac{11}{3} N_c - \frac{2}{3} N_f$. For the ERBL evolution at leading log it is sufficient to truncate at modest n ($n = 2, 4$) for phenomenology, since higher moments evolve away with increasing μ. In general, the evolution

is obtained by setting $\mu \sim \mathcal{O}(Q)$ for hard processes, while for semi-hard kinematics, a matching to ILM at $\mu_0 \simeq 1/\bar{\rho}$ captures large nonperturbative end-point effects. The ILM naturally suppresses $x \to 0, 1$ via the zero-mode transverse profile $\mathcal{F}$, stabilizing convolution integrals in hard kernels. Although $1/Q$ suppressed, $\varphi^{P,T}$ contributions can be sizable at a few GeV.

20.4 Pion gravitational formfactors

As we already mentioned many times, pion occupies a unique position in the spectrum of strongly interacting particles. As the lightest hadron, its properties reflect the Nambu-Goldstone nature of chiral symmetry breaking in QCD. As a composite quark bound state, it simultaneously encodes nonperturbative dynamics of confinement and semiclassical vacuum structure. This dual character makes the pion an exceptionally sensitive probe of the short and long-distance structure of QCD as well as the structure of the QCD vacuum itself [Schäfer and Shuryak, 1998, Diakonov et al., 1997, Nowak et al., 1996].

Among all local operators in quantum field theory, the stress (energy-momentum) tensor $T_{\mu\nu}$ holds a privileged status. It governs the response of the theory to spacetime deformations, defines conserved charges associated with translations, and encodes the flow of energy, momentum, and stress. Its matrix elements between hadronic states define the gravitational form factors (GFFs), quantities that play the role of form factors in hypothetical couplings to gravity. Even though gravitational interactions are far too weak to be used experimentally, these form factors appear in hard exclusive processes, generalized parton distributions, deeply virtual Compton scattering, and dispersion relations connecting spacelike and timelike amplitudes [Polyakov and Schweitzer, 2018b]. They reveal fundamental aspects of hadron structure such as the distribution of mass, pressure, and shear forces, the decomposition of hadron mass into quark and gluon contributions, and the mechanical stability of strongly interacting systems [Polyakov and Schweitzer, 2018b].

A profound feature of the QCD energy-momentum tensor is its anomalous trace,

$$T^\mu_{\ \mu} = \frac{\beta(g^2)}{4g^4} F^a_{\mu\nu} F^{a\mu\nu} + m\bar{\psi}\psi, \tag{20.16}$$

which manifests the quantum breaking of classical scale invariance. The running of the strong coupling introduces a dynamical scale Λ_{QCD}, and the expectation value of the trace anomaly contributes significantly to hadron masses [Pagels and Tomboulis, 1978, Vainshtein et al., 1982, Shifman, 1989]. Understanding how this anomaly is realized in the pion provides deep insight into the interplay between chiral dynamics and conformal symmetry breaking.

The gravitational form factors (GFFs) of the pion encode the response of the system to a probe that couples to the energy-momentum tensor[1] (EMT) [Polyakov and Schweitzer, 2018a] . Although gravitons are not really available for experiments, the same matrix elements can be accessed through moments of generalized parton distributions (GPDs) [Diehl, 2003] and by lattice QCD [Hackett et al., 2023b]. The two scalar functions that parameterize the pion EMT, $A_\pi(Q^2)$ and $D_\pi(Q^2)$, summarize, respectively, how momentum is carried by constituents and how internal forces (pressure and shear) are arranged.

We define the pion EMT matrix element by

$$\langle \pi(p')|T^{\mu\nu}|\pi(p)\rangle = 2\bar{p}^\mu \bar{p}^\nu A_\pi(Q^2) + \frac{1}{2}(q^\mu q^\nu - g^{\mu\nu}q^2) D_\pi(Q^2) + 2m_\pi^2 g^{\mu\nu}\bar{C}(Q^2), \tag{20.17}$$

where $q = p' - p$, $\bar{p} = (p' + p)/2$, and $Q^2 = -q^2$. Energy-momentum conservation enforces $A_\pi(0) = 1$, while the mechanical stability of a bound state implies a negative D-term at the origin, $D_\pi(0) < 0$.

---

[1] Also known as the stress tensor.

20.5 The Energy-Momentum Tensor and the Trace Anomaly

The QCD EMT in a symmetric, gauge-invariant form is

$$T^{\mu\nu} = -F^{a\,\mu\lambda}F^{a\,\nu}{}_\lambda + \frac{1}{4}g^{\mu\nu}F^a_{\rho\sigma}F^{a\,\rho\sigma} + \bar\psi\gamma^{(\mu}i\overset{\leftrightarrow}{D}{}^{\nu)}\psi. \tag{20.18}$$

Classically, $T^\mu{}_\mu = 0$ in the massless limit. Quantum corrections break scale invariance, producing the trace anomaly

$$T^\mu{}_\mu = \frac{\beta(g)}{2g}F^a_{\rho\sigma}F^{a\,\rho\sigma} + m\,\bar\psi\psi, \tag{20.19}$$

with the QCD beta function

$$\beta(g) = \mu\frac{dg}{d\mu} = -\frac{\beta_0}{16\pi^2}g^3 - \frac{\beta_1}{(16\pi^2)^2}g^5 + \cdots, \qquad \beta_0 = 11 - \frac{2}{3}N_f, \quad \beta_1 = 102 - \frac{38}{3}N_f. \tag{20.20}$$

The anomaly implies that scale breaking is driven by gluon dynamics even in the chiral limit. In the vacuum, this is reflected in the nonzero gluon condensate $\langle F^2\rangle$, while for hadrons it controls the scalar channel of the EMT and contributes to their mass budget.

20.6 Decomposition and Physical Interpretation

Projecting Eq. (20.17) in the Breit frame, one finds [Liu et al., 2024f]

$$T^{00}(Q^2) = 2\left(m_\pi^2 + \frac{Q^2}{4}\right)A_\pi(Q^2) + \frac{Q^2}{2}D_\pi(Q^2), \tag{20.21}$$

$$T^{ii}(Q^2) = 2\bar p_i^2\,A_\pi(Q^2) - \frac{1}{6}Q^2 D_\pi(Q^2), \tag{20.22}$$

with no sum over i. The time component tracks energy flow and normalizes $A_\pi(0) = 1$. The spatial trace is directly tied to internal stress. Eliminating A_π or D_π gives convenient relations:

$$A_\pi(Q^2) = \frac{3T^{00}(Q^2) - T^\mu{}_\mu(Q^2)}{Q^2 + 4m_\pi^2}, \tag{20.23}$$

$$D_\pi(Q^2) = \frac{T^\mu{}_\mu(Q^2) - T^{00}(Q^2)}{Q^2}. \tag{20.24}$$

Negative $D_\pi(0)$ ensures that repulsive core pressure is balanced by attractive surface tension, as required by mechanical stability.

20.7 Connection to GPDs and Energy Flow

The GFFs are the second Mellin moments of pion GPDs. For the unpolarized GPD $H_\pi(x,\xi,t)$ one has [Diehl, 2003]

$$\int_{-1}^1 dx\, x\, H_\pi(x,\xi,t) = A_\pi(t) + \xi^2 D_\pi(t), \tag{20.25}$$

with $t = q^2 = -Q^2$. This identity links the GFFs to experimentally accessible observables in deeply virtual Compton scattering (DVCS) and timelike Compton scattering (TCS). Physically, the integral weights partonic momentum flow by x, while the ξ^2 term encodes the stress redistribution characterized by D_π.

20.8 Perturbative Regime and Twist Expansion

At large Q^2, the EMT matrix element factorizes into [Lepage and Brodsky, 1980]

$$\langle\pi|T^{\mu\nu}|\pi\rangle = \int_0^1 dx_1 dx_2 \, \Phi_\pi(x_1,\mu) \, T_H^{\mu\nu}(x_1,x_2,Q^2,\mu) \, \Phi_\pi(x_2,\mu) + \mathcal{O}\left(\frac{1}{Q^4}\right), \tag{20.26}$$

with the leading-order hard kernel scaling like [Shuryak and Zahed, 2021h, Tong et al., 2021, Tong et al., 2022, Liu et al., 2024f]

$$T_H \sim \frac{16\pi\alpha_s C_F}{Q^2} \frac{1}{x_1 x_2} \times \mathcal{P}^{\mu\nu}(x_1,x_2), \tag{20.27}$$

where $\mathcal{P}^{\mu\nu}$ encodes the EMT vertex structure. The distribution amplitude evolves according to the ERBL equation [Efremov and Radyushkin, 1980b, Lepage and Brodsky, 1979]

$$\mu\frac{d}{d\mu}\varphi_\pi(x,\mu) = \int_0^1 dy \, V(x,y) \, \varphi_\pi(y,\mu), \tag{20.28}$$

driving $\varphi_\pi(x,\mu)$ towards the asymptotic form $6x(1-x)$. Twist-3 DAs $\varphi_\pi^{P,T}$ contribute at $\mathcal{O}(1/Q)$ and are numerically important in the few-GeV range, where they correct the leading-twist picture and feed the scalar channel [Shuryak and Zahed, 2021g].

The QCD instanton vacuum offers a semiclassical, microscopic description of the nonperturbative ground state of QCD [Shuryak, 1982f, Schäfer and Shuryak, 1998, Nowak et al., 1996]. Instantons and anti-instantons are topological tunneling configurations that interpolate between vacua of different winding number. Their distribution in size and density can be extracted from semiclassical arguments, phenomenology, and lattice QCD simulations [Schäfer and Shuryak, 1998, Diakonov et al., 1997, Nowak et al., 1996]. The resulting instanton liquid model (ILM) successfully explains the dynamical generation of the constituent quark mass, spontaneous breaking of chiral symmetry, and numerous hadronic observables [Diakonov et al., 1997, Nowak et al., 1996, Kacir et al., 1999]. It also naturally accommodates the gluonic scale (stress tensor trace) anomaly [Novikov et al., 1981a].

Modern high-statistics lattice QCD computations of pion gravitational form factors allow for quantitative comparison with theoretical predictions [Hackett et al., 2023a, Wang et al., 2024]. This motivates a fully detailed, mathematically expanded account of the ILM computation of pion gravitational form factors, including both trace and traceless components, quark and gluon contributions, and their evolution to higher resolution scales. This chapter provides exactly such an expanded, pedagogical exposition, synthesizing semiclassical QCD, chiral dynamics, and light-front quantization [Liu et al., 2024a].

20.9 Breaking of Scale Invariance in QCD and Instanton Vacuum

The QCD vacuum is a medium populated by fluctuating gauge fields whose properties are far from trivial. Instantons are Euclidean classical solutions of the Yang-Mills equations with finite action,

$$S_{\text{inst}} = \frac{8\pi^2}{g^2}, \tag{20.29}$$

and nonzero topological charge [Schäfer and Shuryak, 1998]. Their size ρ and collective coordinates parametrize a manifold of degenerate configurations. Semiclassical analysis yields a size distribution [Schäfer and Shuryak, 1998]

$$n(\rho) \sim \rho^{-5} \left(\rho\Lambda_{\text{QCD}}\right)^b \exp\left(-C\rho^2/\bar{R}^2\right), \tag{20.30}$$

where $b = 11N_c/3 - 2N_f/3$ is the one-loop coefficient of the QCD beta-function and C is a constant of order unity. Perturbation theory controls the small-ρ tail [Schäfer and Shuryak, 1998], while interactions among instantons regulate the infrared [Diakonov et al., 1997, Nowak et al., 1996]. Lattice cooling studies support the picture of a dilute but correlated ensemble with characteristic size $\bar{\rho} \approx 0.3\,\text{fm}$ and average separation $\bar{R} \approx 1\,\text{fm}$ [Schäfer and Shuryak, 1998, Athenodorou et al., 2018].

Instantons induce fermionic zero modes of definite chirality, whose delocalization across the ensemble gives rise to the quark condensate and a constituent quark mass $M(p)$ [Diakonov et al., 1997]. This mechanism provides a microscopic understanding of spontaneous chiral symmetry breaking. Conformal symmetry is broken by ultraviolet fluctuations encoded in the trace anomaly,

$$T^{\mu}_{\;\mu} = \frac{\beta(g^2)}{4g^4} F^a_{\mu\nu} F^{a\mu\nu} + m\bar{\psi}\psi, \tag{20.31}$$

with F^2 counting, in the instanton ensemble, the number of pseudoparticles in a given volume modulo subtractions of perturbative contributions [Novikov et al., 1981a].

The instanton number fluctuates around its mean $\bar{N}$ according to a grand-canonical distribution,

$$P(N) = e^{bN/4} \left(\frac{\bar{N}}{N}\right)^{bN/4}, \tag{20.32}$$

resulting in a topological compressibility

$$\sigma_T = \frac{\langle (N - \bar{N})^2 \rangle}{\bar{N}} = \frac{4}{b}. \tag{20.33}$$

This compressibility reflects the quantum nature of the vacuum and plays an essential role in enabling finite pion matrix elements of gluonic operators [Novikov et al., 1981a, Nowak et al., 1996].

20.10 The Pion Mass Identity from the Trace Anomaly

For a one-pion state normalized as

$$\langle p'|p \rangle = 2E(p)(2\pi)^3 \delta^{(3)}(p - p'), \tag{20.34}$$

the forward EMT matrix element is completely fixed by Lorentz invariance,

$$\langle p|T_{\mu\nu}|p \rangle = 2p_\mu p_\nu, \tag{20.35}$$

and therefore the trace satisfies

$$\langle p|T^{\mu}_{\;\mu}|p \rangle = 2m_\pi^2. \tag{20.36}$$

Using the anomalous expression for the trace yields the pion mass identity [Liu et al., 2024a]

$$m_\pi = -\frac{b}{32\pi^2} \frac{\langle \pi|F^2|\pi \rangle}{2m_\pi} + \frac{\langle \pi|m\bar{\psi}\psi|\pi \rangle}{2m_\pi}. \tag{20.37}$$

In the instanton vacuum the forward matrix element of F^2 is obtained from the sensitivity of the Euclidean pion two-point function to fluctuations in the instanton number. After isolating the connected part of the three-point correlator and employing the Feynman-Hellmann theorem, one finds

$$-\frac{b}{32\pi^2} \frac{\langle \pi|F^2|\pi \rangle}{2m_\pi} = \frac{m_\pi}{2}, \tag{20.38}$$

while differentiation of the Euclidean pion energy with respect to the bare quark mass gives

$$\frac{\langle\pi|m\bar{\psi}\psi|\pi\rangle}{2m_\pi} = \frac{m_\pi}{2}. \tag{20.39}$$

Thus the pion mass decomposes symmetrically:

$$m_\pi = \left.\frac{m_\pi}{2}\right|_{\text{gluon}} + \left.\frac{m_\pi}{2}\right|_{\text{quark}}. \tag{20.40}$$

This equal partition is a special consequence of the Goldstone nature of the pion; in other hadrons the mass decomposition is markedly different. In the chiral limit, the scalar gluonic matrix element vanishes, reflecting the decoupling of massive scalar glueball backgrounds from the massless Goldstone mode [Liu et al., 2024a].

20.11 Gravitational Form Factors and General Structure

The matrix element of the energy-momentum tensor between off-forward pion states takes the most general Lorentz- and parity-invariant form

$$\langle p'|T_{\mu\nu}|p\rangle = 2\bar{p}_\mu\bar{p}_\nu A(q^2) + \frac{1}{2}(q_\mu q_\nu - g_{\mu\nu}q^2)D(q^2), \tag{20.41}$$

where $q = p'-p$ and $\bar{p} = (p+p')/2$. The scalar function $A(q^2)$ describes the distribution of momentum and energy, while $D(q^2)$ encodes mechanical properties such as pressure and shear forces [Polyakov and Schweitzer, 2018b].

Separating the trace and traceless parts,

$$T_{\mu\nu} = \left(T_{\mu\nu} - \frac{1}{4}g_{\mu\nu}T^\alpha_\alpha\right) + \frac{1}{4}g_{\mu\nu}T^\alpha_\alpha, \tag{20.42}$$

one introduces the trace form factor

$$T_\pi(q^2) = \frac{\langle p'|T^\mu_\mu|p\rangle}{2m_\pi^2} = G_\pi(q^2) + \sigma_\pi(q^2), \tag{20.43}$$

where $G_\pi(q^2)$ and $\sigma_\pi(q^2)$ represent gluonic and quark contributions respectively. Chiral symmetry implies the low-energy theorem

$$D(0) = -1, \tag{20.44}$$

reflecting the long-range nature of the pion [Polyakov and Schweitzer, 2018b, Liu et al., 2024a].

20.12 The stress tensor trace Form Factor in the Instanton Vacuum

The ILM provides a microscopic computation of $G_\pi(q^2)$ by relating it to the Euclidean F^2-F^2 vacuum correlator. In the soft regime, $Q^2 \ll 1/\bar{\rho}^2$, the dynamics is dominated by the lightest scalar glueball of mass $m_{0^{++}} \approx 1.25\,\text{GeV}$. One obtains an approximately monopole form

$$G_\pi(Q^2) \simeq (1 - \sigma_\pi(0))\,\frac{1}{1 + Q^2/m_{0^{++}}^2}. \tag{20.45}$$

In the semi-hard regime, $Q\bar{\rho} \sim 1$, nonlocal form factors emerge from Fourier-transforming the instanton gauge profile. These take the form of integrals over Bessel functions J_n and modified Bessel functions K_n,

which are well approximated by analytic expressions. Together with the quark sigma-term contribution,

$$\sigma_\pi(Q^2) = \frac{\sigma_\pi(0)}{1 + Q^2/m_\sigma^2},$$
(20.46)

with $m_\sigma \approx 683\,\text{MeV}$, the ILM yields a complete picture of the trace form factor across all relevant scales [Liu et al., 2024a].

20.13 Traceless Gravitational Form Factors from Light-Front Dynamics

The traceless quark contribution to the EMT dominates at leading order in instanton density and can be computed using the pion light-front wave function obtained by diagonalizing the ILM light-front Hamiltonian. Working in a Drell-Yan frame ($q^+ = 0$), one evaluates matrix elements of the twist-two operator T^{++}, which avoids contributions from higher Fock states.

The gravitational form factors follow from

$$A(Q^2) = \frac{1}{2P^{+2}} \langle p'|T^{++}|p\rangle,$$
(20.47)

and

$$D(Q^2) = \frac{2}{3Q^2} \left[\langle p'|T^\mu_\mu|p\rangle - \frac{Q^2 + 4m_\pi^2}{4P^{+2}} \langle p'|T^{++}|p\rangle \right].$$
(20.48)

Gluonic traceless contributions arise only at next-to-leading order in the instanton density and are suppressed by κ^2. Nonetheless they can be computed and expressed in terms of quark GFFs, with coefficients given by overlap integrals of instanton zero modes [Liu et al., 2024a].

To compare with lattice QCD results, ILM predictions are evolved from the resolution scale $\mu_0 = 1/\bar{\rho} \approx 0.6\,\text{GeV}$ to $\mu = 2\,\text{GeV}$ using leading-order DGLAP evolution of twist-two operators [Hackett et al., 2023a, Wang et al., 2024].

20.14 Radii and Spatial Interpretation

The spatial distribution of energy and pressure within the pion is encoded in the slopes of gravitational form factors at zero momentum transfer. The tensor and scalar radii are defined by

$$\langle r_A^2 \rangle = -6 \frac{A'(0)}{A(0)}, \qquad \langle r_D^2 \rangle = -6 \frac{D'(0)}{D(0)}.$$
(20.49)

For the pion these radii illustrate the contrast between short-range twist-two dynamics and long-range scalar interactions [Polyakov and Schweitzer, 2018b, Liu et al., 2024a].

Additional radii follow from Breit-frame matrix elements of T_{00} and T^μ_μ,

$$\langle r_M^2 \rangle = -6 \frac{dT_\pi^{00}(Q^2)/dQ^2}{T_\pi^{00}(0)}, \qquad \langle r_S^2 \rangle = -6 \frac{dT_\pi^{\mu\mu}(Q^2)/dQ^2}{T_\pi^{\mu\mu}(0)},$$
(20.50)

revealing a large scalar radius controlled by chiral dynamics in agreement with chiral perturbation theory [Polyakov and Schweitzer, 2018b].

In summary, the instanton liquid model provides a remarkably coherent and quantitatively accurate description of the pion's gravitational structure [Schäfer and Shuryak, 1998, Liu et al., 2024a]. Semiclassical gauge configurations generate both the dynamical breaking of scale invariance and the spontaneous

breaking of chiral symmetry. The resulting zero-mode structure yields a constituent quark picture consistent with the Goldstone nature of the pion. Gravitational form factors computed at the ILM resolution scale evolve naturally to lattice QCD scales and agree closely with numerical data [Hackett et al., 2023a, Wang et al., 2024]. The gluonic trace anomaly contributes half of the pion mass, a striking hallmark of conformal symmetry breaking in QCD. The traceless gravitational form factors reveal a mechanically stable pion whose distributions of pressure and shear are governed by chiral and semiclassical dynamics [Polyakov and Schweitzer, 2018b, Liu et al., 2024a].
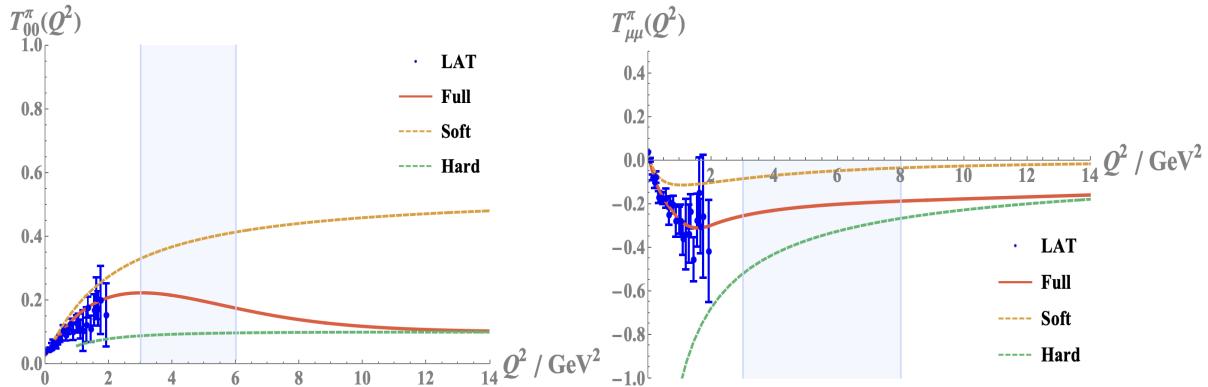
Fig. 20.14.1 The pion 00-EMT (a) and pion trace-EMT (b) versus Q^2, with the soft contribution from the ILM (dashed-orange line) from [Liu et al., 2024a], the hard plus semi-hard contribution (dashed-green line) and the interpolation full sum (solid-red line) are from [Liu et al., 2024f], compared to the lattice results from [Hackett et al., 2023b].
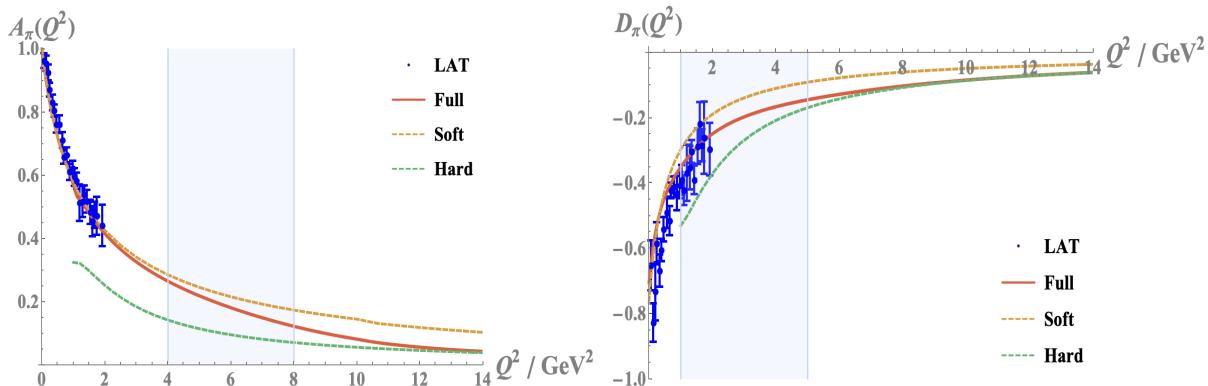
Fig. 20.14.2 The pion A-GFF (a) and pion D-GFF (b) versus Q^2, with the soft contribution from the ILM (dashed-orange line) from [Liu et al., 2024a], the hard plus semi-hard contribution (dashed-green line) and the interpolation full sum (solid-red line) are from [Liu et al., 2024f], compared to the lattice results from [Hackett et al., 2023b].

20.15 Pion Light-Front Wave Function in the ILM

The pion state on the light front is written as

$$|P\rangle = \int \frac{dx}{\sqrt{2x(1-x)}} \int \frac{d^2 k_\perp}{(2\pi)^3} \sum_{s_1,s_2,a} \Phi_\pi^a(x, k_\perp, s_1, s_2)\, b_{s_1}^{a\dagger}(k)\, d_{s_2}^{a\dagger}(P-k)\, |0\rangle, \qquad (20.51)$$

where the wave function factorizes into a momentum profile and a Dirac-isospin factor,

$$\Phi_\pi^a(x, k_\perp) = \frac{1}{\sqrt{N_c}} \, \varphi_\pi(x, k_\perp) \, \bar{u}(k) \, i\gamma_5 \tau^a \, v(P - k). \tag{20.52}$$

The scalar profile contains the instanton zero-mode form factor,

$$F(k) = \left[z(I_0 K_0 - I_1 K_1)' \right]_{z = k\rho/2}^2, \tag{20.53}$$

where modified Bessel functions encode the nonlocal structure of the zero mode [Diakonov et al., 1997, Schäfer and Shuryak, 1998, Nowak et al., 1996].

20.16 Scalar Form Factor from Chiral and Instanton Dynamics

Chiral Ward identities imply a representation for the scalar form factor in terms of the pion decay constant and the sigma field correlator,

$$F_S(q) = -\frac{1}{f_\pi} + \frac{\langle \sigma \rangle}{f_\pi^2} - \frac{m_\pi^2}{f_\pi} \int d^4 x \, e^{iq \cdot x} \, \langle T \, \sigma(x) \sigma(0) \rangle + \cdots . \tag{20.54}$$

To one loop in chiral perturbation theory one finds

$$F_S(Q^2) = -\frac{1}{f_\pi} + \frac{1}{f_\pi^3} \left(Q^2 + \frac{1}{2} m_\pi^2 \right) J(Q), \tag{20.55}$$

where $J(Q)$ is the standard two-pion loop function [Gasser and Leutwyler, 1984]. The sigma-term form factor follows from

$$\sigma_\pi(Q^2) = -\frac{f_\pi}{2} F_S(Q^2). \tag{20.56}$$

Within the ILM the scalar channel is dominated by an emergent sigma meson of mass $m_\sigma \approx 683 \, \text{MeV}$, giving the monopole form

$$\sigma_\pi(Q^2) = \frac{1/2}{1 + Q^2/m_\sigma^2}, \tag{20.57}$$

in agreement with the semiclassical analysis [Liu et al., 2024a].

20.17 Semi-Hard Instanton Effects

At scales $Q\rho \sim 1$ the instanton size ρ becomes relevant. The quark propagator in an instanton background can be schematically written as

$$S_I(x, y) = S_0(x - y) + S_{\text{zero}}(x, y) + S_{\text{NZM}}(x, y), \tag{20.58}$$

where the zero-mode (chiral) and non-zero-mode (NZM) parts capture distinct physics. The NZM term induces an effective vector form factor $\mathbb{G}_V(\rho Q)$ in the EMT, modifying the twist-3 contributions and producing semi-hard corrections:

$$T_{00,\text{NZM}}^\pi(Q^2) \sim \rho Q \, \mathbb{G}_V(\rho Q) \int dx_1 dx_2 \, \mathcal{K}(x_1, x_2) \, \varphi_\pi^P(x_1) \varphi_\pi^P(x_2) + \cdots , \tag{20.59}$$

with $\mathcal{K}$ a calculable kernel. This mechanism implements the transition between soft chiral dynamics and hard partonic scattering, and is essential for a realistic description of the trace channel at moderate Q^2.

20.18 Soft Sector and Matching Across Scales

For $Q \ll \rho^{-1}$, the zero modes dominate and the EMT is governed by chiral symmetry breaking. A practical description across all Q combines soft, NZM, and hard pieces:

$$\mathcal{O}(Q^2) = c_{\text{soft}}(Q^2)\, \mathcal{O}_{\text{soft}}(Q^2) + c_{\text{NZM}}(Q^2)\, \mathcal{O}_{\text{NZM}}(Q^2) + c_{\text{hard}}(Q^2)\, \mathcal{O}_{\text{hard}}(Q^2), \qquad \sum_i c_i(Q^2) = 1, \quad (20.60)$$

with a smooth switch in the few-GeV regime. This interpolation reproduces $A_\pi(0) = 1$, yields a negative $D_\pi(0)$, and matches lattice trends for slopes and radii.

20.19 Mechanical Densities and Internal Forces

The spatial structure of internal forces follows from the Fourier transforms of $D_\pi(Q^2)$ [Polyakov and Schweitzer, 2018a]

$$p_\pi(r) = -\frac{1}{6\pi^2 r} \int_0^\infty dQ \, \frac{Q^3 \sin(Qr)}{2E_\pi(Q)} \, D_\pi(Q^2), \qquad (20.61)$$

$$s_\pi(r) = -\frac{3}{8\pi^2} \int_0^\infty dQ \, \frac{Q^4 j_2(Qr)}{2E_\pi(Q)} \, D_\pi(Q^2), \qquad (20.62)$$

with $E_\pi(Q) = \sqrt{m_\pi^2 + Q^2/4}$. For a dipole fit,

$$D_\pi(Q^2) = \frac{D_\pi(0)}{(1 + Q^2/M_D^2)^2}, \qquad (20.63)$$

the integrals in Eqs. (20.61)-(20.62) can be evaluated analytically in terms of exponential integrals, yielding a positive core pressure and a negative surface pressure. The stability (von Laue) condition

$$\int_0^\infty 4\pi r^2 p_\pi(r) \, dr = 0 \qquad (20.64)$$

is automatically satisfied by any sufficiently fast-falling $D_\pi(Q^2)$. The mechanical radius follows from the slope at the origin,

$$\langle r^2 \rangle_D = \frac{6}{D_\pi(0)} \frac{dD_\pi(Q^2)}{dQ^2}\bigg|_{Q^2=0} = \frac{12}{M_D^2}. \qquad (20.65)$$

Empirically one finds $\sqrt{\langle r^2 \rangle_D} \approx 0.45\text{-}0.55$ fm [Liu et al., 2024f], smaller than the pion charge radius, indicating that confining forces act at shorter distances than electric screening.

20.20 Summary and Outlook

The pion GFFs provide a unifying view of QCD dynamics across scales. The function $A_\pi(Q^2)$ traces how energy and momentum flow through the hadron, while $D_\pi(Q^2)$ encodes the mechanical landscape of pressure and shear that stabilizes it. Perturbative QCD governs the asymptotic region through factorization and ERBL evolution; instanton non-zero modes supply semi-hard corrections that connect to the trace anomaly; and zero modes control the soft domain set by chiral symmetry breaking. The negative D-term emerges as a robust signature of confinement. Future lattice and experimental studies, especially at the Electron-Ion Collider, will refine the gluon contribution and test these mechanisms with higher precision.
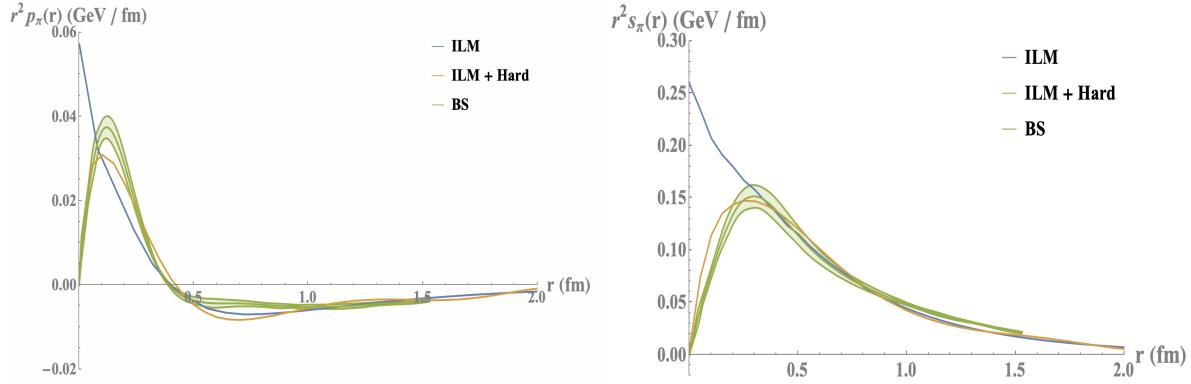
Fig. 20.20.1 The pressure (a) and shear (b) in the pion calculated using the ILM (blue-solid line) and the ILM plus pQCD (orange solid line). The comparison is to the recent results from the Bethe-Salpeter resummation [Xu et al., 2024].

Appendix

20.A Energy-Momentum (stress) Tensor and related vertices

The EMT inserts the following vertices into quark and gluon lines. For quarks,

$$V_q^{\mu\nu}(k',k) = \frac{i}{4}[\gamma^\mu(k'+k)^\nu + \gamma^\nu(k'+k)^\mu] - \frac{i}{2}g^{\mu\nu}(\slashed{k}' + \slashed{k} - 2m). \tag{20.66}$$

For the quark-gluon insertion,

$$V_{qg}^{\mu\nu,a} = ig_s T^a[\gamma^{(\mu}A^{\nu)} - g^{\mu\nu}\slashed{A}], \tag{20.67}$$

and for gluons,

$$V_g^{\mu\nu,\alpha\beta} = -ig_s f^{abc}\big[g^{\mu\alpha}(k_1 - k_2)^\nu + g^{\nu\alpha}(k_1 - k_2)^\mu\big] + \cdots. \tag{20.68}$$

These rules generate the hard kernels that appear in Eq. (20.27).

In the static limit, the spatial components of the EMT decompose as

$$T^{ij}(\boldsymbol{r}) = \left(\frac{r^i r^j}{r^2} - \frac{1}{3}\delta^{ij}\right)s_\pi(r) + \delta^{ij}p_\pi(r). \tag{20.69}$$

Taking the divergence and imposing conservation $\partial_i T^{ij} = 0$ leads to coupled differential constraints that the transforms in Eqs. (20.61)-(20.62) satisfy. The von Laue condition in Eq. (20.64) expresses mechanical equilibrium, while the integrated shear relates to the D-term via

$$-\frac{32\pi m_\pi}{45}\int_0^\infty dr\, r^4 s_\pi(r) = D_\pi(0). \tag{20.70}$$

The instanton liquid model is specified by an average instanton size $\bar{\rho} \simeq 0.33$ fm, a constituent mass $M \simeq 350$ MeV, and a packing fraction $\kappa \sim 0.1$. These values set the crossover between soft ($Q \ll \rho^{-1}$), semi-hard ($Q\rho \sim 1$), and hard ($Q \gg \rho^{-1}$) dynamics. Simple parametrizations such as Eq. (20.63) provide useful analytic control and allow direct interpretation of radii and densities.

20.B Light-front Hamiltonian in terms of the good component

In the previous section we have seen how the instanton-induced 't Hooft interaction in the instanton liquid model can be rewritten on the light front in terms of the good fermionic component only, after eliminating the bad component in the mean-field approximation and resumming the leading tadpole diagrams. The outcome is an effective light-front Lagrangian in which the good component field ψ carries a dynamically generated constituent mass M, and interacts through nonlocal four-fermion operators in the scalar, pseudoscalar and

isovector channels. In this section the authors carry out the canonical Legendre transformation of this Lagrangian to derive the light-front Hamiltonian P^-, first in the zero-size limit of the instantons and then in the finite-size case with explicit nonlocal form factors. The resulting Hamiltonian is expressed entirely in terms of the good component and its associated creation and annihilation operators, and provides the starting point for the bound-state and partonic analysis that follows.

The mean-field Lagrangian in the zero-size limit can be written as

$$L \;=\; \bar{\psi}\,(i\slashed{\partial} - M)\,\psi \;-\; \tfrac{1}{2}\,G_S\left[\delta\sigma\,\hat{D}_+\,\delta\sigma - \sigma^a\,\hat{D}_-\,\sigma^a - \pi\,\hat{D}_-\,\pi + \pi^a\,\hat{D}_+\,\pi^a\right]$$
$$+ G_S\left[\bar{\psi}\psi\,\sigma - \bar{\psi}\tau^a\psi\,\sigma^a - \bar{\psi}i\gamma_5\psi\,\pi + \bar{\psi}i\gamma_5\tau^a\psi\,\pi^a\right], \tag{20.71}$$

where the bosonic fields $\sigma, \sigma^a, \pi, \pi^a$ describe scalar-isoscalar, scalar-isovector, pseudoscalar-isoscalar and pseudoscalar-isovector channels, respectively, and $\delta\sigma = \sigma - N_c\sigma_0$ denotes the fluctuation around the nonzero scalar vacuum expectation value that encapsulates spontaneous chiral symmetry breaking. The operators $\hat{D}_\pm$ are nonlocal kernels generated by the tadpole resummation, schematically of the form

$$\hat{D}_\pm \;=\; 1 \pm G_S\left\langle \bar{\psi}\,\gamma^+\,\frac{-i}{\overleftrightarrow{\partial_-}}\,\psi \right\rangle + \cdots, \tag{20.72}$$

where $\partial_- = \partial/\partial x^-$ is the longitudinal light-front derivative, and the dots indicate channel-dependent details that are not essential for the Hamiltonian structure. The key point is that integrating out the Gaussian bosonic fields in this mean-field Lagrangian generates strings of four-fermion operators with kernels proportional to $\hat{D}_\pm^{-1}$.

Carrying out the Gaussian integration over $\delta\sigma, \sigma^a, \pi, \pi^a$ yields an effective Lagrangian purely in terms of ψ,

$$L \;=\; \bar{\psi}\,(i\slashed{\partial} - M)\,\psi \;+\; \frac{G_S}{2}\left[\bar{\psi}\psi\,\hat{D}_+^{-1}\,\bar{\psi}\psi - \bar{\psi}\tau^a\psi\,\hat{D}_-^{-1}\,\bar{\psi}\tau^a\psi - \bar{\psi}i\gamma_5\psi\,\hat{D}_-^{-1}\,\bar{\psi}i\gamma_5\psi + \bar{\psi}i\gamma_5\tau^a\psi\,\hat{D}_+^{-1}\,\bar{\psi}i\gamma_5\tau^a\psi\right].$$
$$\tag{20.73}$$

This is the mean-field light-front Lagrangian associated with the instanton-induced interaction in the zero-size limit. It contains a free part for a constituent quark of mass M, and a set of nonlocal four-fermion operators that act in the scalar and pseudoscalar isosinglet and isotriplet channels.

The promotion of this Lagrangian to a Hamiltonian proceeds through the symmetric energy-momentum tensor,

$$T^{\mu\nu} \;=\; \frac{1}{2}\left[\bar{\psi}\,i\gamma^\mu\partial^\nu\psi + \bar{\psi}\,i\gamma^\nu\partial^\mu\psi\right] - g^{\mu\nu}L, \tag{20.74}$$

from which the light-front Hamiltonian is obtained as the plus-minus component integrated over the light-front spatial coordinates,

$$P^- \;=\; \int dx^- d^2x_\perp\, T^{+-} \;=\; \int dx^- d^2x_\perp\, \frac{1}{2}\left[\bar{\psi}\,i\gamma^+\partial^+\psi + \bar{\psi}\,i\gamma^-\partial^-\psi\right] - \int dx^- d^2x_\perp\, L. \tag{20.75}$$

Here $x^+ = (x^0 + x^3)/\sqrt{2}$ is the light-front "time" and $x^- = (x^0 - x^3)/\sqrt{2}$ its conjugate coordinate; $\gamma^\pm = (\gamma^0 \pm \gamma^3)/\sqrt{2}$ are the associated Dirac matrices. Inserting the effective Lagrangian (20.73) into (20.75), and using the equations of motion to eliminate time derivatives in favor of spatial ones, one arrives at the Hamiltonian density purely in terms of spatial operators.

Performing these steps, one obtains the Hamiltonian in coordinate space as

$$P^- = \int dx^- d^2 x_\perp \, \bar{\psi}(x) \, \frac{-\partial_\perp^2 + M^2}{2\,i\partial_-} \, \gamma^+ \psi(x)$$

$$-\frac{G_S}{2} \int dx^- d^2 x_\perp \left[\bar{\psi}\psi \, \hat{D}_+^{-1} \, \bar{\psi}\psi - \bar{\psi}\tau^a\psi \, \hat{D}_-^{-1} \, \bar{\psi}\tau^a\psi - \bar{\psi}i\gamma_5\psi \, \hat{D}_-^{-1} \, \bar{\psi}i\gamma_5\psi + \bar{\psi}i\gamma_5\tau^a\psi \, \hat{D}_+^{-1} \, \bar{\psi}i\gamma_5\tau^a\psi \right].$$

$$(20.76)$$

The first term is the familiar kinetic light-front Hamiltonian for a fermion of mass M, in which the longitudinal derivative ∂_- is inverted by the same Green's function that appeared in the elimination of the bad component. The second term is the interaction part, expressed as nonlocal four-fermion operators whose kernels are precisely the tadpole-resummed $\hat{D}_\pm^{-1}$.

For applications to bound states it is convenient to rewrite the Hamiltonian in momentum space. Introducing the measure

$$[d^3k]_+ = \frac{dk^+ \, d^2 k_\perp}{(2\pi)^3 \, 2k^+ \, \epsilon(k^+)}, \qquad (20.77)$$

where $\epsilon(k^+) = \theta(k^+) - \theta(-k^+)$ distinguishes particle and antiparticle regions, and the Fourier transform of the good field,

$$\psi(x^-, x_\perp) = \int [d^3k]_+ \, \psi(k) \, e^{-ik^+ x^- + i\mathbf{k}_\perp \cdot \mathbf{x}_\perp}, \qquad (20.78)$$

the Hamiltonian becomes

$$P^- = \int [d^3k]_+ \int [d^3q]_+ \, \frac{k_\perp^2 + M^2}{2k^+} \, \bar{\psi}(k) \, \gamma^+ \, \psi(q) \, (2\pi)^3 \, \delta_+^{(3)}(k-q)$$

$$+ \int [d^3k]_+ [d^3q]_+ [d^3p]_+ [d^3l]_+ \, (2\pi)^3 \, \delta_+^{(3)}(p+k-q-l) \, V(k,q;p,l), \qquad (20.79)$$

where the delta function $\delta_+^{(3)}(k-q) = \delta(k^+ - q^+) \, \delta^{(2)}(\mathbf{k}_\perp - \mathbf{q}_\perp)$ enforces momentum conservation, and $V(k,q;p,l)$ is the interaction kernel generated by the four-fermion part of (20.76). The first term in (20.79) is the kinetic part, while the second term describes the effective two-body interaction in all channels connected by the 't Hooft interaction.

The explicit form of the kernel in the scalar and pseudoscalar channels can be displayed in terms of the good-component spinors ψ_+. In the zero-size limit one can write

$$V(k,q;p,l) = -\frac{G_S}{2} \alpha_+(k^+ - q^+) \, \bar{\psi}_+(k) \Big(\frac{\boldsymbol{\gamma}_\perp \cdot \mathbf{k}_\perp + M}{2k^+} \gamma^+ + \gamma^+ \frac{\boldsymbol{\gamma}_\perp \cdot \mathbf{q}_\perp + M}{2q^+} \Big) \psi_+(q) \, \bar{\psi}_+(p) \Big(\frac{\boldsymbol{\gamma}_\perp \cdot \mathbf{p}_\perp + M}{2p^+} \gamma^+ + \gamma^+ \frac{\boldsymbol{\gamma}_\perp \cdot \mathbf{l}_\perp + M}{2l^+} \Big) \psi_+(l)$$

$$+ \frac{G_S}{2} \alpha_-(k^+ - q^+) \, \bar{\psi}_+(k) \Big(\frac{\boldsymbol{\gamma}_\perp \cdot \mathbf{k}_\perp + M}{2k^+} i\gamma^+ \gamma_5 + i\gamma_5 \gamma^+ \frac{\boldsymbol{\gamma}_\perp \cdot \mathbf{q}_\perp + M}{2q^+} \Big) \psi_+(q) \, \bar{\psi}_+(p) \Big(\frac{\boldsymbol{\gamma}_\perp \cdot \mathbf{p}_\perp + M}{2p^+} i\gamma^+ \gamma_5 + i\gamma_5 \gamma^+ \frac{\boldsymbol{\gamma}_\perp \cdot \mathbf{l}_\perp + M}{2l^+} \Big) \psi_+(l)$$

$$+ \frac{G_S}{2} \alpha_-(k^+ - q^+) \, \bar{\psi}_+(k) \Big(\frac{\boldsymbol{\gamma}_\perp \cdot \mathbf{k}_\perp + M}{2k^+} \gamma^+ \tau^a + \tau^a \gamma^+ \frac{\boldsymbol{\gamma}_\perp \cdot \mathbf{q}_\perp + M}{2q^+} \Big) \psi_+(q) \, \bar{\psi}_+(p) \Big(\frac{\boldsymbol{\gamma}_\perp \cdot \mathbf{p}_\perp + M}{2p^+} \gamma^+ \tau^a + \gamma^+ \tau^a \frac{\boldsymbol{\gamma}_\perp \cdot \mathbf{l}_\perp + M}{2l^+} \Big) \psi_+(l)$$

$$- \frac{G_S}{2} \alpha_+(k^+ - q^+) \, \bar{\psi}_+(k) \Big(\frac{\boldsymbol{\gamma}_\perp \cdot \mathbf{k}_\perp + M}{2k^+} i\gamma^+ \gamma_5 \tau^a + \tau^a i\gamma_5 \gamma^+ \frac{\boldsymbol{\gamma}_\perp \cdot \mathbf{q}_\perp + M}{2q^+} \Big) \psi_+(q) \, \bar{\psi}_+(p) \Big(\frac{\boldsymbol{\gamma}_\perp \cdot \mathbf{p}_\perp + M}{2p^+} i\gamma^+ \gamma_5 \tau^a + i\gamma_5 \gamma^+ \tau^a \frac{\boldsymbol{\gamma}_\perp \cdot \mathbf{l}_\perp + M}{2l^+} \Big) \psi_+($$

$$(20.80)$$

Although lengthy, this expression makes explicit how the Hamiltonian couples scalar, pseudoscalar and isovector channels through combinations of γ^+, γ_5, $\boldsymbol{\gamma}_\perp$, and the Pauli matrices τ^a. The functions $\alpha_\pm$ are tadpole-resummed vertex functions that encode the nontrivial vacuum structure through longitudinal zero modes; they depend only on the total longitudinal momentum flowing through the interaction.

For many purposes a compact form of the kernel is more transparent. In terms of the effective field ψ (rather than explicitly the projected ψ_+), and suppressing explicit Dirac structures, the interaction kernel in the zero-size limit can be summarized as

$$V(k,q;p,l) = -\frac{G_S}{2}\Big[\alpha_+(k^+ - q^+)\,\bar{\psi}(k)\psi(q)\,\bar{\psi}(p)\psi(l) - \alpha_-(k^+ - q^+)\,\bar{\psi}(k)i\gamma_5\psi(q)\,\bar{\psi}(p)i\gamma_5\psi(l)$$
$$-\alpha_-(k^+ - q^+)\,\bar{\psi}(k)\tau^a\psi(q)\,\bar{\psi}(p)\tau^a\psi(l) + \alpha_+(k^+ - q^+)\,\bar{\psi}(k)i\tau^a\gamma_5\psi(q)\,\bar{\psi}(p)i\tau^a\gamma_5\psi(l)\Big].$$
$$(20.81)$$

In this representation one clearly sees the decomposition into scalar-isoscalar, pseudoscalar-isoscalar, scalar-isovector, and pseudoscalar-isovector channels, with the vertex functions $\alpha_\pm$ distinguishing attractive and repulsive combinations after tadpole resummation.

The vertex functions themselves follow from the resummation of quark tadpoles and take the form

$$\alpha_\pm(P^+) = \left\{1 - 2g_S\int dl^+ d^2l_\perp\,\frac{1}{(2\pi)^3}\frac{\epsilon(l^+)}{P^+ - l^+}\right\}^{-1},\tag{20.82}$$

in the zero-size limit, where $g_S = N_c G_S$ is the 't Hooft coupling scaled with the number of colors. The integral runs over the longitudinal momenta of intermediate tadpole loops, and the denominator encodes the propagation along the light-front direction. The appearance of a nontrivial $\alpha_\pm$ expresses the impact of the instanton-induced vacuum on the light-front Hamiltonian: the vacuum is not trivial, but contributes through these resummed vertex factors.

The above construction extends naturally to the finite-size instanton case, where the nonlocal form factor $F(k)$ associated with the quark zero modes must be retained. In the Lagrangian, this amounts to replacing each quark field by the smeared field $\sqrt{F(i\partial)}\,\psi$, so that each four-fermion vertex is dressed by a product of form factors. In momentum space, this is implemented by inserting factors of $F(k)$ for each external leg. As a result, the Hamiltonian becomes

$$P^- = \int [d^3k]_+[d^3q]_+\,\frac{k_\perp^2 + M^2}{2k^+}\,\bar{\psi}(k)\gamma^+\psi(q)(2\pi)^3\,\delta_+^{(3)}(k-q)$$
$$+ \int [d^3k]_+[d^3q]_+[d^3p]_+[d^3l]_+\,(2\pi)^3\,\delta_+^{(3)}(p+k-q-l)\,\sqrt{F(k)F(q)F(p)F(l)}\,V(k,q;p,l),$$
$$(20.83)$$

where the kernel $V(k,q;p,l)$ is structurally the same as in (20.81), but with the vertex functions modified to

$$\alpha_\pm(P^+) \longrightarrow \left\{1 - 2g_S\int dl^+ d^2l_\perp\,\frac{1}{(2\pi)^3}\frac{\epsilon(l^+)}{P^+ - l^+}\,F(l)\,F(P-l)\right\}^{-1}.\tag{20.84}$$

These replacements reflect the finite size of instantons in the ILM and the corresponding momentum-dependent suppression of high-virtuality contributions. The factors $\sqrt{F}$ in (20.83) appear for each external quark leg, while the combination $F(l)F(P-l)$ enters the resummed tadpole loop in (20.84). Importantly, because the form factor $F(k)$ falls rapidly for large $|k|$, the resulting nonlocal Hamiltonian is well behaved and does not lead to pathological propagation.

To summarize, starting from the mean-field Lagrangian for the instanton-induced 't Hooft interaction on the light front, the canonical construction yields a light-front Hamiltonian of the form

$$P^- = P^-_{\text{kin}} + P^-_{\text{int}},\tag{20.85}$$

where P^-_{kin} describes a constituent quark of mass M with the standard light-front kinetic operator, and P^-_{int} encodes nonlocal four-fermion interactions in the scalar and pseudoscalar channels, dressed by vertex functions $\alpha_\pm$ that resum vacuum tadpoles and by form factors $F(k)$ inherited from the instanton zero modes. All of this is formulated entirely in terms of the good component of the quark field; the bad component has been eliminated as a constraint. The Hamiltonian thus obtained is boost invariant and provides a concrete, frame-independent realization of the nonperturbative instanton vacuum on the light front. It is

this Hamiltonian that will be diagonalized in subsequent sections in the quark-antiquark sector to obtain the light-front wave functions of pions and kaons, and from them their distribution amplitudes and parton distribution functions.

20.C Relation to the Wilsonian picture and light-front criticality

At first sight, the light-front Hamiltonian treatment presented above may appear to be in tension with the Wilsonian perspective emphasized earlier, in particular with the discussion of light-cone criticality in Sec. 2.7. The latter stresses that a formulation defined strictly at the light-front critical surface generically exhibits infrared pathologies associated with longitudinal zero modes and the absence of an intrinsic resolution scale.

The present construction should not, however, be interpreted as a canonical quantization performed directly at that critical point. Rather, the infrared sensitivity characteristic of light-front dynamics manifests itself here through a well-identified, power-counting-enhanced class of diagrams, namely tadpole chains associated with longitudinal zero-mode exchanges. These contributions are not treated perturbatively; instead, they are resummed into effective vertex functions $\alpha_\pm(P^+)$, which encode the vacuum structure and the dominant infrared physics of the theory.

From this viewpoint, the resummation procedure plays a role analogous to a Wilsonian matching step: degrees of freedom responsible for the strongest infrared enhancements are effectively integrated out and absorbed into renormalized operators of the light-front Hamiltonian. Subsequent calculations are then performed with these dressed interactions, which remain finite and well defined in the light-cone limit.

Thus, while the technical implementation differs from a conventional Wilsonian flow, the underlying logic is the same: potentially singular contributions associated with unresolved modes are reorganized into effective couplings before physical observables are computed. In this sense, the analysis above should be viewed as a concrete realization of the Wilsonian philosophy within a light-front Hamiltonian framework, rather than an exception to it.

Chapter 21
Pions on the LF

The pion plays a central role in QCD as both the pseudo-Goldstone boson of spontaneous chiral symmetry breaking (SχSB) and the lightest hadronic bound state. Understanding its structure within the light-front (LF) framework provides an illuminating example of how nonperturbative phenomena-traditionally associated with the vacuum-emerge from hadronic wave functions. In this chapter we will derive, in pedagogical fashion, the pion's decay constant, distribution amplitude (DA), and parton distribution function (PDF) using the nonlocal instanton-induced kernel of Ref. [Liu et al., 2023a]. We will also interpret these results in terms of chiral symmetry realization, angular momentum composition, and QCD evolution.

21.1 Light-Front pion bound-state

In the preceding sections we have constructed an effective light-front (LF) Hamiltonian for quarks derived from the induced multi-flavor interactions of the instanton liquid model (ILM) [Diakonov and Petrov, 1986, Schäfer and Shuryak, 1998, Diakonov, 2003, Nowak et al., 1996], and shown that (within the mean-field (large N_c) approximation and after elimination of the bad) light-cone components. The resulting constituent quark mass and chiral condensate coincide with their rest-frame values. We now use that Hamiltonian to diagonalize the two-body sector (valence $q\bar{q}$) in the light-front and extract the meson spectrum. In particular, for two light quark flavors (u, d) with equal current mass, we examine scalar and pseudoscalar mesons. The key result is that only the pseudoscalar isosinglet and isotriplet modes (the pions) emerge as strongly bound (Goldstone) states, while all other scalar or pseudoscalar modes remain unbound on the light front, in the mean-field approximation and away from the chiral limit [Diakonov et al., 1997, Schäfer and Shuryak, 1998, Nowak et al., 1996, Kacir et al., 1999]. We moreover extract the corresponding light-cone wave function for the pion, which yields a nonperturbative pion distribution amplitude (DA).

The LF Hamiltonian derived can be cast, in the two-body valence approximation, into an eigenvalue equation

$$P^-\big|X, P_i\big\rangle = \frac{m_X^2}{2P^+}\big|X, P_i\big\rangle, \tag{21.1}$$

or equivalently (multiplying by $2P^+$)

$$\hat{H}_{\mathrm{LF}}\big|X, P_i\big\rangle = m_X^2\big|X, P_i\big\rangle. \tag{21.2}$$

In the valence (leading $1/N_c$) sector the meson state is dominated by a constituent-quark and antiquark, and may be written as

$$\big|\mathrm{Meson}\ X, P_i\big\rangle = \frac{1}{\sqrt{N_c}}\int_0^1 \frac{dx}{\sqrt{2x\bar{x}}}\int \frac{d^2k_\perp}{(2\pi)^3}\sum_{s_1,s_2}\Phi_X(x, k_\perp, s_1, s_2)\, b_{s_1}^\dagger(k)\, d_{s_2}^\dagger(P-k)\,|0\rangle, \tag{21.3}$$

with normalization

$$\int_0^1 dx \int \frac{d^2k_\perp}{(2\pi)^3} \sum_{s_1,s_2} \left| \Phi_X(x, k_\perp, s_1, s_2) \right|^2 = 1. \tag{21.4}$$

Here $x = k^+/P^+$, $\bar{x} = 1 - x$, and M denotes the constituent quark mass generated by the ILM instanton-induced dynamics. The light-front Hamiltonian matrix elements between these two-body states lead to bound-state equations in momentum space.

For two light flavors (u, d) with identical current mass m, the relevant mesonic channels are the isosinglet scalar σ, the isosinglet pseudoscalar η_0 (denoted σ_5 in the original paper), the isotriplet pseudoscalar $\pi^{\pm,0}$, and the corresponding non-singlet scalar partners. The flavor structure in the valence sector is

$$\sigma = \frac{1}{\sqrt{2}}(u\bar{u} + d\bar{d}), \qquad \pi = \frac{1}{\sqrt{2}}(u\bar{u} - d\bar{d}), \qquad \pi^\pm = u\bar{d},\ d\bar{u}.$$

By construction of the instanton-induced interaction in the ILM, the scalar-isoscalar (σ) channel and the pseudoscalar isotriplet (π) channel are strongly attractive, while the pseudoscalar isosinglet (η_0) channel and non-singlet scalar/pseudoscalar partners are strongly repulsive ['t Hooft, 1976, Shifman et al., 1980, Schäfer and Shuryak, 1998, Kacir et al., 1999]. As a result, only the π emerges as a bound state, while the others remain unbound or appear only at threshold.

Denoting by Φ_X the light-cone wave function (LCWF) of meson X, the Hamiltonian eigenvalue equation reduces to an integral equation of the general form

$$\left[k_\perp^2 + M^2\right]\Phi_X(x, k_\perp) + \int dx' d^2 q_\perp\, V_X(x, k_\perp; x', q_\perp)\, \Phi_X(x', q_\perp) = m_X^2\, \Phi_X(x, k_\perp).$$

Here V_X is the effective two-body kernel arising from the instanton-induced four-fermion interaction (after eliminating the bad components), projected in the scalar or pseudoscalar channel. In the pseudoscalar (π) channel the kernel is attractive and strong enough to bind.

In the ILM, the interaction kernel (in the two-body light-front Hamiltonian) takes the form (suppressing spinor and color structure for clarity)

$$V_\pi(k, q)\ \sim\ -g_S\, F(k)\, F(q)\, \bar{u}(k)\, \Gamma_\pi\, u(P-k)\, \bar{v}(q)\, \Gamma_\pi\, v(P-q), \tag{21.5}$$

where g_S is the effective coupling associated with the 't Hooft interaction, and Γ_π denotes the spin-flavor Dirac structure appropriate for the pseudoscalar isotriplet channel (e.g. $\gamma^5 \tau^a$ in flavor space, plus the usual LF spinor projectors). The factors $F(k)$, $F(q)$ stem from the zero-mode profile, thus making the effective interaction non-local in momentum space and strongly suppressing large momenta ($\gtrsim 1/\rho$). This non-locality (finite instanton size) is essential for rendering the integrals finite and preserving the boost-invariance of the LF Hamiltonian [Liu et al., 2023b, Liu et al., 2024d]. More specifically, in Euclidean momentum space the form factor is given by

$$F(k) = \left(z\, F_0(z)\right)^2, \qquad z = \tfrac{1}{2}\, k\rho, \qquad F_0(z) = I_0(z)K_0(z) - I_1(z)K_1(z), \tag{21.6}$$

where ρ is the (average) instanton size, and I_ν, K_ν are modified Bessel functions. This form factor ensures that the induced interactions are smeared over a distance scale $\sim \rho$, avoiding the divergences associated with a strictly local four-fermion interaction.

21.2 Pion DA

The good-component light-front spinors for quarks and antiquarks are given by
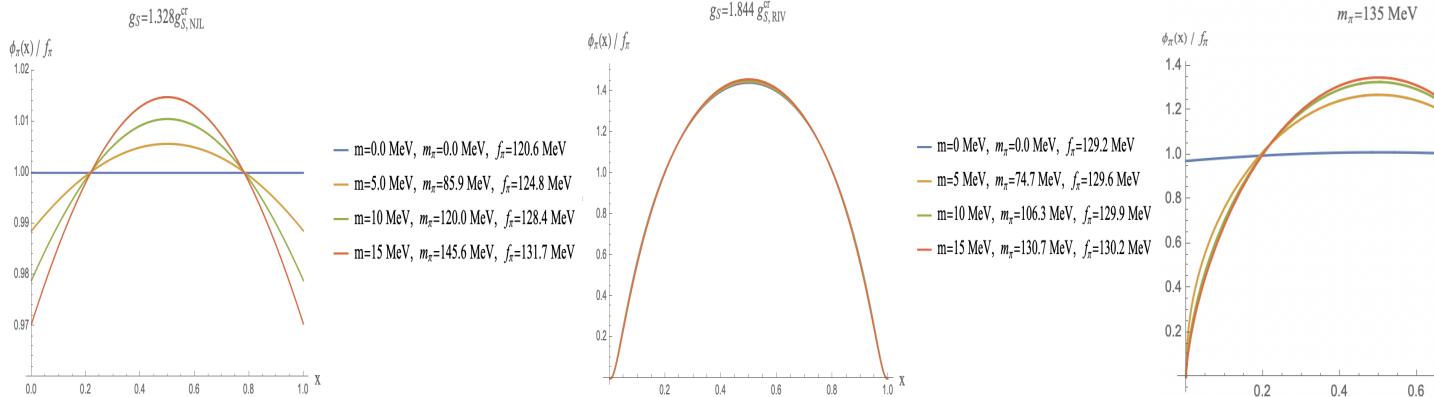
Fig. 21.1.1 a: The pion DA with different pion mass m_π in the zero instanton size limit; b: The pion DA with different pion mass m_π in the ILM with finite instanton size $\rho = (630\text{MeV})^{-1}$; c: The ERBL evolution of pion DA in zero instanton size limit; d: The ERBL evolution of pion DA in RIV with finite instanton size $\rho = (630\text{MeV})^{-1}$.

$$u_s(p) = \frac{1}{\sqrt{2p^+}} \left(\not{p} + M \right) \begin{pmatrix} \chi_s \\ \chi_s \end{pmatrix}, \qquad v_s(p) = \frac{1}{\sqrt{2p^+}} \left(\not{p} - M \right) \begin{pmatrix} \chi_s \\ -\chi_s \end{pmatrix}, \qquad (21.7)$$

with χ_s a two-component spinor (helicity). Thus the pseudoscalar Dirac structure for the pion, in the valence Fock sector, can be written as

$$\Phi_\pi(x, k_\perp, s_1, s_2) = \varphi_\pi(x, k_\perp) \, \bar{u}_{s_1}(k) \, \gamma^5 \tau^a \, v_{s_2}(P - k), \qquad (21.8)$$

where $\varphi_\pi(x, k_\perp)$ is a scalar function encoding the momentum dependence (effectively the radial wave function in LF variables), and τ^a is a Pauli matrix in flavor space selecting the appropriate isospin component of the pion. The normalization of φ_π then follows from eq. (21.8) after squaring/summing/integrating over spin and momentum [Liu et al., 2023b, Liu et al., 2024d].
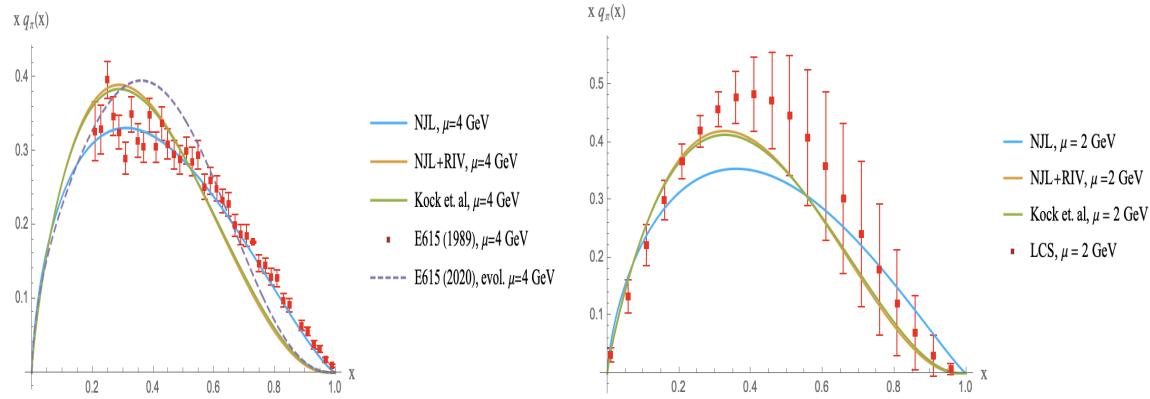
Fig. 21.2.1 a: Pion parton momentum distribution function for zero instanton size (solid-blue) and finite instanton size of $\rho = 0.317$ fm (solid-orange), both of which are evolved to $\mu = 4$ GeV with a pion mass $m_\pi = 135$ MeV. The results are compared to the those extracted from the ILM using the LaMET (solid-green) [Kock et al., 2020, Kock and Zahed, 2021], also evolved to $\mu = 4$ GeV. The E615 data from 1989 (red) are from [Conway et al., 1989], corresponding to a fixed invariant muon pair mass $m_{\mu^+\mu^-} \geq 4.05$ GeV. The improved E615 data from 2020 (dashed-purple) are from [Aicher et al., 2010], using the original E615 experimental data from [Conway et al., 1989].
b: The same pion parton distribution functions as in a, but now evolved to $\mu = 2$ GeV, for comparison with the lattice data using cross sections (LCS) (red) from [Sufian et al., 2020].

In practice, one inserts the explicit zero-mode profile (eq. (21.6)) when computing the overlap integrals. For equal-mass quarks the kernel simplifies to a function depending only on the relative momenta $k_\perp, q_\perp$ and the longitudinal momentum fractions x, x'. One obtains an explicit expression (in the so-called "zero-instanton-size limit" $F \to 1$) for V_π, but in the finite-ρ ILM the factors $F(k)F(q)$ regulate the integrals and modify quantitatively the binding condition. In the zero-instanton-size limit (pointlike interaction), and with a boost-invariant momentum cutoff Λ, the bound-state equation simplifies and yields a relation for the pion mass m_π. In that limit the bound-state condition reads (for π)

$$m_\pi^2 \; - \; \frac{m}{M} \; = \; \frac{g_S}{4\pi^2}\, m_\pi^2 \int_0^1 dy \int_0^{\Lambda^2} dq_\perp^2 \; \frac{1}{q_\perp^2 + M^2 - y\bar{y}\, m_\pi^2},$$

which upon evaluation yields a pion mass that vanishes in the chiral limit $m \to 0$, thus realizing the Goldstone theorem on the light-front. More precisely one finds

$$m_\pi^2 = \frac{2m}{f_\pi^2}\, |\langle \bar{\psi}\psi \rangle| + \mathcal{O}(m^2),$$

with f_π the pion decay constant and $\langle \bar{\psi}\psi \rangle$ the chiral condensate – the same relation as in the rest frame [Gell-Mann et al., 1968, Donoghue et al., 1992]. This demonstrates that the spontaneous breaking of chiral symmetry by instanton effects in the ILM is correctly carried over in the light-front formalism, and that the pion emerges as a genuine light-front Goldstone mode [Diakonov, 1997, Schäfer and Shuryak, 1998, Nowak et al., 1996].

In all other scalar and pseudoscalar channels (e.g., σ_5, η_0, non-singlet scalar/pseudoscalar), the instanton-induced kernel is repulsive or insufficiently attractive; correspondingly the integral equations admit no bound-state solution below the two-constituent quark threshold. In particular the would-be scalar σ is at threshold (mass $\simeq 2M$ in the chiral limit), and the η_0 remains unbound. This result aligns with the expectation from the ILM that only the pseudoscalar-isotriplet modes are strongly bound due to the 't Hooft interaction ['t Hooft, 1976].

The pion decay constant f_π quantifies the overlap between the vacuum axial current and the one-pion state

$$\langle 0|\bar{q}(0)\gamma^\mu\gamma_5 q(0)|\pi(P)\rangle = i f_\pi P^\mu. \tag{21.9}$$

On the light front, we use the "plus" component ($\mu = +$) to avoid instantaneous terms. In terms of the valence LFWF, the pion decay constant reads

$$f_\pi = \sqrt{N_c} \int_0^1 dx \int \frac{d^2 \boldsymbol{k}_\perp}{(2\pi)^3} \frac{\phi_\pi(x, \boldsymbol{k}_\perp)\, \mathcal{S}(x, \boldsymbol{k}_\perp)}{\sqrt{x(1-x)}}, \tag{21.10}$$

where $\mathcal{S}$ contains spinor traces involving $\gamma^+\gamma_5$ and the nonlocal form factors. The factor $\sqrt{x(1-x)}$ arises from the Jacobian of the LF normalization.

Physically, f_π measures how much of the pion internal structure is "aligned" with the axial current. In the instanton framework, f_π is directly proportional to the dynamical quark mass $M(k)$ and to the instanton density, establishing a link between the microscopic (instanton) and macroscopic (hadronic) scales. At high scales, $\phi_\pi(x) \to \phi_\pi(x,\mu)$ evolves according to the Efremov-Radyushkin-Brodsky-Lepage (ERBL) equation [Efremov and Radyushkin, 1980b, Lepage and Brodsky, 1980], which governs its approach to the asymptotic form $\phi_\pi^{as}(x) = 6x(1-x)$. The nonlocal instanton model provides an initial condition at a low scale $\mu_0 \simeq$ 0.6-1 GeV that is broader than the asymptotic shape, consistent with lattice and experimental constraints [Shi et al., 2015b, Zhang et al., 2020].

Appendix

21.A Melosh rotations and spinor algebra

In this appendix we summarize the role of Melosh rotations in connecting canonical spin to light-front helicity. This is essential for understanding how the pion, although a spin-zero bound state, contains nontrivial orbital and spin correlations encoded in its light-front wave function [Melosh, 1974, Keister and Polyzou, 1991, Bakker et al., 2014]. The relativistic nature of LF dynamics implies that the naive nonrelativistic spin-addition rules do not directly apply; Melosh rotations correct for this mismatch.

On the light front, the helicity basis differs from the instant form due to boosts along the x^- direction. The spin wave function is obtained by applying the Melosh rotation:

$$R_M(x, \boldsymbol{k}_\perp) = \frac{m + xM_0 - i\sigma \cdot (\hat{n} \times \boldsymbol{k}_\perp)}{\sqrt{(m + xM_0)^2 + \boldsymbol{k}_\perp^2}}, \tag{21.11}$$

where $\hat{n}$ is the unit vector along the z-axis and M_0 is the invariant mass of the $q\bar{q}$ pair. This rotation connects canonical spin to LF helicity. Using these rotations, the spinor factor in the axial current matrix element is

$$\mathcal{S}(x, \boldsymbol{k}_\perp) = \frac{m^2 + \boldsymbol{k}_\perp^2 - x(1-x)M_\pi^2}{\sqrt{(m^2 + \boldsymbol{k}_\perp^2)/[x(1-x)]}}, \tag{21.12}$$

up to normalization. This factor controls the relativistic suppression of helicity nonconserving components and explains why the pion DA is broader at low scales than the asymptotic form.

21.B From Bethe-Salpeter to LFWFs

Here we outline how the covariant Bethe-Salpeter (BS) description of the pion in the instanton vacuum [Liu et al., 2023b, Liu et al., 2024d] is mapped to a light-front wave function. The key step is to integrate over the LF energy k^-, which enforces on-shell propagation of one of the constituents and produces the familiar LF energy denominator.

To obtain the LF wave function, integrate the BS amplitude over k^-:

$$\Psi_\pi(x, \boldsymbol{k}_\perp) = \int \frac{\mathrm{d}k^-}{2\pi} \, \Gamma_\pi(k; P) \, S(k + \tfrac{P}{2}) S(k - \tfrac{P}{2}). \tag{21.13}$$

Closing the contour in the lower half-plane picks the pole of $S(k^-)$ corresponding to the on-shell quark. This leads to

$$S(k) \approx \frac{\slashed{k} + M(k)}{k^2 - M^2(k) + i\epsilon} \rightarrow \frac{1}{2k^+} \frac{\gamma^+}{k^- - (M^2 + \boldsymbol{k}_\perp^2)/k^+}. \tag{21.14}$$

Performing the k^- integral yields the LF energy denominator $M_\pi^2 - \mathcal{M}^2$. The nonlocality of Γ_π introduces form factors $F((k-\ell)^2)$ that regularize UV behavior and encode the instanton profile. This procedure ensures that chiral Ward identities and the GMOR relation remain valid in the LF representation.

21.C Instanton Form Factors and Normalization

The quark zero mode in an instanton background follows the BPST form [Belavin et al., 1975] and is a central building block of the ILM. In coordinate space (regular gauge)

$$\psi_0(x) = \frac{\rho}{\pi} \frac{1}{(x^2 + \rho^2)^{3/2}} \frac{1 - \gamma_5 \slashed{x}/\sqrt{x^2}}{2} U, \tag{21.15}$$

where ρ is the instanton size and U a color rotation. Its Fourier transform gives the form factor

$$F(k\rho) = 2z[I_0(z)K_1(z) - I_1(z)K_0(z) - I_1(z)K_1(z)/z], \quad z = k\rho/2, \tag{21.16}$$

which is closely related to the function in Eq. (21.6). The nonlocal kernel is

$$\mathcal{K}(k_1, \ldots, k_{2N_f}) = G \prod_i F(k_i\rho)(2\pi)^4 \delta^{(4)}\Big(\sum k_i\Big), \tag{21.17}$$

with G determined by the instanton density n and distribution $d(\rho)$. Using $n \simeq 1$ fm^{-4} and $\rho \simeq 0.33$ fm yields $G \sim$ 5-10 GeV^{-2} [Shuryak, 1982e, Schäfer and Shuryak, 1998, Nowak et al., 1996]. These parameters quantitatively reproduce the observed condensate and f_π values and set the model scale for the DA and PDF.

21.D From Covariant to Light-Front Gap Equation

Finally, we comment on the relation between the covariant gap equation and its LF counterpart. The Euclidean gap equation

$$M(p_E) = m + \int \frac{\mathrm{d}^4\ell_E}{(2\pi)^4} K(p_E, \ell_E) \frac{M(\ell_E)}{\ell_E^2 + M^2(\ell_E)} \tag{21.18}$$

is transformed to LF variables via $\ell^\pm = \ell^0 \pm \ell^3$:

$$M(x, \boldsymbol{\ell}_\perp) = m + \int_0^1 \mathrm{d}y \int \frac{\mathrm{d}^2\boldsymbol{k}_\perp}{(2\pi)^3} K(x, \boldsymbol{\ell}_\perp; y, \boldsymbol{k}_\perp) \frac{M(y, \boldsymbol{k}_\perp)}{\boldsymbol{k}_\perp^2 + M^2(y, \boldsymbol{k}_\perp) - y(1-y)P^{+2}}. \tag{21.19}$$

Boundary terms at $x = 0, 1$ carry zero-mode contributions that generate $\langle \bar{q}q \rangle_{\mathrm{LF}}$. Numerical solutions show the same critical coupling G_{crit} as in covariant approaches, confirming full equivalence when zero modes are retained [Chang et al., 2013, Liu et al., 2023b, Liu et al., 2024d]. This supports the consistency of implementing SχSB and Goldstone dynamics directly on the light front.

Chapter 22
Kaons on the LF

The kaon provides a central bridge between the dynamics of spontaneous chiral symmetry breaking and the explicit breaking introduced by the strange quark mass [Gell-Mann et al., 1968, Donoghue et al., 1992]. Within the light-front formulation [Brodsky et al., 1998a], its description becomes especially transparent because the wave function is expressed directly in terms of boost-invariant momentum fractions. The appearance of an asymmetric mass distribution between the constituent quarks becomes immediately reflected in the internal kinematic structure, the bound-state dynamics, and ultimately the partonic content of the state.

In the instanton liquid model, the nonperturbative vacuum induces a multi-fermion interaction with the correct chiral and flavor structure to generate Goldstone modes [Diakonov et al., 1997, Schäfer and Shuryak, 1998, Nowak et al., 1996]. The u, d, and s quarks enter symmetrically through the 't Hooft determinant ['t Hooft, 1976], but the heavier strange quark produces explicit SU(3) flavor breaking. The kaon thus emerges from the same vacuum structure as the pion, yet with a built-in mass asymmetry that becomes encoded directly into its light-front wave function.

In what follows, the dynamics is organized in the SU(3) subgroups known as U-spin and V-spin, which interchange nonstrange and strange quarks [Liu et al., 2023b]. Because the u and d quarks remain nearly degenerate, both sectors exhibit identical light-front dynamics. It suffices to write the analysis for a single kaon wave function Φ_K, with the understanding that the charged and neutral kaons follow by trivial flavor replacement.

22.1 Flavor structure and the light-front kaon wave function

The relevant quark-antiquark content of the kaon can be formulated in either the U-spin or V-spin representation, both of which rotate nonstrange quarks into strange quarks [Liu et al., 2023b]. For the charged kaons, the $u\bar{s}$ and $s\bar{u}$ configurations define the U-spin doublet, while the neutral $d\bar{s}$ and $s\bar{d}$ belong to the V-spin sector. In either case, isospin symmetry ensures that u and d can be treated equivalently, so that the light-front wave functions obey

$$\Phi_{K^+} = \Phi_{K^-} = \Phi_{K^0} = \Phi_{\bar{K}^0} \equiv \Phi_K.$$

The kaon contains both a pseudoscalar and a scalar channel due to the chirality structure of the instanton-induced interaction. These channels are represented by the light-front wave functions

$$\Phi_{K_5}(x, k_\perp, s_1, s_2) = \phi_{K_5}(x, k_\perp)\, \bar{u}_{s_1}(k)\tau^\pm v_{s_2}(P - k), \tag{22.1}$$

$$\Phi_K(x, k_\perp, s_1, s_2) = \phi_K(x, k_\perp)\, \bar{u}_{s_1}(k)i\gamma^5\tau^\pm v_{s_2}(P - k), \tag{22.2}$$

where the scalar functions ϕ_{K_5} and ϕ_K encode the nonperturbative momentum structure and $\tau^{\pm}$ denote the U- or V-spin raising and lowering operators.

The unequal quark masses M_u and M_s introduce an inherent asymmetry in the longitudinal momentum distribution [Keister and Polyzou, 1991]. The light quark tends to carry a larger momentum fraction because the kinetic term $(k_\perp^2 + M^2)/x$ penalizes the heavier strange quark more strongly as x decreases. This UV-finite, boost-invariant structure is preserved by the instanton form factor $\mathcal{F}$, which depends only on the combination

$$\frac{k_\perp^2 + M_u^2}{x} + \frac{k_\perp^2 + M_s^2}{\bar{x}},$$

and therefore ensures that the nonlocal interaction is consistent with light-front symmetry [Liu et al., 2023b, Liu et al., 2024d].

22.2 Physical content of the kaon bound-state equations

The instanton-induced interaction contains the same essential physics that produces the pion as a Goldstone boson, but extended to three flavors [Nowak et al., 1989, Kacir et al., 1999, Liu et al., 2023b]. Its determinantal structure explicitly couples left- and right-handed quarks and mixes the pseudoscalar and scalar channels. When restricted to the valence two-body sector, the effective Hamiltonian on the light front contains the free kinematic term and a nonlocal kernel determined by the instanton zero-mode profile [Liu et al., 2023b].

The resulting bound-state equation takes the form of an inhomogeneous integral equation. The kernels include the functions $\alpha_{K\pm}$ that incorporate quark-loop dressing of the 't Hooft vertex; these encode the effects of mass generation and the interplay between u and s constituents ['t Hooft, 1976]. The scalar and pseudoscalar channels are repulsive and attractive, respectively, producing an unbound scalar partner but a deeply bound pseudoscalar kaon.

All mathematical expressions for the kernels and their spin traces appear in Appendix 22.A. Here we emphasize their physical meaning. The pseudoscalar interaction is enhanced relative to the scalar channel because instantons induce chirality flips that match the pseudoscalar quantum numbers [Schäfer and Shuryak, 1998, Kacir et al., 1999]. The SU(3)-breaking mass difference $M_s - M_u$ tilts the kernel and shifts the momentum distribution in favor of the lighter quark. The resulting light-front wave function is therefore asymmetric even before evolution to higher scales [Shi et al., 2015b].

22.3 Kaon mass, the scalar channel, and the GOR relation

The mass eigenvalues follow from a spectral equation derived from the bound-state kernel. The pseudoscalar channel yields an eigenvalue m_K in the expected range between $(M_s - M_u)$ and $(M_s + M_u)$, while the scalar kaon partner K_5 is pushed above the cutoff and remains unbound. The physical kaon mass arises from the interplay between chiral symmetry breaking and explicit SU(3) violation [Gell-Mann et al., 1968, Donoghue et al., 1992, Kacir et al., 1999].

When expanded in the limit of small current masses, the mass equation reduces to the Gell-Mann-Oakes-Renner relation,

$$m_K^2 = \frac{m_u + m_s}{f_K^2} |\langle \bar{u}u \rangle + \langle \bar{s}s \rangle| + \cdots,$$

which shows that the kaon remains a pseudo-Goldstone boson despite the heavier strange quark. The condensate receives contributions from both flavors weighted symmetrically, reflecting the structure of the 't Hooft interaction.

The decay constant f_K follows from the normalization of the axial current. In the instanton liquid model it inherits a logarithmic sensitivity to the instanton size and matches the chiral expansion when the constituent masses and form factor are used consistently [Donoghue et al., 1992, Kacir et al., 1999]. The detailed derivation is presented in Appendix 22.B.
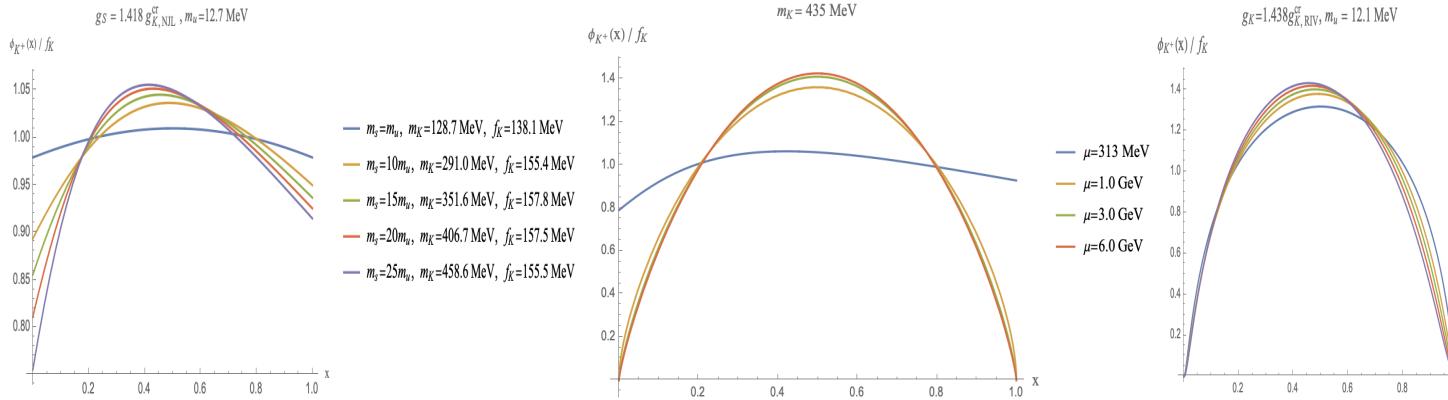
Fig. 22.3.1 a: The positive charged kaon DA versus parton x, for fixed coupling $g_S/g_K^{cr} = 1.418$ and fixed $m_u = 12.7$ MeV, but different ratios m_s/m_u, in the zero instanton size limit; b: The positive charged kaon DA versus parton x, for fixed $m_K = 435$ MeV using the ERBL evolution from the initial $\mu = 0.313$ GeV to $\mu = 6$ GeV; c,d: Same as a,b but in the ILM, for a fixed instanton size $\rho = 0.313$ fm.
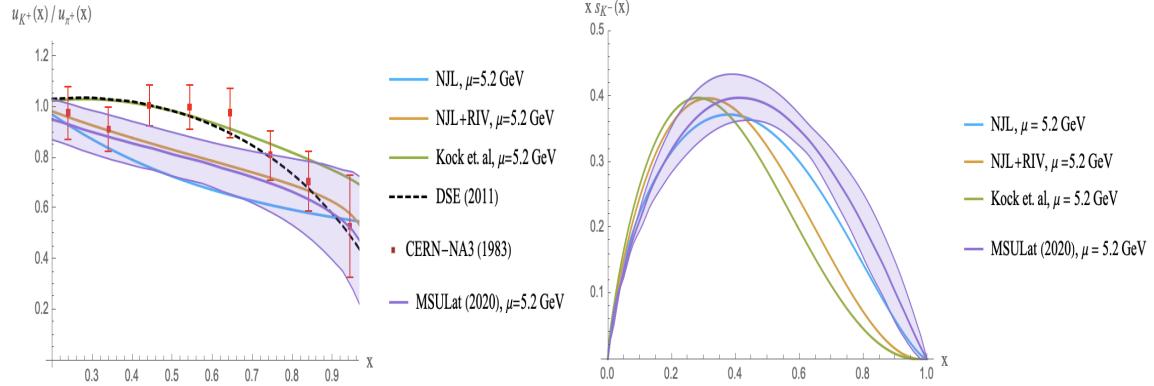
Fig. 22.3.2 a: The ratio of positive charge kaon to pion PDF versus parton x, in the zero instanton size limit, with $m_K = 435$ MeV and evolved to $\mu = 5.2$ GeV (solid-blue), in the ILM with finite instanton size $\rho = 0.318$ fm with $m_K = 431$ MeV and evolved to $\mu = 5.2$ GeV (solid-orange). The comparison is to the results of the ILM using the LaMET extraction in [Kock et al., 2020, Kock and Zahed, 2021] and evolved to $\mu = 5.2$ GeV (solid-green), and the results from the Dyson-Schwinger equation with full Bethe-Salpeter wavefunction [Bashir et al., 2012] (dashed-black). The data for the measured ratio (red) are from [Badier et al., 1980] using muon pair production, using the invariant mass cuts between 4.1 GeV and 8.5 GeV to eliminate the meson production on resonance. The recent lattice data MSULat (band-purple) are from [Lin et al., 2021], using the LaMET construction, at $\mu = 5.2$ GeV. b: The same as in b, but for the strange quark momentum distribution for the negative kaon $x s_{K^-}(x)$ versus x.

22.4 Distribution amplitudes and parton distribution functions

The light-front wave function directly determines both the distribution amplitude (DA) and the parton distribution function (PDF). Because the kaon contains a heavier strange quark, the momentum distribution is skewed toward the nonstrange quark. This phenomenon is already present at the model scale, well before perturbative evolution is applied [Shi et al., 2015b, Liu et al., 2023b].

The DA measures the projection of the wave function onto zero transverse separation. Its asymmetry is a clear signature of SU(3) breaking and is consistent with lattice calculations and Dyson-Schwinger results [Shi et al., 2015b, Zhang et al., 2020]. Under ERBL evolution the DA slowly approaches the asymptotic form, but retains a noticeable skewness at experimentally relevant scales [Liu et al., 2023b].

The PDF is obtained by integrating the absolute square of the wave function over transverse momentum. The strange antiquark distribution peaks at larger momentum fractions than the light quark distribution. This asymmetry has been observed in Drell-Yan experiments and lattice extractions and is a robust prediction of the instanton framework [Liu et al., 2023b].

All explicit integral expressions for the DA and PDF are given in Appendix 22.B. Their forms depend on the instanton form factor or on the transverse cutoff in the zero-size limit, but their qualitative behavior follows directly from the constituent mass hierarchy [Liu et al., 2023b].
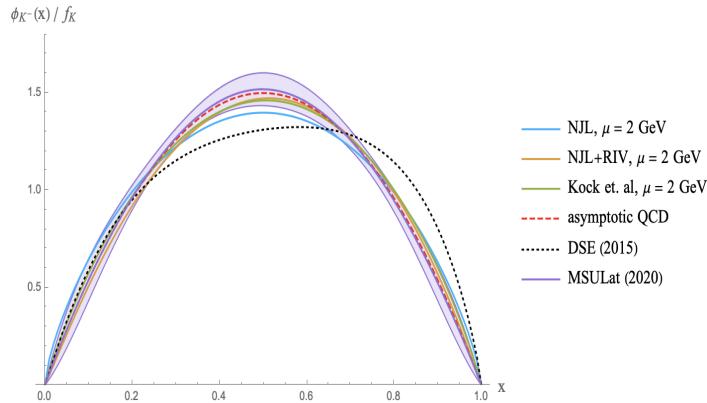
Fig. 22.4.1 Evolution of the negative kaon DA with $m_K = 435$ MeV, from $\mu = 0.313$ GeV to $\mu = 2$ GeV in the zero instanton size limit (solid-blue), and in the ILM with a finite instanton size with $m_K = 431$ MeV (solid-orange) [Liu et al., 2023b]. The results are compared to those obtained also from the ILM (solid-green), using the LaMET construction in [Kock et al., 2020, Kock and Zahed, 2021], also evolved to $\mu = 2$ GeV. The results using the Dyson-Schwinger equation with Bethe-Salpeter wavefunctions (dashed-black) are from [Bashir et al., 2012]. The QCD asymptotic result of $6x\bar{x}$ (dashed-red) is from [Lepage and Brodsky, 1980, Efremov and Radyushkin, 1980a]. The recent lattice data MSULat(2020) (purple-band) are from [Lin et al., 2021] using the LaMET construction.

Appendix

22.A Full Bound-State Equation and Instanton Kernel

In this appendix we collect the explicit light-front bound-state equations and the corresponding instanton-induced kernels that underlie the qualitative discussion in Sec. 22.2. The goal is to make clear how the nonlocal 't Hooft interaction, when projected on the valence sector and expressed in light-front variables, leads to the coupled scalar and pseudoscalar equations for the kaon. Throughout, we keep the notation as close as possible to the main text, so that the physical interpretation of each ingredient remains transparent [Liu et al., 2024e].

The starting point is the effective ILM interaction in the three-flavor sector. After bosonization in the scalar and pseudoscalar channels and restriction to the $q\bar{q}$ Fock sector, one arrives at a light-front Hamiltonian consisting of a free kinetic term plus a nonlocal kernel that encodes instanton zero-mode overlap. The structure of the kernel is constrained by chiral symmetry and SU(3) flavor, and the explicit expressions given below show how this information feeds into the kaon bound-state problem.

22.A.1 Light-front wave functions and Dirac structure

The kaon wave functions in the scalar and pseudoscalar channels are

$$\Phi_{K_5}(x, k_\perp, s_1, s_2) = \phi_{K_5}(x, k_\perp)\bar{u}_{s_1}(k)\tau^\pm v_{s_2}(P - k), \tag{22.3}$$

$$\Phi_K(x, k_\perp, s_1, s_2) = \phi_K(x, k_\perp)\bar{u}_{s_1}(k)i\gamma^5\tau^\pm v_{s_2}(P - k). \tag{22.4}$$

The spinor factors implement the scalar and pseudoscalar Dirac structures, while the scalar functions ϕ_{K_5} and ϕ_K capture the nonperturbative momentum dependence. The use of U- or V-spin raising and lowering operators $\tau^\pm$ ensures that the same formalism applies to both charged and neutral kaons, differing only by flavor labels.

22.A.2 Boost-invariant instanton form factor

The nonlocality of the instanton zero-mode implies

$$\lim_{P^+ \to \infty} \sqrt{\mathcal{F}_u(k)\mathcal{F}_s(P - k)} \to \mathcal{F}\left(\frac{k_\perp^2 + M_u^2}{x} + \frac{k_\perp^2 + M_s^2}{\bar{x}}\right). \tag{22.5}$$

This shows explicitly that, in the infinite-momentum frame, the nonlocal form factor depends only on boost-invariant combinations of the transverse momentum and longitudinal fractions. The same functional form

appears in the pion sector, but with $M_u = M_d$, so that the kaon case illustrates how SU(3) breaking deforms an otherwise universal instanton profile [Liu et al., 2023b].

22.A.3 Complete bound-state equation

The kaon bound-state equation is

$$
m_K^2 \Phi_K(x, k_\perp, s_1, s_2) = \left[\frac{k_\perp^2 + M_u^2}{x} + \frac{k_\perp^2 + M_s^2}{\bar{x}} \right] \Phi_K(x, k_\perp, s_1, s_2)
$$
$$
+ \frac{1}{\sqrt{2x\bar{x}}} \sqrt{\mathcal{F}_u(k)\mathcal{F}_s(P-k)} \int_0^1 \frac{dy}{\sqrt{2y\bar{y}}} \int \frac{d^2 q_\perp}{(2\pi)^3} \sum_{s,s'} \mathcal{V}_{s,s',s_1,s_2} \Phi_K(y, q_\perp, s, s') \sqrt{\mathcal{F}_u(q)\mathcal{F}_s(P-q)}.
$$

$$(22.6)$$

The first line encodes the kinetic energy of quark and antiquark with unequal constituent masses, while the second line represents the nonlocal interaction mediated by the ILM kernel. The structure is entirely analogous to the pion case, but with modified kinematics and flavor factors appropriate to the $u\bar{s}$ system.

22.A.4 Instanton-induced spin kernel

The interaction kernel is

$$
\mathcal{V}_{s,s',s_1,s_2} = -g_K \left[\alpha_{K+} \bar{u}_{s_1}(k)\tau^+ i\gamma^5 v_{s_2}(k') \bar{v}_{s'}(q')\tau^- i\gamma^5 u_s(q) - \alpha_{K-} \bar{u}_{s_1}(k)\tau^+ v_{s_2}(k') \bar{v}_{s'}(q')\tau^- u_s(q) \right.
$$
$$
\left. + \alpha_{K+} \bar{u}_{s_1}(k)\tau^- i\gamma^5 v_{s_2}(k') \bar{v}_{s'}(q')\tau^+ i\gamma^5 u_s(q) - \alpha_{K-} \bar{u}_{s_1}(k)\tau^- v_{s_2}(k') \bar{v}_{s'}(q')\tau^+ u_s(q) \right].
$$

$$(22.7)$$

The structure of $\mathcal{V}$ displays explicitly how the ILM couples pseudoscalar and scalar channels: the terms proportional to α_{K+} involve $i\gamma^5$ and drive the attractive pseudoscalar interaction, while those proportional to α_{K-} generate the repulsive scalar contribution. The dressing functions $\alpha_{K\pm}$ resum tadpole-like quark loops and therefore encode the response of the vacuum to the presence of the kaon state [Liu et al., 2023b].

22.A.5 Dressing functions $\alpha_{K\pm}$

$$
\alpha_{K\pm} = \left[1 \pm g_K \int \frac{dk^+ d^2 k_\perp}{(2\pi)^3} \frac{\epsilon(k^+)}{P^+ - k^+} \left(\mathcal{F}_u(k)\mathcal{F}_s(P-k) + \mathcal{F}_s(k)\mathcal{F}_u(P-k) \right) \right]^{-1}.
$$

$$(22.8)$$

These functions summarize the strength of the effective interaction in each channel. In the chiral limit and in the pion sector, the analogous functions reduce to simple constants fixed by the gap equation; here, the presence of the strange quark mass and the asymmetry between M_u and M_s makes the dressing more intricate and feeds directly into the different binding patterns of K and K_5.

22.A.6 Scalar and pseudoscalar bound-state equations

$$m_{K_5}^2 \phi_{K_5} = \left[\frac{k_\perp^2 + M_u^2}{x} + \frac{k_\perp^2 + M_s^2}{\bar{x}} \right] \phi_{K_5} + \frac{2g_K \alpha_{K-}}{\sqrt{x\bar{x}}} \sqrt{\mathcal{F}_u(k)\mathcal{F}_s(P-k)} \int_0^1 \frac{dy}{\sqrt{y\bar{y}}} \int \frac{d^2 q_\perp}{(2\pi)^3} \left(\frac{q_\perp^2 + y^2 M_s^2 - 2y\bar{y}M_u M_s + \bar{y}^2 M_u^2}{y\bar{y}} \right)$$

(22.9)

$$m_K^2 \phi_K = \left[\frac{k_\perp^2 + M_u^2}{x} + \frac{k_\perp^2 + M_s^2}{\bar{x}} \right] \phi_K - \frac{2g_K \alpha_{K+}}{\sqrt{x\bar{x}}} \sqrt{\mathcal{F}_u(k)\mathcal{F}_s(P-k)} \int_0^1 \frac{dy}{\sqrt{y\bar{y}}} \int \frac{d^2 q_\perp}{(2\pi)^3} \left(\frac{q_\perp^2 + y^2 M_s^2 + 2y\bar{y}M_u M_s + \bar{y}^2 M_u^2}{y\bar{y}} \right)$$

(22.10)

The two equations differ only in the sign in front of the $2y\bar{y}M_u M_s$ term and in the corresponding dressing factors $\alpha_{K\pm}$. This sign difference is ultimately responsible for the attractive versus repulsive character of the pseudoscalar and scalar channels, respectively, and explains why the kaon emerges as a pseudo-Goldstone boson while its scalar partner is unbound.

22.A.7 Auxiliary integrals

The integral

$$\int_0^1 dx \int d^2 k_\perp \frac{1}{x} \left[\mathcal{F}_u^2(k) + \mathcal{F}_s^2(k) - \mathcal{F}_u(k)\mathcal{F}_s(P-k) - \mathcal{F}_s(k)\mathcal{F}_u(P-k) \right]$$

(22.11)

vanishes for large cutoff. This identity plays the same role as in the pion sector: it guarantees that, after appropriate subtractions consistent with the gap equation, the bound-state integral equations remain finite and independent of the UV regularization, with the instanton size ρ providing the only physical scale.

22.B Kaon Mass Spectrum, GOR Limit, DA and PDF

In this appendix we present the spectral equations for the kaon mass, together with the explicit expressions for the DA and PDF in both the ILM and in the zero-size limit. These formulas make concrete the qualitative statements in Secs. 22.3 and 22.4, and show how the interplay between dynamical mass generation and explicit SU(3) breaking controls the kaon structure [Liu et al., 2023b].

The starting point is the resummed kaon propagator in the pseudoscalar channel, obtained by summing quark-loop diagrams with nonlocal ILM form factors. The pole condition for this propagator yields the kaon mass equation, whose small-mass expansion reproduces the Gell-Mann-Oakes-Renner relation. The same Bethe-Salpeter amplitude, when projected on the light front and integrated over transverse momentum, yields the DA and PDF.

22.B.1 Spectral equations for the masses

The mass eigenvalues satisfy

$$1 = \int_0^1 dy \int d^2 q_\perp \frac{V_X(y, q_\perp)}{y\bar{y}m_X^2 - (q_\perp^2 + M^2)} \mathcal{F}_u(q)\mathcal{F}_s(P-q),$$

(22.12)

with potentials

$$V_X = \begin{cases} +\dfrac{2g_K}{(2\pi)^3} \alpha_{K-} \dfrac{q_\perp^2 + y^2 M_s^2 - 2y\bar{y}M_u M_s + \bar{y}^2 M_u^2}{y\bar{y}}, \\[2ex] -\dfrac{2g_K}{(2\pi)^3} \alpha_{K+} \dfrac{q_\perp^2 + y^2 M_s^2 + 2y\bar{y}M_u M_s + \bar{y}^2 M_u^2}{y\bar{y}}. \end{cases}$$

(22.13)

Here $X = K_5$ or K respectively. The structure of V_X encodes the attractive or repulsive nature of each channel and depends sensitively on the constituent masses M_u and M_s. In the limit $M_s \to M_u$ the potentials reduce smoothly to their pion counterparts, confirming that the kaon sector interpolates continuously between SU(2) and SU(3) chiral dynamics.

22.B.2 Gell-Mann-Oakes-Renner relation

Expanding the pseudoscalar kaon mass equation yields

$$m_K^2 = \frac{m_u + m_s}{f_K^2} |\langle \bar{u}u \rangle + \langle \bar{s}s \rangle| + \mathcal{O}(m_u^2, m_s^2, m_u m_s), \tag{22.14}$$

with condensate

$$|\langle \bar{u}u \rangle + \langle \bar{s}s \rangle| = \frac{N_c}{2g_K}(M_u + M_s - m_u - m_s).$$

This relation makes explicit how the ILM saturates the kaonic GMOR relation: the difference between constituent and current masses provides a measure of the quark condensates, while the coupling g_K encapsulates the strength of the underlying instanton-induced interaction [Liu et al., 2023b].

22.B.3 Light-front wave function form

$$\phi_{K^+}(x, k_\perp) = \frac{1}{\sqrt{2x\bar{x}}} \frac{C_K}{m_K^2 - \frac{k_\perp^2 + xM_s^2 + \bar{x}M_u^2}{x\bar{x}}} \sqrt{\mathcal{F}_u(k)\mathcal{F}_s(P-k)}. \tag{22.15}$$

This form illustrates that the light-front wave function is dominated by configurations where the invariant mass of the $u\bar{s}$ pair is close to the physical m_K^2, with the instanton form factors suppressing large virtualities. The overall normalization constant C_K is fixed by requiring that the probability carried by the valence Fock sector be unity or by matching the decay constant f_K.

22.B.4 Parton distribution function

$$u_{K^+}(x) = \frac{C_K^2}{4\pi^2} \int_0^\infty dk_\perp^2 \frac{k_\perp^2 + x^2 M_s^2 + 2x\bar{x}M_s M_u + \bar{x}^2 M_u^2}{[x\bar{x}m_K^2 - (k_\perp^2 + xM_s^2 + \bar{x}M_u^2)]^2} \mathcal{F}_u(k)\mathcal{F}_s(P-k), \tag{22.16}$$

and in ILM variables

$$u_{K^+}(x) = \frac{C_K^2}{2\pi^2} \int_{\rho\frac{\sqrt{\bar{x}M_u^2 + xM_s^2}}{2\lambda_K \sqrt{x\bar{x}}}}^\infty dz \frac{z^2 - \frac{\rho^2}{4\lambda_K^2}(M_s - M_u)^2}{\left(\frac{\rho^2 m_K^2}{4\lambda_K^2} - z^2\right)^2} z^5 (F'(z))^4. \tag{22.17}$$

These expressions show explicitly that the strange-quark mass shifts the distribution toward larger x for the strange antiquark and toward smaller x for the light quark. The ILM representation in terms of the dimensionless variable z highlights the role of the instanton size ρ as the natural UV regulator.

Zero-size limit:

$$u_{K^+}(x) = \frac{C_K^2}{4\pi^2} \theta(x\bar{x}) \left[\frac{(m_K^2 - (M_s - M_u)^2)x\bar{x}\Lambda^2}{(xM_s^2 + \bar{x}M_u^2 - x\bar{x}m_K^2)(xM_s^2 + \bar{x}M_u^2 + \Lambda^2 - x\bar{x}m_K^2)} + \ln\left(1 + \frac{\Lambda^2}{xM_s^2 + \bar{x}M_u^2 - x\bar{x}m_K^2}\right) \right]. \tag{22.18}$$

In this limit the instanton profile is effectively replaced by a sharp transverse cutoff Λ, and the logarithmic dependence reflects the familiar structure of light-front constituent models [Keister and Polyzou, 1991]. The ILM can thus be viewed as providing a physically motivated smearing of this cutoff in terms of a finite-size instanton form factor.

22.B.5 Distribution amplitude

$$\phi_K(x) = \frac{\sqrt{N_c}}{\sqrt{2}\pi^2} \int dk_\perp^2 \frac{\phi_K(x, k_\perp)}{\sqrt{2x\bar{x}}} [xM_s \mathcal{F}_s(P-k) + \bar{x}M_u \mathcal{F}_u(k)]. \tag{22.19}$$

In the ILM:

$$\phi_{K^+}(x) = \frac{\sqrt{N_c}(xM_s + \bar{x}M_u)}{\sqrt{2}\pi^2} C_K \int_{\rho\frac{\sqrt{\bar{x}M_u^2 + xM_s^2}}{2\lambda_K\sqrt{x\bar{x}}}}^{\infty} dz\, \frac{z^5}{\frac{\rho^2 m_K^2}{4\lambda_K^2} - z^2} (F'(z))^4. \tag{22.20}$$

The numerator $(xM_s + \bar{x}M_u)$ makes explicit the skewness of the DA: even before evolution, the heavier strange quark biases the momentum distribution, so that the DA is no longer symmetric around $x = \frac{1}{2}$ as in the pion case [Kock et al., 2020, Kock and Zahed, 2021, Liu et al., 2023b].

Zero-size limit:

$$\phi_{K^+}(x) = \frac{\sqrt{N_c}(xM_s + \bar{x}M_u)}{2\sqrt{2}\pi^2} C_K\, \theta(x\bar{x}) \ln\left(1 + \frac{\Lambda^2}{xM_s^2 + \bar{x}M_u^2 - x\bar{x}m_K^2}\right). \tag{22.21}$$

The decay constant is

$$f_K = C_K \frac{\sqrt{N_c}M}{2\sqrt{2}\pi^2} \int_0^1 dx \frac{xM_s + \bar{x}M_u}{M} \ln\left(1 + \frac{\Lambda^2}{xM_s^2 + \bar{x}M_u^2 - x\bar{x}m_K^2}\right). \tag{22.22}$$

These relations show how the same underlying wave function controls both the DA and the decay constant. In practice, f_K is used to fix C_K, after which the ILM predictions for the DA and PDF follow without additional free parameters, up to the choice of instanton size [Liu et al., 2023b].

Chapter 23
Scalar mesons on the LF

23.1 Physical background and role of scalar mesons

The Instanton Liquid Model (ILM) provides a semiclassical description of the QCD vacuum in terms of an ensemble of instantons and anti-instantons with characteristic size ρ and density $n_{I+\bar{I}}$ [Diakonov et al., 1997, Schäfer and Shuryak, 1998, Nowak et al., 1996]. Quarks propagating in this background acquire exact zero modes of definite chirality in the field of a single (anti-)instanton ['t Hooft, 1976]. By integrating out the gauge fields, one obtains an effective nonlocal multi-fermion interaction - the nonlocal 't Hooft vertex - which encodes both the spontaneous breaking of chiral symmetry and the explicit breaking of the axial $U_A(1)$ symmetry.

At low resolution, the quark propagation is dominated by these zero modes and one can parameterize the quark self-energy in terms of a momentum dependent constituent mass $M(k)$, which is nonzero even in the chiral limit once the scalar 't Hooft interaction exceeds a critical strength [Diakonov et al., 1997, Nowak et al., 1989]. The same interaction generates strong correlations in the scalar channels, giving rise to scalar mesons as quark-antiquark bound states.

From the point of view of chiral symmetry, the scalar-isoscalar σ field plays a special role. In a purely linear sigma model, the σ is the chiral partner of the pion; in the ILM, a similar phenomenon occurs dynamically: the same nonlocal interaction that generates a nonzero quark condensate and hence the pion as a pseudo-Goldstone boson, also binds a scalar $\bar{q}q$ state whose mass tracks the dynamical threshold $2M$ [Diakonov et al., 1997, Nowak et al., 1989]. The isovector scalar a_0 is affected by both single-instanton and instanton-molecule contributions and thus provides a probe of the interplay between these two sectors of the ILM.

Working on the light front adds two crucial elements [Brodsky, 1994]. First, the hadronic states are expanded in Fock components with a clear partonic interpretation: probabilities for finding quarks with given longitudinal momentum fraction x and transverse momentum $k_\perp$. Second, the constrained ("bad") component of the quark field is eliminated, inducing additional nonlocal interactions that are essential to realize spontaneous chiral symmetry breaking on the light front [Liu et al., 2024e, Liu et al., 2024d].

23.2 Instanton-induced scalar interactions and the gap equation

In the ILM, the effective action for two light flavors can be written schematically as

$$\mathcal{L}_I = \frac{G_I}{8(N_c^2 - 1)} \left\{ \frac{2N_c - 1}{2N_c} \left[(\bar{\psi}\psi)^2 - (\bar{\psi}\tau^a\psi)^2 - (\bar{\psi}i\gamma^5\psi)^2 + (\bar{\psi}i\gamma^5\tau^a\psi)^2 \right] + \frac{1}{4N_c} \left[\left(\bar{\psi}\sigma_{\mu\nu}\psi\right)^2 - \left(\bar{\psi}\sigma_{\mu\nu}\tau^a\psi\right)^2 \right] \right\}$$

(23.1)

in the ultra-local limit, where m is the current quark mass [Nowak et al., 1989]. The effective coupling

$$G_I = \int d\rho\, n(\rho) \rho^{N_f} (2\pi\rho)^{2N_f} = \frac{n_{I+\bar{I}}}{2} (4\pi^2\rho^3)^{N_f} \left(\frac{1}{m^*\rho}\right)^{N_f} \tag{23.2}$$

is fixed by the mean-instanton density

$$\frac{n_{I+\bar{I}}}{2} = \int d\rho\, n(\rho) \prod_{f=1}^{N_f} (m_f^*\rho) \tag{23.3}$$

with m_f^* the induced determinantal mass [Schäfer and Shuryak, 1998, Liu et al., 2024d]. At low resolution, the instanton distribution is sharply peaked around the average instanton size $\rho \approx 0.31$ fm, with a mean density $n_{I+\bar{I}} \sim 1$ fm^{-4}.

However, the instanton size is not small in comparison to the size of the light hadrons, e.g. pion, kaon, nucleon ..., and cannot be ignored in general. More importantly, this size fixes the UV scale and provides for a natural cut-off both in Euclidean or light front signature (see below). Finite size instantons yield finite size zero modes, and therefore non-local effective interactions between the light quarks. The net effect is captured by the substitution

$$\psi(x) \to \sqrt{F(i\partial)}\psi(x) \tag{23.4}$$

in the local approximation. Here $F(i\partial)$ is the zero mode profile, that acts as a form factor. In singular gauge its form is more user friendly in momentum space

$$F(k) = \left[(zF_0'(z))^2\right]\Big|_{z=\frac{k\rho}{2}} \tag{23.5}$$

where $F_0(z) = I_0(z)K_0(z) - I_1(z)K_1(z)$ are spherical Bessel functions, and $k = \sqrt{k^2}$ is the Euclidean 4-momentum. Inserting (23.4) into (23.1) yields the non-local form of the effective action in the QCD instanton vacuum in leading order in $1/N_c$

$$\begin{aligned}
\mathcal{L} =& \bar{\psi}[i\slashed{\partial} - m]\psi + \frac{G_S}{2}(\bar{\psi}\sqrt{F(i\partial)}\sqrt{F(i\partial)}\psi)^2 - \frac{G_S}{2}(\bar{\psi}\sqrt{F(i\partial)}\tau^a\sqrt{F(i\partial)}\psi)^2 \\
& - \frac{G_S}{2}(\bar{\psi}\sqrt{F(i\partial)}i\gamma^5\sqrt{F(i\partial)}\psi)^2 + \frac{G_S}{2}(\bar{\psi}\sqrt{F(i\partial)}i\gamma^5\tau^a\sqrt{F(i\partial)}\psi)^2
\end{aligned} \tag{23.6}$$

with $G_S = G_I/4N_c^2$. Instanton-anti-instanton molecular configurations contribute additional nonlocal interactions. As we will detail below, these interactions operate chiefly in the vector channels, but are subleading in the $1/N_c$ book-keeping.

The light quarks through zero modes acquire a momentum dependent mass, in leading order in $1/N_c$ (mean-field approximation)

$$M(k) \approx M\, F(k)\,, \tag{23.7}$$

The constituent quark mass $M \equiv M(0)$ satisfies the gap-equation [Diakonov et al., 1997, Nowak et al., 1996].

$$\frac{m}{M} = 1 - 8g_S \int \frac{d^4k}{(2\pi)^4} \frac{F^2(k)}{k^2 + M^2}\,, \tag{23.8}$$

where $g_S = N_c G_S$ is the scalar 't Hooft coupling. The nonlocal form factor plays the role of a smooth ultraviolet cutoff of order $1/\rho$. In dimensionless variables $z = k\rho/2$, (23.8) can be written more explicitly as

$$\frac{m}{M} = 1 - \frac{4g_S}{\pi^2\rho^2} \int_0^\infty dz\, \frac{z^3}{z^2 + \frac{\rho^2 M^2}{4}}\, F^2(z). \tag{23.9}$$

In the chiral limit $m \to 0$, a nontrivial solution $M \neq 0$ exists only if the scalar coupling exceeds a critical value g_S^{cr}, determined from the condition that the coefficient of M in the linearized gap equation vanishes:

$$g_S^{\mathrm{cr}} = 2\pi^2 \rho^2 \left[8 \int_0^\infty dz\, z\, F^2(z) \right]^{-1} \simeq 2.981\,\pi^2 \rho^2. \tag{23.10}$$

For the standard two-flavor ILM parameters $\rho \approx (636\ \mathrm{MeV})^{-1}$, this yields $g_S^{\mathrm{cr}} \approx 72.6\ \mathrm{GeV}^{-2}$ [Liu et al., 2023b, Liu et al., 2024d]. Once $g_S > g_S^{\mathrm{cr}}$, the constituent mass M grows rapidly with g_S, and the quark condensate

$$\rho^3 \langle \bar\psi \psi \rangle = -\frac{4N_c}{\pi^2}\, \rho M \int_0^\infty dz\, \frac{z^3}{z^2 + \frac{\rho^2 M^2}{4}}\, z\, F^2(z) \tag{23.11}$$

develops in magnitude, signaling the spontaneous breaking of chiral symmetry in the ILM.

23.3 Effective scalar channels in the ILM

The scalar channels are obtained by projecting the nonlocal 't Hooft interaction onto the color-singlet, spin-0 bilinears. For two flavors, the relevant isoscalar and isovector scalar operators are

$$\sigma(x) \sim \bar\psi(x)\psi(x), \qquad a_0^a(x) \sim \bar\psi(x)\tau^a \psi(x), \tag{23.12}$$

where τ^a are Pauli matrices in flavor space.

At leading order in $1/N_c$, the scalar sector of the effective action may be written as

$$\mathcal{L}_S = \bar\psi(i\,\slashed{\partial} - M)\psi + \frac{G_\sigma}{2}\left(\bar\psi\sqrt{F}\sqrt{F}\psi\right)^2 + \frac{G_{a_0}}{2}\left(\bar\psi\sqrt{F}\,\tau^a\sqrt{F}\psi\right)^2, \tag{23.13}$$

with $G_\sigma = -G_{a_0} = G_S$. In the isoscalar scalar channel σ, the net interaction is purely attractive and directly tied to the same scalar vertex that generates the quark condensate. In the isovector channel a_0, the molecular contribution competes with the single-instanton term, resulting in a weaker net attraction. This competition is one of the main reasons that the a_0 is heavier and less bound than the σ in the ILM [Schäfer and Shuryak, 1998, Kacir et al., 1999, Liu et al., 2024d].

23.4 Light-front representation of scalar mesons

We now turn to the light-front Hamiltonian formulation [Brodsky et al., 1998a, Brodsky, 1994]. On the light front, quark fields are decomposed as

$$\psi = \psi_+ + \psi_-, \qquad \psi_\pm = \Lambda_\pm \psi, \qquad \Lambda_\pm = \frac{\gamma^0 \gamma^\pm}{2}, \tag{23.14}$$

where ψ_+ is the dynamical "good" component and ψ_- is the constrained "bad" component. Eliminating ψ_- using its equation of motion generates additional multi-fermion interactions, which in leading order reduce to tadpole contributions that renormalize the couplings in (23.13). The corresponding scalar kernels on the light front carry a characteristic denominator of the form

$$\frac{1}{1 + 2g_X w_+(P^+)}, \tag{23.15}$$

where $w_+(P^+)$ is an even function of P^+ arising from tadpole resummation and g_X is the channel-dependent effective coupling (g_σ, g_{a_0}) [Liu et al., 2024e].

A scalar meson state $|X(P)\rangle$ $(X = \sigma, a_0)$ is expanded in the lowest Fock sector as

$$|X(P)\rangle = \int_0^1 \frac{dx}{\sqrt{2x\bar{x}}} \int \frac{d^2k_\perp}{(2\pi)^3} \sum_{s_1,s_2} \Phi_X(x, k_\perp, s_1, s_2) \, b_{s_1}^\dagger(k) \, d_{s_2}^\dagger(P - k) \, |0\rangle, \tag{23.16}$$

where $x = k^+/P^+$, $\bar{x} = 1 - x$, and $b^\dagger, d^\dagger$ are quark and antiquark creation operators.

Because the scalar has spin zero, the spin structure of the valence wave function is particularly simple. One may factorize the light-front wave function as

$$\Phi_X(x, k_\perp, s_1, s_2) = \frac{C_X}{\sqrt{N_c}} \sqrt{2x\bar{x}} \, \phi_X(x, k_\perp) \, \bar{u}_{s_1}(k) \, v_{s_2}(P - k), \tag{23.17}$$

where $\phi_X(x, k_\perp)$ is a scalar function and C_X is a normalization constant. The latter is fixed by the probabilistic normalization condition

$$\int_0^1 dx \int \frac{d^2k_\perp}{(2\pi)^3} \sum_{s_1,s_2} \left|\Phi_X(x, k_\perp, s_1, s_2)\right|^2 = 1. \tag{23.18}$$

23.5 Light-front bound-state equation for scalar mesons

Using the effective interaction (23.13) and projecting the light-front Hamiltonian onto the two-body Fock sector, one derives the bound-state equation for $\phi_X(x, k_\perp)$. The result can be written in the compact form

$$\begin{aligned}
m_X^2 \, \phi_X(x, k_\perp) = {}& \frac{k_\perp^2 + M^2}{x\bar{x}} \, \phi_X(x, k_\perp) \\
& - \frac{4\sqrt{F(k)F(P-k)}}{\sqrt{2x\bar{x}}} \frac{g_X}{1 + 2g_X w_+(P^+)} \int_0^1 \frac{dy}{\sqrt{2y\bar{y}}} \int \frac{d^2q_\perp}{(2\pi)^3} \left[\frac{q_\perp^2 + (y - \bar{y})^2 M^2}{y\bar{y}}\right] \\
& \times \phi_X(y, q_\perp) \sqrt{F(q)F(P-q)} .
\end{aligned} \tag{23.19}$$

This equation holds for $X = \sigma, a_0$ with the appropriate channel-dependent coupling g_X. The kernel is entirely determined by the constituent mass M, the instanton form factor $F(k)$, and the tadpole function $w_+(P^+)$. The nonlocality of the interaction ensures a finite result without the need of ad hoc cutoffs: the instanton size ρ provides the physical ultraviolet scale [Liu et al., 2023b, Liu et al., 2024d].
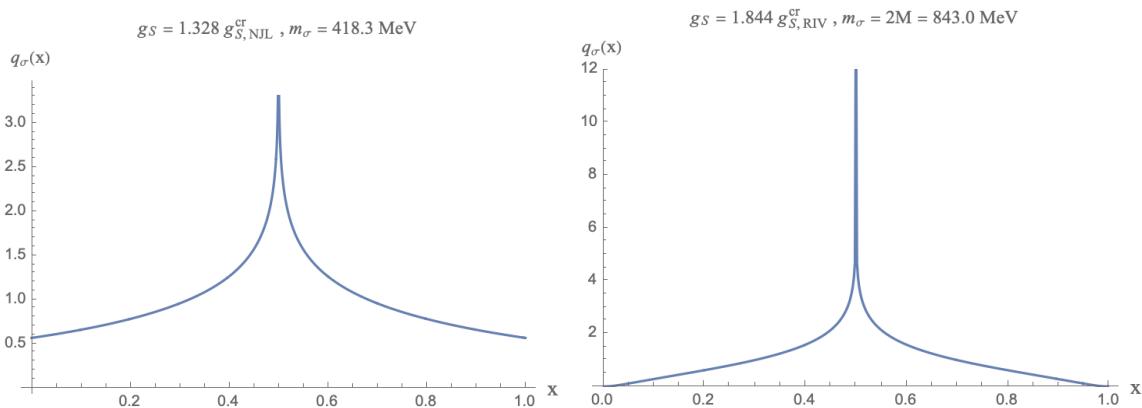
Fig. 23.5.1 a: The sigma PDF in zero instanton size and in the chiral limit, with a treshold sigma mass $2M = 418.9$ MeV; b: The sigma PDF with the finite instanton size $1/\rho = 630$ MeV, with a treshold sigma mass $2M = 418.9$ MeV in the chiral limit;

The same dynamics can be recast in a covariant language by resumming the scalar polarization bubble. In leading order (LO), the vacuum polarization function contributes to the 4-point function through the bubble-chain shown in FIg. 23.5.2.
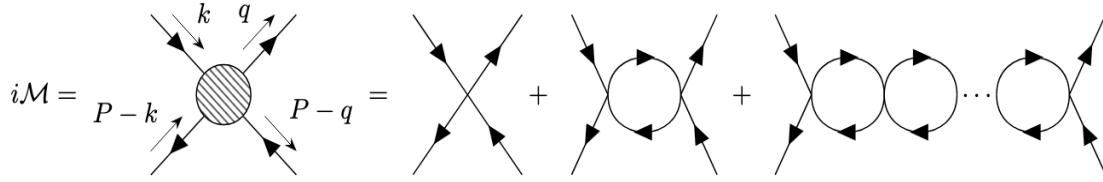
Fig. 23.5.2 Contributions to the vacuum polarization function in the mean-field (bubble) approximation.

The scalar propagator is

$$D_X(P^2) = \frac{iG_X}{1 - G_X \, \Pi_{SS}(P^2)}, \tag{23.20}$$

with scalar polarization

$$\Pi_{SS}(P^2) = -2iN_c \int \frac{d^4k}{(2\pi)^4} \frac{4k \cdot (P - k) - 4M^2}{\left(k^2 - M^2\right)\left((P - k)^2 - M^2\right)} F(k)F(P - k). \tag{23.21}$$

The scalar mass follows from the pole condition

$$1 = G_X \, \Pi_{SS}(m_X^2). \tag{23.22}$$

Integrating over the light-front energy and using the gap equation, one arrives at a light-front form of the mass equation

$$1 - \frac{g_X}{g_S}\left(1 - \frac{m}{M}\right) = -2g_X(m_X^2 - 4M^2) \int_0^1 dx \int \frac{d^2k_\perp}{(2\pi)^3} \frac{F(k)F(P - k)}{x\bar{x}m_X^2 - (k_\perp^2 + M^2)}. \tag{23.23}$$

This equation is particularly useful to study how the scalar masses depend on the current quark mass m and on the coupling ratios g_X/g_S. Numerical solutions of (23.19) and (23.23) exhibit a characteristic behavior. In the chiral limit $m \to 0$, the σ mass satisfies

$$m_\sigma \approx 2M, \tag{23.24}$$

so it lies very close to the constituent quark threshold. The σ is therefore a "threshold" bound state whose mass tracks the order parameter of chiral symmetry breaking, in line with ILM expectations [Diakonov, 1997, Nowak et al., 1996]. As the current mass m increases, the constituent mass M changes only mildly, but the pole equation shifts so that m_σ moves above threshold and the state gradually becomes unbound. This illustrates explicitly how chiral symmetry breaking controls the existence of a light σ. The isovector scalar a_0 is governed by the coupling

$$g_{a_0} = -g_S + 8g_V. \tag{23.25}$$

where g_V arises from a Fierzing of the vector interactions induced by instanton-anti-instanton molecules (see below). Since g_V is parametrically smaller than g_S, the net attraction in the a_0 channel is significantly reduced. As a result, the a_0 mass lies well above the σ and is only weakly bound or even unbound, depending on the precise choice of ILM parameters [Liu et al., 2023b, Liu et al., 2024d].

This pattern is qualitatively consistent with phenomenology, where the light isoscalar scalar meson is anomalously light and broad, while the isovector scalar lies at a substantially higher mass.

$\rho = 0.313$ fm , $g_S = 2.540 \times 2\pi^2 \rho^2$, $g_V = 0.531 \times 2\pi^2 \rho^2$

q_X (x)

— σ PDF , $m_\sigma = 743.2$ MeV
— ρ PDF , $m_\rho = 736.5$ MeV
— π PDF , $m_\pi = 0.0$ MeV
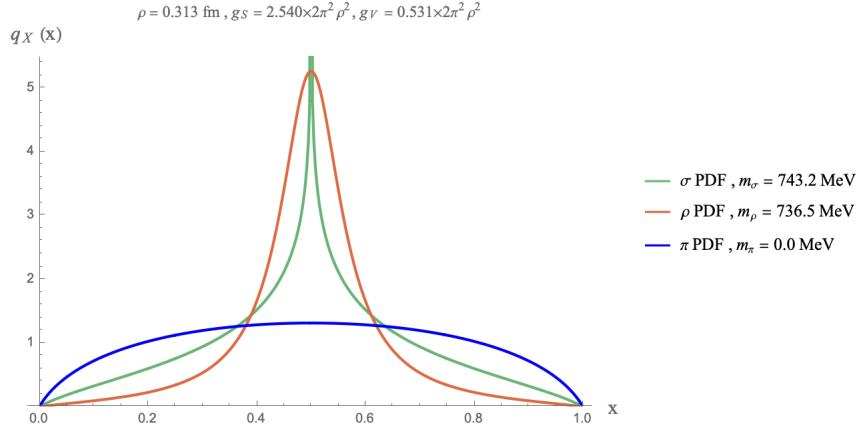
Fig. 23.5.3 Parton density functions in the chiral limit [Liu et al., 2024d].

23.6 Scalar parton distributions on the light front

One of the advantages of the light-front formulation is the direct access it provides to the partonic structure of hadrons. For a spin-0 meson X (such as π or a scalar meson), the leading-twist quark distribution function is defined by [Brodsky et al., 1998a, Belitsky and Radyushkin, 2005]

$$q_X(x) = \int_{-\infty}^{\infty} \frac{d\xi^-}{4\pi} \, e^{ixP^+\xi^-} \, \langle X(P)|\bar{\psi}(0)\gamma^+ W(0,\xi^-)\psi(\xi^-)|X(P)\rangle, \tag{23.26}$$

with W a Wilson line ensuring gauge invariance. In terms of the light-front wave function Φ_X in (23.16), one finds the familiar relation

$$q_X(x) = \int \frac{d^2 k_\perp}{(2\pi)^3} \sum_{s_1,s_2} \left|\Phi_X(x,k_\perp,s_1,s_2)\right|^2. \tag{23.27}$$

Due to charge symmetry, the antiquark distribution satisfies

$$\bar{q}_X(x) = q_X(1-x), \tag{23.28}$$

so that the total valence number and momentum sum rules are manifestly satisfied:

$$\int_0^1 dx \left[q_X(x) - \bar{q}_X(x)\right] = 1, \tag{23.29}$$

$$\int_0^1 dx\, x \left[q_X(x) + \bar{q}_X(x)\right] = 1 \tag{23.30}$$

in the pure two-body truncation.

For scalar mesons in the ILM, $q_X(x)$ is obtained by inserting the solution of (23.19) into (23.27). The resulting distributions are typically broad in x, reflecting the strong binding and the nonlocality of the instanton-induced kernel. In the chiral limit, the σ distribution is particularly delocalized, consistent with its role as a collective mode tied to the quark condensate [Liu et al., 2024e].

23.7 Summary of the scalar sector in the ILM

To summarize, the ILM, through its nonlocal 't Hooft interaction, provides a unified mechanism for spontaneous chiral symmetry breaking and for binding scalar mesons [Diakonov et al., 1997, Schäfer and Shuryak, 1998, Nowak et al., 1996]. The constituent quark mass M is generated dynamically once the scalar coupling exceeds a critical value, and the same coupling controls the attraction in the σ channel, leading to $m_\sigma \approx 2M$ in the chiral limit. Instanon-anti-instanton molecular configurations introduce additional vector-like interactions which weaken the attraction in the isovector scalar channel, explaining naturally why $m_{a_0} \gg m_\sigma$ in typical ILM parameter sets. The light-front formulation yields a well-defined bound-state equation for scalar mesons, fully consistent with the covariant Bethe-Salpeter resummation and directly related to their partonic structure via the light-front wave functions [Liu et al., 2023b, Liu et al., 2024d]. More formal aspects of the gap equation and of the covariant Bethe-Salpeter amplitudes in the scalar channels are collected in the following appendices.

Appendix

23.A Bethe-Salpeter wave functions and quark-meson couplings

After summing the geometric series of scalar polarization bubbles, the full scalar propagator reads

$$D_X(P^2) = \frac{iG_X}{1 - G_X \Pi_{SS}(P^2)}, \qquad X = \sigma, a_0, \tag{23.31}$$

where Π_{SS} is given by Eq. (23.21). Near the pole at $P^2 = m_X^2$, the propagator can be written as

$$D_X(P^2) \simeq \frac{Z_X}{P^2 - m_X^2 + i\epsilon}, \tag{23.32}$$

with residue $Z_X = g_{Xqq}^2$, where g_{Xqq} is the effective quark-meson coupling. Differentiating with respect to P^2 gives the standard relation

$$g_{Xqq}^2 = \left(\frac{\partial \Pi_{SS}(P^2)}{\partial P^2} \right)^{-1} \Bigg|_{P^2 = m_X^2}, \tag{23.33}$$

for $X = \sigma, a_0$. Analogous expressions hold for pseudoscalar and vector mesons with their respective polarization functions [Liu et al., 2024d].

The corresponding Bethe-Salpeter wave functions are

$$\Psi_\sigma(k; P) = g_{\sigma qq} \, S(k) \, \sqrt{F(k)} \, \sqrt{F(P-k)} \, S(k-P), \tag{23.34}$$

$$\Psi_{a_0}(k; P) = g_{a_0 qq} \, S(k) \, \sqrt{F(k)} \, \tau^a \sqrt{F(P-k)} \, S(k-P), \tag{23.35}$$

where $S(k)$ is the dressed quark propagator

$$S(k) = \frac{1}{\not{k} - M(k)} \approx \frac{1}{\not{k} - M}. \tag{23.36}$$

These scalar Bethe-Salpeter amplitudes have the same nonlocal structure as the original 't Hooft interaction: each quark leg is dressed with a form factor $\sqrt{F}$ reflecting the instanton zero mode.

23.B From Bethe-Salpeter amplitudes to light-front wave functions

The light-front wave functions Φ_X that appear in (23.16) can be obtained by integrating the Bethe-Salpeter amplitudes over the light-front energy k^- and projecting on appropriate spin states. One finds

$$\frac{1}{\sqrt{2x\bar{x}}}\,\Phi_X(x,k_\perp,s_1,s_2) = iP^+ \int_{-\infty}^{\infty} \frac{dk^-}{2\pi}\, \bar{u}_{s_1}(k)\, \frac{\gamma^+}{2k^+}\, \Psi_X(k;P)\, \frac{\gamma^+}{2(P^+ - k^+)}\, v_{s_2}(P-k), \qquad (k^+ = xP^+).$$

$$(23.37)$$

Performing the k^- integration by residues and comparing with the factorized form (23.17) yields a relation between the normalization constant C_X and the covariant coupling g_{Xqq}. For scalar and pseudoscalar channels one finds the simple identity

$$g_{Xqq} = -\frac{C_X}{\sqrt{N_c}}, \qquad X = \sigma, a_0, \pi, \eta_0, \qquad\qquad (23.38)$$

so that the normalization determined from the covariant Bethe-Salpeter equation matches exactly the probabilistic normalization of the light-front wave function (23.18).

This provides a powerful consistency check: the scalar meson properties (masses, couplings, and wave-function normalizations) computed in the covariant ILM framework can be translated directly into the light-front language without ambiguity. All observables that can be expressed in terms of the light-front wave functions - such as parton distribution functions and, in principle, distribution amplitudes specialized to scalar channels - are therefore fully determined once the ILM parameters are fixed in the vacuum sector [Liu et al., 2023b, Liu et al., 2024d].

Chapter 24
Vectors on the LF

24.1 Physical Background

Vector mesons, notably the ρ and ω, represent the lowest-lying $J^{PC} = 1^-$ excitations of QCD and provide a crucial testing ground for understanding nonperturbative dynamics. Because they couple directly to the electromagnetic current through $\bar{q}\gamma_\mu q$, they dominate hadronic contributions in many low-energy processes such as e^+e^- annihilation and hadronic τ decay, forming the empirical basis of vector meson dominance [Sakurai, 1969]. Their internal quark structure and dynamical mass generation relate directly to the mechanisms of confinement and chiral symmetry breaking.

Within the ILM described earlier, spontaneous chiral symmetry breaking is driven primarily by near-zero quark modes of single instantons. These modes generate a momentum-dependent constituent mass through the gap equation and produce strong attraction in pseudoscalar and scalar channels. In contrast, vector mesons receive only weak contributions from single instantons, since the 't Hooft interaction flips helicity and therefore does not contribute directly to chirality-preserving vector bilinears. Instead, vector channels are governed by instanton-anti-instanton molecules [Schafer, 1994, Shuryak and Zahed, 2021a], which give rise to nonlocal quark interactions preserving chirality. These molecular interactions are suppressed in the vacuum, but dominate the formation of vector-meson bound states, rendering the vector sector a sensitive probe of molecular correlations.

Light-front (LF) Hamiltonian quantization provides a powerful framework for analyzing such nonlocal interactions. The decomposition of quark fields into dynamical (ψ_+) and nondynamical (ψ_-) components reveals how the constrained field elimination generates additional multi-fermion operators. At leading order in $1/N_c$, these reduce to tadpole contributions that renormalize the effective vertices. The resulting LF Hamiltonian encodes the same nonlocalities appearing in the Euclidean ILM but rephrased in the language of LF wave functions, making explicit the partonic structure of vector mesons. In the LF formulation, the longitudinal and transverse polarizations obey distinct integral equations due to the lack of manifest Lorentz symmetry as noted earlier [Brodsky et al., 1998b]. Nevertheless, it is possible to show that the physical masses coincide, and that Lorentz covariance can be restored by properly removing spurious terms induced by instantaneous interactions [Liu et al., 2024d].

From a phenomenological perspective, the ILM's description of vector mesons is appealing because the instanton size $\rho \approx 1/3$ fm sets the characteristic nonlocality scale, which naturally produces extended vector bound states with charge radii. Furthermore, the ILM predicts broad distribution amplitudes at the intrinsic resolution scale $\mu \sim 1/(2\rho) \approx 0.6$ GeV, a feature consistent with lattice QCD extractions. The consistency between light-front results, covariant Bethe-Salpeter structures, and Euclidean path-integral derivations provides a cross-validated and physically transparent description of mesons in QCD.

24.2 Physical details

The lightest isovector vector meson is the $\rho(770)$ and the lightest isoscalar is the $\omega(782)$, each carrying quantum numbers $J^{PC} = 1^-$. These states are created from the QCD vacuum by the local vector currents

$$J_\mu^a(x) = \bar{\psi}(x)\gamma_\mu \frac{\tau^a}{2}\psi(x), \qquad J_\mu^{(0)}(x) = \bar{\psi}(x)\gamma_\mu\psi(x),$$

and their dominance in hadronic electromagnetic processes forms the foundation of vector meson dominance [Sakurai, 1969].

In the Instanton Liquid Model (ILM), the fermionic zero modes of single instantons lead to a momentum-dependent constituent mass $M(k) \approx MF^2(k)$ as we discussed earlier, which is the key to spontaneous chiral symmetry breaking, with the light pions and sigmas.

However, vector mesons cannot be generated by single instantons alone. The 't Hooft interaction violates chirality and contributes only to channels built from bilinears such as $\bar{\psi}_L\psi_R$. Vector bilinears $\bar{\psi}\gamma_\mu\psi$ are chirality preserving and therefore require instanton-anti-instanton molecular correlations. Such molecules behave as tightly correlated pairs of instantons with approximate dipole structure, and their fermionic zero modes overlap in a manner that produces a nonlocal vector vertex [Shuryak and Zahed, 2021a, Liu et al., 2024d].

The resulting effective interaction in the vector channel is suppressed by the small probability for molecular formation, typically a few percent of the total instanton density. This explains the phenomenological fact that vector mesons are heavier than the pion: their binding arises from weaker interactions than those responsible for chiral symmetry breaking.

To describe vector mesons in a partonic language, light-front (LF) quantization is useful. The However, the main conceptual challenge is to ensure that Lorentz covariance of the vector channel, manifest in the covariant Bethe-Salpeter amplitude, is correctly reproduced in the LF Hamiltonian framework. A central result, derived in [Liu et al., 2024d], is that all spurious Lorentz-violating LF terms can be cancelled by enforcing an identity between LF energy denominators and the covariant ILM propagators. This restores the equality of longitudinal and transverse vector-meson masses.

24.3 Nonlocal Vector Interactions from Instanton Molecules

In the local approximation, the maximally locked instanton-anti-instanton configurations or molecules, induce flavor mixing interactions of the form [Schafer, 1994]

$$\mathcal{L}_{I\bar{I}} = G_{I\bar{I}}\bigg\{ \frac{1}{N_c(N_c-1)}\left[(\bar{\psi}\gamma^\mu\psi)^2 + (\bar{\psi}\gamma^\mu\gamma^5\psi)^2\right] - \frac{N_c-2}{N_c(N_c^2-1)}\left[(\bar{\psi}\gamma^\mu\psi)^2 - (\bar{\psi}\gamma^\mu\gamma^5\psi)^2\right]$$
$$+ \frac{2N_c-1}{N_c(N_c^2-1)}\left[(\bar{\psi}\psi)^2 + (\bar{\psi}\tau^a\psi)^2 + (\bar{\psi}i\gamma^5\psi)^2 + (\bar{\psi}i\gamma^5\tau^a\psi)^2\right] \qquad (24.1)$$
$$- \frac{1}{2N_c(N_c-1)}\left[(\bar{\psi}\gamma^\mu\psi)^2 + (\bar{\psi}\tau^a\gamma^\mu\psi)^2 + (\bar{\psi}\gamma^\mu\gamma^5\psi)^2 + (\bar{\psi}\tau^a\gamma^\mu\gamma^5\psi)^2\right]\bigg\}$$

which are LL and RR chirality preserving. The effective molecule-induced coupling is defined as

$$G_{I\bar{I}} = \int d\rho_I d\rho_{\bar{I}} \int du d^4R \; \frac{1}{8T_{I\bar{I}}^2}(4\pi^2\rho_I^2)(4\pi^2\rho_{\bar{I}}^2)n(\rho_I)n(\rho_{\bar{I}})T_{I\bar{I}}(u,R)^{2N_f}\rho_I^{N_f}\rho_{\bar{I}}^{N_f} \qquad (24.2)$$

Here $R = z_I - z_{\bar{I}}$ is the relative molecular separation, $u_\mu = \frac{1}{2i}\text{tr}(U_{\bar{I}}\tau_\mu^+ U_I^\dagger)$ is the relative molecular orientation with the locked color with $\tau_\mu^+ = (\boldsymbol{\tau}, -i)$, and $T_{I\bar{I}}$ is the hopping quark matrix. (24.2) is readily understood as the unquenched tunneling density for a molecular configuration, whereby a pair of quark lines is removed by the division $T_{I\bar{I}}^2$ to account for the induced 4-Fermi interaction. The strength of the induced molecular

coupling $G_{I\bar{I}}$ to the single coupling G_I is

$$G_{I\bar{I}} = \frac{G_I^2}{128\pi^4 \rho^2}\xi \tag{24.3}$$

where the dimensionless and positive hopping parameter is defined as

$$\xi = \frac{1}{\rho^4}\int du d^4 R \left[\rho T_{I\bar{I}}(u,R)\right]^{2N_f - 2} \tag{24.4}$$

Thanks to the smallness of the instanton plus anti-instanton density $n(\rho)$, the complex many-body dynamics of the ILM can be organized around the dilute limit. For that the $1/N_c$ book-keeping is useful, with $n(\rho) \sim N_c$ and both G_I and $G_{I,\bar{I}}$ of the same order in $1/N_c$, but with a parametrically small ratio $G_{I\bar{I}}/G_I$ from the diluteness. With this in mind, the leading contributions in $1/N_c$ from single and molecular instantons and anti-instantons are respectively

$$\mathcal{L}_I = \frac{G_I}{8N_c^2}\left[(\bar{\psi}\psi)^2 - (\bar{\psi}\tau^a\psi)^2 - (\bar{\psi}i\gamma^5\psi)^2 + (\bar{\psi}i\gamma^5\tau^a\psi)^2\right]$$

$$\mathcal{L}_{I\bar{I}} = \frac{G_{I\bar{I}}}{2N_c^2}\left[4\left[(\bar{\psi}\psi)^2 + (\bar{\psi}\tau^a\psi)^2 + (\bar{\psi}i\gamma^5\psi)^2 + (\bar{\psi}i\gamma^5\tau^a\psi)^2\right]\right.$$

$$\left. - \left[(\bar{\psi}\gamma^\mu\psi)^2 + (\bar{\psi}\tau^a\gamma^\mu\psi)^2 - 3(\bar{\psi}\gamma^\mu\gamma^5\psi)^2 + (\bar{\psi}\tau^a\gamma^\mu\gamma^5\psi)^2\right]\right] \tag{24.5}$$

The induced 't Hooft interaction $\mathcal{L}_I$ does not operate in the light vector channels, but the molecular induced interaction $\mathcal{L}_{I\bar{I}}$ does. The molecular interaction is equally attractive in the scalar σ, a_0 and pseudoscalar π, η' channels. Since the instanton molecules are topologically neutral, the molecular interaction are $U(1)_A$ symmetric. Note that this Lagrangian predicts no splitting between the isoscalar (ω) and isovector (ρ) vector channels. To illustrate how these interactions operate in various mesonic channels, a Fierzing yields

$$\mathcal{L} = \bar{\psi}(i\slashed{\partial} - M)\psi + \frac{G_\sigma}{2}(\bar{\psi}\psi)^2 + \frac{G_{a_0}}{2}(\bar{\psi}\tau^a\psi)^2 + \frac{G_{\eta'}}{2}(\bar{\psi}i\gamma^5\psi)^2 + \frac{G_\pi}{2}(\bar{\psi}i\gamma^5\tau^a\psi)^2$$

$$- \frac{G_\omega}{2}(\bar{\psi}\gamma_\mu\psi)^2 - \frac{G_\rho}{2}(\bar{\psi}\gamma_\mu\tau^a\psi)^2 - \frac{G_{f_1}}{2}(\bar{\psi}\gamma_\mu\gamma^5\psi)^2 - \frac{G_{a_1}}{2}(\bar{\psi}\gamma_\mu\gamma^5\tau^a\psi)^2 \tag{24.6}$$

with the effective couplings

$$G_\sigma = G_S \qquad G_{a_0} = -G_S + 8G_V \qquad G_\pi = G_S \qquad G_{\eta'} = -G_S + 8G_V$$

$$G_\omega = G_V \qquad G_\rho = G_V \qquad G_{a_1} = G_V \qquad G_{f_1} = -3G_V$$

where $G_S = \frac{G_I}{4N_c^2} + \frac{4G_{I\bar{I}}}{N_c^2}$ and $G_V = \frac{G_{I\bar{I}}}{N_c^2}$. As we noted earlier, the non-local form is readily obtained through the substitution

$$\psi(x) \rightarrow \sqrt{F(i\partial)}\psi(x) \tag{24.7}$$

with the leading order $1/N_c$

$$\mathcal{L} = \bar{\psi}[i\slashed{\partial} - M(k)]\psi + \frac{G_S}{2}(\bar{\psi}\sqrt{F(i\partial)}\sqrt{F(i\partial)}\psi)^2 - \frac{G_S}{2}(\bar{\psi}\sqrt{F(i\partial)}\tau^a\sqrt{F(i\partial)}\psi)^2$$

$$- \frac{G_S}{2}(\bar{\psi}\sqrt{F(i\partial)}i\gamma^5\sqrt{F(i\partial)}\psi)^2 + \frac{G_S}{2}(\bar{\psi}\sqrt{F(i\partial)}i\gamma^5\tau^a\sqrt{F(i\partial)}\psi)^2 - \frac{G_V}{2}(\bar{\psi}\sqrt{F(i\partial)}\gamma_\mu\sqrt{F(i\partial)}\psi)^2$$

$$- \frac{G_V}{2}(\bar{\psi}\sqrt{F(i\partial)}\gamma_\mu\tau^a\sqrt{F(i\partial)}\psi)^2 + \frac{3G_V}{2}(\bar{\psi}\sqrt{F(i\partial)}\gamma_\mu\gamma^5\sqrt{F(i\partial)}\psi)^2 - \frac{G_V}{2}(\bar{\psi}\sqrt{F(i\partial)}\gamma_\mu\gamma^5\tau^a\sqrt{F(i\partial)}\psi)^2$$

$$\tag{24.8}$$

24.4 Covariant analysis of vector mesons

In the covariant formulation, the starting point is the dressed quark propagator in the ILM is

$$S(k) = \frac{\slashed{k} + M(k)}{k^2 - M^2(k) + i\epsilon},$$

In $1/N_c$ book-keeping in the ILM, the Bethe-Salpeter equations in the vector channels amount to resumming the bubble graphs as for the scalar with vector sources (mean-field approximation). More specifically, the polarization tensor in the vector channel arises from the one-loop bubble using the dressedquark propagator,

$$\Pi_{\mu\nu}(P) = -i \int \frac{d^4k}{(2\pi)^4} \text{tr}\big[\gamma_\mu(\slashed{k} + M)\gamma_\nu(\slashed{P} - \slashed{k} + M)\big] \frac{F(k)F(P-k)}{(k^2 - M^2)[(P-k)^2 - M^2]}. \tag{24.9}$$

The trace yields

$$\text{tr}\big[\gamma_\mu(\slashed{k} + M)\gamma_\nu(\slashed{P} - \slashed{k} + M)\big] = 4\big[k_\mu(P-k)_\nu + k_\nu(P-k)_\mu - g_{\mu\nu}(k \cdot (P-k) - M^2)\big].$$

Using Feynman parameters and shifting $k \to k - \alpha P$, one obtains the standard transverse structure

$$\Pi_{\mu\nu}(P) = \left(g_{\mu\nu} - \frac{P_\mu P_\nu}{P^2}\right)\Pi_T(P^2), \qquad P^\mu \Pi_{\mu\nu} = 0.$$

The bound-state mass follows from the pole condition

$$1 - g_V \Pi_T(m_V^2) = 0.$$

While in the covariant formulation Lorentz symmetry symmetry is manifest, this is not the case for the light fron formulation. However, the two formulations should yield the same observables, in the $1/N_c$ book-keeping approximation of the ILM. The simplest way to see how this arizes in the leading order or mean-field approximation is as follows: In the driving bubble kernel, the measure can be split through $d^4k \to dk^- dk^+ dk_\perp$, and then the k^--integration carried first,

$$\int_{-\infty}^{\infty} \frac{dk^-}{2\pi} \frac{i}{(k^2 - M^2)[(P-k)^2 - M^2]} \mathcal{F}(k)\mathcal{F}(P-k)\bigg|_{P^2 = m_X^2} \to \frac{\theta(x\bar{x})}{2x\bar{x}P^+} \frac{1}{m_X^2 - \frac{k_\perp^2 + M^2}{x\bar{x}}} \big[zF'(z)\big]^4\bigg|_{z = \frac{\rho k_\perp}{2\lambda_X \sqrt{x\bar{x}}}} \tag{24.10}$$

This can be justified by doing the contour integral along $k'^4 = \frac{-k^3 + ik^4}{\sqrt{2}}$ in Euclidean space. The parameter λ_X is of order 1, and can be determined by matching the integrals on both sides. Its origin goes back to the removing of the spurious poles in the two-body non-local form factor, in the analytical continuation from Euclidean to Minkowski signature [Kock et al., 2020, Kock and Zahed, 2021]. Effectively, λ_X is a measure of the non-locality related to the finite-sized instanton vacuum with effective size cut-off ρ/λ_X which depends on the bound state mass m_X, constituent mass M and instanton size ρ. with typivally [Kock et al., 2020, Kock and Zahed, 2021],

$$\lambda_S = 2.464 \qquad \lambda_V = 3.542 \tag{24.11}$$

24.5 Light-Front Representation of Vector Mesons

A physical vector meson is described on the light front by its lowest Fock component [Liu et al., 2024d]

$$|V(P,\lambda)\rangle = \int_0^1 \frac{dx}{\sqrt{2x\bar{x}}} \int \frac{d^2k_\perp}{(2\pi)^3} \sum_{s_1 s_2} \Phi_V^\lambda(x, k_\perp; s_1, s_2)\, b_{s_1}^\dagger(k)\, d_{s_2}^\dagger(P-k)\, |0\rangle.$$

with the LF momentum variables are

$$k^+ = xP^+, \qquad (P-k)^+ = \bar{x}P^+, \qquad k_\perp, \qquad \bar{x} = 1 - x.$$

In this framework, the vector meson light front wave function factorizes

$$\Phi_V^\lambda(x, k_\perp; s_1, s_2) = \frac{C_{V,\lambda}}{\sqrt{N_c}} \sqrt{2x\bar{x}}\, \phi_V^\lambda(x, k_\perp)\, \bar{u}_{s_1}(k)\gamma^\mu \epsilon_\mu^{(\lambda)} v_{s_2}(P-k).$$

with the spinor bilinears splitting into transverse and longitudinal contributions

$$\bar{u}(k)\gamma^\mu \epsilon_\mu^{(\lambda)} v(P-k) = \bar{u}(k)\left[\gamma^+ \epsilon_{(\lambda^-)} + \gamma^- \epsilon_{(\lambda^+)} - \gamma^i \epsilon_{(\lambda^i)}\right] v(P-k).$$

Because $\epsilon_A^+ = 0$ and $\epsilon_{(0)}^+ \neq 0$, the longitudinal polarization couples to the instantaneous part of the Dirac propagator, producing the LF asymmetry between $\lambda = 0$ and $\lambda = \pm 1$ which must ultimately be removed. The LF wavefunction normalization follows from

$$\int dx \int \frac{d^2k_\perp}{(2\pi)^3} \sum_{s_1 s_2} |\Phi_V^\lambda|^2 = 1.$$

24.6 Transverse Vector Bound-State Equation

The study of light-front (LF) bound states provides a powerful nonperturbative framework for describing relativistic hadrons. In the ILM, quarks acquire a dynamical mass together with nonlocal, chirally symmetric interactions that can be recast in a light-front Hamiltonian formalism. In this formulation, only the so-called good component of the fermion field is dynamical, while the bad component is constrained and must be eliminated. This elimination gives rise to instantaneous fermion-exchange kernels that contribute to the two-body interaction.

The LF Hamiltonian for the ρ/ω mesons contains a kinetic term, and a nonlocal interaction arising from ILM molecular contributions. For the vector mesons with transverse polarization, the instantaneous fermion exchange through the bad component does not contribute. Hence, the bound state equation follows solely from the use of the good component, giving [Liu et al., 2024d]

$$m_V^2 \phi_V^T(x, k_\perp) = \frac{k_\perp^2 + M^2}{x\bar{x}} \phi_V^T(x, k_\perp) - 4g_V \sqrt{F(k)F(P-k)} \int_0^1 dy \int \frac{d^2q_\perp}{(2\pi)^3} \frac{4(q_\perp^2 + M^2)}{\sqrt{2x\bar{x}2y\bar{y}}} \phi_V^T(y, q_\perp)\sqrt{F(q)F(P-q)}.$$

(24.12)

Its derivation from the LF Hamiltonian in the mean-field approximation, uses the reduction

$$\gamma^i \slashed{q} \gamma^i = -\slashed{q} + 2q^i \gamma^i,$$

after summing over $i = 1, 2$, which yields

$$\bar{u}(k)\gamma^i(\slashed{q} + M)\gamma^i v(P-q) = 4(q_\perp^2 + M^2)\, \bar{u}(k)v(P-q),$$

producing the kernel in Eq. (24.12). The equation is an eigenvalue problem for m_V^2, symmetric in $x \leftrightarrow \bar{x}$, with attractive kernel due to positive g_V from instanton molecules. Its solution determines ϕ_V^T and the vector-meson mass.

$\rho = 0.313$ fm , $m_{\omega,\rho} = 780$ MeV , M = 398.2 MeV

$q_{\omega,\rho}$ (x)

Transverse mode
Longitudinal mode
Unpolarized PDF
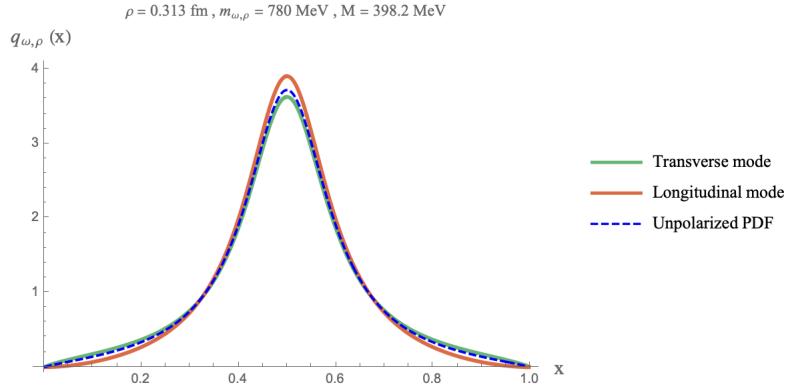
Fig. 24.6.1 Vector mesons PDFs versus parton-x: transverse polarization (solid-green), longitudinal polarization (solid-red) and unpolarized (dashed-blue) [Liu et al., 2024d].

24.7 Longitudinal Vector Bound-State Equation on the Light Front

For vector mesons, the longitudinal polarization contains additional instantaneous contributions not present in the transverse channel. A covariant treatment in the ILM, however, requires that the longitudinal and transverse channels ultimately coincide once nonlocal form factors and Bethe-Salpeter constraints are enforced.

Here, we derive the longitudinal light-front bound-state equation for a neutral vector meson in a quark-antiquark model with an effective vector interaction inspired by the ILM. The goal is to make explicit the role of the instantaneous fermion contribution in the longitudinal channel and to show how, after enforcing a covariant structure for the non-local interaction, the longitudinal equation becomes identical to the transverse one, leading to a unique vector mass and a common light-front wave function. The exact ILM derivation can be found in [Liu et al., 2024d] (Appendix B).

24.7.1 Light-front kinematics and quark fields

For completeness, we recall the light front coordinates

$$x^{\pm} = x^0 \pm x^3, \qquad \boldsymbol{x}_{\perp} = (x^1, x^2), \tag{24.13}$$

and similarly for momenta. The total meson momentum is chosen as

$$P^{\mu} = \left(P^+, \frac{m_V^2}{P^+}, \boldsymbol{0}_{\perp}\right), \tag{24.14}$$

with m_V the physical vector meson mass. In the valence $q\bar{q}$ Fock sector the quark carries longitudinal momentum fraction x and transverse momentum $\boldsymbol{k}_{\perp}$, while the antiquark carries $\bar{x} = 1 - x$ and $-\boldsymbol{k}_{\perp}$.

The Dirac field is decomposed into "good" and "bad" components,

$$\psi_{\pm} = \Lambda_{\pm}\psi, \qquad \Lambda_{\pm} = \frac{1}{2}\gamma^{\mp}\gamma^{\pm}, \tag{24.15}$$

with ψ_+ dynamical and ψ_- constrained. In the presence of an effective non-local interaction V_{ILM} and a constituent quark mass M, the light-front Dirac equation yields the constraint

$$i\partial^+\psi_- = \left(i\gamma^{\perp}\partial_{\perp} + M + V_{\text{ILM}}\right)\psi_+, \tag{24.16}$$

so that

$$\psi_- = \frac{1}{i\partial^+}\left(i\gamma^\perp\partial_\perp + M + V_{\text{ILM}}\right)\psi_+. \tag{24.17}$$

Eliminating ψ_- in favor of ψ_+ generates a *bare* instantaneous fermion interactions in the light-front Hamiltonian, which will play a crucial role in the longitudinal channel. For clarity of the argument, we will ignore the dressing of the bare interactions in the ILM. The full treatement including the dressing in the ILM, is given in [Liu et al., 2024d].

24.7.2 Effective vector interaction and non-local form factor

We consider an effective four-fermion interaction in the vector channel,

$$\mathcal{L}_{\text{int}} = -\frac{g_V}{2}\left[\bar{\psi}(x)\gamma^\mu\mathcal{F}(i\partial)\psi(x)\right]\left[\bar{\psi}(x)\gamma_\mu\mathcal{F}(i\partial)\psi(x)\right], \tag{24.18}$$

where g_V is a coupling and $\mathcal{F}(i\partial)$ is a non-local operator encoding the momentum-dependent ILM form factor. In momentum space the corresponding vertex attaches a form factor $F(k)$ to each quark leg, with k the off-shell quark momentum. For a quark carrying $(xP^+, \boldsymbol{k}_\perp)$ and an antiquark carrying $(\bar{x}P^+, -\boldsymbol{k}_\perp)$ we will denote these factors as

$$F(k) \equiv F(x, \boldsymbol{k}_\perp), \qquad F(P-k) \equiv F(\bar{x}, -\boldsymbol{k}_\perp). \tag{24.19}$$

A convenient shorthand is

$$\mathcal{F}_{x,\boldsymbol{k}_\perp} \equiv \sqrt{F(k)F(P-k)}. \tag{24.20}$$

24.7.3 Vector meson wave function on the light front

The light-front valence state of a neutral vector meson with polarization λ is expanded as

$$\left|V(P,\lambda)\right\rangle_{\text{val}} = \sum_{s_1,s_2}\int_0^1\frac{dx}{\sqrt{x\bar{x}}}\int\frac{d^2\boldsymbol{k}_\perp}{(2\pi)^3}\,\psi_{s_1 s_2}^\lambda(x,\boldsymbol{k}_\perp)\,b_{s_1}^\dagger(xP^+,\boldsymbol{k}_\perp)\,d_{s_2}^\dagger(\bar{x}P^+,-\boldsymbol{k}_\perp)\left|0\right\rangle, \tag{24.21}$$

where s_1, s_2 denote light-front helicities and $b^\dagger, d^\dagger$ are quark and antiquark creation operators.

The spinor structure is encoded in a light-front spin projector $S_{s_1 s_2}^\lambda(x,\boldsymbol{k}_\perp)$, while the dynamical information is in a scalar wave function $\phi_V(x,\boldsymbol{k}_\perp)$. For a longitudinally polarized state ($\lambda = 0$) one may write

$$\psi_{s_1 s_2}^L(x,\boldsymbol{k}_\perp) = S_{s_1 s_2}^L(x,\boldsymbol{k}_\perp)\,\phi_V^L(x,\boldsymbol{k}_\perp), \tag{24.22}$$

where $S_{s_1 s_2}^L$ is constructed from the polarization vector $\varepsilon_L^\mu(P)$ and the Dirac structure γ_μ coupled to the spinors.

The free $q\bar{q}$ invariant mass squared is

$$M_0^2(x,\boldsymbol{k}_\perp) = \frac{\boldsymbol{k}_\perp^2 + M^2}{x\bar{x}}. \tag{24.23}$$

The interacting system satisfies a light-front Hamiltonian eigenvalue problem,

$$\left(P_{\text{free}}^- + P_{\text{int}}^-\right)\left|V(P,\lambda)\right\rangle = \frac{m_V^2}{P^+}\left|V(P,\lambda)\right\rangle, \tag{24.24}$$

which reduces in the valence sector to an integral equation for $\phi_V^\lambda(x,\boldsymbol{k}_\perp)$.

24.7.4 Transverse reference equation

It is convenient to recall first the transverse ($\lambda = \pm 1$) equation, which is free of instantaneous fermion contributions once ψ_- is eliminated. For a transverse polarization one obtains a homogeneous integral equation of the form

$$\left[m_V^2 - M_0^2(x, \boldsymbol{k}_\perp)\right] \phi_V^T(x, \boldsymbol{k}_\perp) = \int_0^1 dy \int \frac{d^2 \boldsymbol{q}_\perp}{(2\pi)^3} \, K_T(x, \boldsymbol{k}_\perp; y, \boldsymbol{q}_\perp) \, \phi_V^T(y, \boldsymbol{q}_\perp), \tag{24.25}$$

where K_T is the transverse kernel generated by the effective vector interaction. In the ILM, a typical structure is

$$K_T(x, \boldsymbol{k}_\perp; y, \boldsymbol{q}_\perp) = -\frac{g_V N_c}{\sqrt{2x\bar{x}\, 2y\bar{y}}} \, \mathcal{F}_{x,\boldsymbol{k}_\perp} \, \mathcal{F}_{y,\boldsymbol{q}_\perp} \, \mathcal{N}_T(x, \boldsymbol{k}_\perp; y, \boldsymbol{q}_\perp), \tag{24.26}$$

where $\mathcal{N}_T$ is the Dirac trace projected onto the transverse polarization. For a pure vector current-current interaction this trace is dominated by terms proportional to $4\left(\boldsymbol{q}_\perp^2 + M^2\right)$; more precisely,

$$\mathcal{N}_T(x, \boldsymbol{k}_\perp; y, \boldsymbol{q}_\perp) = 4\left(\boldsymbol{q}_\perp^2 + M^2\right) + (\text{terms that vanish after symmetric integration}). \tag{24.27}$$

After discarding the odd terms in $\boldsymbol{q}_\perp$ by symmetric integration, the transverse kernel may be represented schematically as

$$K_T(x, \boldsymbol{k}_\perp; y, \boldsymbol{q}_\perp) \simeq -\frac{4 g_V N_c}{\sqrt{2x\bar{x}\, 2y\bar{y}}} \, \mathcal{F}_{x,\boldsymbol{k}_\perp} \left(\boldsymbol{q}_\perp^2 + M^2\right) \mathcal{F}_{y,\boldsymbol{q}_\perp}. \tag{24.28}$$

The precise numerical normalization is not essential for the discussion of the difference between transverse and longitudinal channels; what matters is the dependence on $\boldsymbol{q}_\perp^2 + M^2$ and the overall non-local factors.

24.7.5 Instantaneous fermion exchange and the longitudinal kernel

In contrast, the longitudinal polarization is sensitive to the instantaneous fermion term originating from the constraint (24.17). When the light-front Hamiltonian is reexpressed solely in terms of the good component ψ_+, the effective interaction in the vector channel acquires an additional "seagull" piece, which in the valence sector appears as an instantaneous quark exchange. Diagrammatically, this corresponds to the propagation of a quark line with the instantaneous light-front propagator $\gamma^+/(2p^+)$.

The longitudinal bound-state equation may be written as

$$\left[m_V^2 - M_0^2(x, \boldsymbol{k}_\perp)\right] \phi_V^L(x, \boldsymbol{k}_\perp) = \int_0^1 dy \int \frac{d^2 \boldsymbol{q}_\perp}{(2\pi)^3} \, K_L(x, \boldsymbol{k}_\perp; y, \boldsymbol{q}_\perp) \, \phi_V^L(y, \boldsymbol{q}_\perp). \tag{24.29}$$

The kernel K_L naturally splits into a regular (ladder-type) contribution K_{reg}, identical to that appearing in the transverse channel, and an instantaneous contribution K_{inst}:

$$K_L = K_{\text{reg}} + K_{\text{inst}}, \qquad K_{\text{reg}} \equiv K_T. \tag{24.30}$$

Carrying out the Dirac algebra for the longitudinal polarization vector $\varepsilon_L^\mu(P)$ and using the instantaneous propagator for the internal quark line, one finds a kernel of the form

$$K_L(x, \boldsymbol{k}_\perp; y, \boldsymbol{q}_\perp) = -\frac{g_V N_c}{\sqrt{2x\bar{x}\, 2y\bar{y}}} \, \mathcal{F}_{x,\boldsymbol{k}_\perp} \, \mathcal{F}_{y,\boldsymbol{q}_\perp} \left[\mathcal{N}_T(x, \boldsymbol{k}_\perp; y, \boldsymbol{q}_\perp) + \mathcal{N}_{\text{inst}}(x, \boldsymbol{k}_\perp; y, \boldsymbol{q}_\perp)\right], \tag{24.31}$$

with $\mathcal{N}_T$ as in the transverse case and $\mathcal{N}_{\text{inst}}$ encoding the instantaneous contribution. After performing the light-front energy integration and projecting onto the longitudinal channel, the instantaneous trace can be arranged as

$$\mathcal{N}_{\text{inst}}\big(x, \boldsymbol{k}_\perp; y, \boldsymbol{q}_\perp\big) = -\big[2x\bar{x}\, m_V^2 + \boldsymbol{k}_\perp^2 + M^2\big] + \text{(terms that vanish after symmetric integration)}. \quad (24.32)$$

Here the dependence on m_V^2 reflects the coupling of the longitudinal polarization vector to the total momentum P^μ, while the combination $\boldsymbol{k}_\perp^2 + M^2$ arises from the numerator structure of the instantaneous propagator and the spinor projectors.

Substituting (24.28) and (24.32) into (24.31), and dropping odd terms in $\boldsymbol{q}_\perp$ by symmetric integration, the longitudinal kernel can be written in a schematic but physically transparent form:

$$K_L\big(x, \boldsymbol{k}_\perp; y, \boldsymbol{q}_\perp\big) \simeq -\frac{4g_V N_c}{\sqrt{2x\bar{x}\, 2y\bar{y}}}\, \mathcal{F}_{x,\boldsymbol{k}_\perp}\, \big(\boldsymbol{q}_\perp^2 + M^2\big)\, \mathcal{F}_{y,\boldsymbol{q}_\perp}$$
$$-\frac{g_V N_c}{\sqrt{2x\bar{x}\, 2y\bar{y}}}\, \mathcal{F}_{x,\boldsymbol{k}_\perp}\, \big[2x\bar{x}\, m_V^2 + \boldsymbol{k}_\perp^2 + M^2\big]\, \mathcal{F}_{y,\boldsymbol{q}_\perp}. \quad (24.33)$$

The first line is identical to the transverse kernel, while the second line is the characteristic instantaneous contribution.

24.7.6 Difference between longitudinal and transverse kernels

Equations (24.28) and (24.33) make the origin of the difference between longitudinal and transverse kernels explicit. For fixed $(x, \boldsymbol{k}_\perp)$ one finds

$$K_L\big(x, \boldsymbol{k}_\perp; y, \boldsymbol{q}_\perp\big) - K_T\big(x, \boldsymbol{k}_\perp; y, \boldsymbol{q}_\perp\big) \simeq -\frac{g_V N_c}{\sqrt{2x\bar{x}\, 2y\bar{y}}}\, \mathcal{F}_{x,\boldsymbol{k}_\perp}\, \big[2x\bar{x}\, m_V^2 + \boldsymbol{k}_\perp^2 + M^2\big]\, \mathcal{F}_{y,\boldsymbol{q}_\perp}. \quad (24.34)$$

Thus the *difference* between the longitudinal and transverse kernels is proportional to the combination

$$2x\bar{x}\, m_V^2 + \boldsymbol{k}_\perp^2 + M^2, \quad (24.35)$$

modulated by the non-local form factors. Left untreated, this difference would imply distinct integral equations and potentially different eigenvalues $m_{V,L}^2$ and $m_{V,T}^2$, in apparent conflict with rotational covariance.

24.7.7 Covariant ILM prescription and restoration of equality

In the covariant ILM, the underlying Bethe-Salpeter equation for the vector channel has a Dirac structure proportional to

$$\Gamma^\mu(k; P) \sim \gamma^\mu\, F(k)F(P - k), \quad (24.36)$$

with the form factors chosen such that the full amplitude is rotationally invariant in the meson rest frame. When this covariant structure is projected onto the light front, the combination appearing in (24.35) must match the invariant $k^2 + M^2$ evaluated in an instantaneous approximation with the same non-local dressing.

This requirement motivates the replacement

$$x\bar{x}\, m_V^2 + \boldsymbol{k}_\perp^2 + M^2 \;\longrightarrow\; 2\big(\boldsymbol{k}_\perp^2 + M^2\big)\, F^2(k), \quad (24.37)$$

where $F(k)$ is the ILM quark form factor evaluated at the off-shell momentum corresponding to $(x, \boldsymbol{k}_\perp)$. The numerical factor 2 reflects the two dressed quark legs in the covariant amplitude. A similar replacement-like is shown to be exact in the full treatement in the ILM, in leading order in $1/N_c$. With this in mind, the instantaneous contribution in (24.33) is reshaped into the same functional form as the transverse kernel. More precisely, after (24.37) the longitudinal kernel becomes

$$K_L\big(x, \boldsymbol{k}_\perp; y, \boldsymbol{q}_\perp\big) \simeq K_T\big(x, \boldsymbol{k}_\perp; y, \boldsymbol{q}_\perp\big), \tag{24.38}$$

up to terms that vanish after symmetric integration over $\boldsymbol{q}_\perp$ and higher-order corrections in the ILM expansion.

Consequently, the longitudinal and transverse bound-state equations,

$$\big[m_V^2 - M_0^2(x, \boldsymbol{k}_\perp)\big]\, \phi_V^T(x, \boldsymbol{k}_\perp) = \int_0^1 dy \int \frac{d^2\boldsymbol{q}_\perp}{(2\pi)^3}\, K_T\big(x, \boldsymbol{k}_\perp; y, \boldsymbol{q}_\perp\big)\, \phi_V^T(y, \boldsymbol{q}_\perp), \tag{24.39}$$

$$\big[m_V^2 - M_0^2(x, \boldsymbol{k}_\perp)\big]\, \phi_V^L(x, \boldsymbol{k}_\perp) = \int_0^1 dy \int \frac{d^2\boldsymbol{q}_\perp}{(2\pi)^3}\, K_L\big(x, \boldsymbol{k}_\perp; y, \boldsymbol{q}_\perp\big)\, \phi_V^L(y, \boldsymbol{q}_\perp), \tag{24.40}$$

collapse onto a single integral equation,

$$\big[m_V^2 - M_0^2(x, \boldsymbol{k}_\perp)\big]\, \phi_V(x, \boldsymbol{k}_\perp) = \int_0^1 dy \int \frac{d^2\boldsymbol{q}_\perp}{(2\pi)^3}\, K\big(x, \boldsymbol{k}_\perp; y, \boldsymbol{q}_\perp\big)\, \phi_V(y, \boldsymbol{q}_\perp), \tag{24.41}$$

with a common kernel $K \equiv K_T \simeq K_L$ and a unique scalar light-front wave function ϕ_V.

The physical consequence is that the vector meson mass and wave function are independent of the polarization:

$$\phi_V^L(x, \boldsymbol{k}_\perp) = \phi_V^T(x, \boldsymbol{k}_\perp) \equiv \phi_V(x, \boldsymbol{k}_\perp), \qquad m_{V,L}^2 = m_{V,T}^2 \equiv m_V^2. \tag{24.42}$$

This equality signals the restoration of rotational covariance (within the approximations of the ILM) at the level of the light-front bound-state equation. In practice, this construction provides a consistent starting point for computing longitudinal and transverse distribution amplitudes, parton distributions, and form factors of light vector mesons within the ILM framework.
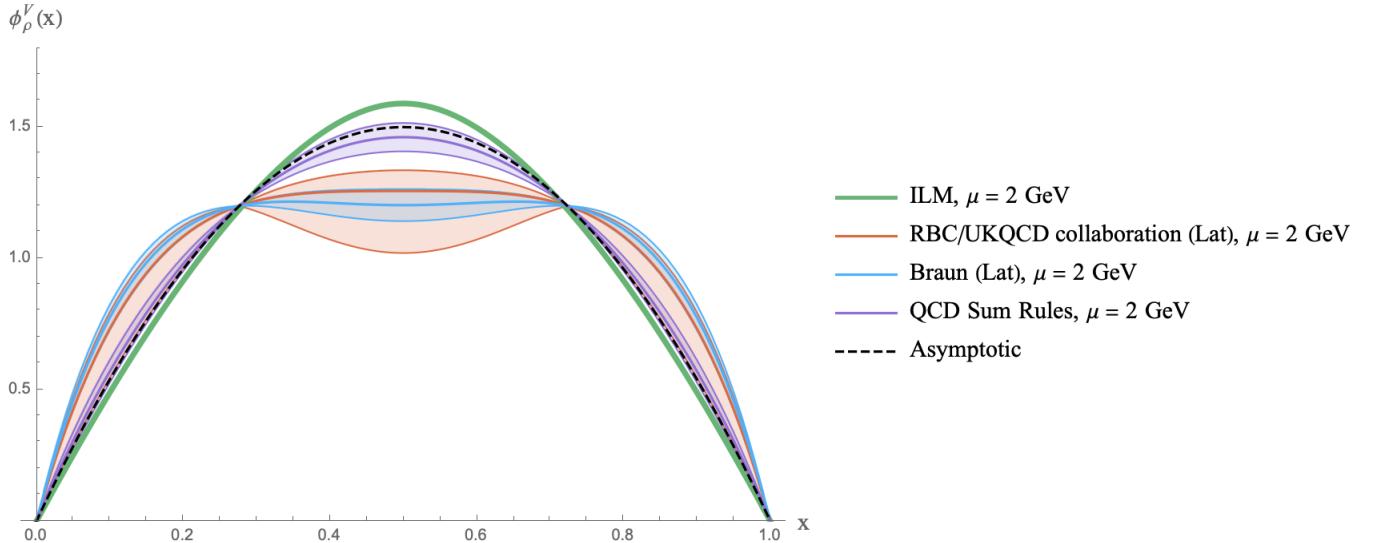
Fig. 24.7.1 Evolved longitudinal ρ DA to $\mu = 2$ GeV in solid-green [Liu et al., 2024d], compared with the lattice in RBC/UKQCD collaboration [Boyle et al., 2008] in filled-red and the lattice [Braun et al., 2017a] in filled-blue. The QCD asymptotic result of $6x\bar{x}$ is in dashed-black and the QCD sum result [Stefanis and Pimikov, 2016] is in filled-purple.

$\phi_\rho^T(\mathbf{x})$
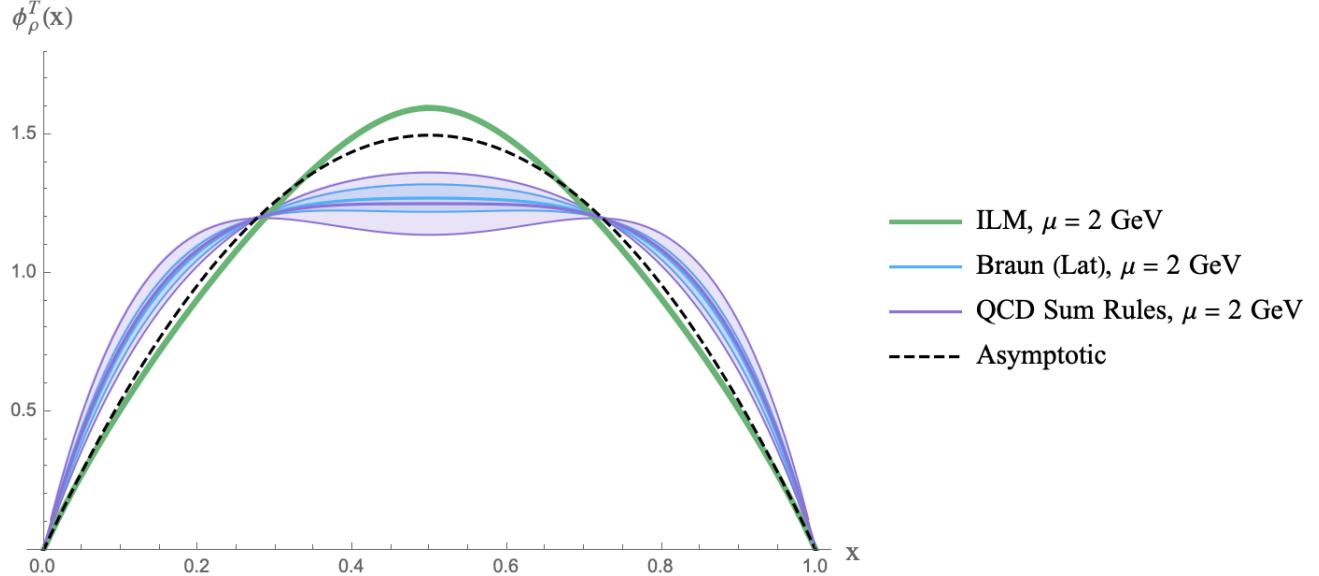
Fig. 24.7.2 Evolved transverse DA for the rho meson at $\mu = 2$ GeV in solid-green [Liu et al., 2024d], and compared with the lattice result at $\mu = 2$ GeV [Braun et al., 2017a] in filled-blue and the QCD sum rule result also at $\mu = 2$ GeV [Ball and Braun, 1996] in filled-purple.

24.8 Decay Constants and Distribution Amplitudes

The decay constant is defined via

$$\langle 0|\bar{\psi}(0)\gamma^\mu \psi(0)|V(P,\lambda)\rangle = f_V m_V \epsilon_{(\lambda)}^\mu.$$

Contracting with $\epsilon_\mu^{(0)}$ and using LF quantization gives

$$f_V = -\frac{2}{\sqrt{2N_c}m_V}\int dx\, d^2k_\perp \frac{\phi_V^L(x,k_\perp)}{\sqrt{2x\bar{x}}}\big[x\bar{x}m_V^2 + k_\perp^2 + M^2\big]F(k)F(P-k).$$

Using the covariance replacement

$$x\bar{x}m_V^2 + k_\perp^2 + M^2 \to 2(k_\perp^2 + M^2)F^2(k),$$

transforms this into the ILM-canonical form involving Bessel functions.

The longitudinal DA is defined by projecting the LF wave function onto the minimal-spin structure and integrating over $\mathbf{k}_\perp$:

$$\phi_V(x) = \frac{\sqrt{2N_c}}{f_V m_V}\int \frac{d^2k_\perp}{16\pi^3}(k_\perp^2 + M^2)F^2(k)\,\phi_V^L(x,k_\perp).$$

The transverse DA follows from replacing ϕ_V^L by ϕ_V^T after covariance restoration ensures equality.

	f_π (MeV)	f_ρ (MeV)	f_ρ^T (MeV)	f_ρ^T/f_ρ
ILM [Liu et al., 2024d]	130.3	203.97	92.48	0.453
Lattice (2GeV) [Braun et al., 2017a]	-	199(4)(1)	124(4)(1)	0.629(8)
PDG (exp) [Tanabashi et al., 2018]	130.3 ± 0.3	210 ± 4	-	-
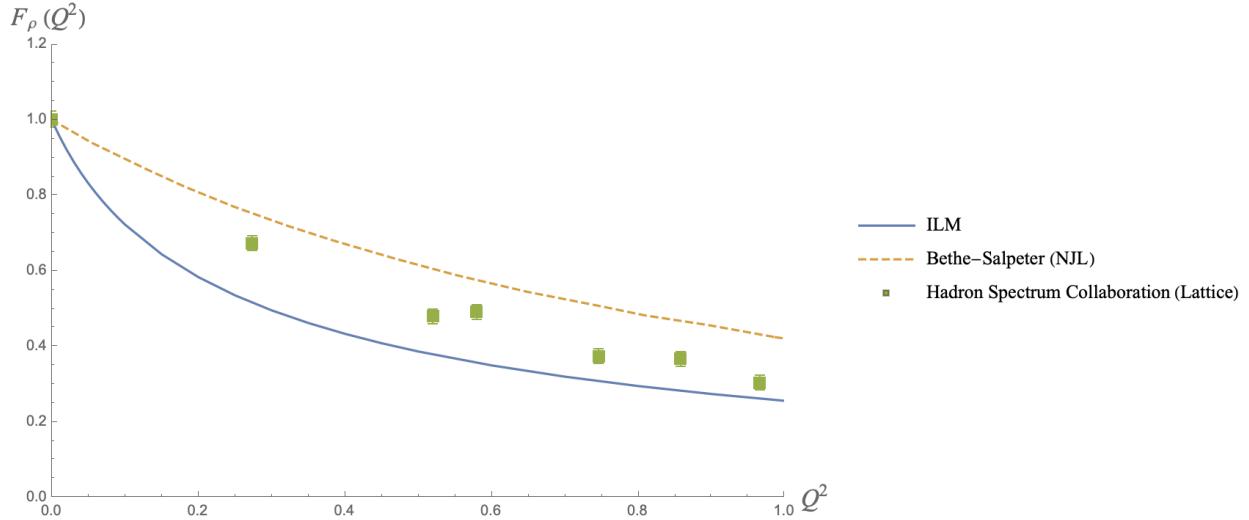
Fig. 24.8.1 ILM calculations [Liu et al., 2024d] are compared with the recent lattice calculation [Shultz et al., 2015], and the model analysis by Bethe-Salpeter equation using the random-phase approximation in the NJL model [Carrillo-Serrano et al., 2015].

24.9 Electromagnetic Structure and Charge Radii

In the Drell-Yan-West frame $q^+ = 0$, the vector meson electromagnetic form factor is given entirely by the valence wave function:

$$F_V(Q^2) = \int_0^1 dx \int \frac{d^2 k_\perp}{16\pi^3} \frac{\phi^*(x, k_\perp + (1-x)q_\perp)\phi(x, k_\perp)}{x\bar{x}} \, \mathcal{S}_V(x, k_\perp, q_\perp),$$

where $\mathcal{S}_V$ is a spin-overlap factor calculable from Dirac algebra. Expanding for small Q^2 gives

$$F_V(Q^2) = 1 - \frac{Q^2}{6} r_V^2 + \cdots .$$

Numerical evaluation in the ILM yields

$$r_V \approx 0.997 \, \text{fm},$$

consistent with the expectation that vector mesons have spatial extent $\sim 2\rho$.

Reference	r_ρ (fm)
ILM [Liu et al., 2024d]	0.997
de Melo [de Melo and Frederico, 1997]	0.608
Bhagwat [Bhagwat and Maris, 2008]	0.735
Krutov [Krutov et al., 2016]	0.748
Carrillo-Serrano[Carrillo-Serrano et al., 2015]	0.819
Owen [Owen et al., 2015]	0.819

24.10 Mass Spectrum and Covariance Restoration

Once the longitudinal and transverse kernels are made identical by enforcing the ILM-covariant replacement, the mass satisfies

$$m_{V,L}^2 = m_{V,T}^2 \equiv m_V^2.$$

The solution of the eigenvalue equation produces a value close to the physical ρ and ω masses when standard ILM parameters ($\rho \approx 1/3\,\mathrm{fm}$, $M \approx 350\,\mathrm{MeV}$) are used. The separation between ρ and ω arises from small isospin-breaking effects not included in the leading ILM analysis.

24.11 Summary

The ILM provides a unified dynamical mechanism for constituent mass generation and vector meson binding. Instanton molecules generate a nonlocal chirality-preserving interaction that produces vector bound states. On the light front, longitudinal and transverse integral equations differ due to instantaneous interactions, but enforcing covariance conditions restores their equality. The resulting LF wave functions allow computation of decay constants, distribution amplitudes, and charge radii in a fully nonperturbative and physically transparent framework.

Appendix

24.A Covariant Bethe-Salpeter Structure of Vector Mesons

The covariant formulation of vector mesons in the Instanton Liquid Model follows from the nonlocal effective action induced by instantons and instanton-anti-instanton molecules. The basic object is the color-singlet vector correlator,

$$\Pi_{\mu\nu}(x-y) = \langle\, 0\,|\, T\{\bar{\psi}(x)\gamma_\mu\psi(x)\, \bar{\psi}(y)\gamma_\nu\psi(y)\}\,|\, 0\,\rangle.$$

In the ILM, this correlator is evaluated by expanding the quark determinant around the instanton ensemble and keeping the lowest nontrivial contributions from zero-mode physics. The dressed quark propagator has the form

$$S(k) = \frac{\slashed{k} + M(k)}{k^2 - M^2(k) + i\epsilon},$$

where $M(k)$ is the constituent mass generated by the single-instanton sector. The nonlocal form factor $F(k)$ encodes the Fourier transform of the instanton zero-mode profile and appears at the quark-meson vertex.

The leading contribution to the vector correlator is obtained by evaluating the quark loop with two vector insertions and nonlocal dressings,

$$\Pi_{\alpha\beta}(P) = -i \int \frac{d^4 k}{(2\pi)^4}\, \mathrm{tr}\left[\Gamma_\alpha(\slashed{k} + M(k))\, \Gamma_\beta(\slashed{P} - \slashed{k} + M(P-k)) \right] \frac{F(k)F(P-k)}{[k^2 - M^2(k)][(P-k)^2 - M^2(P-k)]}.$$
$$(24.43)$$

The Dirac trace decomposes into two pieces,

$$\mathrm{tr}\left[\gamma_\alpha \slashed{k} \gamma_\beta (\slashed{P} - \slashed{k})\right] + M(k)M(P-k)\, \mathrm{tr}[\gamma_\alpha\gamma_\beta],$$

and after use of the identity

$$\mathrm{tr}[\gamma_\alpha\gamma_\rho\gamma_\beta\gamma_\sigma] = 4(g_{\alpha\rho}g_{\beta\sigma} - g_{\alpha\beta}g_{\rho\sigma} + g_{\alpha\sigma}g_{\rho\beta}),$$

one obtains a tensor proportional to

$$g_{\alpha\beta}, \qquad P_\alpha P_\beta,$$

as expected from Lorentz symmetry. The nonlocal factors $F(k)$ and $F(P-k)$ soften the ultraviolet behavior and reflect the instanton size ρ.

The correlator is decomposed as

$$\Pi_{\mu\nu}(P) = \left(g_{\mu\nu} - \frac{P_\mu P_\nu}{P^2}\right) \Pi_T(P^2) + \frac{P_\mu P_\nu}{P^2} \Pi_L(P^2).$$

Because the vector current is conserved and the ILM interactions preserve chirality in the molecular sector, the longitudinal component vanishes at the physical point,

$$P^\mu \Pi_{\mu\nu}(P) = 0,$$

ensuring $\Pi_L(P^2) = 0$ for on-shell vector mesons. The vector meson mass emerges from the zero of the Dyson-resummed propagator,

$$D_{\mu\nu}(P) = \frac{-i}{1 - g_V \Pi_T(P^2)} \left(g_{\mu\nu} - \frac{P_\mu P_\nu}{P^2} \right),$$

giving the bound-state condition

$$1 - g_V \Pi_T(m_V^2) = 0.$$

Near this pole, the propagator assumes the standard form

$$D_{\mu\nu}(P) = \frac{-i Z_V}{P^2 - m_V^2} \left(g_{\mu\nu} - \frac{P_\mu P_\nu}{m_V^2} \right) + \cdots,$$

with residue

$$Z_V^{-1} = \left. \frac{\partial \Pi_T(P^2)}{\partial P^2} \right|_{P^2 = m_V^2}.$$

This allows identification of the covariant Bethe-Salpeter amplitude,

$$\Psi_\mu(k; P) = g_{Vqq}\, S(k)\gamma_\mu S(k - P)\sqrt{F(k)F(P - k)}, \tag{24.44}$$

which enters the LSZ reduction of three-point functions and forms the starting point for LF reduction.

24.B Reduction to Light-Front Dynamics

The transformation from the covariant Bethe-Salpeter amplitude (24.44) to a light-front wave function proceeds by integrating over the LF energy k^- and projecting onto the dynamical spinor components. Explicitly, the LF projection is

$$\Phi_V^\lambda(x, k_\perp) = iP^+ \int \frac{dk^-}{2\pi}\, \bar{u}(k)\frac{\gamma^+}{2k^+} \Psi_\mu(k; P)\epsilon_{(\lambda)}^\mu \frac{\gamma^+}{2(P^+ - k^+)}\, v(P - k).$$

The propagator has poles at

$$k^- = \frac{k_\perp^2 + M^2(k)}{k^+} - i\epsilon, \qquad (P - k)^- = \frac{(P_\perp - k_\perp)^2 + M^2(P - k)}{P^+ - k^+} - i\epsilon,$$

and the contour integral projects the quark line on-shell. Because the nonlocal form factors $F(k)$ are functions of spatial momentum only in the instanton model, they do not contribute poles in k^-. This simplifies the residue calculation, yielding

$$\Phi_V^\lambda(x, k_\perp) = \frac{C_{V,\lambda}}{\sqrt{N_c}}\, \sqrt{2x\bar{x}}\, \phi_V^\lambda(x, k_\perp)\, \bar{u}(k)\gamma^\mu \epsilon_\mu^{(\lambda)} v(P - k),$$

with the scalar LF wave function ϕ_V^λ defined by the on-shell value of the Bethe-Salpeter kernel.

The elimination of ψ_- in the LF Hamiltonian generates additional terms,

$$\psi_- = \frac{1}{i\partial^+} \left[i\gamma^\perp \partial_\perp + M + \text{nonlocal ILM vertex} \right] \psi_+,$$

leading to instantaneous four-fermion interactions. These interactions contribute to longitudinal polarization because the polarization vector satisfies $\epsilon^+_{(0)} \neq 0$, causing longitudinal spin projections to couple directly to instantaneous quark exchange. The induced interaction is governed by a tadpole term,

$$w_+(P^+) = \int dx\, d^2k_\perp\, 2x\, F(k)F(P-k) - \frac{1}{2g_S}\left(1 - \frac{m}{M}\right),$$

which mirrors the structure of the scalar ILM gap equation. This connection highlights the continuity between the nonlocal interactions that generate $M(k)$ and those that produce vector binding.

24.C Longitudinal Bound-State Equation and Covariance Restoration

The longitudinal LF kernel differs from the transverse one because of the presence of the instantaneous interaction. The raw equation takes the form

$$m_V^2\, \phi_V^L(x, k_\perp) = \frac{k_\perp^2 + M^2}{x\bar{x}}\phi_V^L - K_V\phi_V^L + \Delta_{\mathrm{LF}}(x, k_\perp),$$

where K_V is the same nonlocal kernel appearing in the transverse channel. The additional term Δ_{LF} may be written schematically as

$$\Delta_{\mathrm{LF}}(x, k_\perp) = g_V\, \sqrt{F(k)F(P-k)}\frac{x\bar{x}m_V^2 + k_\perp^2 + M(k)M(P-k)}{x\bar{x}}\, \Xi(x, k_\perp), \qquad (24.45)$$

where Ξ represents a smooth function associated with the overlap of spinor numerators.

This term has no analog in the covariant Bethe-Salpeter equation and must therefore be removed or reinterpreted. The comparison of LF and covariant amplitudes shows that the combination

$$x\bar{x}m_V^2 + k_\perp^2 + M(k)M(P-k)$$

naturally appears in LF energy denominators but should be replaced by the covariant denominator arising from quark propagators,

$$k^2 - M^2(k) \qquad \text{and} \qquad (P-k)^2 - M^2(P-k).$$

The ILM approximation $M(k) \approx M$ at low momentum allows one to identify

$$k^2 - M^2 = k_\perp^2 - x\bar{x}P^2,$$

leading to the replacement

$$x\bar{x}m_V^2 + k_\perp^2 + M(k)M(P-k) \approx 2(k_\perp^2 + M^2)F^2(k),$$

derived by matching the structure of the covariant quark loop with the LF energy denominator.

Substituting this relation into (24.45) eliminates Δ_{LF} and renders the longitudinal equation identical to the transverse one. The equality

$$m_{V,L} = m_{V,T}$$

is thus a consequence of enforcing the correct covariant structure inside the LF Hamiltonian.

24.D Decay Constants and Distribution Amplitudes from Light-Front Wave Functions

The longitudinal decay constant is extracted from the matrix element

$$\langle 0|\bar{\psi}(0)\gamma^+\psi(0)|V(P,\lambda=0)\rangle = f_V\, m_V\, \epsilon^+_{(0)}.$$

Using the LF wave function yields

$$f_V = -\frac{2}{\sqrt{2N_c}\, m_V}\int dx \int \frac{d^2k_\perp}{(2\pi)^3}\frac{\phi_V^L}{\sqrt{2x\bar{x}}}\big[x\bar{x}m_V^2 + k_\perp^2 + M^2\big]F(k)F(P-k).$$

Applying the covariance-restoring identity gives the covariant expression involving the Bessel-profile kernel

$$(zF_0(z))^6, \qquad z = k\rho,$$

which arises from the Fourier transform of the instanton zero mode. The integration measure changes accordingly,

$$d^2k_\perp \to \frac{dz\, z}{\rho^2}, \qquad M \to M\, F_0(z).$$

The longitudinal distribution amplitude follows from integration over transverse momenta of the minimal spin component of the LF wave function,

$$\phi_V(x) = \int \frac{d^2k_\perp}{16\pi^3}\phi_V^L(x,k_\perp)\,\mathcal{P}_{\min}(x,k_\perp),$$

where $\mathcal{P}_{\min}$ denotes the projector onto the leading-twist component. After substitution of the Bessel representation and elimination of spurious LF terms, one obtains the compact form given in the main text.

The transverse DA is computed similarly, using the transverse LF wave function ϕ_V^T. At the ILM scale, both DAs are broad, reflecting the extended nonlocality of instanton zero modes.

24.E Tadpole Structures and Gap-Like Mass Equations

The tadpole term $w_+(P^+)$ entering the LF Hamiltonian plays a central role in renormalizing the effective vector kernel. Its explicit form is

$$w_+(P^+) = \int_0^1 dx \int \frac{d^2k_\perp}{(2\pi)^3} 2x\, F(k)F(P-k) - \frac{1}{2g_S}\left(1 - \frac{m}{M}\right).$$

The first term originates from the instantaneous contraction of two nonlocal vector vertices in the LF Hamiltonian, while the second term derives from the ILM gap equation,

$$M = m + g_S \int dk\, F^2(k),$$

which expresses the dynamical constituent mass in terms of the scalar coupling.

Using this relation, one may rewrite the vector bound-state equation in a form analogous to the scalar gap equation. Combining tadpole and dynamical terms yields

$$1 - \frac{g_V}{g_S}\left(1 - \frac{m}{M}\right) = -2g_V(m_V^2 - 4M^2)\int dx\, d^2k_\perp\, \frac{F(k)F(P-k)}{x\bar{x}m_V^2 - (k_\perp^2 + M^2)}.$$

This relation highlights the weaker binding in vector channels due to the suppressed ratio g_V/g_S, reflecting the molecular rather than single-instanton origin of vector interactions. In particular, the vector mass satisfies

$$m_V > 2M,$$

in contrast to the pion, whose mass remains anomalously small because of Goldstone dynamics.

Chapter 25
Transverse-momentum-dependent parton distributions (TMDs)

25.1 Soft functions

The transverse-momentum-dependent parton distributions (TMDs) have become indispensable tools in the theoretical description of high-energy scattering involving hadrons. They encode much more than the longitudinal momentum structure familiar from collinear parton distribution functions; they also reveal the intrinsic transverse motion of partons inside a fast-moving hadron. The dependence on the transverse separation b_T, defined as the Fourier conjugate to the transverse momentum k_T, allows TMDs to probe the three-dimensional momentum structure of hadronic matter [Collins and Soper, 1981a, Collins and Soper, 1982a, Collins et al., 1985b].

The TMDs depend on several scales, including the ultraviolet renormalization scale μ and the rapidity scale ζ that arises from the need to regularize lightlike Wilson lines. This rapidity scale has no analogue in collinear factorization and is intimately connected with the geometry of Wilson lines that extend near the light cone. The logarithmic sensitivity of TMDs to this scale is governed by the Collins-Soper (CS) kernel [Collins and Soper, 1981a], a central nonperturbative function encoding long-distance correlations that appear in soft-gluon exchanges. The CS kernel determines how TMDs evolve with rapidity and is a central building block in the TMD evolution equations. Although the CS kernel can be computed perturbatively for small separations b_T, its behavior at large b_T is intrinsically nonperturbative.

Modern global analyses of TMDs require a reliable parameterization of the nonperturbative CS kernel [Davies et al., 1985, Landry et al., 2003, Konychev and Nadolsky, 2006, Scimemi and Vladimirov, 2018, Scimemi and Vladimirov, 2020, Bacchetta et al., 2020, Bury et al., 2022]. Several groups have proposed forms based on phenomenological considerations, but a compelling nonperturbative calculation rooted directly in QCD dynamics has been difficult to obtain. Recently, the development of large-momentum effective theory (LaMET) [Ji, 2013, Ji, 2014, Ji et al., 2021] has permitted the extraction of the CS kernel from lattice QCD through quasi-TMDs [Shanahan et al., 2020, Shanahan et al., 2021, Avkhadiev et al., 2023]. These calculations are advancing rapidly, but the underlying physics at long distances remains challenging to interpret.

A parallel approach is to compute the nonperturbative soft functions directly in the ILM [Liu et al., 2024g]. Since soft functions are Wilson loops built from Wilson lines, and since Wilson loops are deeply sensitive to long-distance gauge fields, the ILM offers a natural platform for evaluating them. The ability to compute Wilson loops in Euclidean space using instanton ensembles provides a particularly powerful way to extract soft functions that depend on an Euclidean angle θ, which can then be analytically continued to the physical Minkowski rapidity $\chi = i\theta$. This procedure opens a new, fully Euclidean, first-principles route to the CS kernel. For completeness, we note the original attempt to study scattering amplitudes using this approach [Shuryak and Zahed, 2000, Shuryak and Zahed, 2004b].

This chapter provides an expanded account of this construction. We begin with an overview of Wilson lines and their role in TMD factorization, including a detailed discussion of cusp divergences and the structure

of soft functions. We then turn to a comprehensive description of the ILM calculation of Wilson loops with cusp angles, explaining how the instanton profile enters and how the angular dependence factorizes. Both weak-field and strong-field limits are examined, and the resulting CS kernel is analyzed in detail, including its asymptotic form at large transverse separation. Finally, we discuss the matching to perturbation theory at small b_T, the interpretation of the ILM at different gradient-flow cooling levels, and comparisons with lattice and phenomenological results.

25.1.1 Wilson Lines, Wilson Loops, and the Geometry of Soft Functions

Wilson lines arise naturally in QCD whenever one seeks to maintain gauge invariance in matrix elements involving colored fields. If a quark is created at point y and annihilated at x, gauge covariance requires that the operator insert a parallel-transport factor connecting these two points along some path. The straight Wilson line connecting x and y is

$$W[x; y] = \mathcal{P} \exp \left(ig \int_x^y dz^\mu A_\mu(z) \right), \tag{25.1}$$

where $\mathcal{P}$ enforces ordering along the path. In TMD correlators, the path is typically chosen to be nearly lightlike, as required by the kinematics of fast-moving partons.

When two or more Wilson lines are combined to form a closed contour, one obtains a Wilson loop

$$W(C) = \frac{1}{N_c} \text{Tr} \, \mathcal{P} \exp \left(ig \oint_C dx^\mu A_\mu(x) \right). \tag{25.2}$$

Wilson loops are highly sensitive to nonperturbative gauge dynamics. They probe confinement, the static quark potential [Diakonov, 2009, Simonov, 1996], and the color interactions underlying hadronic scattering [Shuryak and Zahed, 2000].

A central geometric feature arises when the contour C contains one or more cusps. A cusp occurs when the tangent direction of the path changes discontinuously. If two straight segments meet at an angle χ, then the loop has a cusp of that angle. In Minkowski signature, the cusp angle may be infinite if the lines are exactly lightlike. Such cusps generate additional divergences beyond the usual ultraviolet divergences associated with self-energy of the lines. The resulting cusp anomalous dimension $\Gamma_{\text{cusp}}(\chi, \alpha_s)$ governs the dependence of the loop on the angle [Polyakov, 1987, Dotsenko and Vergeles, 1980, Brandt et al., 1982, Korchemskaya and Korchemsky, 1992].

Soft functions in TMD factorization are Wilson loops whose geometry is determined by the directions of initial-state and final-state partons [Collins, 2011]. For instance, in the Drell-Yan process, two quarks approach one another from opposite directions along the light cone, producing soft gluon exchange encoded in Wilson lines pointing to the past. Semi-inclusive deep-inelastic scattering (SIDIS) involves a mixture of past- and future-oriented lines, reflecting the different time orderings of the soft exchanges [Vladimirov and Stefanis, 2014]. In all cases, the transverse separation b_T between the lines captures the partonic impact parameter dependence.

An important aspect is that soft functions contain both ultraviolet divergences and rapidity divergences. The former are renormalized in the usual manner, while the latter arise because lightlike Wilson lines extend to infinite rapidity. To regularize these divergences, one can tilt the Wilson lines slightly off the light cone by giving them large but finite rapidity parameters. In Euclidean space, these become finite real angles θ between the Wilson lines. This is the key to the analytic continuation used throughout the ILM analysis.
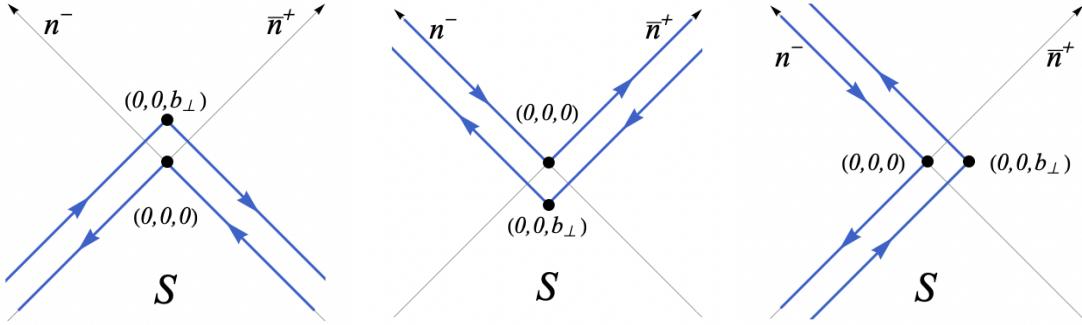
Fig. 25.1.1 The Contours of the Wilson lines for the soft function of the cross section in (a) Drell-Yan, (b) electron-positron annihilation, and (c) SIDIS. Hadron A is moving near the light-cone direction n, and hadron B is moving near the light-cone direction $\bar{n}$ [Vladimirov and Stefanis, 2014].

25.1.2 Analytic Structure of Cusp Singularities and Rapidity Evolution

Renormalization of soft functions leads to a multiplicative structure in which the dependence on the cusp angle is entirely encoded in a function $K(\mu, b_T, \chi)$ plus an angle-independent term $P(\mu, b_T)$ [Vladimirov, 2018]

$$S(\mu, b_T, \chi) = \exp\left[K(\mu, b_T, \chi) + P(\mu, b_T)\right]. \tag{25.3}$$

The evolution with respect to μ follows the renormalization-group equation

$$\frac{dK}{d\ln\mu^2} = -\gamma_K(\chi, \alpha_s), \tag{25.4}$$

where γ_K is the cusp anomalous dimension.

There are two limiting regimes of particular importance. The first is the small-angle limit $\chi \to 0$, which corresponds physically to nearly parallel Wilson lines. In this limit the kernel behaves quadratically in the angle [Korchemsky and Radyushkin, 1992, Mitev and Pomoni, 2016]

$$K(\chi \to 0) \sim K_B(b_T)\chi^2, \tag{25.5}$$

and the corresponding cusp anomalous dimension reduces to the bremsstrahlung function.

The second regime is the large-angle limit $\chi \to \infty$, relevant for TMD factorization where the Wilson lines are effectively lightlike. In this limit one finds

$$K(\chi \to \infty) \sim K_{\mathrm{CS}}(b_T)\chi, \tag{25.6}$$

which defines the CS kernel $K_{\mathrm{CS}}(b_T)$ [Collins and Soper, 1981a, Collins and Soper, 1982a]. This kernel is nonperturbative at large b_T but becomes perturbatively calculable when b_T is small. It plays a central role in controlling the rapidity evolution of TMDs through the Collins-Soper equation.

The ILM analysis hinges on computing $K(\theta)$ for real Euclidean angles θ and analytically continuing to $K(i\chi)$ for Minkowski rapidity χ [Liu et al., 2024g]. A key simplification arises because the angle dependence factorizes in both the weak and strong field instanton regimes, allowing the extraction of the CS kernel from the limit of large imaginary angle.

25.1.3 Soft Functions in the Instanton Liquid Model

The ILM describes the QCD vacuum as a statistical ensemble of instantons and anti-instantons, each represented by a classical gauge configuration localized in space-time. The instanton field is characterized by its size ρ, center z, and color orientation, though for the soft-function calculation the hedgehog structure ensures that path ordering is not needed. The contribution of a single instanton to a Wilson loop is [Shuryak and Zahed, 2000, Liu et al., 2024g]

$$W_I(\rho, z) = \exp\left(i\tau^a \phi_I^a(\rho, z)\right), \tag{25.7}$$

where ϕ_I^a encodes the projection of the instanton field onto the Wilson line. The explicit form is

$$\phi_I^a(\rho, z) = \int_C dx^\mu \, \bar{\eta}_{\mu\nu}^a \frac{(x-z)^\nu \rho^2}{(x-z)^2[(x-z)^2 + \rho^2]}, \tag{25.8}$$

where $\bar{\eta}_{\mu\nu}^a$ is a 't Hooft symbol. Since instantons form a dilute ensemble, the contributions exponentiate,

$$W(C) = \exp\left[\frac{n_{I+A}}{N_c} \int d^4z \left(\mathrm{Tr}_c W_I(\rho, z) - 1\right)\right]. \tag{25.9}$$

This structure holds for any contour, including those relevant for soft functions.
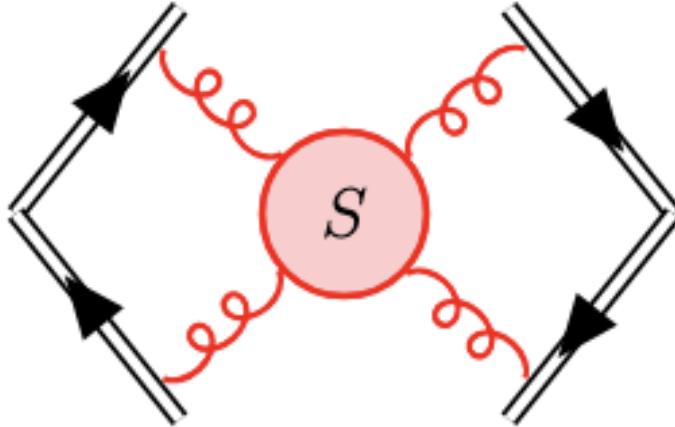
Fig. 25.1.2 Soft function attached to the pertinent Wilson lines in Fig. 25.1.1.

The geometry of the contour for the soft function involves four half-infinite Wilson lines that form two cusps separated by a transverse displacement b_T. Each cusp is characterized by an angle θ in Euclidean space. The evaluation of the instanton contribution requires integrating over the instanton center position z and using explicit parametrizations for the instanton profile along each of the four half-infinite lines. After subtracting the angle-independent self-energy, the resulting expression defines the cusp kernel [Liu et al., 2024g]

$$K(\rho, b_T, \theta) = \ln \frac{W(b_T, \theta)}{W(b_T, 0)}, \tag{25.10}$$

which vanishes for $\theta \to 0$.

25.1.4 Weak-Field Limit and Factorization of Angular Dependence

In the weak-field regime where the instanton profile is small, the expansion of the loop exponent yields

$$\ln W(\rho, b_T, \theta) \approx -\frac{n_{I+A}}{N_c} \int d^4 z\, \phi^2(z, \rho, b_T, \theta). \tag{25.11}$$

The instanton squared profile function at zero angle reads

$$
\phi^2(z, \rho, b_\perp, \theta = 0) = -2\pi^2 \frac{z_3^2 + z_\perp^2 - \frac{1}{4}b_\perp^2}{\sqrt{z_3^2 + \left(z_\perp + \frac{1}{2}b_\perp\right)^2}\sqrt{z_3^2 + \left(z - \frac{1}{2}b_\perp\right)^2}}
$$
$$
\times \left(1 - \frac{\sqrt{z_3^2 + \left(z_\perp + \frac{1}{2}b_\perp\right)^2}}{\sqrt{z_3^2 + \left(z_\perp + \frac{1}{2}b_\perp\right)^2 + \rho^2}}\right)\left(1 - \frac{\sqrt{z_3^2 + \left(z_\perp - \frac{1}{2}b_\perp\right)^2}}{\sqrt{z_3^2 + \left(z_\perp - \frac{1}{2}b_\perp\right)^2 + \rho^2}}\right)
$$
$$
+ \pi^2 \left(1 - \frac{\sqrt{z_3^2 + (z_\perp + \frac{1}{2}b_\perp)^2}}{\sqrt{z_3^2 + (z_\perp + \frac{1}{2}b_\perp)^2 + \rho^2}}\right)^2 + \pi^2 \left(1 - \frac{\sqrt{z_3^2 + (z_\perp - \frac{1}{2}b_\perp)^2}}{\sqrt{z_3^2 + (z_\perp - \frac{1}{2}b_\perp)^2 + \rho^2}}\right)^2. \tag{25.12}
$$

The UV divergence as $z \to 0$ is regulated by the instanton size ρ, and the IR divergence $z \to \infty$ cancels out between the two-anti-parallel Wilson lines. The absence of the z_4 dependence is due to rotational symmetry in Euclidean space.

At finite angle, the expression is manageable but more involved. The integration in (25.11) can be reorganized using a change of variables that separates the angular dependence from the remaining geometry. The result is [Liu et al., 2024g]

$$K^{(1)}(\rho, b_T, \theta) = K_{\text{CS}}^{(1)}(b_T/\rho)\, h(\theta), \tag{25.13}$$

where

$$h(\theta) = \theta \cot \theta - 1, \tag{25.14}$$

and $K_{\text{CS}}^{(1)}$ is a purely radial integral independent of the angle. This factorization is remarkable because it greatly simplifies the analytic continuation and because numerical analysis shows that it persists even in the strong-field regime. The explicit expression for the weak-field kernel is

$$K_{\text{CS}}^{(1)}(b_T) = \frac{4\pi^2 n_{I+A}\rho^4}{N_c} \int_0^\infty dk\, \frac{F_g^2(\rho k)}{k}\left(J_0(kb_T) - 1\right), \tag{25.15}$$

where F_g is the instanton form factor

$$\mathcal{F}_g(k) = \frac{4}{k^2} - 2K_2(k). \tag{25.16}$$

For $b_T \gg \rho$, the oscillatory behavior of the Bessel function ensures that the integral yields a logarithmic dependence,

$$K_{\text{CS}}^{(1)}(b_T) \sim -\frac{4\pi^2 n_{I+A}\rho^4}{N_c}\left[\ln\left(\frac{b_T}{\rho}\right) + 1\right]. \tag{25.17}$$

This logarithmic growth is in excellent agreement with phenomenological models that have long assumed a similar behavior, highlighting the physical relevance of the ILM.
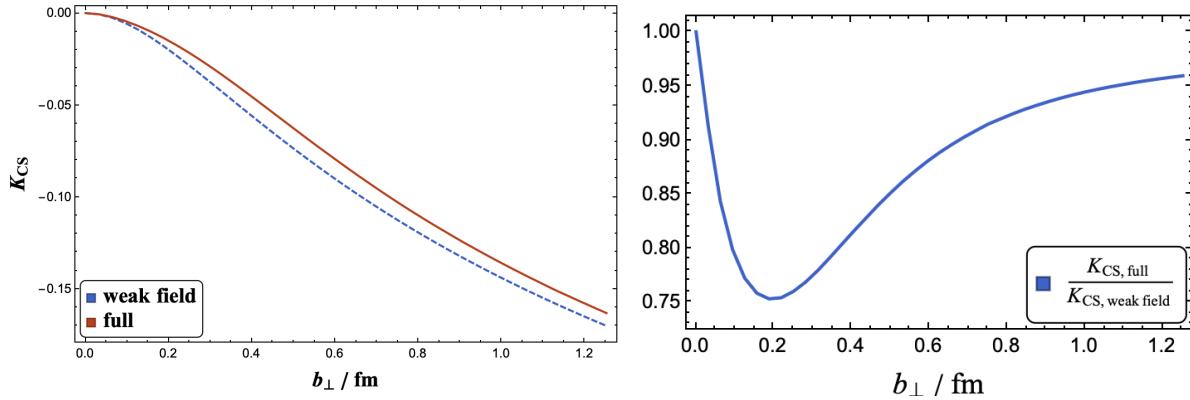
Fig. 25.1.3 (a) Instanton liquid estimation on CS kernel with the full calculation (25.18), and the weak field approximation (25.15). We also plot their ratio in (b).

25.1.5 Strong Field Evaluation and the Full Instanton Contribution

Beyond the weak-field approximation, the instanton profile must be treated exactly. Numerical integration over z shows that the factorization of angular dependence remains extremely accurate even when ϕ is not small. Thus the full kernel can still be written in the form

$$K(\rho, b_T, \theta) \approx K_{\mathrm{CS}}(b_T/\rho)\, h(\theta), \tag{25.18}$$

where K_{CS} is the fully nonperturbative ILM result [Liu et al., 2024g].

The ILM prediction for K_{CS} has several noteworthy properties. At small separations $b_T \ll \rho$, the instanton field appears nearly uniform over the region probed by the Wilson lines, leading to a suppressed contribution. At larger separations $b_T \sim \rho$, the sensitivity to the instanton core becomes pronounced, and the kernel grows in magnitude. At asymptotically large b_T, the kernel approaches the logarithmic form predicted by the weak-field analysis. These features match smoothly onto perturbative expectations at small b_T and phenomenological behavior at large b_T.
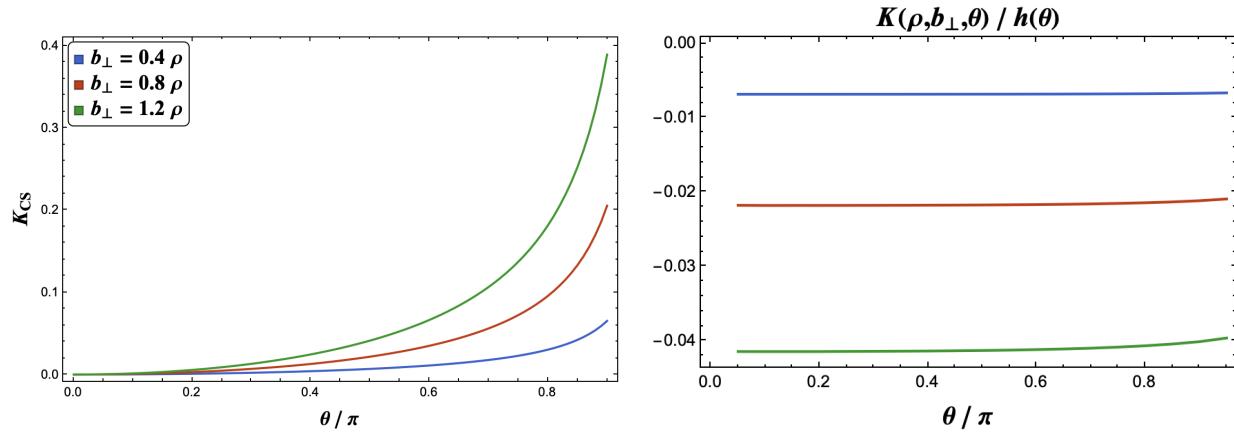
Fig. 25.1.4 The angular dependence of K in (25.18).

25.1.6 Collins-Soper Evolution and Matching to Perturbation Theory

The ILM describes the nonperturbative regime of QCD corresponding to low renormalization scale μ. In gradient flow studies, the flow time t serves as an inverse resolution scale $\mu \sim 1/\sqrt{8t}$. At long flow times, most instanton-anti-instanton pairs dissociate, leaving a dilute ensemble with density $n \approx 1\,\mathrm{fm}^{-4}$. At shorter flow times corresponding to higher resolution $\mu \sim 2\,\mathrm{GeV}$, the effective instanton density increases substantially, consistent with the picture of instanton molecules or tightly bound instanton-antiinstanton pairs.

To construct a full CS kernel valid across all b_T, one must combine the ILM result with perturbation theory. The matching uses the standard b^* prescription of TMD factorization. The perturbative kernel satisfies an RG equation involving Γ_{cusp}, which is now known up to four loop order. The complete expression becomes

$$K_{\mathrm{CS}}(b_T, \mu) = K_{\mathrm{ILM}}(b_T, \mu) + K_{\mathrm{CS}}^{\mathrm{pert}}(b^*, \mu_b) - 2 \int_{\mu_b}^{\mu} \frac{d\mu'}{\mu'} \, \Gamma_{\mathrm{cusp}}(\alpha_s(\mu')), \tag{25.19}$$

where b^* and μ_b are defined in terms of a parameter $b_{\max}$ chosen to optimize the transition region

$$\mu_b = \frac{2e^{-\gamma_E}}{b^*(b_\perp)} \xrightarrow{b_\perp \to \infty} \frac{2e^{-\gamma_E}}{b_{\max}} \tag{25.20}$$

with the asymptotic saturation following from the conventional b^*-parameterization [Collins, 2011],

$$b^*(b_\perp) = \frac{b_\perp}{\sqrt{1 + b_\perp^2/b_{\max}^2}} \,, \tag{25.21}$$

which reduces to $b_\perp$ in the limit $b_\perp \to 0$. Here γ_E is Euler constant, and the optimal non-perturbative distance is $b_{\max} = 0.56$ fm, which is chosen to optimize the interpolation between non-perturbative and perturbative contributions in the lattice results of ASWZ24 [Avkhadiev et al., 2023]. The resulting CS kernel agrees well with lattice calculations and modern phenomenological fits.
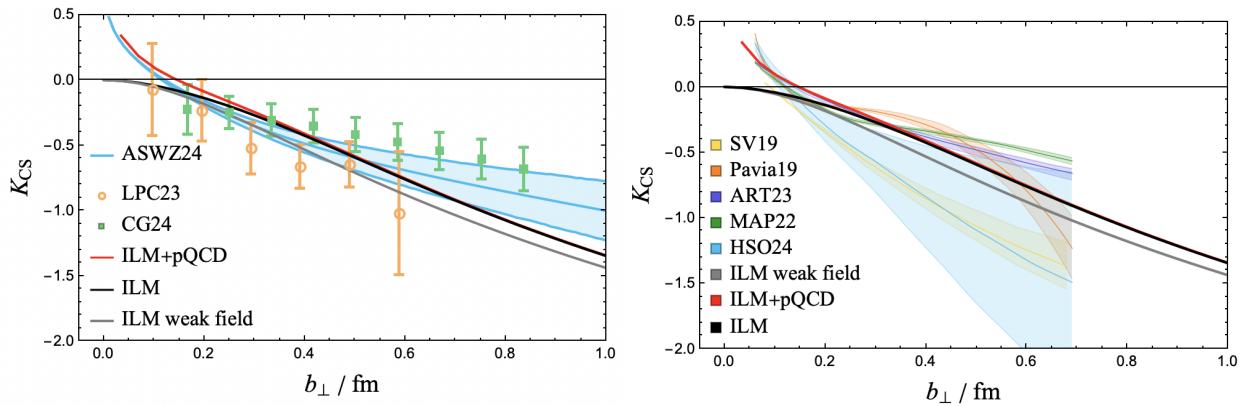
Fig. 25.1.5 (a) The black-solid curve is the ILM result for the CS kernel with $\rho = 0.343$ fm, $n_{I+A} = 7.46$ fm^{-4} [Liu et al., 2024g], compared to the weak field approximation gray-solid curve and the optimized combination with the short-distance perturbative contribution red-solid curve . The results are compared to the recent lattice calculation by ASWZ24 [Avkhadiev et al., 2023], a new lattice calculation using Coulomb-gauge TMD correlators [Zhao, 2024] by CG24 [Bollweg et al., 2024] and results from Lattice Parton Collaboration LPC23 [Chu et al., 2023]. (b) shows the comparison of our results with the phenomenologically extracted CS kernel by SV19 [Scimemi and Vladimirov, 2020], Pavia19 [Bacchetta et al., 2020], MAP22 [Bacchetta et al., 2022], ART23 [Moos et al., 2024], and HSO24 [Gonzalez-Hernandez et al., 2022].

25.1.7 Conclusions

The instanton liquid model provides a natural and physically transparent framework for computing the nonperturbative structure of soft functions and their rapidity evolution. Its success relies on the strong support from gradient-flow lattice studies, which confirm that instantons dominate the long-distance, low-resolution sector of QCD. The ILM captures the essential topological fluctuations of the vacuum and thus provides the correct gauge-field background in which soft Wilson loops can be evaluated.

The resulting CS kernel displays a smooth transition from perturbative to nonperturbative behavior, matching onto perturbative results at small transverse separation and reproducing a logarithmic growth at large separation. The angular dependence factorizes in a universal manner across weak- and strong-field regimes, enabling a straightforward analytic continuation from Euclidean to Minkowski space and offering a new prescription for computing soft functions on the lattice. Comparisons with lattice calculations and phenomenological extractions show very good agreement, highlighting the utility of the ILM in the study of TMD evolution.

The combination of analytical control, numerical tractability, and physical grounding makes the ILM an attractive tool for continued exploration of nonperturbative soft physics in QCD. Its application to the CS kernel sets the stage for future studies of TMD observables in Euclidean frameworks, including potential extensions to generalized TMDs, jet soft functions, and small-x dipole amplitudes.

25.2 TMDs of Pion and Kaon

The transverse-momentum-dependent parton distribution functions (TMDPDFs) of the pion and kaon encode the multidimensional structure of these Nambu-Goldstone bosons in QCD. Whereas standard collinear parton distribution functions (PDFs) characterize the distribution of longitudinal momentum at a fixed renormalization scale, TMDPDFs resolve the simultaneous dependence on the light-cone momentum fraction x and the intrinsic transverse momentum $\mathbf{k}_\perp$ (or equivalently the transverse position $\mathbf{b}_\perp$), thus providing a genuine three-dimensional tomography of hadronic structure [Boussarie et al., 2023]. They play a central role in the description of low-q_T Drell-Yan (DY) production, semi-inclusive deep inelastic scattering (SIDIS), and, prospectively, electron-ion collider (EIC) measurements.

The theoretical description of TMDs is complicated by the appearance of light-like Wilson lines, which are essential for gauge invariance but introduce rapidity divergences that do not appear in collinear factorization. A consistent factorization and renormalization scheme therefore requires soft subtraction and controlled evolution in both the renormalization scale μ and the rapidity scale ζ [Collins, 2011, Rogers, 2016]. The appropriate framework for these tasks is the Collins-Soper-Sterman (CSS) formalism [Collins and Soper, 1981b, Collins et al., 1985a].

At low resolution, where perturbative methods become unreliable, a first-principles description of nonperturbative dynamics becomes essential. In this domain, the QCD instanton liquid model (ILM) [Shuryak, 1982e, Schäfer and Shuryak, 1998, Nowak et al., 1996] provides a concrete semiclassical picture of the QCD vacuum as an ensemble of instantons and anti-instantons with characteristic size $\rho \simeq 1/3\,\mathrm{fm}$. The ILM naturally generates a momentum-dependent dynamical mass for quarks, nonlocal effective interactions, and nontrivial gauge-field configurations that directly influence Wilson-line structures. This framework has been successfully applied to pion and kaon structure [Liu et al., 2023b, Liu et al., 2024d], and in particular the complete TMD analysis [Liu et al., 2024g] which we now review.

25.2.1 Definition of Meson TMDPDFs

The starting point for the TMD description is the gauge-invariant quark correlation function at fixed light-cone momentum fraction x and transverse momentum $\mathbf{k}_\perp$. For a pion with momentum p^μ, the leading-twist TMDPDFs are defined from matrix elements of quark bilinears connected by staple-shaped Wilson lines, whose direction distinguishes SIDIS from DY [Collins, 2011]. Explicitly,

$$q_\pi(x, k_\perp) = \int \frac{dz^-}{2\pi} \int \frac{d^2 b_\perp}{(2\pi)^2} \, e^{ixp^+ z^- - i\mathbf{k}_\perp \mathbf{b}_\perp} \langle \pi | \bar{\psi}(0) \gamma^+ W^{(\pm)}[0; z^-, b_\perp] \psi(z^-, b_\perp) | \pi \rangle, \tag{25.22}$$

$$\Delta q_\pi(x, k_\perp) = \int \frac{dz^-}{2\pi} \int \frac{d^2 b_\perp}{(2\pi)^2} \, e^{ixp^+ z^- - i\mathbf{k}_\perp \mathbf{b}_\perp} \langle \pi | \bar{\psi}(0) \gamma^+ \gamma_5 W^{(\pm)} \psi(z^-, b_\perp) | \pi \rangle, \tag{25.23}$$

$$\delta q_\pi(x, k_\perp) = \int \frac{dz^-}{2\pi} \int \frac{d^2 b_\perp}{(2\pi)^2} \, e^{ixp^+ z^- - i\mathbf{k}_\perp \mathbf{b}_\perp} \langle \pi | \bar{\psi}(0) i\sigma^{\alpha+} \gamma_5 W^{(\pm)} \psi(z^-, b_\perp) | \pi \rangle. \tag{25.24}$$

for the unpolarized, spin and transversity respectively. The Wilson line staples run space-like for SIDIS, and time-like for DY [Kumano and Song, 2021], as illustrated in Fig. 25.1.1. The resummation of the collinear gluons from the final state in the SIDIS process, yields $W^{(+)}$. Similarly, the resummation of the collinear gluons from the initial state in the Drell-Yan process, yields $W^{(-)}$ [Angeles-Martinez et al., 2015, Grosse Perdekamp and Yuan, 2015, Aidala et al., 2013, Barone et al., 2010, D'Alesio and Murgia, 2008].

The transverse coordinate dependence can be obtained by using the Fourier transform

$$\tilde{q}_\pi(x, b_\perp) = \int \frac{d^2 k_\perp}{(2\pi)^2} e^{ik_\perp \cdot b_\perp} q_\pi(x, k_\perp) \tag{25.25}$$

The pion is on-shell with energy $E_{\mathbf{p}} = \sqrt{m_\pi^2 + \mathbf{p}^2}$ and 3-momentum $\mathbf{p}$,

$$p^\mu = p^+ \bar{n}^\mu - \frac{m_\pi^2}{2p^+} n^\mu + p_\perp^\mu \tag{25.26}$$

with hadron mass m_π. Here $n = (1, 0, 0_\perp)$ and $\bar{n} = (0, 1, 0_\perp)$ are the longitudinal and transverse light cone vectors. Similar definitions hold for other hadrons. For a spin-zero target such as the pion or kaon, only two leading-twist TMDs survive

$$f_1^{q/\pi}(x, k_\perp), \qquad h_1^{\perp \, q/\pi}(x, k_\perp). \tag{25.27}$$

The latter, the Boer-Mulders function [Boer and Mulders, 1998], describes a correlation between quark transverse momentum and quark transverse spin inside an unpolarized hadron, and is thus naively T-odd. As shown in the ILM construction, $h_1^\perp$ vanishes at lowest Fock order [Liu and Zahed, 2025] and is generated only through Wilson-line effects or higher Fock-state components.

25.2.2 Rapidity Divergences and Instanton-Induced Soft Separation

The Wilson lines $W^{(\pm)}$ run along nearly light-like directions and engender *rapidity divergences* that cannot be renormalized by ordinary ultraviolet counterterms. The modern treatment of these divergences introduces an independent rapidity scale ζ, soft subtraction factors, and a renormalized TMD [Collins, 2011].

Within the ILM, the nonperturbative gauge-field configurations of instantons induce a distinctive structure for Wilson-line correlators. A remarkable consequence is the "ILM soft separation," whereby the rapidity dependence factorizes from the constituent-quark distribution [Liu and Zahed, 2025]

$$\tilde{f}_1^{q/\pi}(x, b_\perp; \mu \sim 1/\rho, y_q - y_n) \approx \tilde{f}_1^{q/\pi}(x, b_\perp) \, \exp\left[K_{\mathrm{CS}}^{(\mathrm{inst})}(b_\perp/\rho) \, (y_q - y_n) \right]. \tag{25.28}$$

Here $K_{\mathrm{CS}}^{(\mathrm{inst})}$ is the instanton-induced contribution to the Collins-Soper kernel, encoding the cusp behavior of Wilson lines in the semiclassical vacuum. Because the instanton ensemble is dilute, the nonperturbative rapidity dependence is dominated by single-instanton physics.
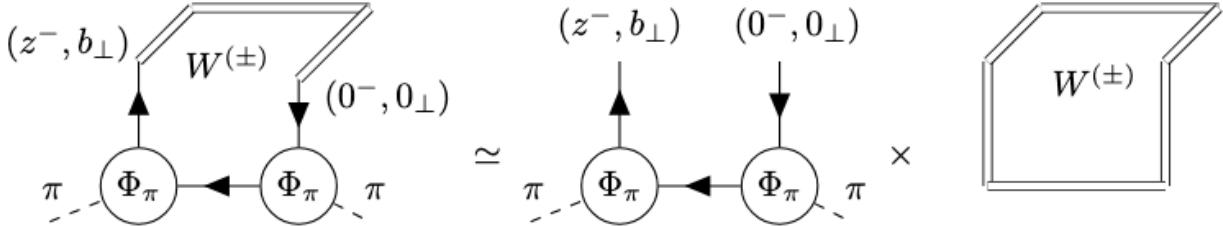
Fig. 25.2.1 Soft separation for the quark pion TMD, which is approximated into a constituent quark distribution without rapidity dependence and a rapidity dependent factor generated by the stapled Wilson line [Liu and Zahed, 2025].

After soft subtraction in the Collins scheme [Collins, 2011], the renormalized TMD at the initial ILM scale is [Liu et al., 2024g]

$$\tilde{F}_1^{q/\pi}(x, b_\perp; \mu_0, \zeta_0) = \tilde{f}_1^{q/\pi}(x, b_\perp) \exp\left[K_{\mathrm{CS}}^{(\mathrm{inst})}\left(\frac{b_\perp}{\rho}\right) \ln\left(\frac{\zeta_0}{1/\rho^2}\right) \right]. \tag{25.29}$$

This expression is a crucial bridge between the nonperturbative ILM description and the perturbative CSS evolution that connects to experimental scales.

25.2.3 Constituent-Quark TMDPDFs from ILM Light-Front Wave Functions

In the ILM, the pion and kaon are treated as bound $q\bar{q}$ states formed through instanton-induced nonlocal interactions. This produces nonlocal light-front wave functions with momentum-dependent constituent quark masses. The pion LFWF in momentum space is [Liu et al., 2023b]

$$\Phi_\pi(x, k_\perp, s_1, s_2) = \frac{1}{\sqrt{N_c}}\left[C_\pi \sqrt{x\bar{x}}\left(m_\pi^2 - \frac{k_\perp^2 + M^2}{x\bar{x}} \right) F\left(\frac{k_\perp}{\lambda_\pi \sqrt{x\bar{x}}}\right) \right] \bar{u}_{s_1}(k_1) i\gamma_5 \tau^a v_{s_2}(k_2), \tag{25.30}$$

with the ILM nonlocal form factor defined earlier. After performing the spin contractions of the LFWF overlap, one finds the unpolarized constituent-quark TMD of the pion at $\mu_0 = 1/\rho$,

$$f_1^{q/\pi}(x, k_\perp) = \frac{C_\pi^2}{(2\pi)^3} \frac{2(k_\perp^2 + M^2)}{\left(x\bar{x}m_\pi^2 - k_\perp^2 - M^2\right)^2} F^2\left(\frac{k_\perp}{\lambda_\pi \sqrt{x\bar{x}}}\right). \tag{25.31}$$

This distribution is valence-dominated, symmetric under $x \leftrightarrow \bar{x}$, and sharply peaked around $x \simeq 0.5$, reflecting the dominance of lowest Fock components at low resolution.

For the kaon, $SU(3)$ flavor symmetry breaking leads to distinct constituent masses M_u and M_s [Liu and Zahed, 2025], producing an asymmetric LFWF

$$f_1^{u/K^+}(x, k_\perp) = \frac{C_K^2}{(2\pi)^3} \frac{2\left(k_\perp^2 + \bar{x}^2 M_u^2 + x^2 M_s^2 + 2x\bar{x}M_u M_s\right)}{\left(x\bar{x}m_K^2 - k_\perp^2 - xM_s^2 - \bar{x}M_u^2\right)^2} F^2\left(\frac{k_\perp}{\lambda_K \sqrt{x\bar{x}}}\right). \tag{25.32}$$

The heavier strange quark biases the kaon distribution toward smaller x, in agreement with phenomenology and lattice-QCD results.
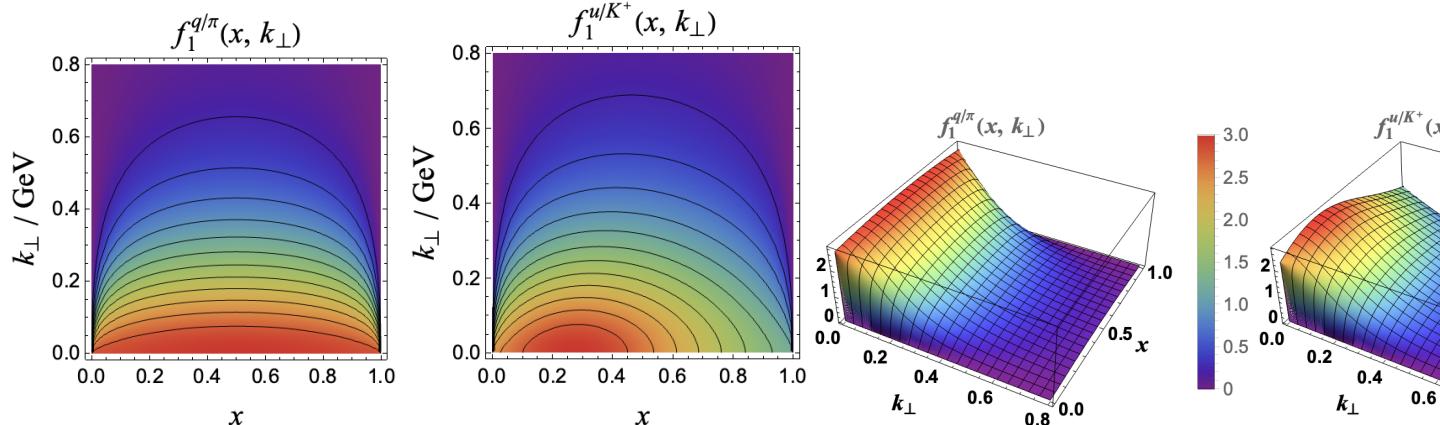
Fig. 25.2.2 Constituent quark TMD distribution in pion (left) (25.31) and kaon (right) (25.32) at low resolution $\mu = 1/\rho$ with $\rho = 0.313$ fm: (a,b) are the density plots, (c,d) the 3D plots, (e,f) the transverse momentum dependent plots for fixed x, and (g,h) the longitudinal momentum dependence for fixed $k_\perp$. The pion parameters are $C_\pi = 7.240$, $m_\pi = 139.0$ MeV, $M = 398.17$ MeV. The kaon parameters are $C_K = 6.60$, $m_K = 458.0$ MeV, $M_u = 394.4$ MeV, $M_s = 556.5$ MeV.

25.2.4 TMD Evolution from the ILM Scale to Experimental Scales

The soft-subtracted TMDs obtained above must be evolved to high momentum scales relevant for experiment. Their scale dependence is governed by the CSS equations [Collins and Soper, 1981b, Collins et al., 1985a],

$$\frac{d}{d\ln\sqrt{\zeta}}\ln F = K_{\mathrm{CS}}(b_\perp, \mu), \tag{25.33}$$

$$\frac{d}{d\ln\mu}\ln F = \gamma_F(\alpha_s(\mu)) - \Gamma_{\mathrm{cusp}}(\alpha_s(\mu))\ln\frac{\zeta}{\mu^2}. \tag{25.34}$$

At small impact parameters $b_\perp \ll 1/\Lambda_{\mathrm{QCD}}$, the TMD factorizes into a convolution of perturbative Wilson coefficients and collinear PDFs,

$$\tilde{F}_1^{q/h}(x, b_\perp; \mu, \mu^2) = \sum_{i=q,\bar{q},g}\int_x^1\frac{dx'}{x'}C_{q/i}\left(\frac{x}{x'}, b_\perp, \mu_b\right)f_{i/h}(x', \mu_b)e^{-S_{\mathrm{Sud}}(\mu_b, \mu)}, \tag{25.35}$$

where $\mu_b = 2e^{-\gamma_E}/b_\perp$, and the Sudakov factor S_{Sud} resums large logarithms. Perturbative expressions for the anomalous dimensions and coefficients are known through N^{3}LO [Braun et al., 2017b].

In the large-$b_\perp$ region, perturbation theory fails, and the ILM provides the correct nonperturbative input. A smooth matching between perturbative and ILM contributions is essential [Liu et al., 2024g, Liu and Zahed, 2025], implemented through a matching function centered near $b_{\mathrm{NP}} \sim \rho$.

The combined ILM + CSS evolution predicts the migration of probability density from valence $x \approx 0.5$ at low scales to small x at higher scales, and a compression of the transverse width as gluon and sea radiation are generated. This qualitative behavior is consistent with extractions from Drell-Yan measurements.

25.2.5 Conclusion

The ILM provides a snapshot of the pion and kaon at their natural low-resolution scale: valence-dominated, with transverse extent of order the instanton size. CSS evolution then builds the experimentally observed

small-x and small-$b_\perp$ structure from perturbative gluon radiation. The resulting meson tomography therefore combines the semiclassical picture of the QCD vacuum with perturbative QCD dynamics.

The emerging picture for the pion is especially striking: at $\mu_0 = 1/\rho$, its TMD is concentrated at $x \simeq 0.5$ in a region of transverse size $b_\perp \simeq \rho$, but at $\mu = 2\,\mathrm{GeV}$ the distribution shifts toward low x and becomes sharply peaked near the origin in impact-parameter space. The kaon exhibits the same behavior, with additional asymmetry reflecting the heavier strange quark.

These results highlight the importance of incorporating both nonperturbative vacuum structure and perturbative evolution in a consistent framework. They also underscore the need for future lattice calculations, Drell-Yan analyses, and EIC measurements to fully resolve the multidimensional structure of pseudoscalar mesons.

Chapter 26
Summary and Discussion

26.1 From vacuum fields to potentials

In this review we have argued that the starting point for any unified description of hadrons must be better understanding of the QCD vacuum itself. While being the true ground state of this theory, it is not an empty but a densely populated medium filled with nonperturbative gluonic and quark configurations, on top of the usual zero point perturbative fluctuations (gluons).

Fluctuations with nontrivial topology - instantons and anti-instantons -dominate the nonperturbative structure of this medium, producing zero modes for light quarks and giving rise to the spontaneous breakdown of the $SU(N_f)$ chiral symmetry. Their impact is well quantified, as they provide a calculable a dynamical mechanism for generating (momentum-dependent) constituent quark masses, pion properties etc. This mechanism of quark effective mass generation, together with the chirality-changing interactions inherent in the instanton ensemble, becomes an essential building block of all effective low-energy Hamiltonians.

The instanton fields affect quark propagation in a specific and channel-dependent way. Correlation functions reveal strong attraction in pseudoscalar and scalar $\bar{q}q$ channels, moderate effects in vector and axial channels, and repulsion in some others. Thus they directly determine which hadrons are light, which are heavy, and which channels host strong dynamical correlations or diquark clustering.

At the same time, confinement-the long-distance property encoded in the area law for Wilson loops- is based on a distinct and complementary piece of the quark-gluon interaction. As Wilson loops are sensitive to gauge field strength, they also obtain large contribution from (topologically neutral) instanton-antiinstanton pairs (molecules). Important novel element of this review is that a combination of instanton-induced topological and non-topological effects produce effective potentials applicable across the full hadronic spectrum, from pions to quarkonia.

The underlying structure of the QCD vacuum is revealed from lattice configurations via $gradient - flow$ cooling. After subsequently smoothing away ultraviolet noise (gluons) one finds that the vacuum is permeated by an intricate network of long, thin, string-like center vortices. As the lattice evolves in Euclidean time, these vortices trace out two-dimensional worldsheets: extended, fluctuating surfaces that weave throughout spacetime. A key feature of this vortex network is the presence of numerous branching and recombination points where several vortex sheets meet or split. In center-projected descriptions, these branch points naturally act as sources and sinks of Abelian magnetic flux, and thus manifest as monopoles and anti-monopoles. Their appearance is not an artifact of projection but reflects genuine geometric singularities inherent to the vortex surfaces.

What is particularly striking is that these same branching regions are strongly correlated with the positions of instantons and anti-instantons once the configuration is gradient-flowed. This correlation is not accidental. Both instantons and vortex branch points arise from localized regions where the gauge field attains nontrivial topology due to singular or rapidly varying geometry. In simple terms, the vortex sheets provide a scaffold

that "guides" the topological charge: when sheets twist, intersect, or fold over themselves, they naturally create the localized lumps of topological charge identified as instantons.

This geometric viewpoint offers a unifying physical intuition. Confinement in the vortex picture stems from the percolation of these extended center flux surfaces, which disorder Wilson loops and enforce an area law. Chiral symmetry breaking, on the other hand, is driven by the presence of instantons, whose zero modes form a near-zero Dirac spectrum. If both monopole worldlines and instanton-like topological lumps originate from the very same vortex geometry, then confinement and chiral symmetry breaking cease to be independent phenomena. Instead, they emerge as two tightly linked consequences of the underlying vortex structure of the vacuum. From this perspective, the apparent duality between monopoles (the topological sources of confinement) and instantons (the topological agents of chiral symmetry breaking) is not mysterious. It reflects the fact that the non-Abelian vacuum organizes itself through a common geometric mechanism: the fluctuating, branching, and knotted center vortices whose topology encodes both magnetic monopole worldlines and topological charge density. Thus, the long-distance physics of QCD string tension, mass gap, and chiral condensate, may all be different faces of the same underlying vortex-driven topological order, as noted formally by the authors [Ramamurti et al., 2018].

Returning to $gradient - flow$ cooling, let us once again emphasize its important role, as a modern form of Renormalization Group. Its modern version reveals relatively dense medium made of strongly correlated instanton-antiinstanton pairs (or molecules). Further cooling converges on dilute "instanton liquid" made of separate instantons. Nontrivial topology of those make them stable under cooling. Only uncovering those subsequent layers of vacuum structure, one can return to physical vacuum (zero or minimal cooling) with confidence that nonperturbative dynamics is fully included.

26.2 Wave functions of multiquark hadrons

The expansion of hadronic spectroscopy in the last decade has revealed that multiquark states are not isolated curiosities but a very important components of the QCD dynamics. Tetraquarks, pentaquarks, hexaquarks, and even twelve-quark configurations arise naturally once the underlying forces and symmetries are examined in a unified framework. Constructing the wave functions of these states requires a careful synthesis of geometric, algebraic, and dynamical inputs. And, last but not least, admixture with them (e.g. baryons and pentaquarks) do not turn out to be small, and offer resolutions of some important puzzles.

The formalism developed in this review rests on three pillars. First, Jacobi coordinates are used to decouple center-of-mass motion from internal dynamics, an essential step when treating systems with more than two constituents. Second, when quarks share equal masses, hyperspherical symmetry offers a powerful simplification: all relative coordinates combine into a single hyperradius and a set of hyperangles. This hypercentral approximation captures dominant features of multiquark dynamics and replaces complicated many-body kinematics by a manageable set of radial and angular functions defined on high-dimensional spheres. Third, the enforcement of Fermi statistics is achieved through the representation theory of permutation groups S_n. The orbital, color, spin, and flavor components of the wave function must combine into overall antisymmetric states; the S_n representations provide a systematic language for achieving and classifying these combinations.

Within this structure, multiquark wave functions can be built explicitly, not only for ground states but also for excited configurations with nontrivial orbital angular momentum. The technical developments discussed in this review (including the use of "monom" bases, optimized coordinate systems, and Mathematica-assisted realizations of S_n representations) enable the solution of multiquark Schrodinger equations with a clarity and control not previously available. In the tetraquark sector, diquark-antidiquark configurations and meson-meson molecular components can be treated within one and the same framework; pentaquark states require a careful analysis of color-spin couplings among four quarks and one antiquark; hexaquarks and larger clusters

reveal high-dimensional analogues of nuclear cluster dynamics, including tendencies toward color-singlet or diquark substructures.

A particularly illuminating outcome of this unified construction is the natural appearance of *mixing* between conventional hadrons and their multiquark counterparts. Such mixing arises because states with the same global quantum numbers inevitably couple through the QCD Hamiltonian. Even if the multiquark configurations do not manifest themselves as sharp experimental resonances, their virtual admixtures significantly influence hadronic properties.

One striking example occurs in the charmonium sector. A nominally "pure" $c\bar{c}$ state such as the χ_{c1} or the excited ψ family generically mixes with four-quark configurations $c\bar{c}q\bar{q}$. In the hyperspherical formalism, these tetraquark components appear naturally when solving the coupled Schrodinger equations: the heavy $c\bar{c}$ pair interacts not only via the central potential but also through instanton-induced forces that are sensitive to the presence of light quark pairs. The resulting wave functions show that conventional charmonium states acquire a nontrivial $c\bar{c}q\bar{q}$ admixture whose probability may reach several percent, precisely the level needed to account for the observed deviations from naive potential-model predictions. This mixing also helps explain the anomalous decay patterns and near-threshold structures observed in the charmonium-like X, Y, and Z states, many of which sit close to open-charm thresholds where tetraquark configurations play an enhanced role.

An even more consequential example is provided by the nucleon. In the rest frame the qqq component dominates, but the full wave function necessarily includes pentaquark configurations $qqqq\bar{q}$. The color, spin, and flavor couplings of four quarks and an antiquark can be organized systematically through S_4 and S_5 representations, revealing a small but robust admixture of configurations such as $[ud][ud]\bar{d}$ or $[ud][us]\bar{s}$. These admixtures provide a natural microscopic explanation for the observed flavor asymmetry $\bar{d} > \bar{u}$ in the proton sea. The mechanism is straightforward in the present framework: once the ud diquark is recognized as the most attractive channel in the instanton-induced interaction, the lowest-energy pentaquark configurations contain $\bar{d}$ more readily than $\bar{u}$, producing the empirically observed excess. The same pentaquark components also impact spin observables by modifying the balance between quark spin and orbital angular momentum inside the nucleon.

These examples illustrate a general principle: multiquark configurations, once included consistently, are not exotic decorations but essential pieces of the full hadronic wave function. In charm and bottom sectors they correct the shortcomings of simple quarkonium models; in the light-quark sector they resolve longstanding puzzles in proton structure; in nuclear systems they suggest hidden correlations that link quark-level dynamics to few-body nuclear forces. In all cases, the unified construction based on Jacobi coordinates, hyperspherical methods, and permutation-group representations provides a mathematically coherent way to build, classify, and analyze these multiquark wave functions.

Crucially, multiquark states need not appear as visible resonances in order to influence hadronic properties. Their virtual admixtures modify the structure of ordinary hadrons: the nucleon contains pentaquark components that explain the flavor asymmetry of the sea; heavy quarkonia receive contributions from virtual four-quark states; and nuclear systems show evidence of underlying multiquark correlations. In this unified framework, wave functions for multiquark clusters are constructed and handled on an equal footing with those of traditional mesons and baryons. This broadens hadronic spectroscopy into a genuinely multi-body domain, where the rich internal structure of QCD becomes manifest.

26.3 Bridging spectroscopy and parton observables

The mainstream of partonic physics has long been driven by experimental data on hard processes such as deep-inelastic scattering, elastic lepton-hadron scattering, and Drell-Yan production. Over several decades, global fits combined with perturbative DGLAP evolution have produced increasingly accurate parton dis-

tribution functions for quarks, antiquarks, and gluons. This phenomenology has been remarkably successful, yet it has also exposed a number of persistent puzzles: the decomposition of the nucleon spin and the unexpectedly large orbital component, the flavor asymmetry of the antiquark sea, and the unusual properties of the Roper resonance. A deeper conceptual issue is that form factors, PDFs, GPDs and related observables come from different experiments or lattice simulations and, in practice, lack a unifying theoretical origin. Spectroscopy and partonic observables have thus historically formed largely disconnected research domains.

The guiding idea of the present program is to reverse this logic and to construct partonic observables directly from the underlying nonperturbative structure that also governs hadronic spectroscopy. Rather than beginning with experimental PDFs and evolving them upward in scale, the approach begins with first-principles dynamics in the rest frame, proceeds through a systematic construction of wave functions, and finally boosts them to the light front. Symbolically, the theoretical chain of development reads

$$(\text{Jacobi coordinates}) \longrightarrow \text{LF Hamiltonian} \longrightarrow \text{LF wave functions} \longrightarrow (\text{formfactors, PDFs, GPDs}\ldots).$$

In this formulation, all observables arise from the same approximations and share a common dependence on all parameters.

The Hamiltonians used throughout the analysis include two dominant nonperturbative phenomena of QCD: effective constituent-like quark masses arising from chiral symmetry breaking and the long-range confining potential. Even with only these ingredients retained, the Schrodinger equations for mesons, baryons, and multiquark states can be solved to an impressive degree of realism. While quark-model spectroscopy of the simplest hadrons has been developed for half a century, the present work extends these methods decisively to multi-quark systems, tetraquarks, pentaquarks, hexaquarks, and even higher clusters. This systematic construction is made possible by the use of Jacobi coordinates to remove center-of-mass motion, hyperspherical methods to exploit approximate dynamical symmetries, and a novel application of representation theory of the permutation groups S_n to enforce Fermi statistics in orbital-color-spin-flavor space. The notions of "monom" and "good coordinate" wave-function representations, aided by symbolic computation tools, help manage the complexity of these multiquark configurations.

Even if such multiquark states are not individually identifiable as resonances in scattering experiments, their theoretical wave functions allow one to quantify their virtual admixtures inside ordinary hadrons. These admixtures naturally modify hadronic properties and help explain several long-standing puzzles, such as the flavor asymmetry of the nucleon sea and the importance of higher-Fock components in spin decompositions. The nucleon, in particular, acquires naturally an admixture of pentaquark configurations, while hybrid $\bar{q}gq$ components provide the light-front analogue of including extra gluons at the Hamiltonian level.

The transition from rest-frame spectroscopy to partonic observables is achieved by boosting the wave functions to the light front. In momentum space the natural variables are the Bjorken fractions x_i, which satisfy the normalization $\sum_i x_i = 1$. Together with modified Jacobi coordinates, these variables define quantum mechanics on simplices such as A_2 for baryons and A_4 for pentaquarks. Constructing complete bases of Laplacian eigenstates on these manifolds uncovers deep mathematical structures and provides a consistent set of tools for light-front quantization. Using either these bases or optimized low-lying approximations, one obtains light-front wave functions that encode the full nonperturbative structure of hadrons at a low instanton-defined scale μ_0. From these, without external phenomenological input, one can compute electromagnetic form factors, PDFs, DAs, GPDs, quasi-distributions, and even gravitational form factors describing the internal pressure and shear forces.

Perhaps the most important conceptual advance is the establishment of a direct bridge between spectroscopy and partonic physics. Rest-frame potentials, instanton-induced interactions, and multiquark admixtures leave characteristic imprints on the boosted light-front wave functions. Twist-three quark-gluon correlations, semi-hard instanton contributions, and the structure of the energy-momentum tensor all reflect the same nonperturbative mechanisms that control the spectroscopy of mesons and baryons. In this way, phenomena that once appeared unrelated: mass splittings, orbital excitations, sea-quark asymmetries, mechanical forces inside hadrons– emerge as different manifestations of a single underlying dynamical picture.

The final step in connecting these results to experimental observables is scale evolution. Traditional DGLAP evolution offers a perturbative, probabilistic description of how PDFs change with the resolution scale μ, but this description is incomplete because PDFs are not the fundamental objects, they correspond to reduced density matrices obtained by integrating out degrees of freedom. A more coherent evolution framework should incorporate additional Fock components directly at the Hamiltonian level, treating extra gluons in the same manner as extra $q\bar{q}$ pairs. The recent realization, particularly in the lattice community, that gradient flow represents a form of renormalization-group evolution opens new possibilities. As the flow time τ increases, hard gluon modes are suppressed, revealing first a dense instanton-antiinstanton ensemble and eventually the dilute instanton liquid. Understanding this evolution semiclassically may ultimately yield a more microscopic connection between vacuum structure, Hamiltonians, and the scale dependence of partonic observables.

In summary, the program described here merges hadronic spectroscopy and partonic physics into a unified theoretical framework. Both domains draw from the same vacuum-derived Hamiltonians, the same multiquark wave functions, and the same light-front quantization procedures. Further developments, including more complete treatments of spin-dependent interactions, improved renormalization of light-front Hamiltonians, and systematic inclusion of higher Fock sectors, promise to strengthen this bridge and bring us closer to a genuinely unified and predictive theory of hadron structure.

26.4 What lies ahead

Needless to say, the program outlined in many papers and in this review is only partially completed, and certain theoretical and phenomenological challenges still are ahead. Significant progress has been made, yet many of the essential ingredients required for a fully unified description of hadronic structure remains to be incorporated.

We started this review with modern semiclassical theory applied to tunneling in quantum mechanics: as Fig.3.1 shows, with two and three loop corrections to instanton density one indeed get good quantitative description of the gap between lowest energy levels. Unfortunately, for gauge theory instantons we are still lacking those: the last semiclassical result here remains the classic paper by ['t Hooft, 1978] fixing the one-loop corrections. That is why the instanton physics is still based on empirical constants (e.g. quark effective mass) or lattice data, rather than straightforward semiclassics.

The quark-model description of the basic mesons and baryons has now been extended to *multiquark hadrons* containing four, five, six, or even nine quarks. Technical difficulties related to incorporation of Fermi statistics have been overcomed. In this work we largely focused on the most symmetric sectors, such as systems composed of quarks of identical flavor or those dominated by light quarks. These cases offer valuable theoretical clarity and reduce computational complexity, but they also represent only a narrow subset of the full multiquark spectrum. The rapidly developing experimental program in heavy-flavor spectroscopy (covering states with charm, bottom, and mixed flavors) poses new challenges and opportunities. Constructing a systematic theoretical framework that can treat arbitrary flavor combinations, account for the interplay between heavy-quark symmetry and light-quark dynamics, and connect smoothly to known quark-model limits remains an important open direction.

Our "bridge" toward partonic physics on the light front (LF) began with the simplest mesons and baryons and has already yielded new insights into quantization methods, renormalization issues, and the interpretation of wave functions as parton amplitudes. The inclusion of higher Fock sectors has been successfully carried out for the $\bar{q}q$ systems, notably in detailed studies of the pion, sigma, and related mesons. For baryons, the baryon-pentaquark mixture has been developed extensively, both in the conventional CM frame and on the LF. This sector has shown particular promise: it provides access to the long-standing puzzles of the nucleon

spin decomposition, the flavor asymmetry of the sea, and the emergence of nontrivial correlations in higher Fock components.

Yet a great deal remains to be accomplished before truly complete picture emerges. For example, we have provided spectroscopic model fitting lattice glueballs, but not yet for *hybrid* sectors, such as $\bar{q}gq$ configurations. Beyond their intrinsic spectroscopic interest, these states are essential for understanding how gluonic degrees of freedom manifest themselves in hadron structure and how they participate in the t ransition between constituent-like and partonic descriptions. Incorporating these sectors consistently into a Hamiltonian approach on the LF presents both conceptual and computational challenges, particularly in relation to gauge invariance, the counting of independent degrees of freedom, and the scaling of the Hilbert space with increasing Fock number. The spectroscopically fitted "effective gluon mass" of about 0.9 GeV qualitatively agree with DGLAP-based disappearence of gluon PDF at $\mu < 1\,GeV$, but this important part of the "bridge" still needs to be quantified.

Equally important is the task of extending DGLAP evolution from its traditional probabilistic formulation for parton distribution functions (PDFs) into a fully Hamiltonian description of the pertinent wave functions. Such a program would allow the evolution of PDFs, generalized parton distributions, and other correlation functions to be understood in terms of transitions among an ever-increasing tower of Fock components. Realizing this vision requires combining nonperturbative LF Hamiltonians with controlled truncation schemes, renormalization procedures, and matching to perturbative renormalization group transformations in the appropriate kinematic regimes.

In summary, while the foundations have been laid and several key mechanisms have been clarified, the long-term goal of a unified, multiscale Hamiltonian description of hadrons– capable of linking spectroscopy, partonic observables, and the full complexity of QCD dynamics, remains a rich and demanding frontier for future work.

Chapter 27
Epilogue

The central theme of this review has been the construction of a bridge between two complementary but historically disconnected frameworks for describing hadrons: the spectroscopy-oriented rest-frame approach and the partonic light-front description. The success of this endeavor rests on a unified treatment of the QCD vacuum, confinement, and chiral symmetry breaking on the one hand, and the scale evolution, operator structure, and factorization properties of high-energy processes on the other. The resulting synthesis offers a continuous view of hadron structure across all relevant distance scales.

Another outcome of this work is the demonstration that instanton physics provides a natural mechanism for embedding nonperturbative QCD dynamics into the light-front formalism. The Instanton Liquid Model, long known to reproduce a broad spectrum of phenomenological signatures in low-energy QCD, proves equally well-suited to generating the nonlocal interactions and dynamical mass functions required to describe hadrons at low resolution. Once these structures are implemented in the light-front Hamiltonian, the resulting wave functions automatically incorporate essential features of the QCD vacuum, including spontaneous chiral symmetry breaking and strong correlations among quark flavors and spins. Important novel features are related with contributions of $I\bar{I}\ molecules$, and incorporation of *gradient flow* version of RG on the lattice.

By constructing light-front wave functions for a wide variety of systems - quarkonia, light mesons, baryons, pentaquarks, tetraquarks, and heavier multiquark states - we have shown that hadronic spectroscopy and partonic observables share a common dynamical infrastructure. The same interactions that reproduce the observed mass spectra and spin splittings also determine the shapes of DAs, PDFs, TMDs and GPDs, as well as the pressure, shear, and energy distributions encoded in the gravitational form factors. This coherence strengthens the central thesis: the spectroscopy of hadrons and the momentum-space structure revealed in scattering experiments emerge from the same underlying dynamics.

Another important contribution of this review is the explicit mapping of low-energy wave functions onto high-energy partonic observables through the use of perturbative evolution equations. The DGLAP and ERBL formalisms ensure that distribution functions computed at the low nonperturbative scale defined by the ILM evolve consistently into the region probed by experiments. This multiscale evolution encapsulates the transition from the nonperturbative "constituent" regime to the perturbative "partonic" regime and shows how the effects of confinement and chiral symmetry breaking are gradually diluted as the resolution increases.

The exploration of gravitational form factors and the energy-momentum tensor further enhances the scope of the program. These quantities, which are becoming increasingly accessible through both lattice simulations and experimental proxy processes, reveal profound aspects of hadron structure that go beyond charge and momentum distributions. The instanton-based light-front framework naturally accommodates these observables, leading to predictions for pressure profiles, mass distributions, and mechanical stability conditions. These results highlight the deep connection between internal forces in hadrons and the dynamics of their underlying quark and gluon degrees of freedom.

Looking ahead, several exciting avenues present themselves. Extending the light-front Hamiltonian to include dynamical gluons will be essential for capturing the full structure of higher-twist observables, gluon distributions, and the gluonic contributions to the energy-momentum tensor. Incorporating higher Fock sectors more systematically will allow for a refined understanding of sea-quark asymmetries and the role of quark-antiquark pairs in baryon structure. The emergent Electron-Ion Collider will provide unprecedented data on GPDs, TMDs, and exclusive processes, offering stringent tests of the framework developed here. Furthermore, improvements in lattice QCD calculations of quasi-PDFs and gravitational form factors will supply additional inputs and benchmarks.

The overarching conclusion of this review is that the boundary between hadronic spectroscopy and partonic descriptions can be bridged with carefully constructed theoretical tools. By embedding the essential nonperturbative physics of instantons and confinement directly into the light-front framework, we obtain a comprehensive theory of hadrons that is simultaneously sensitive to their spectroscopy, their internal forces, and their high-energy scattering signatures. This integrated picture reflects the spirit of QCD itself: a theory whose diverse phenomena, though often studied in isolation, ultimately arise from the same fundamental dynamics.

The hope is that the synthesis presented here will serve not only as a coherent summary of a substantial body of previous work, but as a foundation for future advances. The interplay between vacuum structure, hadronic wave functions, and partonic observables is a fertile ground for new discoveries. As experimental capabilities expand and theoretical techniques evolve, the program outlined in this review will continue to provide a powerful framework for unraveling the multifaceted nature of the strong interaction.

Acknowledgements

References

Abbott et al., 2025. Abbott, R., Hackett, D. C., Pefkou, D. A., Romero-López, F., and Shanahan, P. E. (2025). Lattice evidence that scalar glueballs are small.

Abdul Khalek et al., 2022. Abdul Khalek, R. et al. (2022). Science Requirements and Detector Concepts for the Electron-Ion Collider. *Nucl. Phys. A*, 1026:122447.

Adhikari et al., 2019. Adhikari, L., Li, Y., Li, M., and Vary, J. P. (2019). Form factors and generalized parton distributions of heavy quarkonia in basis light front quantization. *Phys. Rev. C*, 99(3):035208.

Adlarson et al., 2011. Adlarson, P. et al. (2011). ABC Effect in Basic Double-Pionic Fusion — Observation of a new resonance? *Phys. Rev. Lett.*, 106:242302.

Aicher et al., 2010. Aicher, M., Schäfer, A., and Vogelsang, W. (2010). Soft-gluon resummation and the pion distribution. *Phys. Rev. Lett.*, 105:252003.

Aidala et al., 2013. Aidala, C. A., Bass, S. D., Hasch, D., and Mallot, G. K. (2013). The Spin Structure of the Nucleon. *Rev. Mod. Phys.*, 85:655–691.

Aitala et al., 2001. Aitala, E. M. et al. (2001). Direct measurement of the pion valence quark momentum distribution, the pion light cone wave function squared. *Phys. Rev. Lett.*, 86:4768–4772.

Alexandrou et al., 2020. Alexandrou, C., Bacchio, S., Constantinou, M., Finkenrath, J., Hadjiyiannakou, K., Jansen, K., Koutsou, G., Panagopoulos, H., and Spanoudes, G. (2020). Complete flavor decomposition of the spin and momentum fraction of the proton using lattice QCD simulations at physical pion mass. *Phys. Rev. D*, 101(9):094513.

Alford et al., 1998. Alford, M. G., Rajagopal, K., and Wilczek, F. (1998). QCD at finite baryon density: Nucleon droplets and color superconductivity. *Phys. Lett. B*, 422:247–256.

Altarelli and Parisi, 1977. Altarelli, G. and Parisi, G. (1977). Asymptotic Freedom in Parton Language. *Nucl. Phys. B*, 126:298–318.

Amaryan, 2025. Amaryan, M. (2025). 20 Years of Light Pentaquark Searches.

An and Saghai, 2019. An, C. S. and Saghai, B. (2019). Orbital angular momentum of the proton and intrinsic five-quark Fock states. *Phys. Rev. D*, 99(9):094039.

Anderle et al., 2021. Anderle, D. P. et al. (2021). Electron-ion collider in China. *Front. Phys. (Beijing)*, 16:64701.

Angeles-Martinez et al., 2015. Angeles-Martinez, R. et al. (2015). Transverse Momentum Dependent (TMD) parton distribution functions: status and prospects. *Acta Phys. Polon. B*, 46(12):2501–2534.

Anikin et al., 2001. Anikin, I., Dorokhov, A., and Tomio, L. (2001). Pion distribution amplitude within the instanton model. *Phys. Atom. Nucl.*, 64:1329–1336.

Anisovich et al., 2012. Anisovich, A. V., Beck, R., Klempt, E., Nikonov, V. A., Sarantsev, A. V., and Thoma, U. (2012). Properties of baryon resonances from a multichannel partial wave analysis. *Eur. Phys. J. A*, 48:15.

Aoki, 2020. Aoki, S. e. a. (2020). FLAG Review 2019. *Eur. Phys. J. C*, 80:113.

Arvis, 1983. Arvis, J. F. (1983). The Exact $q\bar{q}$ Potential in Nambu String Theory. *Phys. Lett. B*, 127:106–108.

Aslan et al., 2019. Aslan, F. P., Burkardt, M., and Schlegel, M. (2019). Transverse Force Tomography. *Phys. Rev. D*, 100(9):096021.

Athenodorou et al., 2018. Athenodorou, A., Boucaud, P., De Soto, F., Rodríguez-Quintero, J., and Zafeiropoulos, S. (2018). Instanton liquid properties from lattice QCD. *JHEP*, 02:140.

Athenodorou and Teper, 2020. Athenodorou, A. and Teper, M. (2020). The glueball spectrum of su(3) gauge theory in 3+1 dimensions. *JHEP*, 11:172.

Aubert et al., 2003. Aubert, B. et al. (2003). Observation of a narrow meson decaying to $D_s^+\pi^0$ at a mass of 2.32-GeV/c^2. *Phys. Rev. Lett.*, 90:242001.

Avkhadiev et al., 2023. Avkhadiev, A., Shanahan, P. E., Wagman, M. L., and Zhao, Y. (2023). Collins-Soper kernel from lattice QCD at the physical pion mass. *Phys. Rev. D*, 108(11):114505.

Bacchetta et al., 2022. Bacchetta, A., Bertone, V., Bissolotti, C., Bozzi, G., Cerutti, M., Piacenza, F., Radici, M., and Signori, A. (2022). Unpolarized transverse momentum distributions from a global fit of Drell-Yan and semi-inclusive deep-inelastic scattering data. *JHEP*, 10:127.

Bacchetta et al., 2020. Bacchetta, A., Bertone, V., et al. (2020). Extraction of TMDs. *JHEP*, 07.

Badalian, 2023. Badalian, A. M. (2023). The $X(6550), X(6900), X(7280)$ resonances as the $nS, cc\bar{c}\bar{c}$ states.

Badier et al., 1980. Badier, J. et al. (1980). Measurement of the K^-/π^- Structure Function Ratio Using the Drell-Yan Process. *Phys. Lett. B*, 93:354–356.

Bakker et al., 2014. Bakker, B. L. G. et al. (2014). Light-Front Quantum Chromodynamics. *Nucl. Phys. B Proc. Suppl.*, 251-252:165–174.

Bali et al., 2019. Bali, G. S., Braun, V. M., Bürger, S., Göckeler, M., Gruber, M., Hutzler, F., Korcyl, P., Schäfer, A., Sternbeck, A., and Wein, P. (2019). Light-cone distribution amplitudes of pseudoscalar mesons from lattice QCD. *JHEP*, 08:065. [Addendum: JHEP 11, 037 (2020)].

Balitsky and Yung, 1986. Balitsky, I. I. and Yung, A. V. (1986). Collective - Coordinate Method for Quasizero Modes. *Phys. Lett. B*, 168:113–119.

Ball and Braun, 1996. Ball, P. and Braun, V. M. (1996). The Rho meson light cone distribution amplitudes of leading twist revisited. *Phys. Rev. D*, 54:2182–2193.

Balla et al., 1998. Balla, J., Polyakov, M. V., and Weiss, C. (1998). Nucleon matrix elements of higher twist operators from the instanton vacuum. *Nucl. Phys. B*, 510:327–364.

Barabanov et al., 2021. Barabanov, M. Y. et al. (2021). Diquark correlations in hadron physics: Origin, impact and evidence. *Prog. Part. Nucl. Phys.*, 116:103835.

Bardeen and Hill, 1994. Bardeen, W. A. and Hill, C. T. (1994). Chiral dynamics and heavy quark symmetry in a solvable toy field theoretic model. *Phys. Rev. D*, 49:409–425.

Barone et al., 2010. Barone, V., Bradamante, F., and Martin, A. (2010). Transverse-spin and transverse-momentum effects in high-energy processes. *Prog. Part. Nucl. Phys.*, 65:267–333.

Bars, 1976a. Bars, I. (1976a). A Quantum String Theory of Hadrons and Its Relation to Quantum Chromodynamics in Two-Dimensions. *Nucl. Phys. B*, 111:413–440.

Bars, 1976b. Bars, I. (1976b). Exact Equivalence of Chromodynamics to a String Theory. *Phys. Rev. Lett.*, 36:1521.

Bashir et al., 2012. Bashir, A., Chang, L., Cloet, I. C., El-Bennich, B., Liu, Y.-X., Roberts, C. D., and Tandy, P. C. (2012). Collective perspective on advances in Dyson-Schwinger Equation QCD. *Commun. Theor. Phys.*, 58:79–134.

Behtash et al., 2017. Behtash, A., Dunne, G. V., Schäfer, T., Sulejmanpasic, T., and Ünsal, M. (2017). Toward Picard–Lefschetz theory of path integrals, complex saddles and resurgence. *Ann. Math. Sci. Appl.*, 02:95–212.

Belavin et al., 1975. Belavin, A., Polyakov, A., Schwarz, A., and Tyupkin, Y. (1975). *Phys. Lett. B*, 59:85.

Belitsky and Radyushkin, 2005. Belitsky, A. V. and Radyushkin, A. V. (2005). Unpolarized and polarized generalized parton distributions. *Phys. Rept.*, 418:1–387.

Bentz et al., 1999. Bentz, W., Hama, T., Matsuki, T., and Yazaki, K. (1999). NJL model on the light cone and pion structure function. *Nucl. Phys. A*, 651:143–173.

Besson et al., 2003. Besson, D. et al. (2003). Observation of a narrow resonance of mass 2.46-GeV/c**2 decaying to D*+(s) pi0 and confirmation of the D*(sJ)(2317) state. *Phys. Rev. D*, 68:032002. [Erratum: Phys.Rev.D 75, 119908 (2007)].

Bhagwat and Maris, 2008. Bhagwat, M. S. and Maris, P. (2008). Vector meson form factors and their quark-mass dependence. *Phys. Rev. C*, 77:025203.

Bhattacharya et al., 2022. Bhattacharya, S. et al. (2022). Lattice determination of nucleon GPDs via LaMET. *Phys. Rev. D*, 106:114512.

Biddle et al., 2020a. Biddle, J. C., Kamleh, W., and Leinweber, D. B. (2020a). Visualisations of Centre Vortices. *EPJ Web Conf.*, 245:06010.

Biddle et al., 2020b. Biddle, J. C., Kamleh, W., and Leinweber, D. B. (2020b). Visualization of center vortex structure. *Phys. Rev. D*, 102(3):034504.

Bijker et al., 2009. Bijker, R., Santopinto, E., and Santopinto, E. (2009). Unquenched quark model for baryons: Magnetic moments, spins and orbital angular momenta. *Phys. Rev. C*, 80:065210.

Bjorken and Paschos, 1969. Bjorken, J. D. and Paschos, E. A. (1969). Inelastic Electron Proton and gamma Proton Scattering, and the Structure of the Nucleon. *Phys. Rev.*, 185:1975–1982.

Boer and Mulders, 1998. Boer, D. and Mulders, P. J. (1998). Time reversal odd distribution functions in leptoproduction. *Phys. Rev. D*, 57:5780–5786.

Bollweg et al., 2024. Bollweg, D., Gao, X., Mukherjee, S., and Zhao, Y. (2024). Nonperturbative Collins-Soper kernel from chiral quarks with physical masses. *Phys. Lett. B*, 852:138617.

Boucaud et al., 2003. Boucaud, P., De Soto, F., Le Yaouanc, A., Leroy, J., Micheli, J., Moutarde, H., Pene, O., and Rodriguez-Quintero, J. (2003). The Strong coupling constant at small momentum as an instanton detector. *JHEP*, 04:005.

Boussarie et al., 2023. Boussarie, R. et al. (2023). TMD Handbook.

Boyle et al., 2008. Boyle, P. A., Brommel, D., Donnellan, M. A., Flynn, J. M., Juttner, A., and Sachrajda, C. T. (2008). Parton Distribution Amplitudes and Non-Perturbative Renormalisation. *PoS*, LATTICE2008:165.

Brambilla and Wang, 2024. Brambilla, N. and Wang, X.-P. (2024). Off-lightcone Wilson-line operators in gradient flow. *JHEP*, 06:210.

Brandt et al., 1982. Brandt, R. A., Gocksch, A., Sato, M. A., and Neri, F. (1982). LOOP SPACE. *Phys. Rev. D*, 26:3611.

Braun et al., 2016. Braun, V. M. et al. (2016). Light-cone distribution amplitudes of light mesons from lattice QCD. *Phys. Rev. D*, 93(9):094023.

Braun et al., 2017a. Braun, V. M. et al. (2017a). The ρ-meson light-cone distribution amplitudes from lattice QCD. *JHEP*, 04:082.

Braun et al., 2017b. Braun, V. M., Manashov, A. N., Moch, S., and Strohmaier, M. (2017b). Three-loop evolution equation for flavor-nonsinglet operators in off-forward kinematics. *JHEP*, 06:037.

Brodsky and de Teramond, 2006. Brodsky, S. J. and de Teramond, G. F. (2006). Hadronic spectra and light-front wave functions in holographic QCD. *Phys. Rev. Lett.*, 96:201601.

Brodsky and Farrar, 1973. Brodsky, S. J. and Farrar, G. R. (1973). Scaling Laws at Large Transverse Momentum. *Phys. Rev. Lett.*, 31:1153–1156.

Brodsky et al., 1998a. Brodsky, S. J., Pauli, H.-C., and Pinsky, S. S. (1998a). Quantum chromodynamics and other field theories on the light cone. *Phys. Rept.*, 301:299–486.

Brodsky et al., 1998b. Brodsky, S. J., Pauli, H.-C., and Pinsky, S. S. (1998b). Quantum Chromodynamics and Other Field Theories on the Light Cone. *Phys. Rept.*, 301:299.

Brodsky and Shrock, 2011. Brodsky, S. J. and Shrock, R. (2011). Condensates in Quantum Chromodynamics and the Cosmological Constant. *Proc. Nat. Acad. Sci.*, 108:45–50.

Brodsky, 1994. Brodsky, S. J. e. a. (1994). Light-front QCD. *Prog. Part. Nucl. Phys.*, 33:477.

Brodsky, 2015. Brodsky, S. J. e. a. (2015). Light-front dynamics and AdS/QCD correspondence. *Phys. Rept.*, 584:1–105.

Broniowski and Ruiz Arriola, 2017. Broniowski, W. and Ruiz Arriola, E. (2017). Nonperturbative partonic quasidistributions of the pion from chiral quark models. *Phys. Lett. B*, 773:385–390.

Broniowski et al., 2008. Broniowski, W., Ruiz Arriola, E., and Golec-Biernat, K. (2008). Generalized parton distributions of the pion in chiral quark models and their QCD evolution. *Phys. Rev. D*, 77:034023.

Brown and Rho, 1979. Brown, G. E. and Rho, M. (1979). The Little Bag. *Phys. Lett. B*, 82:177–180.

Buchmuller, 1982. Buchmuller, W. (1982). Fine and Hyperfine Structure of Quarkonia. *Phys. Lett. B*, 112:479–483.

Burkardt, 2013. Burkardt, M. (2013). Transverse force on quarks in deep-inelastic scattering. *Phys. Rev. D*, 88:114502.

Bury et al., 2022. Bury, M., Hautmann, F., Leal-Gomez, S., Scimemi, I., Vladimirov, A., and Zurita, P. (2022). PDF bias and flavor dependence in TMD distributions. *JHEP*, 10:118.

Callan et al., 1978. Callan, Jr., C. G., Dashen, R. F., Gross, D. J., Wilczek, F., and Zee, A. (1978). The Effect of Instantons on the Heavy Quark Potential. *Phys. Rev. D*, 18:4684.

Cao et al., 2025. Cao, X., Li, Y., Shi, C., Vary, J. P., and Wang, Q. (2025). Convergence in charmonium structure: light-front wave functions from basis light-front quantization and Dyson-Schwinger equations.

Capstick and Isgur, 1985. Capstick, S. and Isgur, N. (1985). Baryons in a Relativized Quark Model with Chromodynamics. *AIP Conf. Proc.*, 132:267–271.

Capstick and Roberts, 2000. Capstick, S. and Roberts, W. (2000). Quark models of baryon masses and decays. *Prog. Part. Nucl. Phys.*, 45:S241–S331.

Carbonell, 1998. Carbonell, J. e. a. (1998). Explicitly covariant light front dynamics and relativistic few body systems. *Phys. Rept.*, 300:215–347.

Carrillo-Serrano et al., 2015. Carrillo-Serrano, M. E., Bentz, W., Cloët, I. C., and Thomas, A. W. (2015). ρ meson form factors in a confining Nambu–Jona-Lasinio model. *Phys. Rev. C*, 92(1):015212.

Carroll et al., 1968. Carroll, J., Lichtenberg, D. B., and Franklin, J. (1968). Electromagnetic properties of baryons in a quark-diquark model with broken su(6). *Phys. Rev.*, 174:1681–1688.

Chang et al., 2013. Chang, L. et al. (2013). Pion properties and DCSB. *Phys. Rev. Lett.*, 110:132001.

Chang et al., 2014. Chang, L., Mezrag, C., Moutarde, H., Roberts, C. D., Rodríguez-Quintero, J., and Tandy, P. C. (2014). Basic features of the pion valence-quark distribution function. *Phys. Lett. B*, 737:23–29.

Chang and Ma, 1969. Chang, S.-J. and Ma, S.-K. (1969). Feynman rules and quantum electrodynamics at infinite momentum. *Phys. Rev.*, 180:1506–1513.

Chen et al., 2006. Chen, Y. et al. (2006). Glueball spectrum and matrix elements on anisotropic lattices. *Phys. Rev. D*, 73:014516.

Chernyak and Zhitnitsky, 1977. Chernyak, V. and Zhitnitsky, A. (1977). Asymptotic Behavior of Hadron Form-Factors in Quark Model. (In Russian). *JETP Lett.*, 25:510.

Chernyak and Zhitnitsky, 1984. Chernyak, V. and Zhitnitsky, A. (1984). Asymptotic Behavior of Exclusive Processes in QCD. *Phys. Rept.*, 112:173.

Chernyshev et al., 1996. Chernyshev, S., Nowak, M. A., and Zahed, I. (1996). Heavy hadrons and QCD instantons. *Phys. Rev. D*, 53:5176–5184.

Chu et al., 1993. Chu, M. C., Grandy, J. M., Huang, S., and Negele, J. W. (1993). Correlation functions of hadron currents in the QCD vacuum calculated in lattice QCD. *Phys. Rev. D*, 48:3340–3353.

Chu et al., 1994. Chu, M. C., Grandy, J. M., Huang, S., and Negele, J. W. (1994). Evidence for the role of instantons in hadron structure from lattice QCD. *Phys. Rev. D*, 49:6039–6050.

Chu et al., 2023. Chu, M.-H. et al. (2023). Lattice calculation of the intrinsic soft function and the Collins-Soper kernel. *JHEP*, 08:172.

Clement, 2017. Clement, H. (2017). On the History of Dibaryons and their Final Observation. *Prog. Part. Nucl. Phys.*, 93:195.

Collins, 2011. Collins, J. (2011). Foundations of Perturbative QCD. *Cambridge University Press*.

Collins and Soper, 1981a. Collins, J. and Soper, D. (1981a). Back-To-Back Jets in QCD. *Nucl. Phys. B*, 193:381.

Collins and Soper, 1982a. Collins, J. and Soper, D. (1982a). Parton Distribution and Decay Functions. *Nucl. Phys. B*, 197:446.

Collins and Soper, 1981b. Collins, J. C. and Soper, D. E. (1981b). Back-to-back jets in QCD. *Nucl. Phys.*, B193.

Collins and Soper, 1982b. Collins, J. C. and Soper, D. E. (1982b). Parton distribution and decay functions. *Nuclear Physics B*, 194:445.

Collins et al., 1985a. Collins, J. C., Soper, D. E., and Sterman, G. (1985a). Transverse Momentum Distribution in Drell-Yan Pair and W and Z Boson Production. *Nucl. Phys.*, B250.

Collins et al., 1985b. Collins, J. C., Soper, D. E., and Sterman, G. F. (1985b). Transverse Momentum Distribution in Drell-Yan Pair and W and Z Boson Production. *Nucl. Phys. B*, 250:199.

Conway et al., 1989. Conway, J. S. et al. (1989). Experimental Study of Muon Pair Production by π^- on Tungsten. *Phys. Rev. D*, 39:92–122.

Crawford et al., 2025. Crawford, J. A., Can, K. U., Horsley, R., Rakow, P. E. L., Schierholz, G., Stüben, H., Young, R. D., and Zanotti, J. M. (2025). Transverse Force Distributions in the Proton from Lattice QCD. *Phys. Rev. Lett.*, 134(7):071901.

Dakhno and Nikolaev, 1985. Dakhno, L. G. and Nikolaev, N. N. (1985). Does the Failure of Multiple Scattering Theory in $p\alpha$ and $\pi\alpha$ Diffraction Scattering Suggest 12 Quark Bags? *Nucl. Phys. A*, 436:653–687.

D'Alesio and Murgia, 2008. D'Alesio, U. and Murgia, F. (2008). Azimuthal and Single Spin Asymmetries in Hard Scattering Processes. *Prog. Part. Nucl. Phys.*, 61:394–454.

Davies et al., 2018. Davies, C., Koponen, J., Lepage, P. G., Lytle, A. T., and Zimermmane-Santos, A. C. (2018). Meson Electromagnetic Form Factors from Lattice QCD. *PoS*, LATTICE2018:298.

Davies et al., 1985. Davies, C. T. H., Webber, B. R., and Stirling, W. J. (1985). Drell-yan cross-sections at large transverse momentum. *Nucl. Phys. B*, 256.

de Forcrand and Jahn, 2005. de Forcrand, P. and Jahn, O. (2005). The Baryon static potential from lattice QCD. *Nucl. Phys. A*, 755:475–480.

de Melo and Frederico, 1997. de Melo, J. P. B. C. and Frederico, T. (1997). Covariant and light front approaches to the rho meson electromagnetic form-factors. *Phys. Rev. C*, 55:2043.

DeMartini and Shuryak, 2021. DeMartini, D. and Shuryak, E. (2021). Nucleon clustering at kinetic freezeout of heavy-ion collisions via path-integral Monte Carlo. *Nucl. Phys. A*, 1016:122336.

Dhindsa et al., 2025. Dhindsa, N. S., Mathur, N., and Padmanath, M. (2025). Lattice QCD Study of Positive Parity Dibaryons with Maximal Charm and Strangeness.

Diakonov, 1997. Diakonov, D. (1997). Chiral quark - soliton model. In *Advanced Summer School on Nonperturbative Quantum Field Physics*, pages 1–55.

Diakonov, 2003. Diakonov, D. (2003). Instantons at work. *Prog. Part. Nucl. Phys.*, 51:173–222.

Diakonov, 2009. Diakonov, D. (2009). Topology and confinement. *Nucl. Phys. B Proc. Suppl.*, 195:5–45.

Diakonov et al., 2012. Diakonov, D., Petrov, V., and Vladimirov, A. A. (2012). Baryon resonances at large N_c, or Quark Nuclear Physics. *PoS*, QNP2012:084.

Diakonov and Petrov, 1986. Diakonov, D. and Petrov, V. Y. (1986). A Theory of Light Quarks in the Instanton Vacuum. *Nucl. Phys. B*, 272:457–489.

Diakonov et al., 1997. Diakonov, D., Petrov, V. Y., and Polyakov, M. (1997). Pion wave function from the instanton vacuum. *Z. Phys. A*, 359:305–314.

Diakonov et al., 1996. Diakonov, D., Polyakov, M. V., and Weiss, C. (1996). Hadronic matrix elements of gluon operators in the instanton vacuum. *Nucl. Phys. B*, 461:539–580.

Diehl, 2003. Diehl, M. (2003). Generalized parton distributions. *Phys. Rept.*, 388:41–277.

Ding et al., 2024. Ding, H.-T., Gao, X., Hanlon, A. D., Mukherjee, S., Petreczky, P., Shi, Q., Syritsyn, S., Zhang, R., and Zhao, Y. (2024). QCD Predictions for Meson Electromagnetic Form Factors at High Momenta: Testing Factorization in Exclusive Processes. *Phys. Rev. Lett.*, 133(18):181902.

Dirac, 1949. Dirac, P. A. M. (1949). Forms of Relativistic Dynamics. *Rev. Mod. Phys.*, 21:392–399.

Dokshitzer, 1977. Dokshitzer, Y. L. (1977). Calculation of the Structure Functions for Deep Inelastic Scattering. *Sov. Phys. JETP*, 46:641–653.

Donoghue et al., 1992. Donoghue, J. F., Golowich, E., and Holstein, B. R. (1992). *Dynamics of the Standard Model*. Cambridge University Press.

Dotsenko and Vergeles, 1980. Dotsenko, V. S. and Vergeles, S. N. (1980). Renormalizability of Phase Factors in the Nonabelian Gauge Theory. *Nucl. Phys. B*, 169:527–546.

Doumerc and Moriarty, 2008. Doumerc, Y. and Moriarty, J. (2008). Exit problems associated with affine reflection groups. *Probability Theory and Related Fields*, 145(3–4):351–383.

Dove et al., 2021. Dove, J. et al. (2021). The asymmetry of antimatter in the proton. *Nature*, 590(7847):561–565. [Erratum: Nature 604, E26 (2022)].

Durgut, 1976. Durgut, M. (1976). Baryon Bound State in Two-Dimensional SU(N) Gauge Theory. *Nucl. Phys. B*, 116:233–252.

Dyson and Xuong, 1964. Dyson, F. and Xuong, N. H. (1964). Y=2 States in Su(6) Theory. *Phys. Rev. Lett.*, 13(26):815–817.

Efremov and Radyushkin, 1980a. Efremov, A. V. and Radyushkin, A. V. (1980a). Factorization and asymptotical behavior of pion form factor in QCD. *Phys. Lett. B*, 94:245–250.

Efremov and Radyushkin, 1980b. Efremov, A. V. and Radyushkin, A. V. (1980b). Factorization and Asymptotical Behavior of Pion Form-Factor in QCD. *Phys. Lett. B*, 94:245–250.

Eichmann, 2016. Eichmann, G. e. a. (2016). Baryons as relativistic three-quark bound states. *Prog. Part. Nucl. Phys.*, 91:1–100.

Eichten and Feinberg, 1981. Eichten, E. and Feinberg, F. (1981). Spin Dependent Forces in QCD. *Phys. Rev. D*, 23:2724.

Escobar-Ruiz et al., 2015. Escobar-Ruiz, M. A., Shuryak, E., and Turbiner, A. V. (2015). Three-loop Correction to the Instanton Density. I. The Quartic Double Well Potential. *Phys. Rev. D*, 92(2):025046. [Erratum: Phys.Rev.D 92, 089902 (2015)].

Fabre de la Ripelle and Navarro, 1979. Fabre de la Ripelle, M. and Navarro, J. (1979). The first order of the hyperspherical harmonic expansion method. *Annals of Physics*, 123(1):185–232.

Faccioli and DeGrand, 2003. Faccioli, P. and DeGrand, T. A. (2003). Evidence for instanton induced dynamics, from lattice QCD. *Phys. Rev. Lett.*, 91:182001.

Farrar and Jackson, 1975. Farrar, G. R. and Jackson, D. R. (1975). Pion and Nucleon Structure Functions Near $x = 1$. *Phys. Rev. Lett.*, 35:1416.

Ferretti et al., 2013. Ferretti, J., Galatà, G., and Santopinto, E. (2013). Interpretation of the X(3872) as a charmonium state plus an extra component due to the coupling to the meson-meson continuum. *Phys. Rev. C*, 88(1):015207.

Feynman, 1969. Feynman, R. P. (1969). Very high-energy collisions of hadrons. *Phys. Rev. Lett.*, 23:1415–1417.

Flambaum et al., 1997. Flambaum, V. V., Gribakina, A. A., Gribakin, G. F., and Ponomarev, I. V. (1997). Can we apply statistical laws to small systems? the cerium atom.

Fritzsch et al., 1973. Fritzsch, H., Gell-Mann, M., and Leutwyler, H. (1973). Advantages of the Color Octet Gluon Picture. *Phys. Lett. B*, 47:365–368.

Gallimore and Liao, 2024. Gallimore, D. and Liao, J. (2024). A Potential Model Study of the Nucleon's Charge and Mass Radius.

Gao et al., 2017. Gao, F., Chang, L., Liu, Y.-X., Roberts, C. D., and Tandy, P. C. (2017). Exposing strangeness: projections for kaon electromagnetic form factors. *Phys. Rev. D*, 96(3):034024.

Gasser and Leutwyler, 1984. Gasser, J. and Leutwyler, H. (1984). Chiral Perturbation Theory to One Loop. *Annals Phys.*, 158:142.

Gayou et al., 2002. Gayou, O. et al. (2002). Measurement of G(Ep) / G(Mp) in polarized-e p —> e polarized-p to Q**2 = 5.6-GeV**2. *Phys. Rev. Lett.*, 88:092301.

Geiger and Isgur, 1990. Geiger, P. and Isgur, N. (1990). The Quenched Approximation in the Quark Model. *Phys. Rev. D*, 41:1595.

Gell-Mann and Levy, 1960. Gell-Mann, M. and Levy, M. (1960). The axial vector current in beta decay. *Nuovo Cim.*, 16:705.

Gell-Mann et al., 1968. Gell-Mann, M., Oakes, R. J., and Renner, B. (1968). Behavior of Current Divergences Under SU(3) x SU(3). *Phys. Rev.*, 175:2195–2199.

Giannini and Santopinto, 2015. Giannini, M. M. and Santopinto, E. (2015). The baryon spectrum and the hypercentral Constituent Quark Model.

Girardeau, 1960. Girardeau, M. (1960). Relationship between Systems of Impenetrable Bosons and Fermions in One Dimension. *J. Math. Phys.*, 1(6):516.

Głazek and Wilson, 1993. Głazek, S. D. and Wilson, K. G. (1993). Renormalization of Hamiltonians. *Phys. Rev. D*, 48:5863–5872.

Glozman et al., 2012. Glozman, L. Y., Lang, C. B., and Schrock, M. (2012). Symmetries of hadrons after unbreaking the chiral symmetry. *Phys. Rev. D*, 86:014507.

Godfrey and Isgur, 1985. Godfrey, S. and Isgur, N. (1985). Mesons in a Relativized Quark Model with Chromodynamics. *Phys. Rev. D*, 32:189–231.

Gonzalez-Hernandez et al., 2022. Gonzalez-Hernandez, J. O., Rogers, T. C., and Sato, N. (2022). Combining nonperturbative transverse momentum dependence with TMD evolution. *Phys. Rev. D*, 106(3):034002.

Gordillo and Segovia, 2025. Gordillo, M. C. and Segovia, J. (2025). Diffusion Monte Carlo calculation of compact T_{cs0} and $T_{c\bar{s}0}$ tetraquarks.

Gromes, 1984. Gromes, D. (1984). Spin Dependent Potentials in QCD and the Correct Long Range Spin Orbit Term. *Z. Phys. C*, 26:401.

Gross and Wilczek, 1973. Gross, D. J. and Wilczek, F. (1973). Ultraviolet Behavior of Nonabelian Gauge Theories. *Phys. Rev. Lett.*, 30:1343–1346.

Gross et al., 2023. Gross, F. et al. (2023). 50 Years of Quantum Chromodynamics. *Eur. Phys. J. C*, 83:1125.

Grosse Perdekamp and Yuan, 2015. Grosse Perdekamp, M. and Yuan, F. (2015). Transverse Spin Structure of the Nucleon. *Ann. Rev. Nucl. Part. Sci.*, 65:429–456.

Guidal et al., 2005. Guidal, M., Polyakov, M. V., Radyushkin, A. V., and Vanderhaeghen, M. (2005). Nucleon form-factors from generalized parton distributions. *Phys. Rev. D*, 72:054013.

Hackett et al., 2023a. Hackett, D. C., Oare, P., Pefkou, D., and Shanahan, P. (2023a). Pion gravitational form factors from lattice QCD.

Hackett et al., 2023b. Hackett, D. C., Oare, P. R., Pefkou, D. A., and Shanahan, P. E. (2023b). Gravitational form factors of the pion from lattice QCD. *Phys. Rev. D*, 108:114504.

Hasenfratz, 2000. Hasenfratz, A. (2000). Spatial correlation of the topological charge in pure SU(3) gauge theory and in QCD. *Phys. Lett. B*, 476:188–192.

Hatta and Schoenleber, 2024. Hatta, Y. and Schoenleber, J. (2024). Twist analysis of the spin-orbit correlation in QCD. *JHEP*, 09:154.

He et al., 2025a. He, F., Shuryak, E., Wu, W., and Zahed, I. (2025a). Light S-wave pentaquarks on the light front.

He et al., 2025b. He, F., Shuryak, E., Wu, W., and Zahed, I. (2025b). Light S-wave pentaquarks on the light front.

Heinzl, 2001. Heinzl, T. (2001). Light cone quantization: Foundations and applications. *Lect. Notes Phys.*, 572:55–142.

Hieda and Suzuki, 2016. Hieda, K. and Suzuki, H. (2016). Small flow-time representation of fermion bilinear operators. *Mod. Phys. Lett. A*, 31(38):1650214.

Hou et al., 2021a. Hou, T.-J. et al. (2021a). New CTEQ global analysis of quantum chromodynamics with high-precision data from the LHC. *Phys. Rev. D*, 103(1):014013.

Hou et al., 2021b. Hou, T.-J. et al. (2021b). New CTEQ global analysis of quantum chromodynamics with high-precision data from the LHC. *Phys. Rev. D*, 103(1):014013.

Hägler et al., 2008. Hägler, P. et al. (2008). Nucleon GPDs from lattice QCD. *Phys. Rev. D*, 77:094502.

Ilgenfritz and Shuryak, 1989. Ilgenfritz, E.-M. and Shuryak, E. V. (1989). Chiral Symmetry Restoration at Finite Temperature in the Instanton Liquid. *Nucl. Phys. B*, 319:511–520.

Isgur and Karl, 1978. Isgur, N. and Karl, G. (1978). P Wave Baryons in the Quark Model. *Phys. Rev. D*, 18:4187.

Isgur and Karl, 1979a. Isgur, N. and Karl, G. (1979a). Ground State Baryons in a Quark Model with Hyperfine Interactions. *Phys. Rev. D*, 20:1191–1194.

Isgur and Karl, 1979b. Isgur, N. and Karl, G. (1979b). Positive Parity Excited Baryons in a Quark Model with Hyperfine Interactions. *Phys. Rev. D*, 19:2653. [Erratum: Phys.Rev.D 23, 817 (1981)].

Itakura and Maedan, 2000. Itakura, K. and Maedan, S. (2000). Dynamical chiral symmetry breaking on the light front. 2. The Nambu-Jona-Lasinio model. *Phys. Rev. D*, 62:105016.

Jaffe, 1977. Jaffe, R. L. (1977). Multi-Quark Hadrons. 1. The Phenomenology of (2 Quark 2 anti-Quark) Mesons. *Phys. Rev. D*, 15:267.

Jaffe and Wilczek, 2003. Jaffe, R. L. and Wilczek, F. (2003). Diquarks and exotic spectroscopy. *Phys. Rev. Lett.*, 91:232003.

Ji, 1995. Ji, X. (1995). *Phys. Rev. Lett.*, 74:1071.

Ji, 1997a. Ji, X. (1997a). Gauge-invariant decomposition of nucleon spin. *Phys. Rev. Lett.*, 78:610.

Ji, 2013. Ji, X. (2013). Parton Physics on a Euclidean Lattice. *Phys. Rev. Lett.*, 110:262002.

Ji, 2014. Ji, X. (2014). Parton Physics from Large-Momentum Effective Theory. *Sci. China Phys. Mech. Astron.*, 57:1407.

Ji, 2024. Ji, X. (2024). Euclidean Effective Theory for Partons in the Spirit of Steven Weinberg.

Ji et al., 2020a. Ji, X., Liu, Y., and Zahed, I. (2020a). Mass structure of hadrons and light-front sum rules in t' Hooft model.

Ji et al., 2021. Ji, X., Liu, Y.-S., Liu, Y., Zhang, J.-H., and Zhao, Y. (2021). Large-Momentum Effective Theory. *Rev. Mod. Phys.*, 93:035005.

Ji et al., 2004a. Ji, X., Ma, J.-P., and Yuan, F. (2004a). Classification and structure of generalized parton distributions. *Eur. Phys. J. C*, 33:75–90.

Ji et al., 2020b. Ji, X., Zhang, J.-H., and Zhao, Y. (2020b). Approaching Light-Front Dynamics from Euclidean Space. *Phys. Rev. Lett.*, 124:142001.

Ji, 1997b. Ji, X. D. (1997b). Gauge invariant decomposition of nucleon spin. *Phys. Rev. Lett.*, 78:610–613.

Ji, 2021. Ji, X.-D. (2021). Proton mass decomposition: naturalness and interpretation.

Ji et al., 2004b. Ji, X.-d., Ma, J.-P., and Yuan, F. (2004b). Classification and asymptotic scaling of hadrons' light cone wave function amplitudes. *Eur. Phys. J. C*, 33:75–90.

Jia and Vary, 2019. Jia, S. and Vary, J. P. (2019). Basis light front quantization for the charged light mesons with color singlet Nambu–Jona-Lasinio interactions. *Phys. Rev. C*, 99(3):035206.

Jiang et al., 2023. Jiang, X., Sun, W., Chen, F., Chen, Y., Gong, M., Liu, Z., and Zhang, R. (2023). η-glueball mixing from Nf=2 lattice QCD. *Phys. Rev. D*, 107(9):094510.

Jones et al., 2000. Jones, M. K. et al. (2000). G_{Ep}/G_{Mp} ratio by polarization transfer in $e\mathbf{p} \to e\mathbf{p}$. *Phys. Rev. Lett.*, 84:1398–1402.

Kacir et al., 1999. Kacir, M., Prakash, M., and Zahed, I. (1999). Hadrons and QCD instantons: A Bosonized view. *Acta Phys. Polon. B*, 30:287–348.

Karliner et al., 2017. Karliner, M., Nussinov, S., and Rosner, J. L. (2017). $QQ\bar{Q}\bar{Q}$ states: masses, production, and decays. *Phys. Rev. D*, 95(3):034011.

Karliner and Rosner, 2020. Karliner, M. and Rosner, J. L. (2020). First exotic hadron with open heavy flavor: $cs\bar{u}\bar{d}$ tetraquark. *Phys. Rev. D*, 102(9):094016.

Kawanai and Sasaki, 2015. Kawanai, T. and Sasaki, S. (2015). Potential description of charmonium and charmed-strange mesons from lattice QCD. *Phys. Rev. D*, 92(9):094503.

Keister and Polyzou, 1991. Keister, B. D. and Polyzou, W. N. (1991). Relativistic Hamiltonian dynamics in nuclear and particle physics. *Adv. Nucl. Phys.*, 20:225–479.

Kharzeev and Levin, 2017. Kharzeev, D. E. and Levin, E. M. (2017). Deep inelastic scattering as a probe of entanglement. *Phys. Rev. D*, 95(11):114008.

Khoze and Ringwald, 1991. Khoze, V. V. and Ringwald, A. (1991). Valley trajectories in gauge theories.

Kim et al., 2020. Kim, H., Kim, K. S., and Oka, M. (2020). Hexaquark picture for $d^*(2380)$. *Phys. Rev. D*, 102(7):074023.

Klinkhamer and Manton, 1984. Klinkhamer, F. R. and Manton, N. S. (1984). A Saddle Point Solution in the Weinberg-Salam Theory. *Phys. Rev. D*, 30:2212.

Kock et al., 2020. Kock, A. et al. (2020). Pion PDF from Instanton Vacuum via LaMET. *Phys. Rev. D*, 102:014017.

Kock and Zahed, 2021. Kock, A. and Zahed, I. (2021). Pion and kaon distribution amplitudes up to twist-3 in the QCD instanton vacuum. *Phys. Rev. D*, 104(11):116028.

Kokoski and Isgur, 1987. Kokoski, R. and Isgur, N. (1987). Meson Decays by Flux Tube Breaking. *Phys. Rev. D*, 35:907.

Koma and Koma, 2007. Koma, Y. and Koma, M. (2007). Spin-dependent potentials from lattice QCD. *Nucl. Phys. B*, 769:79–107.

Konychev and Nadolsky, 2006. Konychev, A. V. and Nadolsky, P. M. (2006). Universality of the Collins-Soper-Sterman nonperturbative function in gauge boson production. *Phys. Lett. B*, 633:710.

Korchemskaya and Korchemsky, 1992. Korchemskaya, I. A. and Korchemsky, G. P. (1992). On lightlike Wilson loops. *Phys. Lett. B*, 287:169–175.

Korchemsky and Radyushkin, 1992. Korchemsky, G. P. and Radyushkin, A. V. (1992). Infrared factorization, Wilson lines and the heavy quark limit. *Phys. Lett. B*, 279:359–366.

Kraan and van Baal, 1998a. Kraan, T. C. and van Baal, P. (1998a). Monopole constituents inside SU(n) calorons. *Phys. Lett. B*, 435:389–395.

Kraan and van Baal, 1998b. Kraan, T. C. and van Baal, P. (1998b). Periodic instantons with nontrivial holonomy. *Nucl. Phys. B*, 533:627–659.

Krutov et al., 2016. Krutov, A. F., Polezhaev, R. G., and Troitsky, V. E. (2016). The radius of the rho meson determined from its decay constant. *Phys. Rev. D*, 93(3):036007.

Kumano and Song, 2021. Kumano, S. and Song, Q.-T. (2021). Transverse-momentum-dependent parton distribution functions up to twist 4 for spin-1 hadrons. *Phys. Rev. D*, 103(1):014025.

Landry et al., 2003. Landry, F., Brock, R., Nadolsky, P. M., and Yuan, C.-P. (2003). Tevatron Run-1 Z boson data and Collins-Soper-Sterman resummation formalism. *Phys. Rev. D*, 67:073016.

Le Yaouanc et al., 1973. Le Yaouanc, A., Oliver, L., Pene, O., and Raynal, J. C. (1973). Naive quark pair creation model of strong interaction vertices. *Phys. Rev. D*, 8:2223–2234.

Lee and Lu, 1998. Lee, K.-M. and Lu, C.-h. (1998). SU(2) calorons and magnetic monopoles. *Phys. Rev. D*, 58:025011.

Leinweber, 1999. Leinweber, D. B. (1999). Visualizations of the QCD vacuum. In *Workshop on Light-Cone QCD and Nonperturbative Hadron Physics*, pages 138–143.

Lepage and Brodsky, 1979. Lepage, G. and Brodsky, S. J. (1979). Exclusive Processes in Quantum Chromodynamics: Evolution Equations for Hadronic Wave Functions and the Form-Factors of Mesons. *Phys. Lett. B*, 87:359–365.

Lepage and Brodsky, 1980. Lepage, G. P. and Brodsky, S. J. (1980). Exclusive Processes in Quantum Chromodynamics. *Phys. Rev. D*, 22:2157.

Li, 2015. Li, Y. e. a. (2015). Basis light-front quantization approach to positronium. *Phys. Rev. D*, 91:085008.

Li, 2016. Li, Y. e. a. (2016). Parton distribution functions from light-front wave functions. *Phys. Rev. D*, 94:094014.

Li, 2017. Li, Y. e. a. (2017). Heavy quarkonium in basis light-front quantization. *Phys. Rev. D*, 96:034014.

Lin et al., 2021. Lin, H.-W., Chen, J.-W., Fan, Z., Zhang, J.-H., and Zhang, R. (2021). Valence-Quark Distribution of the Kaon and Pion from Lattice QCD. *Phys. Rev. D*, 103(1):014516.

Lin, 2018. Lin, H.-W. e. a. (2018). Parton distributions and lattice QCD. *Prog. Part. Nucl. Phys.*, 100:107–160.

Liu et al., 2024a. Liu, W.-Y., Shuryak, E., Weiss, C., and Zahed, I. (2024a). Pion gravitational form factors in the QCD instanton vacuum. I. *Phys. Rev. D*, 110(5):054021.

Liu et al., 2023a. Liu, W.-Y., Shuryak, E., and Zahed, I. (2023a). Hadronic structure on the light-front VII: Pions and kaons and their partonic distributions. *Phys. Rev. D*, 107:094024.

Liu et al., 2024b. Liu, W.-Y., Shuryak, E., and Zahed, I. (2024b). Glue in hadrons at medium resolution and the qcd instanton vacuum. *Phys. Rev. D*, 110(5):054005.

Liu et al., 2024c. Liu, W.-Y., Shuryak, E., and Zahed, I. (2024c). Glue in hadrons at medium resolution and the QCD instanton vacuum. *Phys. Rev. D*, 110(5):054005.

Liu et al., 2024d. Liu, W.-Y., Shuryak, E., and Zahed, I. (2024d). Hadronic structure on the light front. VIII. Light scalar and vector mesons. *Phys. Rev. D*, 109(7):074029.

Liu et al., 2024e. Liu, W.-Y., Shuryak, E., and Zahed, I. (2024e). Light scalar and vector mesons on the light front from the QCD instanton vacuum.

Liu et al., 2024f. Liu, W.-Y., Shuryak, E., and Zahed, I. (2024f). Pion gravitational form factors in the QCD instanton vacuum. II. *Phys. Rev. D*, 110(5):054022.

Liu et al., 2025. Liu, W.-Y., Shuryak, E., and Zahed, I. (2025). The color force acting on a quark in the pion and nucleon.

Liu and Zahed, 2022. Liu, W.-Y. and Zahed, I. (2022). Pion gravitational form factor at twist-2 in the quark model. *Phys. Rev. D*, 105:014017.

Liu and Zahed, 2025. Liu, W.-Y. and Zahed, I. (2025). Tomography of pions and kaons in the QCD vacuum: Transverse momentum dependent parton distribution functions. *Phys. Rev. D*, 112(3):034039.

Liu et al., 2024g. Liu, W.-Y., Zahed, I., and Zhao, Y. (2024g). Collins-Soper Kernel in the QCD Instanton Vacuum.

Liu et al., 2023b. Liu, Y., Shuryak, E., and Zahed, I. (2023b). Chiral Symmetry Breaking on the Light Front. *Phys. Rev. D*.

Liu and Zahed, 2021. Liu, Y. and Zahed, I. (2021). Small size instanton contributions to the quark quasi-PDF and matching kernel.

Loring et al., 2001. Loring, U., Metsch, B. C., and Petry, H. R. (2001). The Light baryon spectrum in a relativistic quark model with instanton induced quark forces: The Strange baryon spectrum. *Eur. Phys. J. A*, 10:447–486.

Luscher, 1981. Luscher, M. (1981). Symmetry Breaking Aspects of the Roughening Transition in Gauge Theories. *Nucl. Phys. B*, 180:317–329.

Luscher and Palombi, 2010. Luscher, M. and Palombi, F. (2010). Universality of the topological susceptibility in the SU(3) gauge theory. *JHEP*, 09:110.

Luscher and Weisz, 2011. Luscher, M. and Weisz, P. (2011). Perturbative analysis of the gradient flow in non-abelian gauge theories. *JHEP*, 02:051.

Maris and Roberts, 2003. Maris, P. and Roberts, C. D. (2003). Dyson-Schwinger equations: A Tool for hadron physics. *Int. J. Mod. Phys. E*, 12:297–365.

Melosh, 1974. Melosh, H. J. (1974). Quarks and nuclear forces. *Phys. Rev. D*, 9:1095–1101.

Meng et al., 2025. Meng, Y., Liu, C., Tuo, X.-Y., Yan, H., and Zhang, Z. (2025). Lattice calculation of the $\eta_c\eta_c$ and $J/\psi J/\psi$ s-wave scattering length. *Eur. Phys. J. C*, 85(4):458.

Mereghetti et al., 2022. Mereghetti, E., Monahan, C. J., Rizik, M. D., Shindler, A., and Stoffer, P. (2022). One-loop matching for quark dipole operators in a gradient-flow scheme. *JHEP*, 04:050. [Erratum: JHEP 03, 101 (2025)].

Meyer, 2004. Meyer, H. B. (2004). Glueball regge trajectories. Other thesis.

Miesch and Shuryak, 2024. Miesch, N. and Shuryak, E. (2024). Wave functions of multiquark hadrons from representations of the symmetry groups S_n.

Miesch et al., 2023a. Miesch, N., Shuryak, E., and Zahed, I. (2023a). Hadronic structure on the light-front. IX. Orbital-spin-isospin wave functions of baryons. *Phys. Rev. D*, 108(9):094033.

Miesch et al., 2023b. Miesch, N., Shuryak, E., and Zahed, I. (2023b). Hadronic structure on the light-front VIII. Orbital-spin-isospin wave functions of baryons.

Miesch et al., 2024. Miesch, N., Shuryak, E., and Zahed, I. (2024). Baryons and tetraquarks using instanton-induced interactions. *Phys. Rev. D*, 109(1):014022.

Miesch et al., 2025a. Miesch, N., Shuryak, E., and Zahed, I. (2025a). Bridging hadronic and vacuum structure by heavy quarkonia. *Phys. Rev. D*, 111(3):034006.

Miesch et al., 2025b. Miesch, N., Shuryak, E., and Zahed, I. (2025b). D-shell mixing in light baryons and its effect on the orbital motion.

Miesch et al., 2025c. Miesch, N., Shuryak, E., and Zahed, I. (2025c). Pentaquarks made of light quarks and their admixture to baryons.

Mitev and Pomoni, 2016. Mitev, V. and Pomoni, E. (2016). Exact Bremsstrahlung and Effective Couplings. *JHEP*, 06:078.

Moos et al., 2024. Moos, V., Scimemi, I., Vladimirov, A., and Zurita, P. (2024). Extraction of unpolarized transverse momentum distributions from the fit of Drell-Yan data at N^{4}LL. *JHEP*, 05:036.

Morningstar, 2025. Morningstar, C. (2025). Update on Glueballs.

Morningstar and Peardon, 1999. Morningstar, C. J. and Peardon, M. J. (1999). The glueball spectrum from an anisotropic lattice study. *Phys. Rev. D*, 60:034509.

Mosallem and Uzhinskii, 2002. Mosallem, A. M. and Uzhinskii, V. V. (2002). Manifestation of twelve quark bag state of He-4 nucleus in elastic d He-4 scattering.

Musakhanov and Yakhshiev, 2021. Musakhanov, M. and Yakhshiev, U. (2021). Gluons, Light and Heavy Quarks in the Instanton Vacuum. In *9th International Conference on New Frontiers in Physics*.

Musakhanov and Egamberdiev, 2018. Musakhanov, M. M. and Egamberdiev, O. (2018). Dynamical gluon mass in the instanton vacuum. *Phys. Lett. B*, 781:303–309.

Naito et al., 2004. Naito, K., Maedan, S., and Itakura, K. (2004). Light mesons on the light front. *Phys. Rev. D*, 70:096008.

Nakano et al., 2003. Nakano, T. et al. (2003). Evidence for a narrow S = +1 baryon resonance in photoproduction from the neutron. *Phys. Rev. Lett.*, 91:012002.

Nambu and Jona-Lasinio, 1961a. Nambu, Y. and Jona-Lasinio, G. (1961a). Dynamical Model of Elementary Particles Based on an Analogy with Superconductivity. I. *Phys. Rev.*, 122:345–358.

Nambu and Jona-Lasinio, 1961b. Nambu, Y. and Jona-Lasinio, G. (1961b). Dynamical Model of Elementary Particles Based on an Analogy with Superconductivity. II. *Phys. Rev.*, 124:246–254.

Novikov et al., 1981a. Novikov, V., Shifman, M., Vainshtein, A., and Zakharov, V. (1981a). Are All Hadrons Alike? *Nucl. Phys. B*, 191:301.

Novikov et al., 1981b. Novikov, V., Shifman, M. A., Vainshtein, A., and Zakharov, V. I. (1981b). Are All Hadrons Alike? DESY-check = Moscow Inst. Theor. Exp. Phys. Gkae - Itef-81-048 (81,rec.jun.) 32 *P* and Nucl. Phys. B191 (1981) 301-369 and Moscow Inst. Theor. Exp. Phys. Gkae - Itef-81-042 (81,rec.apr.) 70 *P*. (104907). *Nucl. Phys. B*, 191:301–369.

Nowak et al., 1991. Nowak, M. A., Rho, M., and Zahed, I. (1991). Spin factors and geometric phases in arbitrary dimensions. *Phys. Lett. B*, 254:94–102.

Nowak et al., 1993. Nowak, M. A., Rho, M., and Zahed, I. (1993). Chiral effective action with heavy quark symmetry. *Phys. Rev. D*, 48:4370–4374.

Nowak et al., 1996. Nowak, M. A., Rho, M., and Zahed, I. (1996). *Chiral Nuclear Dynamics*. World Scientific.

Nowak et al., 2004. Nowak, M. A., Rho, M., and Zahed, I. (2004). Chiral doubling of heavy light hadrons: BABAR 2317-MeV/c**2 and CLEO 2463-MeV/c**2 discoveries. *Acta Phys. Polon. B*, 35:2377–2392.

Nowak et al., 1989. Nowak, M. A., Verbaarschot, J. J. M., and Zahed, I. (1989). Flavor Mixing in the Instanton Vacuum. *Nucl. Phys. B*, 324:1–33.

Ostrovsky et al., 2002. Ostrovsky, D. M., Carter, G. W., and Shuryak, E. V. (2002). Forced tunneling and turning state explosion in pure Yang-Mills theory. *Phys. Rev. D*, 66:036004.

Owen et al., 2015. Owen, B., Kamleh, W., Leinweber, D., Menadue, B., and Mahbub, S. (2015). Light Meson Form Factors at near Physical Masses. *Phys. Rev. D*, 91(7):074503.

Pagels and Tomboulis, 1978. Pagels, H. and Tomboulis, E. (1978). Vacuum of the Quantum Yang-Mills Theory and Magnetostatics. *Nucl. Phys. B*, 143:485–502.

Pauli and Brodsky, 1985. Pauli, H.-C. and Brodsky, S. J. (1985). Discretized Light-Cone Quantization. *Phys. Rev. D*, 32:1993–2000.

Perry and Wilson, 1993. Perry, R. J. and Wilson, K. G. (1993). Light front Tamm-Dancoff field theory. *Nucl. Phys. B*, 403:587–639.

Petrov and Pobylitsa, 1997. Petrov, V. and Pobylitsa, P. (1997). Pion wave function from the instanton vacuum model.

Petrov et al., 1999. Petrov, V., Polyakov, M. V., Ruskov, R., Weiss, C., and Goeke, K. (1999). Pion and photon light cone wave functions from the instanton vacuum. *Phys. Rev. D*, 59:114018.

Pineda and Vairo, 2001. Pineda, A. and Vairo, A. (2001). The QCD potential at O $(1 / m^2)$: Complete spin dependent and spin independent result. *Phys. Rev. D*, 63:054007. [Erratum: Phys.Rev.D 64, 039902 (2001)].

Pisarski and Stack, 1987. Pisarski, R. D. and Stack, J. D. (1987). Spin Dependent Potential for Heavy Fermions on the Ends of a String. *Nucl. Phys. B*, 286:657–668.

Politzer, 1973. Politzer, H. D. (1973). Reliable Perturbative Results for Strong Interactions? *Phys. Rev. Lett.*, 30:1346–1349.

Polyakov, 1987. Polyakov, A. (1987). Gauge Fields and Strings. *Harwood Academic Publishers*.

Polyakov, 1974. Polyakov, A. M. (1974). Particle Spectrum in Quantum Field Theory. *JETP Lett.*, 20:194–195.

Polyakov, 1988. Polyakov, A. M. (1988). Fermi-Bose Transmutations Induced by Gauge Fields. *Mod. Phys. Lett. A*, 3:325.

Polyakov and Schweitzer, 2018a. Polyakov, M. V. and Schweitzer, P. (2018a). Forces inside hadrons: pressure, surface tension, mechanical radius and all that. *Int. J. Mod. Phys. A*, 33(26):1830025.

Polyakov and Schweitzer, 2018b. Polyakov, M. V. and Schweitzer, P. (2018b). Forces inside hadrons: pressure, surface tension, mechanical radius, and all that. *Int. J. Mod. Phys. A*, 33:1830025.

Praszalowicz, 2024. Praszalowicz, M. (2024). Odyssey of the elusive Θ^+.

Puckett et al., 2012. Puckett, A. J. R. et al. (2012). Final Analysis of Proton Form Factor Ratio Data at $\mathbf{Q^2 = 4.0}$, 4.8 and 5.6 GeV$\mathbf{^2}$. *Phys. Rev. C*, 85:045203.

Qattan and Arrington, 2012. Qattan, I. A. and Arrington, J. (2012). Flavor decomposition of the nucleon electromagnetic form factors. *Phys. Rev. C*, 86:065210.

Radyushkin, 1977. Radyushkin, A. (1977). Deep Elastic Processes of Composite Particles in Field Theory and Asymptotic Freedom.

Radyushkin, 1997. Radyushkin, A. V. (1997). Nonforward parton distributions. *Phys. Rev. D*, 56:5524–5557.

Radyushkin, 2017. Radyushkin, A. V. (2017). Quasi-PDFs and pseudo-PDFs. *Phys. Rev. D*, 96:034025.

Ramamurti et al., 2018. Ramamurti, A., Shuryak, E., and Zahed, I. (2018). Are there monopoles in the quark-gluon plasma? *Phys. Rev. D*, 97(11):114028.

Rapp et al., 1998. Rapp, R., Schäfer, T., Shuryak, E. V., and Velkovsky, M. (1998). Diquark Bose condensates in high density matter and instantons. *Phys. Rev. Lett.*, 81:53–56.

Rapp et al., 2000. Rapp, R., Schäfer, T., Shuryak, E. V., and Velkovsky, M. (2000). High density QCD and instantons. *Annals Phys.*, 280:35–99.

Raya et al., 2024. Raya, K., Bashir, A., Binosi, D., Roberts, C. D., and Rodríguez-Quintero, J. (2024). Pseudoscalar Mesons and Emergent Mass. *Few Body Syst.*, 65(2):60.

Roberts and Williams, 1994. Roberts, C. D. and Williams, A. G. (1994). Dyson-Schwinger equations and their application to hadronic physics. *Prog. Part. Nucl. Phys.*, 33:477–575.

Rogers, 2016. Rogers, T. C. (2016). An overview of transverse-momentum–dependent factorization and evolution. *Eur. Phys. J. A*, 52(6):153.

Ruiz Arriola and Broniowski, 2002. Ruiz Arriola, E. and Broniowski, W. (2002). Pion light cone wave function and pion distribution amplitude in the Nambu-Jona-Lasinio model. *Phys. Rev. D*, 66:094016.

Sakurai, 1969. Sakurai, J. J. (1969). Vector meson dominance and high-energy electron proton inelastic scattering. *Phys. Rev. Lett.*, 22:981–984.

Santopinto and Bijker, 2007. Santopinto, E. and Bijker, R. (2007). Unquenching the quark model. In *11th Conference on Problems in Theoretical Nuclear Physics*, pages 323–330.

Schafer, 1994. Schafer, T. (1994). Instanton–anti-instanton molecules in QCD. *Phys. Rev. D*, 50:3377.

Schäfer and Shuryak, 1995. Schäfer, T. and Shuryak, E. V. (1995). Glueballs and instantons. *Phys. Rev. Lett.*, 75:1707–1710.

Schäfer and Shuryak, 2001. Schäfer, T. and Shuryak, E. V. (2001). Phases of QCD at high baryon density. *Lect. Notes Phys.*, 578:203–217.

Schäfer and Shuryak, 1998. Schäfer, T. and Shuryak, E. (1998). Instantons in QCD. *Rev. Mod. Phys.*, 70:323.

Scimemi and Vladimirov, 2018. Scimemi, I. and Vladimirov, A. (2018). TMD factorization at NNLO. *JHEP*, 03.

Scimemi and Vladimirov, 2020. Scimemi, I. and Vladimirov, A. (2020). Non-perturbative structure of semi-inclusive deep-inelastic and Drell-Yan scattering at small transverse momentum. *JHEP*, 06:137.

Shanahan et al., 2021. Shanahan, P., Wagman, M., and Zhao, Y. (2021). Lattice QCD calculation of the Collins-Soper kernel from quasi-TMDPDFs. *Phys. Rev. D*, 104(11):114502.

Shanahan et al., 2020. Shanahan, P. E., Wagman, M. L., and Zhao, Y. (2020). Lattice Quasi-TMDs. *Phys. Rev. D*, 102:014511.

Shi et al., 2015a. Shi, C., Chen, C., Chang, L., Roberts, C. D., Schmidt, S. M., and Zong, H.-S. (2015a). Kaon and pion parton distribution amplitudes to twist-three. *Phys. Rev. D*, 92:014035.

Shi et al., 2015b. Shi, C. et al. (2015b). Pion distribution amplitude from Dyson-Schwinger equations. *Phys. Rev. D*, 92:014035.

Shifman, 1989. Shifman, M. A. (1989). Anomalies and Low-Energy Theorems of Quantum Chromodynamics. *Sov. Phys. Usp.*, 32:289–309.

Shifman et al., 1979. Shifman, M. A., Vainshtein, A. I., and Zakharov, V. I. (1979). QCD and Resonance Physics. Theoretical Foundations. *Nucl. Phys. B*, 147:385–447.

Shifman et al., 1980. Shifman, M. A., Vainshtein, A. I., and Zakharov, V. I. (1980). Instanton Density in a Theory with Massless Quarks. *Nucl. Phys. B*, 165:45–54.

Shultz et al., 2015. Shultz, C. J., Dudek, J. J., and Edwards, R. G. (2015). Excited meson radiative transitions from lattice QCD using variationally optimized operators. *Phys. Rev. D*, 91(11):114501.

Shuryak, 1982a. Shuryak, E. (1982a). The Role of Instantons in Quantum Chromodynamics. 1. Physical Vacuum. *Nucl. Phys. B*, 203:93–135.

Shuryak, 2019. Shuryak, E. (2019). Light-front wave functions of mesons, baryons, and pentaquarks with topology-induced local four-quark interaction. *Phys. Rev. D*, 100(11):114018.

Shuryak, 2020. Shuryak, E. (2020). Lectures on nonperturbative qcd (nonperturbative topological phenomena in qcd and related theories).

Shuryak and Torres-Rincon, 2020. Shuryak, E. and Torres-Rincon, J. M. (2020). Baryon preclustering at the freeze-out of heavy-ion collisions and light-nuclei production. *Phys. Rev. C*, 101(3):034914.

Shuryak and Zahed, 2004a. Shuryak, E. and Zahed, I. (2004a). A Schematic model for pentaquarks using diquarks. *Phys. Lett. B*, 589:21–27.

Shuryak and Zahed, 2021a. Shuryak, E. and Zahed, I. (2021a). Emergent qcd phenomena in high-energy hadronic collisions. *Phys. Rev. D*, 103:054028.

Shuryak and Zahed, 2021b. Shuryak, E. and Zahed, I. (2021b). Hadronic structure on the light-front IV. Mesons in the instanton vacuum.

Shuryak and Zahed, 2021c. Shuryak, E. and Zahed, I. (2021c). Hadronic structure on the light-front V. Baryons in the instanton vacuum.

Shuryak and Zahed, 2021d. Shuryak, E. and Zahed, I. (2021d). How to observe the QCD instanton/sphaleron processes at hadron colliders?

Shuryak and Zahed, 2021e. Shuryak, E. and Zahed, I. (2021e). Light-front holography, instantons, and the glueball spectrum. *Phys. Rev. D*, 104:114030.

Shuryak and Zahed, 2021f. Shuryak, E. and Zahed, I. (2021f). Meson structure on the light-front III : The Hamiltonian, heavy quarkonia, spin and orbit mixing.

Shuryak and Zahed, 2021g. Shuryak, E. and Zahed, I. (2021g). Nonperturbative quark-antiquark interactions in mesonic form factors. *Phys. Rev. D*, 103(5):054028.

Shuryak and Zahed, 2021h. Shuryak, E. and Zahed, I. (2021h). Nonperturbative quark-antiquark interactions in mesonic form factors. *Phys. Rev. D*, 103:054028.

Shuryak and Zahed, 2022a. Shuryak, E. and Zahed, I. (2022a). Hadronic structure on the light front VII: Nucleon GPDs.

Shuryak and Zahed, 2022b. Shuryak, E. and Zahed, I. (2022b). Hadronic structure on the light front VIII: Delta GPDs.

Shuryak and Zahed, 2023a. Shuryak, E. and Zahed, I. (2023a). Hadronic structure on the light front. III. The Hamiltonian, heavy quarkonia, spin, and orbit mixing. *Phys. Rev. D*, 107(3):034025.

Shuryak and Zahed, 2023b. Shuryak, E. and Zahed, I. (2023b). Hadronic structure on the light front. V. Diquarks, nucleons, and multiquark Fock components. *Phys. Rev. D*, 107(3):034027.

Shuryak, 1982b. Shuryak, E. V. (1982b). Hadrons Containing a Heavy Quark and QCD Sum Rules. *Nucl. Phys. B*, 198:83–101.

Shuryak, 1982c. Shuryak, E. V. (1982c). The role of instantons in quantum chromodynamics. i. physical vacuum. *Nucl. Phys. B*, 203:93–112.

Shuryak, 1982d. Shuryak, E. V. (1982d). The Role of Instantons in Quantum Chromodynamics. *Nucl. Phys. B*, 203:93–135.

Shuryak, 1982e. Shuryak, E. V. (1982e). The Role of Instantons in Quantum Chromodynamics. 1. Physical Vacuum. *Nucl. Phys. B*, 203:93.

Shuryak, 1982f. Shuryak, E. V. (1982f). The Role of Instantons in Quantum Chromodynamics. 1. Physical Vacuum. *Nucl. Phys. B*, 203:93.

Shuryak, 1982g. Shuryak, E. V. (1982g). The Role of Instantons in Quantum Chromodynamics. 3. Quark - Gluon Plasma. *Nucl. Phys. B*, 203:140–156.

Shuryak, 1988. Shuryak, E. V. (1988). Toward the Quantitative Theory of the 'Instanton Liquid' 4. Tunneling in the Double Well Potential. *Nucl. Phys. B*, 302:621–644.

Shuryak, 1989. Shuryak, E. V. (1989). Instantons in QCD. *Nucl. Phys. B*, 328:85–110.

Shuryak, 1993. Shuryak, E. V. (1993). Correlation functions in the QCD vacuum. *Rev. Mod. Phys.*, 65:1–46.

Shuryak, 1999. Shuryak, E. V. (1999). Probing the boundary of the nonperturbative QCD by small size instantons.

Shuryak and Vainshtein, 1982a. Shuryak, E. V. and Vainshtein, A. (1982a). Theory of Power Corrections to Deep Inelastic Scattering in Quantum Chromodynamics. 1. Q**2 Effects. *Nucl. Phys. B*, 199:451–481.

Shuryak and Vainshtein, 1982b. Shuryak, E. V. and Vainshtein, A. (1982b). Theory of Power Corrections to Deep Inelastic Scattering in Quantum Chromodynamics. 2. Q**4 Effects: Polarized Target. *Nucl. Phys. B*, 201:141.

Shuryak and Verbaarschot, 1992. Shuryak, E. V. and Verbaarschot, J. J. M. (1992). On baryon number violation and nonperturbative weak processes at SSC energies. *Phys. Rev. Lett.*, 68:2576–2579.

Shuryak and Verbaarschot, 1993a. Shuryak, E. V. and Verbaarschot, J. J. M. (1993a). Quark propagation in the random instanton vacuum. *Nucl. Phys. B*, 410:37–54.

Shuryak and Verbaarschot, 1993b. Shuryak, E. V. and Verbaarschot, J. J. M. (1993b). Random matrix theory and spectral sum rules for the Dirac operator in QCD. *Nucl. Phys. A*, 560:306–320.

Shuryak and Zahed, 2000. Shuryak, E. V. and Zahed, I. (2000). Instanton induced effects in QCD high-energy scattering. *Phys. Rev. D*, 62:085014.

Shuryak and Zahed, 2004b. Shuryak, E. V. and Zahed, I. (2004b). Understanding the nonperturbative deep inelastic scattering: Instanton induced inelastic dipole dipole cross-section. *Phys. Rev. D*, 69:014011.

Shuryak and Zhirov, 1984. Shuryak, E. V. and Zhirov, O. V. (1984). TESTING MONTE CARLO METHODS FOR PATH INTEGRALS IN SOME QUANTUM MECHANICAL PROBLEMS. *Nucl. Phys. B*, 242:393–406.

Simonov, 1996. Simonov, Y. A. (1996). Confinement. *Phys. Usp.*, 39:313–336.

Simonov, 2021. Simonov, Y. A. (2021). Proton and neutron form factors with quark orbital excitations. *Eur. Phys. J. A*, 57(7):228.

Sonnenschein and Weissman, 2014. Sonnenschein, J. and Weissman, D. (2014). Rotating strings confronting PDG mesons. *JHEP*, 08:013.

Sonnenschein and Weissman, 2015. Sonnenschein, J. and Weissman, D. (2015). A rotating string model versus baryon spectra. *JHEP*, 02:147.

Stefanis and Pimikov, 2016. Stefanis, N. G. and Pimikov, A. V. (2016). Chimera distribution amplitudes for the pion and the longitudinally polarized ρ-meson. *Nucl. Phys. A*, 945:248–268.

Strominger, 1981. Strominger, A. (1981). Loop Space Solution of Two-dimensional QCD. *Phys. Lett. B*, 101:271–276.

Sufian et al., 2020. Sufian, R. S. et al. (2020). Pion valence PDF from Lattice QCD. *Phys. Rev. D*, 102:054508.

't Hooft, 1974. 't Hooft, G. (1974). Magnetic Monopoles in Unified Gauge Theories. *Nucl. Phys. B*, 79:276–284.

't Hooft, 1976a. 't Hooft, G. (1976a). *Phys. Rev.*, D14:3432.

't Hooft, 1976b. 't Hooft, G. (1976b). Symmetry breaking through Bell-Jackiw anomalies. *Phys. Rev. Lett.*, 37:8–11.

't Hooft, 1978. 't Hooft, G. (1978). On the Phase Transition Towards Permanent Quark Confinement. *Nucl. Phys. B*, 138:1–25.

Tanabashi et al., 2018. Tanabashi, M. et al. (2018). Review of Particle Physics. *Phys. Rev. D*, 98(3):030001.

Thomas, 2008. Thomas, A. W. (2008). Interplay of Spin and Orbital Angular Momentum in the Proton. *Phys. Rev. Lett.*, 101:102003.

Tong et al., 2021. Tong, X.-B., Ma, J.-P., and Yuan, F. (2021). Gluon gravitational form factors at large momentum transfer. *Phys. Lett. B*, 823:136751.

Tong et al., 2022. Tong, X.-B., Ma, J.-P., and Yuan, F. (2022). Perturbative calculations of gravitational form factors at large momentum transfer. *JHEP*, 10:046.

Vainshtein et al., 1982. Vainshtein, A. I., Zakharov, V. I., Novikov, V. A., and Shifman, M. A. (1982). ABC's of Instantons. *Sov. Phys. Usp.*, 25:195.

Vary, 2010. Vary, J. P. e. a. (2010). Hamiltonian light-front field theory in a basis function approach. *Phys. Rev. C*, 81:035205.

Veneziano, 1979. Veneziano, G. (1979). U(1) Without Instantons. *Nucl. Phys. B*, 159:213–224.

Verbaarschot, 1991. Verbaarschot, J. J. M. (1991). Streamlines and conformal invariance in Yang-Mills theories. *Nucl. Phys. B*, 362:33–53. [Erratum: Nucl.Phys.B 386, 236–236 (1992)].

Verbaarschot and Zahed, 1993. Verbaarschot, J. J. M. and Zahed, I. (1993). Spectral density of the QCD Dirac operator near zero virtuality. *Phys. Rev. Lett.*, 70:3852–3855.

Vladimirov, 2018. Vladimirov, A. (2018). Structure of rapidity divergences in multi-parton scattering soft factors. *JHEP*, 04:045.

Vladimirov and Stefanis, 2014. Vladimirov, A. A. and Stefanis, N. G. (2014). Key features of the TMD soft-factor structure. *Few Body Syst.*, 55:297–302.

Wang et al., 2024. Wang, B., He, F., Wang, G., Draper, T., Liang, J., Liu, K.-F., and Yang, Y.-B. (2024). Trace anomaly form factors from lattice QCD.

Wang et al., 2022. Wang, G., Yang, Y.-B., Liang, J., Draper, T., and Liu, K.-F. (2022). Proton momentum and angular momentum decompositions with overlap fermions. *Phys. Rev. D*, 106(1):014512.

Weinberg, 1966. Weinberg, S. (1966). Dynamics at infinite momentum. *Phys. Rev.*, 150:1313–1318.

Wiecki, 2015. Wiecki, P. e. a. (2015). Basis light-front quantization approach to light mesons. *Phys. Rev. D*, 91:105009.

Wilson, 1969. Wilson, K. G. (1969). Non-Lagrangian models of current algebra. *Phys. Rev.*, 179:1499–1512.

Witten, 1979. Witten, E. (1979). Current Algebra Theorems for the U(1) Goldstone Boson. *Nucl. Phys. B*, 156:269–283.

Witten, 2010. Witten, E. (2010). A New Look At The Path Integral Of Quantum Mechanics.

Wohler and Shuryak, 1994. Wohler, C. F. and Shuryak, E. V. (1994). Two loop correction to the instanton density for the double well potential. *Phys. Lett. B*, 333:467–470.

Xu et al., 2024. Xu, Y.-Z., Ding, M., Raya, K., Roberts, C. D., Rodríguez-Quintero, J., and Schmidt, S. M. (2024). Pion and kaon electromagnetic and gravitational form factors. *Eur. Phys. J. C*, 84(2):191.

Yakhshiev et al., 2017. Yakhshiev, U. T., Kim, H.-C., Musakhanov, M. M., Hiyama, E., and Turimov, B. (2017). Instanton effects on the heavy-quark static potential. *Chin. Phys. C*, 41(8):083102.

Yang et al., 2018. Yang, Y.-B., Liang, J., Bi, Y.-J., Chen, Y., Draper, T., Liu, K.-F., and Liu, Z. (2018). Proton Mass Decomposition from the QCD Energy Momentum Tensor. *Phys. Rev. Lett.*, 121(21):212001.

Yung, 1988. Yung, A. V. (1988). Instanton Vacuum in Supersymmetric QCD. *Nucl. Phys. B*, 297:47.

Zahed, 2021. Zahed, I. (2021). Mass sum rule of hadrons in the QCD instanton vacuum. *Phys. Rev. D*, 104(5):054031.

Zahed, 2022. Zahed, I. (2022). Spin Sum Rule of the Nucleon in the QCD Instanton Vacuum. *Symmetry*, 14(5):932.

Zelevinsky, 1996. Zelevinsky, V. (1996). Quantum chaos and complexity in nuclei. *Ann. Rev. Nucl. Part. Sci.*, 46:237–279.

Zhang et al., 2020. Zhang, J. et al. (2020). Reconstruction of pion DA using lattice moments. *Phys. Rev. D*, 102:094519.

Zhao, 2013. Zhao, X. e. a. (2013). Time-dependent basis light-front quantization. *Phys. Rev. D*, 88:085030.

Zhao, 2014. Zhao, X. e. a. (2014). Light-front holographic quarkonium. *Phys. Rev. D*, 90:094012.

Zhao, 2024. Zhao, Y. (2024). Transverse Momentum Distributions from Lattice QCD without Wilson Lines. *Phys. Rev. Lett.*, 133(24):241904.

't Hooft, 1976. 't Hooft, G. (1976). Symmetry Breaking Through Bell-Jackiw Anomalies. *Phys. Rev. Lett.*, 37:8–11.